

Methods in biomechanics, volume II

Edited by

Zhen Luo, Peter Quesada and Kerry Danelson

Published in

Frontiers in Bioengineering and Biotechnology



FRONTIERS EBOOK COPYRIGHT STATEMENT

The copyright in the text of individual articles in this ebook is the property of their respective authors or their respective institutions or funders. The copyright in graphics and images within each article may be subject to copyright of other parties. In both cases this is subject to a license granted to Frontiers.

The compilation of articles constituting this ebook is the property of Frontiers.

Each article within this ebook, and the ebook itself, are published under the most recent version of the Creative Commons CC-BY licence. The version current at the date of publication of this ebook is CC-BY 4.0. If the CC-BY licence is updated, the licence granted by Frontiers is automatically updated to the new version.

When exercising any right under the CC-BY licence, Frontiers must be attributed as the original publisher of the article or ebook, as applicable.

Authors have the responsibility of ensuring that any graphics or other materials which are the property of others may be included in the CC-BY licence, but this should be checked before relying on the CC-BY licence to reproduce those materials. Any copyright notices relating to those materials must be complied with.

Copyright and source acknowledgement notices may not be removed and must be displayed in any copy, derivative work or partial copy which includes the elements in question.

All copyright, and all rights therein, are protected by national and international copyright laws. The above represents a summary only. For further information please read Frontiers' Conditions for Website Use and Copyright Statement, and the applicable CC-BY licence.

ISSN 1664-8714
ISBN 978-2-8325-6474-5
DOI 10.3389/978-2-8325-6474-5

About Frontiers

Frontiers is more than just an open access publisher of scholarly articles: it is a pioneering approach to the world of academia, radically improving the way scholarly research is managed. The grand vision of Frontiers is a world where all people have an equal opportunity to seek, share and generate knowledge. Frontiers provides immediate and permanent online open access to all its publications, but this alone is not enough to realize our grand goals.

Frontiers journal series

The Frontiers journal series is a multi-tier and interdisciplinary set of open-access, online journals, promising a paradigm shift from the current review, selection and dissemination processes in academic publishing. All Frontiers journals are driven by researchers for researchers; therefore, they constitute a service to the scholarly community. At the same time, the *Frontiers journal series* operates on a revolutionary invention, the tiered publishing system, initially addressing specific communities of scholars, and gradually climbing up to broader public understanding, thus serving the interests of the lay society, too.

Dedication to quality

Each Frontiers article is a landmark of the highest quality, thanks to genuinely collaborative interactions between authors and review editors, who include some of the world's best academicians. Research must be certified by peers before entering a stream of knowledge that may eventually reach the public - and shape society; therefore, Frontiers only applies the most rigorous and unbiased reviews. Frontiers revolutionizes research publishing by freely delivering the most outstanding research, evaluated with no bias from both the academic and social point of view. By applying the most advanced information technologies, Frontiers is catapulting scholarly publishing into a new generation.

What are Frontiers Research Topics?

Frontiers Research Topics are very popular trademarks of the *Frontiers journals series*: they are collections of at least ten articles, all centered on a particular subject. With their unique mix of varied contributions from Original Research to Review Articles, Frontiers Research Topics unify the most influential researchers, the latest key findings and historical advances in a hot research area.

Find out more on how to host your own Frontiers Research Topic or contribute to one as an author by contacting the Frontiers editorial office: frontiersin.org/about/contact

Methods in biomechanics, volume II

Topic editors

Zhen Luo — University of Technology Sydney, Australia

Peter Quesada — University of Louisville, United States

Kerry Danelson — Wake Forest University, United States

Citation

Luo, Z., Quesada, P., Danelson, K., eds. (2025). *Methods in biomechanics, volume II*.
Lausanne: Frontiers Media SA. doi: 10.3389/978-2-8325-6474-5

Table of contents

- 05 **Identifying special operative trainees at-risk for musculoskeletal injury using full body kinematics**
Lance Frazer, Tylan Templin, Travis David Eliason, Cody Butler, Ben Hando and Daniel Nicolella
- 14 **Computational study of the balloon dilation steps on transcatheter aortic valve replacement**
Jianming Li, Zhuangyuan Meng, Wentao Yan, Wenshuo Wang, Lai Wei and Shengzhang Wang
- 23 **Enhancing biomechanical machine learning with limited data: generating realistic synthetic posture data using generative artificial intelligence**
Carlo Dindorf, Jonas Dully, Jürgen Konradi, Claudia Wolf, Stephan Becker, Steven Simon, Janine Huthwelker, Frederike Werthmann, Johanna Kniepert, Philipp Drees, Ulrich Betz and Michael Fröhlich
- 36 **Successive tendon injury in an *in vivo* rat overload model induces early damage and acute healing responses**
Pooja H. Chainani, Maria Buzo Mena, Diana Yeritsyan, Daniela Caro, Kaveh Momenzadeh, Jenna L. Galloway, Joseph P. DeAngelis, Arun J. Ramappa and Ara Nazarian
- 48 **Design of a simplified cranial substitute with a modal behavior close to that of a human skull**
Natacha Elster, Johanna Boutillier, Nicolas Bourdet, Pascal Magnan, Pierre Naz, Rémy Willinger and Caroline Deck
- 61 **Unveiling interactions between intervertebral disc morphologies and mechanical behavior through personalized finite element modeling**
Estefano Muñoz-Moya, Morteza Rasouligandomani, Carlos Ruiz Wills, Francis Kiptengwer Chemorion, Gemma Piella and Jérôme Noailly
- 88 **Comparison of ground reaction forces as running speed increases between male and female runners**
Xinyan Jiang, István Bíró, József Sárosi, Yufei Fang and Yaodong Gu
- 98 **Investigation of dynamic responses of skin simulant against fragment impact through experiments and concurrent computational modeling**
Punit Kumar Pandey and S. G. Ganpule
- 117 **A wireless buckle transducer for measurement of human forearm tendon tension: operational principles and finite element study**
Alireza Rastegarpanah and Stephen J. G. Taylor
- 129 ***FiberO* for an automated quantitative analysis of fibers orientation and organization in biological fibrous tissues**
Asier Muñoz, Anxhela Docaj, Julen Fernandez and Alessandra Carriero

- 140 **Experimental investigation on the reverse mechano-electrical effect of porcine articular cartilage**
Chunsheng Liu, Le Zhao, Hao Dong, Zekun Hua, Yanqin Wang, Yongxing Wang, Pengcui Li, Xiaochun Wei, Kai Zhang, Yanru Xue, Xiaogang Wu and Weiyi Chen
- 150 **Effects of stair riser height on ankle proprioception in individuals with and without chronic ankle stability**
Xueying Wang, Zheng Wang, Roger Adams, Yang Gao, Jie Lyu and Jia Han
- 157 **Design of novel graded bone scaffolds based on triply periodic minimal surfaces with multi-functional pores**
Rongwu Lai, Jian Jiang, Yi Huo, Hao Wang, Sergei Bosiakov, Yongtao Lyu and Lei Li
- 169 **Statistical shape modeling of shape variability of the human distal tibia: implication for implant design of the tibial component for total ankle replacement**
Jian Yu, Chengke Li, Jinyang Lyu, Shengxuan Cao, Chao Zhang, Xin Ma and Dahang Zhao



OPEN ACCESS

EDITED BY

Zhen (Jeff) Luo, University of Technology
Sydney, Australia

REVIEWED BY

James Yang,
Texas Tech University, United States
Gary B. Wilkerson,
University of Tennessee at Chattanooga,
United States

*CORRESPONDENCE

Lance Frazer,
✉ lance.frazer@swri.org

RECEIVED 13 September 2023

ACCEPTED 21 November 2023

PUBLISHED 06 December 2023

CITATION

Frazer L, Templin T, Eliason TD, Butler C,
Hando B and Nicolella D (2023),
Identifying special operative trainees at-
risk for musculoskeletal injury using full
body kinematics.
Front. Bioeng. Biotechnol. 11:1293923.
doi: 10.3389/fbioe.2023.1293923

COPYRIGHT

© 2023 Frazer, Templin, Eliason, Butler,
Hando and Nicolella. This is an open-
access article distributed under the terms
of the [Creative Commons Attribution
License \(CC BY\)](https://creativecommons.org/licenses/by/4.0/). The use, distribution or
reproduction in other forums is
permitted, provided the original author(s)
and the copyright owner(s) are credited
and that the original publication in this
journal is cited, in accordance with
accepted academic practice. No use,
distribution or reproduction is permitted
which does not comply with these terms.

Identifying special operative trainees at-risk for musculoskeletal injury using full body kinematics

Lance Frazer^{1*}, Tylan Templin¹, Travis David Eliason¹,
Cody Butler², Ben Hando^{2,3} and Daniel Nicolella¹

¹Southwest Research Institute (SwRI), San Antonio, TX, United States, ²United States Air Force, Special Warfare Training Wing Research Flight, Joint Base San Antonio-Lackland, San Antonio, TX, United States, ³Kennell and Associates Inc, Falls Church, VA, United States

Introduction: Non-combat musculoskeletal injuries (MSKIs) during military training significantly impede the US military's functionality, with an annual cost exceeding \$3.7 billion. This study aimed to investigate the effectiveness of a markerless motion capture system and full-body biomechanical movement pattern assessments to predict MSKI risk among military trainees.

Methods: A total of 156 male United States Air Force (USAF) airmen were screened using a validated markerless biomechanics system. Trainees performed multiple functional movements, and the resultant data underwent Principal Component Analysis and Uniform Manifold And Projection to reduce the dimensionality of the time-dependent data. Two approaches, semi-supervised and supervised, were then used to identify at-risk trainees.

Results: The semi-supervised analysis highlighted two major clusters with trainees in the high-risk cluster having a nearly five times greater risk of MSKI compared to those in the low-risk cluster. In the supervised approach, an AUC of 0.74 was produced when predicting MSKI in a leave-one-out analysis.

Discussion: The application of markerless motion capture systems to measure an individual's kinematic profile shows potential in identifying MSKI risk. This approach offers a novel way to proactively address one of the largest non-combat burdens on the US military. Further refinement and wider-scale implementation of these techniques could bring about substantial reductions in MSKI occurrence and the associated economic costs.

KEYWORDS

biomechanics, military, functional movement analysis, kinematics, markerless motion capture, injury risk assessment

Introduction

Non-combat musculoskeletal injuries (MSKIs) that occur during basic and specialized military training continue to be one of the greatest burdens affecting the United States military and their allied partners (Molloy et al., 2020; Rhon et al., 2022). The economic consequences and lost duty days are a substantial encumbrance on the functionality of our armed forces. Recent studies estimate that non-combat injuries are six times more likely than combat-related injuries, put 68,000 servicemembers in non-deployable status every year, and

carry an annual cost that exceeds \$3.7 billion (Grimm et al., 2019). Among MSKI types, lower extremity (LE) injuries are the most common with some reports attributing more than 70% of non-combat injuries to lower extremities (Molloy et al., 2020; Butler et al., 2022). As a result, the US military has promoted the identification of Service members at risk for LE MSKI and the development of effective preventative measures as a top research priority (Teyhen et al., 2020; Rhon et al., 2021).

Over the past decade, a growing interest has developed in the use of biomechanics to evaluate MSKI risk during military training (Sammito et al., 2021). Biomechanical assessments typically include the analysis of an individual's movement (kinematics) (Hando et al., 2021; Bird et al., 2022; Cameron et al., 2022; Eckard et al., 2022; Bird et al., 2023), force transmission through the body (kinetics) (Bird et al., 2022; Hando et al., 2022; Bird et al., 2023), and/or overall fitness (Tomes et al., 2020). These analyses have been fruitful in discovering biomechanical measures associated with injury. For example, Sharma et al. found that imbalanced foot pressure is predictive of medial tibia stress syndrome (shin splints) (Sharma et al., 2011). Step width during gait has been associated with tibial stress, which may affect stress fracture risk (Meardon and Derrick, 2014). Wan and Shan associated muscle mechanics with repetitive stress injuries (Wan and Shan, 2016). While these analyses, among others (Negus and Sih, 2016; Winkelmann et al., 2016; Garnock et al., 2018), have shown promise in identifying Service members at risk for MSKI, to date, there are no examples of successful adoption of biomechanical assessments in military units that have reduced the injury burden. A well-generalizable set of predictive variables and an accurate, reliable injury risk algorithm has yet to be demonstrated. Moreover, the time and effort required to perform biomechanical assessments limit their application at scale, which is particularly important for military applications. To address this latter concern, markerless motion capture technology has emerged as promising to substantially reduce the burden of high throughput testing.

Markerless motion capture systems are an attractive screening tool because of their operational simplicity and equivalence to marker-based systems (Perrott et al., 2017; Martinez et al., 2018; Mosier et al., 2018; Drazan et al., 2021). However, the few studies to investigate their use for injury risk assessments have yielded mixed results, and it is unclear if these systems provide meaningful information to predict MSKI. For example, Eckard et al. and Cameron et al. used results from a markerless motion capture system to compute the Landing Error Scoring System (LESS) and found a significant association between individual subjects' jumping/landing characteristics and lower limb bone stress injury (Cameron et al., 2022; Eckard et al., 2022). While promising, the association was most meaningful among female trainees and may not be strong enough to make actionable decisions for both males and females (Eckard et al., 2022). Moreover, the findings were only applicable to a small percentage of participants who landed in a very particular way (Cameron et al., 2022). In contrast, Hando et al., as well as Bird et al. used markerless motion capture technology coupled with proprietary "scores" but found poor association with injury risk (Hando et al., 2021; Bird et al., 2023). While the ease of implementation offered by markerless systems has alleviated the concern of high throughput testing, the limited and even conflicting results have questioned their predictive value. Yet, even the studies with much more inclusive methods to perform

biomechanical assessments have not yielded satisfactory predictive power (Sanchez-Santos et al., 2017; Rhon et al., 2018; Sammito et al., 2021). Thus, it remains challenging to make a convincing case for biomechanics to assess injury risk.

We believe the application of markerless motion capture and the subsequent analyses of the kinematics obtained from such systems have greater potential to identify MSKI risk than these prior studies suggest. The majority of studies, including those cited earlier, use univariate measures that are decided upon *a priori* and researchers must subjectively choose what may or may not be predictive of injury (Chorba et al., 2010; Lisman et al., 2013; Sefton et al., 2016; Markström et al., 2019; Sammito et al., 2021; Bird et al., 2022; Cameron et al., 2022; Eckard et al., 2022; Hando et al., 2022). Individuals perform specific movements through unique, coordinated patterns of time-dependent joint motions that cannot be adequately described with univariate measures (or even a collection of univariate measures). These unique patterns, or biomechanical fingerprints, that include multiple joint motions across the entire body may reveal subtle differences that are indicative of injury risk. Yet, to our knowledge, no study has investigated the detailed, high-fidelity, full-body kinematics to determine the injury risk of military trainees. With this approach, full, time-dependent joint motions across the entire body are analyzed using dimensionality reduction techniques without choosing beforehand which joints and/or key events are important. We hypothesize that considering the entirety of an individual's kinematic profile is predictive of injury. Therefore, to test this hypothesis and address a gap in injury risk analysis amongst military trainees, the purpose of this study is to evaluate whether an individual's biomechanical movement pattern is indicative of injury risk.

Materials and methods

Participants

United States Air Force (USAF) airmen (male) entering a Special Warfare (SW) 8-week preparatory course designed to ready trainees for the rigors of Special Warfare training served as participants in the study. Details of this course have been described in prior studies from our group (Hando et al., 2022). Trainees with active injuries were excluded from the study. Injury data were obtained from the Medical Health System Management Analysis and Reporting Tool (M2), a centralized data repository that captures data input into the Military Health System's electronic medical records. A published MSKI taxonomy used in US military MSKI research was used to identify International Classification of Diseases (10th Revision, Clinical Modification) codes corresponding to MSKIs (Hando et al., 2023). Subsequent encounters for the same injury were not counted. The trainees were surveilled for the period corresponding to their 8-week training, and those who suffered any MSKI were recorded. For this analysis, the classification matrix was used to further classify participants as sustaining a lower extremity MSKI (yes/no). Only a small sample of individuals had available data, which resulted in 156 participants between October 2017 and April 2020. Because very few females were enrolled in Special Warfare training at the time, there were no females included in our sample.

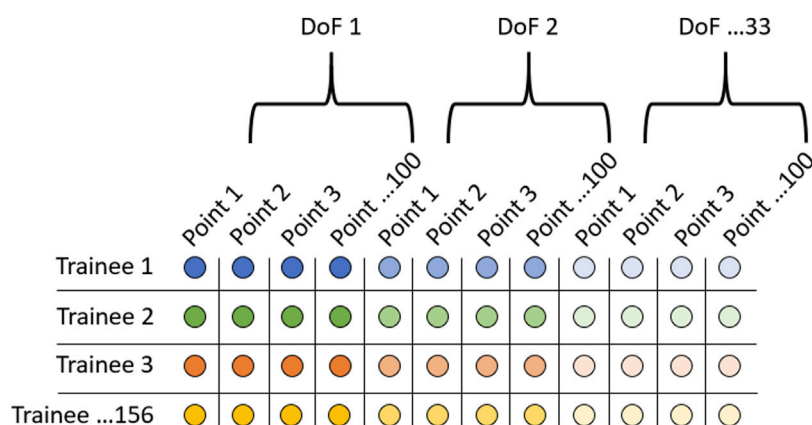


FIGURE 1

Data organization when performing principal component analysis. Rows represent each of the 156 trainees, and each column represents 1 of 3300 points in the kinematic trace. This was performed for each of the 20 kinematic traces (10 movements \times 2 normalizations).

Movement assessment

Within 3 days before the start of the course, kinematic screenings were administered. Eight synced Blackfly/FLIR GigE cameras (50 frames per second) were positioned circumferentially above the participant in a rectangular room measuring 6 m \times 6 m and 3 m in height with green screen flooring. Each of the 156 trainees performed the following kinematic movements directed by certified athletic trainers: 1) squat, 2) countermovement jump, (3–4) single-leg squat (each leg), (5–6) lunge (each leg), (7–8) side-lunge (each leg), (9–10) single-leg jump (each leg). Each movement was processed using a validated markerless biomechanics system (SwRI ENABLE™ v.1.0) (SWRI, 2023). We measured six degrees of freedom (DOFs) for the pelvis (3 translation, three rotational), three DOFs for the torso (3 rotational), three DOFs for the shoulders (rotational), three DOFs for the hips (3 rotational), three DOFs for the knees (rotational), two DOFs for the ankles (flexion/extension, inversion/eversion), and one DOF for the elbows (flexion/extension). In total, 33 DOFs were measured for each individual and for each movement.

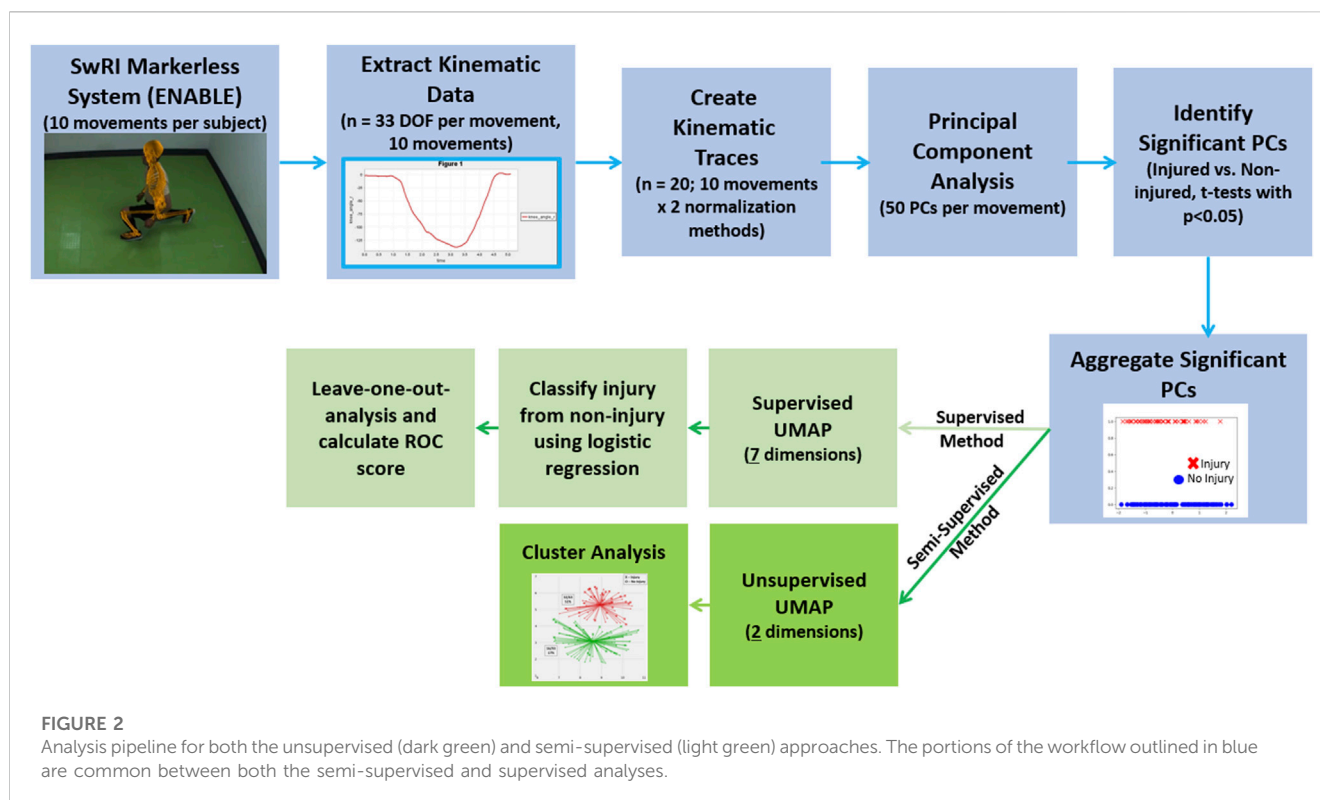
Data analysis

The 33-degree-of-freedom full-body kinematic data obtained from ENABLE™ was analyzed in the aggregate for multiple movements and is referred to herein as an individual's kinematic profile or biomechanical movement pattern. Each joint angle (or joint displacement in the case of the pelvis) vs. time curve was normalized to 100 evenly spaced time points by two different approaches: 1) by time (start to finish of the movement), and 2) by identifying a starting point of the movement and moving forward 3 s in time, which was found to be sufficient to fully capture each movement for each participant. The first normalization technique identifies relative differences in magnitudes at particular parametrically corresponding points of a movement but is insensitive to time, whereas the second normalization technique

is sensitive to the time of a movement but can introduce artificial extrapolations at the end of the data trace if a participant finishes the movement much faster than 3 s. Used in tandem, the two approaches may be complementary (Raffalt et al., 2019). The two normalization techniques across 10 movements created 20 individual kinematic traces for each trainee. Therefore, each trainee's kinematic profile for a particular movement (referred to here as a kinematic trace) contained 3300 points (33 degrees of freedom \times 100 points).

Principal component analysis was performed separately on each of the 20 kinematic traces across all 156 trainees (Figure 1). For each trace, only the first 50 PCs were kept as anything beyond these explained less than 0.5% of the variance and was deemed too prone to noise error from the markerless motion capture system. Two-tailed t-tests were performed on each of the principal components to test for significant differences between injury and non-injury trainees ($p < 0.05$). The significant PCs from each movement were aggregated and served as input to a semi-supervised and supervised analysis pipeline to test the validity of using full-body kinematic data to assess injury risk (Figure 2).

In the semi-supervised approach (the 'semi' is attributed to only using significant PCs), the significant PCs were embedded into 2-dimensional Cartesian space via unsupervised Uniform Manifold and Projection (UMAP) (McInnes et al., 2018). UMAP is a non-linear dimensionality reduction technique and is used in conjunction with the linear PCA to 1) introduce non-linearity to the method, which may detect trends not observable with linear analysis, and 2) further reduce the dimensionality of the PCs, which helps with both supervised learning and visualization (clustering) analysis. The embedded data were then clustered via Gaussian Mixture Models (Reynolds et al., 2009), which is similar to K-Means clustering but does not require that the clusters are circular. The number of clusters was decided via calculating a K-Means silhouette coefficient for 2–10 clusters and selecting the highest score (Shahapure and Nicholas, 2020). The silhouette coefficient is a measure of how close each point in one cluster is to points in the neighboring clusters. A higher score



means the clusters are more closely packed, and thus the highest silhouette coefficient calculated denotes the optimal number of clusters to use.

In the supervised approach, supervised UMAP (performed on the significant PCs) was combined with logistic regression (LR) to classify injurious from non-injurious participants. The performance of the model was evaluated via leave-one-out analyses where 155 of the participants were used to train the supervised UMAP embedding and subsequent LR algorithm. The left-out trainee was then passed through the trained UMAP embedding and then classified via the trained LR. The process was repeated for each of the 156 participants. A receiver operating characteristic curve (ROC) was generated and an associated area under the curve (AUC, which is a measure of separability between two classes, or how well the prediction algorithm can distinguish injury from non-injury, in the present study) was calculated. Values above 0.7 are deemed useful for prediction (Mandrekar, 2010). An optimization procedure was performed to identify the best combination of UMAP components, UMAP neighbors, and the LR regularization parameter (C in the sci-kit learn implementation (Pedregosa et al., 2011; Virtanen et al., 2020)). For each participant, prior injury data (any MSKI), which has been shown to be a strong predictor of MSKI during military training (Rhon et al., 2018), was available. As such, the supervised analysis was repeated two more times to 1) only include prior injury data (logistic regression only), and 2) kinematic data + prior injury data. It should be noted that UMAP is a stochastic algorithm. As opposed to fixing the random seed, each analysis was performed 15 times to test if the results were sensitive to random number generation for both the supervised and semi-supervised methods.

Results

Of the 156 trainees, 48 suffered a lower-body injury. Of these 48 lower body injuries, all were considered overuse injuries that included two stress fractures and two sprains/tears (Table 1).

Of the 1000 principal components tested in this study (50 PCs in each of the 20 movements), 53 were found to be significant (Table 1). All movements yielded significantly different PCs. The lunge movements yielded significant PCs that contained the most variance explained, whereas the countermovement jump had the least.

In the semi-supervised analyses, 2 clusters were selected via the highest silhouette coefficient (0.48). However, *in lieu* of previous work using clustering (Bird et al., 2022), we also implemented 3 clusters (silhouette coefficient = 0.43). In the two-group cluster semi-supervised analysis (Figure 3, left), 51% of the trainees in one of the clusters suffered an MSKI (which we have named the “High Risk” cluster), whereas only 17% of the trainees in the other cluster suffered an MSKI (which we have named the “Low Risk” cluster). The odds ratio was 4.97 ($p < 0.0001$) between these two clusters. In the three-group cluster semi-supervised analysis (Figure 3, right), 49% of the trainees in the “high-risk” cluster suffered an MSKI, 26% of the trainees in the “medium-risk” cluster suffered an MSKI, and only 14% of the trainees in the “low-risk” cluster suffered an MSKI. The repeated analyses had little effect on the clusters.

In the supervised analysis that only included kinematic data, seven UMAP components with the number of neighbors set to 6, and a C value of one was found to be the most optimal combination of hyperparameters in classifying injurious and non-injurious trainees. Using these optimized parameters, an AUC score of 0.74 ± 0.02 (range: 0.70–0.79) was produced (Figure 4 with the best confusion matrix shown in Figure 5). Using the same optimized parameters and the inclusion of prior injury data, an AUC score of 0.75 ± 0.02 (range:

TABLE 1 Injury region and type using Hando et al.'s classification matrix (Hando et al., 2023). 48 total lower extremity injuries occurred in the 156 trainees tracked in this study.

Body region 1 (all categories)		
	Lower Extremity	48
	Spine and Back	8
	Upper Extremity	7
	Head and Neck	3
	Torso	0
	Other	0
Body Region 2 (Top Eight Categories)		
	Knee	19
	Leg Other	15
	Lower Leg	13
	Lumbar Spine	7
	Foot/Toe	6
	Shoulder	6
	Hip	5
	Ankle	3
Injury Types (Top Six Categories)		
	Overuse/Non-Specific	58
	Stress Fracture	2
	Sprain/Joint Damage	1
	Strain/Tear	1

0.71–0.80) was produced. Prior injury data as the sole predictor variable with logistic regression produced an AUC score of 0.62 ± 0.03 (range: 0.57–0.67). The stochastic nature of UMAP had a minor effect on the results (illustrated by the range of AUCs).

Discussion

The purpose of this study was to investigate whether an individual's biomechanical movement pattern is indicative of injury risk. The novelty in our study was the approach taken to assess biomechanical movement. Instead of assessing univariate variables at key events (e.g. maximum knee flexion), the entire waveforms for 33 degrees of freedom in the body were analyzed in aggregate using dimensionality reduction techniques. Moreover, several functional movements were analyzed and considered in tandem in the development of both an unsupervised and supervised approach. Considering the time-dependent movement of multiple joints across the body during particular movements, it was found that a semi-supervised analysis naturally clustered individuals based on movement patterns that were indicative of injury-risk. In a supervised approach, we observed that a binary injury classification algorithm may be possible from kinematics alone. An AUC of 0.74 is a promising result and may have

implications for identifying MSKI risk in vulnerable populations, such as high-school and collegiate athletes, military Service members, first responders, and others. If the results herein can be repeated and improved upon in a much larger, controlled study, a simple kinematic screening test could be implemented as a means to identify at-risk individuals.

Although other studies that have used biomechanics to assess injury risk primarily focused on univariate measures, they demonstrate a perceived strength in result interpretability. For example, Bird et al. were able to show that a short breaking phase and propulsive phase during the countermovement jump was associated with a lower risk of injury in marine officer candidates (Bird et al., 2022). McHugh et al. report high peak propulsive power in the “above average” group for NCAA athletes (McHugh et al., 2021) during the countermovement jump. In another similar study, Rauch et al. demonstrate that NBA basketball players can be clustered and significantly differentiated based on hip flexion during the downward phase of the countermovement jump (CMJ) (Rauch et al., 2020). Indeed, the CMJ is a popular movement for screening, although we found this movement to be the least indicative of injury risk (lowest variance explained in the significant PCs). These studies, among others, demonstrate the benefits of using distinctly chosen predictor variables because these variables are understandable, and they can be interpreted as to what they might be revealing in military trainees (or athletes). Therefore, a criticism against full-body data analyses that use variable, or dimension, reduction methods such as principal components analysis of raw kinematic data could be that the results are difficult to interpret as each PC contains movement information across multiple degrees of freedom (in this study, 33). However, this approach coupled with rigid body dynamics and visualization software makes interpretability possible. To this end, we provide the following explanation on how this can be accomplished.

Using OpenSim (which is the native output of ENABLE™), the principal components that are significant between injury and non-injury participants can be isolated and visualized by perturbing an “average” model with the plus and minus 1 standard deviation of that particular principal component. This type of analysis has substantial implications for training and intervention strategies, as it allows significantly different movement patterns between groups to be visually scrutinized. As a demonstration of this capability and motivation for future work, we visually compared the plus and minus 1 standard deviation of a randomly selected principal component that was significantly different between groups (right side lunge PC#7 that explained 5% of the variance). We found that on average, those that went on to suffer a lower-extremity MSKI performed the side lunge faster than their non-injured counterparts (Figure 6). Moreover, the injured group tended to take a smaller backward step during the initial eccentric phase of the movement. While these observations are not predictive of injury risk in isolation, they provide additional information to researchers and trainers that may help guide actionable interventions. Considering all of the significant PCs, a trainer/practitioner may find insightful differences between each group, such as balance or strength issues and use this information to design intervention strategies aimed at risk mitigation.

The machine learning algorithms implemented in this study were PCA, UMAP, and logistic regression. While the results are positive, we do not believe the results are specific to the choice of

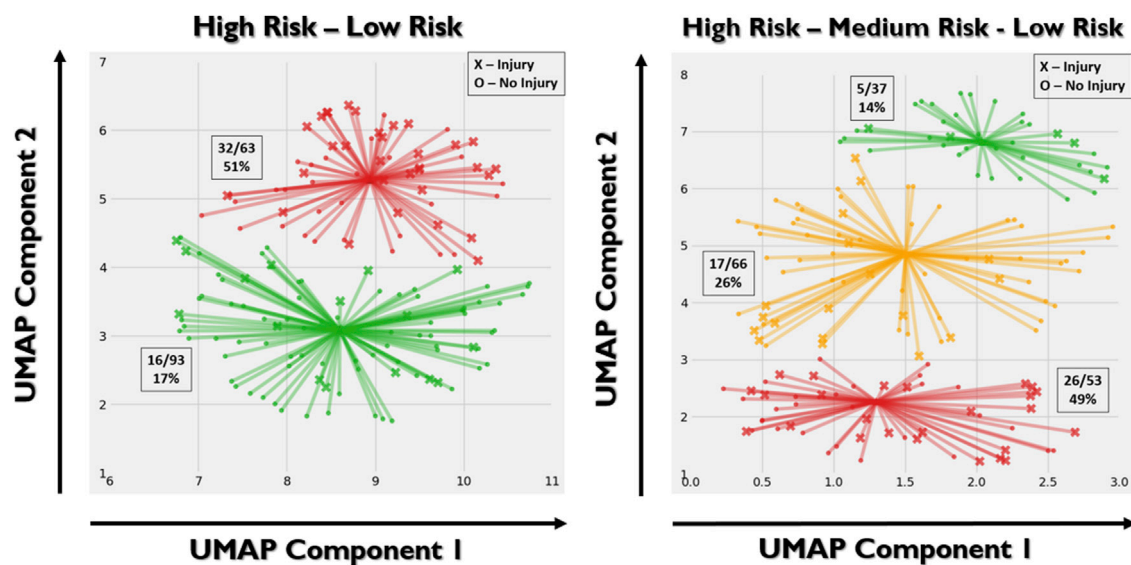


FIGURE 3

Left: two-group gaussian mixture model clustering. X's represent injury and O's represent no injury. Right: three-group clustering. "High-risk" (red), "medium-risk" (yellow), and "low-risk" (green) clusters were defined based on the relative portion of the trainees suffering an MSKI. Based on the stochastic nature of UMAP, each implementation may yield slightly different results even with the same hyperparameters. As such, there is discrepancy between the UMAP embeddings between the two and three group cluster analyses. The X and Y axes represent the two UMAP variables that the PCA variables were compressed to. The value of each UMAP component is unimportant, whereas the spatial relationship between the points is important.

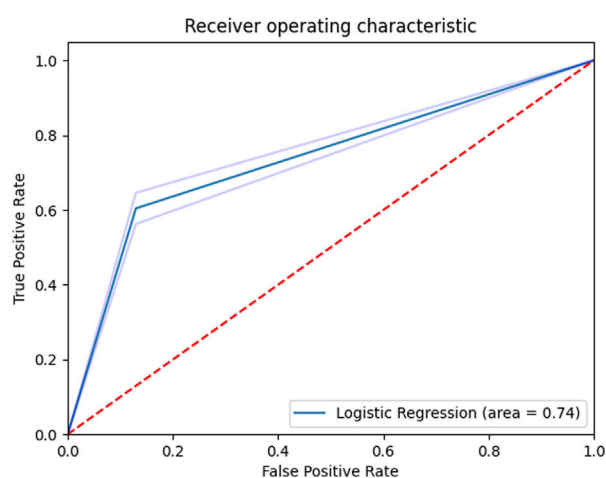


FIGURE 4

Receiver operating characteristic curve for the supervised classifier (kinematics only). Shaded regions denote ± 1 standard deviation.

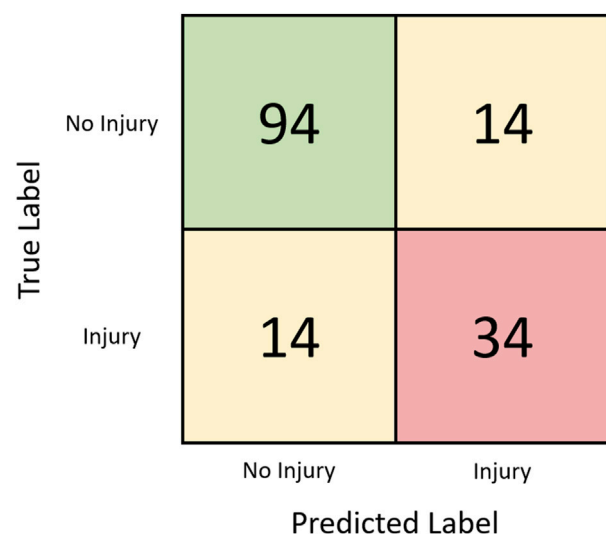


FIGURE 5

Confusion matrix for the kinematic-only supervised classification task assessed via leave-one-out analysis with the best run (AUC = 0.79).

algorithms. PCA is a statistical, easy-to-implement algorithm that reduces the dimensionality of the data. However, it is not the only choice. KPCA, autoencoders, diffusion maps, and other techniques can reduce the burden of high-dimensional data. The benefit of using PCA is that the 1-to-1 linear inverse mapping presents an opportunity to readily visualize the movements associated with each PC, as discussed above. UMAP was selected to further reduce the dimensionality of the data and provide non-linearity that PCA and logistic regression do not provide. Again, other algorithms are

available, but we have found that UMAP is a robust algorithm for dimensionality reduction and is advantageous in that both supervised and unsupervised embeddings are allowable. Moreover, UMAP preserves global data structure such that the relative location of a particular point (and cluster) is meaningful in relation to others. This is evident in the two-cluster analysis in Figure 3. Individuals in the high-risk cluster that were spatially

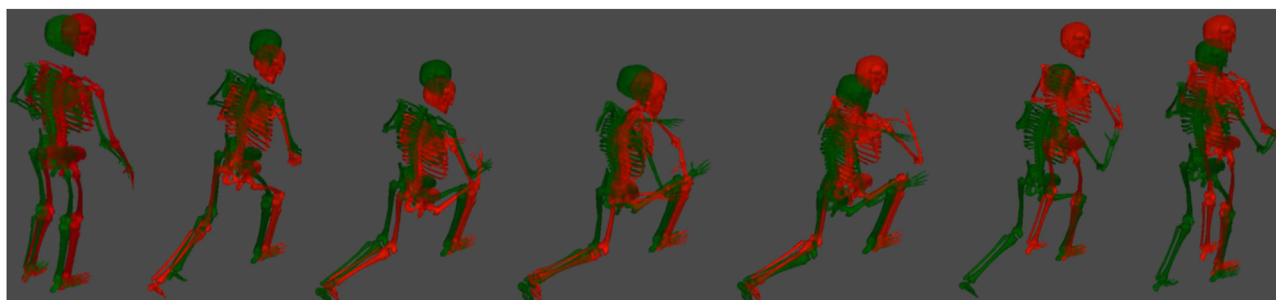


FIGURE 6

Time series of a side lunge (right leg) for both the plus and minus 1 standard deviation of a randomly selected principal component. These models are constructed in OpenSim (native output of ENABLE™) by taking the average kinematics across all participants and perturbing the average motion by a weight factor multiplied by a principal component. The weight factors shown here are plus 1 (green) standard deviation (in this particular PC, plus one was associated with non-injury) and a minus 1 (red) standard deviation, which was associated with injury.

TABLE 2 The number of significant principal components identified for each movement and their respective cumulative variance explained.

	Number of significant PCs ($p < 0.05$)	Total variance (%) explained
Left Lunge	4	17
Right Lunge	3	14
Squat	8	13
Right Side Lunge	9	10
Left Single Leg Squat	7	10
Left Single Leg Jump	6	10
Right Single Leg Squat	5	10
Right Single Leg Squat	5	7
Left Side Lunge	4	5
Countermovement Jump	2	2

closer to the low-risk cluster tended to be non-injurious, which suggests a “medium-risk”. Unsurprisingly then, the semi-supervised three-cluster analysis naturally yielded an intermediate “medium-risk” zone. It should be noted that we observed a minor effect on the random number generation within UMAP, which yielded AUC values between 0.70–0.80. This is likely due to the small sample size as a single change (1 out of 156) in the predicted class changed the AUC by 0.01. Logistic regression is a common binary classifier, but many other options exist to perform binary classification. We find it encouraging that our first choice of algorithms performed well, and perhaps improvement can be made with a more thorough investigation of alternative algorithms.

There were several limitations of this study. The sample size of 156 was low, and it is unknown if the same predictive power would be obtained from a larger military population. Moreover, due to the small sample size, the ability to predict specific lower extremity injuries (Table 2, Body Region 2) was not investigated. The participants were spread over several cohorts, and therefore not every participant performed the exact same training regimen (although, this may be considered a strength, since this could

indicate algorithm generalizability). Age and BMI, and fitness measures were not available for this analysis, but they’ve also been shown to be predictive of injury risk (Rappole et al., 2017; Rhon et al., 2018; Hollander et al., 2020; Butler et al., 2022; Hando et al., 2022). Also, while not necessarily a limitation of this study, force plate data were not available, and the inclusion of kinetic data would provide a more complete biomechanical assessment of an individual and may improve the predictive power of the algorithms used in this study (Guess et al., 2020; Thomas et al., 2022).

In conclusion, we found that full-body kinematics may be predictive of lower extremity MSKI in male trainees that undergo an 8-week Air Force Special Warfare preparatory course. The analysis was performed with data collected from markerless motion capture (ENABLE™). The findings from this preliminary study warrant further investigation and may lead to advanced methods to identify individuals at-risk for injury in military, sport, and healthcare. If at-risk individuals can be readily identified with quick, non-invasive functional movement screens, then tailored interventions, such as specific exercise programs, may be investigated in a controlled study to test its efficacy in reducing the incidence of injury.

Data availability statement

The datasets presented in this article are not readily available because the data comes from Air Force trainees and we have been given special permission to use it. Requests to access the datasets should be directed to cody.butler.3@us.af.mil.

Ethics statement

The studies involving humans were approved by 59th Medical Wing's Institutional Review Board IRB Reference #: FWH20200070E. The studies were conducted in accordance with the local legislation and institutional requirements. The participants provided their written informed consent to participate in this study.

Author contributions

LF: Writing—original draft. TT: Writing—review and editing. TE: Writing—review and editing. CB: Writing—review and editing. BH: Writing—review and editing. DN: Writing—review and editing.

References

- Bird, M. B., Mi, Q., Koltun, K. J., Lovalekar, M., Martin, B. J., Fain, A., et al. (2022). Unsupervised clustering techniques identify movement strategies in the countermovement jump associated with musculoskeletal injury risk during US marine corps officer candidates school. *Front. Physiol.* 13, 868002. doi:10.3389/fphys.2022.868002
- Bird, M. B., Koltun, K. J., Mi, Q., Lovalekar, M., Martin, B. J., Doyle, T. L. A., et al. (2023). Predictive utility of commercial grade technologies for assessing musculoskeletal injury risk in US Marine Corps Officer candidates. *Front. Physiology* 14, 1088813. doi:10.3389/fphys.2023.1088813
- Butler, C., Haydu, L., Bryant, J., Mata, J., Tchandja, J., Hogan, K., et al. (2022). Musculoskeletal injuries during U.S. Air force special Warfare training assessment and selection, fiscal years 2019–2021. *Msmr* 29 (8), 2–6.
- Cameron, K. L., Peck, K. Y., Davi, S. M., Owens, C., Svoboda, C., DiStefano, L. J., et al. (2022). Association between landing error scoring system (LESS) items and the incidence rate of lower extremity stress fracture. *Orthop. J. Sports Med.* 10 (6), 232596712211007. doi:10.1177/23259671221100790
- Chorba, R. S., Chorba, D. J., Bouillon, L. E., Overmyer, C. A., and Landis, J. A. (2010). Use of a functional movement screening tool to determine injury risk in female collegiate athletes. *N. Am. J. Sports Phys. Ther.* 5 (2), 47–54.
- Drazan, J. F., Phillips, W. T., Seethapathi, N., Hullfish, T. J., and Baxter, J. R. (2021). Moving outside the lab: markerless motion capture accurately quantifies sagittal plane kinematics during the vertical jump. *J. biomechanics* 125, 110547. doi:10.1016/j.jbiomech.2021.110547
- Eckard, T. G., Miraldi, S. F. P., Peck, K. Y., Posner, M. A., Svoboda, S. J., DiStefano, L. J., et al. (2022). Automated landing error scoring system performance and the risk of bone stress injury in military trainees. *J. Athl. Train.* 57 (4), 334–340. doi:10.4085/1062-6050-0263.21
- Garnock, C., Witchalls, J., and Newman, P. (2018). Predicting individual risk for medial tibial stress syndrome in navy recruits. *J. Sci. Med. Sport* 21 (6), 586–590. doi:10.1016/j.jsams.2017.10.020
- Grimm, P. D., Mauntel, T. C., and Potter, B. K. (2019). Combat and noncombat musculoskeletal injuries in the US military. *Sports Med. Arthrosc. Rev.* 27 (3), 84–91. doi:10.1097/jsa.0000000000000246
- Guess, T. M., Gray, A. D., Willis, B. W., Guess, M. M., Sherman, S. L., Chapman, D. W., et al. (2020). Force-time waveform shape reveals countermovement jump strategies of collegiate athletes. *Sports* 8 (12), 159. doi:10.3390/sports8120159
- Hando, B. R., Scott, W. C., Bryant, J. F., Tchandja, J. N., Scott, R. M., and Angadi, S. S. (2021). Association between markerless motion capture screenings and musculoskeletal injury risk for military trainees: a large cohort and reliability study. *Orthop. J. Sports Med.* 9 (10), 232596712110416. doi:10.1177/23259671211041656
- Hando, B. R., Scott, W. C., Bryant, J. F., Tchandja, J. N., and Angadi, S. S. (2022). The use of force plate vertical jump scans to identify special Warfare trainees at risk for musculoskeletal injury: a large cohort study. *Am. J. Sports Med.* 50 (6), 1687–1694. doi:10.1177/03635465221083672
- Hando, B. R., Bryant, J., Pav, V., Haydu, L., Hogan, K., Mata, J., et al. (2023). Musculoskeletal injuries in US Air Force Tactical Air Control Party trainees: an 11-year longitudinal retrospective cohort study and presentation of a musculoskeletal injury classification matrix. *BMJ Mil. Health*, e002417. doi:10.1136/military-2023-002417
- Hollander, N. A., Finestone, A. S., Yofe, V., Bader, T., and Magnezi, R. (2020). The association between increased body mass index and overuse injuries in Israel defense forces conscripts. *Obes. Facts* 13 (2), 152–165. doi:10.1159/000505836
- Lisman, P., O'Connor, F. G., Deuster, P. A., and Knapik, J. J. (2013). Functional movement screen and aerobic fitness predict injuries in military training. *Med. Sci. Sports Exerc.* 45 (4), 636–643. doi:10.1249/mss.0b013e31827a1c4c
- Mandrek, J. N. (2010). Receiver operating characteristic curve in diagnostic test assessment. *J. Thorac. Oncol.* 5 (9), 1315–1316. doi:10.1097/jto.0b013e3181ec173d
- Markström, J. L., Grip, H., Schelin, L., and Häger, C. K. (2019). Dynamic knee control and movement strategies in athletes and non-athletes in side hops: implications for knee injury. *Scand. J. Med. Sci. Sports* 29 (8), 1181–1189. doi:10.1111/sms.13432
- Martinez, H. R., Garcia-Sarreón, A., Camara-Lemarro, C., Salazar, F., and Guerrero-González, M. L. (2018). Accuracy of markerless 3D motion capture evaluation to differentiate between on/off status in Parkinson's disease after deep brain stimulation. *Parkinsons Dis.* doi:10.1155/2018/5830364
- McHugh, M. P., Hickok, M., Cohen, J. A., Virgile, A., and Connolly, D. A. J. (2021). Is there a biomechanically efficient vertical ground reaction force profile for countermovement jumps? *Transl. SPORTS Med.* 4 (1), 138–146. doi:10.1002/tsm2.200
- McInnes, L., Healy, J., and Melville, J. (2018). *Umap: Uniform manifold approximation and projection for dimension reduction*. arXiv preprint arXiv:1802.03426
- Meardon, S. A., and Derrick, T. R. (2014). Effect of step width manipulation on tibial stress during running. *J. Biomechanics* 47 (11), 2738–2744. doi:10.1016/j.jbiomech.2014.04.047
- Molloy, J. M., Pendergrass, T. L., Lee, I. E., Chervak, M. C., Hauret, K. G., and Rhon, D. I. (2020). Musculoskeletal injuries and United States army readiness Part I: overview of injuries and their strategic impact. *Mil. Med.* 185 (9–10), e1461–e1471. doi:10.1093/milmed/usaa027
- Mosier, E., Fry, A., Nicoll, J., and Cabarkapa, D. (2018). Test-retest reliability of performance scores using A markerless motion capture system. *Int. J. Exerc. Sci. Conf. Proc.*, 53.
- Negus, C. H., and Sih, B. L. (2016). Physical training outcome predictions with biomechanics, Part II: overuse injury modeling. *Mil. Med.* 181, 85–94. (suppl_5). doi:10.7205/milmed-d-15-00169
- Pedregosa, F., Varoquaux, G., Gramfort, A., Michel, V., Thirion, B., Grisel, O., et al. (2011). Scikit-learn: machine learning in Python. *J. Mach. Learn. Res.* 12, 2825–2830.

Funding

The author(s) declare that no financial support was received for the research, authorship, and of this article.

Conflict of interest

Author BH was employed by Kennell and Associates Inc.

The remaining authors declare that the research was conducted in the absence of any commercial or financial relationships that could be construed as a potential conflict of interest.

Publisher's note

All claims expressed in this article are solely those of the authors and do not necessarily represent those of their affiliated organizations, or those of the publisher, the editors and the reviewers. Any product that may be evaluated in this article, or claim that may be made by its manufacturer, is not guaranteed or endorsed by the publisher.

- Perrott, M. A., Pizzari, T., Cook, J., and McClelland, J. A. (2017). Comparison of lower limb and trunk kinematics between markerless and marker-based motion capture systems. *Gait posture* 52, 57–61. doi:10.1016/j.gaitpost.2016.10.020
- Raffalt, P. C., Kent, J. A., Wurdeman, S. R., and Stergiou, N. (2019). Selection procedures for the largest lyapunov exponent in gait biomechanics. *Ann. Biomed. Eng.* 47 (4), 913–923. doi:10.1007/s10439-019-02216-1
- Rappole, C., Grier, T., Anderson, M. K., Hauschild, V., and Jones, B. H. (2017). Associations of age, aerobic fitness, and body mass index with injury in an operational Army brigade. *J. Sci. Med. Sport* 20 (Suppl. 4), S45–S50. doi:10.1016/j.jsams.2017.08.003
- Rauch, J., Leidersdorf, E., Reeves, T., Borkan, L., Elliott, M., and Ugrinowitsch, C. (2020). Different movement strategies in the countermovement jump amongst a large cohort of NBA players. *Int. J. Environ. Res. Public Health* 17 (17), 6394. doi:10.3390/ijerph17176394
- Reynolds, D. (2009). in *Gaussian mixture models. Encyclopedia of biometrics*. Editors S. Z. Li and A. Jain (Boston, MA: Springer US), 659–663.
- Rhon, D. I., Teyhen, D. S., Shaffer, S. W., Goffar, S. L., Kiesel, K., and Plisky, P. P. (2018). Developing predictive models for return to work using the Military Power, Performance and Prevention (MP3) musculoskeletal injury risk algorithm: a study protocol for an injury risk assessment programme. *Inj. Prev.* 24 (1), 81–88. doi:10.1136/injuryprev-2016-042234
- Rhon, D. I., Fraser, J. J., Sorensen, J., Greenlee, T. A., Jain, T., and Cook, C. E. (2021). Delayed rehabilitation is associated with recurrence and higher medical care use after ankle sprain injuries in the United States military Health system. *J. Orthop. Sports Phys. Ther.* 51 (12), 619–627. doi:10.2519/jospt.2021.10730
- Rhon, D. I., Molloy, J. M., Monnier, A., Hando, B. R., and Newman, P. M. (2022). Much work remains to reach consensus on musculoskeletal injury risk in military service members: a systematic review with meta-analysis. *Eur. J. Sport Sci.* 22 (1), 16–34. doi:10.1080/17461391.2021.1931464
- Sammito, S., Hadzic, V., Karakolis, T., Kelly, K. R., Proctor, S. P., Stephens, A., et al. (2021). Risk factors for musculoskeletal injuries in the military: a qualitative systematic review of the literature from the past two decades and a new prioritizing injury model. *Mil. Med. Res.* 8 (1), 66. doi:10.1186/s40779-021-00357-w
- Sanchez-Santos, M. T., Davey, T., Leyland, K. M., Allsopp, A. J., Lanham-New, S. A., Judge, A., et al. (2017). Development of a prediction model for stress fracture during an intensive physical training program: the royal marines commandos. *Orthop. J. Sports Med.* 5 (7), 232596711771638. doi:10.1177/2325967117716381
- Sefton, J. M., Lohse, K. R., and McAdam, J. S. (2016). Prediction of injuries and injury types in army basic training, infantry, armor, and cavalry trainees using a common fitness screen. *J. Athl. Train.* 51 (11), 849–857. doi:10.4085/1062-6050-51.9.09
- Shahapure, K. R., and Nicholas, C. (2020). Cluster quality analysis using silhouette score, in *2020 IEEE 7th international conference on data science and advanced analytics (DSAA)*, 747–748.
- Sharma, J., Golby, J., Greeves, J., and Spears, I. R. (2011). Biomechanical and lifestyle risk factors for medial tibia stress syndrome in army recruits: a prospective study. *Gait Posture* 33 (3), 361–365. doi:10.1016/j.gaitpost.2010.12.002
- SWRI (2023). *Engine for automatic biomechanical evaluation*, <https://www.swri.org/industry/biomechanics-human-performance/engine-automatic-biomechanical-evaluation-enable>.
- Teyhen, D. S., Shaffer, S. W., Goffar, S. L., Kiesel, K., Butler, R. J., Rhon, D. I., et al. (2020). Identification of risk factors prospectively associated with musculoskeletal injury in a warrior athlete population. *Sports Health* 12 (6), 564–572. doi:10.1177/1941738120902991
- Thomas, C., Jones, P. A., and Dos'Santos, T. (2022). Countermovement jump force-time curve analysis between strength-matched male and female soccer players. *Int. J. Environ. Res. Public Health* 19 (6), 3352. doi:10.3390/ijerph19063352
- Tomes, C. D., Sawyer, S., Orr, R., and Schram, B. (2020). Ability of fitness testing to predict injury risk during initial tactical training: a systematic review and meta-analysis. *Inj. Prev.* 26 (1), 67–81. doi:10.1136/injuryprev-2019-043245
- Virtanen, P., Gommers, R., Oliphant, T. E., Haberland, M., Reddy, T., Cournapeau, D., et al. (2020). SciPy 1.0: fundamental algorithms for scientific computing in Python. *Nat. Methods* 17 (3), 261–272. doi:10.1038/s41592-019-0686-2
- Wan, B., and Shan, G. (2016). Biomechanical modeling as a practical tool for predicting injury risk related to repetitive muscle lengthening during learning and training of human complex motor skills. *Springerplus* 5, 441. doi:10.1186/s40064-016-2067-y
- Winkelmann, Z. K., Anderson, D., Games, K. E., and Eberman, L. E. (2016). Risk factors for medial tibial stress syndrome in active individuals: an evidence-based review. *J. Athl. Train.* 51 (12), 1049–1052. doi:10.4085/1062-6050-51.12.13



OPEN ACCESS

EDITED BY

Peter Quesada,
University of Louisville, United States

REVIEWED BY

Aike Qiao,
Beijing University of Technology, China
Dalin Tang,
Worcester Polytechnic Institute,
United States

*CORRESPONDENCE

Lai Wei,
✉ wei.lai@zs-hospital.sh.cn
Shengzhang Wang,
✉ szwang@fudan.edu.cn

RECEIVED 04 November 2023

ACCEPTED 30 November 2023

PUBLISHED 20 December 2023

CITATION

Li J, Meng Z, Yan W, Wang W, Wei L and Wang S (2023), Computational study of the balloon dilation steps on transcatheter aortic valve replacement. *Front. Bioeng. Biotechnol.* 11:1333138. doi: 10.3389/fbioe.2023.1333138

COPYRIGHT

© 2023 Li, Meng, Yan, Wang, Wei and Wang. This is an open-access article distributed under the terms of the [Creative Commons Attribution License \(CC BY\)](https://creativecommons.org/licenses/by/4.0/). The use, distribution or reproduction in other forums is permitted, provided the original author(s) and the copyright owner(s) are credited and that the original publication in this journal is cited, in accordance with accepted academic practice. No use, distribution or reproduction is permitted which does not comply with these terms.

Computational study of the balloon dilation steps on transcatheter aortic valve replacement

Jianming Li¹, Zhuangyuan Meng¹, Wentao Yan², Wenshuo Wang³, Lai Wei^{3*} and Shengzhang Wang^{1,4,5*}

¹Department of Aeronautics and Astronautics, Institute of Biomechanics, Fudan University, Shanghai, China, ²Shanghai Inspection and Research Institute for Medical Devices, Shanghai, China, ³Department of Cardiac Surgery, Zhongshan Hospital Affiliated to Fudan University, Shanghai, China, ⁴Academy for Engineering and Technology, Institute of Biomedical Engineering Technology, Fudan University, Shanghai, China, ⁵Zhuhai Fudan Innovation Institute, Zhuhai, China

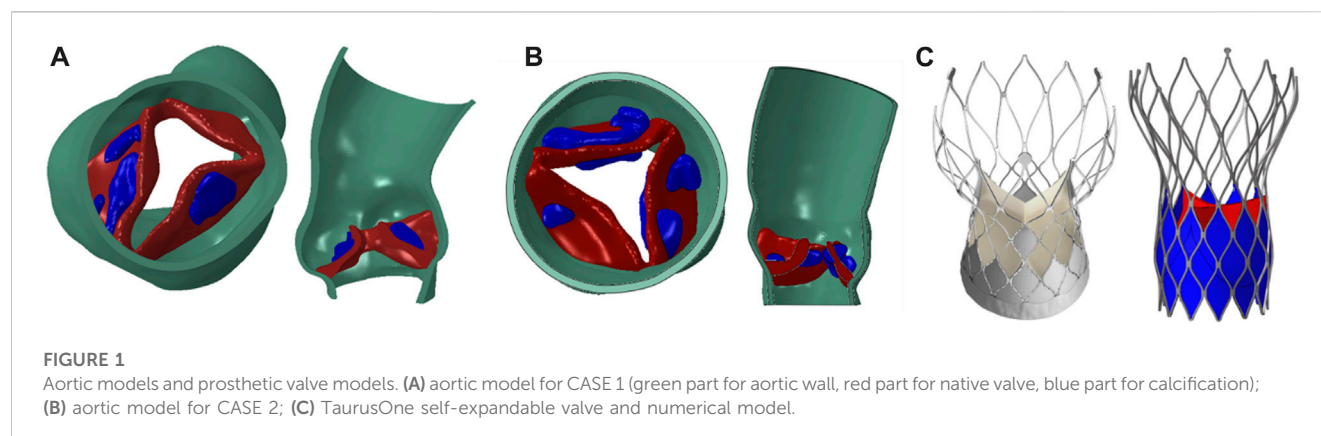
Balloon dilation is a commonly used assistant method in transcatheter aortic valve replacement (TAVR) and plays an important role during valve implantation procedure. The balloon dilation steps need to be fully considered in TAVR numerical simulations. This study aims to establish a TAVR simulation procedure with two different balloon dilation steps to analyze the impact of balloon dilation on the results of TAVR implantation. Two cases of aortic stenosis were constructed based on medical images. An implantation simulation procedure with self-expandable valve was established, and multiple models including different simulation steps such as balloon pre-dilation and balloon post-dilation were constructed to compare the different effects on vascular stress, stent morphology and paravalvular leakage. Results show that balloon pre-dilation of TAVR makes less impact on post-operative outcomes, while post-dilation can effectively improve the implantation morphology of the stent, which is beneficial to the function and durability of the valve. It can effectively improve the adhesion of the stent and reduce the paravalvular leakage volume more than 30% after implantation. However, balloon post-dilation may also lead to about 20% or more increased stress on the aorta and increase the risk of damage. The balloon dilation makes an important impact on the TAVR outcomes. Balloon dilation needs to be fully considered during pre-operative analysis to obtain a better clinical result.

KEYWORDS

transcatheter aortic valve replacement, numerical simulation, self-expandable valve, post-dilation, pre-dilation

1 Introduction

Aortic stenosis is a common heart disease caused by aortic valve calcification. Aortic stenosis causes reduction of cardiac output and may be accompanied by aortic regurgitation (AR), resulting in systemic insufficiency of blood supply, which may lead to cardiac hypertrophy and severe failure in long term (Pibarot et al., 2019; Spitzer et al., 2019). Transcatheter aortic valve replacement (TAVR) is a minimally invasive treatment technique which delivers the compressible artificial valve through a microcatheter to complete the replacement. It has been widely used in the treatment of high-risk patients. However, due to



factors such as non-intuitive surgery and complex anatomy, post-operative complications are the main problems. Atrioventricular conduction may be disturbed by the contact stimulation from prosthetic stent, which needs to be regulated by implantation of pacemaker. The existence of post-operative paravalvular leak is related to higher late mortality, cardiac death and secondary hospitalization (Maisano et al., 2015). In addition, paravalvular leak is also associated with the formation of thrombosis, thus increasing the risk of post-operative stroke (Bianchi et al., 2019).

Clinically, due to the severity of valve stenosis, the valve stent cannot pass smoothly. Therefore, the operator will use balloon dilation to fully open the original valve before valve implantation, which is called balloon pre-dilation. After the valve is released, a balloon is used again for secondary dilation, which is called post-dilation, allowing the valve stent to fully expand to achieve support. These two steps usually play an important role in TAVR procedure (McInerney et al., 2021).

Computational modelling and simulation have been widely used to study TAVR, such as the relationship between calcification distribution and TAVR results and the influence of stent positioning (Auricchio et al., 2014; Morganti et al., 2016; Sturla et al., 2016; Vy et al., 2016; Luraghi et al., 2020). In addition, numerical simulation can be used to evaluate the risk of different operation strategy and predict post-operative outcomes. Morganti et al. (Morganti et al., 2014) established the implantation process of balloon-expandable valve based on two patient-specific models, and then established the simulation model of self-expandable valve to study the influence of valve positioning on the post-operative outcomes (Morganti et al., 2016). Using a combination method of structural simulation and computational fluid dynamics, Bianchi et al. (Bianchi et al., 2019) pointed out the effective reduction of post-operative paravalvular leak with over-dilation for balloon-expandable valve.

However, in many TAVR simulation studies, the balloon dilation steps were not mentioned in detail or considered in TAVR simulation, which typically included two main steps: stent crimping and releasing. The effect of balloon dilation on simulation result is not clear so far. In this study, two patient-specific aortic models were established, and a complete transcatheter self-expandable valve implantation process would be constructed in the model to verify the effectiveness of the balloon dilation step and analyze the impact of balloon dilation on the post-operative results.

TABLE 1 Material parameters for aortic model.

Component	Elastic modulus (MPa)	Poisson's ratio
Aortic wall	2	0.45
Leaflets	3.3	0.45
Calcification	12.6	0.3

2 Methods

2.1 Aortic root and TAVR models

In this study, CTA image data of two patients diagnosed with severe aortic stenosis were retrospectively analyzed and chosen for model reconstruction. Patient-specific aortic models were reconstructed in MIMICS 19.0 (Materialise, Belgium) from the left ventricular outflow tract to the ascending aorta, including the aortic wall, native valve and calcification. The models were repaired and smoothed in Geomagic Studio 2013 (Geomagic Inc. United States) to generate a standard geometry format, and finally meshed in Hypermesh 2019 (Altair, United States), as shown in Figures 1A,B. The native valve and calcification were meshed with tetrahedral elements. The aortic wall was meshed with triangles on inner surface and then offset outward to generate a solid mesh with total thickness of 1.5 mm. The total number of elements of each model was about 250,000, which satisfied the mesh independence requirement (Li et al., 2022). In the process of TAVR simulation, aortic model can be assumed as linear elastic material (Bailey et al., 2016) to reduce the computational cost, and detailed material parameters were listed in Table 1. The circumference of native annulus was 71.7 mm and 73.7 mm for two cases, respectively, corresponding to a diameter of 22.8 mm and 23.8 mm. Therefore, according to the clinical recommendations, a 26 mm size self-expandable valve was chosen for implantation simulation for both two cases.

Based on the commercial transcatheter heart valve products TaurusOne (Peijia Medical Inc. China), the self-expandable valve model (TO) used in this study was constructed, as shown in Figure 1C. The self-expandable stent was made of hyperelastic nitinol alloy material, which involves a phase transformation between Austenite and Martensite during loading and unloading

TABLE 2 Material parameters for self-expandable stent.

Parameter	Description	Value
E_A	Austenite elastic modulus	45,000 MPa
ν_A	Austenite Poisson's ratio	0.33
E_M	Martensite elastic modulus	30,000 MPa
ν_M	Martensite Poisson's ratio	0.33
ε^L	Transformation strain	0.032
σ_L^s	Start of transformation loading	250 MPa
σ_L^E	End of transformation loading	550 MPa
σ_U^s	Start of transformation unloading	60 MPa
σ_U^E	End of transformation unloading	20 MPa
ρ	Material density	4,500 kg/m ³

process. The properties of nitinol were defined in Abaqus 2019 (Dassault System, France) by VUMAT. Parameters for these two stents are listed in Table 2.

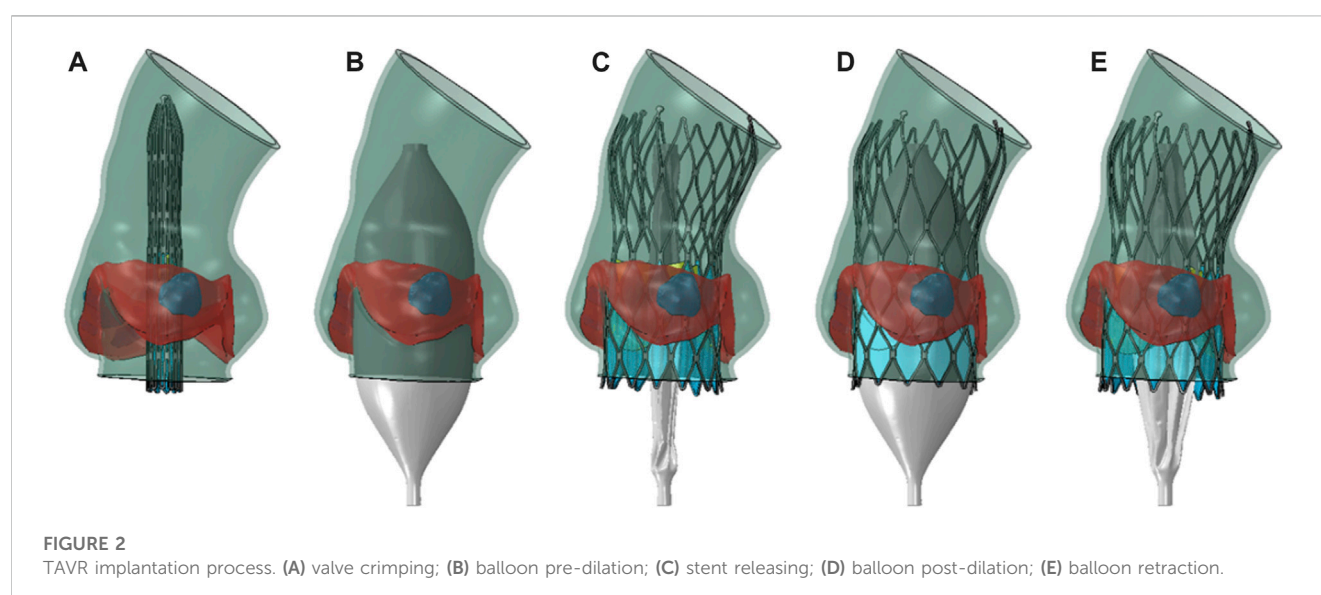
2.2 TAVR implantation procedure

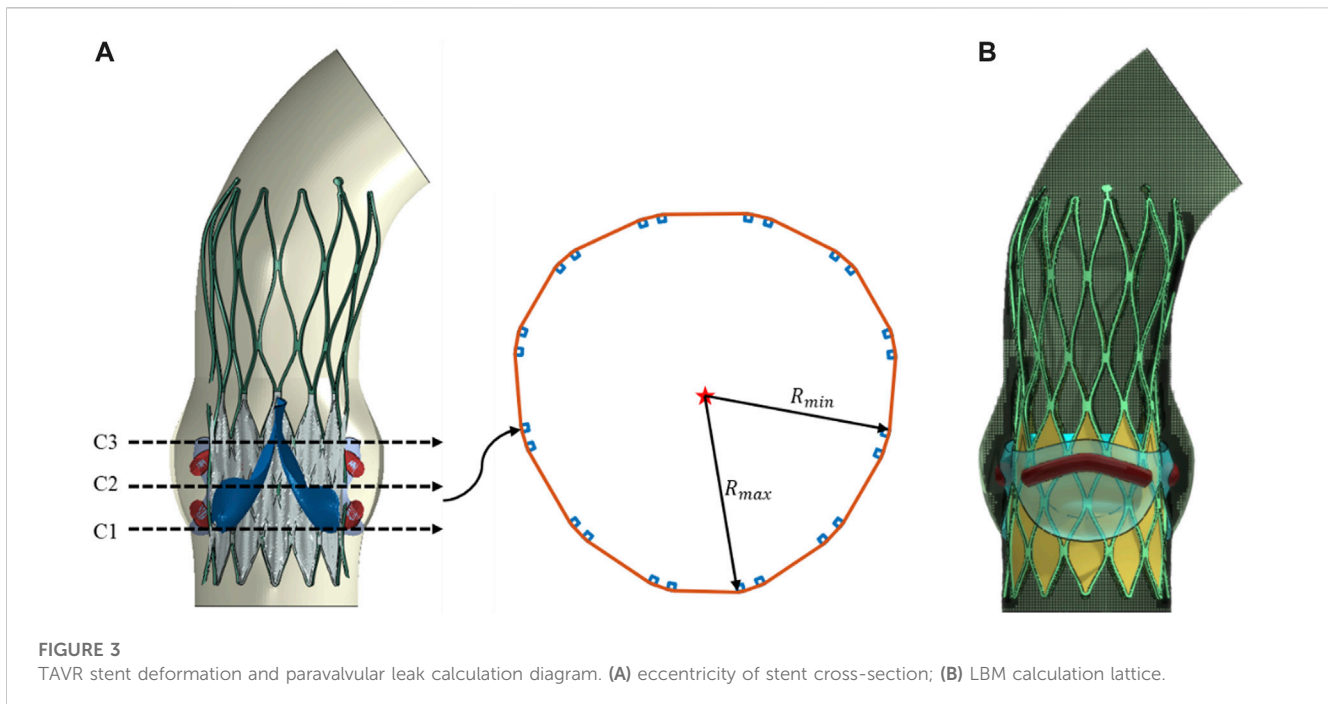
Nitinol can autonomously return to its original shape after the constraints are removed, and the valve implantation process is generally completed with crimping and releasing steps (Morganti et al., 2016; Nappi et al., 2021). In this study, the complete TAVR process in clinical operation was restored, and the steps of balloon pre-dilation and post-dilation were added to simulate a more realistic self-expandable valve implantation process. The complete self-expandable valve implantation process established was shown in Figure 2.

1. Valve crimping: A rigid cylindrical tube and the prosthetic valve were assembled concentrically and adjusted to the appropriate

implantation height. A radially inward displacement boundary condition was applied to the cylindrical tube surface, causing it to shrink radially to a diameter of 7 mm. The general contact between the stent, the skirt and the rigid cylindrical surface was set. The radius of the valve was reduced under the driving of the rigid cylinder to obtain the crimped state.

2. Balloon pre-dilation: A 23 mm balloon was inflated using the method of fluid cavity, which increases the volume of liquid inside the balloon to reach the inflation state. The contact happened among the balloon, the native valve and the aortic wall, causing the native valve to open. In order to improve the calculation efficiency, the calculation of this step was performed simultaneously with the stent crimping step, by setting no contact between the TAVR valve and the aortic model to make them two independent processes.
3. Stent releasing: In this step, the volume of liquid inside the balloon was reduced to deflate the pre-dilation balloon. The balloon gradually shrunk under the action of external pressure and elastic recovery, and the native valve and aortic wall recovered. In the meanwhile, a radial outward displacement condition was applied to the rigid cylindrical tube to increase its diameter. Due to the superelasticity of the material, the self-expandable stent gradually recovered its shape and came into contact with the native valve and aortic wall. Finally, the constraint of the rigid cylindrical tube on the prosthetic valve was released, and the valve interacted with the aorta to reach a stable state.
4. Balloon post-dilation: Second balloon dilation was performed after the valve released completely. During this process, the balloon surface interacted with the self-expandable valve and the aorta and lead to deformation. Inter-contacts and self-contacts of all components in the model were taken into account.
5. Balloon retraction: The post-dilation balloon gradually retracted. Due to the elimination of internal support by the balloon, the self-expandable valve slight contracted under the elastic recovery force of the aortic root and native valve, and eventually the whole model reached a final balance.





In order to study the impact of balloon dilation on the implantation outcomes with self-expandable valve, adjustments were made in the simulation procedure to establish four compared models, without balloon dilation (TO), only considering balloon pre-dilation (TO-pre), only considering balloon post-dilation (TO-post), both considering pre-dilation and post-dilation (TO-prepost).

2.3 Calculation of stent deformation and paravalvular leak

Three valve frame sections with from the area of the sewn prosthetic valve were extracted for deformation analysis after valve implantation (Nappi et al., 2021). The cross-sectional eccentricity of the stent was used to evaluate the degree of deformation of the stent, which was calculated as R_{max}/R_{min} , represented the ratio of the maximum to minimum distance from the point on the cross-section to the geometric center, as shown in Figure 3 (a).

Computational fluid dynamics (CFD) was used for post-operative paravalvular leak analysis. Due to the tiny penetrations or gaps in the models after valve implantation, it was difficult to construct an effective and stable computational mesh using traditional CFD methods, such as finite volume method. Therefore, the Lattice Boltzmann Method (LBM) was employed to calculate the regurgitation caused by paravalvular leak. LBM is a meshless method, which is easy to match with complex geometric boundaries. The calculation was completed in the software XFlow 2019 (Dassault System, France).

Through mesh convergence analysis using regurgitation flow as the inspection index, the global lattice size was finally determined to be 0.4 mm, with local refinement to 0.1 mm on the stent wall and native valve. Paravalvular leak primarily occurs during diastole, when blood flows to the ventricle side from the aorta. The calculation was considered as steady flow, with average diastolic aortic pressure of 13,500 Pa applying for inlet condition in ascending aorta side and

diastolic left ventricular pressure of 500 Pa applying for outlet in ventricle side. Blood was assumed as Newtonian fluid with density of 1,050 kg/m³ and kinematic viscosity of 0.0035 Pa·s. In order to calculate the final regurgitation degree in clinical usage, the cardiac cycle was assumed as 0.8 s and the diastolic period accounted for about 65%.

3 Results

3.1 Aortic stress distribution

Figure 4 shows the stress distribution of the aortic root with different balloon dilation in two cases. In both cases, areas of high stress were found at the inferior edge of the aortic sinuses and in the intra-triangle. The stress at the inferior edge of the sinus increased due to the global dilation of the aortic root caused by the valve stent, while the high stress in the triangular area of the sinus was due to the pull effect in different direction acting on the commissure edge of the native valve when the stent pushes them aside. Balloon dilation made no effect on the location of stress concentration. The peak stress results at the aortic root in the two cases were listed in Table 3. In the two cases, the peak stress of the aorta in the TO and TO-pre models did not vary significantly, indicating that pre-dilation had little impact on the final stress results of the aortic root. Both the TO-post and TO-prepost models that included the post-dilation step showed a significant increase in aortic stress, indicating that post-dilation caused the stent to exert a greater force on the aorta.

3.2 Deformation of prosthetic stent

Figure 5 shows the cross-sectional deformation and eccentricity after stent implantation in each model for two cases. The morphology of the stent showed an important relationship with the distribution of

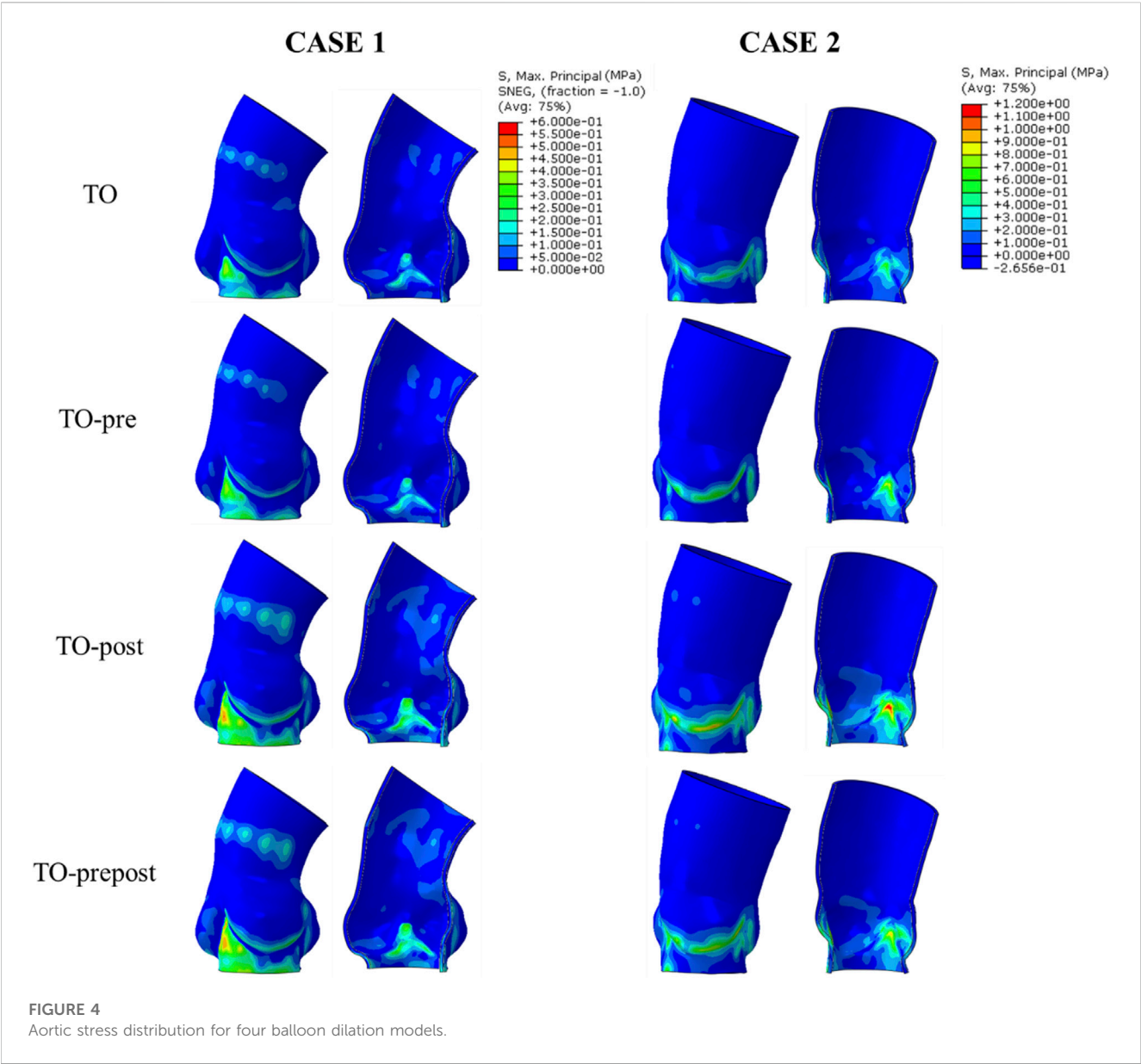
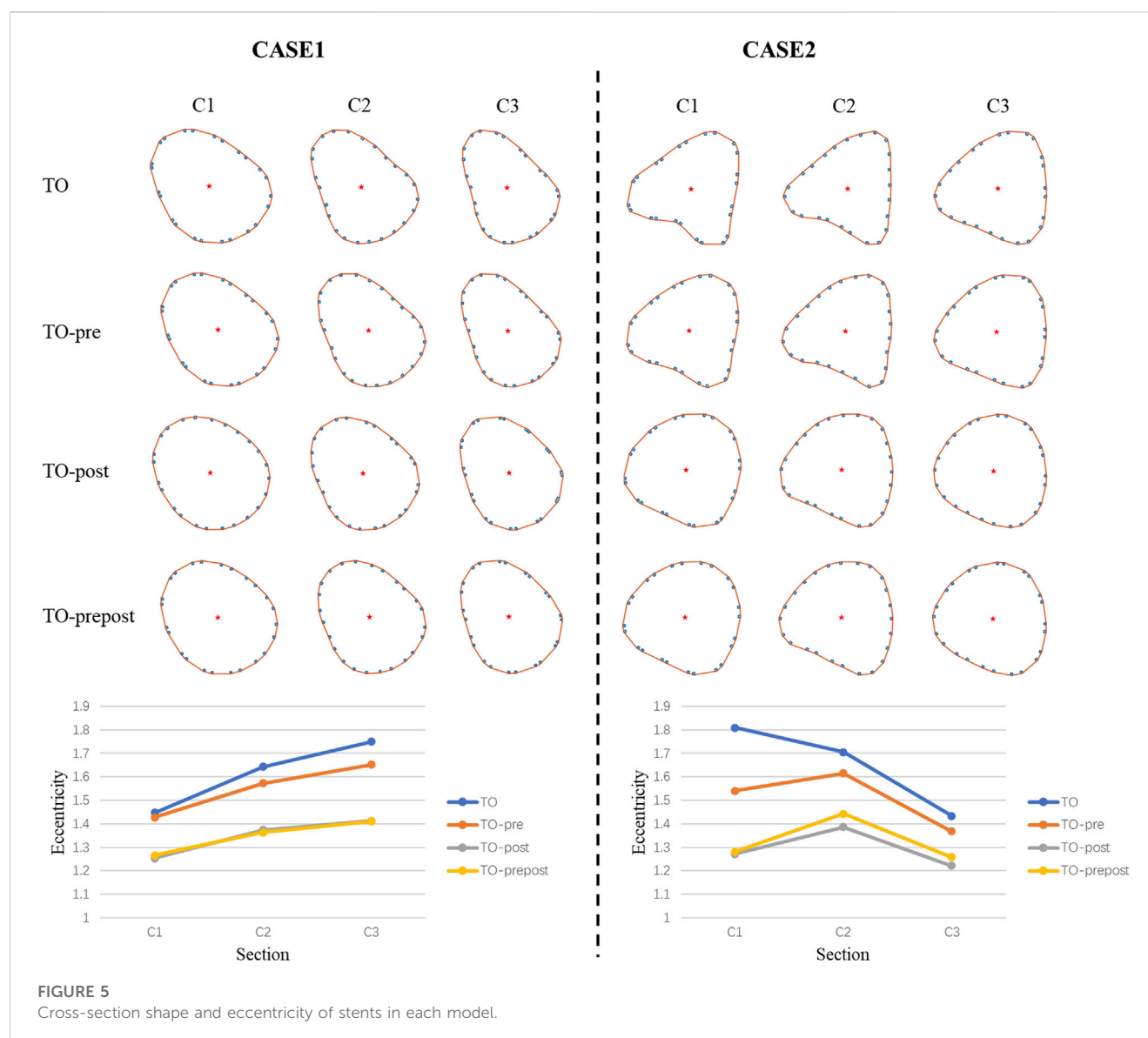


TABLE 3 Aortic stress in different models for two cases.

	Model	Peak stress (MPa)	Percentage increase compared to TO model
CASE1	TO	0.66	0%
	TO-pre	0.58	-12.2%
	TO-post	0.78	18.2%
	TO-prepost	0.74	12.1%
CASE2	TO	0.76	0%
	TO-pre	1.00	31.6%
	TO-post	1.35	77.7%
	TO-prepost	1.21	59.2%



calcification. In CASE 1, the cross-section of the stent was constrained by the shape of the native valve to be an elliptical shape. The balloon post-dilation made it to open more fully along the short axis. In CASE 2, because there was also a large amount of calcification on the ventricular side of the native valve, the stent was limited by the calcification mass, and the cross-section was in the shape of a concave arc triangle. The balloon post-dilation effectively reduced the degree of concavity of the stent, allowing it to better restore its original shape. In the two cases, the eccentricity of stent showed almost no difference between TO-post and TO-prepost model, and both of their eccentricity were significantly lower than TO model. However, cross-sectional morphology and eccentricity of the TO-pre model were not significantly improved compared to the TO model.

3.3 Analysis of paravalvular leak

Since the calcified valve could not fully expand, the stent was blocked by the apposition area of the leaflets during releasing, so that

it could not fit well to the wall at the commissure edge, forming a significant gap area, as shown in Figure 6. After balloon dilation, the adherence of the stent in the TO-prepost model was significantly improved, and the gaps at the commissure edge were eliminated or reduced.

Figure 7 shows the location of paravalvular leak in each model for the two cases. The occurrence of paravalvular leak was mainly concentrated at the commissure edge of the native valve, which was consistent with the location of the gap formed by stent inadequate apposition. The regurgitant volume could be calculated from flow. Assuming a normal physiological cardiac output of 5.0 L after TAVR, the regurgitant fraction of paravalvular leakage was calculated and the regurgitation grading of paravalvular leakage was obtained according to the clinical criteria (Dvir et al., 2018). Table 4 lists the regurgitation flow in each model. Since the degree of calcification in CASE 2 was more severe than that in CASE 1, and the calcification was distributed on both sides of the valve, the regurgitation volume of each model in CASE 2 was much higher than that of the CASE 1. For CASE 1, the stroke regurgitation

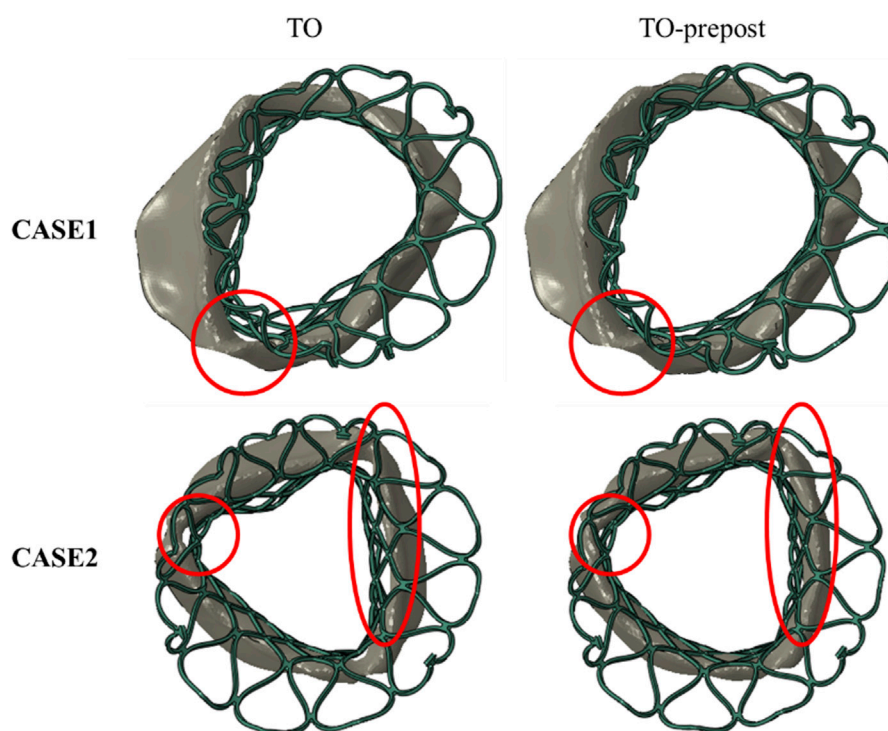


FIGURE 6
Stent adherence after implantation with/without balloon dilation in two cases.

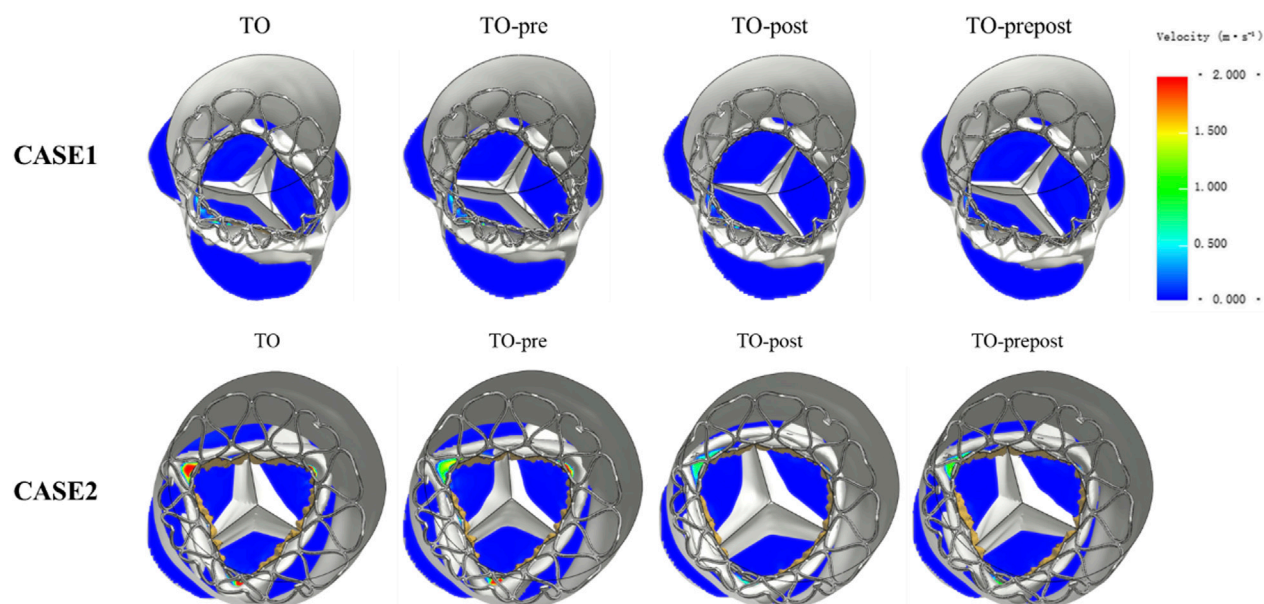


FIGURE 7
Paravalvular leak patterns for different models.

volume of the TO-post model decreased by 36.3% and the TO-prepost model decreased by 29.7%, and the degree of regurgitation decreased from “mild” to “moderate to mild”. For CASE 2, the TO-post model’s stroke regurgitation volume decreased by 56.9%, the

TO-prepost model decreased by 54.6%. The regurgitation degree decreased from “moderate to severe” to “moderate”. In these two cases, there was almost no change in the regurgitation volume and paravalvular leak degree of the TO-pre model.

TABLE 4 Regurgitation degree in different models for two cases.

	Model	Flow (mL/s)	Regurgitant volume (mL)	Regurgitant fraction (%)	Regurgitant grading
CASE1	TO	8.6	4.5	6.7	Mild to moderate
	TO-pre	8.9	4.6	6.9	Mild to moderate
	TO-post	5.5	2.8	4.3	Mild
	TO-prepost	6.0	3.1	4.7	Mild
CASE2	TO	33.7	17.5	26.3	Moderate to severe
	TO-pre	33.8	17.6	26.4	Moderate to severe
	TO-post	14.5	7.6	11.3	Moderate
	TO-prepost	15.3	7.9	11.9	Moderate

4 Discussion

This study constructed a complete patient specific aortic model based on CTA imaging, including the aortic root and native valve with calcification. The implantation process of self-expandable valve considering balloon pre-dilation and post-dilation in the pathological model was established, and the effect of two balloon dilation methods was compared. The results showed that balloon dilation has a significant impact on post-operative outcomes.

Both balloon pre-dilation and post-dilatation are part of the surgical procedures for TAVR, but the main purpose of pre-dilation is to open of the native calcified leaflets. The simulation results indicated that pre-dilation only makes a little impact on post-operative aortic stress, stent morphology and paravalvular leak. The balloon post-dilation step is usually used when the implanted valve did not expand enough, so it plays a major role in post-operative outcomes. Balloon post-dilation significantly increase the interaction between the stent and the aortic wall, resulting in increased stress in the aortic root and better valve anchorage. However, stress concentration will also increase the risk of aortic rupture during valve implantation. In addition, higher stress may cause calcification and tissue shedding on aorta, which may block vessels in the brain and lead to stroke. Some studies had also demonstrated the association of shedding tissue with stroke (Nombela-Franco et al., 2012; Van Mieghem et al., 2015). According to the research of Abbasi et al., insufficiently deployed stent will cause increased stress on the prosthetic leaflets, which may reduce the durability of the valve (Abbasi and Azadani, 2015; Nappi et al., 2021). Balloon post-dilation can fully expand the valve stent, effectively reduce the eccentricity of the stent and maintain a better circular cross-section, therefore improve the performance and durability of the valve. The area of post-operative paravalvular leak may be a potential location for long-term thrombosis (Bianchi et al., 2019), and the degree of paravalvular leak is related to the patient's long-term survival rate (Maisano et al., 2015). Balloon post-dilation improves the adherence of the stent and effectively reduces the degree of paravalvular leak, which is also consistent with clinical findings (Barbanti et al., 2014; Miyasaka et al., 2018).

In summary, the main reason why the balloon post-dilation step can improve TAVR outcomes is that the balloon expansion process makes the valve a better deployed state. The mechanical mechanism

behind it is mainly that the balloon fully deforms the calcified native leaflets, which “soften” the whole structure by a larger force. The second explanation is related to the special mechanical properties of loading and unloading of nickel-titanium materials. Although in a same compressed diameter, the nitinol stent acts out different radial force between the loading and unloading process (Tzamtzis et al., 2013; Stoeckel et al., 2019). For the process of simply releasing the stent, the stent experiences the unloading process to recover its deformation and reaches equilibrium with the blood vessel under the action of chronic outward force. However, the balloon post-dilation step allows the stent to be released to a larger diameter first. After the balloon is retracted, due to the recovery of the blood vessel, the stent is subjected to a loading process and will produce a corresponding higher radial resistance force compared to the chronic outward force in releasing process. So the stent can reach a better final expanded state.

Limitations were also existed. Calcification was simplified as linear elastic material. However, balloon dilation often destroys the integrity of calcification actually, thereby helping the valve to expand effectively. Pre-dilation was thought to be helpful in fully stent deployment clinically (Pagnesi et al., 2016; Dumonteil et al., 2019), but the calcification mass could not be destroyed in this simulation study, so it still made a greater impact on the results even with pre-dilation. The analysis of paravalvular leak in this study made an assumption of rigid vessel walls and steady-state flow calculations, ignoring the diameter changes and paravalvular gap changes caused by aorta compliance during a cardiac cycle, which may cause the calculation results to be underestimated. Fluid-structure interaction analysis that fully considers all components can better capture the information of the fluid, which is also the direction of our future work. In addition, this study only analyzed balloon dilation through simulation and lacked sufficient *in vitro* verification or clinical data support. We hope to supplement these necessary work in future.

5 Conclusion

This study established a complete simulation process for TAVR based on patient specific model, including balloon pre-dilation and post-dilation, and compared the impact of two balloon dilation on post-operative outcomes. Balloon pre-dilation makes a limited impact on the results, while post-dilation plays a major role in

affecting the post-operative outcomes. Balloon post-dilation allows the stent to fully expand and adhere to the wall better, reducing post-operative paravalvular leak, but inevitably leading to a higher vascular stress and increase the risk of injury. Balloon dilation needs to be fully considered in TAVR analysis.

Data availability statement

The original contributions presented in the study are included in the article/Supplementary material, further inquiries can be directed to the corresponding authors.

Author contributions

JL: Conceptualization, Methodology, Software, Writing—original draft. ZM: Formal Analysis, Methodology, Writing—original draft. WY: Formal Analysis, Visualization, Writing—review and editing. WW: Resources, Supervision, Writing—review and editing. LW: Resources, Supervision, Writing—review and editing. SW: Funding acquisition, Supervision, Writing—review and editing.

References

- Abbasi, M., and Azadani, A. N. (2015). Leaflet stress and strain distributions following incomplete transcatheter aortic valve expansion. *J. Biomech.* 48, 3663–3671. doi:10.1016/j.jbiomech.2015.08.012
- Auricchio, F., Conti, M., Morganti, S., and Reali, A. (2014). Simulation of transcatheter aortic valve implantation: a patient-specific finite element approach. *Comput. Method. Biomech.* 17, 1347–1357. doi:10.1080/10255842.2012.746676
- Bailey, J., Curzen, N., and Bressloff, N. W. (2016). Assessing the impact of including leaflets in the simulation of TAVI deployment into a patient-specific aortic root. *Comput. Method. Biomech.* 19, 733–744. doi:10.1080/10255842.2015.1058928
- Barbanti, M., Petronio, A. S., Capodanno, D., Ertori, F., Colombo, A., Bedogni, F., et al. (2014). Impact of balloon post-dilation on clinical outcomes after transcatheter aortic valve replacement with the self-expanding CoreValve prosthesis. *JACC Cardiovasc. Interv.* 7, 1014–1021. doi:10.1016/j.jcin.2014.03.009
- Bianchi, M., Marom, G., Ghosh, R. P., Rotman, O. M., Parikh, P., Gruberg, L., et al. (2019). Patient-specific simulation of transcatheter aortic valve replacement: impact of deployment options on paravalvular leakage. *Biomech. Model. Mechan.* 18, 435–451. doi:10.1007/s10237-018-1094-8
- Dumonteil, N., Terkelsen, C., Frerker, C., Collart, F., Wöhrle, J., Butter, C., et al. (2019). Outcomes of transcatheter aortic valve replacement without predilation of the aortic valve: insights from 1544 patients included in the SOURCE 3 registry. *Int. J. Cardiol.* 296, 32–37. doi:10.1016/j.ijcard.2019.06.013
- Dvir, D., Bourguignon, T., Otto, C. M., Hahn, R. T., Rosenhek, R., Webb, J. G., et al. (2018). Standardized definition of structural valve degeneration for surgical and transcatheter bioprosthetic aortic valves. *Circulation* 137, 388–399. doi:10.1161/circulationaha.117.030729
- Li, J., Yan, W., Wang, W., Wang, S., and Wei, L. (2022). Comparison of balloon-expandable valve and self-expandable valve in transcatheter aortic valve replacement: a patient-specific numerical study. *J. Biomechanical Eng.* 144, 104501. doi:10.1115/1.4054332
- Luraghi, G., Matas, J. F. R., Beretta, M., Chiozzi, N., Iannetti, L., and Migliavacca, F. (2020). The impact of calcification patterns in transcatheter aortic valve performance: a fluid-structure interaction analysis. *Comput. Method. Biomech.* 24, 375–383. doi:10.1080/10255842.2020.1817409
- Maisano, F., Taramasso, M., and Nietlispach, F. (2015). *Prognostic influence of paravalvular leak following TAVI: is aortic regurgitation an active incremental risk factor or just a mere indicator?* Oxford: Oxford University Press.
- McInerney, A., Vera-Urquiza, R., Tirado-Conte, G., Marroquin, L., Jimenez-Quevedo, P., Nuñez-Gil, I., et al. (2021). Pre-dilation and post-dilation in transcatheter aortic valve replacement: indications, benefits and risks. *Interventional Cardiol. Rev. Res. Resour.* 16, e28. doi:10.15420/icr.2020.35
- Miyasaka, M., Tada, N., Taguri, M., Kato, S., Enta, Y., Otomo, T., et al. (2018). Incidence, predictors, and clinical impact of prosthesis-patient mismatch following transcatheter aortic valve replacement in Asian patients: the OCEAN-TAVI registry. *JACC Cardiovasc. Interv.* 11, 771–780. doi:10.1016/j.jcin.2018.01.273
- Morganti, S., Brambilla, N., Petronio, A. S., Reali, A., Bedogni, F., and Auricchio, F. (2016). Prediction of patient-specific post-operative outcomes of TAVI procedure: the impact of the positioning strategy on valve performance. *J. Biomech.* 49, 2513–2519. doi:10.1016/j.jbiomech.2015.10.048
- Morganti, S., Conti, M., Aiello, M., Valentini, A., Mazzola, A., Reali, A., et al. (2014). Simulation of transcatheter aortic valve implantation through patient-specific finite element analysis: two clinical cases. *J. Biomech.* 47, 2547–2555. doi:10.1016/j.jbiomech.2014.06.007
- Nappi, F., Mazzocchi, L., Spadaccio, C., Attias, D., Timofeva, I., Macron, L., et al. (2021). CoreValve vs. Sapien 3 transcatheter aortic valve replacement: a finite element analysis study. *Bioengineering* 8, 52. doi:10.3390/bioengineering8050052
- Nombela-Franco, L., Webb, J. G., de Jaegere, P. P., Toggweiler, S., Nuis, R., Dager, A. E., et al. (2012). Timing, predictive factors, and prognostic value of cerebrovascular events in a large cohort of patients undergoing transcatheter aortic valve implantation. *Circulation* 126, 3041–3053. doi:10.1161/circulationaha.112.110981
- Pagnesi, M., Jabbour, R. J., Latib, A., Kawamoto, H., Tanaka, A., Regazzoli, D., et al. (2016). Usefulness of predilation before transcatheter aortic valve implantation. *Am. J. Cardiol.* 118, 107–112. doi:10.1016/j.amjcard.2016.04.018
- Pibarot, P., Messika-Zeitoun, D., Ben-Yehuda, O., Hahn, R. T., Burwash, I. G., Van Mieghem, N. M., et al. (2019). Moderate aortic stenosis and heart failure with reduced ejection fraction: can imaging guide us to therapy? *JACC Cardiovasc. Imaging* 12, 172–184. doi:10.1016/j.jcmg.2018.10.021
- Spitzer, E., Hahn, R. T., Pibarot, P., de Vries, T., Bax, J. J., Leon, M. B., et al. (2019). Aortic stenosis and heart failure: disease ascertainment and statistical considerations for clinical trials. *Card. Fail. Rev.* 5, 99–105. doi:10.15420/cfr.2018.41.2
- Stoeckel, D., Pelton, A., and Duerig, T. (2019). Self-expanding nitinol stents: material and design considerations. *Eur. Radiol.* 14, 292–301. doi:10.1007/s00330-003-2022-5
- Sturla, F., Ronzoni, M., Vitali, M., Dimasi, A., Vismara, R., Preston-Maher, G., et al. (2016). Impact of different aortic valve calcification patterns on the outcome of transcatheter aortic valve implantation: a finite element study. *J. Biomech.* 49, 2520–2530. doi:10.1016/j.jbiomech.2016.03.036
- Tzamtzis, S., Viquerat, J., Yap, J., Mullen, M. J., and Burriesci, G. (2013). Numerical analysis of the radial force produced by the Medtronic-CoreValve and Edwards SAPIEN after transcatheter aortic valve implantation (TAVI). *Med. Eng. Phys.* 35, 125–130. doi:10.1016/j.medengphys.2012.04.009
- Van Mieghem, N. M., El Faquir, N., Rahhab, Z., Rodríguez-Olivares, R., Wilschut, J., Ouhlous, M., et al. (2015). Incidence and predictors of debris embolizing to the brain during transcatheter aortic valve implantation. *JACC Cardiovasc. Interv.* 8, 718–724. doi:10.1016/j.jcin.2015.01.020
- Vy, P., Auffret, V., Badel, P., Rochette, M., Le Breton, H., Haigron, P., et al. (2016). Review of patient-specific simulations of transcatheter aortic valve implantation. *Int. J. Adv. Eng. Sci. Appl. Math.* 8, 2–24. doi:10.1007/s12572-015-0139-9

Funding

The author(s) declare financial support was received for the research, authorship, and/or publication of this article. This study was partially supported by National Natural Science Foundation of China (No. 11872152, 32,071,310) and Zhuhai Fudan Innovation Institute.

Conflict of interest

The authors declare that the research was conducted in the absence of any commercial or financial relationships that could be construed as a potential conflict of interest.

Publisher's note

All claims expressed in this article are solely those of the authors and do not necessarily represent those of their affiliated organizations, or those of the publisher, the editors and the reviewers. Any product that may be evaluated in this article, or claim that may be made by its manufacturer, is not guaranteed or endorsed by the publisher.



OPEN ACCESS

EDITED BY

Zhen (Jeff) Luo, University of Technology
Sydney, Australia

REVIEWED BY

Tianzhe Bao,
University of Health and Rehabilitation
Sciences, China
Chang Won Jeong,
Wonkwang University, Republic of Korea

*CORRESPONDENCE

Carlo Dindorf,
✉ carlo.dindorf@rptu.de

[†]These authors have contributed equally to this work and share senior authorship

RECEIVED 05 December 2023

ACCEPTED 22 January 2024

PUBLISHED 14 February 2024

CITATION

Dindorf C, Dully J, Konradi J, Wolf C, Becker S, Simon S, Huthwelker J, Werthmann F, Kniepert J, Drees P, Betz U and Fröhlich M (2024), Enhancing biomechanical machine learning with limited data: generating realistic synthetic posture data using generative artificial intelligence.
Front. Bioeng. Biotechnol. 12:1350135.
doi: 10.3389/fbioe.2024.1350135

COPYRIGHT

© 2024 Dindorf, Dully, Konradi, Wolf, Becker, Simon, Huthwelker, Werthmann, Kniepert, Drees, Betz and Fröhlich. This is an open-access article distributed under the terms of the [Creative Commons Attribution License \(CC BY\)](https://creativecommons.org/licenses/by/4.0/). The use, distribution or reproduction in other forums is permitted, provided the original author(s) and the copyright owner(s) are credited and that the original publication in this journal is cited, in accordance with accepted academic practice. No use, distribution or reproduction is permitted which does not comply with these terms.

Enhancing biomechanical machine learning with limited data: generating realistic synthetic posture data using generative artificial intelligence

Carlo Dindorf^{1*}, Jonas Dully¹, Jürgen Konradi², Claudia Wolf², Stephan Becker¹, Steven Simon¹, Janine Huthwelker², Frederike Werthmann³, Johanna Kniepert³, Philipp Drees³, Ulrich Betz^{2†} and Michael Fröhlich^{1†}

¹Department of Sports Science, University of Kaiserslautern-Landau, Kaiserslautern, Germany, ²Institute of Physical Therapy, Prevention and Rehabilitation, University Medical Centre, Johannes Gutenberg University Mainz, Mainz, Germany, ³Department of Orthopedics and Trauma Surgery, University Medical Centre, Johannes Gutenberg University Mainz, Mainz, Germany

Objective: Biomechanical Machine Learning (ML) models, particularly deep-learning models, demonstrate the best performance when trained using extensive datasets. However, biomechanical data are frequently limited due to diverse challenges. Effective methods for augmenting data in developing ML models, specifically in the human posture domain, are scarce. Therefore, this study explored the feasibility of leveraging generative artificial intelligence (AI) to produce realistic synthetic posture data by utilizing three-dimensional posture data.

Methods: Data were collected from 338 subjects through surface topography. A Variational Autoencoder (VAE) architecture was employed to generate and evaluate synthetic posture data, examining its distinguishability from real data by domain experts, ML classifiers, and Statistical Parametric Mapping (SPM). The benefits of incorporating augmented posture data into the learning process were exemplified by a deep autoencoder (AE) for automated feature representation.

Results: Our findings highlight the challenge of differentiating synthetic data from real data for both experts and ML classifiers, underscoring the quality of synthetic data. This observation was also confirmed by SPM. By integrating synthetic data into AE training, the reconstruction error can be reduced compared to using only real data samples. Moreover, this study demonstrates the potential for reduced latent dimensions, while maintaining a reconstruction accuracy comparable to AEs trained exclusively on real data samples.

Conclusion: This study emphasizes the prospects of harnessing generative AI to enhance ML tasks in the biomechanics domain.

KEYWORDS

machine learning, deep learning, spine, variational autoencoder, data augmentation, statistical parametric mapping

1 Introduction

Biomechanics, the study of human movement and its mechanical principles, holds great promise for advancing our understanding of human locomotion, aiding clinical diagnoses, and enhancing athletic performance (Barnes and Kilding, 2015; Ferreira et al., 2016; Ceyssens et al., 2019; Valamatos et al., 2022). In biomechanical data analysis, Artificial Intelligence (AI) and Machine Learning (ML) methods have gained traction (Halilaj et al., 2018; Phinyomark et al., 2018; Dindorf et al., 2022a), yielding promising results, such as in studies involving post-stroke patients (Lau et al., 2009) or Parkinson's disease (Wahid et al., 2015). These approaches excel in handling intricate, multidimensional data, offering objective insights, and pinpointing distinctive group-specific disparities (Horst et al., 2019; Dindorf et al., 2021a). Notably, these methods often outperform traditional statistical analysis methods in related databases (Bzdok et al., 2018; Halilaj et al., 2018; Phinyomark et al., 2018). However, their potential is frequently constrained by persistent challenges such as data scarcity.

Data scarcity refers to a situation in which the available data for analysis or decision-making are limited in quantity, quality, or relevance, often presenting challenges in drawing meaningful insights or conclusions (Alzubaidi et al., 2023). Unlike certain fields, such as image classification, which benefit from vast databases containing millions of images (Deng et al., 2009), biomechanical data frequently encounter limitations, typically comprising only hundreds or a few thousand data points (Horst et al., 2021). These limitations stem from various challenges, including difficulties in participant recruitment, resource constraints, ethical considerations, specialized expertise requirements, and the often expensive and intricate nature of the measurements. Consequently, the development and effectiveness of ML algorithms tailored to biomechanical tasks are impeded by the lack of comprehensive datasets.

Data augmentation is a widely used technique in ML and data science, aimed at artificially expanding the size of a dataset by applying various transformations or modifications to existing data (Bicer et al., 2022). The primary objective of data augmentation is to diversify the training dataset, making it more robust, and reducing overfitting (Lashgari et al., 2020). By introducing variations in the data, the model becomes better at generalizing to unseen examples, consequently enhancing its performance on real-world data. The utilization of data augmentation in ML improves a model's capacity for generalization, which is particularly pronounced in deep learning scenarios (Bicer et al., 2022). For example, in computer vision tasks, data augmentation may encompass randomly rotating or flipping images, changing their color balance, or cropping them differently (Jiang et al., 2020). Similarly, natural language processing techniques can involve paraphrasing sentences, adding synonyms, or introducing typographical errors into the text data (Kang et al., 2021; Bayer et al., 2023).

However, in biomechanics, kinematic data are often presented as tabular or time-series data for dynamic measurements (Horst et al., 2021). In the domain of clinical gait analysis, certain techniques such as magnitude perturbation, temporal perturbation, random rotation, and noise injection have been employed (Kiprijanovska et al., 2020; Tunca et al., 2020;

Paragliola and Coronato, 2021). Alternatively, data augmentation for tabular data may involve generating additional samples by interpolating between existing data points or by applying sampling techniques primarily used for imbalanced datasets (for example, the synthetic minority oversampling technique: SMOTE) (Dindorf et al., 2021a; Iglesias et al., 2023).

Furthermore, there exists considerable promise in leveraging generative models for data generation purposes. Generative models such as Variational Autoencoders (VAEs), Generative Adversarial Networks (GANs), and autoregressive models like transformer-based models represent powerful ML models capable of creating new data samples that closely resemble the training data to which they were exposed (Bicer et al., 2022). These models learn the underlying data distributions and generate data points with similar characteristics. This makes them valuable not only for data augmentation but also for content generation (Hussain et al., 2020) and anomaly detection (Yang et al., 2022). Regarding data augmentation, the synthetic data generated by these models can be combined with the original data, resulting in a larger and diversified dataset for training ML models.

Several studies have explored the application of generative models in analyzing human movement data, highlighting the potential of generative models in the biomechanical domain. Researchers have developed (Takeishi and Kalousis, 2021) a generative model for the human gait that ensures physically realistic outputs by integrating a VAE with a differentiable physics engine, demonstrating its efficacy in gait style transfer. Similarly, Liu et al. (2020) employed a conditional GAN to replicate the kinematic attributes of individuals with lateral collateral ligament injuries in their feet and ankles. Additionally, Luo and Tjahjadi, (2020) utilized conditional GANs to create a parametric three-dimensional (3D) model of the human body, including an underlying skeleton, enabling the synthesis of asymmetrical gait samples. Furthermore, Song et al. (2020) harnessed a Deep Convolutional GAN to create binary images that captured three distinct abnormal gait patterns, encompassing falls, reels, and drags.

Although several studies have emphasized the utility of generative AI in the domain of gait data, only one has addressed posture analysis using 3D spinal computed tomography scans of the lumbar spine (Huang and Zhang, 2023). In response to this pressing issue, we explored whether generative AI can bridge the gap in data scarcity by creating synthetic yet realistic stereographic 3D spinal posture data. By leveraging the capabilities of the VAE, we embarked on the task of generating synthetic posture data. The goal is not only to evaluate whether it is possible to train a VAE on posture data and generate synthetic data, but also to scrutinize whether these synthesized postures can be discerned from genuine data by means of Statistical Parametric Mapping (SPM) and a classification task challenging both domain experts and ML classifiers. Furthermore, this study extends beyond data generation. We explored the practical implications of incorporating synthetic data into the learning process. A critical aspect of this inquiry is the use of an autoencoder (AE) for feature learning based on posture data.

AEs are widely used for denoising tasks in clinical biomechanical data. Previous studies (Mohammadian Rad et al., 2018; Elkholy et al., 2019) have demonstrated their effectiveness in improving the

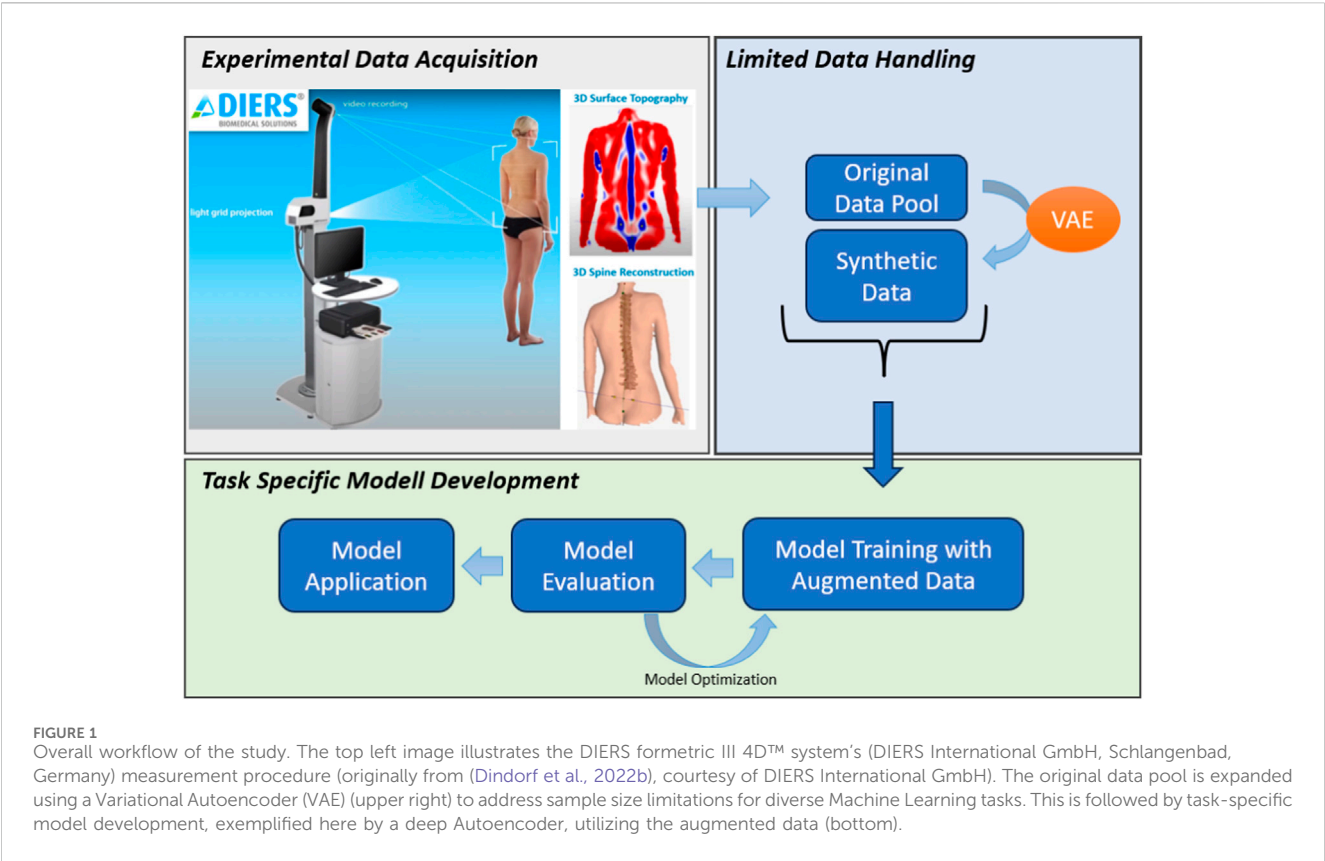


TABLE 1 Subject characteristics and related trials.

	Subjects (n)	Male (n); Female (n)	Age (years)	Hight (cm)	BMI (kg/m ²)	Further information
Healthy ^a (asymptomatic)	201	69; 132	41.28 (13.42)	172.51 (8.19)	23.49 (3.21)	18–70 years; free of pain; no history of surgery or fracture between C7 and pelvis; no medical or therapeutic treatment (C7- pelvis) last 12 months; no medical or therapeutic treatment due to musculoskeletal problems (musculoskeletal system except C7-pelvis) last 6 months; BMI ≤30.0; gait stability; an age- and sex-accorded walking speed and spinal function as well as an appropriate joint mobility to theoretically be able to perform a physiological gait pattern; WHO register (INT: DRKS00010834)
Healthy ^b (asymptomatic)	25	12; 13	34.68 (12.07)	176.28 (8.83)	24.01 (3.45)	Repeated measurements at three points in time; walking without walking aids and pain; no acute or chronic diseases; no pregnancy; BMI <30; WHO register (INT: DRKS00014325)
Back pain	32	14; 18	44.53 (14.84)	174.00 (11.00)	26.01 (4.79)	Area of pain: 6% thoracic spine (TS), 72% lumbar spine (LS), and 22% TS + LS; no acute fractures, walking restraints, or acute/chronic illnesses that prevent safe walking; WHO register (INT: DRKS00013145)
Spinal fusion	34	20; 14	56.26 (15.40)	171.00 (11.00)	26.95 (4.43)	Spinal fusion somewhere between C7 and L5; no acute fractures, walking restraints, or acute/chronic illnesses that prevent safe walking; WHO register (INT: DRKS00013145)
Osteoarthritis	60	29; 31	64.00 (11.27)	171.00 (9.15)	25.68 (2.35)	30 knee osteoarthritis and 30 hip osteoarthritis; walking without walking aids; no walking impairments that prevent safe walking; no acute or chronic diseases; no pelvic or spinal surgery; no pregnancy; BMI <30; WHO register (INT: DRKS00017240)

^aThe dataset is part of the dissertation project of Janine Huthweller. For more details see (Huthweller et al., 2023).
^bThe dataset is part of the dissertation project of Friederike Werthmann.
Abbreviations: BMI: body mass index, SD: standard deviations, WHO: world health organization, TS: thoracic spine, LS: lumbar spine, C: cervical, L: lumbal.

discriminative capabilities of models. In various domains, it has been observed that feeding features reconstructed by AEs to a discriminative model as input often yields superior accuracy compared with using the original data (Marchi et al., 2015; Zhao T. et al., 2017; Tu et al., 2020). The latent space of the AE proves to be a valuable resource for automatic feature extraction, a technique that has shown significant utility in other studies (Nguyen et al., 2018; Zaroug et al., 2020; Yang and Yin, 2021). For example, by utilizing latent space in conjunction with other ML models, enhanced performance in various tasks has been demonstrated (Hernandez et al., 2020).

Given the pivotal role of AEs in biomechanical data analysis, enhancing their reconstruction accuracy holds immense value. Consequently, we sought to elucidate whether augmenting the training dataset with generated synthetic postures can lead to reduced reconstruction errors and a more compact feature representation of an AE without sacrificing reconstruction accuracy.

2 Materials and methods

The comprehensive workflow is outlined in Figure 1 for a concise overview. Subsequent sections will furnish detailed insights into each step delineated in the figure.

2.1 Subjects and data acquisition

In four separate studies, data were collected from 353 participants. Depending on the study design, as outlined in Table 1, each subject underwent postural data collection for the spine on one or three distinct days. During each session, an average of 12–14 individual images was captured for each subject. This data collection encompassed both healthy individuals and those with various pathologies, such as back pain, spinal fusion, and osteoarthritis. The DIERS formetric III 4D™ system, specifically DICAM v3.7 analyzing software (DIERS International GmbH, Schlangenbad, Germany), was employed as a non-invasive means of rasterstereography, also known as surface topography (ST). Detailed information regarding the participants' characteristics is presented in Table 1. This method enables comprehensive spinal measurements across all body planes without requiring invasive radiation-based techniques or extensive preparation.

We utilized fifty-four static parameters from the system, including measurements such as pelvic obliquity (°), pelvic inclination (dimples) (°), pelvic rotation (°), as well as the orientation of VP, T1–T12, and L1–L4 in all planes (°), as part of our modeling process. Supplementary Table S1 provides a comprehensive description of these parameters.

Subsequently, for each participant, we randomly selected three samples without replacement for further calculations. We employed the isolation forest technique (500 trees) to effectively identify and address multivariate outliers. This approach has been demonstrated to be effective in various studies involving kinematic data (Dindorf et al., 2021b; Yee et al., 2021). Consequently, from our initial dataset of 1059 samples, we removed 66 outliers using this method, resulting in a final total of 993 samples, derived from 338 subjects for further analysis.

Although multiple classes of healthy subjects and pathologies were present (Table 1), a single VAE was trained using all the available data. This decision was based on several key considerations.

Insufficient sample sizes were available for each individual class, making it impractical to effectively train separate VAEs for each class.

Previous studies have highlighted the difficulty of discriminating between respective classes, such as distinguishing healthy postures from pathological ones, using ML classifiers (Dindorf et al., 2021b). This suggests that there is limited class-specific information that can be exploited.

Opting for a single VAE offers the advantage of capturing shared patterns and common features that potentially exist across various classes. This approach aims to uncover the underlying similarities that might be overlooked by class-specific models.

By employing a single VAE, the model was designed to learn a universal latent space that remained independent of class labels. This allowed the model to focus on extracting general representations that were common to all classes without being biased by class-specific distinctions.

2.2 General workflow and evaluation procedure

Model development, training, and evaluation of the VAE and AE were integrated into a grouped k-fold cross-validation process ($k = 5$). In each cross-validation fold, the data underwent random partitioning, with approximately 70% assigned to training, 10% to validation, and 20% to testing (the proportion of test data for each fold is given by $k = 5$). It was ensured that subject-specific data, considering multiple measurements per subject, remained separate across the sets. The corresponding specific workflow is illustrated in Figure 2. The utilization of grouped k-fold splitting, a method that prevents subject-specific data from being concurrently included in the training, validation, and test sets, offers several advantages. This approach facilitates improved hyperparameter tuning and early detection of overfitting. Furthermore, this method enhances the robustness of the model evaluation by considering the variability across different training instances. Additionally, by ensuring that subject-specific data are not mixed across the training and evaluation sets, it becomes possible to assess how well the models can be generalized to new, previously unseen subjects or data points, thereby providing a more comprehensive evaluation of the model's performance. The steps pertaining to this workflow are described in detail in the following sections.

2.3 VAE implementation

For data generation in our study, we opted for a VAE over a GAN for several compelling reasons. GANs typically require a more extensive and diverse dataset to perform effectively. They thrive when presented with substantial amounts of data that capture intricate patterns and nuances. GANs are sensitive to hyperparameter choices and can suffer from issues such as mode collapse (Saxena and Cao, 2022). In this case, the posture data were

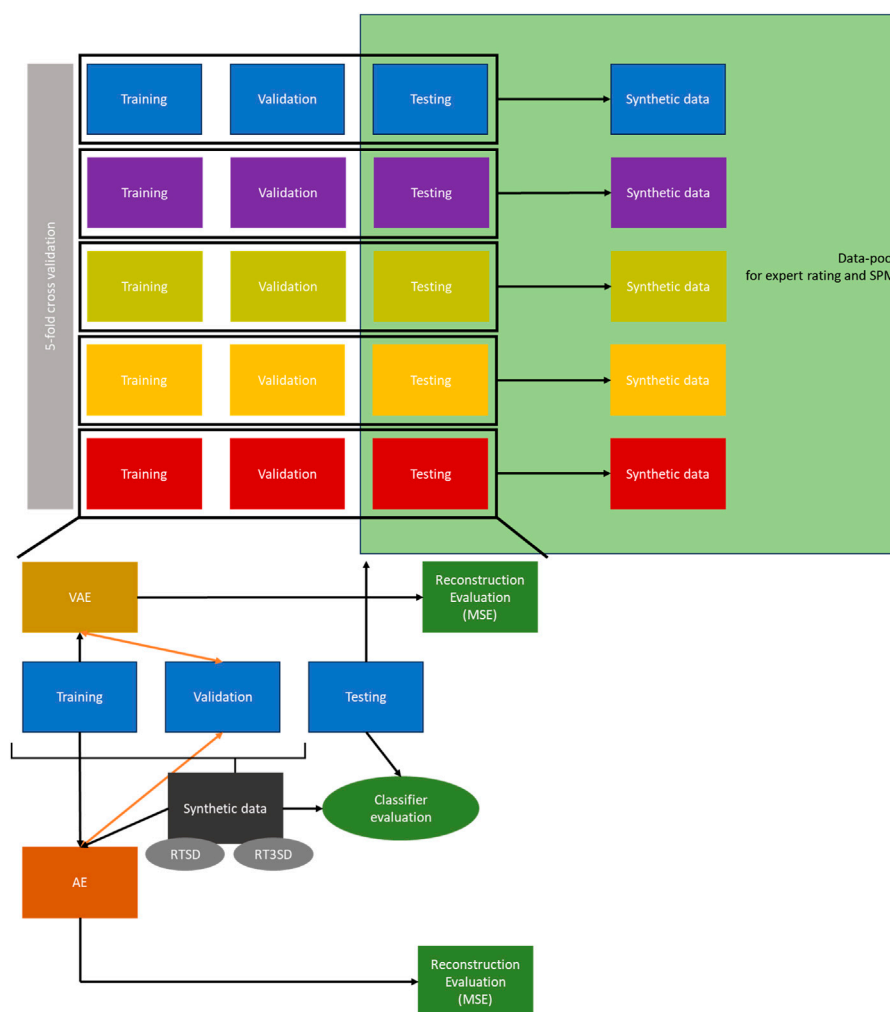


FIGURE 2

Workflow of the generation, testing and evaluation of the synthetic data. RTSD = dataset with 50% real, 50% synthetic data; RT3SD = dataset with 25% real, 75% synthetic data; MSE = Mean Squared Error; SPM = Statistical Parametric Mapping; AE = Autoencoder; VAE = Variational Autoencoder.

not sufficiently extensive to fully harness the potential of the GAN. Our preliminary study, which involved exploratory work with the available posture data, confirmed that VAE outperformed GANs when considering our dataset in terms of both the data quality and stability observed during the training process.

A VAE is an artificial neural network employed for generative tasks. It functions by encoding the input data into a lower-dimensional latent space and then decoding it back into the original data space. The key innovation of a VAE is its ability to model probability distributions in a latent space, allowing it to generate new similar data samples by sampling from these distributions. This makes VAEs particularly useful for tasks, such as data generation, denoising, and representation learning. In short the general information flow in a VAE can be described as the following (please refer to (Zhao S. et al., 2017) for a detailed description):

The encoder takes input data x and produces parameters for a probability distribution over the latent space. Let z be the latent variable, $q(z|x)$ is the approximate posterior distribution, $p(z)$ is the prior distribution (usually a standard Gaussian), and $\mu(x)$ and $\sigma(x)$

are the mean and standard deviation predicted by the encoder. The latent variable z is sampled from the distribution:

$$Z \sim N(\mu(x), \sigma(x)^2)$$

The decoder takes the sampled latent variable z and reconstructs the input data x . The conditional distribution of the data given the latent variable is modeled as $p(x|z)$. The reconstructed data \hat{x} is sampled from this distribution.

The training objective for a VAE is based on the Evidence Lower Bound (ELBO), which is defined as follows:

$$\text{ELBO} = E_{(q(z|x))} [\log p(x|z)] - \text{KL}[q(z|x) \parallel p(z)]$$

The first term is the reconstruction term, encouraging the model to generate data similar to the input. The second term is the regularization term, penalizing the divergence between the learned latent distribution $q(z|x)$ and the prior distribution $p(z)$.

The information flows from the input data through the encoder to the latent space, and then from the latent space through the

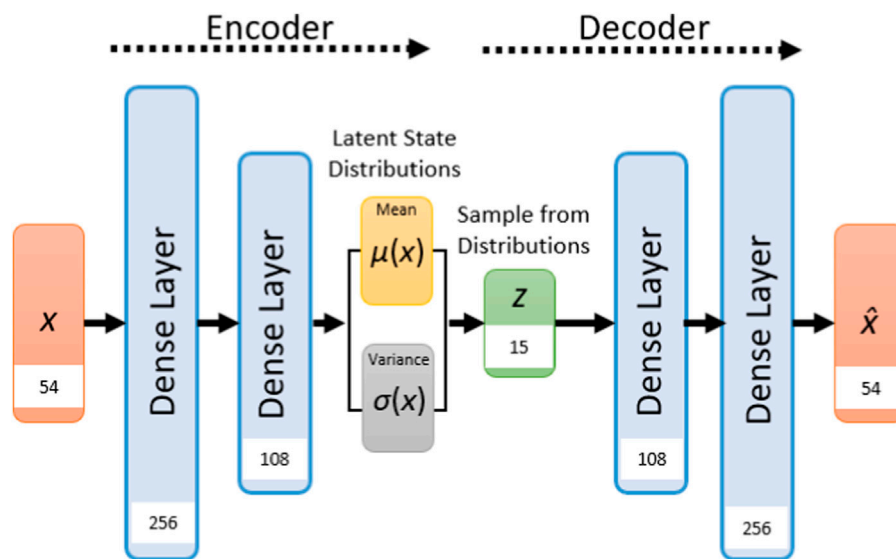


FIGURE 3
Visualization of the VAE architecture in the current study. The values in the white boxed represent the layer sizes.

decoder to reconstruct the data. The objective during training is to maximize the ELBO, thereby encouraging the model to learn a useful latent representation of the input data.

It aims at a smaller latent dimension than the original number of features to capture the most important features and reduce the complexity of data representation by learning a more compact representation of the data. Furthermore, this proved useful because the smaller latent dimensions acted as a form of regularization, preventing the VAE from overfitting the training data (Mahmud et al., 2020). In addition, it has been suggested that when the latent dimension is smaller, the decoder must generate data with fewer degrees of freedom, which can lead to more coherent and structured generated samples (Zhao et al., 2019).

To determine the model architecture, a grid hyperparameter search was performed based on the accuracy of the combined losses (reconstruction loss and KL divergence loss) in the validation set. We varied the latent vector length (5, 10, 15, and 20), two hidden layer sizes for the encoder and decoder (54, 108, 256, and 500), batch size (32, 64, and 128), learning rate (0.01, 0.001, and 0.0001), and number of epochs (200, 400, 600, and 1,000). The VAE model employs an Adam optimizer to minimize the combined loss function. Based on each training set, scaling was applied using StandardScaler from Scikit-learn (Pedregosa et al., 2011). The final model has the following configuration:

The encoder network operated on the input posture data (shape: 54) through two dense layers with specific sizes of 256 and 108, utilizing both Rectified Linear Unit (ReLU) activation functions. These layers reduced the input data to a latent space of 15 dimensions. This is followed by a symmetric decoder section comprising two corresponding dense layers, both employing ReLU activation, and an additional final layer employing linear activation. The epochs were set to 400 with a learning rate of 0.001, and a batch size of 128. For a visual representation of the architecture of the VAE please refer to Figure 3.

Although the intermediate losses employed during VAE training are pivotal for the training process, they may not be as informative or comparable. Instead, we report the Mean Squared Error (MSE) to evaluate the reconstruction errors and conduct model comparisons.

2.4 Evaluation synthetic data

To evaluate the distinguishability of synthetic data from real data, we adopted three distinct approaches: (a) judgment by domain experts, (b) implementation of an ML classifier, and (c) statistical evaluation using SPM.

First, we generated synthetic data for each VAE model during cross-validation of the required size (see below). Therefore, random sampling from a standard Gaussian distribution was performed to generate latent vectors. These latent vectors are then passed through the decoder component of the trained VAE model. Subsequently, we combined the original data from the test set with synthetic data, enabling us to perform the identification tasks denoted as (a), (b), and (c). For expert-based evaluation (a) and SPM analysis (c), we rescaled the feature values to match the scale and distribution of the original data. This was done to ensure that the experts could assess the data in an accustomed manner while preserving the fidelity of their evaluation process:

a) In the expert-based evaluation, we opted for a random subset of 100 real and 100 synthetic data samples because a comprehensive assessment was economically infeasible due to constraints on the experts. Therefore, for each fold, we randomly selected and combined ten real samples from the test set with ten synthetic samples generated by the respective VAE model. Each sample underwent an independent evaluation by three experts, and the final expert-based classification was determined via a majority vote. These experts possessed extensive experience working with spinal data and were familiar with the dataset. During the evaluation, the data were presented visually, similar to the illustration in Figure 4.

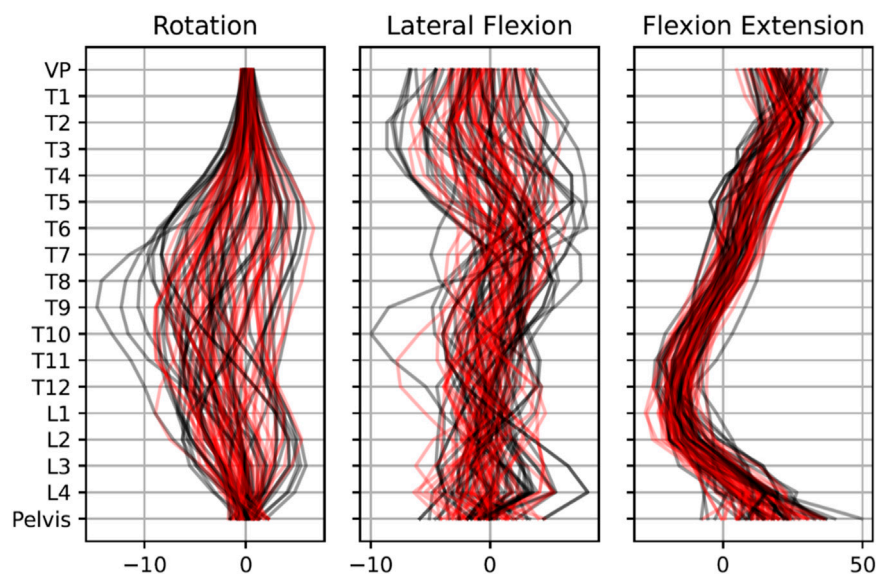


FIGURE 4
Visual comparison of 50 exemplary real (black line) and 50 exemplary synthetic (red line) data samples. Data are rescaled to original feature space.

The expert ratings were organized, and the accuracy for each rater and across all ratings was calculated using MATLAB (MathWorks, Natick, Massachusetts, United States). The loose majority voting was calculated based on (Ballabio et al., 2019). Fleiss' kappa was calculated using the SPSS software (IBM, Armonk, New York, United States).

b) We conducted a supervised classification task to discriminate between real (all test set samples) and synthetic samples equal in size to the test set. To achieve this, we employed a k-nearest neighbour classifier with $k = 10$. The other parameters were set to the default scikit-learn parameters (Pedregosa et al., 2011). To gauge the effectiveness of the classifier in distinguishing between the two data types, we leveraged the cross-validation accuracy score derived from a 5-fold cross-validation procedure.

c) For further evaluation of the synthetic data based on (Bicer et al., 2022) the statistical difference between the synthetic and real data for each vertebrae in the anatomical plane were compared employing a non-parametric 1D two-tailed unpaired t -test ($\alpha = 0.05$) using the spm1d package (Pataky et al., 2013) in MATLAB. Hence, in the actual dataset, a single sample was randomly chosen for each subject. A synthetic dataset of equal size ($n = 338$) was created by randomly selecting synthetic samples generated during the cross-validation folds.

2.5 Use case evaluation AE

For present studies that use case evaluation, the primary emphasis should be dimensionality reduction. We do not focus on the generative capabilities or probabilistic modeling offered by VAEs. Our objective is to establish a deterministic mapping from the input data to a latent representation, ensuring that similar input data points are consistently mapped to similar points in the latent space

without introducing any randomness. To satisfy these criteria, we chose to utilize an AE because it does not introduce a probabilistic element that could result in variations within the latent-space representations. Second, AEs are simpler to implement and incur less computational overhead. Unlike VAEs, AEs do not require complex probabilistic modeling or variational inference techniques.

We evaluated the potential usefulness of artificially created posture data using the VAE training of the AE in three different scenarios:

- Utilizing only the unaugmented data as training data, referred to as *RTD* (100% real training data).
- Employing the real data combined with synthetic data in equal proportions in the training dataset, denoted as *RTSD* (50% real, 50% synthetic).
- Expanding the real data with synthetic data three times its size, labelled as *RT3SD* (25% real, 75% synthetic).

For augmented data generation, we randomly selected one trained VAE model that resulted from the cross-validation process and created synthetic data of the respective sizes, as described in the previous section.

The AE was trained during grouped k-fold cross-validation, similar to the training of the VAE ($k = 5$), to assess how well the AE could generalize its learned representations to new, previously unseen subjects. Scaling was applied based on each training set (without synthetic data) using StandardScaler from Scikit-learn.

Similar to VAE, a grid hyperparameter search guided by the validation set accuracy using unaugmented data was performed. The latent dimension was set to be equal to that of the VAE, and the number of hidden layers was set to three. The hidden layer sizes (25, 50, 100, 250, and 500) of the encoder and decoder, batch sizes (32,

TABLE 2 MSE results for the VAE and AE for each cross-validation fold, as well as mean and SD (bold values) over all folds. Data: RTD = 100% real training data; RTSD = 50% real, 50% synthetic; RT3SD = 25% real, 75% synthetic.

Fold	VAE			AE (latent dim. 15)						AE (latent dim. 7)					
	Train MSE	Val. MSE	Test MSE	RTD		RTSD		RT3SD		RTD		RTSD		RT3SD	
				Train MSE	Test MSE	Train MSE	Test MSE	Train MSE	Test MSE	Train MSE	Test MSE	Train MSE	Test MSE	Train MSE	Test MSE
1	0.01	0.14	0.15	0.02	0.17	0.01	0.01	0.01	0.01	0.17	0.34	0.10	0.07	0.05	0.06
2	0.01	0.13	0.13	0.07	0.19	0.01	0.02	0.01	0.02	0.18	0.33	0.07	0.08	0.11	0.12
3	0.01	0.11	0.13	0.04	0.18	0.01	0.02	0.01	0.01	0.18	0.30	0.08	0.08	0.10	0.09
4	0.01	0.10	0.12	0.01	0.15	0.01	0.01	0.01	0.01	0.14	0.35	0.09	0.08	0.06	0.06
5	0.01	0.18	0.11	0.01	0.14	0.01	0.09	0.01	0.09	0.17	0.29	0.03	0.39	0.04	0.37
Mean	0.01	0.13	0.13	0.03	0.17	0.01	0.03	0.01	0.03	0.17	0.32	0.07	0.14	0.08	0.14
SD	0.00	0.03	0.01	0.03	0.02	0.00	0.03	0.00	0.04	0.02	0.02	0.03	0.14	0.03	0.13

64, and 128), and learning rates (0.01, 0.001, and 0.0001) were varied. Early stopping was integrated into the training procedure, which involved monitoring the validation loss and restoring the best weights when necessary, with a patience setting of 10 epochs and a maximum of 1,000 epochs. This approach led to the final deep AE configuration as follows:

The model was structured with an encoder section featuring three dense layers (500, 250, and 50 units in the first, second, and third layers, respectively), which collectively reduced the input data into a 15-dimensional latent space. This was followed by a symmetric decoder section consisting of three corresponding dense layers. All of these layers utilize ReLU activation functions, except for the final layer of the encoder and decoder, which employs a linear activation function. To train the AE, we employed the MSE loss function in combination with the Adam optimizer (learning rate = 0.001) and a batch size of 64.

Finally, we explored the potential for reducing the latent dimension while maintaining the same reconstruction accuracy as in the unaugmented data by augmenting the training data while preserving other hyperparameters. This exploration was guided by a manual search procedure that considered the accuracy of the validation set.

2.6 Statistics and further calculations

Modeling was implemented using the TensorFlow (Abadi et al., 2016) and Keras (Chollet, 2015) frameworks. Visualization was performed employing matplotlib (Hunter, 2007). Visual exploration of the latent space was performed with Uniform Manifold Approximation and Projection for Dimension Reduction (UMAP) (McInnes et al., 2018).

3 Results

3.1 VAE and synthetic data evaluation

The reconstruction errors of the trained VAE are listed in Table 2. Subsequently, the trained VAE was employed to generate synthetic data. Both generated synthetic data samples as well as real posture data samples are visually presented and compared alongside each other in Figure 4. Notably, there were no discernible systematic differences between the real and synthetic data when viewed visually. This was also statistically confirmed by the SPM, which showed that for no vertebrae, the difference between the real and synthetic data was significant (Figure 5).

The results of the ML and expert-based evaluations assessing the separability of real and synthetically generated posture data using the VAE are presented in Table 3. Both the ML classifier and human experts struggled to accurately distinguish between synthetic and real data, with experts exhibiting a notably poorer performance than the ML classifier.

The first rater’s accuracy was 52.00%, the second one achieved 51.00%, and the third rater rated 53.50% of all cases correctly. The interrater reliability is calculated at $\kappa = .073$ indicating that only slight agreement between the raters (Landis and Koch, 1977). Loose majority vote (50%) shows data was more often rated as real (real = 307, synthetic = 293).

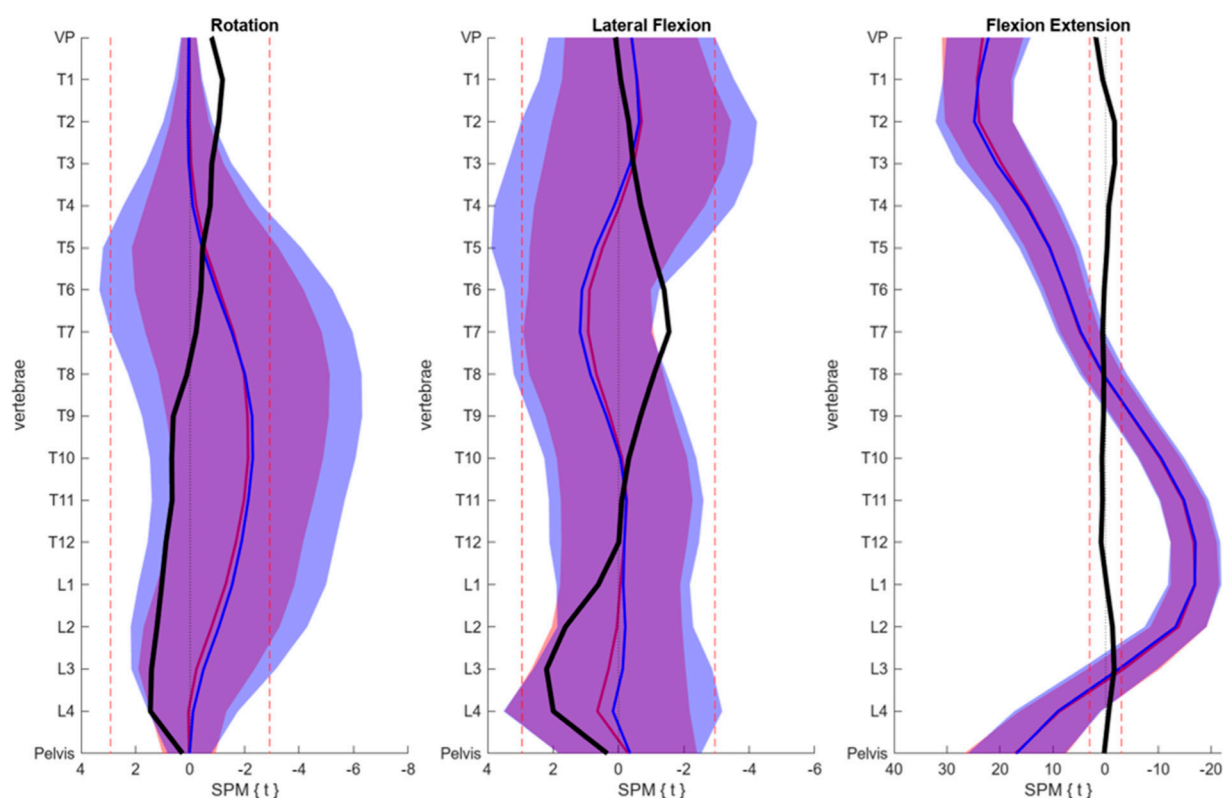


FIGURE 5
SPM results displayed for each anatomical plane. The blue line and area each represent the mean and SD of the real data, while the red line corresponds to synthetic data. The red dotted lines indicate the critical t-values, signifying the absence of significant differences in-between. Additionally, the black line depicts the t-values observed for each vertebra.

3.2 Use case evaluation AE

The reconstruction errors for the AE and the real and augmented datasets are listed in Table 2. An evident enhancement of more than five times in the accuracy of the test set reconstruction becomes strikingly apparent when the training data are expanded with synthetic data using the VAE. This improvement was particularly prominent when using synthetic data of equal proportions in training (RTSD). Extending the original data to three times its size (RT3SD) only slightly reduced the test-set reconstruction error.

The impact of this augmentation on the reconstruction quality becomes apparent when visually comparing the performance of the AE with and without the inclusion of synthetic data. This comparison demonstrates the superior reconstruction with the augmented dataset (see Figure 6).

Explorative reduction of the latent dimension from 15 to seven while keeping the other hyperparameters leads to a slightly better reconstruction performance of the AE while training with the augmented data compared to training only on the unaugmented data with a latent space of 15. In contrast, when using only the unaugmented data RTD with three latent dimensions, the performance deteriorated significantly.

Visualization exploration of the latent space using UMAP (McInnes et al., 2018) (Figure 7) shows no clearly visible clusters

and no clear grouping of the datasets used for the study (healthy, back pain, spinal fusion, osteoarthritis).

4 Discussion

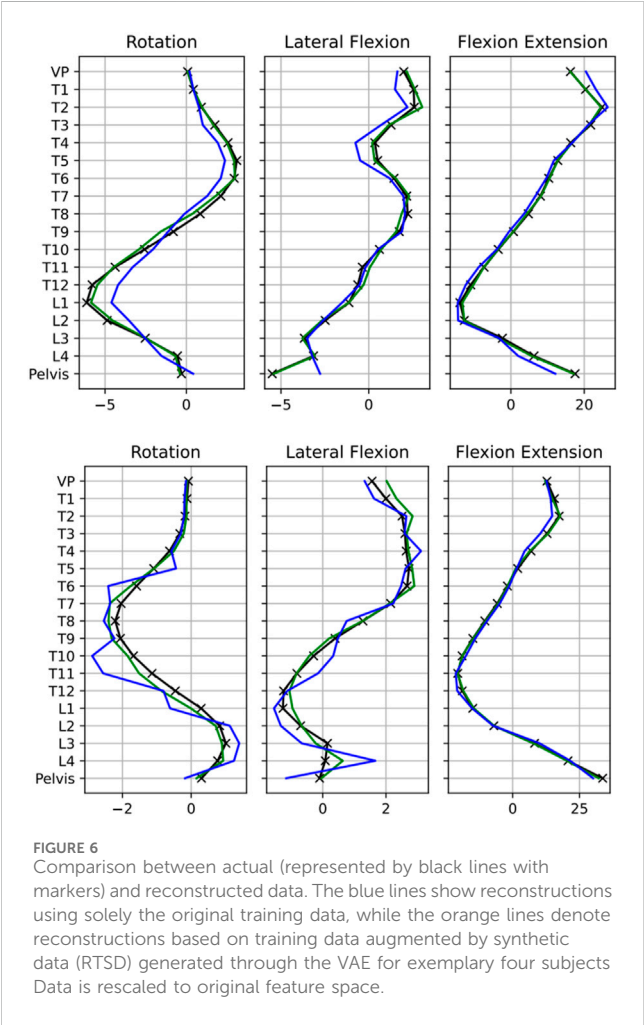
This study addresses a critical issue in the field of biomechanics: scarcity of data for the development of ML models. Our exploration of the use of generative AI to generate synthetic posture data offers promising insights into how limited data challenges can be mitigated and how biomechanical ML can be enhanced.

The promising results regarding loss reduction, as well as the low MSE values for data reconstruction, indicate the VAE's ability to capture the underlying features of the data distribution and show that it is generally possible to develop a VAE model on posture data. Our results align with those of recent biomechanical studies that have successfully applied Variational VAEs to capture essential data distribution features (Huang and Zhang, 2023; Kneifl et al., 2023).

Addressing the quality of synthetic data is of pivotal concern when it is applied to ML tasks. The synthetic data closely mirror the characteristics of the real data (Sharifi Renani et al., 2021). However, evaluating the quality of the synthetic data in the absence of a definitive benchmark dataset is challenging. Although various quantitative metrics have been suggested (Zhou et al., 2019), their applicability in the biomechanical context remains limited (Bicer et al., 2022). To overcome this challenge,

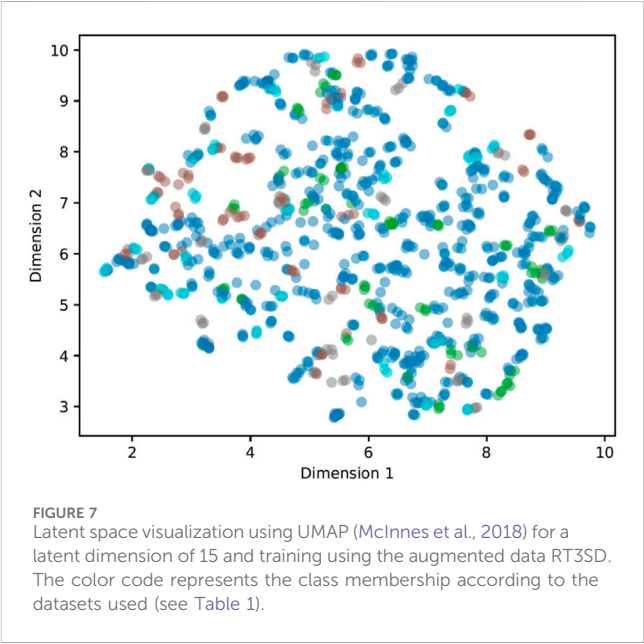
TABLE 3 Separability as classification results or real and synthetic posture data comparing experts and human performance.

Accuracy		ML evaluation		Human experts' evaluation	
		66.53% \pm 2.72%		52.17% (κ = .073)	
		Actual real	Actual synthetic	Actual real	Actual synthetic
Confusion Matrix	Predicted real	562	234	160	147
	Predicted synthetic	431	759	140	153



we adopted a comprehensive evaluation approach for synthetic data, encompassing both objective assessments through ML classification and SPM and subjective evaluations through expert ratings.

Visually, the synthetic data closely resemble the real data. On a statistical basis, employing SPM, no discernible differences were detected between the real and synthetic data. Moreover, when evaluated by both ML classifiers and domain experts, distinguishing between real and synthetically generated posture data proved highly challenging. The experts exhibited minimal-to-negligible consensus, underscoring the inherent challenges of such assessments. This multifaceted evaluation collectively indicates that the synthetic data generated by the VAE exhibit a high level of quality and maintain consistency with the real-world posture data. Consequently, it can be



concluded that the proposed VAE is highly effective for generating synthetic posture data that accurately emulate real data.

Incorporating synthetically generated posture data into the ML process, here with the use case example of an AE, yielded notable improvements in training and test set reconstruction accuracy. This is in line with several studies that demonstrated that AE benefits from larger datasets (Zhao et al., 2015). When incorporating synthetic data, a remarkable improvement in the accuracy of the test set reconstruction became evident, with a more than seven-fold reduction in the test set MSE compared with using unaugmented data for training. These results suggest that augmenting the training data for training an AE with synthetic examples by means of a VAE not only enhances the model's ability to reconstruct the data it was trained on but also improves its generalization to unseen test data, which has also been reported in other works (Wan et al., 2017; Kornish et al., 2018).

It is important to note that alternative approaches to data augmentation have the potential to enhance model performance when dealing with limited data. For instance, transfer learning, an ML technique, allows a model to leverage the knowledge gained from a previous task to enhance its generalizability to a new task. Transfer learning compensates for the scarcity of labeled data by transferring knowledge from other well-labeled data sources. To address the shortage of abnormal gait data, researchers have (Pandit et al., 2019; Martinez and Leon, 2020) employed various neural networks pretrained on extensive

datasets. One approach of interest could involve combining transfer learning with subsequent training on augmented data.

Visual exploration of the latent space revealed a notable absence of distinct clusters and clear groupings among the datasets used in this study, encompassing postures categorized as healthy and those associated with back pain, spinal fusion, and osteoarthritis. This finding underlines the challenges in discriminating between healthy and pathological postures, a hurdle that previous research has highlighted when employing ML classifiers without the benefit of feature learning techniques (Dindorf et al., 2021b). Considering these challenges, the findings of this study are comprehensible and contribute to the current state of research by demonstrating that even the application of feature learning through an AE does not yield a discernible enhancement in discriminability.

Notably, our VAE was not trained separately for each class for the aforementioned reasons, which may have resulted in a mixed latent space in which class-specific information was not well separated. Consequently, class-specific discriminative characteristics may not be as pronounced in the synthetic data, potentially impeding the formation of discernible clusters. Future research should consider including dynamic movement data from the spine as a promising direction. The dynamic aspects of posture and movement could potentially offer more distinctive class differences, potentially facilitating the identification of clusters; hence, there is significant inter-subject variability in spine movement, for example, during gait (Prost et al., 2021). In the context of distinguishing between biological sexes, recent findings have indicated a significant improvement in classification accuracy when utilizing dynamic data as opposed to relying solely on static data (Dindorf et al., 2021c). This highlights the potential of using dynamic data to enhance the accuracy of classification models for specific applications.

Although our research has yielded promising insights into the use of generative AI to address data scarcity in biomechanical ML, it is crucial to acknowledge several limitations that should be considered when interpreting the results and planning future studies. Despite the favorable results in distinguishing synthetic data from real data, it is important to mention that there may still be subtle differences between the two. Synthetic data, although visually and quantitatively similar, may not capture all of the intricacies of real-world biomechanical postures, potentially leading to limitations in specific applications where extreme precision is required.

This study primarily relied on a specific dataset obtained from a particular group of subjects via surface topography. The effectiveness of the generative AI approach may vary when applied to different biomechanical datasets or to data collected using diverse measurement techniques. The ability of the model to be generalized to broader and more diverse populations requires further investigation.

Although our results demonstrate the benefits of augmenting the training dataset with synthetic data, the optimal balance between real and synthetic data remains an open question. The study could only show that with the current AE expanding the real data with synthetic data to three times their size (RT3SD) slightly improved the reconstruction performance compared to real data combined with synthetic data of equal proportions (RTSD). Further research is required to explore the potential impacts of varying proportions of synthetic data.

The use of synthetic data in healthcare raises ethical concerns. On one hand, it mitigates privacy risks by minimizing the demand for additional patient data, thereby reducing the risk of data breaches. However, synthetic data may not fully represent the complexities of actual patient data, potentially leading to biased or inaccurate outcomes. The extent to which accountability applies, in this case, must be discussed in a context-specific manner.

Future directions may involve extending the application of generative AI to other biomechanical domains such as dynamic spinal data. An increase in the volume of accessible posture data has the potential to significantly enhance the applicability of GANs. Therefore, a future comparative analysis between GANs and the approach presented in this study, if feasible, is considered important. Additionally, investigating the impact of synthetic data on various ML architectures or distinct tasks, such as regression or classification, is a promising area of research. In the context of gait data, deep generative models combined with differentiable physics engines have been proposed to ensure that the generated data are in line with physical laws (physically informed modeling) (Takeishi and Kalousis, 2021). The adoption of this methodology in the context of posture data could ensure the realism of the generated data and should be evaluated in future studies. Furthermore, an intriguing direction for future research could be the exploration of an extended VAE that conditions data generation or reconstruction on additional information, such as class labels, or other attributes, such as biological sex. This exploration is particularly relevant as existing studies highlight the presence of biological sex differences in spinal data (Yukawa et al., 2018; Mohan and Huynh, 2019; Ludwig et al., 2023). These models, known as Conditional Variational Autoencoders (CVAEs) (Zhao T. et al., 2017), can accentuate the class membership, potentially leading to the generation of more realistic posture data by incorporating additional subject characteristics. To the best of our knowledge, this application has not been explored in the biomechanical domain.

5 Conclusion

In summary, our study underscores the potential of generative AI, specifically VAEs, in addressing data-scarcity challenges within the biomechanics field. By generating synthetic posture data that closely mirror real-world observations, our study presents a viable approach path for expanding datasets, strengthening model performance, and advancing biomechanical applications.

Data availability statement

The datasets for this article are not publicly available due to concerns regarding participant/patient anonymity. Requests to access the datasets should be directed to the corresponding author.

Ethics statement

The studies involving humans were approved by the Medical Chamber Rhineland-Palatinate and registered with the WHO (INT: DRKS00010834, DRKS00014325, DRKS00013145, and DRKS00017240). The studies were conducted in accordance with

the local legislation and institutional requirements. The participants provided their written informed consent to participate in this study.

Author contributions

CD: Conceptualization, Formal Analysis, Investigation, Methodology, Software, Validation, Visualization, Writing–original draft, Writing–review and editing. JD: Conceptualization, Formal Analysis, Investigation, Methodology, Software, Visualization, Writing–original draft, Writing–review and editing. JKo: Funding acquisition, Investigation, Project administration, Supervision, Writing–original draft, Writing–review and editing. CW: Investigation, Writing–original draft, Writing–review and editing. SB: Conceptualization, Writing–original draft, Writing–review and editing. SS: Writing–original draft, Writing–review and editing. JH: Data curation, Investigation, Writing–review and editing. FW: Data curation, Investigation, Writing–review and editing. JKn: Data curation, Investigation, Writing–review and editing. PD: Funding acquisition, Project administration, Resources, Writing–review and editing. UB: Funding acquisition, Project administration, Resources, Writing–review and editing. MF: Funding acquisition, Project administration, Resources, Writing–review and editing.

Funding

The author(s) declare financial support was received for the research, authorship, and/or publication of this article. This research received support from the AI Junior Research Funding Program at the University of Kaiserslautern-Landau.

References

- Abadi, M., Barham, P., Chen, J., Chen, Z., Davis, A., Dean, J., et al. (2016). “[TensorFlow]: a system for {Large-Scale} machine learning,” in *{TensorFlow}: a system for {Large-Scale} machine learning*. Editor K. Keeton (United States: USENIX Association), 265–283.
- Alzubaidi, L., Bai, J., Al-Sabaawi, A., Santamaría, J., Albahri, A. S., Al-dabbagh, B. S. N., et al. (2023). A survey on deep learning tools dealing with data scarcity: definitions, challenges, solutions, tips, and applications. *J. Big Data* 10 (1), 46–82. doi:10.1186/s40537-023-00727-2
- Ballabio, D., Todeschini, R., and Consonni, V. (2019). Recent advances in high-level fusion methods to classify multiple analytical chemical data. *Data Handl. Sci. Technol.* 31, 129–155. doi:10.1016/B978-0-444-63984-4.00005-3
- Barnes, K. R., and Kilding, A. E. (2015). Strategies to improve running economy. *Sports Med.* 45 (1), 37–56. doi:10.1007/s40279-014-0246-y
- Bayer, M., Kaufhold, M.-A., Buchhold, B., Keller, M., Dallmeyer, J., and Reuter, C. (2023). Data augmentation in natural language processing: a novel text generation approach for long and short text classifiers. *Int. J. Mach. Learn. Cybern.* 14 (1), 135–150. doi:10.1007/s13042-022-01553-3
- Bicer, M., Phillips, A. T. M., Melis, A., McGregor, A. H., and Modenese, L. (2022). Generative deep learning applied to biomechanics: a new augmentation technique for motion capture datasets. *J. Biomech.* 144, 111301. doi:10.1016/j.jbiomech.2022.111301
- Bzdok, D., Altman, N., and Krzywinski, M. (2018). Statistics versus machine learning. *Nat. Methods* 15 (4), 233–234. doi:10.1038/nmeth.4642
- Ceyssens, L., Vanelderden, R., Barton, C., Malliaras, P., and Dingenen, B. (2019). Biomechanical risk factors associated with running-related injuries: a systematic review. *Sports Med.* 49 (7), 1095–1115. doi:10.1007/s40279-019-01110-z
- Chollet, F. (2015). *Keras*. Available at: <https://github.com/fchollet/keras>.
- Deng, J., Dong, W., Socher, R., Li, L.-J., Li, K., and Fei-Fei, Li (2009). “ImageNet: a large-scale hierarchical image database,” in *ImageNet: a large-scale hierarchical image database* (IEEE).
- Dindorf, C., Bartaguiz, E., Gassmann, F., and Fröhlich, M. (2022a). Conceptual structure and current trends in artificial intelligence, machine learning, and deep learning research in sports: a bibliometric review. *Int. J. Environ. Res. Public Health* 20 (1), 173. doi:10.3390/ijerph20010173
- Dindorf, C., Konradi, J., Wolf, C., Taetz, B., Bleser, G., Huthwelker, J., et al. (2021b). Classification and automated interpretation of spinal posture data using a pathology-independent classifier and explainable artificial intelligence (XAI). *Sensors* 21 (18), 6323. doi:10.3390/s21186323
- Dindorf, C., Konradi, J., Wolf, C., Taetz, B., Bleser, G., Huthwelker, J., et al. (2021c). General method for automated feature extraction and selection and its application for gender classification and biomechanical knowledge discovery of sex differences in spinal posture during stance and gait. *Comput. Methods Biomech. Biomed. Engin* 24 (3), 299–307. doi:10.1080/10255842.2020.1828375
- Dindorf, C., Konradi, J., Wolf, C., Taetz, B., Bleser, G., Huthwelker, J., et al. (2022b). “Visualization of interindividual differences in spinal dynamics in the presence of intraindividual variabilities,” in *Visualization of interindividual differences in spinal dynamics in the presence of intraindividual variabilities*. Editors C. Gillmann, J. Schmidt, S. Jänicke, and D. Wiegrefe (Leipzig: Leipzig University).
- Dindorf, C., Teufel, W., Taetz, B., Becker, S., Bleser, G., and Fröhlich, M. (2021a). Feature extraction and gait classification in hip replacement patients on the basis of kinematic waveform data. *Biomed. Hum. Kinet.* 13 (1), 177–186. doi:10.2478/bhk-2021-0022
- Elkholy, A., Makihara, Y., Gomaa, W., Rahman Ahad, M. A., and Yagi, Y. (2019). “Unsupervised GEI-based gait disorders detection from different views,” in *Unsupervised GEI-based gait disorders detection from different views* (IEEE).
- Ferreira, M. I., Barbosa, T. M., Costa, M. J., Neiva, H. P., and Marinho, D. A. (2016). Energetics, biomechanics, and performance in masters’ swimmers: a systematic review. *J. Strength Cond. Res.* 30, 2069–2081. doi:10.1519/jsc.0000000000001279

Acknowledgments

The authors would like to thank all the participants involved in this study. They also appreciate the support received from their colleagues during the recruitment process. Finally, the authors express their gratitude to Kjell Heitmann, Amira Basic, and Helmut Diers for their multifarious endorsements and technological support.

Conflict of interest

The authors declare that the research was conducted in the absence of any commercial or financial relationships that could be construed as a potential conflict of interest.

Publisher’s note

All claims expressed in this article are solely those of the authors and do not necessarily represent those of their affiliated organizations, or those of the publisher, the editors and the reviewers. Any product that may be evaluated in this article, or claim that may be made by its manufacturer, is not guaranteed or endorsed by the publisher.

Supplementary material

The Supplementary Material for this article can be found online at: <https://www.frontiersin.org/articles/10.3389/fbioe.2024.1350135/full#supplementary-material>

- Halilaj, E., Rajagopal, A., Fiterau, M., Hicks, J. L., Hastie, T. J., and Delp, S. L. (2018). Machine learning in human movement biomechanics: best practices, common pitfalls, and new opportunities. *J. Biomech.* 81, 1–11. doi:10.1016/j.jbiomech.2018.09.009
- Hernandez, V., Kulić, D., and Venture, G. (2020). Adversarial autoencoder for visualization and classification of human activity: application to a low-cost commercial force plate. *J. Biomech.* 103, 109684. doi:10.1016/j.jbiomech.2020.109684
- Horst, F., Lapuschkin, S., Samek, W., Müller, K.-R., and Schödlhorn, W. I. (2019). Explaining the unique nature of individual gait patterns with deep learning. *Sci. Rep.* 9 (1), 2391. doi:10.1038/s41598-019-38748-8
- Horst, F., Slijepcevic, D., Simak, M., and Schödlhorn, W. I. (2021). Gutenberg Gait Database, a ground reaction force database of level overground walking in healthy individuals. *Sci. Data* 8 (1), 232. doi:10.1038/s41597-021-01014-6
- Huang, K., and Zhang, J. (2023). Three-dimensional lumbar spine generation using variational autoencoder. *Med. Eng. Phys.* 120, 104046. doi:10.1016/j.medengphys.2023.104046
- Hunter, J. D. (2007). Matplotlib: a 2D graphics environment. *Comput. Sci. Eng.* 9 (3), 90–95. doi:10.1109/MCSE.2007.55
- Hussain, S., Anees, A., Das, A., Nguyen, B. P., Marzuki, M., Lin, S., et al. (2020). High-content image generation for drug discovery using generative adversarial networks. *Neural Netw.* 132, 353–363. doi:10.1016/j.neunet.2020.09.007
- Huthwelker, J., Konradi, J., Wolf, C., Westphal, R., Schmidtman, I., Schubert, P., et al. (2023). Reference values and functional descriptions of transverse plane spinal dynamics during gait based on surface topography. *Hum. Mov. Sci.* 88, 103054. doi:10.1016/j.humov.2022.103054
- Iglesias, G., Talavera, E., González-Prieto, Á., Mozo, A., and Gómez-Canaval, S. (2023). Data Augmentation techniques in time series domain: a survey and taxonomy 2023.
- Kang, T., Perotte, A., Tang, Y., Ta, C., and Weng, C. (2021). UMLS-based data augmentation for natural language processing of clinical research literature. *J. Am. Med. Inf. Assoc.* 28 (4), 812–823. doi:10.1093/jamia/ocaa309
- Kiprijanovska, I., Gjoreski, H., and Gams, M. (2020). Detection of gait abnormalities for fall risk assessment using wrist-worn inertial sensors and deep learning. *Sensors* 20 (18), 5373. doi:10.3390/s20185373
- Kneifl, J., Rosin, D., Avci, O., Röhrle, O., and Fehr, J. (2023). Low-dimensional data-based surrogate model of a continuum-mechanical musculoskeletal system based on non-intrusive model order reduction. *Arch. Appl. Mech.* 93 (9), 3637–3663. doi:10.1007/s00419-023-02458-5
- Kornish, D., Ezekiel, S., and Cornacchia, M. (2018). “DCNN augmentation via synthetic data from variational autoencoders and generative adversarial networks,” in *DCNN augmentation via synthetic data from variational autoencoders and generative adversarial networks* (IEEE).
- Landis, J. R., and Koch, G. G. (1977). The measurement of observer agreement for categorical data. *Biometrics* 33 (1), 159. doi:10.2307/2529310
- Lashgari, E., Liang, D., and Maoz, U. (2020). Data augmentation for deep-learning-based electroencephalography. *J. Neurosci. Methods* 346, 108885. doi:10.1016/j.jneumeth.2020.108885
- Lau, H., Tong, K., and Zhu, H. (2009). Support vector machine for classification of walking conditions of persons after stroke with dropped foot. *Hum. Mov. Sci.* 28 (4), 504–514. doi:10.1016/j.humov.2008.12.003
- Liu, X., Zhao, C., Zheng, B., Guo, Q., Zhang, Z., Wulamu, A., et al. (2020). Synthesizing foot and ankle kinematic characteristics for lateral collateral ligament injuries detection. *IEEE Access* 8, 188429–188440. doi:10.1109/access.2020.3029616
- Ludwig, O., Dindorf, C., Kelm, J., Simon, S., Nimmrichter, F., and Fröhlich, M. (2023). Reference values for sagittal clinical posture assessment in people aged 10 to 69 years. *Int. J. Environ. Res. Public Health* 20 (5), 4131. doi:10.3390/ijerph20054131
- Luo, J., and Tjahjadi, T. (2020). Multi-set canonical correlation analysis for 3D abnormal gait behaviour recognition based on virtual sample generation. *IEEE Access* 8, 32485–32501. doi:10.1109/access.2020.2973898
- Mahmud, M. S., Huang, J. Z., and Fu, X. (2020). Variational autoencoder-based dimensionality reduction for high-dimensional small-sample data classification. *Int. J. Comp. Intel. Appl.* 19 (01). doi:10.1142/S1469026820500029
- Marchi, E., Vesperini, F., Eyben, F., Squartini, S., and Schuller, B. (2015). “A novel approach for automatic acoustic novelty detection using a denoising autoencoder with bidirectional LSTM neural networks,” in *A novel approach for automatic acoustic novelty detection using a denoising autoencoder with bidirectional LSTM neural networks* (IEEE).
- Martinez, M., and Leon, P. L. de (2020). Falls risk classification of older adults using deep neural networks and transfer learning. *IEEE J. Biomed. Health Inf.* 24 (1), 144–150. doi:10.1109/jbhi.2019.2906499
- McInnes, L., Healy, J., and Melville, J. (2018). UMAP: Uniform Manifold approximation and projection for dimension reduction.
- Mohammadian Rad, N., van Laarhoven, T., Furlanello, C., and Marchiori, E. (2018). Novelty detection using deep normative modeling for IMU-based abnormal movement monitoring in Parkinson's disease and autism spectrum disorders. *Sensors* 18 (10), 3533. doi:10.3390/s18103533
- Mohan, M., and Huynh, L. (2019). Sex differences in the spine. *Curr. Phys. Med. Rehabil. Rep.* 7 (3), 246–252. doi:10.1007/s40141-019-00234-7
- Nguyen, T.-N., Huynh, H.-H., and Meunier, J. (2018). “Estimating skeleton-based gait abnormality index by sparse deep auto-encoder,” in *Estimating skeleton-based gait abnormality index by sparse deep auto-encoder* (IEEE).
- Pandit, T., Nahane, H., Lade, D., and Rao, V. (2019). “Abnormal gait detection by classifying inertial sensor data using transfer learning,” in *Abnormal gait detection by classifying inertial sensor data using transfer learning* (IEEE).
- Paragliola, G., and Coronato, A. (2021). “A deep learning-based approach for the classification of gait dynamics in subjects with a neurodegenerative disease,” in *A deep learning-based approach for the classification of gait dynamics in subjects with a neurodegenerative disease* (Cham: Springer), 452–468.
- Pedregosa, F., Varoquaux, G., Gramfort, A., Michel, V., Thirion, B., Grisel, O., et al. (2011). Scikit-learn: machine learning in Python.
- Phinyomark, A., Petri, G., Ibáñez-Marcelo, E., Osis, S. T., and Ferber, R. (2018). Analysis of big data in gait biomechanics: current trends and future directions. *J. Med. Biol. Eng.* 38 (2), 244–260. doi:10.1007/s40846-017-0297-2
- Prost, S., Blondel, B., Pomero, V., Authier, G., Boulay, C., Jouve, J. L., et al. (2021). Description of spine motion during gait in normal adolescents and young adults. *Eur. Spine J.* 30 (9), 2520–2530. doi:10.1007/s00586-021-06918-w
- Saxena, D., and Cao, J. (2022). Generative adversarial networks (GANs). *ACM Comput. Surv.* 54 (3), 1–42. doi:10.1145/3446374
- Sharifi Renani, M., Eustace, A. M., Myers, C. A., and Clary, C. W. (2021). The use of synthetic IMU signals in the training of deep learning models significantly improves the accuracy of joint kinematic predictions. *Sensors* 21 (17), 5876. doi:10.3390/s21175876
- Song, Z., Wang, S., Yang, J., and Bai, D. (2020). “A novel approach to abnormal gait recognition based on generative adversarial networks,” in *A novel approach to abnormal gait recognition based on generative adversarial networks* (Singapore: Springer), 3–15.
- Takeishi, N., and Kalousis, A. (2021). “Variational autoencoder with differentiable physics engine for human gait analysis and synthesis,” in *NeurIPS 2021 Workshop on Deep Generative Models and Downstream Applications 2021*.
- Tu, Y., Mak, M.-W., and Chien, J.-T. (2020). “Information maximized variational domain adversarial learning for speaker verification,” in *Information maximized variational domain adversarial learning for speaker verification* (IEEE).
- Tunca, C., Salur, G., and Ersoy, C. (2020). Deep learning for fall risk assessment with inertial sensors: utilizing domain knowledge in spatio-temporal gait parameters. *IEEE J. Biomed. Health Inf.* 24 (7), 1994–2005. doi:10.1109/JBHI.2019.2958879
- Valamatos, M. J., Abrantes, J. M., Carnide, F., Valamatos, M.-J., and Monteiro, C. P. (2022). Biomechanical performance factors in the track and field sprint start: a systematic review. *Int. J. Environ. Res. Public Health* 19 (7), 4074. doi:10.3390/ijerph19074074
- Wahid, F., Begg, R. K., Hass, C. J., Halgamuge, S., and Ackland, D. C. (2015). Classification of Parkinson's disease gait using spatial-temporal gait features. *IEEE J. Biomed. Health Inf.* 19 (6), 1794–1802. doi:10.1109/JBHI.2015.2450232
- Wan, Z., Zhang, Y., and He, H. (2017). “Variational autoencoder based synthetic data generation for imbalanced learning,” in *IEEE Symposium Series on Computational Intelligence Honolulu (Hig.) 2017 – SSCI. IEEE*, 1–7. Symposium.
- Yang, J., and Yin, Y. (2021). Novel soft smart shoes for motion intent learning of lower limbs using LSTM with a convolutional autoencoder. *IEEE Sensors J.* 21 (2), 1906–1917. doi:10.1109/jsen.2020.3019053
- Yang, Z., Zhang, T., Bozchalooi, I. S., and Darve, E. (2022). Memory-augmented generative adversarial networks for anomaly detection. *IEEE Trans. Neural Netw. Learn. Syst.* 33 (6), 2324–2334. doi:10.1109/TNNLS.2021.3132928
- Yee, J., Low, C. Y., Hashim, N. M., Hanapih, F. A., Theng Koh, C., Che Zakaria, N. A., et al. (2021). “Systematic development of machine for abnormal muscle activity detection,” in *Systematic development of machine for abnormal muscle activity detection* (IEEE).
- Yukawa, Y., Kato, F., Suda, K., Yamagata, M., Ueta, T., and Yoshida, M. (2018). Normative data for parameters of sagittal spinal alignment in healthy subjects: an analysis of gender specific differences and changes with aging in 626 asymptomatic individuals. *Eur. Spine J.* 27 (2), 426–432. doi:10.1007/s00586-016-4807-7
- Zaroug, A., Lai, D. T. H., Mudie, K., and Begg, R. (2020). Lower limb kinematics trajectory prediction using long short-term memory neural networks. *Front. Bioeng. Biotechnol.* 8, 362. doi:10.3389/fbioe.2020.00362
- Zhao, J., Mathieu, M., Goroshin, R., and LeCun, Y. (2015). Stacked what-where auto-encoders.
- Zhao, S., Song, J., and Ermon, S. (2017). Towards deeper understanding of variational autoencoding models.
- Zhao, T., Zhao, R., and Eskenazi, M. (2017). Learning discourse-level diversity for neural dialog models using conditional variational autoencoders.
- Zhao, S., Song, J., and Ermon, S. (2019). InfoVAE: balancing learning and inference in variational autoencoders. *AAAI* 33 (01), 5885–5892. doi:10.1609/aaai.v33i01.33015885
- Zhou, S., Gordon, M. L., Krishna, R., Narcomey, A., Fei-Fei, L., and Bernstein, M. S. (2019). HYPE: a benchmark for human eYe perceptual evaluation of generative models.



OPEN ACCESS

EDITED BY

Peter Quesada,
University of Louisville, United States

REVIEWED BY

Barbara Barboni,
University of Teramo, Italy
Domiziano Tarantino,
University of Naples Federico II, Italy

*CORRESPONDENCE

Ara Nazarian,
✉ anazaria@bidmc.harvard.edu

RECEIVED 24 October 2023

ACCEPTED 16 January 2024

PUBLISHED 07 March 2024

CITATION

Chainani PH, Buzo Mena M, Yeritsyan D, Caro D, Momenzadeh K, Galloway JL, DeAngelis JP, Ramappa AJ and Nazarian A (2024), Successive tendon injury in an *in vivo* rat overload model induces early damage and acute healing responses.

Front. Bioeng. Biotechnol. 12:1327094.
doi: 10.3389/fbioe.2024.1327094

COPYRIGHT

© 2024 Chainani, Buzo Mena, Yeritsyan, Caro, Momenzadeh, Galloway, DeAngelis, Ramappa and Nazarian. This is an open-access article distributed under the terms of the [Creative Commons Attribution License \(CC BY\)](https://creativecommons.org/licenses/by/4.0/). The use, distribution or reproduction in other forums is permitted, provided the original author(s) and the copyright owner(s) are credited and that the original publication in this journal is cited, in accordance with accepted academic practice. No use, distribution or reproduction is permitted which does not comply with these terms.

Successive tendon injury in an *in vivo* rat overload model induces early damage and acute healing responses

Pooja H. Chainani^{1,2}, Maria Buzo Mena¹, Diana Yeritsyan¹, Daniela Caro¹, Kaveh Momenzadeh¹, Jenna L. Galloway³, Joseph P. DeAngelis^{1,4}, Arun J. Ramappa^{1,4} and Ara Nazarian^{1,2,4,5*}

¹Musculoskeletal Translational Innovation Initiative, Carl J. Shapiro Department of Orthopaedic Surgery, Beth Israel Deaconess Medical Center, Harvard Medical School, Boston, MA, United States, ²Department of Mechanical Engineering, Boston University, Boston, MA, United States, ³Center for Regenerative Medicine, Massachusetts General Hospital, Harvard Medical School, Boston, MA, United States, ⁴Carl J. Shapiro Department of Orthopaedic Surgery, Beth Israel Deaconess Medical Center, Harvard Medical School, Boston, MA, United States, ⁵Department of Orthopaedic Surgery, Yerevan State Medical University, Yerevan, Armenia

Introduction: Tendinopathy is a degenerative condition resulting from tendons experiencing abnormal levels of multi-scale damage over time, impairing their ability to repair. However, the damage markers associated with the initiation of tendinopathy are poorly understood, as the disease is largely characterized by end-stage clinical phenotypes. Thus, this study aimed to evaluate the acute tendon responses to successive fatigue bouts of tendon overload using an *in vivo* passive ankle dorsiflexion system.

Methods: Sprague Dawley female rats underwent fatigue overloading to their Achilles tendons for 1, 2, or 3 loading bouts, with two days of rest in between each bout. Mechanical, structural, and biological assays were performed on tendon samples to evaluate the innate acute healing response to overload injuries.

Results: Here, we show that fatigue overloading significantly reduces *in vivo* functional and mechanical properties, with reductions in hysteresis, peak stress, and loading and unloading moduli. Multi-scale structural damage on cellular, fibril, and fiber levels demonstrated accumulated micro-damage that may have induced a reparative response to successive loading bouts. The acute healing response resulted in alterations in matrix turnover and early inflammatory upregulations associated with matrix remodeling and acute responses to injuries.

Discussion: This work demonstrates accumulated damage and acute changes to the tendon healing response caused by successive bouts of *in vivo* fatigue overloads. These results provide the avenue for future investigations of long-term evaluations of tendon overload in the context of tendinopathy.

KEYWORDS

tendinopathy, mechanobiology, fatigue, tendon overload, *in vivo*, acute healing, injury

1 Introduction

Tendons are highly aligned, fibrous tissues connecting muscle to bone and are subjected to substantial amounts of daily loads; the Achilles tendon, the largest in the body, experiences loads up to 12.5 times the body weight during running (Komi et al., 1992; Svensson et al., 2016). Thus, tendons are prone to ruptures and overuse injuries, such as tendinopathies, from their daily continuous stresses and strains. Tendinopathy causes functional impairments, painful symptoms, and decreased quality of life in 30%–50% of the elderly, workplace, and athletic populations (Andarawis-Puri and Flatow, 2011; Kaux et al., 2011; Neviaser et al., 2012; Maffulli et al., 2020). Achilles tendinopathy has a lifetime incidence of 52% for athletes involved in running activities (Tarantino et al., 2023). Clinical cases of tendinopathy present morphological changes (i.e., increased cross-sectional area) as well as diminished mechanical and material properties (Arya and Kulig, 2010; Helland et al., 2013; Wiesinger et al., 2020). Despite its prevalence and substantial healthcare burden, the pathogenesis is largely unknown and clinically characterized in its later stages when the condition is accompanied by pain as well as degenerative symptoms, limiting treatment options.

External mechanical stimuli from physical activity drive tendon homeostasis, adaptation, and repair responses. For example, macroscale loads cause microscopic tensile, compressive, shear, and fluid changes to the ECM due to the hierarchical and viscoelastic properties of the tendon. Native tendon cells (tenocytes) sense and convert mechanical stimuli into cell signals through cell-cell and cell-matrix interactions and respond through mechanotransduction pathways of tissue remodeling and adaptation. Force transmission through the tendon sets off a cascade of biological responses that can strengthen the tendon through matrix synthesis and degradation of damaged collagen and the surrounding ECM (Lipman et al., 2018). However, abnormal loading conditions—such as overload—ultimately trigger a cascade of mechanobiological signals due to deviations from the cellular tensional homeostasis (Pentzold and Wildemann, 2022). Lack of sufficient rest periods between abnormal loading conditions causes an increase in the deposition of mechanically weaker type III collagen, collagen fiber disruption, net degradation of tendon ECM, apoptosis, and inflammation, leaving the tendon susceptible to further injury (Andarawis-Puri et al., 2014; Spiesz et al., 2015; Thorpe et al., 2015; Zamboulis et al., 2020). The accumulation of fatigue damage coupled with insufficient recovery time results in a chronic degenerative cycle resulting from a “failed” tendon healing response, ultimately leading to tendinopathy.

Thus, multiscale investigations of tendon damage are critical to understanding how damage propagates spatially and temporally. *In vivo* animal models of tendon overuse and overload (such as treadmill running, repetitive reaching, climbing, direct tendon loading, and synergist ablation) have been used in such work (Williamson et al., 2021; Bloom et al., 2023). Recently developed *ex vivo* model systems—designed to mimic *in vivo* tendon biomechanics and load the tendon in isolation—demonstrated that cyclically loading tendons to physiological stresses and strains results in temporal inflammatory as well as matrix degradation responses (Benage et al., 2022). Sub-failure tendon changes such as decreased stiffness and collagen disorganization, indicative of early signs of degeneration, have been revealed in cyclic fatigue loading in rat and mouse models (Soslowsky et al., 2000; Soslowsky et al., 2002;

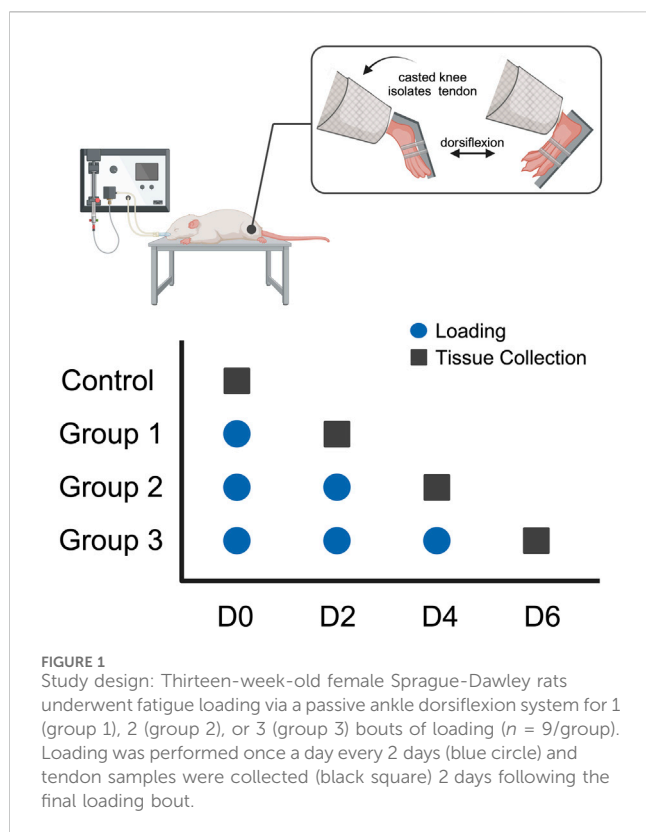
Fung et al., 2009; Ng et al., 2011; Andarawis-Puri et al., 2012; Andarawis-Puri et al., 2014). Various overuse studies have reported increased levels of non-tenogenic cell types and rounded cellular morphology. These may activate mechanotransduction pathways, altering matrix turnover and inflammatory pathways, which may play roles in tendon structural and mechanical degeneration (Williamson et al., 2021).

Whereas *in vivo* overuse models have identified several damage markers associated with overuse tendinopathy in a physiologically relevant manner, models cannot measure a tendon’s stresses and strains during fatigue loading or selectively loading the tendon in isolation from connecting tissues. *Ex vivo* dynamic loading models address these limitations and allow for a coupled understanding of the mechanobiological changes associated with specified fatigue loads but in isolation from the body’s natural environment and reactionary responses to injuries. Therefore, the objective of this study was to assess multiscale mechanobiological and structural changes of the Achilles tendon acute healing in response to successive cyclic fatigue loading, using our previously validated system that applies cyclic loads to the rat Achilles tendon while measuring the tendon’s stresses and strains (Williamson et al., 2023). To determine the effects of fatigue loading on tendon sub-failure changes and the subsequent acute healing response, we assessed changes to *in vivo* mechanical and multiscale morphological properties and biological response through gene expression. We hypothesized that successive fatigue loading would result in decreased *in vivo* mechanical properties, collagen micro-damage, cellular infiltration, and a disruption to the innate inflammatory response and collagen and matrix turnover.

2 Materials and methods

2.1 Experimental design

All procedures were approved by the Institutional Animal Care and Use Committee (IACUC). In this study, female rats were chosen due to existing studies indicating that women have a greater burden associated with tendon disorders, with greater disabilities and diminished tendon function (Sarver et al., 2017; Pentzold and Wildemann, 2022). Thirteen-week-old female Sprague Dawley rats ($n = 36$) were anesthetized using isoflurane. The left hindlimb of each animal was fixed in full-leg extension using a splint to isolate the Achilles tendon. The foot was attached to an ankle joint actuator that allowed for passive ankle dorsiflexion up to 40° relative to full plantarflexion, and the rat was secured in a prone position in a full-body platform. The ankle was cyclically dorsiflexed to an angle that loaded the tendon for 500 cycles to the exponential region at ~1 Hz to mimic normal gait, as described in a previously published protocol (Williamson et al., 2023; Chainani et al., 2024). Each rat was subjected to either 0 (control), 1 (group 1), 2 (group 2), or 3 (group 3) bouts of 500 loading cycles (one bout per day, $n = 9$ per group) with 2 days of cage activity between each loading (Figure 1). Mechanical measurements before and after each loading were performed to assess the effect of loading on tendon mechanical properties. Two days after each group’s final loading, the rats were euthanized via CO₂ inhalation. No loading or mechanical measurements were performed on the control group. The loaded Achilles tendon tissue was harvested for RT-qPCR gene expression



analysis ($n = 5$ per group), histological assessment ($n = 3$ per group), and transmission electron microscopy analysis of transverse sections ($n = 1$ per group).

2.2 Mechanical data analysis

The torque and angle loading data from five baseline measurements before the loading regimen and five post-loading measurements immediately after the last loading bout were converted to stress and strain using the Achilles tendon moment arm and cross-sectional area obtained from pilot studies. The hysteresis curves were analyzed using a custom-developed MATLAB code (MathWorks, Natick, MA, United States) to calculate percentage differences in hysteresis, peak stress, and loading and unloading moduli between baseline measurements and after the final bout of loading for each group.

2.3 Histology

Following euthanasia, tendon tissues were dissected at the calcaneus and proximal to the myotendinous junction and immediately fixed in 10% neutral buffered formalin. The tissue samples were formalin-fixed paraffin-embedded (FFPE) via routine paraffin protocol and sectioned and stained at the BIDMC Histology Core. Sections of 5 μm thickness from each sample were stained with hematoxylin & eosin (H&E) to assess changes in cell shape and size and with Masson's Trichrome staining to assess collagen structural changes with a standard protocol by the BIDMC Histology

Core. Slides were imaged at $\times 10$ using a brightfield full slide scanning microscope (Olympus VS120 Virtual Slide Scanner, Olympus, Japan).

2.4 Histological image analysis

Using the open-source image-processing program Fiji (National Institutes of Health, MD, United States), H&E, and Masson's Trichrome stained images were pre-processed and analyzed to extract cellular morphology and collagen orientation. For H&E stained images, the regions of interest were manually segmented, and a color deconvolution algorithm was performed to isolate the hematoxylin stain, and the cell nuclei were segmented using the Phansalkar thresholding method and watershed segmentation. The circularity, nuclear aspect ratio, area fraction, and cellularity were analyzed for each image. The Masson's Trichrome stained images were manually cropped to the region of interest and converted to greyscale. Using the OrientationJ plugin in Fiji, the collagen orientation was extracted for each image. The circular variance was calculated for each group to measure the spread of orientations per group.

2.5 Transmission electron microscopy

Tendon tissues were dissected as previously described for the histological samples. Tissues were immersion fixed in 2% glutaraldehyde (Electron Microscopy Sciences, Hatfield, PA, United States) in 0.1M Sodium Cacodylate (Sigma-Aldrich, Burlington, MA, United States) pH 7.4 for at least 1 h at room temperature and then at 4°C overnight. Tissues were washed with 0.1M Sodium Cacodylate and then post-fixed for 1 h at 4°C in 1% osmium tetroxide (Electron Microscopy Sciences) in 0.1M Sodium Cacodylate. Cells were washed in DI water and incubated in 2% aqueous uranyl acetate (Electron Microscopy Sciences) overnight at 4°C. The following day, tissues were washed with DI water and then dehydrated at 4°C in a graded ethanol series. Tissues were then brought to room temperature and dehydrated with 100% ethanol (Sigma-Aldrich), followed by propylene oxide (Electron Microscopy Sciences). Infiltration with LX112 resin (Ladd Research Industries, Williston, VT, United States) was followed by embedding in flat-bottom Beem capsules (Electron Microscopy Sciences). The resulting blocks were sectioned using a Leica Ultracut E ultramicrotome (Leica Microsystems, Wetzlar, Germany), and sections were placed on formvar and carbon-coated grids (Electron Microscopy Sciences). Sections of 70 nm thickness from the midsection of the tendon were cut perpendicular to the longitudinal axis of the tendon. The sections were contrast stained with 2% uranyl acetate followed by lead citrate (Sigma-Aldrich) and imaged in a JEOL 1400 transmission electron microscope (JEOL, Peabody, MA, United States) equipped with a Gatan Orius SC1000 digital CCD camera (Gatan, Pleasanton, CA, United States).

Four regions of interest (ROI) were identified at $\times 2,500$ magnification in each quadrant of the sample grid. Ten micrographs per sample from five regions of interest within the tendon were chosen from four quadrants and the center of the transverse section of the tissue, taken at a final magnification of $\times 25,000$.

2.6 Collagen fibril image analysis

The ten representative images from each sample were preprocessed and quantified for collagen morphological parameters using the freely available Fiji image-processing package (Rigozzi et al., 2010). The quantified measurements from these ten images were averaged to provide a representative value for each sample. To correct for uneven backgrounds, the original images were subtracted by their Gaussian filtered (radius = 40 pixels) image to generate a new image with a “flat field” (Zhou et al., 2013). A median filter (radius = 5 pixels) was applied, followed by auto-thresholding to generate a binary mask. Outliers smaller than 5 pixels were removed. The resulting binary images were subjected to watershed segmentation and particle analysis to quantify each collagen fibril’s perimeter, area, radius, and total collagen area fraction. Fibrils on the edges of the images were excluded to remove samples that did not provide a complete characterization for quantification. These measurements described collagen morphological properties (collagen area fraction and collagen fibril radius) and a fibril-fibril interaction parameter (specific fibril surface) (Rigozzi et al., 2010). The distribution of fibril radii was presented in a histogram.

2.7 Quantitative gene expression

Following euthanasia, the loaded Achilles tendons were dissected free of soft tissue, as described previously, and harvested and stored in 1 mL of TRIzol reagent (Invitrogen, Waltham, MA, United States), fast frozen with liquid nitrogen, and stored at -80°C for further processing.

Total RNA from all tissue types was extracted from an established methodology. Tendon tissue was homogenized in 1 mL TRIzol with a Polytron homogenizer (850 Homogenizer, ThermoFisher Scientific, Waltham, MA, United States). RNA extraction and purification were performed using a PureLink RNA mini kit (Invitrogen, Waltham, MA, United States) per manufacturer instructions. A spectrophotometer (NanoDrop Technologies, Wilmington, DE, United States) was used to determine RNA concentrations and purity ratios.

For cDNA synthesis, 500 ng RNA for each sample was converted into cDNA using the PrimeScript RT reagent Kit with gDNA Eraser (TaKaRa Bio, Kusatsu, Shiga, Japan) according to the manufacturer’s protocol. SYBR Green-based quantitative PCR (qPCR) detection was then performed using PerfeCTA SYBR Green FastMix, Low ROX (Qiagen, Hilden, Germany) on a Mx3000P QPCR System (Stratagen, La Jolla, CA, United States). For each target mRNA, 2 μL diluted cDNA was amplified in an 11 μL SYBR Green PCR total reaction containing 5 μL SYBR Green and 0.6 μL (10 μM) of the forward and reverse primer. Samples were assessed for gene expression of matrix proteins (collagen types 1, 3, decorin, biglycan), matrix metalloproteinases (MMP-2, MMP-3, MMP-13), tissue inhibitors of matrix metalloproteinases (TIMP-1, TIMP-2), inflammatory cytokines (IL-1 β , VEGF, TGF β , TNF α), tenocyte markers (scleraxis, tenomodulin), and mechanotransducers (YAP and TAZ) (Table 1). All primers were designed to span an intron. Gene expression values were normalized to the housekeeping gene, GAPDH, and the control group. Gene expression values were normalized to the housekeeping gene, GAPDH, and the control

group], and the data was analyzed with the $2^{-\Delta\Delta C_t}$ values (Livak and Schmittgen, 2001). At the end of each RT-qPCR run, the melting curves were checked to confirm a single product disassociation point and technical replicates were averaged if Ct values were within a tight range.

2.8 Statistical analysis

Statistical analysis used GraphPad (version 9.3.0 for Windows; GraphPad Software, San Diego, CA, United States). The ROUT method was used to remove any outliers before analysis. The Kolmogorov-Smirnov test was used to test for normality. A one-way analysis of variance (ANOVA) test was used for normally distributed data to test the significance between groups on the mechanical, gene expression, and morphological properties. Otherwise, the Kruskal-Wallis test was performed. Statistical significance was assessed at p -values less than 0.05.

3 Results

3.1 Decreased *in vivo* mechanical properties with successive loading

Successive bouts of loading resulted in larger decreases in the *in vivo* mechanical properties of the fatigue-loaded Achilles tendons (Figure 2). There was a significant difference in hysteresis reduction, a mechanical property of viscoelastic tissues measuring their damping capacity, between the loading groups, with an even greater difference between groups 1 and 3. The decrease in peak stress and loading modulus of the dorsiflexion cycle was significant between group 1 and groups 2 and 3; however, there were no differences in the unloading moduli between the loading groups.

3.2 Differential gene expression in matrix and inflammatory markers with successive loads

There was an increase in type I collagen gene expression in groups 1 and 2, with a significant increase in group 2 compared to control (Figure 3A). There was a significant reduction in type I collagen gene expression, while there was an increase in type III collagen gene expression in group 3. However, there were no significant changes in the expression of biglycan and decorin, small leucine-rich proteoglycans (SLRPs) responsible for regulating the tendon’s collagen fibrillogenesis and extracellular matrix assembly.

There was an approximately 200-fold relative upregulation of MMP-13 in group 2, followed by a decrease in group 3, while still significantly upregulated around 65-fold compared to the control group (Figure 3B). MMP-2 expression reached significance in group 3 compared to groups 1 and control. The corresponding tissue inhibitor TIMP-1 was upregulated by 9.3-fold in group 2, followed by a decrease to 3.75-fold upregulation in group 3. MMP-3 expression had an increasing trend in group 1, followed by reductions in expression levels in subsequent groups, with no significance.

TABLE 1 Forward and reverse gene sequences for qPCR.

Gene	Forward Sequence (5' → 3')	Reverse Sequence (5' → 3')
<i>GAPDH</i>	ACCCCTCCTGGGTTTGTAGT	CATCCAAGCATTCAACCGGC
<i>Col1a1</i>	GCGAAGGCAACAGTCGATTC	GGACCTGGTCTGGGGATACT
<i>Col3a1</i>	GCCTACATGGATCAGGCCAA	CATGGCCTTGCGTGTTTGAT
<i>DCN</i>	CGGTGGCAAATACCCGGATTA	AGGGGATTGTCAGGGTCGTA
<i>BGN</i>	GACAAACCGACAGCCTGACA	ATGAGCAGCCCATCATCAA
<i>MMP2</i>	AGTTGGCCACATCTGGTTG	TTTGGCAGAAGTTGGGGTCAT
<i>MMP3</i>	GGTGGATGCTGTCTTTGAAGC	CTCCATGAAAAGACTCAGAGGA
<i>MMP13</i>	ACCCAGCCCTATCCCTTGAT	TCTCGGGATGGATGCTCGTA
<i>TIMP1</i>	CCAGGTCCGAGTTGCAGAAA	TCCTGAGTCTCCCTAGAGCC
<i>IL-1β</i>	GCTACCTATGTCTTGCCCGT	TCACACACTAGCAGGTCGTC
<i>TNFα</i>	ATCGGTCCCAACAAGGAGGA	CGCTTGGTGGTTTGCTACG
<i>VEGF</i>	ACGACAGAAGGGGAGCAGAA	AGATGTCCACCAGGGTCTCA
<i>TGFβ</i>	CAGAACCCCATGTGCTGCC	CAGCCACTCAGGCGTATCAG
<i>Scx</i>	AACAGATCTGCACCTTCTGCC	CTTCGAATCGCCGTCTTTCTG
<i>Tnmd</i>	AGACAAGCAAGCGAGGAAGAC	CACGACAGATGACTCGACCTC
<i>YAP1</i>	TTCGGCAGGCAATACGAA	TGGCTGCGGAGAGCTAATTC
<i>TAZ</i>	GTGGGAGATGACCTTCACGG	CAAGATTGGGCTGGGACACT

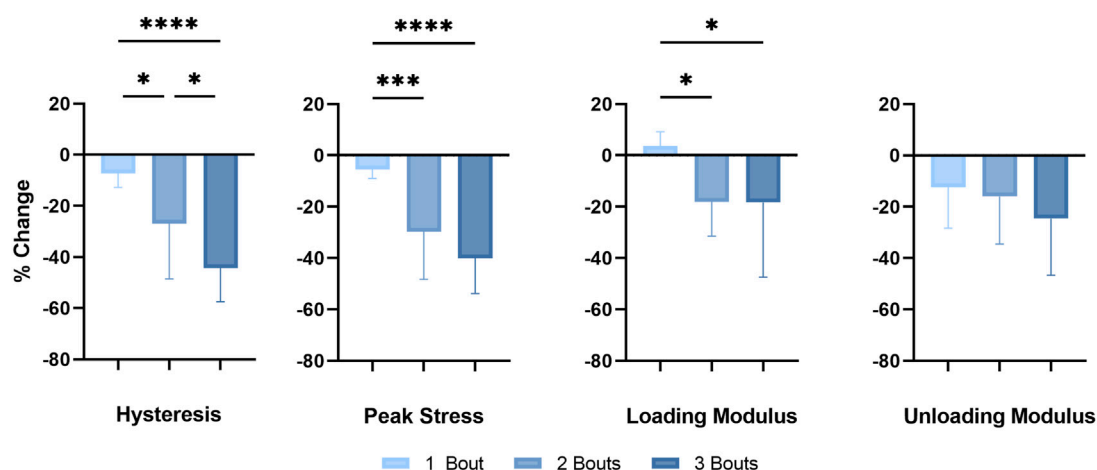


FIGURE 2

In vivo mechanical properties: Successive fatigue-load injuries from passive ankle dorsiflexion result in reduced mechanical properties, specifically in the percent change in hysteresis, the peak stress of each applied cycle, and the loading and unloading modulus between the uninjured *in vivo* tendon properties and properties following the final loading bout of each respective group. The data is presented as mean \pm STD with statistical difference denoted by stars (*) between each number of load (* = $p < 0.05$, ** = $p < 0.01$, *** = $p < 0.001$, and **** = $p < 0.0001$).

The pro-inflammatory cytokine IL-1 β exhibited an average increase of roughly 14 to 15-fold across all three groups (Figure 3C). TNF- α , VEGF, and TGF β did not change significantly throughout the loading groups. However, there was a slight upregulation for VEGF in group 2 and for TGF β in group 1; however, neither reached significance.

3.3 Alterations in tenocyte and mechanotransduction markers

Scleraxis (Scx) had a 2.7-fold increase in gene expression following 1 bout of loading, with a slight decline for the remaining two groups, while still upregulated around 2-fold.

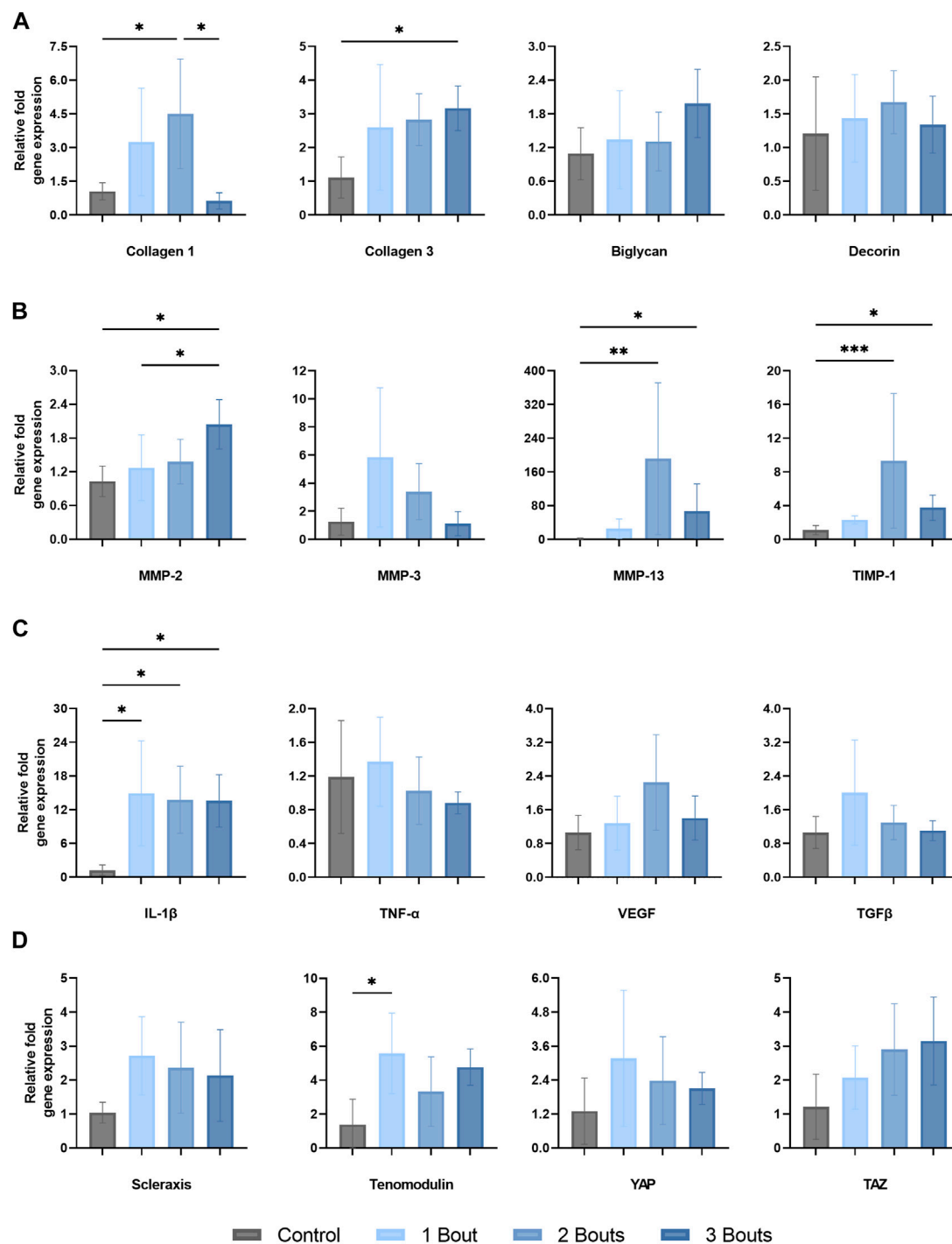


FIGURE 3

Gene expression levels of Achilles tendon mRNA relative to GAPDH of (A) matrix proteins (type I and III collagen, biglycan, and decorin), (B) matrix metalloproteinases and tissue inhibitor-1 (MMP-2, MMP-3, MMP-13, TIMP-1), (C) proinflammatory (IL-1 β , TNF- α , and VEGF) and anti-inflammatory (TGF β) cytokines and (D) tenocyte markers (scleraxis, tenomodulin), and mechanotransducers (YAP and TAZ). The data is presented as mean \pm STD with statistical difference denoted by stars (*) between each number of load (* = $p < 0.05$, ** = $p < 0.01$, and *** = $p < 0.001$).

Tenomodulin (Tnmd) was significantly upregulated by 5.6-fold for group 1 compared to the control group while staying relatively upregulated for the other groups. The mechanoresponsive transcriptional co-activators, Yes-Associated Protein (YAP) and Transcriptional co-activator with PDZ binding motif (TAZ), co-

regulators of cellular proliferation and differentiation, had opposite trends between groups. While YAP expression increased 3.1-fold for group 1 and had a decreasing trend for the remaining groups, TAZ initially was upregulated by 2.1-fold and continued to increase (Figure 3D).

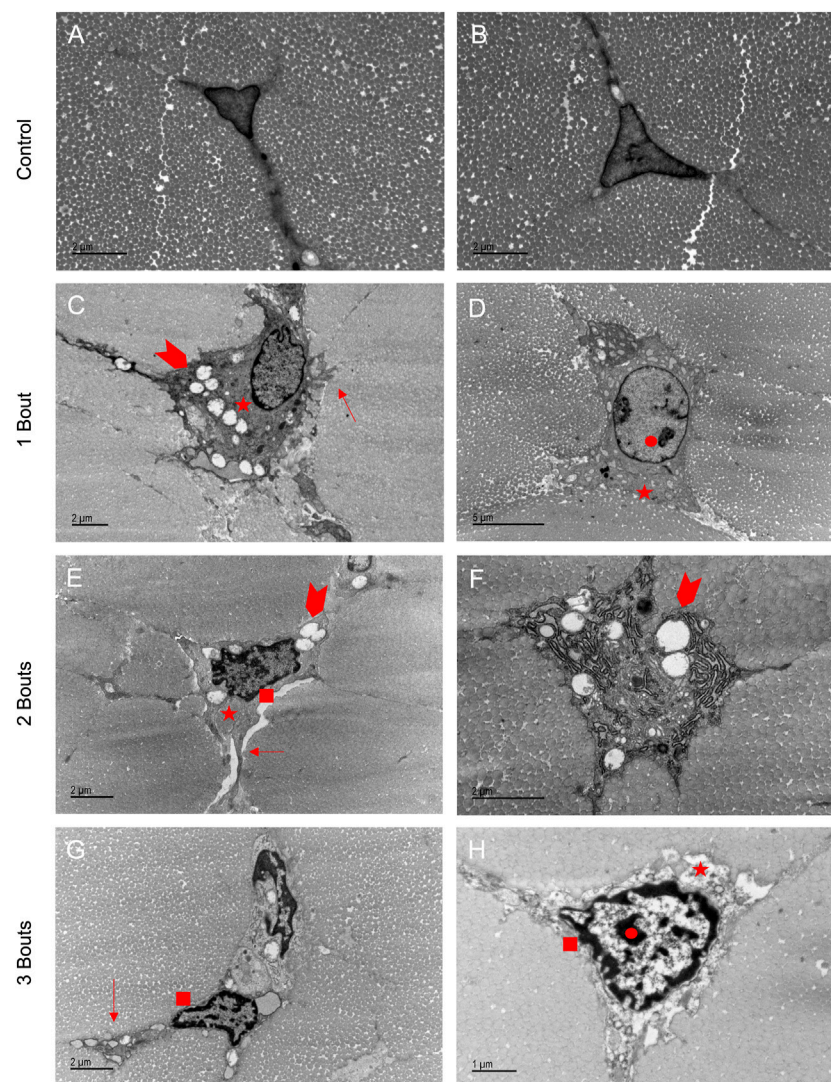


FIGURE 4

Loaded groups exhibited characteristics of apoptosis in TEM images: Healthy tenocytes exhibited characteristic elongated shapes with extensions into the matrix (A, B). Loaded cells had accumulations of vesicles, vacuoles, and mitochondria (arrowheads) (C, E, F). The shapes became more rounded with protrusions in the boundaries (arrows) (C, E, G). Thickened pericellular matrix separated the cell from surrounding fibrils (stars) (C, D, E, H). Some cells had dilated endoplasmic reticulum (F). Apoptotic processes were demonstrated by areas of dense chromatin (circle) (D, H) and rings of chromatin around the cell boundary (square) (E, G, H), with some cells in group 3 having separated nuclei (G).

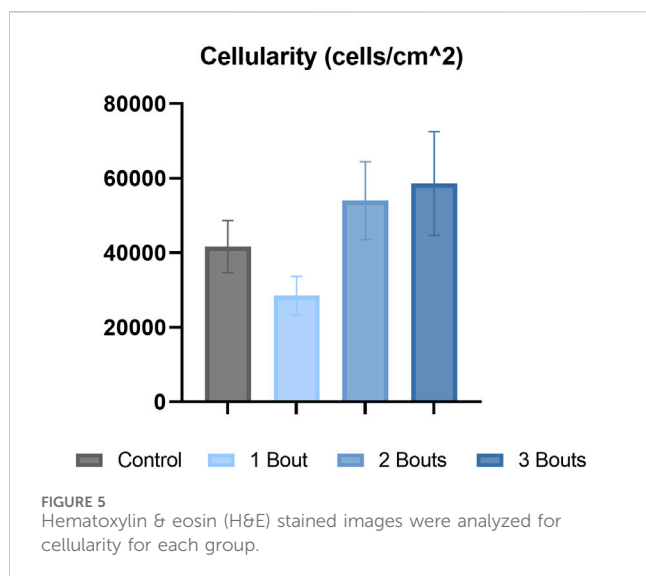
3.4 Cellular damage indicated early apoptotic processes

Tenocytes in the control group had the characteristic elongated cell shape with cell extensions into the network of collagen fibrils (Figures 4A, B). With fatigue overloading, cells became malformed and rounded, with accumulations of intracellular vacuoles, vesicles, and mitochondria (Figures 4C–H). The characteristic cytoplasm was preserved in the control groups, but with overload, there were disrupted cytoplasmic processes dominated by the nucleus, with some protrusions on the outer boundary of cells (Figures 4C–E, G, H). Healthy tenocytes contained uncondensed chromatin, and with successive bouts of loading, the chromatin started to form condensed regions (Figures 4D, E, H) and some developed rings of chromatin in the outer border of the cell (Figures 4C, G). In most

tenocytes of the loaded groups, a thickened pericellular matrix of non-collagenous matrix formed, separating the cell from the surrounding fibrils. Damaged cells also exhibited dilated rough endoplasmic reticulum (Figure 4F). In group 3, tenocytes showed signs of apoptosis with nuclei fragmentation (Figure 4G).

3.5 Macro- and micro-structure indicates cellular and fibril adaptation response

The control group's nuclei had an average circularity of 0.5, slightly increasing to 0.55 for the groups with loading bouts. Similarly, the nuclear aspect ratio between the major and minor axes increased by approximately 10% between the control and the experimental groups. Both area fraction and cellularity decreased for



group 1 compared to the control group and subsequently increased for groups 2 and 3 (Figure 5). Qualitatively, groups 2 and 3 exhibited areas of dense cellularity, and each group demonstrated a progressive increase in areas of fiber kinks (Figures 6, 7). The collagen orientation's circular variance averaged 0.15 for all groups, with a subtle decrease between consecutive loading bouts and an average angle 45° angle. Neither of these structural properties showed statistical significance.

The histograms showed that the control group had a wide distribution of collagen fibrils with larger diameters. In contrast, group 1 had fewer large-diameter fibrils and more small-diameter ones. As the number of loads increased, the distribution began to normalize (Figure 8). The collagen area fraction stayed consistent throughout the groups, while the mean minor fibril radius and specific fibril surface decreased for the loaded groups compared to the control group (Table 2).

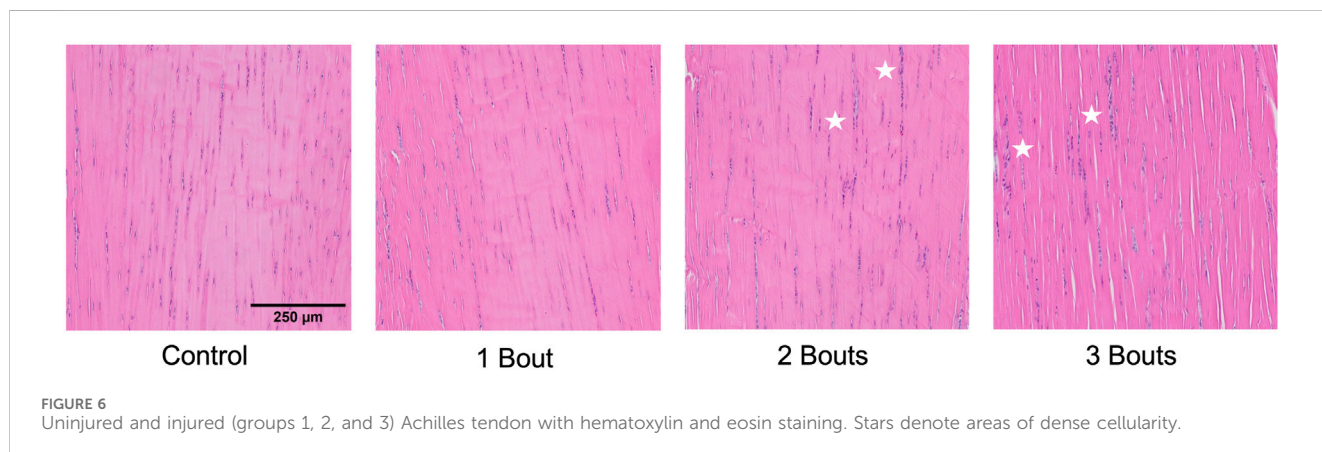
4 Discussion

While previous animal models have mainly focused on long-term effects in tendinopathy due to overuse, our study offers novel insights by

examining the immediate functional and mechanobiological responses to repeated fatigue loading. We accomplished this by conducting qualitative and quantitative assessments of mechanical properties, gene expression, and multi-scale tendon structure in rat Achilles tendons subjected to sub-failure fatigue loading and subsequent healing. Our findings demonstrate that all loading regimens resulted in significant reductions in hysteresis, peak stress, loading, and unloading moduli, along with notable alterations in the expression of inflammation and matrix turnover markers. Furthermore, the loading regimens caused both micro- and macro-structural damage. This research provides a unique perspective on the immediate impacts of overuse injuries, shedding light on the complex interplay of mechanical, mechanobiological, and structural changes in tendons during the acute healing phase.

The continual reduction in mechanical properties following each loading group suggests an accumulation of fatigue damage from successive loading regimens. The hysteresis loss with increased loading regimens is consistent with studies of *in vivo* fatigue loading of the rat patellar tendon (Andarawis-Puri et al., 2012). The changes in hysteresis, a viscoelastic property quantifying energy loss and damping capacity during tissue loading, may suggest alterations to the non-collagenous components in the extracellular matrix, loss in fibril crimp, and a reduced ability for the tendon to protect itself from further damage (Williamson et al., 2021). While our results showed reduced loading and unloading moduli following repetitive loading regimens, another study demonstrated an initial stiffness reduction followed by increased stiffness with further loading. The consistent reduction in moduli may result from continuous damage where only fibers in high tension are loaded, and subsequent decreases can be due to a lack of recovery for the fibers not in tension and ruptured collagen fibers that were previously loaded. The reduction in peak stress following fatigue loading suggests the tendon's impaired ability to bear further stress and load redistribution from damaged to undamaged collagen fibers.

The successive mechanical stimuli caused alterations in mechanotransduction markers. YAP and TAZ are mechanotransducers of the Hippo signaling pathway that are considered to be activated by ECM stiffness and cell shape, whose activity enables cell responses to mechanical cues (Lavagnino et al., 2015). Their activity is required for fibroblast proliferation, and a stiffer ECM can activate a positive fibrotic feedback loop, maintaining or even activating injury states. These



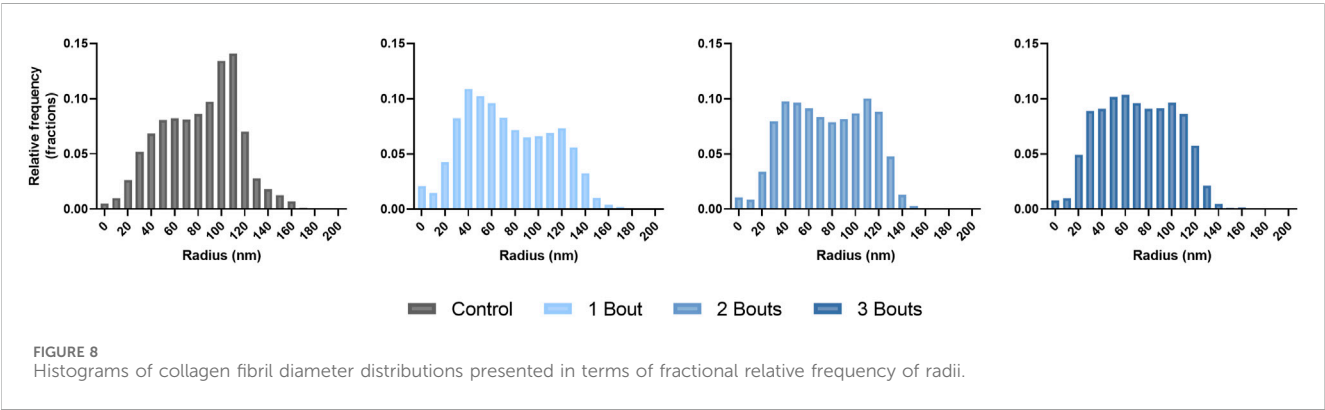
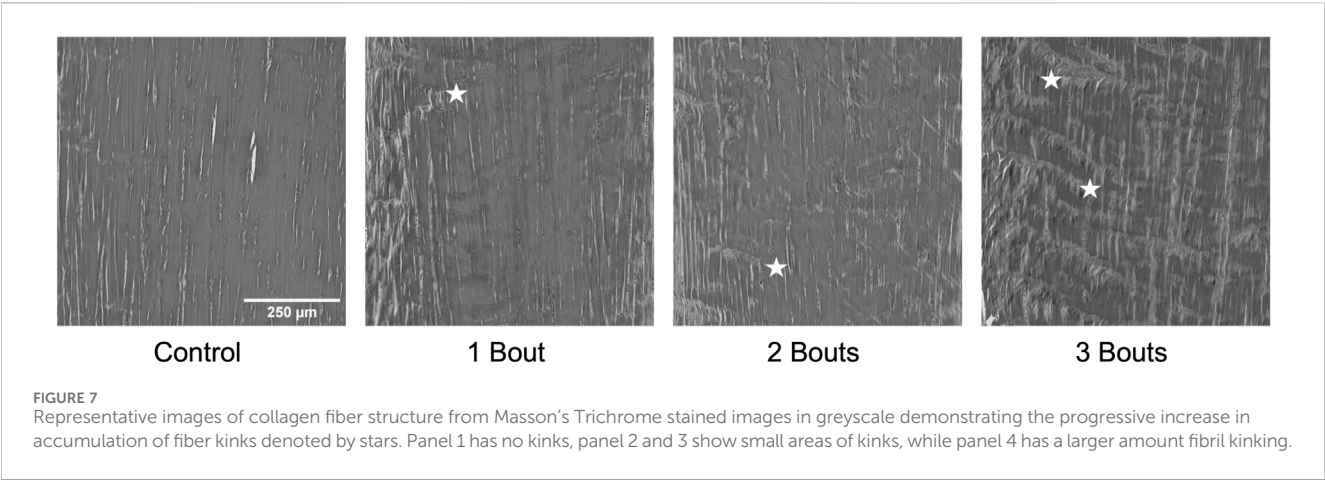


TABLE 2 Collagen morphological properties (collagen area fraction and fibril minor radius) and a fibril-fibril interaction parameter (specific fibril surface) for $n = 1$ sample for the control and loading groups.

Loading Group	Area Fraction (%)	Minor Radius (nm)	Specific Fibril Surface ($\mu\text{m } \mu\text{m}^{-2}$)
0	78.37	83.53	0.0124
1	81.90	73.30	0.0117
2	81.70	75.35	0.0116
3	80.99	70.72	0.0110

transcription factors also regulate other proteins responsible for matrix stiffening and cell contractility, supporting collagen remodeling. However, these transducers' are inhibited upon cell detachment and with a rounder cell morphology (Dupont, 2016; Cai et al., 2021). In our study, YAP and TAZ were both upregulated for group 1. Interestingly, although these are co-transducers, our study showed a gradual decrease in YAP expression with increased TAZ expression for groups 2 and 3. The initial increase in YAP/TAZ may respond to the initial increase in matrix stiffness, as seen with the increase in loading modulus in group 1. With the initiation of apoptotic processes and decreased tendon stiffness, YAP gene expression gradually decreased between groups. While TAZ continued to increase, this may be due to the acute healing time point and a lag in the co-activators response. YAP and TAZ are

considered to be regulated at the protein level by phosphorylation events. In this study, their changes are reported on the transcriptional level. YAP/TAZ regulation which can be considered to be due to upstream signalling pathways in the Hippo pathway, such as focal adhesion sensing of the ECM and adherens junctions mediating cellular adhesion (Heng et al., 2021). Scleraxis, a transcription factor, is crucial for tenocyte differentiation and mechanically stimulated adult tendon growth. Scleraxis expression is known to positively regulate tenomodulin, a type II transmembrane glycoprotein, and a tendon-specific maturation marker, in a tendon cell lineage-dependent manner (Shukunami et al., 2006; Shukunami et al., 2018; Liu et al., 2021). Our findings show increased Scx and Tnmd expression across all groups, indicating tenocyte differentiation processes. The decreasing

trend in expression between groups for both genes may indicate a loss in tenocyte differentiation and cell maturation into aberrant tissues. The increase in *Tnmd* expression between groups 2 and 3 may demonstrate an attempt to recover tenocyte maturation.

Recent work has hypothesized that inflammatory responses from overuse tendon injuries may precede tendon degeneration and pain (D'Addona et al., 2017). The initial responses to tendon injuries involve an inflammatory phase lasting 24 h to 1 week. This involves the migration and recruitment of inflammatory cells, which induces pro-inflammatory cytokines, such as IL-1 β , TNF α , VEGF, and growth factors, including TGF β (D'Addona et al., 2017). While our results show no significant difference in the expression of TNF α , VEGF, and TGF β , the expression of IL-1 β was consistently elevated following each loading group. Changes in cytokine levels alter the expression of type I and III collagen and matrix metalloproteinases (MMPs), which are involved in the remodeling and degradation of the extracellular matrix. Tendon remodeling is mediated by the balance of MMPs and their tissue inhibitors (TIMPs) (Del Buono et al., 2013). An imbalance between these two types of enzymes can disrupt homeostasis and collagen formation, contributing to the degenerative process leading to tendinopathy. IL-1 β induces degenerative tendon changes, including expression of MMP-1, -3, -8, and -13 and downregulation of collagen type I expression (D'Addona et al., 2017). MMP-13 is associated with matrix degradation, specifically the disruption of type I and III collagen in the early phases of wound healing. The significant increase in MMP-13 expression may signify an imbalance in the matrix remodeling process. The gradual increase in MMP-2 expression, which degrades smaller and denatured collagen fragments, demonstrates an active degradation of damaged collagen fibers from repetitive loading.

Our results of a decreased type I collagen expression after three loading bouts with an increase in type III collagen expression may indicate early signs of an impaired wound healing response and contribute to the decreased mechanical properties seen following fatigue loading. Increased collagen disorganization has been reported to precede symptoms of tendon injury and tendon rupture in previous studies (Docking et al., 2015), where alterations to collagen synthesis have been shown as early as 24 h post-loading (Magnusson et al., 2010), with increases in type I and III collagen, and the proportion of type III to I collagen. In the early healing stage, type III collagen is rapidly produced and irregularly placed as a "patch" to repair the damaged area (Maffulli et al., 2000). While type I collagen is eventually produced in normal tendons to replace type III collagen, tendinopathic tendon's impaired healing mechanisms lead to increased production and accumulation of type III collagen (Millar et al., 2021). While the deposition of type III collagen is a rapid healing response to successive overloading, its disorganized arrangement contributes to the tendon's inferior mechanics, predisposing the tendon to tendon ruptures (Maffulli et al., 2000). Our study showed a gradual increase in type I collagen expression for groups 1 and 2, followed by a sharp decrease for group 3. Meanwhile, there was a consistently elevated type III collagen expression between experimental groups. The shift in type I collagen expression with a consistent upregulation of type III collagen indicates the tendons' response to produce type III collagen in recovery from successive injuries.

Cellular morphology became disrupted in loaded groups before the widespread appearance of collagen fiber kinking. While healthy tenocytes had cell extensions, demonstrating deep cell-matrix connections, the thickened pericellular matrix indicated broken cell-cell and cell-matrix interactions. The presence of vacuoles, vesicles, and mitochondria features confirms increased metabolic processes. The cellular damage is consistent with features seen in an *in situ* tendon fatigue model and human tendinopathic samples (Zabrzynski et al., 2018; Ros et al., 2019). Tenocytes exhibited features of apoptosis processes, forming dense chromatin regions, followed by a ring on the cell's outer border and separation of nuclei. There was no formation of a "beaded necklace" or release of apoptotic bodies, as seen in the cell death process. This may correspond to samples being imaged at an early time point following healing. This early evidence of apoptosis indicates a disruption in cellular homeostasis, potentially interrupting the cellular signaling necessary for reparative processes and mechanotransduction and leading to downstream inflammation and imbalance in matrix turnover. As seen in our results, IL-1 β and MMP-2, two genes involved in the positive regulation of apoptotic processes, were upregulated, indicating a feedback mechanism in which apoptotic processes may begin in overloaded tendons (Van Opdenbosch and Lamkanfi, 2019; Kim et al., 2021). Apoptosis has been suggested to play a role in tendon overuse injuries, as demonstrated in clinical tendinopathy and other preclinical overuse models of tendinopathy (Scott et al., 2007; Millar et al., 2009; Ros et al., 2019).

There were no significant differences in collagen orientation, cellular morphology, and proliferation macro-structurally. However, qualitative changes included increased collagen fiber crimping and cellular proliferation in various tendon regions. Low cellularity levels detected within group 1 with respect to the control group could be attributed to cell death. In contrast, the subsequent increase in cellularity for groups 2 and 3 could indicate an increase in cellular response to injury. While there were trends among experimental groups, there was no significance, probably due to the low sample size. The increase in cell number can be attributed to IL-1 β , Scx, and YAP, all upregulated in all groups. Along with these macro-structural damage accumulations, the reduced expression of type I collagen and increased production of mechanically weaker type III collagen may result in the tendon experiencing lower mechanical and material properties (Arya and Kulig, 2010). On the fibrillar level, the increase in lower-diameter fibrils may indicate a microscale adaptation response, where collagen fibrils gradually grow following previous injuries. Since this study assessed early responses to successive fatigue injuries, there may be a lag in the appearance of macro-structural damage, as mechanobiological changes precede gross tissue changes.

While this study demonstrated the ability to use an *in vivo* overuse passive loading model to induce accumulated tendon damage, it is essential to acknowledge certain limitations associated with the work. Although we quantified *in vivo* functional changes resulting from successive loading bouts, it is important to note that comparisons between loading groups to assess healing were not feasible due to the nature of the prescribed fatigue loading regimen. This regimen was tailored to each animal based on the unique properties of their Achilles tendon loading-unloading curves rather than using a load- or displacement-

controlled approach. The variability in the gene expression levels may have been attributed to the subject-specific loading protocol and the nature of *in vivo* experiments. Future studies employing load- or displacement-control modes could provide more precise quantifications of alterations during the healing period. While our *in vivo* mechanical measurements contributed to our understanding of the effects of the fatigue loading protocol, additional insights can be gained from traditional viscoelastic, dynamic, and failure tests and provide a comprehensive view of changes in tendon material properties. Our conversions from ankle dorsiflexion angle to strain rely on *ex vivo* measured strain values, and future work will explore non-invasive methods for quantifying *in vivo* tendon strains throughout loading using ultrasound. Tendon structure was quantified only at the acute healing time points. Investigating tendon structure under varying loading conditions can provide valuable insights into dynamic changes in collagen structure and damage. While our study reported gene expression of collagen, matrix, and inflammatory markers, the inclusion of other damage markers, including apoptosis-related genes, can enhance our understanding of the degenerative and remodeling response following fatigue injuries, given that TEM imaging demonstrated processes preceding apoptosis. Tendons comprise collagen, glycosaminoglycans, and water, collectively contributing to their viscoelastic material properties. A deeper understanding of changes in tendon composition and production can be achieved through assays that quantify the content and synthesis of these key tendon components. While this study focused on assessing tendon changes during the acute healing period, it is crucial to recognize that the inflammatory phase lasts up to 1 week. Future studies will aim to comprehensively characterize the alterations in tendon mechanobiological responses and functional changes in response to fatigue injuries.

We demonstrated early mechanical, biological, and structural damage to successive fatigue loading injuries from our novel passive loading system. This is the first animal model that establishes a direct connection between successive *in vivo* fatigue loads and mechanobiological and functional tendon changes. Our findings demonstrate the early, adaptive responses of tendons to overloading and show promise for longer-term investigations into the underlying mechanisms of cellular signaling and damage and matrix turnover in response to *in vivo* injuries caused by overuse and aging to enhance our ability to predict and address early-stage tendinopathy, ultimately improving the prognosis for individuals facing such conditions.

Data availability statement

The raw data supporting the conclusion of this article will be made available by the authors, without undue reservation.

Ethics statement

The animal study was approved by Beth Israel Deaconess Medical Center Animal Care and Use Committee. The study was

conducted in accordance with the local legislation and institutional requirements.

Author contributions

PC: Writing–review and editing, Data curation, Formal Analysis, Investigation, Methodology, Visualization, Writing–original draft. MM: Data curation, Formal Analysis, Methodology, Writing–review and editing. DY: Data curation, Formal Analysis, Methodology, Writing–review and editing. DC: Data curation, Formal Analysis, Methodology, Writing–review and editing. KM: Data curation, Formal Analysis, Methodology, Writing–review and editing. JG: Writing–review and editing, Methodology, Investigation. JD: Writing–review and editing, Conceptualization, Resources. AR: Conceptualization, Resources, Writing–review and editing, Funding acquisition. AN: Conceptualization, Funding acquisition, Resources, Writing–review and editing, Project administration, Supervision.

Funding

The authors declare financial support was received for the research, authorship, and/or publication of this article. This work was supported by the Joe Fallon Research Fund and the Dr. Louis Meeks BIDMC Sports Medicine Trainee Research Fund at BIDMC Orthopaedic Surgery Department. Research reported in this publication was supported by the Boston University Micro and Nano Imaging Facility and the Office of the Director, National Institutes of Health of the National Institutes of Health under Award Number S10OD024993. This study was also supported by the BIDMC Histology and the Electron Microscopy Cores.

Conflict of interest

The authors declare that the research was conducted in the absence of any commercial or financial relationships that could be construed as a potential conflict of interest.

Publisher's note

All claims expressed in this article are solely those of the authors and do not necessarily represent those of their affiliated organizations, or those of the publisher, the editors and the reviewers. Any product that may be evaluated in this article, or claim that may be made by its manufacturer, is not guaranteed or endorsed by the publisher.

Author disclaimer

The content is solely the responsibility of the authors and does not necessarily represent the official views of the National Institute of Health.

References

- Andarawis-Puri, N., and Flatow, E. L. (2011). Tendon fatigue in response to mechanical loading. *J. Musculoskelet. Neuronal Interact.* 11, 106–114.
- Andarawis-Puri, N., Philip, A., Laudier, D., Schaffler, M. B., and Flatow, E. L. (2014). Temporal effect of *in vivo* tendon fatigue loading on the apoptotic response explained in the context of number of fatigue loading cycles and initial damage parameters. *J. Orthop. Res.* 32, 1097–1103. doi:10.1002/jor.22639
- Andarawis-Puri, N., Sereysky, J. B., Jepsen, K. J., and Flatow, E. L. (2012). The relationships between cyclic fatigue loading, changes in initial mechanical properties, and the *in vivo* temporal mechanical response of the rat patellar tendon. *J. Biomech.* 45, 59–65. doi:10.1016/j.jbiomech.2011.10.008
- Arya, S., and Kulig, K. (2010). Tendinopathy alters mechanical and material properties of the Achilles tendon. *J. Appl. Physiol.* (1985) 108, 670–675. doi:10.1152/jappphysiol.00259.2009
- Benage, L. G., Sweeney, J. D., Giers, M. B., and Balasubramanian, R. (2022). Dynamic load model systems of tendon inflammation and mechanobiology. *Front. Bioeng. Biotechnol.* 10, 896336. doi:10.3389/fbioe.2022.896336
- Bloom, E. T., Lin, L. M., Locke, R. C., Giordani, A., Krassan, E., Peloquin, J. M., et al. (2023). Overload in a rat *in vivo* model of synergist ablation induces tendon multiscale structural and functional degeneration. *J. Biomech. Eng.* 145, 081003. doi:10.1115/1.4062523
- Cai, X., Wang, K. C., and Meng, Z. (2021). Mechanoregulation of YAP and TAZ in cellular homeostasis and disease progression. *Front. Cell Dev. Biol.* 9, 673599. doi:10.3389/fcell.2021.673599
- Chainani, P. H., Williamson, P. M., Yeritsyan, D., Momenzadeh, K., Kheir, N., DeAngelis, J. P., et al. (2024). A passive ankle dorsiflexion testing system for an *In Vivo* model of overuse-induced tendinopathy. doi:10.3791/65803
- D'addona, A., Maffulli, N., Formisano, S., and Rosa, D. (2017). Inflammation in tendinopathy. *Surgeon* 15, 297–302. doi:10.1016/j.surge.2017.04.004
- Del Buono, A., Oliva, F., Osti, L., and Maffulli, N. (2013). Metalloproteases and tendinopathy. *Muscles Ligaments Tendons J.* 3, 51–57. doi:10.11138/mltj/2013.3.1.051
- Docking, S. I., Ooi, C. C., and Connell, D. (2015). Tendinopathy: is imaging telling us the entire story? *J. Orthop. Sports Phys. Ther.* 45, 842–852. doi:10.2519/jospt.2015.5880
- Dupont, S. (2016). Role of YAP/TAZ in cell-matrix adhesion-mediated signalling and mechanotransduction. *Exp. Cell Res.* 343, 42–53. doi:10.1016/j.yexcr.2015.10.034
- Fung, D. T., Wang, V. M., Laudier, D. M., Shine, J. H., Basta-Pjakic, J., Jepsen, K. J., et al. (2009). Subrupture tendon fatigue damage. *J. Orthop. Res.* 27, 264–273. doi:10.1002/jor.20722
- Helland, C., Bojsen-Moller, J., Raastad, T., Seynnes, O. R., Moltubakk, M. M., Jakobsen, V., et al. (2013). Mechanical properties of the patellar tendon in elite volleyball players with and without patellar tendinopathy. *Br. J. Sports Med.* 47, 862–868. doi:10.1136/bjsports-2013-092275
- Heng, B. C., Zhang, X., Aubel, D., Bai, Y., Li, X., Wei, Y., et al. (2021). An overview of signaling pathways regulating YAP/TAZ activity. *Cell Mol. Life Sci.* 78 (2), 497–512. doi:10.1007/s00018-020-03579-8
- Kaux, J. F., Forthomme, B., Goff, C. L., Crielaard, J. M., and Croisier, J. L. (2011). Current opinions on tendinopathy. *J. Sports Sci. Med.* 10, 238–253.
- Kim, R. J., An, S. H., Gwark, J. Y., and Park, H. B. (2021). Antioxidant effects on hypoxia-induced oxidative stress and apoptosis in rat rotator cuff fibroblasts. *Eur. Cell Mater* 41, 680–693. doi:10.22203/ecm.v041a44
- Komi, P. V., Fukashiro, S., and Jarvinen, M. (1992). Biomechanical loading of Achilles tendon during normal locomotion. *Clin. Sports Med.* 11, 521–531. doi:10.1016/s0278-5919(20)30506-8
- Lavagnino, M., Wall, M. E., Little, D., Banes, A. J., Guilak, F., and Arnoczky, S. P. (2015). Tendon mechanobiology: current knowledge and future research opportunities. *J. Orthop. Res.* 33, 813–822. doi:10.1002/jor.22871
- Lipman, K., Wang, C., Ting, K., Soo, C., and Zheng, Z. (2018). Tendinopathy: injury, repair, and current exploration. *Drug Des. Devel Ther.* 12, 591–603. doi:10.2147/dddt.s154660
- Liu, H., Xu, J., Lan, Y., Lim, H. W., and Jiang, R. (2021). The scleraxis transcription factor directly regulates multiple distinct molecular and cellular processes during early tendon cell differentiation. *Front. Cell Dev. Biol.* 9, 654397. doi:10.3389/fcell.2021.654397
- Livak, K. J., and Schmittgen, T. D. (2001). Analysis of relative gene expression data using real-time quantitative PCR and the $2^{-\Delta\Delta Ct}$ method. *Methods* 25 (4), 402–408. doi:10.1006/meth.2001.1262
- Maffulli, N., Ewen, S. W., Waterston, S. W., Reaper, J., and Barrass, V. (2000). Tenocytes from ruptured and tendinopathic achilles tendons produce greater quantities of type III collagen than tenocytes from normal achilles tendons. An *in vitro* model of human tendon healing. *Am. J. Sports Med.* 28, 499–505. doi:10.1177/03635465000280040901
- Maffulli, N., Longo, U. G., Kadakia, A., and Spiezia, F. (2020). Achilles tendinopathy. *Foot Ankle Surg.* 26, 240–249. doi:10.1016/j.fas.2019.03.009
- Magnusson, S. P., Langberg, H., and Kjaer, M. (2010). The pathogenesis of tendinopathy: balancing the response to loading. *Nat. Rev. Rheumatol.* 6, 262–268. doi:10.1038/nrrheum.2010.43
- Millar, N. L., Silbernagel, K. G., Thorborg, K., Kirwan, P. D., Galatz, L. M., Abrams, G. D., et al. (2021). Tendinopathy. *Nat. Rev. Dis. Prim.* 7, 1. doi:10.1038/s41572-020-00234-1
- Millar, N. L., Wei, A. Q., Molloy, T. J., Bonar, F., and Murrell, G. A. (2009). Cytokines and apoptosis in supraspinatus tendinopathy. *J. Bone Jt. Surg. Br.* 91, 417–424. doi:10.1302/0301-620x.91b3.21652
- Neviaser, A., Andarawis-Puri, N., and Flatow, E. (2012). Basic mechanisms of tendon fatigue damage. *J. Shoulder Elb. Surg.* 21, 158–163. doi:10.1016/j.jse.2011.11.014
- Ng, G. Y., Chung, P. Y., Wang, J. S., and Cheung, R. T. (2011). Enforced bipedal downhill running induces Achilles tendinosis in rats. *Connect. Tissue Res.* 52, 466–471. doi:10.3109/03008207.2011.562334
- Pentzold, S., and Wildemann, B. (2022). Mechanical overload decreases tenogenic differentiation compared to physiological load in bioartificial tendons. *J. Biol. Eng.* 16, 5. doi:10.1186/s13036-022-00283-y
- Rigozzi, S., Muller, R., and Snedeker, J. G. (2010). Collagen fibril morphology and mechanical properties of the Achilles tendon in two inbred mouse strains. *J. Anat.* 216, 724–731. doi:10.1111/j.1469-7580.2010.01225.x
- Ros, S. J., Muljadi, P. M., Flatow, E. L., and Andarawis-Puri, N. (2019). Multiscale mechanisms of tendon fatigue damage progression and severity are strain and cycle dependent. *J. Biomech.* 85, 148–156. doi:10.1016/j.jbiomech.2019.01.026
- Salver, D. C., Kharaz, Y. A., Sugg, K. B., Gumucio, J. P., Comerford, E., and Mendias, C. L. (2017). Sex differences in tendon structure and function. *J. Orthop. Res.* 35, 2117–2126. doi:10.1002/jor.23516
- Scott, A., Cook, J. L., Hart, D. A., Walker, D. C., Duronio, V., and Khan, K. M. (2007). Tenocyte responses to mechanical loading *in vivo*: a role for local insulin-like growth factor 1 signaling in early tendinosis in rats. *Arthritis Rheum.* 56, 871–881. doi:10.1002/art.22426
- Shukunami, C., Takimoto, A., Nishizaki, Y., Yoshimoto, Y., Tanaka, S., Miura, S., et al. (2018). Scleraxis is a transcriptional activator that regulates the expression of Tenomodulin, a marker of mature tenocytes and ligamentocytes. *Sci. Rep.* 8, 3155. doi:10.1038/s41598-018-21194-3
- Shukunami, C., Takimoto, A., Oro, M., and Hiraki, Y. (2006). Scleraxis positively regulates the expression of tenomodulin, a differentiation marker of tenocytes. *Dev. Biol.* 298, 234–247. doi:10.1016/j.ydbio.2006.06.036
- Soslowsky, L. J., Thomopoulos, S., Esmail, A., Flanagan, C. L., Iannotti, J. P., Williamson, J. D., 3rd, et al. (2002). Rotator cuff tendinosis in an animal model: role of extrinsic and overuse factors. *Ann. Biomed. Eng.* 30, 1057–1063. doi:10.1114/1.1509765
- Soslowsky, L. J., Thomopoulos, S., Tun, S., Flanagan, C. L., Keefer, C. C., Mastaw, J., et al. (2000). Neer Award 1999. Overuse activity injures the supraspinatus tendon in an animal model: a histologic and biomechanical study. *J. Shoulder Elb. Surg.* 9, 79–84. doi:10.1016/s1058-2746(00)90033-8
- Spiesz, E. M., Thorpe, C. T., Chaudhry, S., Riley, G. P., Birch, H. L., Clegg, P. D., et al. (2015). Tendon extracellular matrix damage, degradation and inflammation in response to *in vitro* overload exercise. *J. Orthop. Res.* 33, 889–897. doi:10.1002/jor.22879
- Svensson, R. B., Heinemeier, K. M., Couppe, C., Kjaer, M., and Magnusson, S. P. (2016). Effect of aging and exercise on the tendon. *J. Appl. Physiol.* (1985) 121, 1237–1246. doi:10.1152/jappphysiol.00328.2016
- Tarantino, D., Mottola, R., Resta, G., Gnasso, R., Palmeri, S., Corrado, B., et al. (2023). Achilles tendinopathy pathogenesis and management: a narrative review. *Int. J. Environ. Res. Public Health* 20, 6681. doi:10.3390/ijerph20176681
- Thorpe, C. T., Chaudhry, S., Lei, I. I., Varone, A., Riley, G. P., Birch, H. L., et al. (2015). Tendon overload results in alterations in cell shape and increased markers of inflammation and matrix degradation. *Scand. J. Med. Sci. Sports* 25, e381–e391. doi:10.1111/sms.12333
- Van Oudenbosch, N., and Lamkanfi, M. (2019). Caspases in cell death, inflammation, and disease. *Immunity* 50, 1352–1364. doi:10.1016/j.immuni.2019.05.020
- Wiesinger, H. P., Seynnes, O. R., Kesters, A., Muller, E., and Rieder, F. (2020). Mechanical and material tendon properties in patients with proximal patellar tendinopathy. *Front. Physiol.* 11, 704. doi:10.3389/fphys.2020.00704
- Williamson, P. M., Freedman, B. R., Kwok, N., Beeram, I., Pennings, J., Johnson, J., et al. (2021). Tendinopathy and tendon material response to load: what we can learn from small animal studies. *Acta Biomater.* 134, 43–56. doi:10.1016/j.actbio.2021.07.046
- Williamson, P. M., Yeritsyan, D., Peacock, T., Chainani, P., Momenzadeh, K., Ascutto, D., et al. (2023). A passive ankle dorsiflexion testing system to assess mechanobiological and structural response to cyclic loading in rat Achilles tendon. *J. Biomech.* 156, 111664. doi:10.1016/j.jbiomech.2023.111664
- Zabrzynski, J., Gagat, M., Paczesny, L., Lapaj, L., and Grzanka, D. (2018). Electron microscope study of the advanced tendinopathy process of the long head of the biceps brachii tendon treated arthroscopically. *Folia Morphol. Warsz.* 77, 371–377. doi:10.5603/fm.a2017.0105
- Zamboulis, D. E., Thorpe, C. T., Ashraf Kharaz, Y., Birch, H. L., Screen, H. R., and Clegg, P. D. (2020). Postnatal mechanical loading drives adaptation of tissues primarily through modulation of the non-collagenous matrix. *Elife* 9, e58075. doi:10.7554/elifesciences.58075
- Zhou, Y., Hong, W., and Lu, L. (2013). Imaging beads-retained prey assay for rapid and quantitative protein-protein interaction. *PLoS One* 8, e59727. doi:10.1371/journal.pone.0059727



OPEN ACCESS

EDITED BY

Peter Quesada,
University of Louisville, United States

REVIEWED BY

Yuan Feng,
Shanghai Jiao Tong University, China
Shailesh Govind Ganpule,
Indian Institute of Technology Roorkee, India

*CORRESPONDENCE

Natacha Elster,
✉ natacha.elster@isl.eu

RECEIVED 20 September 2023

ACCEPTED 27 February 2024

PUBLISHED 22 March 2024

CITATION

Elster N, Boutillier J, Bourdet N, Magnan P, Naz P, Willinger R and Deck C (2024), Design of a simplified cranial substitute with a modal behavior close to that of a human skull. *Front. Bioeng. Biotechnol.* 12:1297730. doi: 10.3389/fbioe.2024.1297730

COPYRIGHT

© 2024 Elster, Boutillier, Bourdet, Magnan, Naz, Willinger and Deck. This is an open-access article distributed under the terms of the [Creative Commons Attribution License \(CC BY\)](https://creativecommons.org/licenses/by/4.0/). The use, distribution or reproduction in other forums is permitted, provided the original author(s) and the copyright owner(s) are credited and that the original publication in this journal is cited, in accordance with accepted academic practice. No use, distribution or reproduction is permitted which does not comply with these terms.

Design of a simplified cranial substitute with a modal behavior close to that of a human skull

Natacha Elster^{1*}, Johanna Boutillier¹, Nicolas Bourdet², Pascal Magnan¹, Pierre Naz¹, Rémy Willinger² and Caroline Deck²

¹French-German Research Institute of Saint-Louis, Saint-Louis, France, ²ICube Laboratory, Strasbourg University, Strasbourg, France

Individuals exposed to the propagation of shock waves generated by the detonation of explosive charges may suffer Traumatic Brain Injury. The mechanism of cranial deflection is one of many hypotheses that could explain the observed brain damage. To investigate this physical phenomenon in a reproducible manner, a new simplified cranial substitute was designed with a mechanical response close to that of a human skull when subjected to this type of loading. As a first step, a Finite Element Model was employed to dimension the new substitute. The objective was indeed to obtain a vibratory behavior close to that of a dry human skull over a wide range of frequencies up to 10 kHz. As a second step, the Finite Element Model was used together with Experimental Modal Analyses to identify the vibration modes of the substitute. A shaker excited the structure via a metal rod, while a laser vibrometer recorded the induced vibrations at defined measurement points. The results showed that despite differences in material properties and geometry, the newly developed substitute has 10/13 natural frequencies in common with those of dry human skulls. When filled with a simulant of cerebral matter, it could therefore be used in future studies as an approximation to assess the mechanical response of a simplified skull substitute to a blast threat.

KEYWORDS

experimental modal analysis, finite element model, human skull substitute, parametric study, vibrations

1 Introduction

Individuals subjected to high-speed loadings such as detonating explosive charges can be injured in many ways depending on their distance from the explosion. The person may be blasted, riddled by munition fragments or surrounding materials, thrown against obstacles, and even burned if too close to the epicenter. The head can be severely affected by such events (Wojcik et al., 2010), particularly by the propagation of shock waves. To explain the observed cerebral lesions (Trudeau et al., 1998; Armonda et al., 2006; Hoge et al., 2008; Warden et al., 2009; Hicks et al., 2010; Rosenfeld et al., 2013; Magnuson and Ling, 2018), several injury mechanisms were proposed in literature. One of those is of particular interest: the cranial deflection. This hypothesis implies that the load applied when shock waves reach the human skull can induce brain lesions due to compression and shear loading on the underlying cerebral matter (Bolander, 2011; Chandra and Sundaramurthy, 2015).

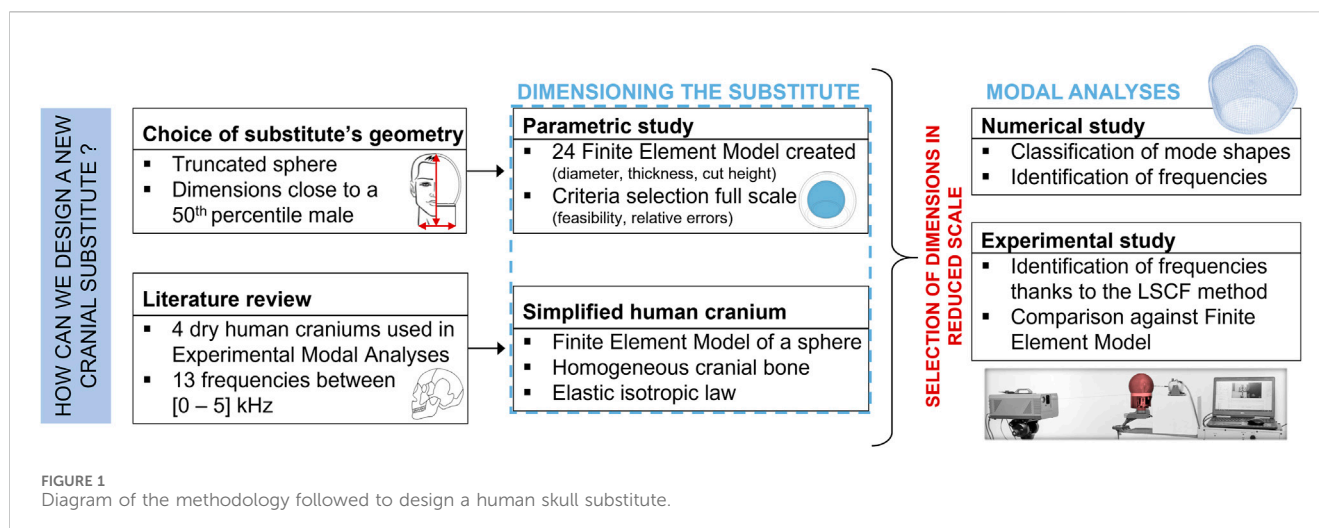


FIGURE 1
Diagram of the methodology followed to design a human skull substitute.

Literature describes several geometric human head substitutes developed to investigate this specific phenomenon. Dal Cengio Leonardi et al. (2011) filled Synbone spheres with either Sylgard gel (527 A&B) or aqueous glycerin; Goeller et al. (2012) created an ellipsoidal model in polycarbonate and filled it with either water or Sylgard gel 527; and finally Hua et al. (2014) designed a polycarbonate spherical shell filled with water. Those substitutes were then instrumented with pressure sensors inside their shell, while strain gauges were glued to their outer surfaces. Shock waves of varying durations between 0.4 ms and 6.0 ms, with maximum amplitudes ranging from 40 kPa to 210 kPa were applied to each substitute. Several metrics of interest were collected such as the time of wave arrival, the first peak values of the internal pressures and the shell strains, as well as the extreme values. Results showed that internal pressures and shell strains are related; however, only time-domain analyses were performed in those mentioned studies (Elster et al., 2023). Since the time history of quasi-ideal blast waves could be approximated by pulse signals with broad frequency spectra, it would be interesting to analyze blast related results in the frequency domain as well. Indeed, the shock front could excite a large range of cranial vibration modes. It would therefore be worth using Experimental Modal Analyses (EMA) to characterize the vibration modes of the head substitutes beforehand, and then as a second step to compare the obtained results with the frequencies extracted from the strain signals recorded during blast events.

In Fujiwara et al. (1989) a cranial substitute able to reproduce the first vibration mode shape of a dry human skull was designed. The current study aims to create a new skull substitute that could replace a human one for frequency-domain analysis, considering a larger number of natural frequencies than in Fujiwara's study. Indeed, EMA has been performed on four 50th percentile dry human male skulls in the literature (Franke, 1956; Gurdjian et al., 1970; Khalil et al., 1979; Taleb et al., 1993). In the range [0–5] kHz, 13 natural frequencies were found in all experiments combined. The present study aims to design a new cranial substitute based on these frequencies.

To reach this goal, the manufacturing method of the substitute must first be selected and the mechanical properties of the material need to be characterized. Secondly, the geometry

and dimensions of the substitute are then adapted to approximate a 50th percentile dry human skull, while maintaining a close vibratory response. The third part is dedicated to simultaneously perform Numerical and Experimental Modal Analyses to identify all vibration modes of the substitute. Finally, the obtained results are compared in terms of frequencies with those described in the literature on dry human skulls to evaluate the relevance of the new cranial substitute.

2 Material and methods

The methodology adopted to design the new cranial substitute is summarized in Figure 1. A simplified geometry was chosen to approximate the human skull: a hollow truncated sphere. For enhanced feasibility and cost-effectiveness, an additive manufacturing process was thus selected: Polyjet 3D-printing technology (@Stratasys, 2019). The material chosen is the IORA Black resin developed by the firm iSQUARED², whose mechanical properties are far from those of the cranial bone in terms of Young's modulus, density and Poisson ratio (Elster et al., 2022). Hence, since the substitute is meant to have a vibratory response akin to that of a dry human skull, a parametric study must be performed on its dimensions to compensate for the existing disparities. In addition, a reduced scale was considered to select the optimal geometry due to experimental constraints of the blast testing field. Finally, once the dimensions have been settled, numerical and experimental studies are carried out simultaneously to characterize the vibratory response of the new substitute, and to compare its behavior with literature data.

2.1 Parametric study

The first step consists in creating a Finite Element Model (FEM) of a sphere approximating a human skull. This sphere has an outer diameter of 180 mm like the skullcap (Got et al., 1983; Bushby et al., 1992; Haeussinger et al., 2011), and a constant thickness of 7 mm to mimic the frontal cranial bone (Got et al.,

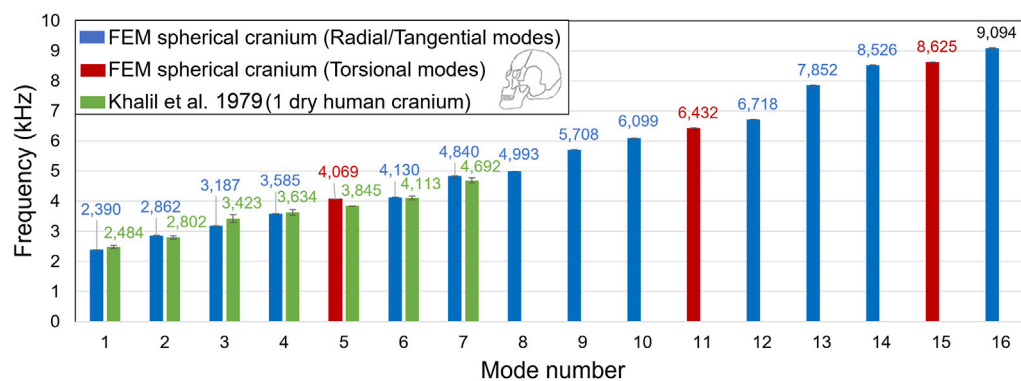


FIGURE 2
Comparison of the numerical frequencies computed from a FEM of a spheric-approximated human skull to those measured experimentally on a dry human skull of the 50th percentile in the literature (Khalil et al., 1979).

1983; Lynnerup, 2001; Haeussinger et al., 2011). For the purpose of simplification, the cranial bone is assumed to be made of a homogeneous and isotropic material, following a linear elastic behavior law with a Young's modulus of 5,000 MPa (Verschuere et al., 2006; Delille, 2007; Auperrin, 2009), a Poisson ratio of 0.2 (McElhaney et al., 1970; Nishimoto et al., 1995) and a mass density of 1,700 kg/m³ (McElhaney et al., 1970; Nishimoto et al., 1995). The LS-Dyna software is used to mesh the structure, using 30996 hexahedral solid elements with 3 element layers through thickness, and an average element size of 3.1 mm. The implicit solver with the element formulation #18 is selected. This formulation is tailored for hexahedral elements with eight integration points during an implicit linear resolution (LS-DYNA R11 Keyword Manual Volume I, 2018). Free boundary conditions are imposed. In the frequency range [0–10] kHz, 16 vibration modes are computed for the spherical model: 3 torsional modes and 13 radial/tangential modes. This FEM is validated according to the vibration theory of thin spherical shells (Wilkinson, 1966): the relative errors calculated between the FEM and analytical natural frequencies are ranging from 0.01% to 0.93%. Moreover, Figure 2 compares the frequencies of the FEM with experimental results described by Khalil et al. (1979), where a human skull was struck by an impact hammer, resulting in an impulse signal between 20 Hz and 5,000 Hz. The first seven frequencies of the FEM are close to several frequencies measured on the dry human skull, with relative errors ranging from 0.4% to 6.9%.

In future studies, the newly developed substitute is intended to be exposed to the detonation of explosive charges in free-field conditions. The experimental ground where the detonations will be carried out has limitations. These include the maximum admissible explosive mass and the allowable distances between the instrumented substitute and the center of the detonation. Given the exposure parameters being sought, it is essential to work in a reduced scale of 5/6 ratio. The similarity laws and scale effects will have to be applied in future blast tests. In the context of explosives, the similarity laws indicate that reduced-scale studies can be employed to ascertain the characteristics of a full-scale blast wave, and *vice versa* (Baker et al., 1983). Additionally, scale

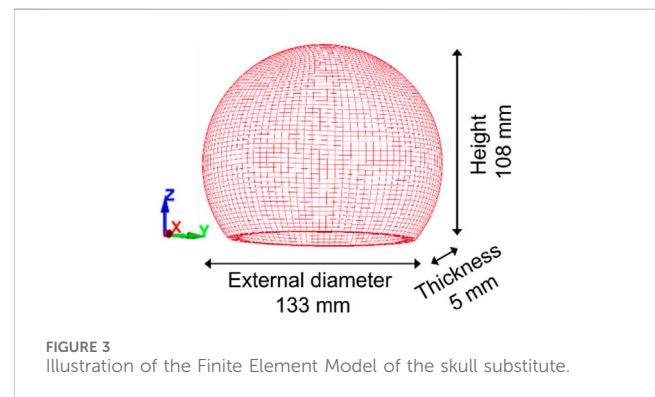


FIGURE 3
Illustration of the Finite Element Model of the skull substitute.

effects extend to the displacement of the exposed structure (Baker et al., 1991).

With this in mind, the dimensions of the new cranial substitute have to be selected. Working with a hollow truncated sphere, three parameters have to be defined: the external diameter of the shell, its thickness, and its height. A parametric study is thus performed to evaluate the influence of each parameter on the natural frequencies of the substitute. Several design criteria must be taken into account to define the possibilities of each setting. First, the substitute has to be large enough to contain the sensors, while being smaller than 148 mm in diameter, which is the size of the printing plate. Four external diameters are chosen: 120 mm, 125 mm, 133 mm and 142 mm. In addition, based on a preliminary study, a minimum thickness of 5 mm in reduced scale is required for the substitute to withstand a blast. Therefore, the thicknesses chosen are 5 mm, 5.8 mm and 7.5 mm. Finally, three truncation ratios are defined: 5/8, 3/4, and 7/8 of the volume. As a result, twenty-four combinations of dimensions were tested during the parametric study. To select the most suitable combination, three selection criteria were applied: the physical feasibility, and the relative and absolute gaps in terms of frequencies against the spheric-approximated skull FEM values. Ultimately, the chosen dimensions are: an external diameter of 133 mm, a thickness of 5 mm, and a height of 108 mm (Elster et al., 2022).

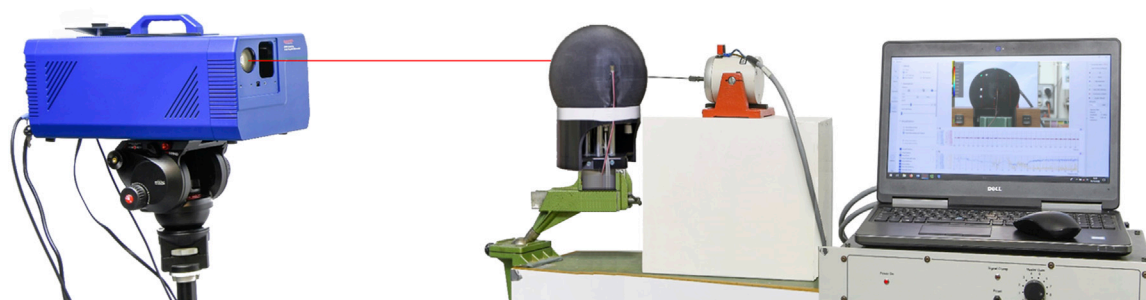


FIGURE 4
Setup used to perform an Experimental Modal Analysis on the 3D-printed prototype of the human skull substitute.

2.2 Finite Element Model of the substitute

After selecting the optimal dimensions, the FEM of the new skull substitute is created, as illustrated in Figure 3. The model is meshed with 14400 hexahedral elements of average size 3.1 mm with 3 elements through thickness. Again, element formulation #18 is used, with an elastic isotropic constitutive law. Nodes located at the bottom of the FEM are embedded. The material properties of the IORA Black resin were determined experimentally in a previous study, giving a Young's modulus of $2,663 \pm 228$ MPa, a Poisson ratio of 0.38 ± 0.04 , and a mass density of $1,170 \text{ kg/m}^3$ (Elster et al., 2022).

Computed vibrations modes can be visually classified into four different types: torsional, biaxial, radial, and axial modes. Radial and axial modes can be further described using the thin-shell theory (Rossing, 1982; Xie et al., 2017; Du et al., 2019), for which two parameters (n, m) are defined: n represents the number of symmetry lines passing through the center of the cavity; and m is the number of circles that can be drawn in top view.

2.3 Experimental Modal Analysis of the substitute

An Experimental Modal Analysis aims to extract the vibration modes of a structure. The structure under test is subjected to external forces through a frequency sweep in given input points; while resulting vibrations are recorded at strategic locations called outputs (Ewins, 2000). A modal identification method then exploits the experimental signals and determines the associated natural frequencies and mode shapes of the structure.

In this study, a prototype of the skull substitute is 3D-printed using the Polyjet technology, applying resin droplets to the printing plate layer by layer. Each layer is then immediately cured by UV radiation and the structure can be used immediately after printing. Theoretically, the molecular bonds between the layers are maintained and material properties are preserved both in the printing plane and in thickness, allowing assumptions of isotropy and material homogeneity to be considered (Williams et al., 2011). In the current study, the in-fill density was 100% for a layer thickness of 0.028 mm. The skull substitute is then glued on a Dural plate (AU4G), circular in cross-section and 5 mm thick, using notches for attachment. A transition

piece printed in the same material as the substitute is bonded directly to the substitute thanks to epoxy glue. The dimensions of this part are close to the neck in reduced scale: it is an open cylinder with a diameter of 120 mm and a length of 90 mm (Gordon et al., 1988; Vasavada et al., 2008). The prototype is finally clamped at its base and subjected to an EMA using the setup illustrated in Figure 4. An up-chirp signal of amplitude 2V and frequency ranging from 5 Hz to 12 kHz is transmitted to a shaker (LDS V200), whose metal rod is in contact with the substitute near its midline. A scanning laser vibrometer (OptoMET SWIR) is used to record the time history of the vibration velocity in a given output point at a recording speed of 49 mm/s and a sampling rate of 51.2 kS/s. Ten repetitions are conducted for each measurement to ensure the reproducibility of results.

To limit the number of outputs, six measurement lines are defined, as illustrated in Figure 5A: three horizontal lines “top”, “midline”, “bottom”; and three vertical lines “left”, “middle”, “right”. Taking symmetries into account, the substitute is then turned six times to reconstruct data for the entire structure in three dimensions (Figure 5B). For each position, the input point is at the extreme left on the midline. On average, 51 measurement points are defined per rotation.

The experimental data measured during the vibration tests are post-processed using a moving average filter with a kernel of 3 points. A modal identification algorithm is then applied to extract the parameters of the vibration modes: the Least-Squares Complex Frequency (LSCF) algorithm in output-only conditions is used (Verboven, 2002; Peeters and Van der Auweraer, 2005), considering a Single Input Single Output system for each measurement point. First, the velocities recorded at the output points are computed in the frequency-domain to create stabilization diagrams, as illustrated for three theoretical measurement points in Figure 6 (black curves). To robustly identify each frequency, p polynomials are generated to describe the frequency evolution at each measurement point. For every polynomial r , where $1 < r < p$, its roots are plotted directly on the frequency evolution against the polynomial order, here in red (stable roots) and blue (unstable roots). Stable roots form a stabilization line, indicating a natural frequency of the structure; while unstable roots are purely mathematical. Figure 6 plots the magnitude against frequency for three points, showing that amplitude peaks correspond to stabilization lines.

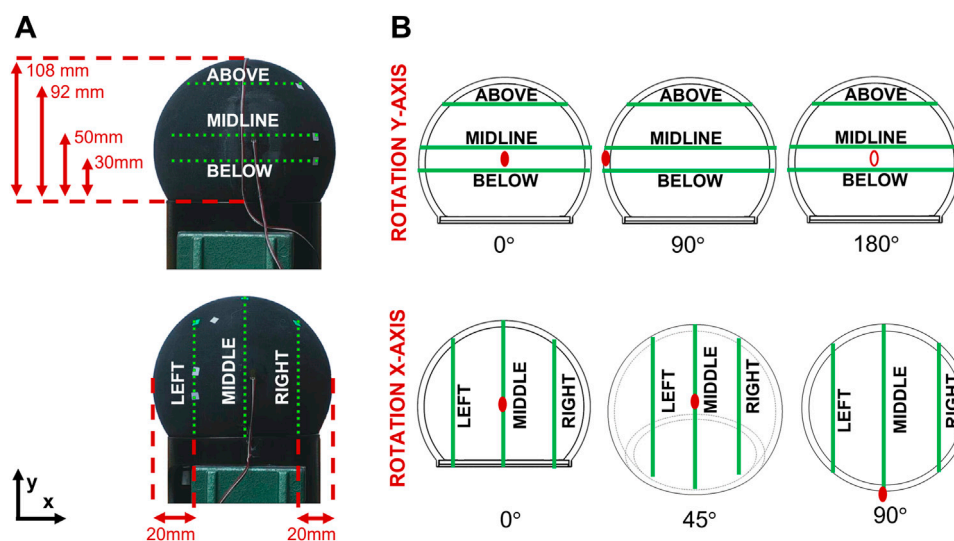


FIGURE 5 Positioning of the 3D-printed prototype in the Experimental Modal Analyses. (A) Horizontal and vertical measurement lines. (B) Six possible rotations along the x- and y- axes. The red dots show the rotation of the substitute.

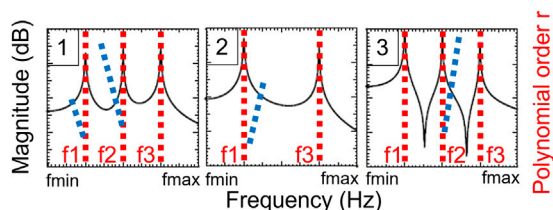


FIGURE 6 Stabilization diagrams for three theoretical measurement points using the Least Squares Complex Frequency method. The dotted lines in red represent the stable roots, and in blue the unstable roots. The graph shows the history of the data magnitude versus frequency.

From the stabilization diagrams, the natural frequencies can be extracted using two criteria: the amplitude spectrum with a tolerance of ± 25 Hz, and the stabilization lines showing the convergence of the roots towards the frequencies with increasing polynomial order, where the maximal polynomial order p is 300. When all conditions are satisfied, the frequency is selected. Associated mode shapes are then constructed from the imaginary part of the measured data.

3 Results

This section presents the results of modal analyses carried out first numerically thanks to a FEM of the new cranial substitute; and second experimentally on the 3D-printed prototype. Both analyses are conducted simultaneously to characterize the vibration modes of the substitute, while eliminating spurious experimental data and validating the FEM at the same time. Mode shapes are first identified by comparing the measured experimental deformations with the FEM computed cut lines amplitudes. Once the numerical and experimental pairing is established, the natural frequency identification errors are quantified to assess how close both models are.

3.1 Identification of mode shapes

3.1.1 Numerical results

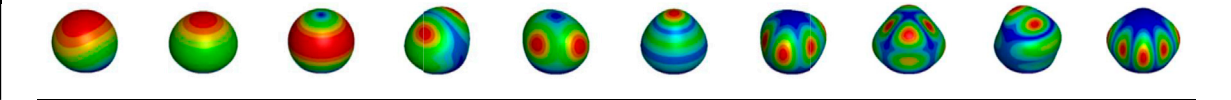
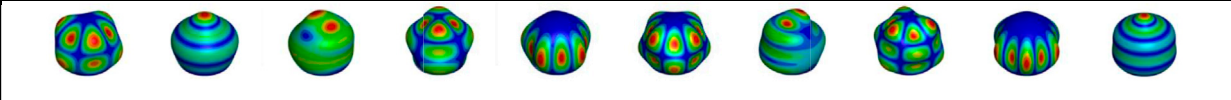
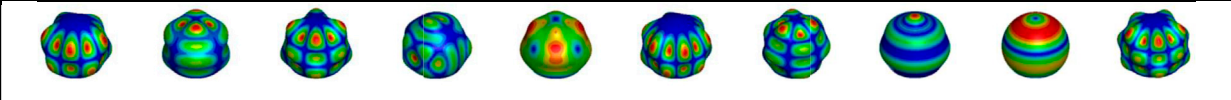
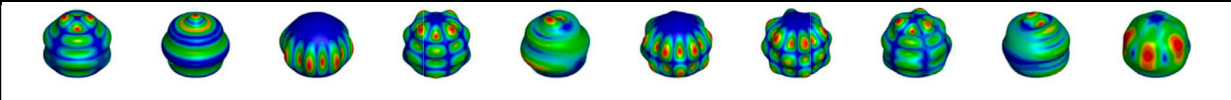
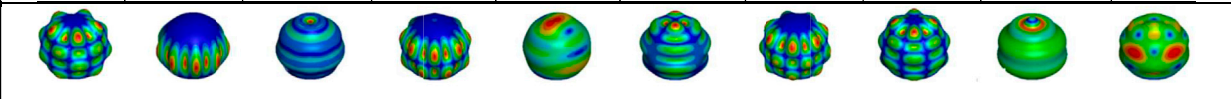
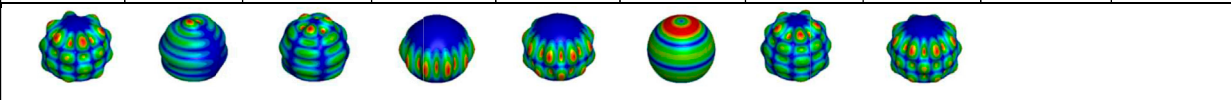
First of all, looking at the FEM mode shapes gathered in Table 1, 58 numerical vibration modes are identified in the frequency range [0–10] kHz: 3 torsional modes, 5 biaxial modes and finally 50 radial modes, 8 of which are axial. The torsional modes are scattered over the spectrum, the first one being at 2,272 Hz (mode 3), then 6,303 Hz (mode 29), and 9,686 Hz (mode 56). The same applies to the biaxial modes, since the first is found at 4,278 Hz (mode 13) and the last at 9,069 Hz (mode 50). As the thickness of the substitute's shell is small compared to its diameter (5 mm thick for an external diameter of 133 mm), the so-called radial modes, for which the deformations observed are predominantly normal to the surface, can be described by the parameters (n, m) according to the thin-shell vibration theory (Rossing, 1982; Xie et al., 2017; Du et al., 2019). For axial modes, n equals 0 and m varies between 1 and 8; while the predominantly radial modes have a parameter n between 1 and 9; for a parameter m varying between 0 and 8.

3.1.2 Experimental results

The mode shapes corresponding to the 51 experimentally detected frequencies are depicted. Only 23 of them, i.e., 45%, are “complete” mode shapes, meaning that the same frequency is detected for each of the three rotations around either the x or y axis. Figure 7 shows an example of a complete mode shape detected at $2,953 \pm 26$ Hz, with deformations recorded for the x -axis rotations of the vertical measurement lines in side and isometric views (A); and those obtained during the y -axis rotations of the horizontal measurement lines in top and isometric views (B). The colors represent the magnitude of the measured deformations in normalized values, where the maximum magnitude is shown in red and the minimum in blue.

In a second step, the 2D complete and incomplete experimental mode shapes are analyzed to identify the parameters (n, m) of the radial modes. As an example, Figure 8 shows four modes shapes

TABLE 1 Computational mode shapes of the Finite Element Model of the skull substitute in the range [0–10] kHz displayed in isometric view.

									
1.Radial (1, 0) 946 Hz	2.Axial (0, 1) 2,008 Hz	3.Torsion X 2,272 Hz	4.Radial (1, 1) 2,976 Hz	5.Radial (2, 1) 3,004 Hz	6.Axial (0, 2) 3,400 Hz	7.Radial (3, 1) 3,475 Hz	8.Radial (2, 2) 3,636 Hz	9.Radial (1, 3) 3,738 Hz	10.Radial (4, 1) 3,844 Hz
									
11.Radial (3, 2) 4,070 Hz	12.Axial (0, 3) 4,144 Hz	13.Biaxial (1, 3) 4,278 Hz	14.Radial (2, 3) 4,308 Hz	15.Radial (5, 1) 4,322 Hz	16.Radial (4, 2) 4,561 Hz	17.Radial (1, 4) 4,730 Hz	18.Radial (3, 3) 4,905 Hz	19.Radial (6, 1) 4,985 Hz	20.Axial (0, 4) 5,141 Hz
									
21.Radial (5, 2) 5,214 Hz	22.Radial (2, 4) 5,284 Hz	23.Radial (4, 3) 5,597 Hz	24.Biaxial (1, 5) 5,853 Hz	25.Biaxial (2, 3) 5,896 Hz	26.Radial (6, 2) 6,054 Hz	27.Radial (3, 4) 6,098 Hz	28.Axial (0, 5) 6,297 Hz	29.Torsion X 6,303 Hz	30.Radial (5, 3) 6,442 Hz
									
31.Radial (2, 5) 6,739 Hz	32.Axial (0, 6) 6,864 Hz	33.Radial (8, 1) 6,920 Hz	34.Radial (4, 4) 6,980 Hz	35.Radial (1, 5) 7,073 Hz	36.Radial (7, 2) 7,078 Hz	37.Radial (6, 3) 7,445 Hz	38.Radial (3, 5) 7,616 Hz	39.Radial (1, 6) 7,634 Hz	40.Biaxial (1, 2) 7,913 Hz
									
41.Radial (5, 4) 7,988 Hz	42.Radial (9, 1) 8,166 Hz	43.Axial (0, 7) 8,260 Hz	44.Radial (8, 2) 8,272 Hz	45.Radial (1, 7) 8,386 Hz	46.Radial (2, 6) 8,390 Hz	47.Radial (7, 3) 8,598 Hz	48.Radial (4, 5) 8,673 Hz	49.Axial (0, 8) 8,916 Hz	50.Biaxial (4, 5) 9,069 Hz
									
51.Radial (6, 4) 9,124 Hz	52.Radial (1, 8) 9,348 Hz	53.Radial (3, 6) 9,482 Hz	54.Radial (10, 1) 9,567 Hz	55.Radial (9, 2) 9,619 Hz	56.Torsion X 9,686 Hz	57.Radial (5, 5) 9,808 Hz	58.Radial (8, 3) 9,890 Hz	(n, m) parameters	

Parameters (n, m) respectively describe the number of lines of symmetry passing through the center of the cavity; and the number of circles in top view.

detected during rotation of the horizontal measurement lines along the y-axis in top view. Color coding once again represents the magnitude of vibrations in normalized values. The symmetry lines drawn in black are deduced from the amplitude variations of the cut lines. The illustrated mode shapes have a parameter m equal to 1 for a parameter n varying between 1 and 4. Ultimately, 34/51 experimental mode shapes are formally identified using (n, m) parameters,

representing 67% of the detected experimental frequencies. It should be noted that out of these 34 natural frequencies, 14 of them are associated in pairs with the same vibration mode, which implies that 7 modes are detected twice (once during x-rotations and once during y-rotations). Thus 27 vibration modes are formally authenticated experimentally for the 3D-printed prototype: 3 biaxial modes, 0 torsional modes and 24 radial modes.

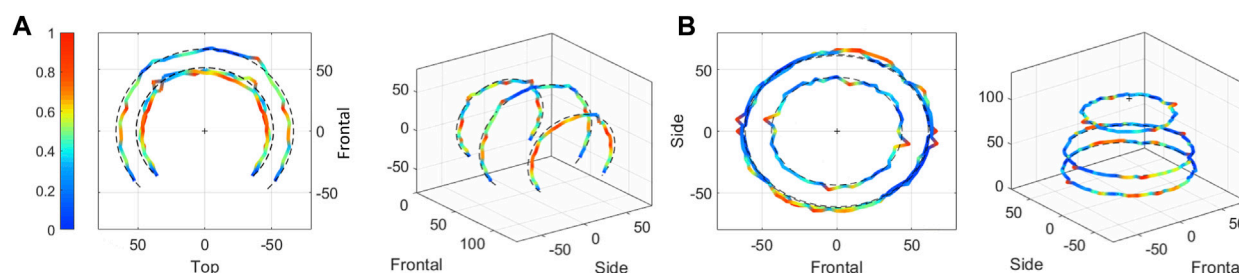


FIGURE 7
Example of a "complete" mode shape obtained during the Experimental Modal Analysis of the 3D-printed prototype. The calculated natural frequency is $2,953 \pm 26$ Hz. Color coding is the normalized magnitude of vibrations for each mode shape, and the measurement lines are defined in Figure 5. (A) Rotations of the vertical measurement lines along the x-axis in side and isometric views. (B) Rotations of the horizontal measurement lines along the y-axis in top and isometric views.

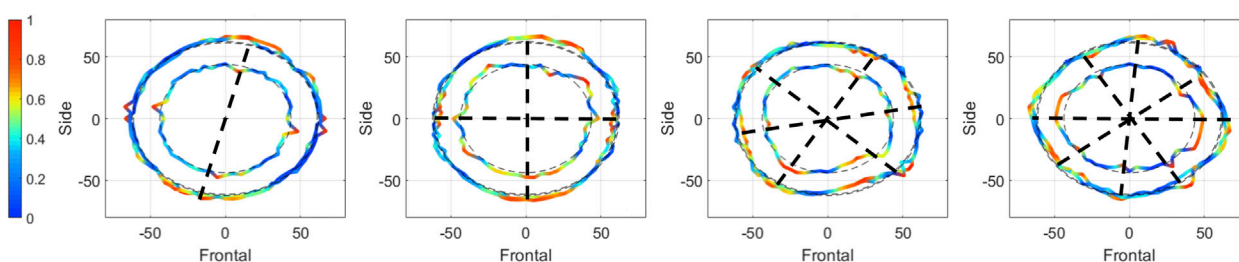


FIGURE 8
Example of four mode shapes obtained during the Experimental Modal Analysis of the 3D-printed prototype. The mode shapes are detected during rotations of the horizontal measurement lines along the y-axis and are represented here in top view. The black dotted lines represent the symmetry lines defining the parameter n . Color coding is the normalized magnitude of vibrations for each mode shape, and the measurement lines are defined in Figure 5.

3.1.3 Numerical and experimental comparison

Finally, a comparison between experimental and computational data is required. Each experimental mode shapes are compared with computational ones in order to both validate the FEM and eliminate spurious data from the experimental set. An example is presented in Figure 9 for the mode ($n = 2, m = 1$). The experimental frequency is $3,139 \pm 30$ Hz, against 3,004 Hz for the FEM. In side view, a shift is observed between the left and right parts (A); while in top view, the largest cut lines display four parts with high amplitudes of vibrations (B). All comparisons between experimental and numerical sets are presented in the [Supplementary Data SA](#) as 2D plots along either the x or y axis of rotation. The color coding represents the mode shapes amplitudes in normalized values per set.

3.2 Quantification of errors in terms of natural frequencies

After matching the experimental and numerical data through visual identification of the mode shapes, errors made on the natural frequencies are quantified. Table 2 compares the results of the FEM and 3D-printed prototype of the skull substitute. In total, 58 vibration modes were computed with the FEM and 51 were found experimentally. By comparing the two data sets, 34 common modes (including 7 detected twice) were formally authenticated: 3/5 bi-axial modes, 0/3 torsional modes and 24/50 radial modes. The computed

relative errors are small (0.3%–5.7%), corresponding to absolute errors between 18 Hz and 280 Hz. Unfortunately, it is clear that not all vibration modes were detected using the experimental protocol outlined in this study. The factors that may explain this shortcoming will be discussed further below.

4 Discussion

At the end of this study, some issues still need to be addressed. First, on which frequency interval has the vibratory behavior of the new cranial substitute been evaluated? Second, could this substitute be used instead of dry human skulls for high-speed loading experiments? Finally, the outlook of this study will be discussed, including the use of a brain simulant in conjunction with the skull substitute for blast loadings.

4.1 What is the validity of the modal analyses performed on the substitute?

The quantification of disparities between the experimental and numerical vibration modes of the cranial substitute evidenced a good fit between the FEM and the 3D-printed prototype. However, it is worth noting that not all vibration modes were detected experimentally, mainly because of the

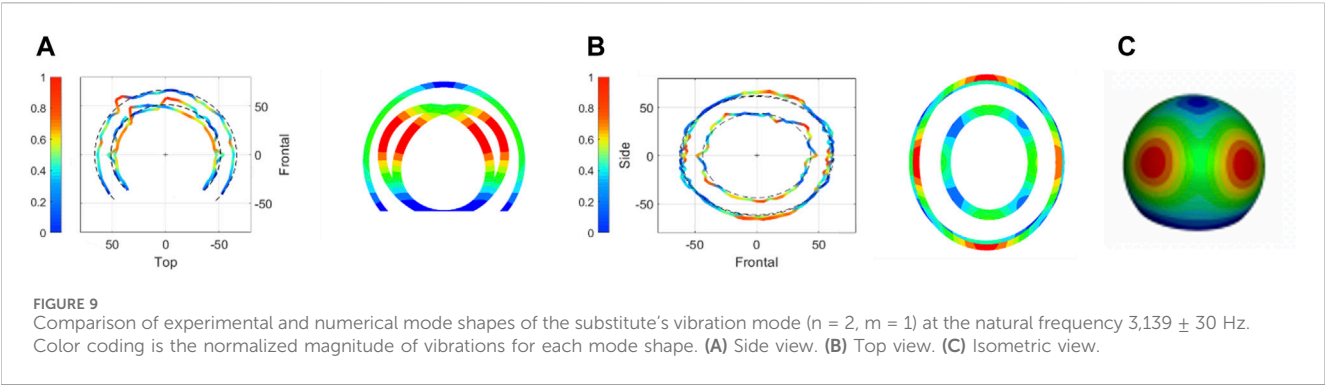


TABLE 2 Comparison of the natural frequencies of the Finite Element Model and the 3D-printed prototype of the cranial substitute.

Parameters (n, m)	Experimental frequency (HZ)	Computational frequency (HZ)	Relative gap (%)	Absolute gap (HZ)
(0, 1)	$2,102 \pm 23$	2,008	4.7	94
(1, 1)	$2,953 \pm 26$	2,976	0.8	23
(2, 1)	$3,139 \pm 30$	3,004	4.5	135
(3, 1)	$3,512 \pm 52$	3,475	1.1	37
(2, 2)	$3,610 \pm 36$	3,636	0.7	26
(1, 3)	$3,824 \pm 83$	3,738	2.3	86
(4, 1)	$3,954 \pm 66$	3,844	2.9	110
Bi-axial	$4,145 \pm 97$	4,278	3.1	133
(5, 1)	$4,344 \pm 79$	4,322	0.5	22
(2, 3)	$4,371 \pm 21$	4,308	1.5	63
(4, 2)	$4,587 \pm 78$	4,561	0.6	26
(6, 1)	$5,168 \pm 60$	4,985	3.7	183
(3, 3)	$5,185 \pm 98$	4,905	5.7	280
(2, 4)	$5,302 \pm 27$	5,284	0.3	18
Bi-axial	$5,698 \pm 116$	5,853	2.7	155
(6, 2)	$6,081 \pm 95$	6,054	0.4	27
(3, 4)	$6,126 \pm 100$	6,098	0.4	28
(5, 3)	$6,642 \pm 156$	6,442	3.1	199
(4, 4)	$6,939 \pm 13$	6,980	0.6	41
(1,5)	$7,175 \pm 113$	7,073	1.4	102
(6, 3)	$7,221 \pm 60$	7,445	3.0	224
(5, 4)	$7,914 \pm 93$	7,988	0.9	75
(7, 3)	$8,448 \pm 139$	8,598	1.8	150
(4, 5)	$8,604 \pm 107$	8,673	0.8	69
Bi-axial	$8,885 \pm 4$	9,069	2.0	184
(6, 4)	$8,921 \pm 162$	9,124	2.2	203
(1, 8)	$9,223 \pm 28$	9,348	1.3	125

experimental setup. A force was applied to the structure using a shaker and a metal rod instead of an impact hammer to ensure a broad frequency range that is easily reproducible. The electrical signal transmitted from the signal generator to the shaker was an up-chirp with a constant amplitude of 2V and a frequency varying between 5 Hz and 12 kHz. Since the applied input signal remains unknown, merely output-only conditions could be set for the modal identification step. Hence, only the magnitude of the recorded velocities could be exploited, and not the magnitude, phase, and coherence function information, as opposed to using the LSCF algorithm with input-output conditions. To obtain more information during vibration tests, the input signal could be measured by positioning a triaxial accelerometer in the vicinity of the input point. Furthermore, the use of a laser vibrometer simplifies the modal analysis, as it is only necessary to define a set of measurement points to start an automatic analysis. While most radial modes are effectively detected using this method, biaxial modes pose a greater challenge, and torsional modes cannot be formally identified because the laser points perpendicular to the outer surface of the substitute. Once again, the use of a triaxial accelerometer could have been useful for these modes, but as there were fewer of them, the choice fell on the ease of implementation, the non-addition of the accelerometers' masses, and the simplicity of the results' processing.

Another factor to consider when discussing the validity of the modal analyses performed is the sensitivity of the numerical results to the mechanical properties of the material. A sensitivity analysis revealed that a variation of $\pm 10\%$ in Young's modulus causes a uniform frequency shift of $\pm 4\%$ in the direction as the modulus change. Additionally, a change of $\pm 20\%$ in the Poisson ratio leads to more significant non-uniform variations, reaching up to 15%. Notably, this variation affects the time of emergence of certain vibration modes, especially as the material approaches incompressibility. Plus, structural damping cannot be implemented in the current study, which explains a plausible frequency shift of the calculated vibration modes.

The disparities quantified during the comparison of the two modal analysis datasets (experimental and computational) can be further explained by several factors. First, despite the moving average filtering applied to the signals; high-frequency noise taints the dataset. These uncertainties can lead to identification errors when using the LSCF algorithm to select the natural frequencies that are compared to the FEM. Another source of bias can arise from the stage of matching experimental and numerical data, as this relies mainly on the visual appearance of the mode shapes.

To assess whether the FEM is a good fit to the experimental data despite the observed discrepancies, the literature is consulted. Schedlinski et al. (2004) performed an EMA on a car body in white and then created a FEM. The model validation was performed between 0 and 100 Hz: of the 42 modes computed with the numerical model, 17 experimental modes were found to be common. The numerical model was then recalibrated using Young's modulus. A similar approach was adopted by Sellami et al. (2017) for the validation of their FE model of a wind turbine in free vibration over the range [0–250] Hz. Numerically, 15 vibration modes were computed over this range, while 7/15 modes were detected with an impact hammer and 15/15 modes with the use of an accelerometer and a shaker. The study by Frankovský et al. (2022)

created the FE model of a flat rectangular steel plate. The model was validated between 0 and 2000 Hz using only the first six experimental vibration modes. Hence, taking into account previously outlined experimental limitations, the Finite Element Model (FEM) of the skull substitute can be considered to be validated. This is further supported by the large number of vibration modes considered and the broad frequency range of interest. Indeed, more than 65% of the experimental data agree with the numerical results between 0 and 10 kHz. Plus, low relative and absolute errors were computed between the two Modal Analysis techniques, although only six measurement cut lines were considered.

4.2 Does the new substitute have a vibratory response close to dry human skulls?

The main objective of this newly designed cranial substitute is to reproduce the vibratory response of the human skull under high-speed loading. Unfortunately, in the literature, only four published studies describe EMA performed on 50th percentile dry human skulls (Franke, 1956; Gurdjian et al., 1970; Khalil et al., 1979; Taleb et al., 1993). In these experiments, a total of four male skulls were excited by an impact hammer whose signal varied in frequency from 0 Hz to a maximum of 5 kHz. The induced vibrations were measured by an accelerometer placed at various locations. In the end, a total of 13 natural frequencies were measured, all bibliographic studies combined. Khalil et al. (1979) detected the majority of these natural frequencies (11/13) on a single male skull. Only this particular study recorded frequencies above 1.5 kHz. There is also a significant discrepancy between the various bibliographic data. This can be partly explained by the boundary conditions used (simple-support, free boundary conditions, unspecified), the instrumentation of the skull, but also by the high variability of the mechanical properties of the skull, which depends on the age of the subjects and the preservation of the specimens (Fallenstein et al., 1969). Due to incomplete data on the rare mode shapes available (Khalil et al., 1979; Taleb et al., 1993), they cannot currently be compared with the data presented in the study. Therefore, the results can here only be matched in terms of frequencies because of the lack of modal analyses performed on human skulls in the literature. This limits the validation of the spheric-approximated skull FEM presented in Section 2.1; as well as the comparison with the 3D-printed prototype of the human skull substitute.

Table 3 compares several numerical and experimental natural frequencies of the substitute to those described in the literature. Of the 13 frequencies associated with dry human skulls, 10 are common to the FEM, and 8 are common to the 3D-printed prototype. These 8 experimental frequencies between 2 kHz and 5 kHz are close to the ones detected by Khalil et al. (1979) on a dry skull. This stems from the fact that, during the design of the skull substitute with the parametric study, the chosen dimensions were adjusted to favor Khalil's frequencies. Indeed, a wide-range excitation signal was used in his study, thanks to an impulse generated by an impact hammer within a frequency range of [20–5,000] Hz. A large number of measurement points was also considered, representing more than 100 outputs, compared to 1 output for Franke (1956), 3 outputs for Gurdjian et al. (1970) and 29 outputs for Taleb et al. (1993).

TABLE 3 Comparison of frequencies (Hz) identified on the substitute using Finite Element Modelling and Experimental Modal Analysis with those found on dry human skulls in the literature.

FEM	EMA	Dry skulls	Number of skulls (references)]		Experimental errors (%)
X	X	700	1	Taleb et al. (1993)	X
946	X	866 ± 42	3	Franke (1956); Gurdjian et al. (1970); Taleb et al. (1993)	X
X	X	1,342 ± 59	3	Khalil et al. (1979); Taleb et al. (1993)	X
X	X	1,770 ± 20	1	Khalil et al. (1979)	X
2,008	2,102 ± 23	1,893 ± 14	1	Khalil et al. (1979)	9.9
2,272	X	2,484 ± 47	1	Khalil et al. (1979)	X
2,976	2,953 ± 26	2,802 ± 58	1	Khalil et al. (1979)	5.8
3,475	3,512 ± 52	3,423 ± 130	1	Khalil et al. (1979)	2.5
3,636	3,610 ± 36	3,634 ± 96	1	Khalil et al. (1979)	0.7
3,844	3,954 ± 66	3,845	1	Khalil et al. (1979)	2.8
4,278	4,145 ± 97	4,113 ± 62	1	Khalil et al. (1979)	3.9
4,308	4,371 ± 21	4,284 ± 63	1	Khalil et al. (1979)	2.0
4,561	4,587 ± 78	4,692 ± 87	1	Khalil et al. (1979)	2.9

Regarding the comparison between the current skull substitute and the bibliographic data, relative errors were calculated for the natural frequencies, ranging from 0.7% to 9.9%. They can be attributed to several factors that can affect the overall vibratory response. First, the skull substitute weighs 245 g against almost 390 g for the cranial vault and around 800 g for an entire skull (Got et al., 1983). The vibration modes of a structure depend on its mass, rigidity and damping matrices. A variation in those properties lead to a modification of the observed mode shapes, and more specifically to a shift in frequency when mass is added or removed. Therefore, a parametric study was required to select the geometry of the skull substitute. This was essential to compensate for the observed disparities, attributed to the known differences in mechanical properties between the cranial bone and the IORA black resin. The most appropriate geometry for the substitute was a hollow truncated sphere in this case. However, the geometry evidently influences the obtained results even though it was dimensioned such as a maximal number of its natural frequencies were common with dry human skulls. Indeed, the substitute has a spherical shell, while the skull is made up of several bones, notably the cranial vault, the mandible and the maxilla, that are characterized by their sutures, crevices, and cavities. Furthermore, the vibratory response of a structure depends on its macroscopic composition. In the current study, the 3D-printed prototype is made of an homogeneous material, yet the cranial bone is composed of several layers (Saladin, 2003) that have specific material properties: the diploë as well as the inner and outer tables of the cortical bone. Lastly, the prototype of the cranial substitute was embedded at its base; but in the study carried out by Khalil et al. (1979), the dry skull was placed in simple support conditions. Varying the boundary conditions causes a change in the number of degrees of freedom at the contact section, and thus modify the vibration modes.

This research is not the first one attempting to reproduce the vibratory response of a dry human skull. The study by Fujiwara et al. (1989) is particularly noteworthy since they created a

human skull substitute filled with degassed water that had a first vibration mode resonating at 500 Hz. They could reproduce part of the first mode shape of a dry human skull they had placed in simple support conditions. In this study however, only the first vibration mode was studied and the skull substitute was filled with a cerebral matter simulant, thus increasing the mass of the structure and thereby modifying its vibratory response. In the current study, despite the use of a very simple and approximate geometry for a new skull substitute, a good number of its natural frequencies are in common with those of dry human skulls, thus fulfilling the requirements.

4.3 Towards the design of a head substitute

As stated in the introduction, the ultimate goal of this research is to investigate the cranial deflection hypothesis. This hypothesis is one of the plausible injury mechanisms that could explain the occurrence of brain damage in individuals exposed to explosions. It could be investigated by studying the outer surface deformation signals of the subject in both time and frequency domains. To this end, a new human skull substitute with a simplified geometry was designed to ensure the reproducibility of results.

Although the created substitute meets those specific requirements, it is important to highlight that the design considered only the vibratory behavior of a human skull. Additional steps are required to incorporate skin and brain simulants, among others, to develop a head substitute that could be used to further investigate other injury mechanisms. The most commonly used brain simulant for these kind of studies is the ballistic gel (Ganpule et al., 2016; Salzar et al., 2017). This material replicates the properties of soft tissues during impacts (Jussila, 2004), but its preservation conditions depend on both the duration and the temperature (Cronin and Falzon, 2011). The sylgard gel is another simulant frequently used (Merkle

et al., 2009; Dal Cengio Leonardi et al., 2011; Goeller et al., 2012), even though there is once again a limitation on the preservation duration after hardening. To overcome these issues while maintaining the proper density of brain tissue, some authors prefer turning to saline solutions (Salzar et al., 2017) or water (Goeller et al., 2012; Hua et al., 2014; Josey et al., 2016; Banton et al., 2018). One study stands out: an anthropomorphic head substitute was created by replicating the skin with urethane rubber, skull with polyurethane, cerebrospinal fluid with water and finally the brain with a silicone gel (Ouellet et al., 2012). However, shell deformations were not recorded in this study, and the vibratory response of the substitute was not assessed.

Adding the soft tissues will consequently lead to a modification of the vibratory behavior of the substitute. Hence, supplementary computational and experimental modal analyses will be required. Unfortunately, the literature lacks experiments carried out *in-vivo* for future comparison. One study involved volunteers who were impacted in the frontal zone, while accelerometers were placed on their occipital, vertex and temporal bones (Gurdjian et al., 1970). Three natural frequencies were measured *in-vivo*: 300 Hz, 560 Hz and 920 Hz. In addition, six *in-vivo* subjects were subjected to random noise transmitted to their temporal bone; while accelerations were measured in their left and right temporal bones (Hakansson et al., 1994). Between 14 and 19 frequencies were found for each subject, with considerable variability in the measurements. For example, the first resonance frequency ranged from 828 Hz to 1,164 Hz depending on the individual. Further *in-vivo* vibration studies are thus required to develop a more robust head substitute that takes into account additional soft tissues.

5 Conclusion

In conclusion, numerical and experimental analyses were carried out to establish the vibration modes of a newly designed cranial substitute. When considering only six measurement lines on the 3D-printed prototype of the substitute, more than 65% of experimental results are in agreement with the Finite Element Model of said substitute. The developed prototype and the FEM respectively have 8/13 and 10/13 natural frequencies in common with dry human skulls in the frequency range [0–10] kHz, with acceptable levels of errors. Hence, this new substitute could be used in the future as a first approximation of a human skull for vibration studies. After being filled with a brain matter simulant to be determined, it could be once again subjected to modal analyses before being subjected to high dynamic solicitations, such as blast loading, in order to investigate the cranial deflection injury mechanism.

Data availability statement

The original contributions presented in the study are included in the article/**Supplementary Material**, further inquiries can be directed to the corresponding author.

Ethics statement

Ethical approval was not required for the study involving humans in accordance with the local legislation and institutional requirements. Written informed consent to participate in this study was not required from the participants or the participants' legal guardians/next of kin in accordance with the national legislation and the institutional requirements.

Author contributions

NE: Conceptualization, Data curation, Formal Analysis, Software, Writing—original draft. JB: Conceptualization, Investigation, Writing—review and editing. NB: Conceptualization, Investigation, Methodology, Writing—review and editing. PM: Investigation, Writing—review and editing. PN: Project administration, Supervision, Validation, Writing—review and editing. RW: Project administration, Supervision, Validation, Writing—review and editing. CD: Investigation, Methodology, Project administration, Supervision, Validation, Writing—review and editing.

Funding

The author(s) declare that no financial support was received for the research, authorship, and/or publication of this article.

Acknowledgments

Special thanks are extended to the staff of Strasbourg University and to the Acoustic and Soldier's Protection group from the French-German Research Institute of Saint Louis, especially to Sebastien De Mezzo, Laurent Gross and Stéphane Heck for conceiving and instrumenting the cranial substitute.

Conflict of interest

The authors declare that the research was conducted in the absence of any commercial or financial relationships that could be construed as a potential conflict of interest.

Publisher's note

All claims expressed in this article are solely those of the authors and do not necessarily represent those of their affiliated organizations, or those of the publisher, the editors and the reviewers. Any product that may be evaluated in this article, or claim that may be made by its manufacturer, is not guaranteed or endorsed by the publisher.

Supplementary material

The Supplementary Material for this article can be found online at: <https://www.frontiersin.org/articles/10.3389/fbioe.2024.1297730/full#supplementary-material>

References

- Armonda, R. A., Bell, R. S., Vo, A. H., Ling, G., DeGraba, T. J., Crandall, B., et al. (2006). Wartime traumatic cerebral vasospasm: recent review of combat casualties. *Neurosurgery* 59 (6), 1215–1225. doi:10.1227/01.neu.0000249190.46033.94
- Auperrin, A. (2009). *Caractérisation tissulaire pour la détermination du comportement de l'os crânien: essais mécaniques et imagerie médicale*. Français: Thèse de l'Université de Valenciennes et du Hainaut Cambrésis. HAL ID tel-00454865. Available at: <https://theses.hal.science/tel-00454865>
- Baker, W. E., Cox, P. A., Kulesz, J. J., Strehlow, R. A., and Westine, P. S. (1983). *Explosion hazards and evaluation*. Elsevier Science.
- Baker, W. E., Wilfred, E., Westine, P. S., and Dodge, F. T. (1991). *Similarity methods in engineering dynamics: theory and practice of scale modeling*. Elsevier.
- Banton, R., Piehler, T., Zander, N., Benjamin, R., and Duckworth, J. (2018). "Comparison of numerical simulations with experiments of blast-induced pressure wave impact on a surrogate head model," in Conference Proceedings of the Society for Experimental Mechanics Series, 181–187.
- Bolander, R. (2011). *A multi-species analysis of biomechanical responses of the head to a shock wave*. Wayne State University Dissertations, 406. Available at: https://digitalcommons.wayne.edu/oa_dissertations/406/.
- Bushby, K. M. D., Cole, T., Matthews, J. N., and Goodship, J. A. (1992). Centiles for adult head circumference. *Archives Dis. Child.* 67 (10), 1286–1287. doi:10.1136/adc.67.10.1286
- Chandra, N., and Sundaramurthy, A. (2015). "Acute pathophysiology of blast injury - from Biomechanics to experiments and computations," in *Brain neurotrauma molecular, neuropsychological and rehabilitation aspects*, F. H. Kobeissy Editor, 199–258.
- Cronin, D. S., and Falzon, C. (2011). Characterization of 10% ballistic gelatin to evaluate temperature, aging and strain rate effects. *Exp. Mech.* 51 (7), 1197–1206. doi:10.1007/s11340-010-9438-z
- Dal Cengio Leonardi, A. (2011). *An investigation of the biomechanical response from shock wave loading to the head*. Wayne State University Dissertations, 306. Available at: https://digitalcommons.wayne.edu/oa_dissertations/306/.
- Dal Cengio Leonardi, A., Bir, C., Ritzel, D., VandeVord, P., and Dingell, J. D. (2011). "The effects of apertures on internal pressure measured during shock wave exposure," in ASME Summer Bioengineering Conference, Pennsylvania, USA (Farmington). Available at: <https://doi.org/10.1115/SBC2011-53586>.
- Delille, R. (2007). *Contribution à la compréhension du comportement mécanique de l'os du crâne humain sous différents moyens de conservation et de sollicitation*. Thèse de l'Université de Valenciennes et du Hainaut Cambrésis. HAL ID: tel-00270740. Available at: <https://theses.hal.science/tel-00270740>.
- Du, Y., Huo, R., Pang, F., Li, S., Huang, Y., and Zhang, H. (2019). Free vibration of spherical cap subjected to various pressure boundary conditions. *Adv. Mech. Eng.* 11 (9), 168781401987926–12. doi:10.1177/1687814019879261
- Elster, N., Boutillier, J., Magnan, P., Naz, P., Willinger, R., and Deck, C. (2023). A critical review of experimental analyses performed on animals, postmortem human subjects, and substitutes to explore primary blast-induced Traumatic Brain injuries. *Front. Mech. Eng.* 9. doi:10.3389/fmech.2023.1185231
- Elster, N., Boutillier, J., Bourdet, N., Magnan, P., Naz, P., Willinger, R., et al. (2022). 'Design of a simplified cranial substitute and Modal Analysis', in *DYMAT* 26.
- Erwins, D. J. (2000). *Modal testing: theory, practice and application*. 2nd edition. Wiley.
- Fallenstein, G. T., Hulce, V. D., and Melvin, J. W. (1969). Dynamic mechanical properties. *J. Biomechanics* 2, 1–9. doi:10.1016/0021-9290(69)90079-7
- Franke, E. (1956). Response of the human skull to mechanical vibrations. *J. Acoust. Soc. Am.* 28 (6), 1277–1284. doi:10.1121/1.1908622
- Frankovský, P., Delyová, I., Sivák, P., Bocko, J., Živčák, J., and Kicko, M. (2022). Modal analysis using digital image correlation technique. *Materials* 15. doi:10.3390/ma15165658
- Fujiwara, S., Yanagida, Y., and Mizoi, Y. (1989). Impact-induced intracranial pressure caused by an accelerated motion of the head or by skull deformation: an experimental study using physical models of the head and neck, and ones of the skull. *Forensic* 43, 159–169. doi:10.1016/0379-0738(89)90132-1
- Ganpule, S., Salzar, R., and Perry, B. (2016). Role of helmets in blast mitigation: insights from experiments on PMHS surrogate. *Int. J. Exp. Comput. Biomechanics* 4 (1), 13. doi:10.1504/ijecb.2016.10002680
- Goeller, J., Wardlaw, A., Treichler, D., O'Bruba, J., and Weiss, G. (2012). Investigation of cavitation as a possible damage mechanism in blast-induced traumatic brain injury. *J. Neurotrauma* 29 (10), 1970–1981. doi:10.1089/neu.2011.2224
- Gordon, C. C., Churchill, T., Clauser, C. E., Bradtmiller, B., McCONVILLE, J. T., Tebbetts, I., et al. (1988). *Anthropometric survey of U.S. Army personnel: summary statistics interim report*.
- Got, C., Guillon, F., Patel, A., Mack, P., Brun-Cassan, F., Fayon, A., et al. (1983). "Morphological and biomechanical study of 146 human skulls used in experimental impacts, in relation with the observed injuries," in 27th Stapp Car Crash Conference, Bron, France.
- Gurdjian, E. S., Hodgson, V. R., and Thomas, L. M. (1970). Studies on mechanical impedance of the human skull: preliminary report. *J. Biomechanics* 3 (3), 239–247. doi:10.1016/0021-9290(70)90025-4
- Haeussinger, F. B., Heinzel, S., Hahn, T., Scheckmann, M., Ehls, A. C., and Fallgatter, A. J. (2011). Simulation of near-infrared light absorption considering individual head and prefrontal cortex anatomy: implications for optical neuroimaging. *PLoS ONE* 6 (10), e26377. doi:10.1371/journal.pone.0026377
- Hakansson, B., Brandt, A., Carlsson, P., and Tjellström, A. (1994). Resonance frequencies of the human skull *in vivo*. *J. Acoust. Soc. Am.* 95 (3), 1474–1481. doi:10.1121/1.408535
- Hicks, R. R., Fertig, S. J., Desrocher, R. E., Koroshetz, W. J., and Pancrazio, J. J. (2010). Neurological effects of blast injury. *J. Trauma - Inj. Infect. Crit. Care* 68 (5), 1257–1263. doi:10.1097/ta.0b013e3181d8956d
- Hoge, C. W., McGurk, D., Thomas, J. L., Cox, A. L., Engel, C. C., and Castro, C. A. (2008). Mild traumatic brain injury in U.S. Soldiers returning from Iraq. *N. Engl. J. Med.* 358 (5), 453–463. doi:10.1056/nejmoa072972
- Hua, Y., Kumar Akula, P., Gu, L., Berg, J., and Nelson, C. A. (2014). Experimental and numerical investigation of the mechanism of blast wave transmission through a surrogate head. *J. Comput. Nonlinear Dyn.* 9. doi:10.1115/1.4026156
- Josey, T., Donahue, L., Sawyer, T., and Ritzel, D. V. (2016). "Blast response of a fluid-filled elastic shell," in *Military aspects of blast and shock*.
- Jussila, J. (2004). Preparing ballistic gelatine - review and proposal for a standard method. *Forensic Sci. Int.* 141 (2–3), 91–98. doi:10.1016/j.forsciint.2003.11.036
- Khalil, T. B., Viano, D. C., and Smith, D. L. (1979). Experimental analysis of the vibrational characteristics of the human skull. *J. Sound Vib.* 63 (3), 351–376. doi:10.1016/0022-460x(79)90679-5
- LS-DYNA R11 Keyword Manual Volume I (2018). Available at: <https://lsdyna.ansys.com/manuals/>.
- Lynnnerup, N. (2001). Cranial thickness in relation to age, sex and general body build in a Danish forensic sample. *Forensic Sci. Int.* 117 (1–2), 45–51. doi:10.1016/s0379-0738(00)00447-3
- Magnuson, J., and Ling, G. (2018). "Explosive blast mild traumatic brain injury," in *Traumatic brain injury - pathobiology* (Advanced Diagnostics and Acute Management. InTech). Available at: <http://dx.doi.org/10.5772/intechopen.74035>.
- Mcelhaney, J., Fogle, J. L., Melvin, J. W., Haynes, R. R., Roberts, V. L., and Alem, N. M. (1970). Mechanical properties of cranial bone. *J. Biomech.* 3 (1969), 495–511. doi:10.1016/0021-9290(70)90059-x
- Merkle, A. C., Wang, I. D., Armiger, R. A., Carkhuff, B. G., and Roberts, J. C. (2009). "Development of a human head physical surrogate model for investigating blast injury," in ASME International Mechanical Engineering Congress and Exposition, Proceedings, 2, 91–93.
- Nishimoto, T., Murakami, S., Abe, T., and Ono, K. (1995). Mechanical properties of human cranium and effect of cranial fractures on extradural hematoma, 11. *Trans. Jpn. Soc. Mech. Eng.* doi:10.1299/kikaia.61.2386
- Ouellet, S., Bouamoul, A., Gauvin, R., Binette, J. S., Williams, K. V., and Martineau, L. (2012). "Development of a biofidelic head surrogate for blast-induced traumatic brain injury assessment," in Personal Armor System Symposium.
- Peeters, B., and Van der Auweraer, H. (2005). "PolyMAX: a revolution in operational modal analysis," in Proceedings of the 1st International Operational Modal Analysis Conference, IOMAC 2005, January 2005.
- Rosenfeld, J. V., McFarlane, A. C., Bragge, P., Armonda, R. A., Grimes, J. B., and Ling, G. S. (2013). Blast-related traumatic brain injury. *Lancet Neurology* 12, 882–893. doi:10.1016/s1474-4422(13)70161-3
- Rossing, T. D. (1982). Chladni's law for vibrating plates. *Am. J. Phys.* 50 (3), 271–274. doi:10.1119/1.12866
- Saladin, K. (2003). in *Anatomy and physiology: the unity of form and function*. Editor T.M.-H Company. 3rd edition.
- Salzar, R. S., Treichler, D., Wardlaw, A., Weiss, G., and Goeller, J. (2017). Experimental investigation of cavitation as a possible damage mechanism in blast-induced traumatic brain injury in post-mortem human subject heads. *J. Neurotrauma* 34 (8), 1589–1602. doi:10.1089/neu.2016.4600
- Schedlinski, C., Wangner, F., Bohnert, K., Frappier, J., Irrgang, A., Lehmann, R., et al. (2004). "Experimental modal analysis and computational model updating of a car body in white," in Proceedings of the 2004 International Conference on Noise and Vibration Engineering (ISMA), 1925–1938. Available at: <https://www.semanticscholar.org/paper/Experimental-Modal-Analysis-and-Computational-Model-Schedlinski-Wagner/f243ae93cf3c857f19834b59a62751e83bd665>.
- Sellami, T., Jelassi, S., Darcherif, A. M., Berriri, H., and Mimouni, M. F. (2017). Experimental validation of a numerical 3-D finite model applied to wind turbines design under vibration constraints: TREVISe platform. *Mech. Industry* 18 (8), 806. doi:10.1051/meca/2017046

@Stratasys (2019). *Notice technique sur les systèmes et matériaux de la technologie PolyJet*.

Taleb, L., Willinger, R., Fellmann, G., and Kopp, C. M. (1993). Analyse modale de la boîte crânienne humaine *in vitro*. *Mécanique industrielle Matériaux* 46 (2), 92–95.

Trudeau, D. L., Anderson, J., Hansen, L. M., Shagalov, D. N., Schmoller, J., Nugent, S., et al. (1998). Findings of mild traumatic brain injury in combat veterans with PTSD and a history of blast concussion. *J. Neuropsychiatry Clin. Neurosci.* 10 (3), 308–313. doi:10.1176/jnp.10.3.308

Vasavada, A. N., Danaraj, J., and Siegmund, G. P. (2008). Head and neck anthropometry, vertebral geometry and neck strength in height-matched men and women. *J. Biomechanics* 41 (1), 114–121. doi:10.1016/j.jbiomech.2007.07.007

Verboven, P. (2002). *Frequency domain system identification for Modal Analysis*. Brussels: Thesis of Vrije Universiteit Brussel. Available at: <https://researchportal.vub.be/en/publications/frequency-domain-system-identification-for-modal-analysis>.

Verschuere, P., Delye, H., Berckmans, D., Verpoest, I., Goffin, J., Vander Sloten, J., et al. (2006). “Analysis of fracture characteristics of cranial bone for Fe modelling,” in

International IRCOBI Conference on the Biomechanics of Impact, Proceedings, 357–360.

Warden, D. L., French, L. M., Shupenko, L., Fargus, J., Riedy, G., Erickson, M. E., et al. (2009). Case report of a soldier with primary blast brain injury. *NeuroImage* 47 (Suppl. 2), T152–T153. doi:10.1016/j.neuroimage.2009.01.060

Wilkinson, J. P. D. (1966). Natural frequencies of closed spherical sandwich shells. *J. Acoust. Soc. Am.* 40 (4), 801–806. doi:10.1121/1.1910151

Williams, C. B., Mistree, F., and Rosen, D. W. (2011). A functional classification framework for the conceptual design of additive manufacturing technologies. *J. Mech. Des. Trans. ASME* 133 (12), 1–11. doi:10.1115/1.4005231

Wojcik, B. E., Stein, C. R., Bagg, K., Humphrey, R. J., and Orosco, J. (2010). Traumatic brain injury hospitalizations of U.S. army soldiers deployed to Afghanistan and Iraq. *Am. J. Prev. Med.* 38 (1 Suppl. L), S108–S116. doi:10.1016/j.amepre.2009.10.006

Xie, K., Chen, M., and Li, Z. (2017). A semi-analytical method for vibration analysis of thin spherical shells with elastic boundary conditions. *J. Vibroengineering* 19 (4), 2312–2330. doi:10.21595/jve.2016.17154



OPEN ACCESS

EDITED BY

Naomichi Ogihara,
The University of Tokyo, Japan

REVIEWED BY

Joeri Kok,
Maastricht University, Netherlands
Nicolas Newell,
Imperial College London, United Kingdom

*CORRESPONDENCE

Estefano Muñoz-Moya,
✉ estefano.munoz@upf.edu

RECEIVED 09 February 2024

ACCEPTED 25 April 2024

PUBLISHED 10 June 2024

CITATION

Muñoz-Moya E, Rasouligandomani M,
Ruiz Wills C, Chemorion FK, Piella G and
Noailly J (2024), Unveiling interactions between
intervertebral disc morphologies and
mechanical behavior through personalized
finite element modeling.
Front. Bioeng. Biotechnol. 12:1384599.
doi: 10.3389/fbioe.2024.1384599

COPYRIGHT

© 2024 Muñoz-Moya, Rasouligandomani, Ruiz
Wills, Chemorion, Piella and Noailly. This is an
open-access article distributed under the terms
of the [Creative Commons Attribution License
\(CC BY\)](https://creativecommons.org/licenses/by/4.0/). The use, distribution or reproduction in
other forums is permitted, provided the original
author(s) and the copyright owner(s) are
credited and that the original publication in this
journal is cited, in accordance with accepted
academic practice. No use, distribution or
reproduction is permitted which does not
comply with these terms.

Unveiling interactions between intervertebral disc morphologies and mechanical behavior through personalized finite element modeling

Estefano Muñoz-Moya^{1*}, Morteza Rasouligandomani¹,
Carlos Ruiz Wills¹, Francis Kiptengwer Chemorion^{1,2},
Gemma Piella¹ and Jérôme Noailly¹

¹BCN MedTech, Department of Engineering, Universitat Pompeu Fabra, Barcelona, Spain, ²Department of Information Technology, InSilicoTrials Technologies, Trieste, Italy

Introduction: Intervertebral Disc (IVD) Degeneration (IDD) is a significant health concern, potentially influenced by mechanotransduction. However, the relationship between the IVD phenotypes and mechanical behavior has not been thoroughly explored in local morphologies where IDD originates. This work unveils the interplays among morphological and mechanical features potentially relevant to IDD through Abaqus UMAT simulations.

Methods: A groundbreaking automated method is introduced to transform a calibrated, structured IVD finite element (FE) model into 169 patient-personalized (PP) models through a mesh morphing process. Our approach accurately replicates the real shapes of the patient's Annulus Fibrosus (AF) and Nucleus Pulposus (NP) while maintaining the same topology for all models. Using segmented magnetic resonance images from the former project *MySpine*, 169 models with structured hexahedral meshes were created employing the Bayesian Coherent Point Drift++ technique, generating a unique cohort of PP FE models under the *Disc4All* initiative. Machine learning methods, including Linear Regression, Support Vector Regression, and eXtreme Gradient Boosting Regression, were used to explore correlations between IVD morphology and mechanics.

Results: We achieved PP models with AF and NP similarity scores of 92.06% and 92.10% compared to the segmented images. The models maintained good quality and integrity of the mesh. The cartilage endplate (CEP) shape was represented at the IVD-vertebra interfaces, ensuring personalized meshes. Validation of the constitutive model against literature data showed a minor relative error of 5.20%.

Discussion: Analysis revealed the influential impact of local morphologies on indirect mechanotransduction responses, highlighting the roles of heights, sagittal areas, and volumes. While the maximum principal stress was influenced by morphologies such as heights, the disc's ellipticity influenced the minimum principal stress. Results suggest the CEPs are not influenced by

their local morphologies but by those of the AF and NP. The generated free-access repository of individual disc characteristics is anticipated to be a valuable resource for the scientific community with a broad application spectrum.

KEYWORDS

patient-specific, intervertebral disc, morphing algorithm, finite element method, machine learning, model repository, patient-personalized, morphological analysis

1 Introduction

Lumbar degenerative spine diseases are the primary cause of low back pain (LBP), standing as a leading global health burden. They affect an estimated 266 million individuals worldwide annually and are a primary cause of work absenteeism, as highlighted by the meta-analysis of Ravindra et al. (2018). Intervertebral disc (IVD) degeneration (IDD) is identified as the primary cause of LBP. It results from multiple factors, including heredity, aging, inadequate metabolite transport, and mechanical loading. These factors can collectively compromise the disc's integrity and increase the risk of physical disruption under physiological mechanical loads (Adams and Roughley, 2006). Despite the broad and profound impact of IDD, there is still a lack of effective early detection of risk factors and therapies.

The IVD, the largest avascular tissue in the human body, provides the spine with load support and flexibility while finely articulating the anterior vertebral column. This function results from fully functional interactions among the highly specialized disc tissues. The disc tissues define three main anatomic regions: (i) the center, with the gelatinous nucleus pulposus (NP), populated by chondrocyte-like cells with a density of around 5,000 cells/mm³ (Kodama et al., 2023). It predominantly contains proteoglycans reinforced with type-II collagen fibers for structural integrity that promote tissue hydration and hydrostatic pressurization through osmotic swelling (Urban et al., 2000); (ii) the circumference, with the annulus fibrosus (AF), a fiber-reinforced lamellar ring structure with concentric layers of type-I collagen aligned according to a criss-cross pattern that alternates in angles from 28° to 44° concerning the transverse plane of the disc (Natarajan et al., 2004; Nerurkar et al., 2007; Pezowicz, 2010; Raza and Michalek, 2021), laterally confines the NP and contributes to tensile strength when the periphery of the disc is directly stretched, undergoes shear deformations, or bulges under the effect of the intradiscal pressure (Kiani et al., 2002; Bhattacharjee and Ghosh, 2014); and (iii) the cranial and caudal ends, with the top and bottom cartilage endplates (CEP), a 500–1,000 μ m-thick layer of hyaline-like cartilage that consists mainly of type-II collagen, proteoglycans, and water (Roberts et al., 1989; Urban et al., 2004; Moon et al., 2013). It covers the NP's cranial and caudal ends and the AF's inner part adjacent to the vertebral subchondral bone, i.e., the bony endplate (BEP).

The risk factors for IDD encompass a range of physiological and genetic contributors. These include excessive movements and loads (Paul et al., 2013), genetic predispositions (Mayer et al., 2013), previous spinal surgeries (Hashimoto et al., 2018), anomalies in the vertebral endplates (Bonnheim et al., 2022), and a reduction in proteoglycans accompanied by decreased water content in the discs (Knudson and Knudson, 2001). Even recent research has underscored the significant role of disc morphology in IDD,

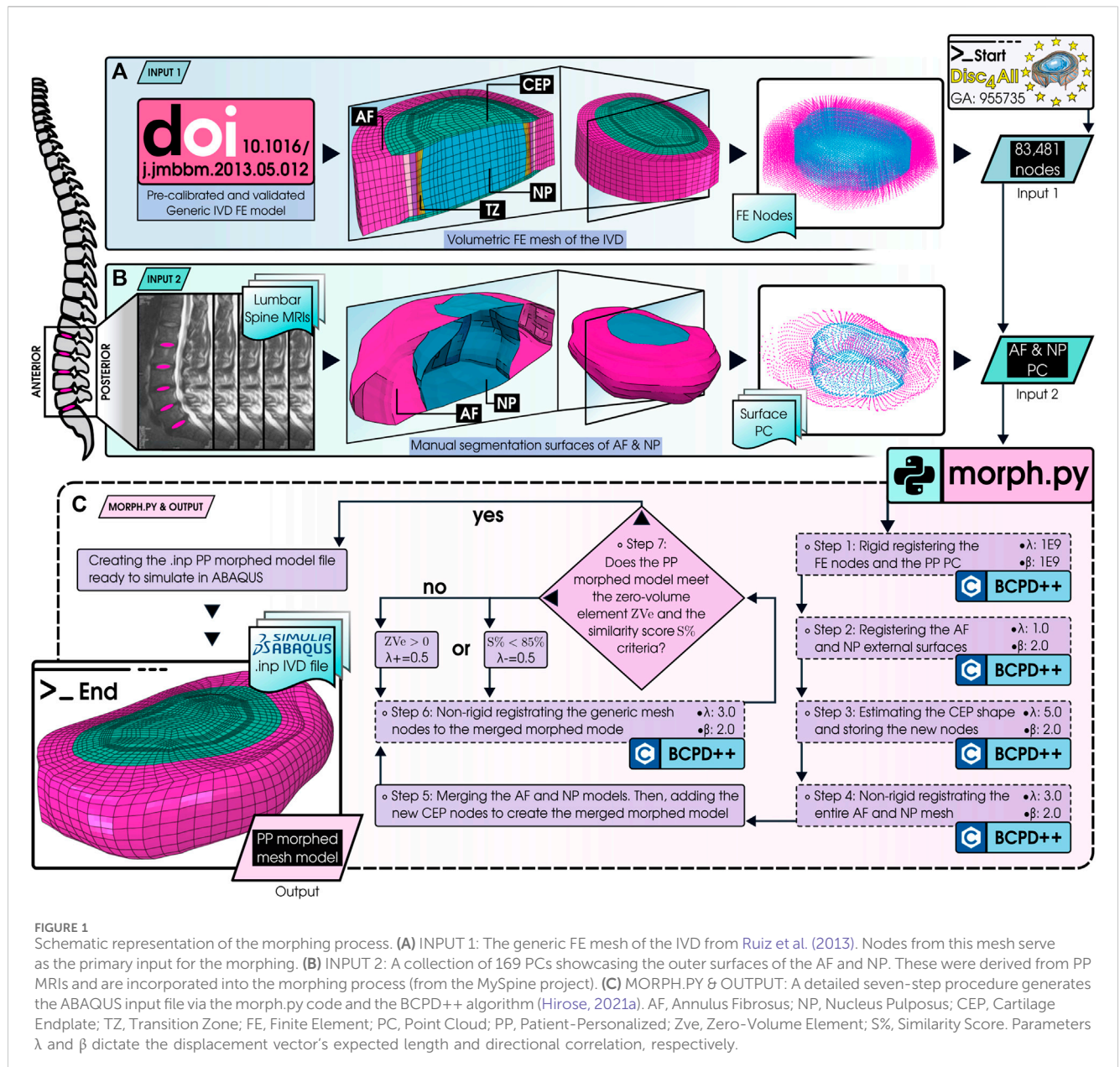
mainly focusing on the disc's height and associated stiffness (Tavana et al., 2024).

Significant advancements have been made in understanding the biological interactions relevant to IDD through *in silico* modeling techniques (Baumgartner et al., 2021). These advancements address challenges such as the complex nonlinear behavior of IVD components, the invasive nature of studying human internal structures, and the difficulties in replicating physiological conditions like pressure variations and nutrient supply in *in vivo* and *in vitro* environments (Sato et al., 1999).

Computational modeling of the IVD predominantly employs finite element (FE) analysis, agent-based models, and network models (Bermudez-Lekerika et al., 2022). Furthermore, experimental *in vivo* measurements, such as those by Wilke et al. (1999), have provided valuable data on disc pressures during varied activities, offering unique physiological IVD mechanical loads for FE analyses. These simulations have explored early IDD aspects, including cell nutritional stress (Ruiz et al., 2018), cell viability (Ruiz et al., 2016), the effects of sustained compression (Malandrino et al., 2011), and the impact of nutrient supply (Malandrino et al., 2014).

Despite these advances, integrating these insights into FE models to create patient-personalized (PP) IVD models to study IDD remains challenging. One major hurdle is the presence of oversimplified geometrical representations (Meijer et al., 2011). A recent study by Fleps et al. (2024) aimed to bridge this gap by investigating the influence of IVD morphology on its mechanical behaviors through FE analysis. However, the study primarily focused on the AF external surface during the morphing process, while (Du et al., 2021) emphasized the importance of accurately modeling the IVD's internal structures, such as the nucleus, for improved precisions of the simulated mechanical responses. Early FE explorations have suggested that the specific configuration of these internal components impacts the prediction of local mechanical fields while not significantly affecting the overall flexibility of the organ (Noailly et al., 2007). Consequently, the literature may not fully grasp the importance of personalizing internal components such as the NP. Likewise, the possible importance of the multiplicity of local morphological features might have been neglected, as overall organ measurements like mid-height or coronal and sagittal distances have been traditionally explored (Urquhart et al., 2014; Teichtahl et al., 2015; Bach et al., 2019; Kizilgöz and Ulusoy, 2019), potentially neglecting the non-linear interactions between IVD phenotypes and mechanics.

Another significant impediment is the variation in tissue-level FE meshes across different studies. These discrepancies in mesh topologies often hinder the automation of simulations, large-scale result production, replication of results, clinical applicability, and



multi-scale strategies using PP models. Ruiz et al. (2013) attempted to standardize an IVD mesh for the L4-L5 spinal segment to minimize result fluctuations, especially in the transition zone (TZ) between the NP and AF. However, this approach falls short in evaluating CEP diffusion distances due to using a simplified generic model.

This research aims to discern the influence of disc local morphologies on the biomechanical responses of the IVD and to provide a comprehensive free-access repository of PP IVD model geometries, underscoring our dedication to standardization and furthering the scientific understanding of IDD. We employed an advanced mesh morphing technique to adapt a previously calibrated, validated FE mesh (Ruiz et al., 2013) to PP IVD models, addressing the challenge of standardizing IVD meshes. These adaptations enable the execution of FE simulations under

average daily physiological loads (Wilke et al., 1999), evaluating the effects of morphological factors on the multiphysics response. Our methodology incorporates a biphasic swelling model implemented in a User MATERIAL (UMAT) subroutine in ABAQUS 2020, allowing exploring the porous media of the IVD (Ruiz et al., 2018) and maintaining a consistent topology. Machine learning regression algorithms were used to refine our understanding of the relationship between IVD morphology and mechanical responses within targeted regions of interest.

1.1 Contributions of the work

- An automatic mesh morphing procedure was established to transform a structured IVD FE mesh, previously calibrated

(Ruiz et al., 2013), into IVD PP models based on segmented medical images.

- The model was validated using experimental data from the literature.
- The interplay between morphology and mechanical responses was revealed through tissue-level simulations and machine-learning algorithms.
- A repository of 169 PP FE models of the IVD was created for the scientific community. Available for free use at the Zenodo open repository (Muñoz-Moya et al., 2023), accessible through our online user interface (<https://ivd.spineview.upf.edu/>).

2 Materials and methods

2.1 Overview

A cohort of 169 geometrical models of the lumbar spine IVD (Pfirman scale range from 1 to 4) was acquired through T2-weighted magnetic resonance imaging (MRI) from the former project *MySpine* (FP7-269909) to generate the morphed FE meshes. These models were developed following the innovative approach introduced by Castro-Mateos et al. (2014), which enables accurate 3D segmentation of IVD annulus and nucleus, with increased resolution as axial and transversal MRI slices (isotropic voxels of $0.68 \times 0.68 \times 0.68 \text{ mm}^3$) are combined. This method is effective for all degrees of IDD, including discs with protrusions or herniations. The segmentation algorithm, employing a feature selector, iteratively deforms an initial shape, which is projected into a statistical shape model space at first and then into a B-Spline space to improve accuracy. Expert clinicians validated the initial manual segmentation and the generated 3D morphologies.

The point cloud (PC) of the AF and NP external surfaces could be extracted from the MRIs, but the segmented models did not incorporate the CEP (Figure 1B). To overcome this limitation, our morphing process estimates the shape of the CEP (presented in Figure 1C). This algorithm tailors an IVD FE generic mesh (previously calibrated through a comprehensive mesh convergence analysis (Ruiz et al., 2013), and originally developed by Noailly et al. (2010), presented in Figure 1A) to the PC of the PP models while preserving the relative dimensions of the elements and the mesh structure at material discontinuities. The entire mesh of the IVD contains 83,481 nodes, and the disc tissues—namely AF, NP, and CEP—were discretized with 19,392 second-order hexahedral elements (20 nodes).

The collagen fibers of the AF were modeled with 7,680 second-order quadrilateral rebar elements (8 nodes) embedded in the hexahedral elements of the annulus to model the fiber-reinforcement of the tissue. These rebars follow the concentric mesh structure of the annulus hexahedral elements to represent the functional mechanical behavior of the annulus structure within the IVD (Noailly et al., 2010).

The primary purpose of the pipeline presented in Figure 1 is to create a FE PP mesh file (.inp) compatible with the ABAQUS mechanical solver, with a mesh structure able to preserve simulation convergence and minimize poro-mechanical instabilities under physiological loading conditions (Ruiz et al.,

2013). Furthermore, our algorithm guarantees the non-convexity of the elements, contributing to the simulations' accuracy.

The simulations adopt the same boundary conditions, material properties, and physiological loads used by Ruiz et al. (2018) for healthy discs, based on *in vivo* intradiscal pressure measurements by Wilke et al. (1999). Each PP FE model has the same number of elements and nodes and the same connectivity. The sole difference among the PP models lies in the coordinates of the nodes within the FE mesh.

To validate our model's capacity to represent the mechanical behavior of a normal healthy disc, we compared our simulations with the *in vitro* vertical creep displacement tests by Malandrino et al. (2015b). We employ the morphing algorithm to obtain the morphology of the IVD used in these experiments and consider its effects on the validation simulation.

Thanks to the consistent topology across the 169 PP morphed models, extracting mechanical responses from targeted zones, such as the NP's center, the anterior and posterior TZs (regions prone to early degeneration, observed by (Smith et al., 2011) through clinical images), and the CEP—was straightforward and systematic for all models. Accordingly, local mechanical predictions could consistently correlate with various morphological factors, such as heights, areas, and volumes. The relevance of each factor was then ranked by leveraging SHAP (SHapley Additive exPlanations) values (Ning et al., 2022).

2.2 Morphing process

The Bayesian Coherent Point Drift ++ (BCPD++) (Hirose, 2021a; Hirose, 2021b) was employed to adapt the structured generic IVD FE mesh (Ruiz et al., 2013) to the PP point cloud (AF and NP). This Bayesian framework allows the inclusion of prior knowledge about the distribution of potential transformations, such as degrees of translation, rotation, and scaling among the points. Overall, the BCPD++ algorithm was chosen to facilitate the automation of transforming FE meshes.

- Algorithm convergence is guaranteed by variational Bayesian inference while introducing motion coherence using a prior distribution of displacement vectors.
- Rigid and non-rigid registration can be executed within a single algorithm.
- The algorithm works with both structured and unstructured shapes.
- Point-to-point correspondences are not assumed to be one-to-one.

To adapt the mesh to the PP models and estimate the CEP shape, the BCPD++ algorithm was regulated through our in-house Python script named *morph.py* (Figure 1C). Additionally, the script substitutes the original hexahedral elements of the BEP (Noailly et al., 2007; Malandrino et al., 2011; Ruiz et al., 2013) from the generic mesh with 3,552 eight-node shell elements in the top and bottom regions of the disc, consequently reducing the computation time of both the morphing and the FE simulations.

In brief, the algorithm has two main parameters that were controlled hereby: λ , which controls the expected length of the

displacement vectors, and β , which controls the directional correlation among the displacement vectors. λ and β facilitate the balance of rigid and non-rigid registrations by using large or small values of each parameter, which enables the control of the distortion of the deformation field.

To accurately estimate the CEP, it is crucial to set a specific target thickness range to ensure that modeled healthy discs do not fall below the expected thickness values. Moon et al. (2013) found, via MRI observations, that the central thickness of a healthy disc—considered the minimum thickness across the entire CEP—measured in the sagittal plane averages 0.54 ± 0.12 mm across all lumbar levels. This finding is consistent with our generic model, which specifies a CEP thickness at the center of the disc of 0.545 mm, initially based on histological measurements (Noailly et al., 2007). Consequently, ensuring that the average CEP thickness of the discs generated by the morphing process falls within this range becomes a key objective, particularly for discs not in advanced degeneration stages. Additionally, focusing on the central thickness allows for the creation of CEPs with variable thickness across the tissue, adapting its shape to match the morphology of the AF and NP, thereby introducing a more realistic and nuanced approach to modeling healthy and degenerated discs.

The process of creating the PP models is divided into seven key steps, presented in Figure 1C.

- **Step 1: Initial Alignment**—The IVD generic FE mesh and the PP point cloud are aligned using a rigid registration process. This step employs a theoretically infinitely large value for both λ and β to achieve a perfect initial alignment without any deformation of the models. Here, $\lambda = 1E9$ and $\beta = 1E9$ are suggested by Hirose (2021b) to represent the infinity.
- **Step 2: Surface Adaptation**—A Non-rigid registration of the external surface nodes of the generic FE mesh (source) to the external surface point clouds of the PP geometrical model (target) is conducted to replicate the external surfaces of both the AF and NP. This ensures that the PP model surfaces include the structured topology of the FE mesh. Here, $\lambda = 1.0$ and $\beta = 2.0$ are used.
- **Step 3: CEP Thickness Control**—This step repeats the non-rigid registration process of Step 2, but this time, the source includes the volumetric nodes of the CEPs within the generic mesh (top and bottom CEP of the disc). The registration targets the points of the PP geometrical model's AF and NP external surfaces. A higher λ than in Step 2 prevents the distortion of the CEP node cloud: it keeps the NP interfacing nodes of the CEP on the same plane as the external surface of the NP while simultaneously aligning the CEP outer nodes with the neighboring AF outer surface, thus avoiding the creation of zero-volume elements. In this way, the CEP was generated between the NP and AF, allowing us to estimate the real position of CEP, even without direct tissue segmentation. The new nodal coordinates of the CEP are retained for later use in Step 5. The values used are $\lambda = 5.0$ and $\beta = 2.0$. Notably, the thickness of the CEP can be dynamically adjusted by varying λ : increasing λ enhances the thickness, whereas decreasing it reduces the thickness. However, this causes part of the NP volume to be used to increase the thickness of the CEP.
- **Step 4: Volumetric Mesh Morphing**—The volumetric AF and the NP generic meshes are non-rigidly registered as sources to the morphed outer surface (obtained in step 2) as a target. This morphing is performed without the CEP nodes (estimated in step 3). This allows the volumetric mesh of the AF and NP to be obtained with the external shape provided by the PP model. Here, $\lambda = 3.0$ and $\beta = 2.0$ are used.
- **Step 5: Model Merging**—The AF and NP volumetric meshes are integrated into a single merged morphed model. The transition zone nodes (at the AF and NP boundary) maintain the NP shape. The CEP nodes (estimated in step 3) are then added. However, since the registration processes are carried out separately, the model may have overlapping nodes, which is addressed in step 6.
- **Step 6: Final Mesh Registration**—All nodes of the FE mesh (including AF, NP, CEP, and TZ) are non-rigidly registered to the merged morphed model (obtained in Step 5). Since the source and the target now have the same number of points, locating their corresponding nodes becomes straightforward. Moreover, BCPD++ maintains the proportion of the relative distances of the source nodes to be deformed and adapted to the PP model, aiding in maintaining the original FE model's mesh quality. Finally, the morph.py script creates an ABAQUS.inp file with the same boundary conditions, material properties, and physiological loads as used by Ruiz et al. (2018). The values used are $\lambda = 3.0$ and $\beta = 2.0$.
- **Step 7: Quality Evaluation**—Two criteria were employed to evaluate the procedure's quality:
 1. **Zero-Volume Element Check (ZVE)**: The initial step involves inspecting the ABAQUS.inp file for zero-volume elements. If such elements are detected, the process iterates Step 6 again with an increased (+0.5) λ value. This adjustment aims to minimize deformation in the relative distances between nodes, enhancing the mesh integrity.
 2. **Similarity Score (S%)**: The absence of zero-volume elements leads to the second evaluation criterion, which utilizes the Hausdorff distance (HD) to measure the similarity between the original model and the morphed model. The process begins by establishing a Hausdorff distance reference value of error. This reference value is calculated between the original model and a version of the model enlarged by 10% (achieved by scaling each coordinate by 1.1), which is assumed to represent an error percentage ($e\%$) of 10% to the original. Next, the Hausdorff distance between the original model and the morphed version thereof is determined, and the corresponding error is calculated through a cross-multiplication, assuming direct proportionality with the 10% of error as the baseline. Finally, the similarity (S%) is calculated by subtracting the error to 100%. The target is to achieve at least an 85% similarity score. If this target is not met, the λ value used in Step 6 is lowered (−0.5) to achieve a closer match in subsequent iterations. The Hausdorff distance is sensitive to outliers: as it focuses on the maximum distance between the respective points of the two sets to be compared, a single point can disproportionately affect the similarity score. Therefore, the median is used for every comparison to reduce the effect of any extreme discrepancies that might exist only at a few points in the models. Thus, the similarity score S% is formulated as:

$$e\% = \frac{HD_{\text{median}}(\text{original, morphed})}{HD_{\text{median}}(\text{original, enlarged})} \times 10\% \quad (1)$$

$$S\% = 100\% - e\%$$

Where $HD_{\text{median}}(\text{original, enlarged})$ represent the median Hausdorff distance between the original model and its version enlarged by 10%. $HD_{\text{median}}(\text{original, morphed})$ denote the median Hausdorff distance between the original model and the morphed model.

- Exception: If there is any morphed model that presents at the same time zero-volume elements and a similarity score lower than 85% ($ZVe > 0$ & $S\% < 85\%$), then the model is discarded.

Once all the IVD morphed models were prepared, the mesh quality was contrasted with the generic FE mesh of Ruiz et al. (2013). This allowed us to assess whether the BCPD++ algorithm could maintain the proportionality of the nodes' relative distances without inducing excessive deformation.

Each BCPD++ process was accelerated inside and outside the variational Bayes inference using Nystrom's method alongside KD-tree search. Furthermore, a downsampling strategy was implemented to manage the number of model points, standardizing on a voxel size of 0.1 across all instances. This approach to acceleration and downsampling adheres to the default parameters as suggested by Hirose (2021b).

2.3 Constitutive modeling of the IVD

The generic mesh of the IVD, including the morphed models (healthy and degenerated disc geometries), uses the same constitutive model, adapted by Ruiz et al. (2018) and Noailly et al. (2010). This model was implemented within an ABAQUS UMAT subroutine, allowing the biomechanical parameters to accurately reflect the properties of healthy disc tissues (Ruiz et al., 2016; Ruiz et al., 2018). This model primarily aims to isolate and examine the effects of disc morphology on biomechanical behavior, ensuring that the constitutive properties remain consistent across healthy and degenerated disc geometries.

The IVD material model considers 1) a solid phase comprising structural macromolecules such as collagen, elastin, and proteoglycans, alongside cells and 2) a fluid phase consisting of water and solutes (Malandrino et al., 2015a). The biphasic-swelling (BS) theory, as detailed by Mow et al. (1980), Mow et al. (1989), delineates both the equilibrium and transient mechanics of charged soft tissues in IVDs. This theory presents each tissue as a composite material featuring a charged solid porous phase saturated by interstitial fluid, thereby enabling the simulation of fluid pressurization and movement within the disc.

This study characterizes the behavior of the entire disc through an osmo-poro-hyper-viscoelastic model. This comprehensive model integrates the constitutive tissue of the bony endplate, treated as a linear poroelastic material (Malandrino et al., 2011) through shell elements. Furthermore, the annulus, nucleus, cartilage, and transition zone, represented with second-order hexahedral elements, employ the BS model used to simulate poromechanical

interactions within a poro-hyperelastic matrix saturated with intra- and extra-fibrillar fluid (Wilson et al., 2005b), including the Donnan osmotic pressure gradient effects (Urban and Maroudas, 1981). In addition, the model considers viscoelastic collagen fibers present only in the AF Wilson et al. (2006a) as rebar elements.

The total stress tensor σ_{tot} is expressed as the superimposition of the effective stress σ_{eff} (defined in Section 2.3.1) of the solid skeleton within the pores, a fluid pore pressure component p , and Darcy's law:

$$\sigma_{\text{tot}} = \sigma_{\text{eff}} - p\mathbf{I} \quad (2)$$

$$\mathbf{q} = \kappa \nabla p \quad (3)$$

Where \mathbf{I} is the identity tensor, \mathbf{q} is the fluid mass flow to the spatial gradient of pore pressure ∇p , and κ is the hydraulic permeability tensor of the tissue. Also, the fluid flow can be expressed by:

$$\mathbf{q} = \mathbf{u}_f n_f \quad (4)$$

Where \mathbf{u}_f is the pore fluid velocity, and n_f represents the total water fraction, i.e., the porosity of the medium.

Due to the fixed charges, the cation concentration inside the tissue is higher than in the surrounding body fluid (Wilson et al., 2005b). This excess of ion particles within the matrix creates the Donnan osmotic pressure, $\Delta\pi$, which drives the fluid flow, causing the swelling of the tissue (Urban et al., 1979). Incorporating the osmotic pressure into Eq. 2, where Schroeder et al. (2007) adapted this equation to the IVD, the hydrostatic fluid pressure p is defined as:

$$p = u_w + \Delta\pi \quad (5)$$

u_w is the water chemical potential, linked with the pore pressure degree-of-freedom generated by the interstitial fluid permeation effects through the permeability (introduced in Section 2.3.5) by applying Darcy's law to describe a relationship between fluid flow and the swelling pressure. Therefore, fluid flow between the different tissues of the model depends on the tissue-specific mappings of permeability. $\Delta\pi$ represents the osmotic pressure gradient generated by the difference between the internal and external salt concentrations (more details in Section 2.3.3).

2.3.1 Solid matrix—non-fibrillar part

The macroscopic stress-strain response of the solid matrix is determined by the initial shear modulus, G_m , the initial (in the unloaded and non-swollen state) volume fraction, $n_{s,0}$, and the current deformations of the homogenized poroelastic continuum. This response follows the Cauchy stress of the non-fibrillar matrix to describe the material's finite strain behavior, as Wilson et al. (2005a), Wilson et al. (2005b), Wilson et al. (2006a), Wilson et al. (2006b) detailed initially and then adapted by Schroeder et al. (2008) for the IVD:

$$\sigma_{\text{eff}} = -\frac{1}{6} \frac{\ln(J)}{J} G_m \mathbf{I}_1 \left[-1 + \frac{3(J + n_{s,0})}{(-J + n_{s,0})} + \frac{3J \ln(J) n_{s,0}}{(-J + n_{s,0})^2} \right] + \frac{G_m}{J} (\mathbf{B} - J^{\frac{2}{3}} \mathbf{I}_1) \quad (6)$$

Where J is the determinant of the deformation gradient tensor \mathbf{F} , and \mathbf{I}_1 is the first invariant of the left Cauchy–Green strain tensor $\mathbf{B} = \mathbf{F} \cdot \mathbf{F}^T$.

2.3.2 Annulus fibrosus collagen fibers—fibrillar part

In the AF, collagen fibers exhibit a unidirectional viscoelastic mechanical response. This behavior is modeled by incorporating finite strains in a Zener viscoelastic model with two non-linear springs. Assuming that the fibrils only resist tension, the Cauchy fibril stress tensor in a unit area for viscoelastic fibrils (Wilson et al., 2006a; Wilson et al., 2006b) can be expressed as:

$$\sigma_f = \frac{\psi}{J} P_f \bar{e}_f \bar{e}_f \quad (7)$$

Where ψ is the elongation of the fibril, P_f is the first Piola-Kirchhoff fibril stress, and \bar{e}_f is the current fibril direction.

2.3.3 Pressure component—osmotic swelling

The Donan osmotic potential describes swelling behavior (Malandrino et al., 2015a), assuming that electrolyte flux can be neglected in mechanical studies of charged materials. Accordingly, the internal and external osmotic pressures are represented by the classical Van't Hoff equation (Huyghe and Janssen, 1997), and assuming that the osmotic components are instantaneously equilibrated with the external bath, the osmotic pressure gradient $\Delta\pi$ is given by (Wilson et al., 2005b):

$$\Delta\pi = \phi_{\text{int}} RT \left(\sqrt{c_{f,\text{ext}}^2 + 4 \left(\frac{\gamma_{\text{ext}}^+}{\gamma_{\text{int}}^+} \right)^2 c_{\text{ext}}^2} \right) - 2\phi_{\text{ext}} RT c_{\text{ext}} \quad (8)$$

Where R is the gas constant, and T is the absolute temperature. The internal and external osmotic coefficients ϕ_{int} and ϕ_{ext} multiply the terms related to concentrations of mobile cations and anions, respectively. The average of the internal and external activity coefficients of the ions is represented by γ_{int}^+ and γ_{ext}^+ (assuming $\gamma^{\pm} = \sqrt{\gamma^+ \gamma^-}$). These osmotic and activity coefficients were implemented as Huyghe and Janssen (1997); Huyghe et al. (2003) proposed and as other authors such as (Wilson et al., 2005b; Schroeder et al., 2007) and Galbusera et al. (2011) adopted in their respective studies. The external concentration of salt and the proteoglycan fixed charge density are denoted by c_{ext} and $c_{f,\text{ext}}$, respectively.

2.3.4 Tissue model parameters and relation to composition measurements

To elucidate the relationship between biphasic/poroelastic models and IVD deformations quantified by J , it's essential to connect the variables in the equations for the non-fibrillar solid matrix's effective stress (Eq. 6) and the osmotic potential (Eq. 8). The proteoglycan fixed charge density is determined by the ratio of the normal fixed charge density (c_f) in milliequivalents per milliliter of total fluid to the extra-fibrillar water ($n_{f,\text{ext}}$), as defined by Ruiz et al. (2016):

$$c_{f,\text{ext}} = \frac{n_f c_f}{n_{f,\text{ext}}} \quad (9)$$

Where $n_{f,\text{ext}}$ is derived as:

$$n_{f,\text{ext}} = n_f - \varphi_{ci} \rho_{c,\text{tot}} \quad (10)$$

In this Equation, φ_{ci} indicates the intrafibrillar water content per unit mass of collagen, and $\rho_{c,\text{tot}}$ signifies the total collagen content as a proportion of the tissue's total wet weight (WW).

To ascertain water content, the initial step involves measuring the tissue sample's wet weight (WW) (Huyghe et al., 2003; Malandrino et al., 2015a; Ruiz et al., 2016), followed by lyophilization to obtain the dry weight (DW). These measurements facilitate the calculation of the initial total water content ($n_{f,0}$) and, subsequently, the initial solid fraction and the current fluid fraction:

$$n_{f,0} = \frac{\text{WW} - \text{DW}}{\text{WW}} \quad (11)$$

$$n_{s,0} = 1 - n_{f,0} \quad (12)$$

$$n_f = \frac{n_{f,0} - 1 + J}{J} \quad (13)$$

Thus, using $n_{f,0}$ as a foundational value, the equations seamlessly connect $n_{s,0}$ and n_f with the IVD deformations represented by J , establishing a coherent framework for relating IVD composition measurements to mechanical modeling parameters. Then, the total fluid volume ratio is calculated using the void volume in the medium (dV_v) and the total volume of the medium (dV):

$$n_w = \frac{dV_v}{dV} \quad (14)$$

To estimate the proteoglycan and total collagen contents, previous works propose digesting the dried samples in a papain solution. The digested solutions were then used (i) to determine the content of sulfated glycosaminoglycans (sGAG) through a dimethyl methylene blue (DMMB) assay (Farndale et al., 1986) and (ii) to achieve a measure for collagen content according to hydroxyproline measurements through the chloramine-T assay (Huszar et al., 1980).

We calculated the initial fixed charge density ($c_{f,0}$) per total hydrated tissue volume, from which c_f (Eq. 9) is derived to be dependent of J , using the expression (Narmoneva et al., 1999):

$$c_{f,0} = \frac{z_{cs} c_{cs}}{\text{MW}_{cs}} \quad (15)$$

$$c_f = c_{f,0} \frac{n_{f,0}}{n_{f,0} - 1 + J} \quad (16)$$

Here, z_{cs} , MW_{cs} , and c_{cs} are the valency (2 mEq/mmol), the molecular weight (513,000 $\mu\text{g}/\text{mmol}$), and the concentration (in $\mu\text{g}/\text{mL}$) of chondroitin sulfate, respectively. The sGAG content measured through the DMMB assay is assumed to be equivalent to the chondroitin sulfate content, i.e., c_{cs} is the amount of sGAG divided by the sample's water content. To obtain $\rho_{c,\text{tot}}$ in Eq. 17, the initial collagen content ($\mu\text{g}/\text{mg}$ DW) was estimated from hydroxyproline content by using 7.6 as the mass ratio of collagen to hydroxyproline (Sivan et al., 2006):

$$\rho_{c,\text{tot}} = \% \text{hydroxyproline} \cdot 7.6 \quad (17)$$

2.3.5 Permeability

The tissue's AF and NP hydraulic permeability (κ) are strain-dependent according to the following expression as Wilson et al. (2006a) developed and then adapted by (Schroeder et al., 2007) for the IVD:

$$\kappa = \alpha (1 - n_{f,\text{ext}})^{-M} \quad (18)$$

TABLE 1 Material properties used for all the different disc model morphologies.

Parameters		Tissue		
		AF	NP	CEP
G	MPa	0.84	1.0	1.0
$c_{f,0}^* \rightarrow c_{f,0}$	% mEq/mL	18 \rightarrow 20	29 \rightarrow 30	16.6 \rightarrow 17
$n_f^* \rightarrow n_{f,0}$	% WW	70.4 \rightarrow 75	74.5 \rightarrow 80	58.9 \rightarrow 66
$\rho_{c,tot}$	% DW	65	15	24
c_{ext}	mEq/mL	0.15	0.15	0.15
α	mm ⁴ /Ns	1.6×10^{-4}	1.6×10^{-4}	1.7×10^{-2}
M	—	1.2	1.2	1.2

G : Shear modulus, $c_{f,0}$: Initial fixed charge density, $n_{f,0}$: Initial fraction of water, $\rho_{c,tot}$: Initial collagen content concerning the total dry weight, c_{ext} : External concentration of salt, α : Initial permeability at zero strain, M : Positive constant that governs volumetric strain dependency, DW: Dry weight, and WW: Wet weight. (*): Values at the beginning of the swelling step. G of AF is from Ruiz et al. (2016), contributing the 84%, and 16% for fibers. α of CEP was back-calculated (Ruiz et al., 2018) and then validated against the experimental study of Accadbled et al. (2008). G of NP and CEP is for the non-fibrillar matrix. These values, with the rest of all tissue's material compositions, are from the work of Ruiz et al. (2018).

Where α stands for the initial permeability at zero strain, and M is a positive constant that governs volumetric strain dependency, and $n_{f,ext}$ is calculated in Eq. 10.

The CEP is also strain-dependent, following this equation (Mow et al., 1980; Argoubi and Shirazi-Adl, 1996):

$$\kappa = \alpha \left[\frac{e(1+e_0)^2}{e_0(1+e)} \right]^2 \exp \left[M \left(\frac{1+e}{1+e_0} - 1 \right) \right] \quad (19)$$

Where e is the void ratio, which is the ratio of the current pore volume (i.e., fluid) to the current volume of the solid matrix, and e_0 is the initial void ratio. The void ratio is related to the initial and current water content/porosity of the tissue, $n_{f,0}$ and n_f according to the following expression:

$$e = \frac{n_f}{1-n_f} \quad \text{and} \quad e_0 = \frac{n_{f,0}}{1-n_{f,0}} \quad (20)$$

All tissue compositions for both non-degenerated and degenerated IVD were considered for a Grade I IVD and were taken from the literature (Table 1). All mechanical behavior has been detailed in the Supplementary Section S1. See the works of Huyghe et al. (2003); Malandrino et al. (2015a); Ruiz et al. (2013), Ruiz et al. (2016), Ruiz et al. (2018) for more information on the evolution of the used model.

2.4 Mechanical simulations

This simulation was conducted following a free swelling step of 17 h (as per the BS theory outlined in Section 2.3.3). No external loads were applied on the morphed IVD to simulate free swelling, which stood for an initialization of the expected equilibrium osmotic pressurization of the disc, according to the Eq. 8. The pre-swelling initial values for fixed charge density and water content, denoted by c_f^* and n_f^* in Table 1, were set to gradually reach the $c_{f,0}$ and $n_{f,0}$ values proposed in the literature by the end of the swelling process (Ruiz et al., 2018).

Three daily load cycles were then simulated to identify which morphological factors significantly affected the mechanical response during average human activities. Accordingly, each cycle started

with an 8-h resting period (creep step) under 0.11 MPa compression (load step of 10 s), which simulated overnight best rest. It was followed by 16 h of average day activity (creep step) under a load of 0.54 MPa compression (load step of 10 s), as illustrated in Figure 2A. These load values were selected based on average activity and resting intradiscal pressures as measured *in vivo* by Wilke et al. (1999), as proposed by Ruiz et al. (2016). The compressive loads were applied to the BEP shell elements (as mentioned in Section 2.2) of the top, while the nodes of the caudal BEP remained fully constrained ($U_x = U_y = U_z = 0$). The simulation also accounted for atmospheric external pressure (Figure 2B).

Given the incorporation of swelling into our simulations, it is necessary to detect potential deviations between the real geometry from the MRI models and the geometry following the morphing process, which includes swelling. To address this, we selected three IVD models with varying mid-heights (MH) for detailed analysis (See Table 2). Post-swelling, these were used to re-evaluate the Similarity Score (refer to Section 2.2 for details).

3 Model validation

The constitutive model and the morphing process were validated using the experimental tests reported by Malandrino et al. (2015b), performed with a 500 N sustained compressive load, similar to a physiological upper body standing weight of 50 kg (Heuer et al., 2007; Ruiz et al., 2016; Hassan et al., 2020), which can produce fluid loss from the IVD and height reduction (Adams and Hutton, 1983). In his works, creep compression tests were briefly done on L3-L4 segments extracted from four lumbar spines. The IVDs were placed in a neutral position in the spine tester (WISI) of the Institute of Orthopedic Research and Biomechanics (Ulm, Germany) (Wilke et al., 1994), with their mid-transverse planes normal to the vertical direction. Only vertical, i.e., axial displacements, were permitted during the loading period. An initial compressive preload of 300 N was applied for 180 s and then withdrawn for 180 s. This cycle was repeated

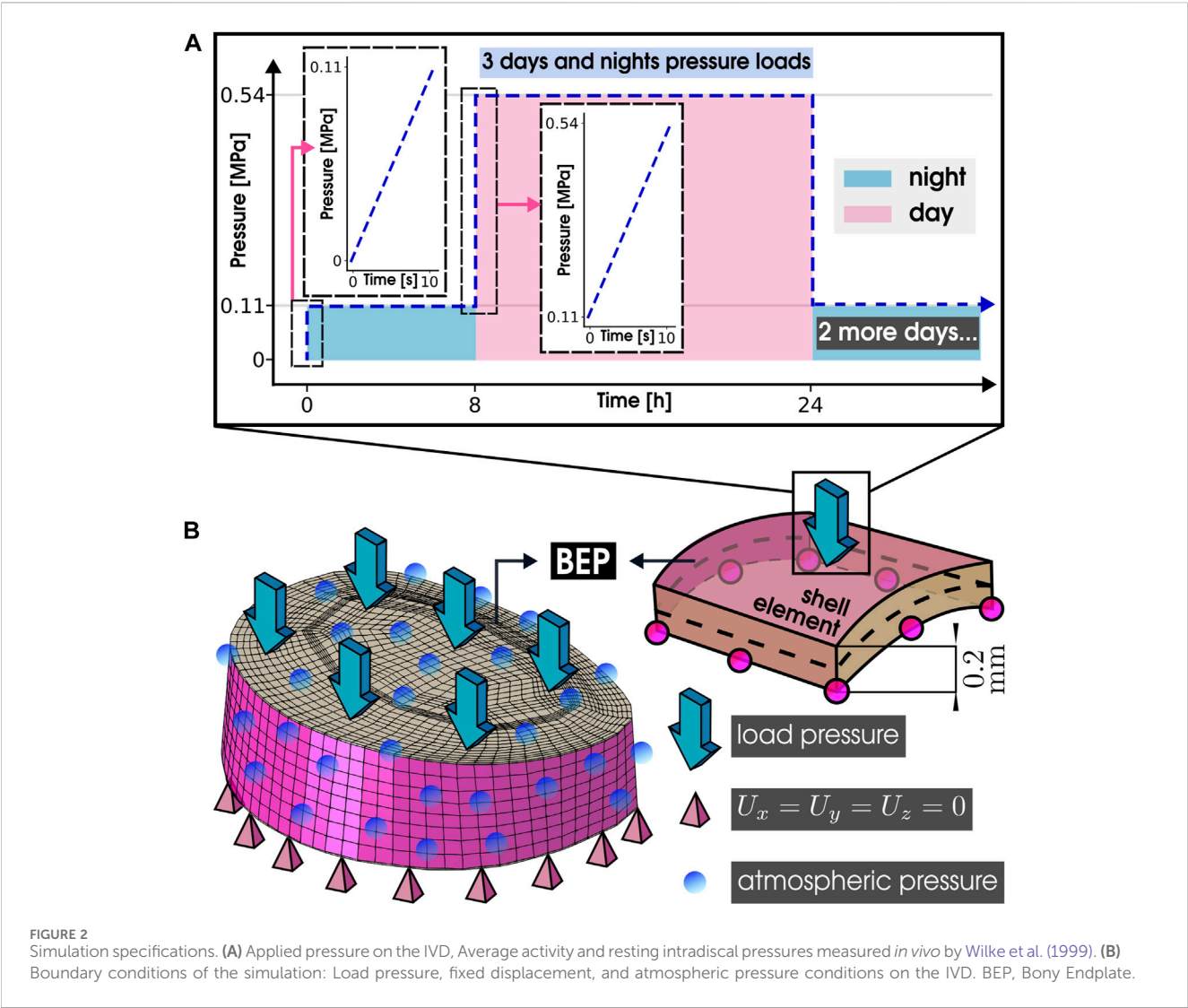


TABLE 2 Morphed IVD Models used to check similarity score post-swelling. Mid-height: MH.

ID	Level	MH [mm]	SpineView link
MY0092	L4-L5	8.04	https://ivd.spineview.upf.edu/?filenamePrefix=MY0092_L4L5
MY0002	L5-S1	14.20	https://ivd.spineview.upf.edu/?filenamePrefix=MY0002_L5S1
MY0065	L3-L4	17.41	https://ivd.spineview.upf.edu/?filenamePrefix=MY0065_L3L4

three times to precondition the IVD. Subsequently, the load was increased to 500 N in 10 s and sustained for 3 h, with creep responses recorded as displacements.

We selected an IVD exemplifying healthy disc characteristics to align with the mechanical properties defined in our model. This selection was followed by the morphing process detailed in Section 2.2, aimed at replicating the morphology reported in the study of Malandrino et al. (2015b) (height of 12.1 mm, sagittal distance of 37.6 mm, and coronal distance of 47.4 mm). We conducted a comparative analysis to ascertain our constitutive model’s accuracy and the morphing process’s effectiveness. This involved contrasting the displacement of the disc’s top zone as measured in

both the experimental setup and the simulation outcomes of the referenced study against the results from our simulation.

4 Data mining

To explain the connection between morphological attributes and the early stages of disc degeneration across our 169 IVD PP FE model dataset, we analyzed the mechanical simulation outcomes as detailed in Section 2.4. This analysis was strategically focused on five distinct zones of interest, chosen for their critical relevance to the onset of disc degeneration. We analyzed morphological factors based on their

significance in the qualitative assessment of Pfirrmann grading and their visibility in sagittal and coronal clinical images. Concurrently, we concentrated on mechanical variables that are pivotal for understanding stresses and the mechanisms of indirect mechanotransduction.

For the predictive analysis, we employed three regression models: Linear Regression (LR), Support Vector Machine Regression (SVR), and Extreme Gradient Boosting Regression (XGBoostR). Each model was trained according to the morphological factors of the morphed IVDs, and we explored the relationship between morphological measurements and mechanical responses by using the SHAP (SHapley Additive exPlanations) values that ranked the impact of each factor in each regression model. The models' inputs were the morphological features, and the targets were the mechanical responses.

The selection process for the optimal model for each mechanical variable was based on predictive performance, utilizing the R-squared (r^2) metric to identify the model with superior predictive power. Furthermore, the Mean Squared Error (MSE) was used to assess whether the chosen model would exhibit high predictive accuracy and keep minimal prediction error.

4.1 Zones of interest for evaluation

To discern possible mechanical changes because of the morphological variability in regions likely relevant to IDD pathophysiology, we focused on particular regions susceptible to being altered in early IDD. On one hand, the center of the nucleus pulposus is a natural candidate region, according to Pfirrmann's grading. On the other hand, our mesh structure contains a region, the transition zone, that is worth exploring. This zone, as defined in our FE meshes, emerged out of a need for computational stability to ensure the FE mesh convergence and cope with the negative effects of weak discontinuities between the nucleus pulposus and the annulus fibrosus elements (Ruiz et al., 2013). Interestingly, though, a transition between the nucleus and the annulus exists, as revealed by several quantitative MRI, synchrotron imaging, cell phenotypes, and structural and composition measurements through the IVD (Marchand and Ahmed, 1990; Bruhlmann et al., 2002; Disney et al., 2023; Kapoor et al., 2023). Hence, the definition of this region in the FEM results in a more realistic description of the IVD, in contrast to an abrupt change of material properties from the NP to the AF.

Therefore, our analysis focused on the finite element simulations of the local tissue mechanics in these corresponding volumes that show signs of alterations in early-degeneration stages positioned along the sagittal plane of the disc: the transition zones (Posterior Transition Zone, PTZ; Anterior Transition Zone, ATZ), and the Center of the Nucleus Pulposus (CNP). Furthermore, we analyzed the mechanical features calculated over the central regions of the top and bottom CEP surfaces (TC and BC, respectively) to underscore the potential significance of the CEP in different disc morphologies. For each volume (PTZ, CNP, ATZ), average mechanical responses were calculated over 27 nodes contained in the volume (Figure 3E). For each surface (TC and BC), average mechanical values were computed over 529 nodes belonging to the surface (Figure 3D).

The selection of 27 nodes within each volume is grounded on the definition of a minimal-size transition zone to avoid numerical instabilities in our generic model, as defined by Ruiz et al. (2013). The TZ, characterized by a composition of 5 second-order

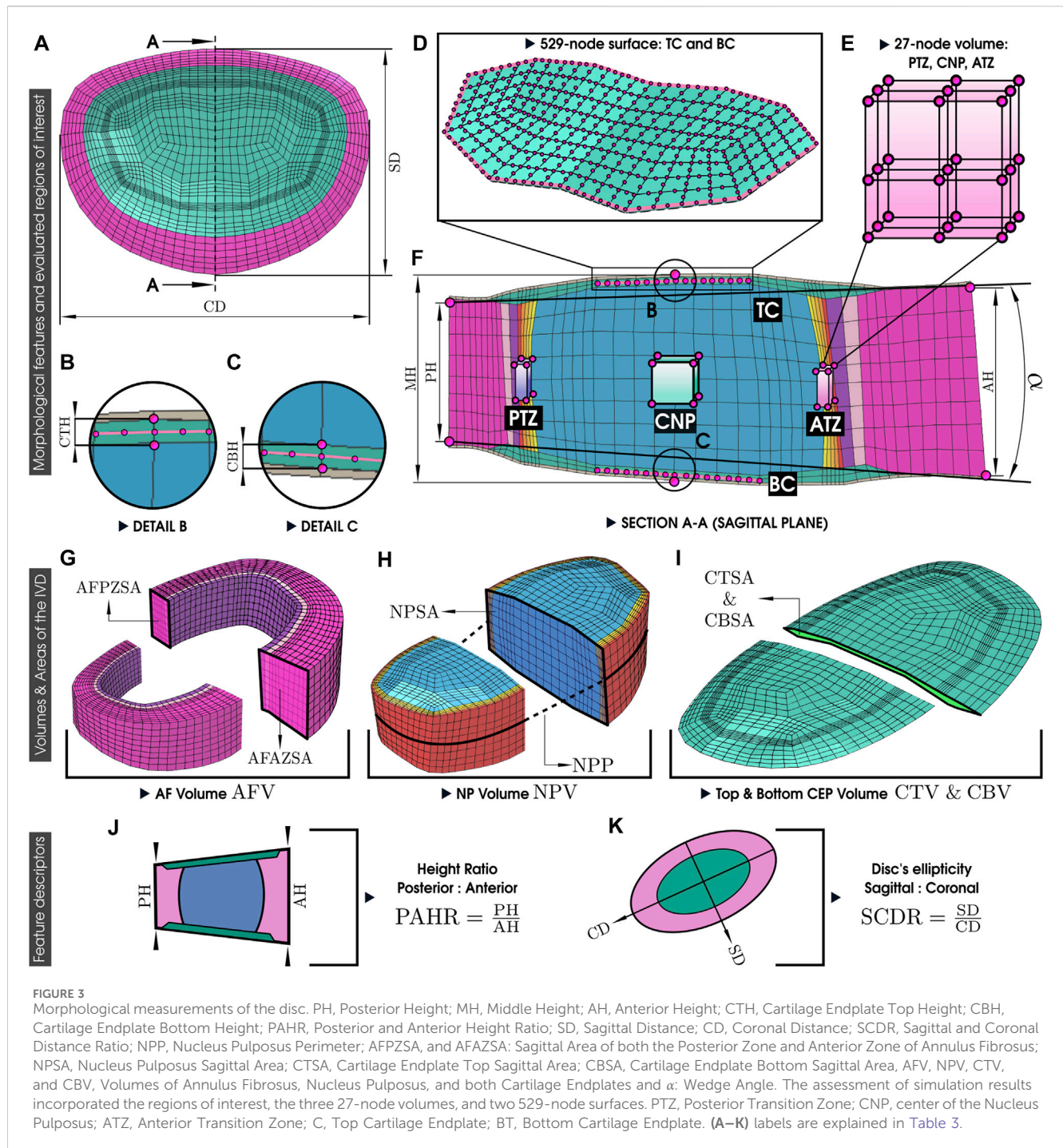
hexahedral elements in thickness, opts for an internal volume excluding the nodes at the nucleus or annulus interface. Given the second-order nature of the hexahedral elements, the thickness includes 11 nodes, with those at positions 3, 6, and 9 being specifically chosen. Adopting a 27-node volume for the CNP facilitates a more coherent comparison by leveraging the vertex nodes of the 8 central hexahedral elements within the nucleus. Meanwhile, the CEP surface selection aims to minimize the influence of the AF, focusing solely on its relation to the NP.

4.2 IVD model morphological features

Despite numerous studies using Pfirrmann's classification to assess varying degrees of degeneration and morphological measurements, the specific morphological factors associated with IDD remain elusive. Previous studies, including observational and *ex vitro* research, have focused on the significance of disc height reduction at the posterior, middle, and anterior sections of IDD. These studies, however, have often presented inconclusive outcomes regarding the morphological attributes of IDD (Urquhart et al., 2014; Teichtahl et al., 2015; Bach et al., 2019; Kizilgöz and Ulusoy, 2019; Fleps et al., 2024; Tavana et al., 2024). Hence, it becomes necessary to explore the entire morphology of the discs, combining all the possible factors to understand the interplay between them.

As the morphological variations are reflected by different node coordinates in each model and the direct mechanical and tissue property environment of each region is kept consistent with the entire set of PP models, 20 morphological factors were extracted from finite element (FE) model meshes, with a consistent topology across all models. This enhances the precision of measuring heights and distances, both observable in the sagittal and coronal planes and measurable in clinical images, particularly in sagittal lumbar MRI. Further morphological features, such as the volumes, can only be calculated after 3D image segmentations but are expected to be relevant to the functional mechanics of the IVD, according to the known importance of volumetric mechanical deformations in highly hydrated materials. Therefore, we propose these features as possible novel biomarkers in the study of IDD.

Figure 4 provides an in-depth visual guide to these factors. More specifically, the explored morphological factors of the PP IVD models were: Posterior Height (PH); Middle Height (MH); Anterior Height (AH); Cartilage Endplate Top Height (CTH); Cartilage Endplate Bottom Height (CBH); Sagittal Distance (SD); Coronal Distance (CD); Nucleus Pulposus Perimeter (NPP); Sagittal Area of both the Anterior Zone and Posterior Zone of Annulus Fibrosus (AFAZSA and AFPZSA); Nucleus Pulposus Sagittal Area (NPSA); Cartilage Endplate Top Sagittal Area (CTSA); Cartilage Endplate Bottom Sagittal Area (CBSA); Volumes of Annulus Fibrosus Nucleus Pulposus, and both Cartilage Endplates (AFV, NPV, CTV, and CBV); the Wedge Angle (α), defined as the angle formed by the line connecting the upper heights of PH and AH with the line connecting the base of PH and AH. Two different ratios were evaluated as well, signifying the IVD's intrinsic asymmetry when the sagittal and coronal plane are observed: the Posterior and Anterior Height Ratio (PAHR)—representing the ratio of PH to AH, Sagittal and Coronal Distance Ratio (SCDR)—indicating the disc's ellipticity:



$$\text{PAHR} = \frac{\text{PH}}{\text{AH}} \quad \text{and} \quad \text{SCDR} = \frac{\text{SD}}{\text{CD}} \quad (21)$$

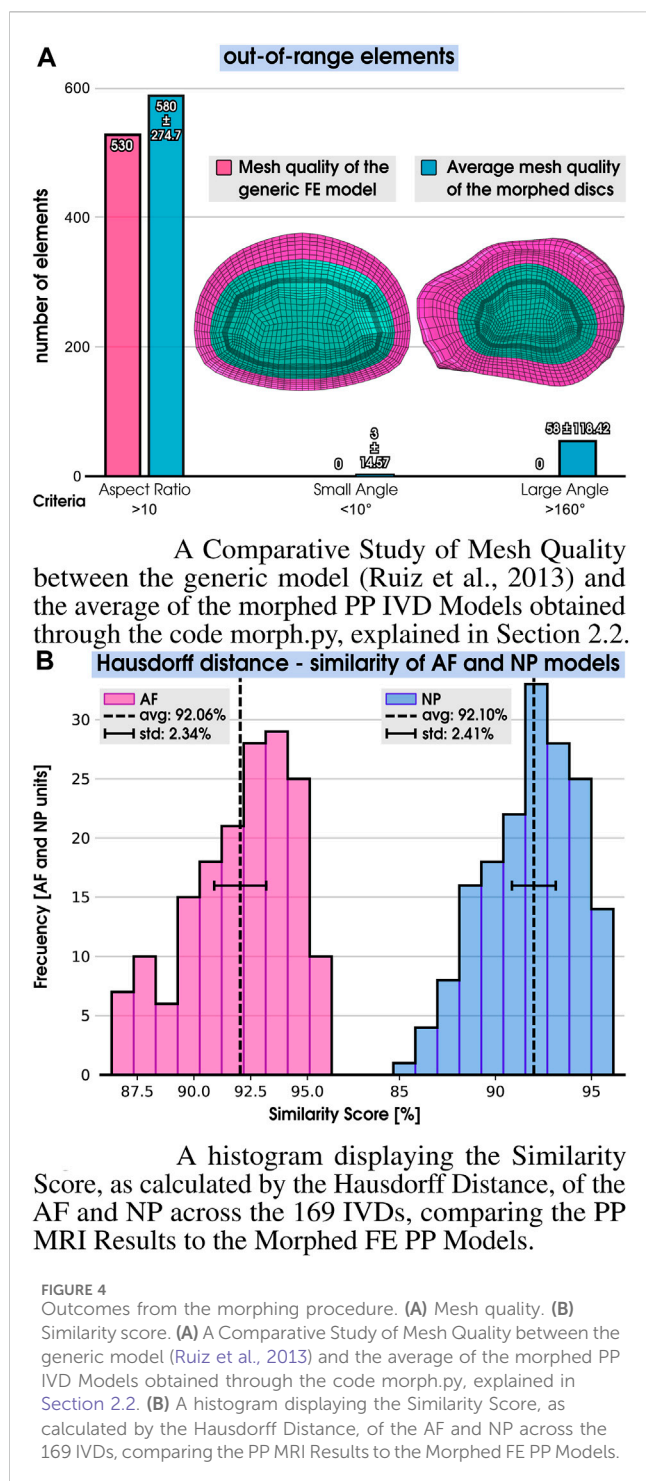
A brief description of the morphological features and their location in Figure 3 is detailed in Table 3.

4.3 Target variables out of the FE simulations

To refine the selection of mechanical variables for analysis, our approach extends beyond principal stresses and hydrostatic

pressure, elements previously examined Tavana et al. (2024); Fleps et al. (2024), to explore potential non-linear interplays with IVD morphology. Moreover, we have incorporated mechanical variables known to affect indirect mechanotransduction phenomena, such as the different strain-dependent or stress parameters related to fluid and proteoglycan contents possibly related to IDD through IVD nutritional aspects (Roberts et al., 1996; Magnier et al., 2009; Travascio et al., 2009; Shirazi-Adl et al., 2010; Malandrino et al., 2015a; Ruiz et al., 2016; De Geer, 2018).

In this context, we selected 11 key mechanical variables, modeled as the response of the 169 PP IVD models to the



imposed mechanical loads as target variables. These variables were derived from averages across the three 27-node volumes (PTZ, CNP, and ATZ) and two 529-node surfaces (TC and BC), as introduced previously. They include the indirect mechanotransduction-related variables: Fluid Volume Ratio (n_w); Pore Fluid Effective Velocity ($\|\mathbf{v}_f\|$); Hydrostatic Pressure (p); Principal Stress I (σ_I); Principal Stress III (σ_{III}); Water Content (n_f); Fixed Charge Density (c_f); Extrafibrillar Fixed Charge Density ($c_{f,ext}$); Extrafibrillar Water Content ($n_{f,ext}$); Swelling/Osmotic Pressure ($\Delta\pi$); Void Ratio (e). A description

of the variables related to the constitutive model through the equations is detailed in Table 4.

4.4 Machine learning models

We adopted three machine-learning regression models, i.e., LR, SVR, and XGBoostR, each trained using the disc morphological features to predict the target simulated variables. We partitioned our IVD dataset, consisting of features (X) and targets (y), 60% for training (X_{train} , y_{train}), 20% for validation (X_{val} , y_{val}), and the remaining 20% for testing (X_{test} , y_{test}). We chose the model and the optimal hyperparameters by maximizing the highest R-squared (r^2) value while ensuring a low mean squared error (MSE).

The implementation relies on the sklearn library in Python. For each of the five regions of interest (PTZ, CNP, ATZ, TC, and BC), we employed the following steps.

4.4.1 Hyperparameter optimization process

We used K-Fold cross-validation for the hyperparameter optimization for the SVR and XGBoostR models (the LR model has no hyperparameters). The training dataset (X_{train} , y_{train}) was split into 20 folds. We fixed the random state value at 42 during the shuffling process to maintain consistency and reproducibility. The ranges of the initial hyperparameters for both models are shown in Table 5).

Our strategies for hyperparameter optimization included.

- **Grid Search:** This strategy conducts an exhaustive search through a predefined set of hyperparameters, creating a “grid” of parameter combinations to try. It then trains a model for each combination and evaluates the model’s performance using cross-validation.
- **Randomized Search:** Unlike Grid Search, Randomized Search does not exhaustively try all parameter settings. Instead, it samples a given number of candidates from a parameter space with a specified distribution. This method is more efficient, especially when dealing with many or continuous parameters. By randomly drawing a subset of parameter combinations, it can explore more unique sets of parameters than Grid Search, potentially leading to better results.
- **Bayesian optimization:** The Tree-structured Parzen Estimator (TPE), which is a Bayesian optimization algorithm, is used through the Optuna Study (a framework for hyperparameter optimization). It constructs a probabilistic model based on past trial results and uses this model to suggest the next set of hyperparameters.

For each regression type (SVR and XGBoostR), we chose the best-performing model from the optimized models obtained through grid search, randomized search, and Bayesian optimization on the validation set (X_{val} , y_{val}).

4.4.2 Selecting the best machine-learning model

After identifying the optimal hyperparameters, we merged the training and validation sets to create a combined training-validation

TABLE 3 IVD model morphological features.

Morphological variables				Figure 3
Posterior height	PH	mm	Measured in the sagittal plane	F
Middle height	MH	mm	Measured in the sagittal plane	F
Anterior height	AH	mm	Measured in the sagittal plane	F
Cartilage top height	CTH	mm	Measured in the sagittal plane	B
Cartilage bottom height	CBH	mm	Measured in the sagittal plane	C
Posterior-anterior ratio	PAHR	—	PH/AH Eq. 21	J
Sagittal distance	SD	mm	Measured in the top plane	A
Coronal distance	CD	mm	Measured in the top plane	A
Sagittal-coronal ratio	SCDR	—	SD/CD Eq. 21	K
Nucleus pulposus perimeter	NPP	mm	Measured around the Nucleus	H
Posterior zone area	AFPZSA	mm ²	Measured in the sagittal plane	G
Anterior zone area	AFAZSA	mm ²	Measured in the sagittal plane	G
Nucleus pulposus area	NPSA	mm ²	Measured in the sagittal plane	H
Cartilage top area	CTSA	mm ²	Measured in the sagittal plane	I
Cartilage bottom area	CBSA	mm ²	Measured in the sagittal plane	I
Annulus fibrosus volume	AFV	mm ³	Tissue volume	G
Nucleus pulposus volume	NPV	mm ³	Tissue volume	H
Cartilage top volume	CTV	mm ³	Tissue volume	I
Cartilage bottom volume	CBV	mm ³	Tissue volume	I
Wedge angle	α	°	Angle between PH and AH	F

TABLE 4 Mechanical variables evaluated in each region of interest (Figures 3D, E).

Mechanical variables		Description	Equation
n_w	%	Total fluid volume ratio	Eq. 14
$\ \mathbf{v}_f\ $	mm/s	Magnitude of velocity at which fluid moves through the porous	Eq. 4
p	MPa	The mechanical stress due to the fluid pressure within the IVD	Eq. 5
σ_I	MPa	The maximum principal stress within the tissue	Eq. 2
σ_{III}	MPa	The minimum principal stress within the tissue	Eq. 2
n_f	%	Percentage of water by volume within the tissue	Eq. 13
c_f	mEq/mL	Density of fixed charges within the tissue matrix	Eq. 16
$c_{f,ext}$	mEq/mL	Density of fixed charges outside the collagen fibers	Eq. 9
$n_{f,ext}$	%	Percentage of water by volume outside the collagen fibers	Eq. 10
$\Delta\pi$	MPa	The tissue exerts pressure as it swells due to water uptake	Eq. 8
e	%	The ratio of the volume of voids to the volume of solid material	Eq. 20

FLUVR, Fluid Volume Ratio; FLVEL, Pore Fluid Effective Velocity; HidPre, Hydrostatic Pressure; SMax, Principal Stress I, SMin, Principal Stress III; WCont, Water Content; FCHD, Fixed Charge Density; EFCHD, Extrafibrillar Fixed Charge Density; EWCont, Extrafibrillar Water Content; SwePre, Swelling Pressure; VOIDR, Void Ratio.

set $(X_{train, val}, y_{train, val})$. This was used to train the final SVR and XGBoostR models. Since LR does not require hyperparameter optimization, it was directly trained using the training-validation set. We evaluated the performance of the final model using the testing set (X_{test}, y_{test}) . Thus, the model (either LR, SVR, or XGBoostR) with the higher r^2 score was selected.

TABLE 5 Initial values for hyperparameter optimization of Grid Search, Randomized Search, and Bayesian optimization for SVR and XGBoostR models.

SVR params	Hyperparameter optimization model		
	Grid search	Randomized search	Bayesian optimization
C	0.1, 1, 10, 100	Log-scaled, 1e-3 to 1e3	Log-scaled, 1e-3 to 1e2
ϵ	0.0001, 0.001, 0.01, 0.1	Linear scale, 0.001 to 0.1	Log-scaled, 1e-3 to 1e1
<i>kernel</i>	Li, Po, RBF, Sig	Li, Po, RBF, Sig	Li, Po, RBF, Sig
γ	Scale, auto, -3 to 3	Scale, auto, -3 to 3	Scale, auto
δ_{Po}	N/A	[2, 5]	[2, 5]
XGBoostR params	Hyperparameter optimization model		
	Grid search	Randomized search	Bayesian optimization
$n_{\text{estimators}}$	100, 500, 1000	Integer range, 50 to 2000	Integer range, 50 to 2000
η	0.01, 0.1, 1	Uniform scale, 0.01 to 1	Log-scaled, 0.01 to 1
$\text{max}_{\text{depth}}$	3, 5, 7	Integer range, 1 to 10	Integer range, 1 to 10
$\text{min}_{\text{child weight}}$	1, 3, 5	Integer range, 1 to 10	Integer range, 1 to 10
Subsample	0.5, 0.7, 0.9	Uniform scale, 0.1 to 0.7	Log-scaled, 0.3 to 7
Colsample	0.5, 0.7, 0.9	Uniform scale, 0.1 to 0.7	Log-scaled, 0.3 to 7

The hyperparameters for SVR included the penalty parameter C , the epsilon (ϵ) tolerance for errors, the *kernel* function, and the coefficient gamma (γ), a parameter specific to certain kernel functions. The kernel functions used include *linear* (Li), *poly* (Po), *rbf* (RBF), and *sigmoid* (Sig), and the degree (δ_{Po}) of the polynomial function was also considered. The hyperparameters for XGBoostR included the number of gradient-boosted trees ($n_{\text{estimators}}$), the learning rate (η), the maximum depth of the trees ($\text{max}_{\text{depth}}$), the minimum child weight ($\text{min}_{\text{child weight}}$), the subsample ratio (subsample), and the column sample by the tree (colsample).

4.4.3 Influential morphological factors on the mechanical responses

We employed SHAP values to determine each feature's contribution towards the prediction. We used the Normalized Mean Absolute SHAP Value (Ning et al., 2022), scaled to a range from 0 to 1, as a reliable metric to rank the morphological factors by impact on each mechanical response.

4.4.4 Morphological impact in terms of mechanical variation magnitude

The SHAP values reflect the influence of each morphological variable on each local mechanical prediction, but they do not measure the magnitude of the triggered variation of these mechanical predictions. Hence, to complement the information provided by the SHAP values, we defined a new metric, the PR% (Eq. 22). The PR% quantifies the capacity of a specific morphological feature to uniquely impact the magnitude of a particular mechanical response (PR) relative to the full range of variation of the same mechanical response over the 169 finite element simulations performed with the personalized models (SR), i.e.,:

$$\text{PR\%} = \frac{\text{PR}}{\text{SR}} \times 100\% \quad (22)$$

The calculation of PR was done with the best (i.e., with the highest r^2) trained correlation model (LR; SVR; XGBoostR) by calculating a possible range of mechanical response as a result of the sole variation of the considered morphological descriptor,

determined over the entire cohort ($n = 169$). Non-varied morphological features were set to their respective average values for each PR calculation, determined over the entire cohort through the chosen regression model. The PR values are also referred to as the ranges of the regression-predicted variations of magnitude of the mechanical responses (specific to each morphological parameter). The SR values were also referred to as the range of the FE-simulated variations of the magnitude of the mechanical responses over the entire cohort of models.

For each PR%, a low %value indicates that a specific morphology cannot capture *per se* the entire range of variation of the magnitude of the mechanical response. In such a case, the range of mechanical response shall result from the combined variations of multiple morphological features. In contrast, a high PR% value indicates that a leading unique morphological feature can explain *per se* the variation of the magnitude of a specific mechanical response.

5 Results

5.1 Morphing process

A total of 169 PP IVD FE models were successfully created out of the 169 segmented volumes. Each FE model was devoid of zero-volume elements ($ZVe = 0$), and all models shared the same components and connectivity as the generic FE mesh model, described in Figure 1A. The mesh quality of the generic model and the average mesh quality of all morphed discs, in terms of element aspect ratio and angular distortions, were compared by

TABLE 6 Morphological features (Section 4.2) of the created 169 IVDs morphed models obtained by the morphing process (Section 2.2).

Morphological features		Measured values			
		MIN	MAX	avg \pm std	GM
PH	mm	4.000	14.541	8.257 \pm 1.548	10.508
MH	mm	5.269	18.254	12.307 \pm 2.182	14.330
AH	mm	6.064	24.614	11.838 \pm 2.822	13.694
CTH	mm	0.230	1.292	0.534 \pm 0.148	0.545
CBH	mm	0.182	1.518	0.493 \pm 0.151	0.545
PAHR	—	0.364	1.641	0.721 \pm 0.171	0.767
SD	mm	30.395	46.604	37.742 \pm 3.372	37.959
CD	mm	41.471	61.847	50.143 \pm 4.036	49.463
SCDR	—	0.605	0.930	0.754 \pm 0.050	0.767
NPP	mm	63.237	119.308	86.613 \pm 11.718	94.734
AFPZSA	mm ²	0.231	1.115	0.542 \pm 0.170	0.525
AFAZSA	mm ²	0.432	2.026	1.053 \pm 0.306	1.316
NPSA	mm ²	1.012	3.813	2.313 \pm 0.513	2.878
CTSA	mm ²	0.057	0.418	0.145 \pm 0.044	0.178
CBSA	mm ²	0.037	0.276	0.138 \pm 0.045	0.193
AFV	mm ³	4.274	18.097	9.637 \pm 2.708	10.146
NPV	mm ³	2.373	13.158	5.566 \pm 1.673	8.134
CTV	mm ³	0.184	1.399	0.432 \pm 0.156	0.624
CBV	mm ³	0.133	1.367	0.436 \pm 0.184	0.667
α	°	0.081	23.692	5.981 \pm 3.476	4.694

The minimum (MIN), maximum (MAX), and average (avg \pm std) values of the entire cohort for each of the morphed models and the values of the generic model (GM) are presented. PH, Posterior Height; MH, Middle Height; AH, Anterior Height; CTH, Cartilage Endplate Top Height; CBH, Cartilage Endplate Bottom Height; PAHR, Posterior and Anterior Height Ratio; SD, Sagittal Distance; CD, Coronal Distance; SCDR, Sagittal and Coronal Distance Ratio; NPP, Nucleus Pulposus Perimeter; AFPZSA, and AFAZSA, Sagittal Area of both the Posterior Zone and Anterior Zone of Annulus Fibrosus; NPSA, Nucleus Pulposus Sagittal Area; CTSA, Cartilage Endplate Top Sagittal Area; CBSA, Cartilage Endplate Bottom Sagittal Area, AFV, NPV, CTV, and CBV, Volumes of Annulus Fibrosus, Nucleus Pulposus, and both Cartilage Endplates and α : Wedge Angle.

employing the ABAQUS 2020 mesh quality check functions (Figure 4A). The average aspect ratio increased by 9.4% in the morphed models, with 580 out-of-range elements and a standard deviation (std) of 274.7, compared to 530 in the generic mesh, out of a total of 19,392 hexahedral elements in each model. Small and large angles escalated by 3 (std of 14.57) and 58 (std of 118.42), respectively, in the morphed models.

None of these increases led to error elements, convergence issues, or negative Jacobians during the simulations. Considering all the out-of-range elements of the three mesh quality categories within the created cohort, it represents only 3.3% of the 19,392 elements.

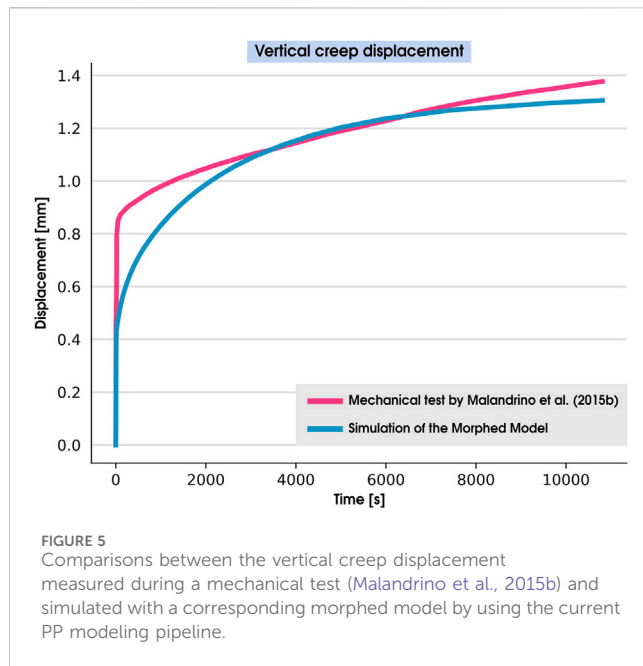
The morphological measurements of the resulting morphed models are listed in Table 6 and detailed in Section 4.2. Here, we can observe that the average CEP height at the disc's center for the top (CTH) and bottom (CBH) zones were 0.534 ± 0.148 and 0.493 ± 0.151 , respectively. This agrees with that observed by Moon et al. (2013), although the out-of-range minimum and maximum values are also shown among the generated models corresponding to discs in advanced stages of degeneration.

The similarity score (Figure 4B) between each morphed model and its AF and NP counterpart surfaces in the segmented geometrical models was computed using the Hausdorff distance (as detailed in Section 2.2), as seen in step 7 of Figure 1C). On average, the AF and NP yielded a similarity score of 92.06% and 92.10%, respectively. Moreover, the morphing algorithm consistently achieved a similarity score of at least 85%.

No model was discarded for further morphing or during the simulations since all of them met the quality criteria: $ZVe = 0$ & $S\% \geq 85\%$.

5.2 Model validation

Figure 5 presents the time history of the vertical displacements of the cranial BEP during the 3-h creep experiment reported in Malandrino et al. (2015b) alongside the simulations of the PP model performed in this work. The simulated creep response was similar to the experimentally measured one (Malandrino et al., 2015b), with a relative error at the end of the simulation of 5.20% between our simulation and the *in vitro* measurements.



5.3 Mechanical simulations

5.3.1 Evaluation process and initial values after swelling

The mechanical response was evaluated during the day activity part of the simulated loading history. Over three simulated days (detailed in Section 2.4), the mechanical response for day activity reached equilibrium on the second day. Hence, this specific step was selected for further analysis.

The average values for the initial fixed charge densities and water contents in the AF and NP zones after the swelling step for each of the 169 morphed IVDs were calculated as $c_{f,0} = 0.204 \pm 0.003$ and $n_f = 75.056 \pm 0.302\%$ for AF, and $c_{f,0} = 0.309 \pm 0.003$ and $n_f = 79.692 \pm 0.162\%$ for NP. These evaluations helped to ensure that the simulations met the estimates detailed in Table 1.

There were no problems with the convergence or the quality of the elements during the simulation for any model, and the Similarity Score (S%) (Eq. 1) for the three models before and after the Swelling are reported in Table 7.

5.3.2 Data mining of the mechanical simulations

5.3.2.1 Magnitude of the mechanical responses

Table 8 presents the extreme values of the mechanical responses calculated across the cohort of 169 morphed IVD models (detailed in Table 4) on the three volumes (PTZ, CNP, ATZ) and surfaces (CEP: CT and CB), including the FE-simulated range of variation (SR) and the simulation variation percentage (SV%). The SV% quantifies the relative change in the mechanical response magnitudes, benchmarking the maximum value against the absolute minimum observed in the cohort. This metric is given by the formula:

$$SV\% = \frac{|MAX - MIN|}{\min(|MAX|, |MIN|)} \times 100\% \quad (23)$$

TABLE 7 Similarity scores (S%) pre- and post-swelling for IVD models.

ID	Pre-swelling		Post-swelling	
	S% (AF)	S% (NP)	S% (AF)	S% (NP)
MY0092	91.41	91.05	92.80	92.97
MY0002	93.78	91.72	92.53	89.60
MY0065	90.44	92.00	88.90	89.71

The variables that had percentage variations greater than 100% between maximum and minimum values of the entire cohort were the fluid velocity ($\|v_f\|$) for all the evaluated zones and the maximum stress (σ_I) in the posterior, anterior, and CEP bottom zones (PTZ, ATZ, and BT). Changes of 50%–100% were reflected by the hydrostatic pressure (p) in the PTZ and ATZ and the minimum stress (σ_{III}) in the PTZ, ATZ, and BT. Changes between 30% and 50% were calculated for the osmotic pressures ($\Delta\pi$) of the PTZ and ATZ and for the hydrostatic pressures and principal stresses of the CNP and of the CEPs (CT and BT). Values between 10% and 30% were calculated for the fixed charge densities (c_f and $c_{f,exf}$) and void ratio (e) of all zones of interest. The most insignificant changes ($< 10\%$) were obtained for the fluid content-related variables (n_w , n_f and $n_{f,exf}$).

In general, the magnitudes of the mechanical responses most affected by the morphological changes were fluid velocity, hydrostatic pressure, and principal stresses. The most significant changes were in the posterior and anterior zones (PTZ and ATZ). In contrast, the magnitude variation in the CNP was smaller, especially for the principal stresses. The osmotic pressure and void ratio magnitude variations were also lower in the CNP compared to the PTZ and ATZ, although similar in percentage variation to the ones in the CEPs (CT and BT).

5.3.2.2 Interpreting machine learning models

Figure 6 shows the contribution of each morphological variable (rows) to the prediction of each mechanical response (columns) for the regression models in the three volumes (PTZ, CNP, and ATZ), while Figure 7 explains the interaction for the two CEP surfaces (TC and BT). The absolute normalized SHAP values reported there quantify the average contribution of a feature to the model predictions across the entire dataset, with a value of 1 representing a maximal contribution. Only the top 5 morphological features are reported in this text so that each mechanical variable does not unnecessarily saturate the figure with less influential features. All morphological features of each volume, PTZ, CNP, and ATZ, and surfaces, TC and BC, of interest are listed in (Supplementary Figures S1–S5, respectively). Specific variables, such as $\|v_f\|$, were assessed after the day's loading, just before the creep step (see Figure 2), because they showed significant changes with deformations within a brief period.

5.3.2.3 Influential morphological factors on zones of interest

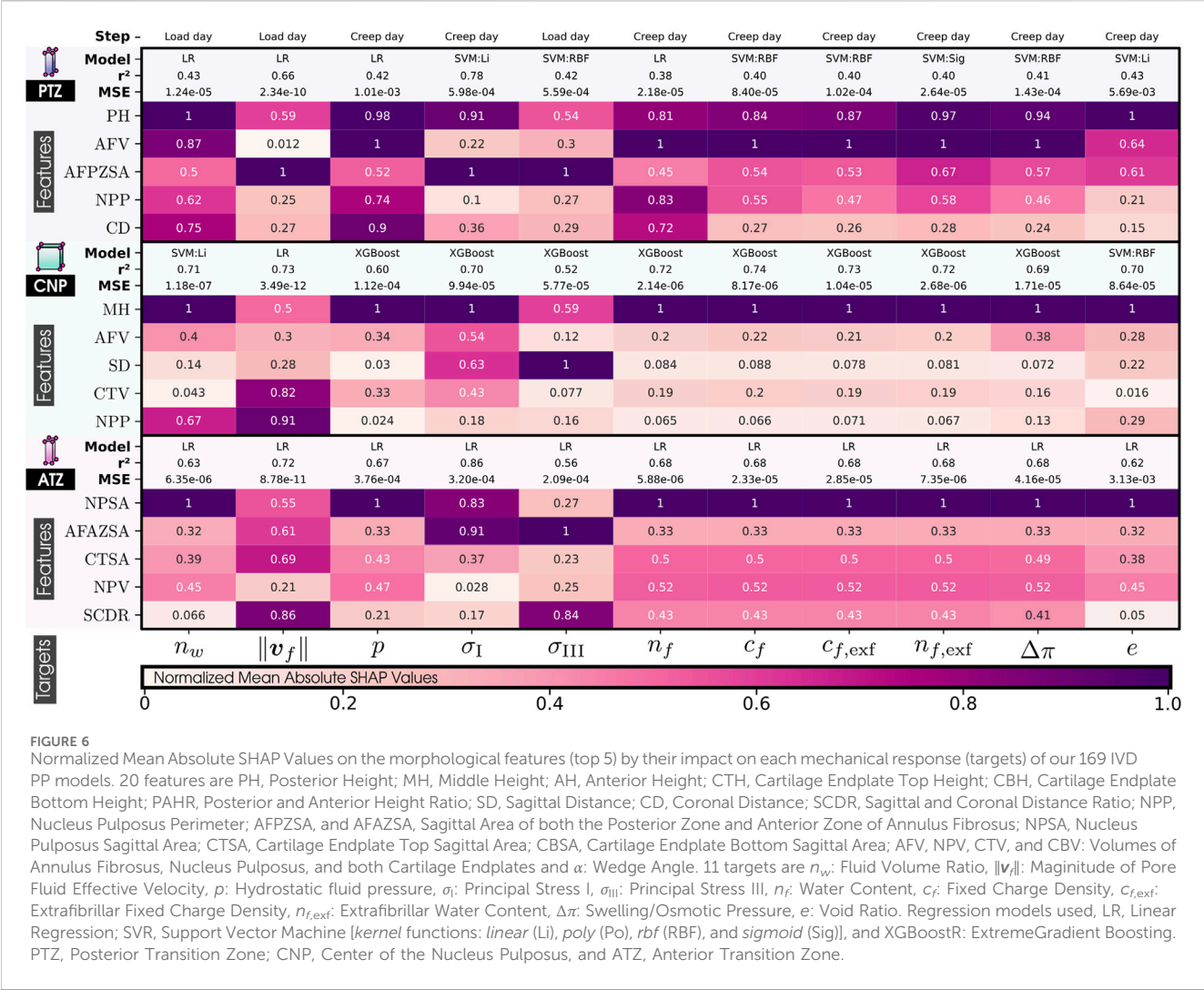
The analysis of Figures 6, 7 indicates that MH is a pivotal morphological feature influencing the trained model of the mechanical behavior across the nucleus and cartilaginous regions

TABLE 8 Summary of Mechanical Variables from the Cohort of 169 Morphed IVDs: Detailing Minimum (MIN), Maximum (MAX) Values, the Simulation Range of Variation (SR), and the Simulation Variation Percentage (SV%) for mechanical response.

Posterior transition zone (PTZ)	n_w %	$\ v_f\ $ mm/s	p MPa	σ_I MPa	σ_{III} MPa	n_f %	c_f mEq/mL	$c_{f,exf}$ mEq/mL	$n_{f,exf}$ %	$\Delta\pi$ MPa	e %
MIN	7.71e-01	1.63e-05	2.24e-01	-3.28e-01	-3.22e-01	7.66e-01	3.10e-01	3.28e-01	7.19e-01	-2.84e-01	3.36e+00
MAX	7.96e-01	1.58e-04	4.47e-01	-7.01e-02	-1.88e-01	7.97e-01	3.71e-01	3.95e-01	7.53e-01	-2.04e-01	3.89e+00
SR	2.48e-02	1.42e-04	2.22e-01	2.58e-01	1.33e-01	3.04e-02	6.06e-02	6.69e-02	3.41e-02	8.04e-02	5.30e-01
SV%	3.22%	868.58%	99.25%	368.20%	70.73%	3.97%	19.54%	20.42%	4.74%	39.51%	15.76%
Center of nucleus pulposus (CNP)	n_w %	$\ v_f\ $ mm/s	p MPa	σ_I MPa	σ_{III} MPa	n_f %	c_f mEq/mL	$c_{f,exf}$ mEq/mL	$n_{f,exf}$ %	$\Delta\pi$ MPa	e %
MIN	8.03e-01	4.65e-06	3.40e-01	-3.18e-01	-2.44e-01	7.61e-01	3.41e-01	3.62e-01	7.14e-01	-2.99e-01	4.09e+00
MAX	8.08e-01	2.94e-05	4.71e-01	-2.37e-01	-1.78e-01	7.81e-01	3.81e-01	4.07e-01	7.36e-01	-2.44e-01	4.21e+00
SR	4.68e-03	2.47e-05	1.31e-01	8.09e-02	6.60e-02	1.98e-02	4.04e-02	4.48e-02	2.20e-02	5.45e-02	1.24e-01
SV%	0.58%	531.10%	38.46%	34.15%	37.02%	2.60%	11.84%	12.38%	3.09%	22.33%	3.04%
Anterior transition zone (ATZ)	n_w %	$\ v_f\ $ mm/s	p MPa	σ_I MPa	σ_{III} MPa	n_f %	c_f mEq/mL	$c_{f,exf}$ mEq/mL	$n_{f,exf}$ %	$\Delta\pi$ MPa	e %
MIN	7.76e-01	1.20e-05	2.21e-01	-3.22e-01	-2.77e-01	7.68e-01	3.17e-01	3.36e-01	7.21e-01	-2.78e-01	3.46e+00
MAX	7.98e-01	9.85e-05	4.10e-01	-8.11e-02	-1.79e-01	7.93e-01	3.67e-01	3.91e-01	7.49e-01	-2.12e-01	3.95e+00
SR	2.21e-02	8.65e-05	1.89e-01	2.41e-01	9.85e-02	2.48e-02	4.95e-02	5.47e-02	2.77e-02	6.66e-02	4.89e-01
SV%	2.85%	719.72%	85.50%	296.94%	55.11%	3.23%	15.60%	16.29%	3.84%	31.48%	14.11%
Cartilage endplate top (CT)	n_w %	$\ v_f\ $ mm/s	p MPa	σ_I MPa	σ_{III} MPa	n_f %	c_f mEq/mL	$c_{f,exf}$ mEq/mL	$n_{f,exf}$ %	$\Delta\pi$ MPa	e %
MIN	5.91e-01	5.60e-03	3.12e-01	-3.01e-01	-6.23e-01	6.14e-01	1.95e-01	2.59e-01	4.51e-01	-1.89e-01	1.58e+00
MAX	6.04e-01	2.18e-02	4.13e-01	-2.35e-01	-4.57e-01	6.37e-01	2.14e-01	2.92e-01	4.78e-01	-1.57e-01	1.66e+00
SR	1.25e-02	1.62e-02	1.01e-01	6.64e-02	1.66e-01	2.21e-02	1.93e-02	3.23e-02	2.71e-02	3.15e-02	8.11e-02
SV%	2.12%	289.31%	32.34%	28.25%	36.33%	3.60%	9.90%	12.46%	6.01%	20.05%	5.15%
Cartilage endplate bottom (BT)	n_w %	$\ v_f\ $ mm/s	p MPa	σ_I MPa	σ_{III} MPa	n_f %	c_f mEq/mL	$c_{f,exf}$ mEq/mL	$n_{f,exf}$ %	$\Delta\pi$ MPa	e %
MIN	5.87e-01	4.54e-03	3.19e-01	-3.19e-01	-7.18e-01	6.07e-01	1.97e-01	2.62e-01	4.42e-01	-2.01e-01	1.55e+00
MAX	6.06e-01	1.81e-02	4.58e-01	-9.80e-02	-4.74e-01	6.34e-01	2.21e-01	3.03e-01	4.75e-01	-1.60e-01	1.67e+00
SR	1.90e-02	1.36e-02	1.39e-01	2.21e-01	2.44e-01	2.74e-02	2.43e-02	4.10e-02	3.32e-02	4.12e-02	1.23e-01
SV%	3.24%	298.47%	43.49%	225.60%	51.50%	4.51%	12.36%	15.62%	7.52%	25.75%	7.97%

The SV% values are highlighted to indicate their ranges:

< 10%	10-30%	30-50%	50-100%	> 100%
-------	--------	--------	---------	--------



(CNP, TC, and BC). Overall, this result highlights a strong correlation between the axial dimension of the disc and the regional biomechanical responses calculated across the organ. Notably, within the nucleus, MH's influence was so significant that it diminished the relative importance of other morphological factors.

In the posterior zone (Figure 6), the local height, PH, and the posterior sagittal area, AFPZSA, emerged as the most influential features, pointing out the importance of local disc morphology in controlling the mechanical response of the respective region. The overall volume of the AF, AFV, is also a determinant factor in this zone.

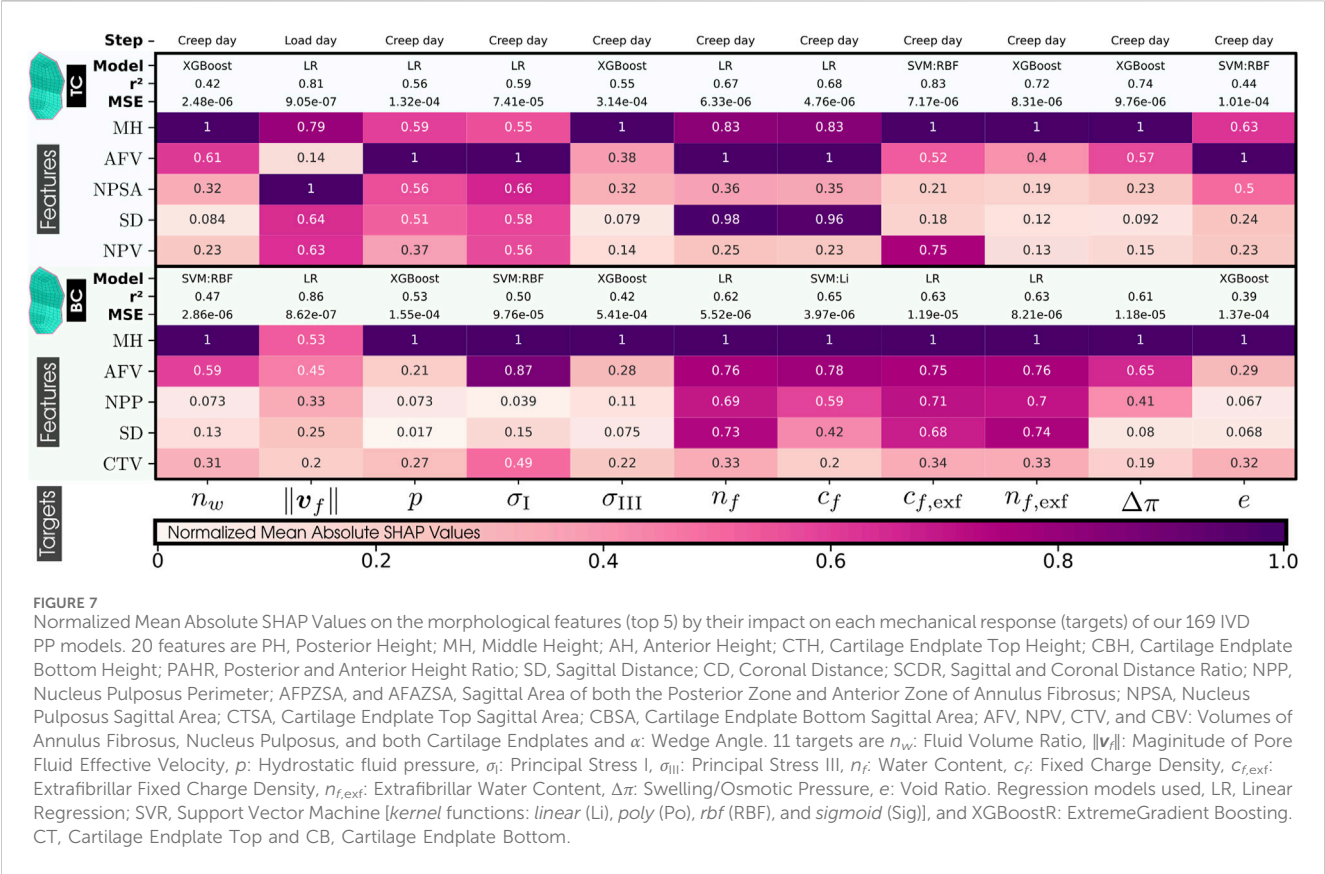
In contrast, the ATZ (Figure 6) is predominantly influenced by the nearest sagittal areas, including those of the anterior and nucleus regions (AFPZSA and NPSA). This suggests that the biomechanics of the ATZ is intricately connected to the IVD's anterior spatial arrangement, i.e., local morphological attributes. Interestingly, the ATZ's mechanics are less dependent on its own height compared to other regions like the CNP and PTZ.

Even though the cartilaginous regions (TC and BC) analysis reveals a nuanced relationship where the central disc height (Figure 7)—a parameter composed of the heights of both CEPs

and the nucleus—exerts a dominant influence, their own local morphology does not affect them. Instead, the mechanical dynamics are shaped by an intricate mix of morphologies beyond the immediate locality, including the sagittal area and perimeter of the nucleus (NPSA and NPP). Moreover, these zones also show sensitivity to the volume of the annulus (AFV), mirroring patterns observed in the PTZ and ATZ.

5.3.2.4 Influential morphological factors on the mechanical responses

Critical variables for nutrient transport (Figure 6), such as those that measure water quantities (Malandrino et al., 2011; Ruiz et al., 2016), charge densities, and pressures, are highly affected by local morphological factors, such as the MH in the CNP and the sagittal area of the nucleus in the ATZ. Both zones, thought to be critical in the early disc degeneration stages, depend on NP-related morphology. This pattern is similarly observed in the cartilaginous regions, where the disc's central height impacts indirect mechanotransduction variables. However, in the posterior region, they are predominantly affected by the PH, its associated sagittal area (AFPZSA), and the Annulus Fibrosus's volume (AFV).



Conversely, when it comes to stress-related mechanical variables such as the principal stresses, σ_I and σ_{III} , a divergence is observed in the influencing morphological factors. Within the nucleus, the maximum stress correlates mainly with the vertical dimension, MH, whereas the minimum stress is associated with the sagittal distance, SD. In the ATZ, maximum stress linkage is seen with the NP's and AF's sagittal areas (NPSA and AFAZSA). In contrast, the minimum stress is influenced solely by the sagittal area of the annulus (AFAZSA). For the posterior region, PTZ, something similar to the previous one is observed; the maximum stress is more about vertical morphologies, and the minimum stress is related to AF and SCDR.

Pore fluid velocity exhibits zone-specific dependencies. In the PTZ, it is primarily governed by its adjacent sagittal area, the AFPZSA. Within the nucleus, the perimeter of the nucleus and cartilage volume take precedence. For the ATZ, this variable is more sensitive to the sagittal-coronal distances ratio (SCDR), underscoring responsiveness to the disc's general shape or ellipticity. This attribute parallels the sensitivity of the minimum principal stress, σ_{III} .

Focusing on the CEP surfaces (Figure 7), both principal stresses are significantly conditioned by the MH. Notably, the maximum stress is additionally modulated by the volume of the Annulus Fibrosus, suggesting that both the height and the volumetric attributes of the IVD components collectively influence the mechanical stresses exerted within these regions.

5.3.2.5 Morphological impact in terms of mechanical variation magnitude

The top 5 PR% values (Eq. 22) were calculated for each mechanical variable by using the results of the morphing

(Table 6) for the values of the morphological features in the calculation of the PR values. They are represented in Figures 8, 9 for the targeted volumes (PTZ, CNP, ATZ) and surfaces (CEP: CT and CB), respectively. The 100% represents the SR value of each mechanical response (detailed in Table 8).

The magnitudes with the highest simulation variation percentage in their magnitude (SV%), the fluid velocity ($\|v_f\|$), was particularly sensitive to CEP morphologies (represented by the volumes CTV and CBV, and by the sagittal area CTSA), especially in the CNP and ATZ areas (Figure 8). The variability of another mechanical response with a high SV% is the maximum stress magnitude, which was mostly controlled by height-related measurements (PH, MH, and AH), while minimum stress (SV% > 50%) levels were influenced by AF dimensions and disc ellipticity (AFPZSA, SD, CD, SCDR). The rest of the mechanical magnitudes changed when the corresponding local morphologies varied, i.e., the CNP by the mid-height (MH) and the PTZ by the posterior height (PH). Remarkably, though, the magnitudes of the mechanical variables in the ATZ were first most affected by the sagittal area of the NP (NPSA) and then by its corresponding local IVD morphology, the anterior disc height (AH). The magnitudes of the mechanical variables in the CEP (Figure 9) were predominantly affected by AF and NP morphologies (mid-height, MH; AF volume, AFV; sagittal area and volume of the NP, NPV, and NPSA) and not by their own morphologies.

In the nucleus center (CNP), the hydrostatic pressure (p), the stresses (σ_I and σ_{III}), the water contents (n_f and $n_{f,exf}$), the fixed charge densities (c_f and $c_{f,exf}$), and the osmotic pressure ($\Delta\pi$)

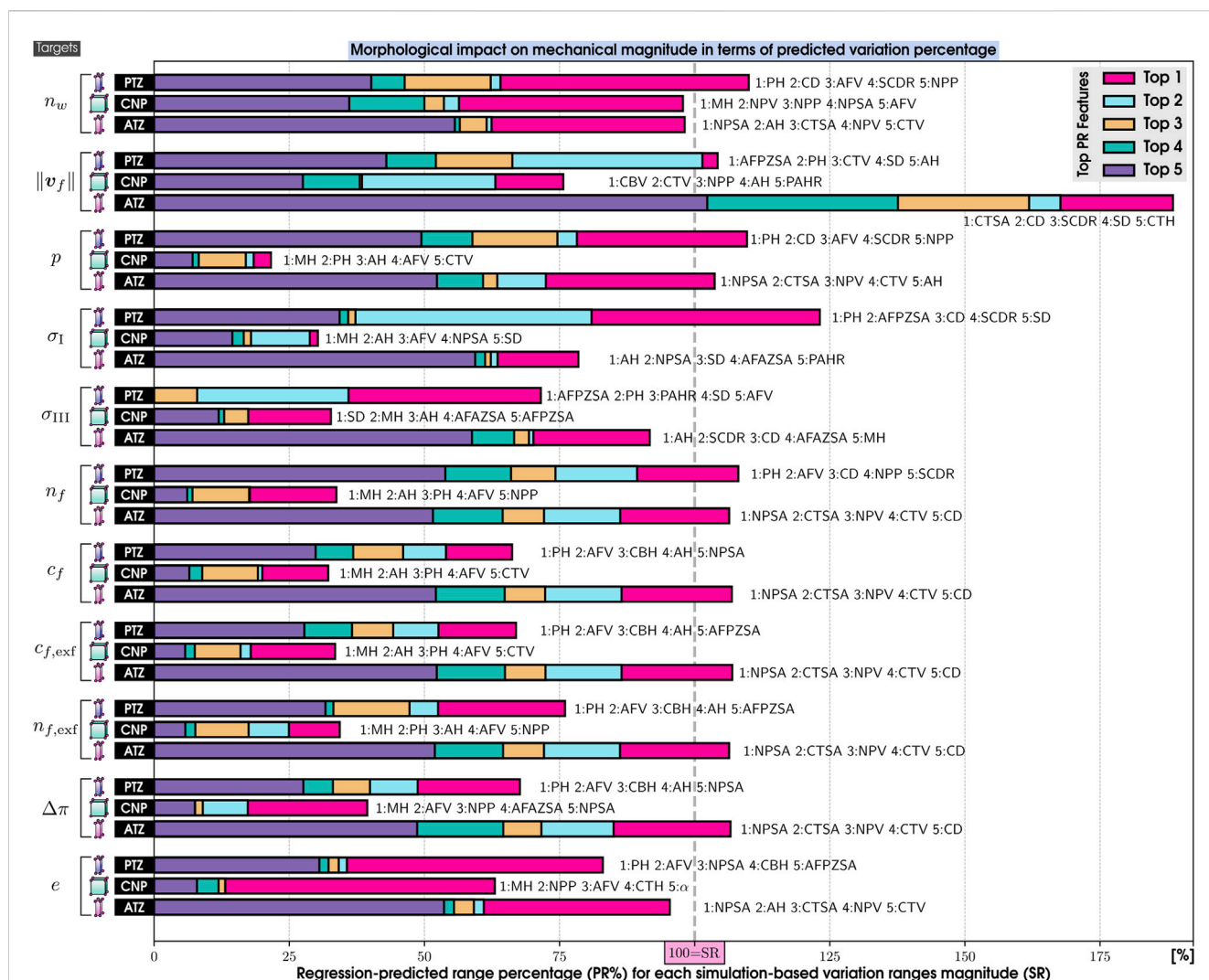


FIGURE 8

Overlapping bar chart, with the top 5 Morphological impacts (top 1 at the base and top 5 at the peak) on mechanical magnitudes (targets) in terms of predicted variation percentage (PR%) of our 169 IVD PP models. PR%, Regression-predicted range percentage; SR, Simulation-based variation ranges magnitude. The 20 features are PH, Posterior Height; MH, Middle Height; AH, Anterior Height; CTH, Cartilage Endplate Top Height; CBH, Cartilage Endplate Bottom Height; PAHR, Posterior and Anterior Height Ratio; SD, Sagittal Distance; SCDR, Sagittal and Coronal Distance Ratio; NPP, Nucleus Pulposus Perimeter; AFPZSA, and AFAZSA, Sagittal Area of both the Posterior Zone and Anterior Zone of Annulus Fibrosus; NPSA, Nucleus Pulposus Sagittal Area; CTSA, Cartilage Endplate Top Sagittal Area; CBSA, Cartilage Endplate Bottom Sagittal Area; AFV, NPV, CTV, and CBV: Volumes of Annulus Fibrosus, Nucleus Pulposus, and both Cartilage Endplates and α : Wedge Angle. 11 targets are n_w : Fluid Volume Ratio, $\|v_f\|$: Magnitude of Pore Fluid Effective Velocity, p : Hydrostatic fluid pressure, σ_I : Principal Stress I, σ_{III} : Principal Stress III, n_f : Water Content, c_f : Fixed Charge Density, $c_{f,exf}$: Extrafibrillar Fixed Charge Density, $n_{f,exf}$: Extrafibrillar Water Content, $\Delta\pi$: Swelling/Osmotic Pressure, e : Void Ratio. PTZ, Posterior Transition Zone; CNP, Center of the Nucleus Pulposus, and ATZ, Anterior Transition Zone.

magnitude variation had low PR%, below of 50%. Surprisingly, the principal stress magnitudes (σ_I and σ_{III}) in the CNP could not be affected by more than 30% of the SR by individual morphological features. This is also consistent with the low SV%, so the magnitude does not vary as much as in the PTZ and ATZ.

The SHAP values, detailed in the Bee Swarm Plot (Figure 10A), indicated how strongly a morphological feature variation increased or decreased the magnitude of the stress in each region of interest. The stress graphs show that the regression-predicted variations in stress magnitude in the CNP (PR = e-02) were one order of magnitude lower than those in the

PTZ and ATZ (PR = e-01) regions. However, the non-linearity observed in the CNP for both stresses and in the PTZ for the minimum stress shows that the minimum and maximum magnitudes do not necessarily correspond to the minimum and maximum values of the specific evaluated morphology. In the CNP, the cumulative impact of all morphological features on both stress variations (Figure 10B) had to be considered to reach or exceed 100% of the SR.

For further insight into the interplay between morphology and mechanical magnitude across all five zones of interest (PTZ, CNP, CT, and CB), please refer to the (Supplementary Figures S6 through S10).

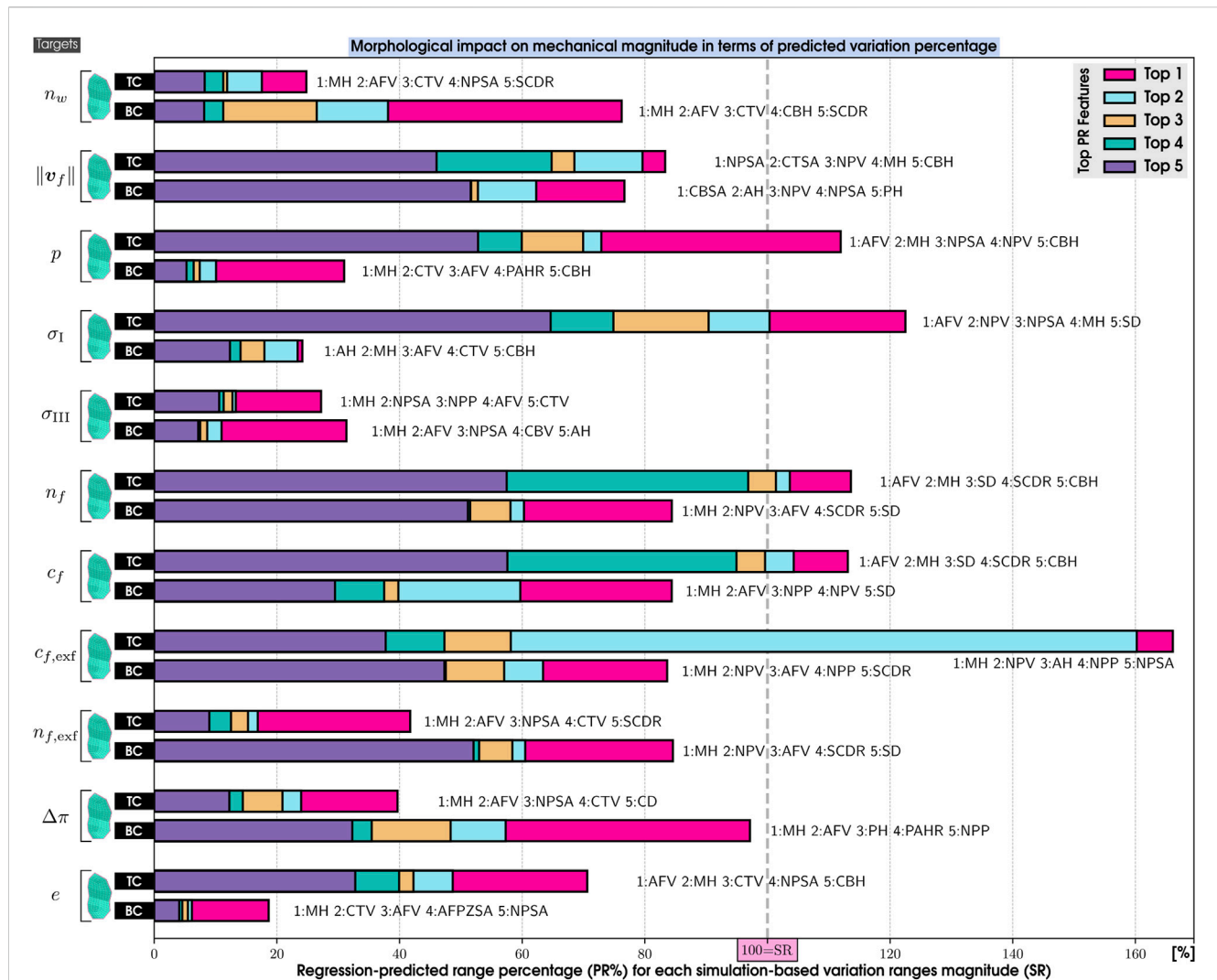


FIGURE 9
Overlapping bar chart, with the top 5 Morphological impacts (top 1 at the base and top 5 at the peak) on mechanical magnitudes (targets) in terms of predicted variation percentage (PR%) of our 169 IVD PP models. PR%, Regression-predicted range percentage; SR, Simulation-based variation ranges magnitude. The 20 features are PH, Posterior Height; MH, Middle Height; AH, Anterior Height; CTH, Cartilage Endplate Top Height; CBH, Cartilage Endplate Bottom Height; PAHR, Posterior and Anterior Height Ratio; SD, Sagittal Distance; CD, Coronal Distance; SCDR, Sagittal and Coronal Distance Ratio; NPP, Nucleus Pulposus Perimeter; AFPZSA, and AFAZSA, Sagittal Area of both the Posterior Zone and Anterior Zone of Annulus Fibrosus; NPSA, Nucleus Pulposus Sagittal Area; CTSA, Cartilage Endplate Top Sagittal Area; CBSA, Cartilage Endplate Bottom Sagittal Area; AFV, NPV, CTV, and CBV: Volumes of Annulus Fibrosus, Nucleus Pulposus, and both Cartilage Endplates and α : Wedge Angle. 11 targets are n_w : Fluid Volume Ratio, $\|v_f\|$: Magnitude of Pore Fluid Effective Velocity, p : Hydrostatic fluid pressure, σ_I : Principal Stress I, σ_{III} : Principal Stress III, n_f : Water Content, c_f : Fixed Charge Density, $c_{f,exf}$: Extrafibrillar Fixed Charge Density, $n_{f,exf}$: Extrafibrillar Water Content, $\Delta\pi$: Swelling/Osmotic Pressure, e : Void Ratio. CT, Cartilage Endplate Top and CB, Cartilage Endplate Bottom.

6 Discussion

6.1 Morphing process, accuracy, and validation

Our morphing process successfully produced 169 PP IVD models, with the mesh quality remaining consistent with the generic FE mesh model, even if minor increases in out-of-range elements occurred. Notably, the increase in aspect ratio criterion and small and large angles did not affect the convergence or the simulations, demonstrating the overall quality of the generated mesh and the ability of the algorithm to restrict the excessive growth of hexahedral edges. Precise deformation control was

reflected by the similarity scores for AF and NP, which were 92.06% and 92.10%, respectively (Figure 4B). The BCPD++ algorithm maintained the relative distances and positions between FE mesh nodes, which prevented any single edge of a hexahedral element from growing disproportionately, achieving a patient-personalized FE model of the IVD efficiently, based on segmented medical images, with full respect to important tissue-specific mesh structures (Ruiz et al., 2013). Arguably, this approach does not allow the modeling of structural tissue damage, such as fissures or annular tears. Yet, the effect of these damages can be captured with proper homogenized continuum models and parameters, as proposed by Malandrino et al. (2015b).

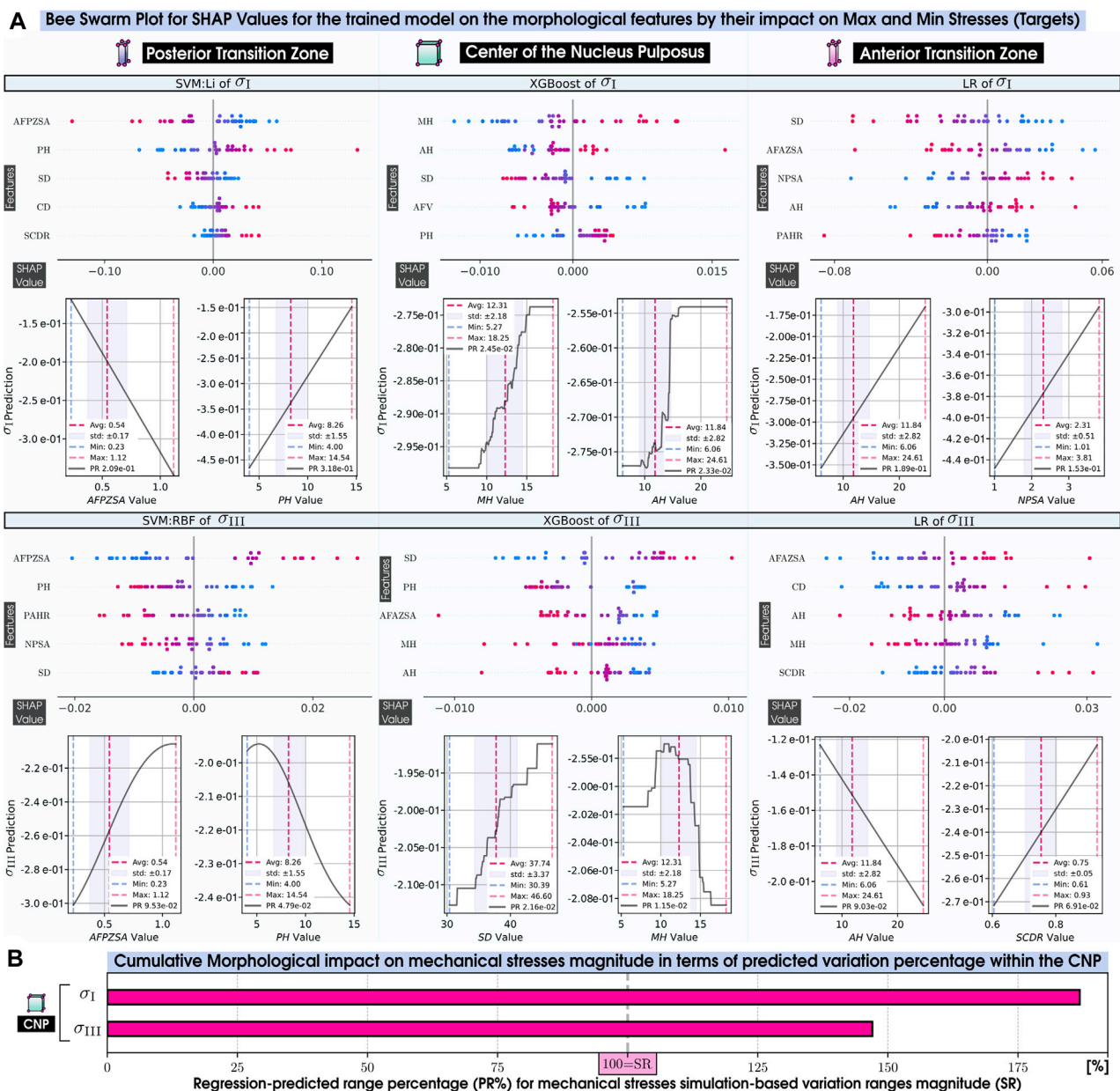


FIGURE 10 Morphological impact on mechanical stresses. **(A)** Bee Swarm Plot for SHAP Values for the trained model on the morphological features by their impact on Max and Min Stresses (Targets). **(B)** Cumulative morphological impact of the 20 features on the mechanical stresses within the CNP. PR, Regression-predicted variation ranges magnitude; SR, Simulation-based variation ranges magnitude. PTZ, Posterior Transition Zone; CNP, Center of the Nucleus Pulposus; and ATZ, Anterior Transition Zone. The description of the morphological features can be found in Table 3.

As mentioned in Section 4.2, most of the research related to morphology and degeneration focuses on the diversity of disc heights. For instance, mid-height (MH) discs ranging from 5 to 16 mm have been used to determine relationships between IDD and MH (Teichtahl et al., 2015). In the present study, we examined the MH, which ranged from 5 to 18 mm. Other studies have correlated the three heights of the IVD with lumbar disc herniation (Kizilgöz and Ulusoy, 2019), with corresponding values of posterior, middle, and anterior as PH: 2–13 mm, MH: 3–15 mm, and AH: 3–18 mm, respectively. Our cohort includes discs with values of PH: 4–14 mm, MH: 5–18 mm, and AH: 6–24 mm,

thus representing a diverse array of shapes that cover an extensive range of morphologies in healthy and degenerated discs. This further validates the method's capability to preserve vital geometric characteristics.

The average CEP height at the center of the disc for the top (CTH) and bottom (CBH) zones measured 0.534 ± 0.148 mm and 0.493 ± 0.151 mm, respectively. These averages align with the findings by Moon et al. (2013) of 0.54 ± 0.12 mm, showcasing the robustness of our modeling approach. Additionally, the range of values captured includes minimum and maximum measurements corresponding to the variation expected in discs exhibiting advanced

degeneration, reflecting the diversity of IVD conditions in the population.

The importance of our pipeline and methodology becomes particularly evident when compared to other techniques, such as the one proposed by Fleps et al. (2024), which also used segmented medical images to achieve personalized IVD model geometries. However, these only captured the outer surface of the AF, neglecting to personalize the Nucleus Pulposus individually. Our findings highlight the critical role of the NP in influencing indirect mechanotransduction responses. Specifically, parameters crucial for nutrient transport, including charge densities, water content, and osmotic pressure (represented by c_f , n_f , $c_{f,ext}$, $n_{f,ext}$, and $\Delta\pi$), as mentioned in Section 4, especially in the posterior and anterior zone (PH and AH) and both cartilaginous regions, top and bottom (TC and BC), cannot be accurately replicated with the same level of personalized precision using such external-surface-focused techniques. Furthermore, our morphing technique has been uniquely tested on a significantly larger sample of IVD morphologies [$n = 169$ vs. $n = 22$ in Fleps et al. (2024)].

One of the primary challenges we faced in this study was the inability to replicate the morphology of the CEP due to the inherent limitation of MRI scans in delineating the external surface of this thin tissue. To overcome this obstacle, we implemented a model customization strategy. Specifically, we adjusted the dimensions of the CEP to fill the volume between the NP's cranial and caudal surfaces and the external AF. This adaptation involves manipulating the λ variable in the third step of our morphing process, as explained in Section 2.2. Since the AF/IVD and the NP external surface are directly provided by image segmentations, a certain level of personalization of the CEP is uniquely achieved for each set of segmented disc tissue surfaces, although direct verification or validation of the FE CEP morphology was not possible. Remarkably, the algorithm allows the parameterization of the CEP thickness, in that case, adjusting the cranial and caudal external surfaces of the NP coherently. Though this feature was not used in the current study, it paves the way to systematically explore the relative importance of the CEP through models and simulations. Such explorations might support simulation-based identifications of advanced early image biomarkers associated with the risk of IDD or targeting of CEP engineering-based new regenerative strategies.

Another limitation of our study pertains to the NP-AF boundary transition zone (TZ), which, despite its relevance introduced in the Methods and noted by Ruiz et al. (2013), is difficult to define precisely in terms of material properties and size. Yet, the delineation of this region enhances the realism of the IVD model by providing a gradual material property transition from the NP to the AF, as opposed to an abrupt shift, as suggested by measurements of gradual shifts in cell phenotypes (Bruehlmann et al., 2002), MRI signal (Kapoor et al., 2023), and fiber structure (Disney et al., 2023). Arguably, this region's local properties and exact size are difficult to assess. Even so, the TZ is physically interesting, as it represents a singular volume of increased radial compression at the periphery of the inner IVD, where the NP material is pressed against the confining annulus material because of the lateral expansion of the nucleus under external mechanical loads. This mechanism potentially influences the transport of

nutrients to the cells in the TZ, as suggested by FE models and simulations (Ruiz et al., 2016; Ruiz et al., 2018). Such regional particular tissue physics coincides with the reported local emergence of relatively early signs of tissue disorganization in IVD (Leung et al., 2006; Smith et al., 2011). Moreover, the used segmentations, refined through image fusion (Castro-Mateos et al., 2014), may not have fully captured the shape of the complex NP-AF boundary, even with an improved resolution of 0.68 mm isotropic voxels. Acknowledging this limitation might be crucial to accurately represent this intricate boundary in future models, though some segmentations did represent inward bulging of the AF in degenerated discs¹.

Additionally, it is essential to recognize our models' limitations related to the IVD-vertebrae interface. Arguably, the detailed mechanics of the BEP-CEP system cannot be fully captured with the current meshes, as these do not include full vertebrae.

Finally, the validation of the simulations against the research by Malandrino et al. (2015b), with a relative error of just 5.20%, demonstrated the ability to capture the real morphology with the morphing process, and the osmo-poro-hyper-viscoelastic model (referenced in Section 2.3) and the mechanical and tissue properties (listed in Table 1) in representing the time-dependent behavior of a healthy IVD under compression, as simulated hereby to represent average load cycles of daily life.

6.2 Mechanical simulations of daily loads

The mechanical simulation results stabilized by the second day. Examination of fixed charge densities and water content ($c_{f,0}$ and n_f) across the morphed PP models confirmed that second-day equilibrium was achieved regardless of the particularities of the modeled morphologies. This verification of the consistency of model initialization was crucial to comparatively analyze the mechanical behaviors of the different disc models after the simulated swelling when reaching the $c_{f,0}$ and $n_{f,0}$ proposed values in Table 1.

The analysis revealed that the post-swelling Similarity Scores of the models with mid heights ranging from 8 to 17 mm remained relatively stable, as detailed in Table 7. This stability suggests that despite its potential to modify the morphed shape, the swelling process does not significantly impact the geometry. This resilience in shape demonstrates the simulations' effectiveness in capturing the true geometry of the IVD for both the AF and NP throughout the present PP modeling process.

A key finding of this research was the correlation between the mechanical responses within specific local volumes in the IVD (Posterior Transition Zone—PTZ, Center of the Nucleus Pulposus—CNP, and Anterior Transition Zone—ATZ) and the corresponding local morphological characteristics of the disc. Overall, results suggested that local disc shapes preponderantly

¹ e.g., https://ivd.spineview.upf.edu/?filenamePrefix=MY0004_L1L2, https://ivd.spineview.upf.edu/?filenamePrefix=MY0073_L4L5

altered local disc mechanics and shall be considered in personalized modeling. The mechanical variables in the CEP were significantly influenced by the middle height (MH) and the AF and NP volumes (AFV and NPV), except the fluid velocity ($\|\mathbf{v}_f\|$) that depended more on the CEP sagittal areas (CTSA and CBSA). This demonstrates the impact of the morphology of specific disc regions on biomechanical variables in other regions, probably caused by particular volume distributions, i.e., the mechanical variables in the reduced volume of the CEP are impacted by the deformation of larger volumes from other regions. Likewise, the ATZ, a region reported to be affected (Section 4.1) already in early stages of IDD (Leung et al., 2006; Smith et al., 2011), was more influenced by adjacent morphological features, such as the NP and CEP sagittal areas (NPSA and CTSA) than by its own height.

The local mechanical variables reported to impact indirect mechanotransduction phenomena, possibly involved in early IDD (see Section 4.3), are highly influenced by the corresponding local morphology. Such outcome suggests that indirect mechanotransduction is affected by disc height and local morphological factors in each evaluated zone, as we explain above. Meanwhile, maximum and minimum principal stresses (σ_I and σ_{III}) are respectively impacted by different morphological features. On one hand, the MH, PH, and the nucleus sagittal area (NPSA) predominantly affected the maximum principal stress, σ_I . On the other hand, the minimum principal stress, σ_{III} , was more influenced by ellipticity-related variables (ellipticity, SCDR, and sagittal distance, SD) and the posterior and anterior Annulus Fibrosus sagittal areas (AFPZSA and AFAZSA). These insights suggest that in-depth evaluations of IDD require a nuanced analysis that considers local morphological features. Specifically, the assessment of tensile stresses demands a detailed consideration of local axial morphologies, and the compressive stresses call for an exploration of horizontal dimensions related to the ellipticity of the disc to fully understand the mechanical interplays that might contribute to IDD.

In General, the PR% for the volumes and surfaces (Figures 8, 9) captured less than 100% of the SR, indicating that regression-based ranges were included within the simulation-based-ranges. However, in the ATZ, the velocity was particularly sensitive to the cartilage sagittal area (CTSA) and to the ellipticity of the disc (SD, CD, SCDR), so much that every top 5 features exceeded 100% of the SR. This emphasizes the importance of the cartilage endplate in critical areas in the early stages of IDD, such as the anterior zone of the IVD.

Additionally, our influential morphology results (Figure 6) align with prior experimental findings that emphasize the central role of the mid-height (MH), influencing the center of the nucleus (CNP) behaviors (Teichtahl et al., 2015; Kizilgöz and Ulusoy, 2019). However, our analysis suggests that the influence is not necessarily reflected in the magnitude of the mechanical response. The MH highly influences the behavior of the CNP, but the magnitude (Figure 8) of the hydrostatic pressure, stresses, water contents, charged densities, and the osmotic pressure do not exceed 50% magnitude variation. Nevertheless, the cumulative impact of all morphological features on both stress variations (Figure 10B) exceeded 100%, implying the necessity for a holistic morphological approach to understanding CNP mechanics.

These calculations reveal the challenge of isolating a single morphological factor as a single leading controller of the mechanical response of the disc. First, we point out possible non-linear relationships between morphology and mechanics. For example, while mid-height (MH) may be a predominant factor, its increase does not necessarily correlate linearly with the disc mechanical behavior (Figure 10A). Second, the influence of morphology is not defined by a single factor (as observed in Figures 6, 7); adjacent morphologies can significantly alter the expected mechanical outcomes by their influence and magnitudes (Figures 8, 9), thereby complicating the ability to attribute mechanical behavior to a singular morphological aspect. This complexity accentuates the need for a comprehensive customization approach of the IVD 3D morphology, including the AF and the NP, in FE simulations for achieving more accurate and realistic simulations.

Some of our morphological features, while typically not assessed in radiographic evaluations, influenced significantly the predicted internal biomechanics of the IVD and could serve, thus, as novel and potentially crucial image-based biomarkers in a clinical context. For instance, the sagittal areas of the annulus and nucleus (AFPZSA, AFAZSA, and NPSA) are readily identifiable on MRIs. Other features, such as the volumes of the annulus, nucleus, and CEPs (AFV, NPV, and CTV and CBV), as well as the nucleus pulposus perimeter (NPP), can be quantified through 3D segmentation (refer to Figure 3 for morphological factors). Current progress in medical image analysis and processing let us envision the forthcoming availability of automated tool capable of generating 3D lumbar spine models from 2D images, e.g., as proposed for osteoporosis assessments (Lopez Picazo et al., 2018).

Although the present study uniquely revealed the intricate interactions among intervertebral disc morphology and internal biomechanics, it has some limitations. Our boundary conditions represent a normal subject with diverse physiological physical activity during the day and lying at night, as reflected by *in vivo* measurements of intradiscal pressures (Wilke et al., 1999). Although this should be studied following a person's typical activities, the current approach serves as a standard loading scheme to evaluate a large number of PP models. Since the objective was to focus only on morphology, material properties specific to each degree of degeneration have not been considered. This limitation shall be addressed in future studies, in particular, seizing the opportunity to incorporate Pfirrmann grade-specific material properties (Malandrino et al., 2015b; Barthelemy et al., 2016; Ruiz et al., 2016). Performing morphing for both the AF and NP was challenging due to its difficulty. However, we have achieved it with acceptable levels of similarity to the real model without damaging the mesh, becoming one of the strengths of our work.

The tensile and the compressive stresses are, respectively, the maximum and the minimum principal stresses, which are the local eigenvalues of the stress tensor. Yet, we disregard the analysis of the orientations of these eigenvectors because regardless of the latter, the stress is, indeed, suffered by the materials. Looking at the local orientations of the eigenvectors would be interesting to analyze for future work.

Although the generated IVD files (.inp) are ABAQUS files, these are in ASCII format and can be converted so that models can be reused with alternative open-source software suites, such as FEBio (Maas et al., 2012), MoFEM (Kaczmarczyk et al., 2020), High-Performance Computing (HPC), among others.

7 Conclusion

This work provides the first FE model database to study IDD and thoroughly analyzes the intricate relationships between the morphological characteristics of the IVD and its indirect mechanotransduction behavior, employing sophisticated simulation, machine learning techniques, and the BCPD ++ algorithm. The generation and morphing of 169 IVD models revealed remarkable accuracy and adaptability in aligning the generic FE mesh model with MRI-derived PP models without compromising the mesh's element integrity or the quality of their complicated and varied morphology.

The validation, which yielded acceptable relative errors, underscores the effectiveness and fidelity of our PP modeling approach to replicate healthy IVD behavior under compression. To the best of our knowledge, our comprehensive dataset of 169 simulations of PP FEM of the IVD is unique, as are our collection of mechanical results and data mining analyses. These offer the most detailed insights into data about how local morphologies intricately influence mechanical responses in specific zones of the IVD, including the ones that might be relevant in early IDD. Thanks to the current modeling pipeline, this cohort could be augmented to achieve even more precise results. These insights shall not only enrich our understanding of IVDs' structural and functional behavior but shall also have significant implications for future research and simulation-based early prevention, diagnostics, and therapeutic interventions for IDD.

This study led to an open-access repository (Muñoz-Moya et al., 2023) -accessible through our online user interface (<https://ivd.spineview.upf.edu/>). We hope that our research can contribute to standardizing methods for promoting translational IVD and IDD research through *in silico* methods that can be coupled with medical data. This initiative aims to provide a strong foundation for innovation in IVD research, paving the way for further investigations into the multifaceted nature of IVD mechanics, with potential implications for IDD diagnosis, treatment, and prevention strategies.

Data availability statement

The generated/analyzed datasets of 169 IVD PS FE models can be found for free use at the open repository Zenodo Muñoz-Moya et al., 2023, accessible through our online user interface: <https://zenodo.org/records/8325042>.

Ethics statement

The studies involving humans were approved by the MySpine 2010 MySpine patient-specific spinal treatment simulation. The studies were conducted in accordance with the local legislation and institutional requirements. Written informed consent for

participation was not required from the participants or the participants' legal guardians/next of kin in accordance with the national legislation and institutional requirements.

Author contributions

EM-M: Conceptualization, Data curation, Formal Analysis, Investigation, Methodology, Software, Validation, Visualization, Writing—original draft, Writing—review and editing. MR: Investigation, Methodology, Software, Writing—review and editing. CR: Conceptualization, Investigation, Methodology, Software, Writing—review and editing. FC: Visualization, Writing—review and editing. GP: Conceptualization, Formal Analysis, Methodology, Software, Supervision, Writing—review and editing. JN: Conceptualization, Data curation, Formal Analysis, Funding acquisition, Investigation, Methodology, Project administration, Resources, Software, Supervision, Visualization, Writing—review and editing.

Funding

The author(s) declare that financial support was received for the research, authorship, and/or publication of this article. This project has received funding from the European Union's Horizon 2020 research and innovation program under the Marie Skłodowska-Curie grant agreement (Grant No. MSCA- 2020-ITN-ETN GA: 955735) and the European Research Council (ERC-2021-CoG-O-Health-101044828). GP is supported by ICREA under the ICREA Acadèmia programme.

Conflict of interest

Author FC was employed by company InSilicoTrials Technologies.

The remaining authors declare that the research was conducted in the absence of any commercial or financial relationships that could be construed as a potential conflict of interest.

The author(s) declared that they were an editorial board member of Frontiers, at the time of submission. This had no impact on the peer review process and the final decision.

Publisher's note

All claims expressed in this article are solely those of the authors and do not necessarily represent those of their affiliated organizations, or those of the publisher, the editors and the reviewers. Any product that may be evaluated in this article, or claim that may be made by its manufacturer, is not guaranteed or endorsed by the publisher.

Supplementary material

The Supplementary Material for this article can be found online at: <https://www.frontiersin.org/articles/10.3389/fbioe.2024.1384599/full#supplementary-material>

References

- Accadbled, F., Laffosse, J.-M., Ambard, D., Gomez-Bouchet, A., de Gauzy, J. S., and Swider, P. (2008). Influence of location, fluid flow direction, and tissue maturity on the macroscopic permeability of vertebral end plates. *Spine* 33, 612–619. doi:10.1097/brs.0b013e318166e0d7
- Adams, M., and Hutton, W. (1983). The effect of posture on the fluid content of lumbar intervertebral discs. *Spine* 8, 665–671. doi:10.1097/00007632-198309000-00013
- Adams, M. A., and Roughley, P. J. (2006). What is intervertebral disc degeneration, and what causes it? *Spine* 31, 2151–2161. doi:10.1097/01.brs.0000231761.73859.2c
- Argoubi, M., and Shirazi-Adl, A. (1996). Poroelastic creep response analysis of a lumbar motion segment in compression. *J. Biomechanics* 29, 1331–1339. doi:10.1016/0021-9290(96)00035-8
- Bach, K., Ford, J., Foley, R., Januszewski, J., Murtagh, R., Decker, S., et al. (2019). Morphometric analysis of lumbar intervertebral disc height: an imaging study. *World Neurosurg.* 124, e106–e118. doi:10.1016/j.wneu.2018.12.014
- Barthelemy, V., van Rijsbergen, M., Wilson, W., Huyghe, J., van Rietbergen, B., and Ito, K. (2016). A computational spinal motion segment model incorporating a matrix composition-based model of the intervertebral disc. *J. Mech. Behav. Biomed. Mater.* 54, 194–204. doi:10.1016/j.jmbbm.2015.09.028
- Baumgartner, L., Wuertz-Kozak, K., Le Maitre, C. L., Wignall, F., Richardson, S. M., Hoyland, J., et al. (2021). Multiscale regulation of the intervertebral disc: achievements in experimental, *in silico*, and regenerative research. *Int. J. Mol. Sci.* 22, 703. doi:10.3390/ijms22020703
- Bermudez-Lekerika, P., Crump, K. B., Tseranidou, S., Nüesch, A., Kanelis, E., Alminnawi, A., et al. (2022). Immuno-modulatory effects of intervertebral disc cells. *Front. Cell Dev. Biol.* 10, 924692. doi:10.3389/fcell.2022.924692
- Bhattacharjee, M., and Ghosh, S. (2014). “Silk biomaterials for intervertebral disk (IVD) tissue engineering,” in *Silk biomaterials for tissue engineering and regenerative medicine (elsevier)*, 377–402. doi:10.1533/9780857097064.3.377
- Bonnheim, N. B., Wang, L., Lazar, A. A., Zhou, J., Chachad, R., Sollmann, N., et al. (2022). The contributions of cartilage endplate composition and vertebral bone marrow fat to intervertebral disc degeneration in patients with chronic low back pain. *Eur. Spine J.* 31, 1866–1872. doi:10.1007/s00586-022-07206-x
- Bruehlmann, S. B., Rattner, B., Matyas, R., and Duncan, N. A. (2002). Regional variations in the cellular matrix of the annulus fibrosus of the intervertebral disc. *J. Anat.* 201, 159–171. doi:10.1046/j.1469-7580.2002.00080.x
- Castro-Mateos, I., Pozo, J. M., Eltes, P. E., Rio, L. D., Lazary, A., and Frangi, A. F. (2014). 3d segmentation of annulus fibrosus and nucleus pulposus from t2-weighted magnetic resonance images. *Phys. Med. Biol.* 59, 7847–7864. doi:10.1088/0031-9155/59/24/7847
- De Geer, C. M. (2018). Intervertebral disk nutrients and transport mechanisms in relation to disk degeneration: a narrative literature review. *J. Chiropr. Med.* 17, 97–105. doi:10.1016/j.jcm.2017.11.006
- Disney, C., Vo, N., Bodey, A., Bay, B., and Lee, P. (2023). Image quality and scan time optimisation for *in situ* phase contrast x-ray tomography of the intervertebral disc. *J. Mech. Behav. Biomed. Mater.* 138, 105579. doi:10.1016/j.jmbbm.2022.105579
- Du, Y., Tavana, S., Rahman, T., Baxan, N., Hansen, U. N., and Newell, N. (2021). Sensitivity of intervertebral disc finite element models to internal geometric and non-geometric parameters. *Front. Bioeng. Biotechnol.* 9, 660013. doi:10.3389/fbioe.2021.660013
- Farndale, R., Buttle, D., and Barrett, A. (1986). Improved quantitation and discrimination of sulphated glycosaminoglycans by use of dimethylmethylene blue. *Biochimica Biophysica Acta (BBA) - General Subj.* 883, 173–177. doi:10.1016/0304-4165(86)90306-5
- Fleps, I., Newman, H. R., Elliott, D. M., and Morgan, E. F. (2024). Geometric determinants of the mechanical behavior of image-based finite element models of the intervertebral disc. *J. Orthop. Res.* 42, 1343–1355. doi:10.1002/jor.25788
- Galbusera, F., Schmidt, H., Noailly, J., Malandrino, A., Lacroix, D., Wilke, H.-J., et al. (2011). Comparison of four methods to simulate swelling in poroelastic finite element models of intervertebral discs. *J. Mech. Behav. Biomed. Mater.* 4, 1234–1241. doi:10.1016/j.jmbbm.2011.04.008
- Hashimoto, K., Aizawa, T., Kanno, H., and Itoi, E. (2018). Adjacent segment degeneration after fusion spinal surgery—a systematic review. *Int. Orthop.* 43, 987–993. doi:10.1007/s00264-018-4241-z
- Hassan, C. R., Lee, W., Komatsu, D. E., and Qin, Y.-X. (2020). Evaluation of nucleus pulposus fluid velocity and pressure alteration induced by cartilage endplate sclerosis using a poro-elastic finite element analysis. *Biomechanics Model. Mechanobiol.* 20, 281–291. doi:10.1007/s10237-020-01383-8
- Heuer, F., Schmitt, H., Schmidt, H., Claes, L., and Wilke, H.-J. (2007). Creep associated changes in intervertebral disc bulging obtained with a laser scanning device. *Clin. Biomech.* 22, 737–744. doi:10.1016/j.clinbiomech.2007.04.010
- Hirose, O. (2021a). Acceleration of non-rigid point set registration with downsampling and Gaussian process regression. *IEEE Trans. Pattern Analysis Mach. Intell.* 43, 2858–2865. doi:10.1109/TPAMI.2020.3043769
- Hirose, O. (2021b). A bayesian formulation of coherent point drift. *IEEE Trans. Pattern Analysis Mach. Intell.* 43, 2269–2286. doi:10.1109/TPAMI.2020.2971687
- Huszar, G., Maiooco, J., and Naftolin, F. (1980). Monitoring of collagen and collagen fragments in chromatography of protein mixtures. *Anal. Biochem.* 105, 424–429. doi:10.1016/0003-2697(80)90481-9
- Huyghe, J., and Janssen, J. (1997). Quadriphasic mechanics of swelling incompressible porous media. *Int. J. Eng. Sci.* 35, 793–802. doi:10.1016/s0020-7225(96)00119-x
- Huyghe, J. M., Houben, G. B., Drost, M. R., and van Donkelaar, C. C. (2003). An ionised/non-ionised dual porosity model of intervertebral disc tissue. *Biomechanics Model. Mechanobiol.* 2, 3–19. doi:10.1007/s10237-002-0023-y
- Kaczmarczyk, Ł., Ullah, Z., Lewandowski, K., Meng, X., Zhou, X.-Y., Athanasiadis, I., et al. (2020). Mofem: an open source, parallel finite element library. *J. Open Source Softw.* 5, 1441. doi:10.21105/joss.01441
- Kapoor, R., Rangankar, V. P., Kumar, D., Raina, S., Revikumar, A., and Mohanan, K. (2023). Apparent diffusion coefficient and t2* mapping on 3t mri in normal and degenerative lumbar intervertebral discs. *Pol. J. Radiology* 88, 275–285. doi:10.5114/pjr.2023.128882
- Kiani, C., Chen, L., Wu, Y. J., Yee, A. J., and Yang, B. B. (2002). Structure and function of aggrecan. *Cell Res.* 12, 19–32. doi:10.1038/sj.cr.7290106
- Kizilgöz, V., and Ulusoy, G. (2019). Is there any relationship between lumbar intervertebral disc space height and lumbar disc herniations? a study of radiographic evaluation. *J. Turkish Spinal Surg.* 30.
- Knudson, C. B., and Knudson, W. (2001). Cartilage proteoglycans. *Seminars Cell & Dev. Biol.* 12, 69–78. doi:10.1006/scdb.2000.0243
- Kodama, J., Wilkinson, K. J., and Otsuru, S. (2023). Nutrient metabolism of the nucleus pulposus: a literature review. *North Am. Spine Soc. J. (NASSJ)* 13, 100191. doi:10.1016/j.xnsj.2022.100191
- Leung, Y. Y. L., Chan, D., and Cheung, K. M. C. (2006). Regeneration of intervertebral disc by mesenchymal stem cells: potentials, limitations, and future direction. *Eur. Spine J.* 15, 406–413. doi:10.1007/s00586-006-0183-z
- Lopez Picazo, M., Magallon Baro, A., Del Rio Barquero, L. M., Di Gregorio, S., Martelli, Y., Romera, J., et al. (2018). 3-d subject-specific shape and density estimation of the lumbar spine from a single anteroposterior dxa image including assessment of cortical and trabecular bone. *IEEE Trans. Med. Imaging* 37, 2651–2662. doi:10.1109/tmi.2018.2845909
- Maas, S. A., Ellis, B. J., Ateshian, G. A., and Weiss, J. A. (2012). Febio: finite elements for biomechanics. *J. Biomechanical Eng.* 134, 011005. doi:10.1115/1.4005694
- Magnier, C., Boiron, O., Wendling-Mansuy, S., Chabrand, P., and Deplano, V. (2009). Nutrient distribution and metabolism in the intervertebral disc in the unloaded state: a parametric study. *J. Biomechanics* 42, 100–108. doi:10.1016/j.jbiomech.2008.10.034
- Malandrino, A., Jackson, A. R., Huyghe, J. M., and Noailly, J. (2015a). Poroelastic modeling of the intervertebral disc: a path toward integrated studies of tissue biophysics and organ degeneration. *MRS Bull.* 40, 324–332. doi:10.1557/mrs.2015.68
- Malandrino, A., Noailly, J., and Lacroix, D. (2011). The effect of sustained compression on oxygen metabolic transport in the intervertebral disc decreases with degenerative changes. *PLoS Comput. Biol.* 7, e1002112. doi:10.1371/journal.pcbi.1002112
- Malandrino, A., Noailly, J., and Lacroix, D. (2014). Numerical exploration of the combined effect of nutrient supply, tissue condition and deformation in the intervertebral disc. *J. Biomechanics* 47, 1520–1525. doi:10.1016/j.jbiomech.2014.02.004
- Malandrino, A., Pozo, J. M., Castro-Mateos, I., Frangi, A. F., van Rijsbergen, M. M., Ito, K., et al. (2015b). On the relative relevance of subject-specific geometries and degeneration-specific mechanical properties for the study of cell death in human intervertebral disk models. *Front. Bioeng. Biotechnol.* 3, 5. doi:10.3389/fbioe.2015.00005
- Marchand, F., and Ahmed, A. M. (1990). Investigation of the laminate structure of lumbar disc annulus fibrosus. *Spine* 15, 402–410. doi:10.1097/00007632-199005000-00011
- Mayer, J. E., Iatridis, J. C., Chan, D., Qureshi, S. A., Gottesman, O., and Hecht, A. C. (2013). Genetic polymorphisms associated with intervertebral disc degeneration. *Spine J.* 13, 299–317. doi:10.1016/j.spinee.2013.01.041
- Meijer, G. J. M., Homminga, J., Veldhuizen, A. G., and Verkerke, G. J. (2011). Influence of interpersonal geometrical variation on spinal motion segment stiffness: implications for patient-specific modeling. *Spine* 36, E929–E935. doi:10.1097/brs.0b013e3181fd7f7f
- Moon, S. M., Yoder, J. H., Wright, A. C., Smith, L. J., Vresilovic, E. J., and Elliott, D. M. (2013). Evaluation of intervertebral disc cartilaginous endplate structure using magnetic resonance imaging. *Eur. Spine J.* 22, 1820–1828. doi:10.1007/s00586-013-2798-1
- Mow, V., Gibbs, M., Lai, W., Zhu, W., and Athanasiou, K. (1989). Biphasic indentation of articular cartilage—ii. a numerical algorithm and an experimental study. *J. Biomechanics* 22, 853–861. doi:10.1016/0021-9290(89)90069-9
- Mow, V. C., Kuei, S. C., Lai, W. M., and Armstrong, C. G. (1980). Biphasic creep and stress relaxation of articular cartilage in compression: theory and experiments. *J. Biomechanical Eng.* 102, 73–84. doi:10.1115/1.3138202

- Muñoz-Moya, E., Rasouligandomani, M., Ruiz Wills, C., Chemorion, F., Piella, G., and Noailly, J. (2023) *Repository of ivd patient-specific fe models*. doi:10.5281/zenodo.8325042
- Narmoneva, D., Wang, J., and Setton, L. (1999). Nonuniform swelling-induced residual strains in articular cartilage. *J. Biomechanics* 32, 401–408. doi:10.1016/s0021-9290(98)00184-5
- Natarajan, R. N., Williams, J. R., and Andersson, G. B. (2004). Recent advances in analytical modeling of lumbar disc degeneration. *Spine* 29, 2733–2741. doi:10.1097/01.brs.0000146471.59052.e6
- Nerurkar, N. L., Elliott, D. M., and Mauck, R. L. (2007). Mechanics of oriented electrospun nanofibrous scaffolds for annulus fibrosus tissue engineering. *J. Orthop. Res.* 25, 1018–1028. doi:10.1002/jor.20384
- Ning, Y., Ong, M. E. H., Chakraborty, B., Goldstein, B. A., Ting, D. S. W., Vaughan, R., et al. (2022). Shapley variable importance cloud for interpretable machine learning. *Patterns* 3, 100452. doi:10.1016/j.patter.2022.100452
- Noailly, J., Planell, J. A., and Lacroix, D. (2010). On the collagen criss-cross angles in the annuli fibrosi of lumbar spine finite element models. *Biomechanics Model. Mechanobiol.* 10, 203–219. doi:10.1007/s10237-010-0227-5
- Noailly, J., Wilke, H.-J., Planell, J. A., and Lacroix, D. (2007). How does the geometry affect the internal biomechanics of a lumbar spine bi-segment finite element model? consequences on the validation process. *J. Biomechanics* 40, 2414–2425. doi:10.1016/j.jbiomech.2006.11.021
- Paul, C. P. L., Schoorl, T., Zuiderbaan, H. A., Zandieh Doulabi, B., van der Veen, A. J., van de Ven, P. M., et al. (2013). Dynamic and static overloading induce early degenerative processes in caprine lumbar intervertebral discs. *PLoS ONE* 8, e62411. doi:10.1371/journal.pone.0062411
- Pezowicz, C. (2010). Analysis of selected mechanical properties of intervertebral disc annulus fibrosus in macro and microscopic scale. *J. Theor. Appl. Mech.* 48, 917–932.
- Ravindra, V. M., Senglaub, S. S., Rattani, A., Dewan, M. C., Härtl, R., Bisson, E., et al. (2018). Degenerative lumbar spine disease: estimating global incidence and worldwide volume. *Glob. Spine J.* 8, 784–794. PMID: 30560029. doi:10.1177/2192568218770769
- Raza, A., and Michalek, A. J. (2021). Radial trend in murine annulus fibrosus fiber orientation is best explained by vertebral growth. *Eur. Spine J.* 30, 3450–3456. doi:10.1007/s00586-021-06999-7
- Roberts, S., Memange, J., and Urban, J. P. G. (1989). Biochemical and structural properties of the cartilage end-plate and its relation to the intervertebral disc. *Spine* 14, 166–174. doi:10.1097/00007632-198902000-00005
- Roberts, S., Urban, J. P. G., Evans, H., and Eisenstein, S. M. (1996). Transport properties of the human cartilage endplate in relation to its composition and calcification. *Spine* 21, 415–420. doi:10.1097/00007632-199602150-00003
- Ruiz, C., Foata, B., González Ballester, M. A., Karppinen, J., and Noailly, J. (2018). Theoretical explorations generate new hypotheses about the role of the cartilage endplate in early intervertebral disk degeneration. *Front. Physiology* 9, 1210. doi:10.3389/fphys.2018.01210
- Ruiz, C., Malandrino, A., van Rijsbergen, M., Lacroix, D., Ito, K., and Noailly, J. (2016). Simulating the sensitivity of cell nutritive environment to composition changes within the intervertebral disc. *J. Mech. Phys. Solids* 90, 108–123. doi:10.1016/j.jmps.2016.02.003
- Ruiz, C., Noailly, J., and Lacroix, D. (2013). Material property discontinuities in intervertebral disc porohyperelastic finite element models generate numerical instabilities due to volumetric strain variations. *J. Mech. Behav. Biomed. Mater.* 26, 1–10. doi:10.1016/j.jmbbm.2013.05.012
- Sato, K., Kikuchi, S., and Yonezawa, T. (1999). *In vivo* intradiscal pressure measurement in healthy individuals and in patients with ongoing back problems. *Spine* 24, 2468. doi:10.1097/00007632-199912010-00008
- Schroeder, Y., Elliott, D., Wilson, W., Baaijens, F., and Huyghe, J. (2008). Experimental and model determination of human intervertebral disc osmo-viscoelasticity. *J. Orthop. Res.* 26, 1141–1146. doi:10.1002/jor.20632
- Schroeder, Y., Sivan, S., Wilson, W., Merkher, Y., Huyghe, J. M., Maroudas, A., et al. (2007). Are disc pressure, stress, and osmolarity affected by intra- and extrafibrillar fluid exchange? *J. Orthop. Res.* 25, 1317–1324. doi:10.1002/jor.20443
- Shirazi-Adl, A., Taheri, M., and Urban, J. (2010). Analysis of cell viability in intervertebral disc: effect of endplate permeability on cell population. *J. Biomechanics* 43, 1330–1336. doi:10.1016/j.jbiomech.2010.01.023
- Sivan, S., Merkher, Y., Wachtel, E., Ehrlich, S., and Maroudas, A. (2006). Correlation of swelling pressure and intrafibrillar water in young and aged human intervertebral discs. *J. Orthop. Res.* 24, 1292–1298. doi:10.1002/jor.20144
- Smith, L. J., Nerurkar, N. L., Choi, K.-S., Harfe, B. D., and Elliott, D. M. (2011). Degeneration and regeneration of the intervertebral disc: lessons from development. *Dis. Models Mech.* 4, 31–41. doi:10.1242/dmm.006403
- Tavana, S., Shek, C., Rahman, T., Baxan, N., and Newell, N. (2024). The influence of geometry on intervertebral disc stiffness. *J. Biomechanics* 111915doi, 111915. doi:10.1016/j.jbiomech.2023.111915
- Teichtahl, A. J., Urquhart, D. M., Wang, Y., Wluka, A. E., Heritier, S., and Cicuttini, F. M. (2015). A dose–response relationship between severity of disc degeneration and intervertebral disc height in the lumbosacral spine. *Arthritis Res. Ther.* 17, 297. doi:10.1186/s13075-015-0820-1
- Travascio, F., Jackson, A. R., Brown, M. D., and Gu, W. Y. (2009). Relationship between solute transport properties and tissue morphology in human annulus fibrosus. *J. Orthop. Res.* 27, 1625–1630. doi:10.1002/jor.20927
- Urban, J., Maroudas, A., Bayliss, M., and Dillon, J. (1979). Swelling pressures of proteoglycans at the concentrations found in cartilaginous tissues. *Biorheology* 16, 447–464. doi:10.3233/bir-1979-16609
- Urban, J. P., Smith, S., and Fairbank, J. C. (2004). Nutrition of the intervertebral disc. *Spine* 29, 2700–2709. doi:10.1097/01.brs.0000146499.97948.52
- Urban, J. P. G., and Maroudas, A. (1981). Swelling of the intervertebral disc *in vitro*. *Connect. Tissue Res.* 9, 1–10. doi:10.3109/03008208109160234
- Urban, J. P. G., Roberts, S., and Ralphs, J. R. (2000). The nucleus of the intervertebral disc from development to degeneration. *Am. Zoologist* 40, 53–061. doi:10.1093/icb/40.1.53
- Urquhart, D. M., Kurniadi, I., Triangto, K., Wang, Y., Wluka, A. E., O'Sullivan, R., et al. (2014). Obesity is associated with reduced disc height in the lumbar spine but not at the lumbosacral junction. *Spine* 39, E962–E966. doi:10.1097/brs.0000000000000411
- Wilke, H., Neef, P., Caimi, M., Hoogland, T., and Claes, L. E. (1999). New *in vivo* measurements of pressures in the intervertebral disc in daily life. *Spine* 24, 755–762. doi:10.1097/00007632-199904150-00005
- Wilke, H. J., Claes, L., Schmitt, H., and Wolf, S. (1994). A universal spine tester for *in vitro* experiments with muscle force simulation. *Eur. Spine J.* 3, 91–97. doi:10.1007/bf02221446
- Wilson, W., Huyghe, J., and van Donkelaar, C. (2006a). A composition-based cartilage model for the assessment of compositional changes during cartilage damage and adaptation. *Osteoarthr. Cartil.* 14, 554–560. doi:10.1016/j.joca.2005.12.006
- Wilson, W., Huyghe, J. M., and van Donkelaar, C. C. (2006b). Depth-dependent compressive equilibrium properties of articular cartilage explained by its composition. *Biomechanics Model. Mechanobiol.* 6, 43–53. doi:10.1007/s10237-006-0044-z
- Wilson, W., van Donkelaar, C., van Rietbergen, B., and Huiskes, R. (2005a). A fibril-reinforced poroviscoelastic swelling model for articular cartilage. *J. Biomechanics* 38, 1195–1204. doi:10.1016/j.jbiomech.2004.07.003
- Wilson, W., van Donkelaar, C. C., and Huyghe, J. M. (2005b). A comparison between mechano-electrochemical and biphasic swelling theories for soft hydrated tissues. *J. Biomechanical Eng.* 127, 158–165. doi:10.1115/1.1835361



OPEN ACCESS

EDITED BY

Zhen Luo,
University of Technology Sydney, Australia

REVIEWED BY

Malek Adouni,
Abdullah Al Salem University, Kuwait
Qiang Chen,
Southeast University, China

*CORRESPONDENCE

Yaodong Gu,
✉ guyaodongnb@aliyun.com

RECEIVED 29 January 2024

ACCEPTED 12 July 2024

PUBLISHED 29 July 2024

CITATION

Jiang X, Bíró I, Sárosi J, Fang Y and Gu Y (2024),
Comparison of ground reaction forces as
running speed increases between male and
female runners.
Front. Bioeng. Biotechnol. 12:1378284.
doi: 10.3389/fbioe.2024.1378284

COPYRIGHT

© 2024 Jiang, Bíró, Sárosi, Fang and Gu. This is
an open-access article distributed under the
terms of the [Creative Commons Attribution
License \(CC BY\)](#). The use, distribution or
reproduction in other forums is permitted,
provided the original author(s) and the
copyright owner(s) are credited and that the
original publication in this journal is cited, in
accordance with accepted academic practice.
No use, distribution or reproduction is
permitted which does not comply with these
terms.

Comparison of ground reaction forces as running speed increases between male and female runners

Xinyan Jiang^{1,2,3}, István Bíró^{2,3}, József Sárosi³, Yufei Fang¹ and
Yaodong Gu^{1,4*}

¹Department of Radiology, Ningbo No. 2 Hospital, Ningbo, China, ²Doctoral School on Safety and Security Sciences, Obuda University, Budapest, Hungary, ³Faculty of Engineering, University of Szeged, Szeged, Hungary, ⁴Faculty of Sports Science, Ningbo University, Ningbo, China

Introduction: The biomechanics associated with human running are affected by gender and speed. Knowledge regarding ground reaction force (GRF) at various running speeds is pivotal for the prevention of injuries related to running. This study aimed to investigate the gait pattern differences between males and females while running at different speeds, and to verify the relationship between GRFs and running speed among both males and females.

Methods: GRF data were collected from forty-eight participants (thirty male runners and eighteen female runners) while running on an overground runway at seven discrete speeds: 10, 11, 12, 13, 14, 15 and 16 km/h.

Results: The ANOVA results showed that running speed had a significant effect ($p < 0.05$) on GRFs, propulsive and vertical forces increased with increasing speed. An independent t-test also showed significant differences ($p < 0.05$) in vertical and anterior-posterior GRFs at all running speeds, specifically, female runners demonstrated higher propulsive and vertical forces than males during the late stance phase of running. Pearson correlation and stepwise multiple linear regression showed significant correlations between running speed and the GRF variables.

Discussion: These findings suggest that female runners require more effort to keep the same speed as male runners. This study may provide valuable insights into the underlying biomechanical factors of the movement patterns at GRFs during running.

KEYWORDS

gender, running speed, biomechanics, impulse, ground reaction force

1 Introduction

Since the 1970s, running has surged in popularity both as a recreational pursuit and a competitive sport (Van Mechelen, 1992; Van Der Worp et al., 2015; Quan et al., 2021). In recent years, the number of females competing in running events has increased significantly (Hollander et al., 2021). In comparative studies of aerobic exercises, running demonstrates a heightened predisposition to overuse injuries in contrast to activities like walking, swimming, and cycling (Francis et al., 2019). The etiology of running-related injuries (RRIs) is multifaceted, with predominant attributions to anatomical, biomechanical factors and training load (Buist et al., 2010; Vannatta et al., 2020; Xu et al., 2022; Zhou and Ugbohue, 2024). Gender has been posited as a potential risk factor, influencing the overall risk of

injury (Buist et al., 2010; Van Der Worp et al., 2015; Hollander et al., 2021). Female runners might exhibit a heightened susceptibility to certain RRIs, including patellofemoral pain and tibial stress fractures, compared to male runners (Wright et al., 2015; Almonroeder and Benson, 2017). However, understanding remains limited concerning sex-specific disparities in the etiology of RRIs.

Gender-related differences in kinematics and kinetics during running have previously been reported. Besson et al. (2022) found that female runners showed larger hip and knee joint motion in the non-sagittal plane than male runners. Almonroeder and Benson (2017) also noticed that hip adduction and internal rotation are greater in females than in males. A study conducted by Sinclair and Selfe (2015) showed that among recreational runners, females demonstrated significantly larger extension and abduction moments in the knee joint, as well as greater patellofemoral contact forces and pressures than males, which may relate to the greater risk of patellofemoral pain in female runners. Most studies of gender differences in running biomechanics have focused on lower limb joint biomechanics. Studies examining differences in ground reaction forces (GRFs) between runners of different genders are limited and inconsistent. Bazuelo-Ruiz et al. (2018) conducted a prospective study and found that females have a significantly greater loading rate and peak propulsive force, and a smaller active peak force than males. Isherwood et al. (2021) also observed that females exhibited a greater loading rate than males. However, the findings of a study conducted by Greenhalgh. (2012) indicate that no significant differences in GRF were observed between males and females. During running, runners experience vertical GRF between 1.5 and 3 times their body weight, which is believed to be a significant risk factor for lower limb injuries (Grabowski and Kram, 2008; Logan et al., 2010). Several studies have investigated the correlation between RRIs and GRF parameters. Loading rate, vertical impact force, peak braking force and impulses have all been demonstrated to be associated with RRIs in previous investigations (Zadpoor and Nikooyan, 2011; Napier et al., 2018; Gao et al., 2023). The connection between GRFs and RRIs has inspired researchers to examine the potential of gait retraining as a preventive measure against injuries (Napier et al., 2018; Dempster et al., 2021).

During running training sessions, speed is commonly adjusted and serves as an indicator of the task's physical intensity (Floria et al., 2019). As running speed increases, there is often a rise in stride length, frequency, joint range of motion, joint moment, joint load, and vertical impact force (Grabowski and Kram, 2008; Schache et al., 2011; Orendurff et al., 2018). Runners are believed to experience greater forces on their bodies as they run faster. Specifically, within a speed range of 2–7 m/s, runners achieve a longer stride length by producing increased GRFs (Mercer et al., 2005; Hamner and Delp, 2013; Schache et al., 2014). However, not all biomechanical parameters change with increased running speed. Floria et al. (2019) observed no impact of speed on coordination variability when compared to three different running speeds. Girard et al. (2019) accomplished a study on the impact of varying running speeds, from 10 to 25 km/h, on the extent and variation of asymmetry in essential biomechanical aspects. They concluded that the speed of running does not affect the mechanical asymmetry of the lower limb. A prospective study conducted by

Muñoz-Jimenez et al. (2015) revealed no significant differences in foot strike patterns, frequencies or percentages between low-speed and high-speed running. While numerous studies have examined running biomechanics at varying speeds, most have focused on a single gender. It remains to be studied how different speeds affect the running mechanics of male and female runners and the gender differences between them.

In summary, current research lacks sufficient evidence regarding the impact of potential confounding factors such as running speed and gender. There are certain questions to answer, including whether females and males adapt differently to varying speed gradients, the effect of speed on GRFs during overground running, and the possibility of predicting speed changes from GRF parameters. Therefore, our study aimed to investigate the differences in GRFs between male and female runners across a range of speeds (10–16 km/h) and to analyze the correlation between GRF parameters and running speed in both genders. We hypothesize that GRF parameters are related to the running speed, and we also hypothesize that GRF parameters are associated with the gender of runners. Comprehensively clarifying the mechanical factors that influence running performance through GRFs is crucial for understanding human locomotor functions. Insights into the key variables critical for faster running will be beneficial for improving performance.

2 Materials and methods

2.1 Participants

Thirty male (age: 25.80 ± 3.44 years, height: 1.76 ± 0.05 m, body mass: 75.70 ± 6.14 kg) and eighteen female recreational runners (age: 24.89 ± 2.77 years, height: 1.63 ± 0.04 m, body mass: 54.83 ± 5.15 kg) participated in this study. All runners self-identified as rearfoot strike pattern runners. The exclusion criteria for the study were: 1) any lower limb injury within the past 6 months; 2) any low back or lower limb pain during running; 3) less than 3 years of running experience. The study protocol received approval from the institutional review board of Ningbo University, and all runners provided informed written consent before the testing.

2.2 Experimental procedures

After 10 min of laboratory familiarization and a warm-up, all runners performed running tests on a 20 m runway at seven speeds: 10, 11, 12, 13, 14, 15, and 16 km/h. Each participant completed three successful trials at each speed ($\pm 2\%$) on the runway. The trial was considered successful only if runners struck the force plate with their right foot fully on without targeting, and the speed was within 2% of the prescribed running speed. Runners were required to maintain a steady-state speed until they exited the runway. Running speed was measured by two infrared timing gates placed 3 m apart alongside the runway just before and after the force plate. The order of running speeds was non-random for practical reasons (Schache et al., 2011; Orendurff et al., 2018; Aljohani and Kipp, 2020). Adequate rest was provided between speed increases to prevent fatigue. Additionally,

our experimenters had monitored the participants' fatigue levels throughout the process. If a participant had reported experiencing fatigue during the experiment, they would have been allowed to rest before continuing. All runners wore the same natural running shoes to avoid shoe effects. Ground reaction forces (GRFs) were recorded by an in-ground force plate (AMTI, Watertown, MA, United States) located in the middle of the runway. Data was collected by the force plate using a sampling frequency of 1,000 Hz.

2.3 Data analysis

GRFs for each runner were underwent processing using a Butterworth fourth-order low-pass filter with a cut-off frequency set at 20 Hz via MATLAB software (Vision 2019b; The MathWorks, Inc., Natick, MA). Foot strikes were determined by identifying moments when the vertical GRF exceeded a threshold of 20 N, which indicated the beginning of the initial contact phase and the toe-off phase (Jiang et al., 2021). Then, vertical and anterior-posterior GRFs were normalized relative to each runner's body weight (BW). Due to high variability within and between subjects, medial-lateral GRFs were excluded from this study (Munro et al., 1987). The GRF variables of interest were extracted and computed from the vertical and anterior-posterior directions, including braking impulse, propulsive impulse, peak braking force, peak propulsive force, vertical impulse, vertical average loading rate (VALR), peak vertical impact force and peak vertical impact force. Based on prior investigations focusing on running GRFs, the selection of these variables as the most related components for analysis (Logan et al., 2010; Zadpoor and Nikooyan, 2011; Jiang et al., 2021).

VALR was calculated by determining the average slope between 20% and 80% of the vertical GRF at the first peak (Yu et al., 2021). The first and second vertical GRFs were defined as the peak vertical impact force and active force, respectively. The anterior-posterior GRF represented the braking phase with negative values and the propulsion phase with positive values (Bazuelo-Ruiz et al., 2018; Jiang et al., 2021). For each direction of interest, impulses were computed from the area between the zero line and the GRF curve, which were calculated using the trapezoidal integration approach as follows:

$$\text{Impulse} = \sum_{i=1}^{n-1} \frac{1}{2} (F_{i+1} + F_i) \times (t_{i+1} - t_i)$$

In this equation, n is the number of frames, i is the i -th frame, F is the ground reaction force and t is the time value.

2.4 Statistical analysis

Average data for each participant were included in the analysis. The normality of the GRF variables was checked via Shapiro-Wilk tests. Pearson's correlation coefficients were computed to evaluate the relationship between GRF variables and running speed. Correlations were defined as: no relationship or little ($r \leq 0.25$), low to fair ($0.25 < r < 0.50$), moderate to good ($0.50 < r < 0.75$), and strong ($r \geq 0.75$) (Portney and Watkins, 2009). The significance level for determining whether a correlation is statistically significant was set at 0.05. To further determine the level of variance in running speed that was explained

by the specific GRF variables, two stepwise linear regressions were performed (one for males and one for females). The discrete GRF variables that were significantly correlated with the running speed were input into one model as the independent variables, while the running speed was considered the dependent variable. The criteria for entering or removing variables from the model were set at alpha levels of 0.05 and 0.10, respectively. The data were analyzed via SPSS software (version 25.0, IBM Corporation, Armonk, NY, United States).

Meanwhile, both vertical and anterior-posterior GRFs were normalized into 101 data points by using the cubic spline interpolation approach to represent stance phase (from 0% to 100%). Given the one-dimensional time-varying characters of GRF curves, a two-tailed independent t -test with statistical parametric mapping (SPM) analyses was used to determine gender differences in each running speed, and a one-way repeated measures ANOVA with SPM was used to determine the main effect of running speed in both males and females.

3 Results

The relationship between discrete GRF variables and running speed is detailed in Figure 1. In female runners, seven variables showed significant correlations with running speed. Specifically, braking impulse ($r = 0.617$, $p < 0.001$), propulsive impulse ($r = 0.568$, $p < 0.001$), peak propulsive force ($r = 0.822$, $p < 0.001$), VALR ($r = 0.687$, $p < 0.001$) and peak vertical impact force ($r = 0.702$, $p < 0.001$) increased linearly with running speed, whereas vertical impulse ($r = -0.814$, $p < 0.001$) and peak vertical active force ($r = -0.205$, $p = 0.021$) decreased linearly. In male runners, six variables were significantly correlated with running speed. Peak propulsive force ($r = 0.627$, $p < 0.001$), VALR ($r = 0.639$, $p < 0.001$) and peak vertical impact force ($r = 0.691$, $p < 0.001$) increased linearly with speed, whereas the braking impulse ($r = -0.177$, $p = 0.010$), peak braking force ($r = -0.597$, $p < 0.001$) and vertical impulse ($r = -0.707$, $p < 0.001$) decreased linearly.

The results of stepwise linear regression analysis for females and males were shown in Tables 1, 2, respectively. For females, the analysis identified peak propulsive force, peak vertical impact force, propulsive impulse, VALR and vertical impulse as the best predictors of the running speed ($R^2 = 0.901$, $p < 0.001$), explaining 90% of the variation. For males, the best predictors were vertical impulse, peak vertical impact force, peak propulsive force, braking impulse, VALR and peak braking force ($R^2 = 0.855$, $p < 0.001$), accounting for 85.5% of the variance in running speed.

SPM analyses revealed significant main effects of speed on the anterior-posterior and vertical GRF waveforms for female runners, as shown in Figure 2. Both propulsive force (45%–98%, $p < 0.001$) and vertical force (1%–18%, $p < 0.001$; 60%–88%, $p < 0.001$) increased with running speed. Notably, peak propulsive force, propulsive impulse, braking impulse, vertical impulse, VALR, and peak vertical impact force all demonstrated significant speed main effects. Similarly, for male runners, Figure 3 indicated significant main effects of speed on their anterior-posterior and vertical GRF waveforms. Increased running speed resulted in greater braking force (12%–47%, $p < 0.001$), propulsive force (67%–98%, $p < 0.001$), and vertical force (7%–23%, $p < 0.001$; 47%–95%, $p < 0.001$). Significant main effects of speed were also found in male

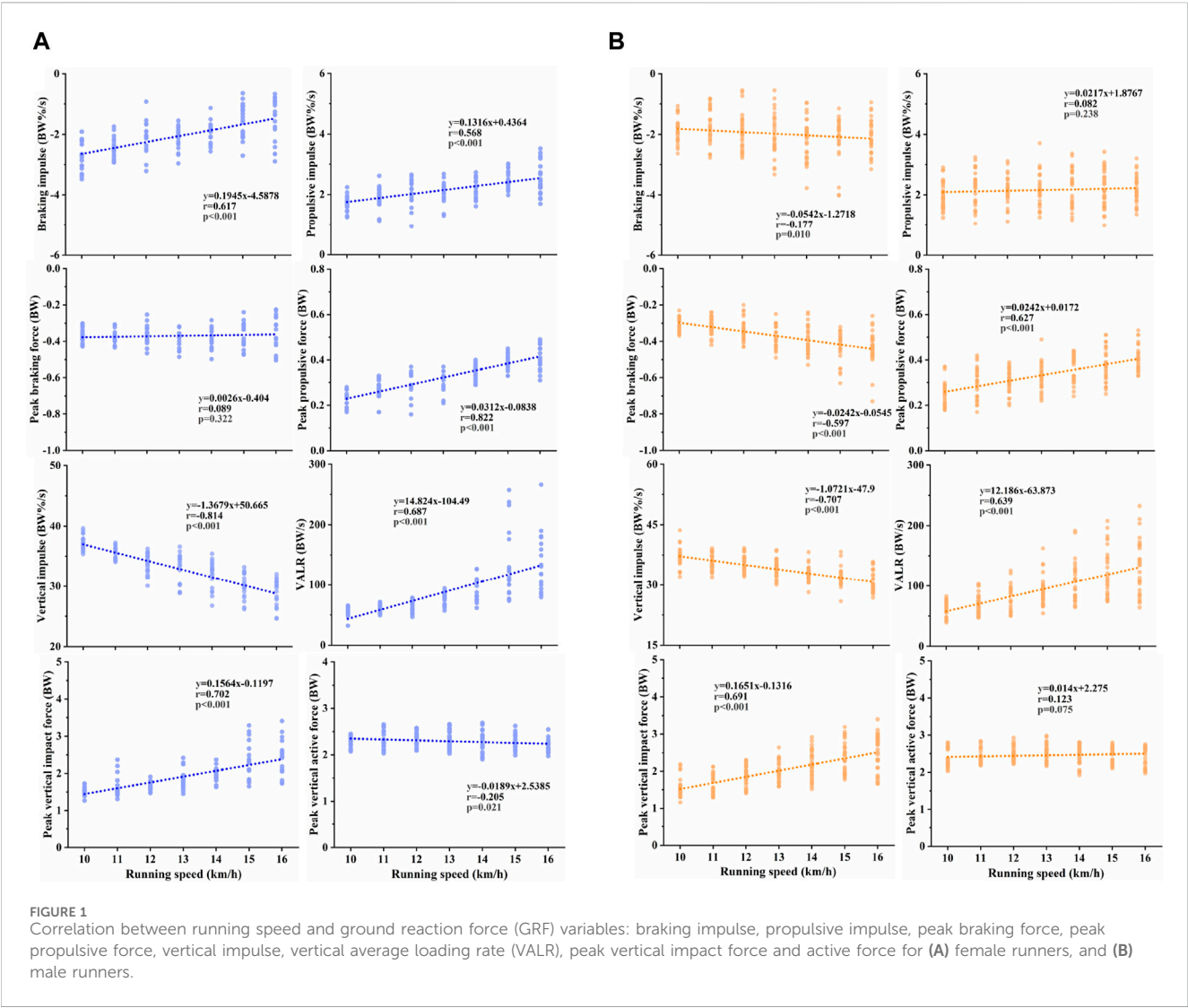


TABLE 1 Results of stepwise linear regression for running speed in female runners.

Variables	R	R ²	Adjusted R ²	F	p
Peak propulsive force	0.820	0.673	0.670	255.245	<0.001
Peak propulsive force + peak vertical impact force	0.917	0.842	0.839	326.931	<0.001
Peak propulsive force + peak vertical impact force + propulsive impulse	0.934	0.872	0.869	276.457	<0.001
Peak propulsive force + peak vertical impact force + propulsive impulse + VALR	0.942	0.888	0.884	240.288	<0.001
Peak propulsive force + peak vertical impact force + propulsive impulse + VALR + vertical impulse	0.949	0.901	0.897	217.968	<0.001

runners' peak propulsive force, peak braking force, vertical impulse, VALR, and peak vertical impact force.

Figure 4 presented the results of gender differences in anterior-posterior GRFs at each running speed, as determined by independent t-tests and SPM analyses. Females exhibited a larger braking force at speeds of 10 km/h (13%–57%, $p < 0.001$) and 11 km/h (12%–58%, $p < 0.001$). During the later stance phase, females demonstrated more propulsive force than males at all tested speeds. Specifically, this increase was observed during 93%–100% of the

stance phase at 10 km/h ($p = 0.003$), 94%–100% at 11 km/h ($p = 0.012$), 92%–100% at 12 km/h ($p = 0.004$), 94%–100% at 13 km/h ($p = 0.015$), 93%–100% at 14 km/h ($p = 0.008$), 89%–100% at 15 km/h ($p < 0.001$), and 84%–100% at 16 km/h ($p < 0.001$). Figure 5 illustrated gender differences in vertical GRFs at each running speed. During the later stance phase, females exhibited higher forces than males at all selected speeds. Specifically, this increase was observed during 70%–100% of the stance phase at 10 km/h ($p < 0.001$), 84%–100% at 11 km/h ($p < 0.001$), 83%–100% at 12 km/h ($p < 0.001$),

TABLE 2 Results of stepwise linear regression for running speed in male runners.

Variables	R	R ²	Adjusted R ²	F	p
Vertical impulse	0.707	0.499	0.497	207.322	<0.001
Vertical impulse + peak vertical impact force	0.830	0.689	0.686	229.037	<0.001
Vertical impulse + peak vertical impact force + peak propulsive force	0.868	0.754	0.750	210.155	<0.001
Vertical impulse + peak vertical impact force + peak propulsive force + braking impulse	0.914	0.835	0.832	258.860	<0.001
Vertical impulse + peak vertical impact force + peak propulsive force + braking impulse + VALR	0.920	0.847	0.843	225.883	<0.001
Vertical impulse + peak vertical impact force + peak propulsive force + braking impulse + VALR + peak braking force	0.925	0.855	0.851	200.043	<0.001

86%–100% at 13 km/h ($p < 0.001$), 86%–100% at 14 km/h ($p < 0.001$), 79%–100% at 15 km/h ($p < 0.001$), and 86%–100% at 16 km/h ($p < 0.001$). However, males showed larger force during 34%–56% of the stance phase at 13 km/h ($p < 0.001$), 31%–51% at 15 km/h ($p < 0.001$), and 31%–53% at 16 km/h ($p < 0.001$), which included peak vertical active force.

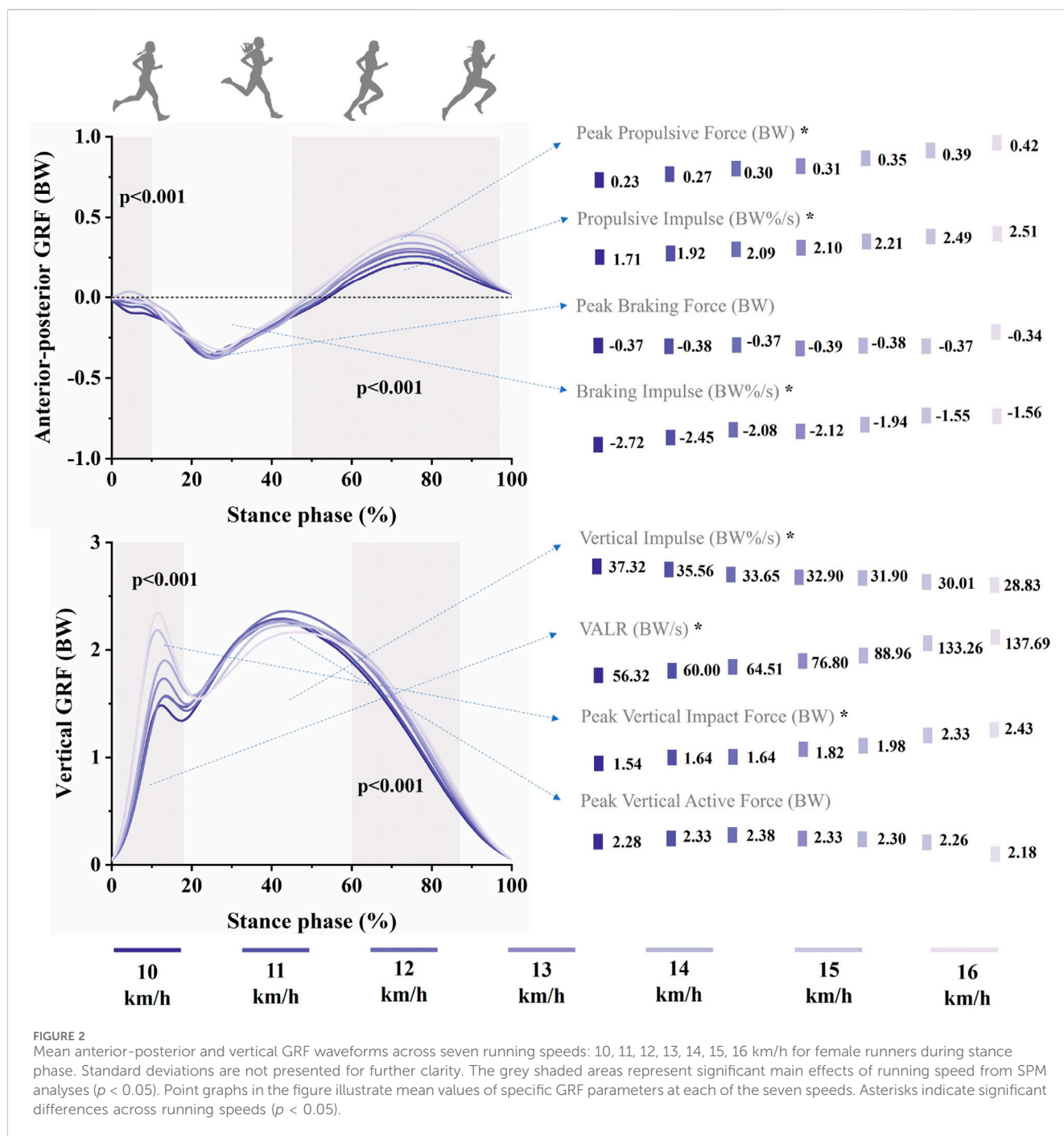
4 Discussion

The primary purpose of our study was to explore gait pattern differences in ground reaction forces (GRFs) between male and female runners across seven running speeds. We hypothesized that specific GRF characteristics would vary between genders across different speeds and that GRFs would correlate with running speed. The primary finding of our study was that female runners exhibit higher propulsive and vertical forces than male runners at all tested speeds. Our findings indicated that distinct running patterns for male and female runners are identifiable through GRFs at each speed, particularly during the later stance phase. We also observed that running speed significantly influences GRFs for all runners, with both genders exhibiting increased trends in early and mid-late stance as speed increased. The stepwise regression analysis revealed that certain discrete GRF variables could predict running speed, thereby providing partial support for our hypothesis.

Distinction in the incidence rates of specific injuries among male and female runners has indicated the necessity to distinguish running mechanics (Van Gent et al., 2007; Boyer et al., 2017; Hollander et al., 2021). The differences in propulsive force between males and females at each running speed suggest that female runners may require more effort to accelerate the body to maintain forward momentum, in order to keep the same speed as male runners. Previous studies also found that propulsive force in females was higher when compared with males at the same speed during running (Bazuelo-Ruiz et al., 2018; Stickley et al., 2018). Females have a larger braking force during the first half of stance at running speeds of 10 km/h and 11 km/h, which indicated that the mass center of females accelerated more backward than males at slower speeds. Faster running speeds require a higher amount of propulsive force, but not necessarily a lower amount of braking force (Morin et al., 2015). Previous studies have analyzed gender differences on parameters extracted from vertical GRF

(Greenhalgh, 2012; Bazuelo-Ruiz et al., 2018), but none have prospectively conducted time series curve analysis on GRF throughout the stance phase. A novel finding in this study was that females have higher vertical GRF during the later stance phase at each running speed compared with males. Higher vertical GRF may be considered an inevitable result of needing a higher percentage of available strength to propel the body towards toe-off (Cavanagh and Kram, 1989). Female runners exhibited a greater peak vertical impact force at faster running speeds, which may induce potential shock increases in the musculoskeletal system and thus lead to running-related injuries (Davis et al., 2016; Vannatta et al., 2020). This may provide a potential explanation for the higher patellofemoral pain and tibial stress fracture rates among female runners (Wright et al., 2015; Almonroeder and Benson, 2017).

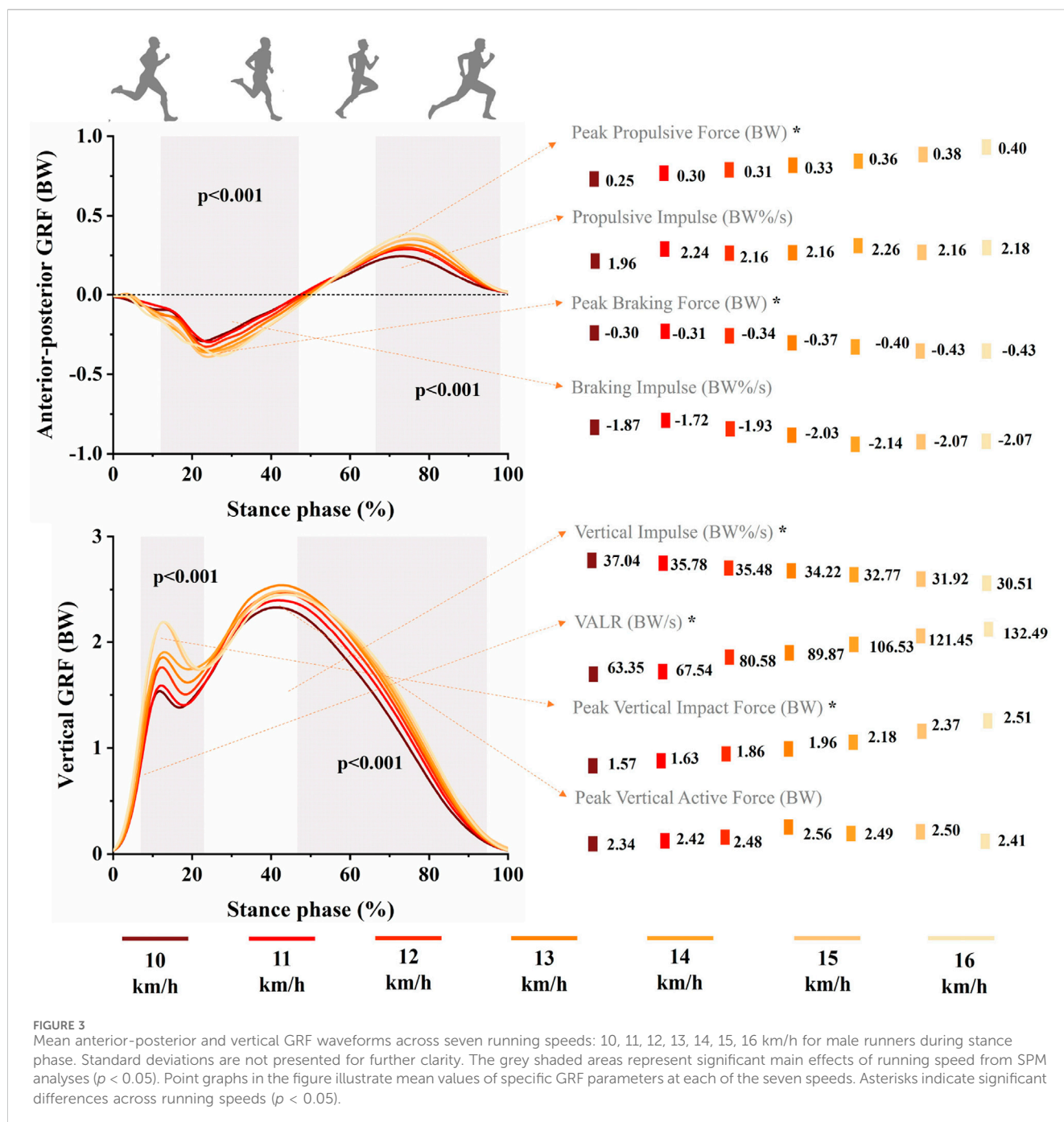
In 2016, Yokoyama et al. (2016) identified three running speed categories: slow (2.7–2.9 m/s), moderate (3.5–3.7 m/s), and fast (4.4–4.5 m/s) for experienced runners. In this study, we opted for a speed range of 10–16 km/h, corresponding to 2.78–4.44 m/s. This selection spans the spectrum from slow to fast running, facilitating a more comprehensive examination of the effect of running speed on gait mechanisms. Furthermore, the incremental difference of 1 km/h (0.28 m/s) between each chosen running speed allows for a more detailed investigation of the impact of speed on GRFs. As running speed increases, male and female runners exhibit different GRF characteristics. The results of our study demonstrated that running speed had a significant effect on propulsive force during the second half of stance in both females and males. Runners typically exhibit a forward inclination of the trunk, with foot contact striking the ground behind the body's center of mass. Consequently, from a biomechanical perspective, the aim is to maximize the propulsive component of GRF to maintain faster running speeds (Schache et al., 2014). Additionally, male runners exhibited increased braking force at higher speeds, suggesting greater impact during the braking phase of high-speed running, aligning with previous findings (Hollis et al., 2019). The runner-ground interaction during the braking phase is crucial, playing a significant role in lower extremity injury risk (Davis et al., 2016; Williams et al., 2020; Jiang et al., 2021). At initial ground contact, the lower extremity experiences rapid loading with forces exceeding 1.5 times the runner's body weight (Grabowski and Kram, 2008; Logan et al., 2010). With increased speed, runners displayed an increased peak vertical impact force, producing greater external loads on their bodies. The forefoot underwent considerable



loading. Previous studies investigated running speed as it related to GRFs and found similar correlations (Breine et al., 2019; Hollis et al., 2019). Interestingly, we observed no significant differences in peak vertical active force across speeds. The relationship between peak vertical impact force and lower limb injuries, however, remains a topic of controversy (Napier et al., 2018; Matijevich et al., 2019).

The current results also showed significant correlations (i.e., Pearson correlation and stepwise multiple linear regression) between running speed and the GRF variables, which are compatible with the findings by Breine et al. (2019) and Fukuchi et al. (2017). The GRF variables chosen in this study together explained

approximately 90% of the variance associated with increases in running speed. Key contributors and predictors of higher running speeds for both genders included peak propulsive force, vertical impulse, peak vertical impact force and VALR. Schache et al. (2014) suggested that, to achieve higher running speeds, runners tend to exert greater force against the ground rather than increasing the frequency of their strides. This conclusion is also consistent with the higher values we recorded for the propulsive force. Consistent with our hypothesis, variations in vertical GRF were responsive to changes in running speed, indicating the necessity for the legs to generate more vertical force to attain faster speeds. Notably, braking impulse and peak braking force emerged as significant factors only



in male runners. This could be explained by the fact that male runners, having relatively larger body weights, experience greater gravity and inertia effects during the braking phase, which emphasizes the importance of the braking phase in their running mechanics (Chang et al., 2000).

This study verified whether running speeds influence the GRF on overground running and whether these likely influences depended on gender differences. However, several limitations must be acknowledged. The selected running speeds are based on absolute values, not relative to each runner's physiological capabilities. We chose absolute speeds to quantify the impact of speed more accurately on a runner's GRF and minimize potential biomechanical differences

that could arise from differences in relative speeds (Petersen et al., 2014; Jiang et al., 2023). Furthermore, the intervals between the selected running speeds are relatively small. Utilizing speeds based on each runner's physiological capabilities could have introduced confounding variables into our experimental results. Nevertheless, it is important to acknowledge that this constitutes a limitation of the present study. Notably, even at identical speeds, runners may experience differing physiological intensities (Mo et al., 2020). Another limitation is that the order of running speeds was not randomized. This decision was primarily made to prevent fatigue effects by minimizing the total duration of time spent in the laboratory, which was kept under 2 h (Orendurff et al., 2018).

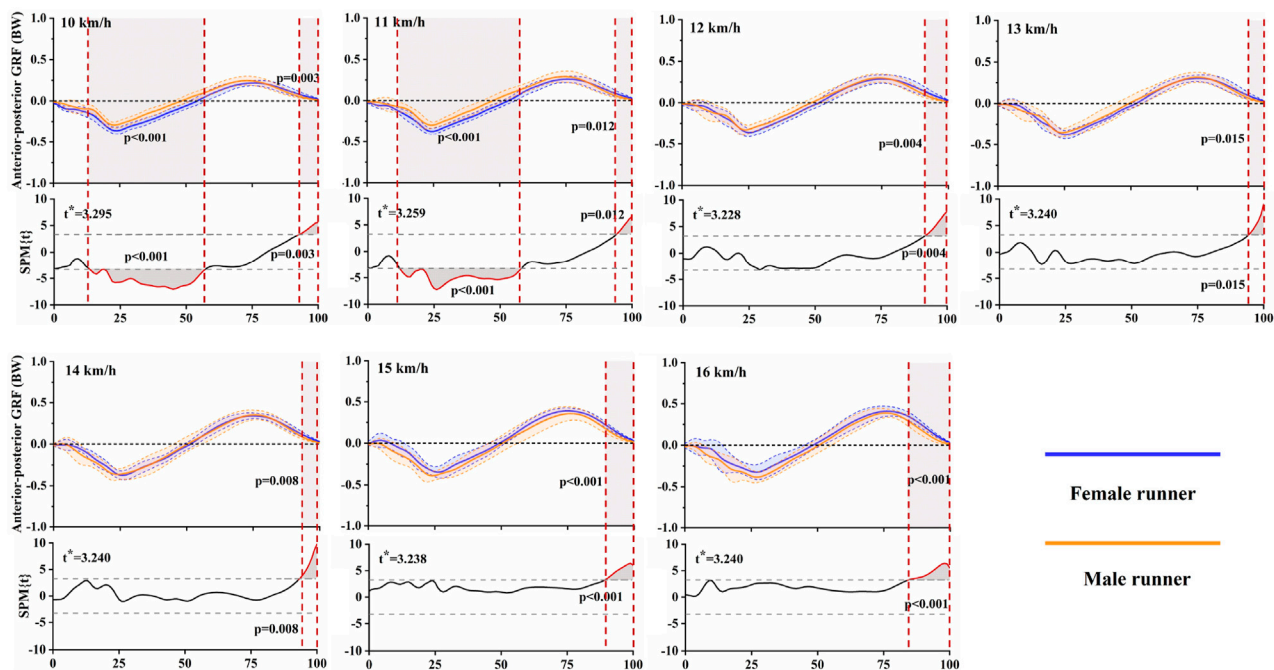


FIGURE 4
Mean (standard deviation) anterior-posterior GRF waveforms for both female and male runners at each running speed, accompanied by the SPM results. Grey shaded areas represent significant differences between female and male runners during the running stance phase ($p < 0.05$).

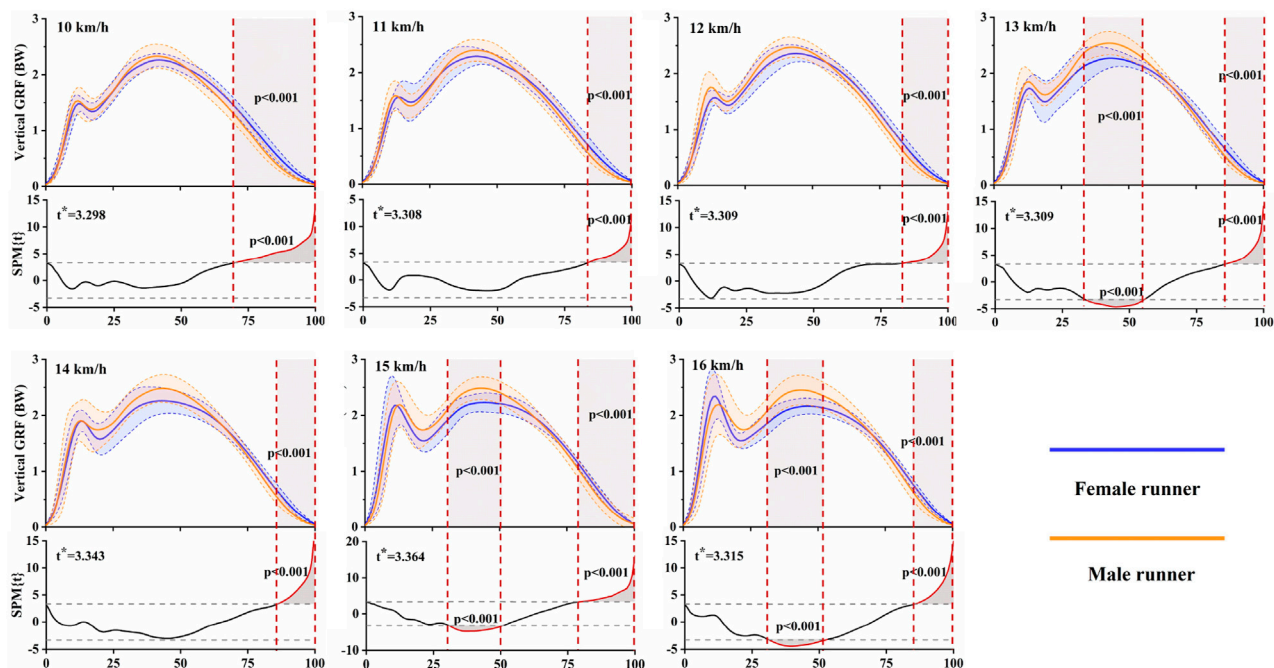


FIGURE 5
Mean (standard deviation) vertical GRF waveforms for both female and male runners at each running speed, accompanied by the SPM results. Grey shaded areas represent significant differences between female and male runners during the running stance phase ($p < 0.05$).

Randomizing the running speeds could be challenging and potentially unsafe, especially when attempting to achieve high running speeds without first gradually progressing through lower speeds (Chang and

Cen, 2024; Dorris et al., 2024). It is also important to consider that the observed changes at higher speeds might result from both the external force exerted during ground contact and muscle force production in

anticipation of or in response to surface interaction (Logan et al., 2010; Hamner and Delp, 2013; Schache et al., 2014). The knee joint is the most susceptible to injury during running (Vannatta et al., 2020; Zhou and Ugbohue, 2024). While the current study only focuses on GRF, future research will integrate the biomechanics of the knee joint with GRF to investigate the impact of running speed on runners (Adouni et al., 2023; Adouni et al., 2019; Al Khatib et al., 2022). Moreover, our findings are based on data from healthy runners and may not reflect GRF pattern changes in runners with running-related injuries (RRIs). Future research should include runners with RRIs to investigate gender and speed influences on RRI risk factors within this population.

5 Conclusion

In conclusion, this study found that increased running speeds (10–16 km/h) on an overground runway led to adaptations in ground reaction forces (GRFs), which were observed in both male and female runners. Despite gender differences, a similar trend in these adaptations was evident. The most significant effects of increased running speed were apparent in the early and late stance phases, with both vertical and anterior-posterior GRFs increasing proportionally. Moreover, female runners exhibited higher propulsive and vertical forces than males in the late stance phase at all speeds, suggesting that females might exert more effort to maintain the same speed as male runners. These findings provide valuable insights into the underlying biomechanical factors of the movement patterns at GRFs during running. Future analyses should focus on enhancing our understanding of the correlation between running-related injuries and gender differences.

Data availability statement

The original contributions presented in the study are included in the article/Supplementary Material, further inquiries can be directed to the corresponding author.

Ethics statement

The studies involving humans were approved by the Ethical committee of Ningbo University. The studies were conducted in accordance with the local legislation and institutional requirements. The participants provided their written informed consent to participate in this study.

References

- Adouni, M., Alkhatib, F., Gouissem, A., and Faisal, T. R. (2023). Knee joint biomechanics and cartilage damage prediction during landing: a hybrid MD-FE-musculoskeletal modeling. *PloS one* 8, e0287479. doi:10.1371/journal.pone.0287479
- Adouni, M., Faisal, T. R., Gaith, M., and Dhaher, Y. Y. (2019). A multiscale synthesis: characterizing acute cartilage failure under an aggregate tibiofemoral joint loading. *Biomech. Model. Mechan.* 18, 1563–1575. doi:10.1007/s10237-019-01159-9
- Aljohani, M., and Kipp, K. (2020). Use of self-organizing maps to study sex-and speed-dependent changes in running biomechanics. *Hum. Mov. Sci.* 72, 102649. doi:10.1016/j.humov.2020.102649
- Al Khatib, F., Gouissem, A., Mbarki, R., and Adouni, M. (2022). Biomechanical characteristics of the knee joint during gait in obese versus normal subjects. *Int. J. Environ. Res. Public Health* 2, 989. doi:10.3390/ijerph19020989
- Almonroeder, T. G., and Benson, L. C. (2017). Sex differences in lower extremity kinematics and patellofemoral kinetics during running. *J. Sports. Sci.* 35, 1575–1581. doi:10.1080/02640414.2016.1225972
- Bazuelo-Ruiz, B., Durá-Gil, J. V., Palomares, N., Medina, E., and Llana-Belloch, S. (2018). Effect of fatigue and gender on kinematics and ground reaction forces variables in recreational runners. *PeerJ* 6, e4489. doi:10.7717/peerj.4489

Author contributions

XJ: Data curation, Investigation, Methodology, Writing—original draft. IB: Investigation, Methodology, Validation, Writing—review and editing. JS: Conceptualization, Project administration, Writing—review and editing. YF: Formal Analysis, Methodology, Writing—review and editing. YG: Conceptualization, Funding acquisition, Investigation, Resources, Writing—review and editing.

Funding

The author(s) declare that financial support was received for the research, authorship, and/or publication of this article. This study was sponsored by the Zhejiang Provincial Natural Science Foundation of China for Distinguished Young Scholars (LR22A020002), Zhejiang Provincial Key Research and Development Program of China (2021C03130), Zhejiang Provincial Natural Science Foundation (LTGY23H040003), Ningbo key R&D Program (2022Z196), Research Academy of Medicine Combining Sports, Ningbo (No. 2023001), the Project of NINGBO Leading Medical and Health Discipline (Nos 2022-F15 and 2022-F22), Ningbo Natural Science Foundation (2022J1CGY010532, 2022J1CGY010607), Public Welfare Science and Technology Project of Ningbo, China (2023S145), and Zhejiang Rehabilitation Medical Association Scientific Research Special Fund (ZKKY2023001).

Conflict of interest

The authors declare that the research was conducted in the absence of any commercial or financial relationships that could be construed as a potential conflict of interest.

Publisher's note

All claims expressed in this article are solely those of the authors and do not necessarily represent those of their affiliated organizations, or those of the publisher, the editors and the reviewers. Any product that may be evaluated in this article, or claim that may be made by its manufacturer, is not guaranteed or endorsed by the publisher.

- Besson, T., Macchi, R., Rossi, J., Morio, C. Y., Kunimasa, Y., Nicol, C., et al. (2022). Sex differences in endurance running. *Sports Med.* 52, 1235–1257. doi:10.1007/s40279-022-01651-w
- Boyer, K. A., Freedman Silvernail, J., and Hamill, J. (2017). Age and sex influences on running mechanics and coordination variability. *J. Sports. Sci.* 35, 2225–2231. doi:10.1080/02640414.2016.1265139
- Breine, B., Malcolm, P., Galle, S., Fiers, P., Frederick, E. C., and De Clercq, D. (2019). Running speed-induced changes in foot contact pattern influence impact loading rate. *Eur. J. Sport Sci.* 19, 774–783. doi:10.1080/17461391.2018.1541256
- Buist, I., Bredeweg, S. W., Bessem, B., Van Mechelen, W., Lemmink, K. A., and Dierckx, R. L. (2010). Incidence and risk factors of running-related injuries during preparation for a 4-mile recreational running event. *Br. J. Sports. Med.* 44, 598–604. doi:10.1136/bjsm.2007.044677
- Cavanagh, P. R., and Kram, R. (1989). Stride length in distance running: velocity, body dimensions, and added mass effects. *Med. Sci. Sports. Exerc.* 21, 467–479. doi:10.1249/00005768-198908000-00020
- Chang, H. B., and Cen, X. Z. (2024). Can running technique modification benefit patellofemoral pain improvement in runners? A systematic review and meta-analysis. *Int. J. Biomed. Eng. Technol.* 45, 83–101. doi:10.1504/IJBET.2024.138706
- Chang, Y.-H., Huang, H.-W. C., Hamerski, C. M., and Kram, R. (2000). The independent effects of gravity and inertia on running mechanics. *J. Exp. Biol.* 203, 229–238. doi:10.1242/jeb.203.2.229
- Davis, I. S., Bowser, B. J., and Mullineaux, D. R. (2016). Greater vertical impact loading in female runners with medically diagnosed injuries: a prospective investigation. *Br. J. Sports. Med.* 50, 887–892. doi:10.1136/bjsports-2015-094579
- Dempster, J., Duthiel, F., and Ugbole, U. C. (2021). The prevalence of lower extremity injuries in running and associated risk factors: a systematic review. *Phys. Act. Health* 5, 133–145. doi:10.5334/paah.109
- Dorris, H., Oh, J., and Jacobson, N. (2024). Wearable movement data as a potential digital biomarker for chronic pain: an investigation using deep learning. *Phys. Act. Health* 8, 83–92. doi:10.5334/paah.329
- Floria, P., Sánchez-Sixto, A., Harrison, A. J., and Ferber, R. (2019). The effect of running speed on joint coupling coordination and its variability in recreational runners. *Hum. Mov. Sci.* 66, 449–458. doi:10.1016/j.humov.2019.05.020
- Francis, P., Whatman, C., Sheerin, K., Hume, P., and Johnson, M. I. (2019). The proportion of lower limb running injuries by gender, anatomical location and specific pathology: a systematic review. *J. Sport. Sci. Med.* 18, 21–31.
- Fukuchi, R. K., Fukuchi, C. A., and Duarte, M. (2017). A public dataset of running biomechanics and the effects of running speed on lower extremity kinematics and kinetics. *PeerJ* 5, e3298. doi:10.7717/peerj.3298
- Gao, Z., Zhu, Y., Fang, Y., Fekete, G., Kovács, A., Baker, J. S., et al. (2023). Automated recognition of asymmetric gait and fatigue gait using ground reaction force data. *Front. Physiol.* 14, 1159668. doi:10.3389/fphys.2023.1159668
- Girard, O., Morin, J.-B., Ryu, J., Read, P., and Townsend, N. (2019). Running velocity does not influence lower limb mechanical asymmetry. *Front. Sports Act. Living* 1, 36. doi:10.3389/fspor.2019.00036
- Grabowski, A. M., and Kram, R. (2008). Effects of velocity and weight support on ground reaction forces and metabolic power during running. *J. Appl. Biomech.* 24, 288–297. doi:10.1123/jab.24.3.288
- Greenhalgh, A. (2012). Gender differences in the kinetics and kinematics of distance running: implications for footwear design. *Int. J. Sports. Sci. Eng.* 6, 118–128.
- Hamner, S. R., and Delp, S. L. (2013). Muscle contributions to fore-aft and vertical body mass center accelerations over a range of running speeds. *J. Biomech.* 46, 780–787. doi:10.1016/j.jbiomech.2012.11.024
- Hollander, K., Rahlf, A. L., Wilke, J., Edler, C., Steib, S., Junge, A., et al. (2021). Sex-specific differences in running injuries: a systematic review with meta-analysis and meta-regression. *Sports Med.* 51, 1011–1039. doi:10.1007/s40279-020-01412-7
- Hollis, C. R., Koldenhoven, R. M., Resch, J. E., and Hertel, J. (2019). Running biomechanics as measured by wearable sensors: effects of speed and surface. *Sports Biomech.* 20, 521–531. doi:10.1080/14763141.2019.1579366
- Isherwood, J., Wang, H., and Sterzing, T. (2021). Running biomechanics and running shoe perception of Chinese men and women. *Footwear Sci.* 13, 55–67. doi:10.1080/19424280.2020.1853827
- Jiang, X., Xu, D., Fang, Y., Bíró, I., Baker, J. S., and Gu, Y. (2023). PCA of running biomechanics after 5 km between novice and experienced runners. *Bioengineering* 10, 876. doi:10.3390/bioengineering10070876
- Jiang, X., Zhou, H., Quan, W., Hu, Q., Baker, J. S., and Gu, Y. (2021). Ground reaction force differences between bionic shoes and neutral running shoes in recreational male runners before and after a 5 km run. *Int. J. Environ. Res. Public Health* 18, 9787. doi:10.3390/ijerph18189787
- Logan, S., Hunter, I., Hopkins, J. T., Feland, J. B., and Parcell, A. C. (2010). Ground reaction force differences between running shoes, racing flats, and distance spikes in runners. *J. Sport. Sci. Med.* 9, 147–153.
- Matijevich, E. S., Branscombe, L. M., Scott, L. R., and Zelik, K. E. (2019). Ground reaction force metrics are not strongly correlated with tibial bone load when running across speeds and slopes: implications for science, sport and wearable tech. *PLoS one* 14, e0210000. doi:10.1371/journal.pone.0210000
- Mercer, J. A., Bezodis, N. E., Russell, M., Purdy, A., and Delion, D. (2005). Kinetic consequences of constraining running behavior. *J. Sport. Sci. Med.* 4, 144–152.
- Mo, S., Lau, F. O., Lok, A. K., Chan, Z. Y., Zhang, J. H., Shum, G., et al. (2020). Bilateral asymmetry of running gait in competitive, recreational and novice runners at different speeds. *Hum. Mov. Sci.* 71, 102600. doi:10.1016/j.humov.2020.102600
- Morin, J.-B., Slawinski, J., Dorel, S., Couturier, A., Samozino, P., Brughelli, M., et al. (2015). Acceleration capability in elite sprinters and ground impulse: push more, brake less? *J. Biomech.* 48, 3149–3154. doi:10.1016/j.jbiomech.2015.07.009
- Muñoz-Jimenez, M., Latorre-Román, F., Soto-Hermoso, V., and García-Pinillos, F. (2015). Influence of shod/unshod condition and running speed on foot-strike patterns, inversion/eversion, and vertical foot rotation in endurance runners. *J. Sports. Sci.* 33, 2035–2042. doi:10.1080/02640414.2015.1026377
- Munro, C. F., Miller, D. I., and Fuglevand, A. J. (1987). Ground reaction forces in running: a reexamination. *J. Biomech.* 20, 147–155. doi:10.1016/0021-9290(87)90306-X
- Napier, C., Maclean, C., Maurer, J., Taunton, J., and Hunt, M. (2018). Kinetic risk factors of running-related injuries in female recreational runners. *Scand. J. Med. Sci. Sports* 28, 2164–2172. doi:10.1111/sms.13228
- Orendurff, M. S., Kobayashi, T., Tulchin-Francis, K., Tullock, A. M. H., Villarosa, C., Chan, C., et al. (2018). A little bit faster: lower extremity joint kinematics and kinetics as recreational runners achieve faster speeds. *J. Biomech.* 71, 167–175. doi:10.1016/j.jbiomech.2018.02.010
- Petersen, J., Nielsen, R. O., Rasmussen, S., and Sørensen, H. (2014). Comparisons of increases in knee and ankle joint moments following an increase in running speed from 8 to 12 to 16 km·h⁻¹. *Clin. Biomech.* 29, 959–964. doi:10.1016/j.clinbiomech.2014.09.003
- Portney, L. G., and Watkins, M. P. (2009). *Foundations of clinical research: applications to practice*. Upper Saddle River, NJ: Pearson/Prentice Hall.
- Quan, W., Ren, F., Sun, D., Fekete, G., and He, Y. (2021). Do novice runners show greater changes in biomechanical parameters? *Appl. Bionics Biomech.* 2021, 1–8. doi:10.1155/2021/8894636
- Schache, A. G., Blanch, P. D., Dorn, T. W., Brown, N. A., Rosemond, D., and Pandey, M. G. (2011). Effect of running speed on lower limb joint kinetics. *Med. Sci. Sport Exerc.* 43, 1260–1271. doi:10.1249/MSS.0b013e3182084929
- Schache, A. G., Dorn, T. W., Williams, G. P., Brown, N. A., and Pandey, M. G. (2014). Lower-limb muscular strategies for increasing running speed. *J. Orthop. Sport. Phys.* 44, 813–824. doi:10.2519/jospt.2014.5433
- Sinclair, J., and Selve, J. (2015). Sex differences in knee loading in recreational runners. *J. Biomech.* 48, 2171–2175. doi:10.1016/j.jbiomech.2015.05.016
- Stickley, C. D., Andrews, S. N., Parke, E. A., and Hetzler, R. K. (2018). The effectiveness of scaling procedures for comparing ground reaction forces. *J. Biomech.* 77, 55–61. doi:10.1016/j.jbiomech.2018.06.021
- Van Der Worp, M. P., Ten Haaf, D. S., Van Cingel, R., De Wijer, A., Nijhuis-Van Der Sanden, M. W., and Staal, J. B. (2015). Injuries in runners: a systematic review on risk factors and sex differences. *PLoS ONE* 10, e0114937. doi:10.1371/journal.pone.0114937
- Van Gent, R., Siem, D., Van Middelkoop, M., Van Os, A., Bierma-Zeinstra, S., and Koes, B. (2007). Incidence and determinants of lower extremity running injuries in long distance runners: a systematic review. *Br. J. Sports. Med.* 41, 469–480. doi:10.1136/bjsm.2006.033548
- Van Mechelen, W. (1992). Running injuries: a review of the epidemiological literature. *Sports Med.* 14, 320–335. doi:10.2165/00007256-199214050-00004
- Vannatta, C. N., Heinert, B. L., and Kernozek, T. W. (2020). Biomechanical risk factors for running-related injury differ by sample population: a systematic review and meta-analysis. *Clin. Biomech.* 75, 104991. doi:10.1016/j.clinbiomech.2020.104991
- Williams, L. R., Standiford, T. W., Creer, A., Fong, H. B., and Powell, D. W. (2020). Ground reaction force profiles during inclined running at iso-efficiency speeds. *J. Biomech.* 113, 110107. doi:10.1016/j.jbiomech.2020.110107
- Wright, A. A., Taylor, J. B., Ford, K. R., Siska, L., and Smoliga, J. M. (2015). Risk factors associated with lower extremity stress fractures in runners: a systematic review with meta-analysis. *Br. J. Sports. Med.* 49, 1517–1523. doi:10.1136/bjsports-2015-094828
- Xu, D., Quan, W., Zhou, H., Sun, D., Baker, J. S., and Gu, Y. (2022). Explaining the differences of gait patterns between high and low-mileage runners with machine learning. *Sci. Rep.* 12, 2981. doi:10.1038/s41598-022-07054-1
- Yokoyama, H., Ogawa, T., Kawashima, N., Shinya, M., and Nakazawa, K. (2016). Distinct sets of locomotor modules control the speed and modes of human locomotion. *Sci. Rep.* 6, 36275. doi:10.1038/srep36275
- Yu, L., Mei, Q., Xiang, L., Liu, W., Mohamad, N. I., István, B., et al. (2021). Principal component analysis of the running ground reaction forces with different speeds. *Front. Bioeng. Biotechnol.* 9, 629809. doi:10.3389/fbioe.2021.629809
- Zadpoor, A. A., and Nikooyan, A. A. (2011). The relationship between lower-extremity stress fractures and the ground reaction force: a systematic review. *Clin. Biomech.* 26, 23–28. doi:10.1016/j.clinbiomech.2010.08.005
- Zhou, H., and Ugbole, U. C. (2024). Biomechanical analysis of lower limbs based on unstable condition sports footwear: a systematic review. *Phys. Act. Health* 8, 93–104. doi:10.5334/paah.332



OPEN ACCESS

EDITED BY

Zhen (Jeff) Luo, University of Technology
Sydney, Australia

REVIEWED BY

Ahmed Alshareef,
University of South Carolina, United States
Antonio Pellegrino,
University of Bath, United Kingdom

*CORRESPONDENCE

S. G. Ganpule,
✉ ganpule@me.iitr.ac.in

RECEIVED 17 May 2024

ACCEPTED 02 August 2024

PUBLISHED 27 August 2024

CITATION

Pandey PK and Ganpule SG (2024) Investigation of dynamic responses of skin simulant against fragment impact through experiments and concurrent computational modeling. *Front. Bioeng. Biotechnol.* 12:1422685. doi: 10.3389/fbioe.2024.1422685

COPYRIGHT

© 2024 Pandey and Ganpule. This is an open-access article distributed under the terms of the [Creative Commons Attribution License \(CC BY\)](https://creativecommons.org/licenses/by/4.0/). The use, distribution or reproduction in other forums is permitted, provided the original author(s) and the copyright owner(s) are credited and that the original publication in this journal is cited, in accordance with accepted academic practice. No use, distribution or reproduction is permitted which does not comply with these terms.

Investigation of dynamic responses of skin simulant against fragment impact through experiments and concurrent computational modeling

Punit Kumar Pandey¹ and S. G. Ganpule^{1,2*}

¹Department of Mechanical and Industrial Engineering, Indian Institute of Technology Roorkee, Roorkee, India, ²Department of Design, Indian Institute of Technology Roorkee, Roorkee, India

Perforation of the skin by fragment impact is a key determinant of the severity of an injury and incapacitation during modern asymmetric warfare. Computational models validated against experimental data are thus desired for simulating the responses of a skin simulant against fragment impact. Toward this end, experiments and concurrent computational modeling were used to investigate the dynamic responses of the skin simulant against fragment impact. Fragment simulating projectiles (FSPs) of masses 1.10 g and 2.79 g were considered herein, and the responses of the skin simulant were investigated in terms of the threshold velocity, energy density, peak displacement, and failure mechanisms. The results illustrate numerous salient aspects. The skin simulant failure involved cavity shearing followed by elastic hole enlargement, and these results were sensitive to the strain rate. The best agreement between the simulated and experimental results was achieved when the input stress–strain curves to the simulation were based on the full spectrum of strain rates. When a single stress–strain curve corresponding to a specific strain rate was used as the input, the threshold velocity and peak displacement of the skin simulant were either underpredicted or overpredicted depending on the strain rate considered. The threshold velocity was also sensitive to the input failure strain; here, the best agreement was obtained when the failure strain was based on the theoretical limiting strain. When the FSP materials were changed to plastics, the threshold velocities increased by up to 33%; however, the energy densities and generated stresses exceeded the contusion and laceration thresholds of the skin.

KEYWORDS

skin simulant, fragment, impact, threshold velocity, failure, strain rate sensitivity

Abbreviations: FSP, fragment simulating projectile; V_i , impact velocity; V_r , residual velocity; V_{th} , threshold velocity; E_{th} , threshold energy; A , cross-sectional (c/s) area; E_{th}/A , energy density; BB, ball bearing; PVC, polyvinyl chloride; SHPB, split Hopkinson pressure bar.

1 Introduction

The skin is the outermost part of the human body and acts as an initial barrier against any external loading (Limbert, 2017; Chanda, 2018; Wahlsten et al., 2019). Perforation of the skin by high-velocity projectiles, such as bullets and fragments, is considered sufficient for human incapacitation on the battlefield (Allen and Sperrazza, 1956; Henderson, 2010; Breeze and Clasper, 2013; Zecevic et al., 2015). The majority of skin-penetrating combat injuries are caused by fragments generated from ammunition such as improvised explosive devices, grenades, antipersonnel warheads, and explosive mines (Bowyer et al., 1995; Champion et al., 2003; Breeze and Clasper, 2013; Carr et al., 2017; Regasa et al., 2018). Thus, skin or skin simulant response against fragment impact is a topic of considerable interest.

The ballistic responses of skin or skin simulants against fragment impact are typically evaluated experimentally by launching fragments on skin or skin simulants at high velocities (Sperrazza and Kokinakis, 1968; Breeze and Clasper, 2013; Breeze et al., 2013; Hazell, 2022). Conducting large numbers of such ballistic experiments is challenging and costly. Thus, robust computational models benchmarked against experiments are desired as alternatives (Breeze and Clasper, 2013; Breeze et al., 2014). Accordingly, existing constitutive models of soft materials can be calibrated using the ballistic experiment data; these calibrated constitutive models and their material parameters or stress-strain response curves may be used in higher-order computational models, such as 3D head and 3D anatomically accurate computational models. Higher-order models have greater utility in simulating real-life scenarios, such as penetrating ballistic impact.

There are several challenges in simulating the responses of skin or skin simulants under high loading rates. First, the available experimental stress-strain responses of the skin or skin simulants at high strain rates ($>10^1 \text{ s}^{-1}$) are sparse. Most of the available data are acquired at quasi-static strain rates (Joodaki and Panzer, 2018; Jor et al., 2013; Kalra et al., 2016; Sachs et al., 2021). A few investigations provide stress-strain response at high strain rates under compression (Shergold et al., 2006; Joodaki and Panzer, 2018); such data are not readily available for skin under tension, and only one study (Khodadadi et al., 2019b) provides the simulant data under tension (albeit not up to failure).

Obtaining data under skin tension is more challenging than compression owing to several technical challenges in the tensile testing of such soft materials on the split Hopkinson pressure bar (SHPB). The specimen geometries, such as dog-bone shape, and critical connections between the specimen and input/output bars pose significant technical difficulties during tensile loading (Chen, 2016; Guo and Wang, 2020; Upadhyay et al., 2021). Designing and attaching grips to the tensile specimens to effectively transfer uniaxial loads to their gage sections (i.e., measurement zones) are particularly tricky. Achieving appropriate load transfer without inducing any damage to the specimen edges and minimizing the edge effects thus becomes critical. Improper gripping techniques can also lead to the development of a triaxial stress state within the specimen (Upadhyay et al., 2021). Moreover, fully characterizing the tensile properties of soft materials (up to the failure point) often requires large tensile deformations, which are challenging to achieve within the limitations of the SHPB system (Siviour and Jordan, 2016).

First, high-strain-rate experimental data of skin or skin simulants required for constitutive modeling are lacking, and

most of the computational modeling of skin or skin simulant responses in literature use either quasi-static data or data obtained at a single strain rate (see Joodaki and Panzer (2018) and the references therein). Second, the experimental data for relevant loading scenarios (e.g., fragment or bullet impact) desired for model calibration and validation are scant. Toward this end, to bridge the aforementioned gaps, we simulated the responses of a skin simulant under fragment impact. The high-strain-rate stress-strain responses of the skin simulant under tension were retrieved from literature, and the data were extrapolated adequately up to the failure strains (estimated theoretically). The sensitivity of the model to the material parameters (i.e., input stress-strain curves and failure strain), thickness of the skin simulant, as well as shape, size, and material of the fragment were investigated.

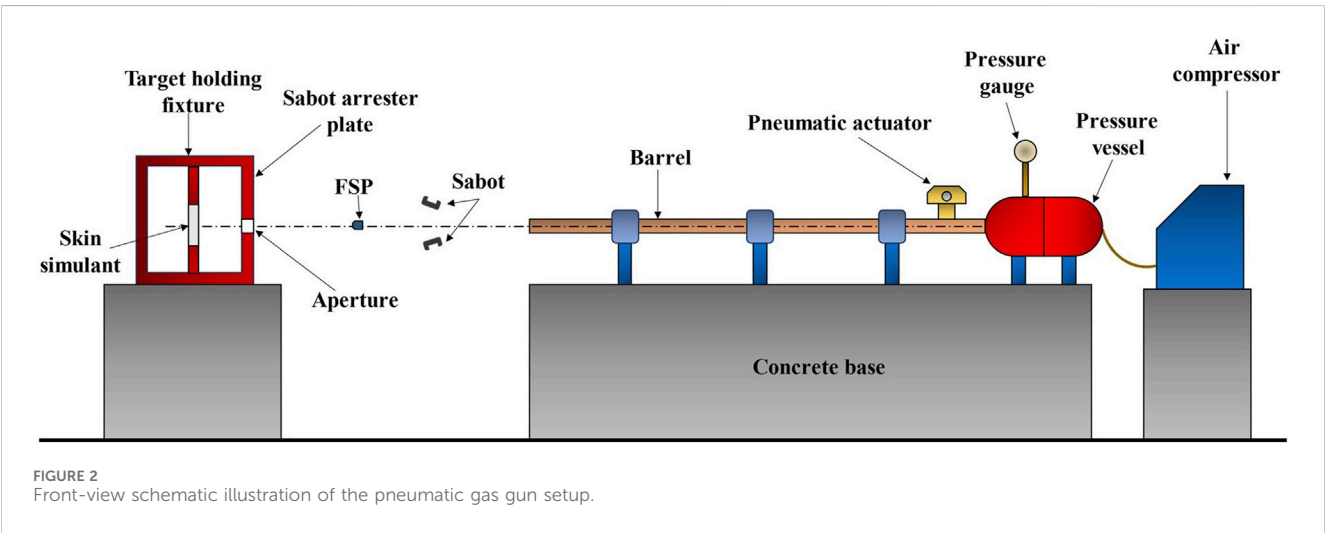
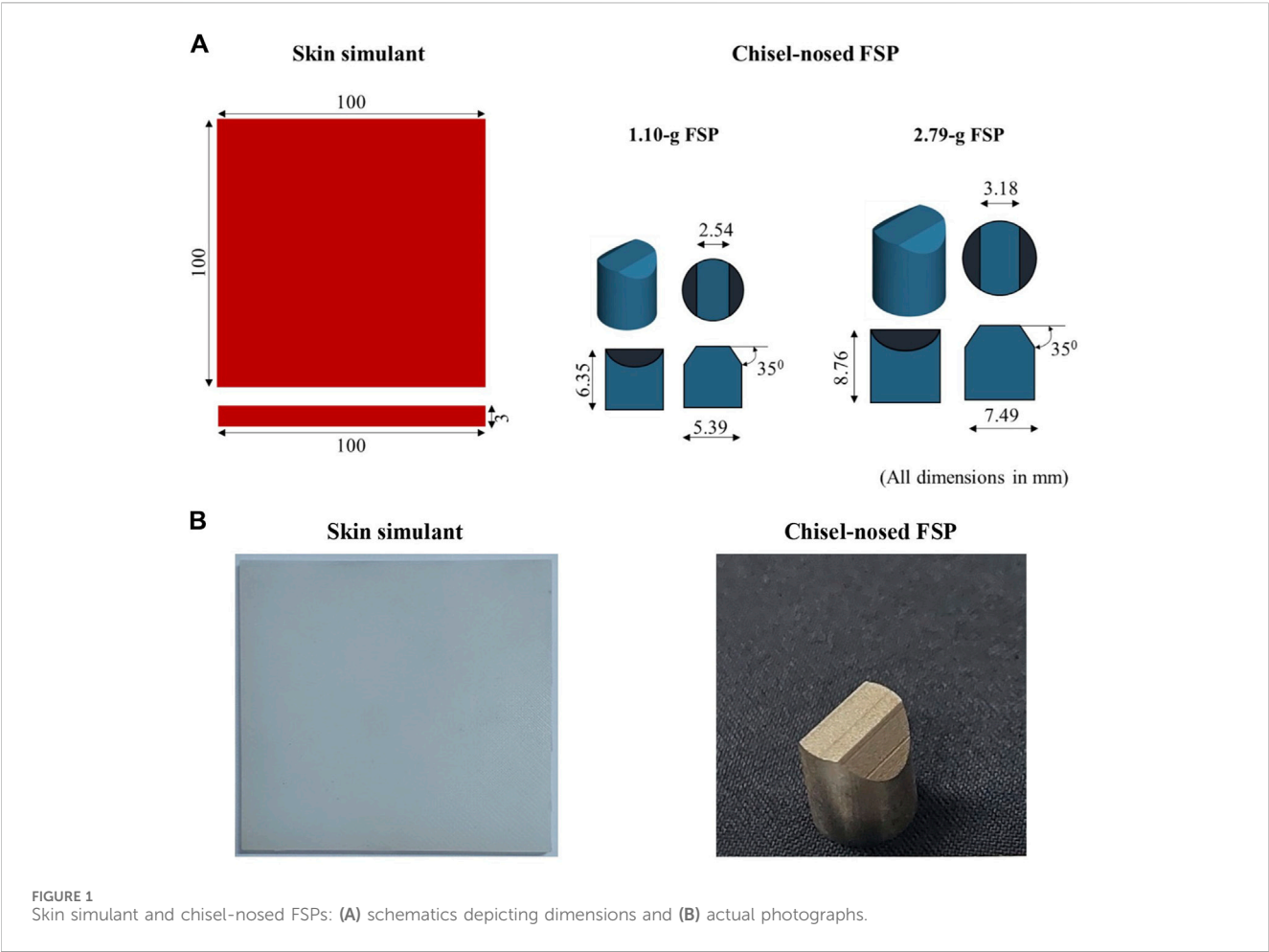
2 Method

2.1 Experiments

Experiments were conducted to investigate the responses of the skin simulant to fragment impact. These data were used to validate the numerical model. A two-part silicone substance (Smooth-On, Inc., Macungie, PA) with a shore hardness of 30A was used as the skin simulant; this material exhibits a stress-strain response similar to human skin (Chanda et al., 2017; Chanda and Upchurch, 2018; Marechal et al., 2021). The skin simulant was prepared in the form of a rectangular plate of size 100 mm \times 100 mm \times 3 mm, where the 3 mm thickness was selected based on the average thickness documented for human skin in literature (Sperrazza and Kokinakis, 1968; Yoganandan and Pintar, 1997; Chanda, 2018). Mild-steel chisel-nosed fragment simulating projectiles (FSPs) of masses 1.10 g and 2.79 g (Figure 1) were manufactured according to the standard sizes specified in NATO STANAG 2920 (NATO, 2003; Bolduc and Jager, 2016).

A pneumatic gas gun setup (Figure 2) was used to conduct the experiments. The setup comprised an air compressor, a pressure vessel, a pressure gage, an electric actuator, and a seamless barrel. To accommodate FSPs of different sizes in a fixed-diameter barrel, a split sabot having an outer diameter equal to the diameter of the barrel with a cavity tailored to the specific FSP size was used. The sabots were accelerated by the sudden release of compressed air from the pressure vessel. After exiting the barrel, the sabot opened due to air drag, and the FSP moved faster than the sabot owing to its lower mass and lower air drag. Upon traveling further, the sabot was arrested by the sabot arrester plate, allowing the FSP to pass through an aperture and impact the skin simulant.

The required velocities of the FSPs were attained by adjusting the effective barrel length (i.e., distance between the sabot and open end of the barrel) and compressed air pressure in the pressure vessel. The FSPs were launched onto the skin simulant in the velocity range of 49–170 m s^{-1} , with a variation of $\pm 5 \text{ m s}^{-1}$ for a given effective barrel length and air pressure. A high-speed camera (Phantom v411, Vision Research, Inc., Wayne, NJ) was installed to capture the ballistic test events; the captured high-speed images were used to obtain the velocities of the FSPs. The frame rate of the high-speed



camera was 16,000 frames per second. A total of 46 impact experiments were performed. Table 1 presents the impact velocities (V_i) and corresponding results of the impact events (i.e., perforation or non-perforation) for the two FSPs. Each sample was impacted once to avoid the response effects from previous loading.

2.2 Finite-element model

2.2.1 Finite-element discretization

A finite-element model was considered to simulate the responses of the skin simulant against fragment impact. The model was built to mimic the experiments described in Section 2.1. The skin simulant

TABLE 1 Observed results (perforation or non-perforation) at various impact velocities (V_i) for the two FSPs.

1.10 g FSP			2.79 g FSP		
Exp. No.	V_i (m/s)	Result	Exp. No.	V_i (m/s)	Result
1	41	Non-perforation	1	49	Non-perforation
2	53	Non-perforation	2	56	Non-perforation
3	62	Non-perforation	3	57	Non-perforation
4	67	Non-perforation	4	59	Non-perforation
5	68	Non-perforation	5	63	Non-perforation
6	71	Non-perforation	6	65	Non-perforation
7	71	Non-perforation	7	66	Non-perforation
8	76	Non-perforation	8	68	Perforation
9	79	Non-perforation	9	69	Perforation
10	83	Non-perforation	10	76	Perforation
11	89	Non-perforation	11	76	Perforation
12	88	Perforation	12	81	Perforation
13	88	Perforation	13	85	Perforation
14	88	Perforation	14	86	Perforation
15	90	Perforation	15	89	Perforation
16	90	Perforation	16	93	Perforation
17	92	Perforation	17	93	Perforation
18	92	Perforation	18	94	Perforation
19	95	Perforation	19	97	Perforation
20	95	Perforation	20	97	Perforation
21	96	Perforation	21	100	Perforation
22	99	Perforation	22	108	Perforation
23	136	Perforation	23	135	Perforation

and FSPs were discretized using linear hexahedral elements with reduced integration (ELFORM 1 of LS-DYNA) (Figure 3). The central part (i.e., impact zone) of the skin simulant having dimensions of 10 mm × 10 mm × 3 mm was finely meshed with elements of size 0.4 mm × 0.4 mm × 0.4 mm. The mesh converged (<5% difference in the residual velocity) at this mesh resolution (Supplementary Figure S1). To optimize the computational efficiency, the mesh size was increased gradually toward the outer boundaries of the skin simulant plate up to a mesh size of 1.6 mm × 2.0 mm × 0.4 mm. This resulted in 60,000 elements for the skin simulant. All four edges of the skin simulant were fully constrained to replicate the experimental boundary conditions. The 1.10 g and 2.79 g FSPs were meshed with elements of size 0.25 mm × 0.25 mm × 0.25 mm, resulting in 24,288 and 50,880 hexahedral elements, respectively.

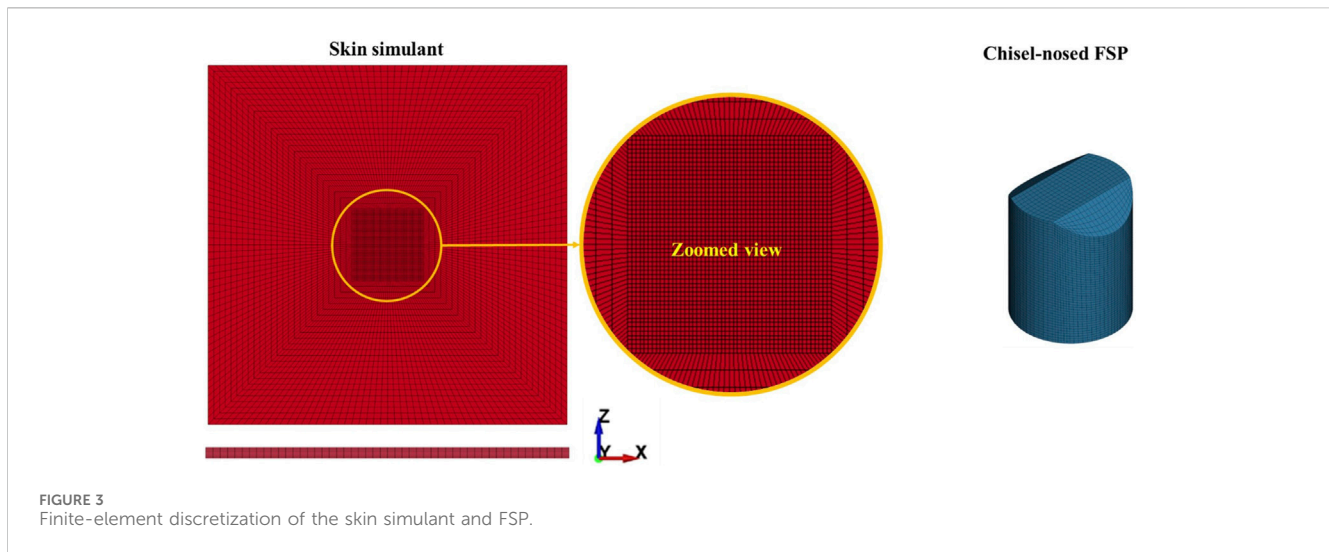
A two-way, surface-to-surface eroding contact was used to model the interactions between the skin simulant and FSPs. The eroding contact is useful when there is a probability of element deletion upon meeting the failure criterion. The contact surfaces in the eroding contact were continuously updated to account for

the element deletions (LSTC, 2021). Simulations were performed using a non-linear, transient, explicit dynamic scheme in which the initial velocity of the FSPs was set according to the experimental impact velocity (V_i). The simulations were then performed with 32 processors (Intel® Xeon® Gold 6,134, processor speed 3.00 GHz) and a massively parallel processing (MPP) solver in LS-DYNA V971 R4.7 (LSTC, 2021). Time steps of the order of 10^{-9} s were used in the simulations to ensure stability; each simulation iteration required ~22 min of CPU time for a total simulation time of 1.5 ms.

2.2.2 Constitutive model of the skin simulant

The skin simulant was modeled using a phenomenological material; this material model is based on the Ogden hyperelasticity (Ogden, 1972), whose energy function is given by

$$W = \sum_{i=1}^3 \sum_{j=1}^m \frac{\mu_j}{\alpha_j} \left(\lambda_i^{\alpha_j} - 1 \right) + K (J - 1 - \ln J), \tag{1}$$



where μ (shear modulus), α (strain hardening exponent), and K (bulk modulus) are the material constants; λ is the principal stretch, $\lambda^* = \lambda J^{-1/3}$ is the deviatoric principal stretch, and $J = \lambda_1 \lambda_2 \lambda_3$ is the Jacobian.

The principal stresses can be computed as

$$\sigma_i = \frac{1}{\lambda_p \lambda_q} \frac{\partial W}{\partial \lambda_i} \quad (2)$$

The subscripts p and q in Equation 2 refer to the two coordinate directions perpendicular to i . Substituting Equation 1 into Equation 2, we have

$$\sigma_i = \frac{1}{\lambda_p \lambda_q} \frac{\partial W}{\partial \lambda_i} = \sum_{j=1}^m \frac{\mu_j}{J} \left[\lambda_i^{\alpha_j} - \sum_{p=1}^3 \frac{\lambda_p^{\alpha_j}}{3} \right] + K \frac{J-1}{J}. \quad (3)$$

Kolling et al. (2007) proposed the equivalent forms of Equations 1, 3 as follows

$$W = \sum_{i=1}^3 g(\lambda_i) + K (J - 1 - \ln J). \quad (4)$$

$$\sigma_i = \frac{1}{J} \left(f(\lambda_i) - \frac{1}{3} \sum_{j=1}^3 f(\lambda_j) \right) + K \frac{J-1}{J}. \quad (5)$$

Equations 4, 5 facilitate the calculation of $g(\lambda)$, $f(\lambda)$, W , and σ directly from the tabulated data without the need to explicitly calculate the fitting parameters μ and α . This approach is especially convenient when modeling rate-dependent hyperelastic behaviors (Kolling et al., 2007). Next, $g(\lambda_i)$ and $f(\lambda_i)$ can be estimated from the uniaxial stress-strain data (Equations 6–14). $g(\lambda_i)$ is defined as

$$g(\lambda_i) = \sum_{j=1}^m \frac{\mu_j}{\alpha_j} (\lambda_i^{\alpha_j} - 1). \quad (6)$$

$g(\lambda)$ can be written in terms of $W_u(\lambda)$, where $W_u(\lambda)$ is the deformation energy per unit undeformed volume expressed in terms of the uniaxial engineering stress (σ_u) and uniaxial engineering strain (ϵ_u) as follows:

$$W_u(\lambda) = \int_0^\epsilon \sigma_u d\epsilon_u = \int_0^\lambda \sigma_u d\lambda. \quad (7)$$

Equation 1 can be evaluated for the uniaxial test. For a nearly incompressible material, $J \approx 1$ and $\lambda_p^* \approx \lambda_q^* \approx \lambda_i^* - \frac{1}{2}$. Substituting these in Equation 1, we have

$$W_u(\lambda_i) = \sum_{j=1}^m \frac{\mu_j}{\alpha_j} (\lambda_i^{\alpha_j} - 1) + 2 \sum_{j=1}^m \frac{\mu_j}{\alpha_j} (\lambda_i^{*\alpha_j - \frac{\alpha_j}{2}} - 1), \quad (8)$$

$$W_u(\lambda_i^{-\frac{1}{2}}) = \sum_{j=1}^m \frac{\mu_j}{\alpha_j} (\lambda_i^{*\alpha_j - \frac{\alpha_j}{2}} - 1) + 2 \sum_{j=1}^m \frac{\mu_j}{\alpha_j} (\lambda_i^{*\alpha_j} - 1), \quad (9)$$

and hence

$$g(\lambda_i) = W_u(\lambda_i) - 2W_u(\lambda_i^{-\frac{1}{2}}) + 4W_u(\lambda_i^{\frac{1}{2}}) - \dots \quad (10)$$

Equation 10 represents an infinite series. However, the terms of the series can be truncated upon meeting a desired tolerance. For

$$|\lambda_i^{(-1/2)^x} - 1| \leq 0.01$$

$$g(\lambda_i) = W_u(\lambda_i - 1) + \sum_{x=1}^{\infty} (-2)^x W_u(\lambda_i^{(-1/2)^x} - 1). \quad (11)$$

Next, $f(\lambda_i)$ is evaluated as

$$f(\lambda_i) = \sum_{j=1}^m \mu_j \lambda_i^{\alpha_j}. \quad (12)$$

$f(\lambda_i)$ can be written in terms of σ_u as (for the detailed derivation, please refer to Kolling et al. (2007))

$$f(\lambda_i) = \lambda_i \sigma_{ui} (\lambda_i - 1) + \lambda_i^{(-\frac{1}{2})} \sigma_{ui} (\lambda_i^{(-\frac{1}{2})} - 1) + \lambda_i^{(\frac{1}{2})} \sigma_{ui} (\lambda_i^{(\frac{1}{2})} - 1) + \dots \quad (13)$$

where the terms of the series in Equation 13 can be truncated upon meeting a desired tolerance. For

$$|\lambda_i^{(-1/2)^x} - 1| \leq 0.01$$

$$f(\lambda_i) = \lambda_i \sigma_{ui} (\lambda_i - 1) + \sum_{x=1}^{\infty} \lambda_i^{(-1/2)^x} \sigma_{ui} \times (\lambda_i^{(-1/2)^x} - 1). \quad (14)$$

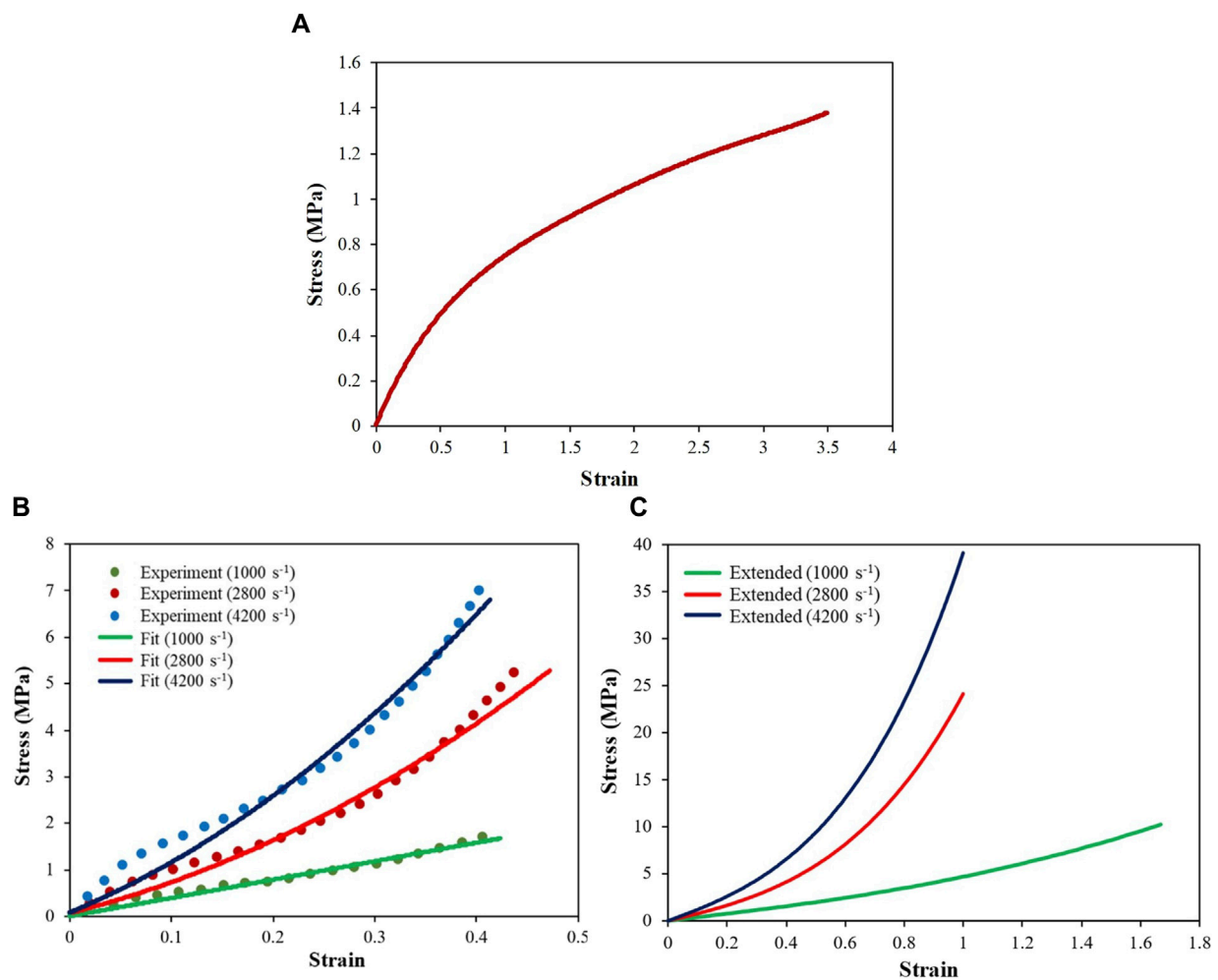


FIGURE 4
Engineering stress–strain responses of the skin simulant at different strain rates: **(A)** quasi-static response; **(B)** high-strain-rate responses fitted with stress–strain curves using experimental data (Khodadadi et al., 2019b); **(C)** extended stress–strain curves up to failure strain.

Equation 5 provides an exact fit to the experimental uniaxial stress–strain curves. Kolling et al. (2007) showed that although this model needs only the uniaxial stress–strain response, it yields satisfactory results for various types of loading and is not limited to only uniaxial loading.

Equation 5 considers the strain rate effect by permitting the users to input several uniaxial engineering stress–strain curves (in tabulated form), each corresponding to a different strain rate. When the strain rate in the simulation differs from the input strain rate (and associated stress–strain response), the model determines the constitutive behavior by interpolating between the input stress–strain curves. The model described above was implemented as MAT-181 in LS-DYNA (LSTC, 2021). The rate-dependent stress–strain response under uniaxial tension was adopted from literature (Khodadadi et al., 2019a; Khodadadi et al., 2019b), and a similar response was assumed for compression. At the quasi-static strain rate (Figure 4A), the experimental stress response was available up to failure strain. However, at higher strain rates (i.e., 1,000 s⁻¹, 2,800 s⁻¹, and 4,200 s⁻¹), the experimental stress response (Figure 4B) was available up to a strain of ~0.40. We extended each stress–strain curve (Figure 4C) corresponding to the higher strain rates up to the limiting failure strain by fitting the experimental data using Equation 3. The

limiting or maximum possible failure strain at each strain rate was estimated by fitting the experimental data using a Gent model (details below). These extended stress–strain data were used as the inputs to the simulation. The stress–strain data at each strain rate were input in tabular form. The strain energy and principal stresses at each time step were calculated using Equations 4, 5.

Since the experimental data up to failure strain were not available at high strain rates, we estimated the limiting strains by fitting the experimental stress–strain curve at each strain rate using the Gent (Gent, 1996; Rashid et al., 2014) hyperelastic strain energy function (Equation 15). Note that we used the same experimental stress–strain curves at each strain rate for both the Ogden and Gent models. The Gent model facilitates estimation of the limiting chain extensibility (Horgan and Saccomandi, 2003; Upadhyay et al., 2021):

$$W = -\frac{\mu}{2} J_m \ln \left(1 - \frac{I_1 - 3}{J_m} \right), \quad (15)$$

where the shear modulus μ and chain extensibility parameter J_m are the fitting parameters; J_m denotes the maximum value of $I_1 - 3$,

TABLE 2 Estimated failure strains from the Gent model.

Strain rate (s^{-1})	Failure strain, ϵ_m (mm mm $^{-1}$)
1,000	1.67
2,800	1.02
4,200	1

which represents the fully stretched state (i.e., limiting state, $W \rightarrow \infty$).

$$\therefore J_m = (I_1)_m - 3. \quad (16)$$

For the uniaxial case,

$$(I_1)_m = \lambda_m^2 + \frac{2}{\lambda_m}, \quad (17)$$

$$\lambda_m = 1 + \epsilon_m, \quad (18)$$

where λ_m is the maximum or limiting stretch and ϵ_m is the limiting strain. Once J_m is determined, I_{1m} , λ_m , and ϵ_m can be obtained using Equations 16–18. Since ϵ_m represents the strain at the fully stretched state of the material, we refer to ϵ_m as the failure strain. The estimated failure strain at each strain rate is presented in Table 2.

In addition to the aforementioned stress–strain data, density and bulk modulus values of 1,080 kg m $^{-3}$ and 2.5 GPa, respectively, were used (Mühr, 2005; Smooth-on). The FSPs were modeled as linear and elastic components, and mild steel was used as the FSP material unless stated otherwise.

2.3 Ballistic response estimation

The ballistic responses of the skin simulant were estimated through both experiments and simulations by evaluation the key metrics, namely, threshold velocity (V_{th}), threshold energy (E_{th}), energy density (E_{th}/A), residual velocity (V_r), and peak deformation of the skin simulant.

2.3.1 Threshold velocity (V_{th})

V_{th} is defined as the minimum FSP velocity required to induce perforation. In the simulation, V_{th} was obtained through an iterative process, where the FSP velocity was incremented by 1 m s $^{-1}$ until perforation was observed. In the experiments, the FSPs were launched with a range of impact velocities, resulting in both perforation and non-perforation of the skin simulant. V_{th} was subsequently determined based on these experimental conditions using a statistical approach in accordance with the NATO STANAG 2920 standard (NATO, 2003). V_{th} was calculated from the arithmetic mean of six impact velocities to account for the experimental scatter. These six velocities comprised three minimum velocities that caused perforation and three maximum velocities that did not cause perforation.

2.3.2 Threshold energy (E_{th}) and energy density (E_{th}/A)

Here, E_{th} is the kinetic energy corresponding to V_{th} of the respective FSP. Then, E_{th}/A is the ratio of E_{th} to the cross-sectional area of the FSP (A). Thus, E_{th}/A normalizes the threshold energy of

the FSP by its cross-sectional area. The energy density is a particularly useful metric for comparing the threshold energies across multiple projectiles.

2.3.3 Residual velocity (V_r)

V_r is the velocity of the FSP after complete perforation of the skin simulant. A comparative analysis of V_r was conducted across a range of V_i values in both the experiments and simulations.

2.3.4 Peak deformation of the skin simulant

The peak deformation of the skin simulant was quantified by the maximum deformation until the onset of failure for the perforation cases and until unloading for the non-perforation cases. To visually represent the peak deformation in the experiment images, the stretched part of the skin simulant was highlighted with red shading. This technique was employed for better visualization due to blurring of the high-speed images after magnification. A detailed description of the shading protocol is provided in Supplementary Figure S2.

2.4 Parametric studies

The sensitivity of the strain rate to the response of the skin simulant was studied using a full spectrum (i.e., quasi-static, 1,000 s $^{-1}$, 2,800 s $^{-1}$, and 4,200 s $^{-1}$) of stress–strain curves and a single stress–strain curve (corresponding to the specific strain rate) as the inputs. To investigate the effects of the FSP material, two other types of FSPs made of ball bearing (BB) and polyvinyl chloride (PVC) plastics were considered. These FSPs are used as less lethal projectiles during law enforcement operations (Pavier et al., 2015; Jin et al., 2019). The material properties of the various FSPs are tabulated in Table 3. Furthermore, to investigate the influence of skin thickness, we varied the thickness of the simulant in the range of 1–5 mm (Laurent et al., 2007; Joodaki and Panzer, 2018; Chen et al., 2020; Fenton et al., 2020) in increments of 1 mm. For these parametric studies, the FSP of mass 1.10 g was used.

3 Results

3.1 Ballistic responses of the skin simulant

The ballistic responses of the skin simulant were investigated in terms of the V_{th} , E_{th}/A , V_r , deformation, and failure pattern. For each of the aforementioned parameters, the experimental and numerical results are depicted and compared.

3.1.1 Threshold velocity (V_{th}), energy density (E_{th}/A), and residual velocity (V_r)

Table 4 shows the V_{th} and E_{th}/A values for the 1.10 g and 2.79 g FSPs. The V_{th} and E_{th}/A decreased by ~29% and ~33%, respectively, as the mass of the FSP increased from 1.10 g to 2.79 g. The differences in V_{th} and E_{th}/A between the experiments and simulations were within ~10%. Interestingly, in absolute terms, the E_{th}/A value was within a narrow range of 0.12–0.18 J mm $^{-2}$. A reasonable agreement (within ~15%) between the experimental and simulated values was obtained for V_r as well (Figure 5). Note that at all velocities below V_{th} , the FSPs did not perforate the target,

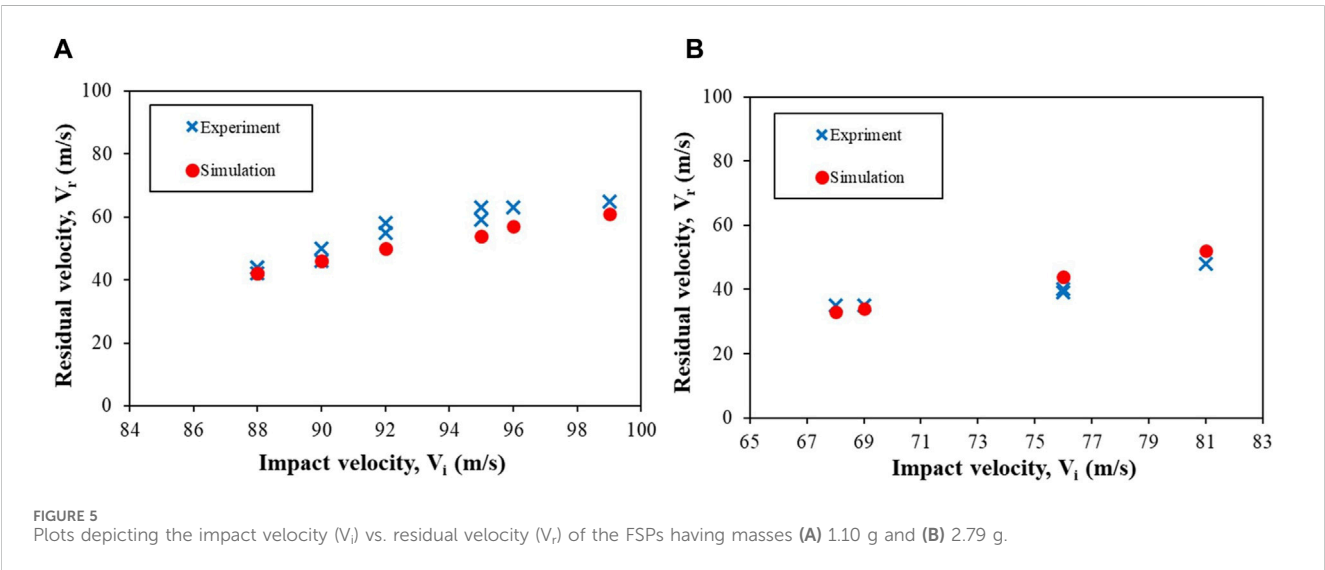
TABLE 3 Material properties of the FSPs.

Material	Density (kg m ⁻³)	Elastic modulus (MPa)	Poisson's ratio
Mild steel ^a (Deka et al., 2008)	7,860	210,000	0.28
BB plastic (Jin et al., 2019)	2,010	2,320	0.30
PVC plastic (Pavier et al., 2015)	1,340	2,300	0.30

^aFor all simulations (except parametric studies), the FSP material was mild steel.

TABLE 4 Threshold velocities (V_{th}) and energy densities (E_{th}/A) of the skin simulant for the 1.10 g and 2.79 g FSPs.

FSP		V_{th} (m/s)		E_{th}/A (J mm ²)	
Mass (g)	Cross-sectional area, A (mm ²)	Experiment	Simulation	Experiment	Simulation
1.10	22.78	86	86	0.18	0.18
2.79	44.11	68	61	0.15	0.12



resulting in $V_r = 0$. Therefore, only velocities that caused perforation of the skin simulant are included in Figure 5.

(higher impact velocities, column iii) of the FSP was lower than that during non-perforation (lower impact velocities, column i).

3.1.2 Deformation of the skin simulant

Figure 6 shows the peak displacements (deformations) of the skin simulant in the direction of impact for various V_i values. Results corresponding to representative V_i values below (column i), similar to (column ii), and above (column iii) V_{th} are depicted. The simulation and experimental results are shown in the upper and lower halves of each panel, respectively. A reasonable qualitative and quantitative agreement was obtained between the experiment and simulation for each case, with the differences in peak displacements between the experiments and simulations being <1.5 mm (i.e., $<5\%$) for the 1.10 g FSP and <4 mm (i.e., $<15\%$) for the 2.79 g FSP. Moreover, the peak displacements in the experiments and simulations occurred at reasonably similar time points. The peak displacement of the skin simulant was a function of V_i . Interestingly, the peak displacement of the skin simulant during perforation

3.1.3 Failure mechanism

Figure 7 shows the typical failure mechanism during the interaction of the FSP with the skin simulant. In each panel, the simulation image (upper half) is presented along with the corresponding experimental image (lower half). The skin simulant failed under the combination of shearing and elastic hole enlargement. Upon initial impact, the FSP stretched the skin simulant to a certain extent (Figure 7ii). Thereafter, the FSP sheared the skin simulant, resulting in the creation of a cavity (Figure 7iii); this was followed by lateral stretching of the skin simulant (Figure 7iv), a phenomenon typically known as elastic hole enlargement (Rosenberg et al., 2012). After complete perforation of the FSP, the laterally stretched skin simulant retracted elastically (Figure 7v). The combination of cavity creation in the stretched state followed by elastic retraction resulted in the final cavity size being

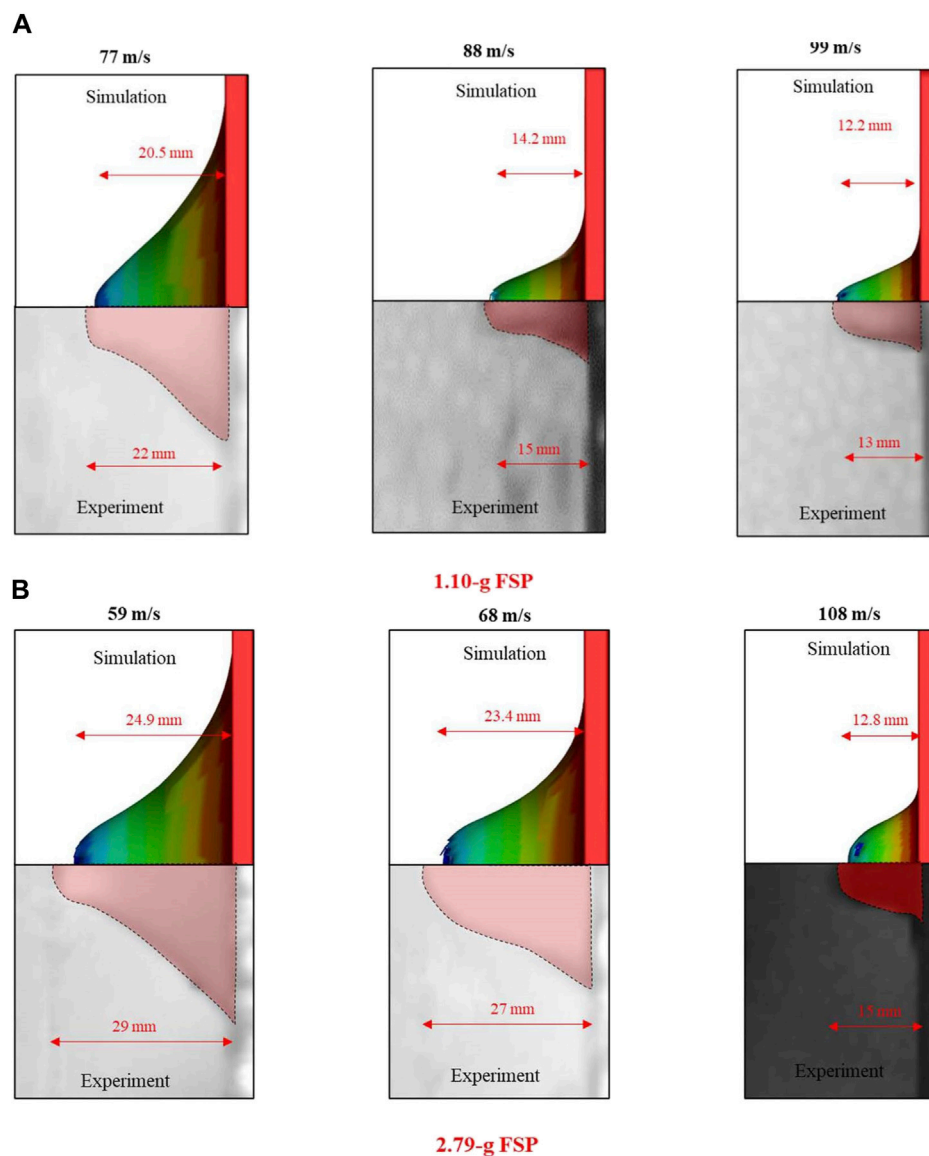


FIGURE 6

Peak displacements of the skin simulant in the direction of impact for different impact velocities (V_i): (A) 1.10 g and (B) 2.79 g FSPs. The first, second, and third columns of each sub-part correspond to impact velocities below, similar to, and above the threshold velocity (V_{th}), respectively. The direction of travel of the FSP is from right to left in the images. In the experiment images, the red area is the stretched skin simulant, black and dark gray areas are parts of the metal fixture, and light gray area is the background of the experimental setup.

smaller than the FSP size (Figure 7vi). The failure patterns between the experiments and simulations were similar.

The mechanism of skin simulant failure is further illustrated using the von Mises stress distribution on the skin simulant's rear surface (Figure 8). The stress concentration was pronounced in the vicinity of the impact zone. As the FSP made initial contact with the skin simulant, its rectangular nose engaged with the skin simulant, generating an elliptical stress contour (Figure 8A). Subsequently, as the skin simulant continued to stretch, the circular section of the FSP came into contact with the simulant, resulting in a circular stress contour (Figures 8B,C). The elements of the skin simulant beneath the impacting face of the FSP experienced extensive stretching, causing them to reach the failure strain. This marked the initiation and propagation of failure (Figure 8D). Once the

element failed in the direction of the thickness, the skin simulant started unloading, resulting in elastic recovery (Figure 8E). The localized failure of the skin simulant (Figure 8D) followed by elastic recovery (Figure 8E) produced the final cavity, whose size was smaller than that of the FSP (Figure 8F).

3.2 Parametric studies

3.2.1 Sensitivity of the skin simulant response to the input stress–strain curve

We investigated the sensitivity of the skin simulant response (i.e., V_{th} and peak displacement) to the input stress–strain curve. By default, the stress–strain curves corresponding to four strain rates

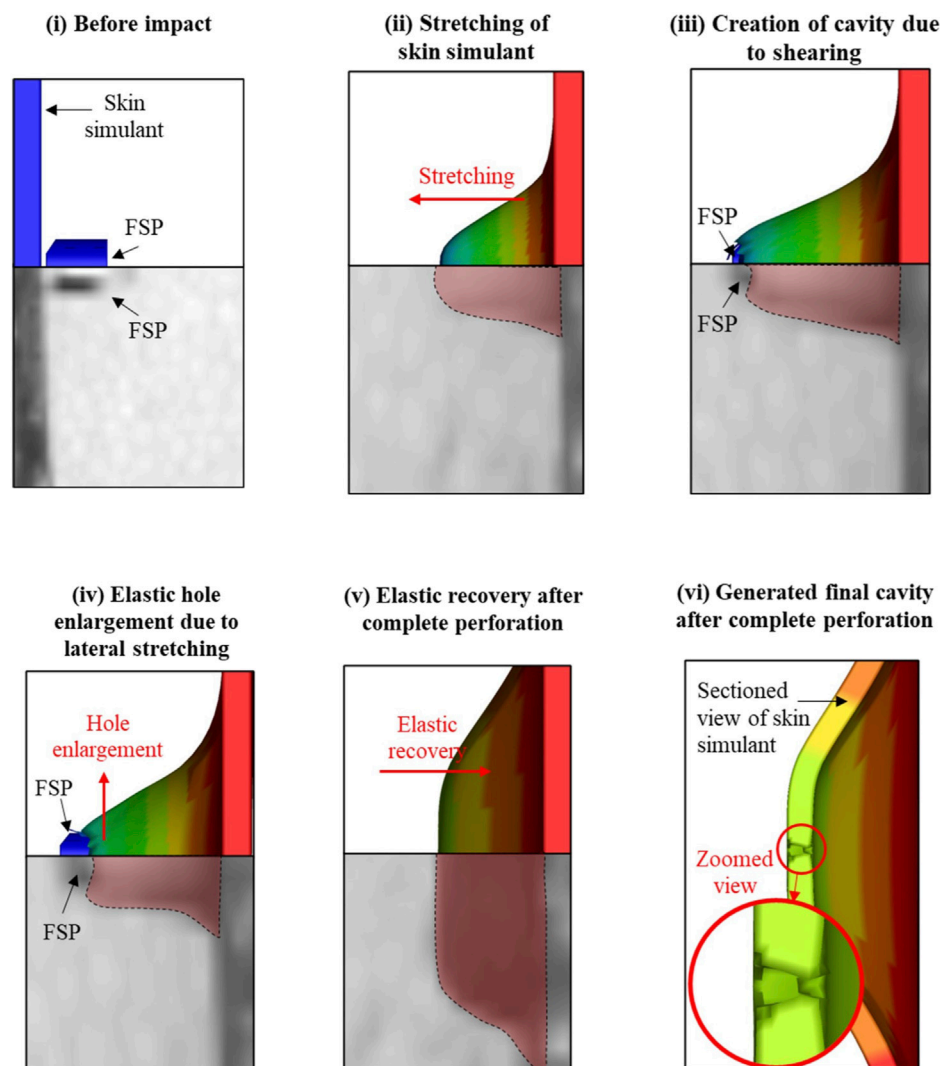


FIGURE 7
Failure process during the interaction of the FSP with the skin simulant.

(i.e., quasi-static, $1,000 \text{ s}^{-1}$, $2,800 \text{ s}^{-1}$, and $4,200 \text{ s}^{-1}$) were used as inputs. In subsequent simulations, the stress-strain curve corresponding to a single strain rate was used as the input (i.e., $1,000 \text{ s}^{-1}$, $2,800 \text{ s}^{-1}$, or $4,200 \text{ s}^{-1}$).

Figure 9 shows the V_{th} values corresponding to the aforementioned cases, which were sensitive to the input stress-strain curves and were hence rate dependent. The maximum value of V_{th} was obtained when the stress-strain curve corresponding to the highest strain rate was used. The V_{th} values from the simulations best matched with the experimentally obtained V_{th} when multiple stress-strain curves corresponding to the full spectrum of strain rates (i.e., quasi-static, $1,000 \text{ s}^{-1}$, $2,800 \text{ s}^{-1}$, and $4,200 \text{ s}^{-1}$) were used.

Strain-rate-dependent behavior was also observed in the peak displacement of the skin simulant. The peak displacements (Figure 10) of the skin simulant at various V_i values were in reasonable agreement with the experimental findings when multiple stress-strain curves corresponding to the full spectrum of strain rates were used. When a single

stress-strain curve corresponding to a strain rate of $1,000 \text{ s}^{-1}$ was used, the peak displacements corresponding to velocities of 88 m s^{-1} and 99 m s^{-1} were overpredicted. On the contrary, when a single stress-strain curve corresponding to the strain rate of either $2,800 \text{ s}^{-1}$ or $4,200 \text{ s}^{-1}$ was used, the peak displacement corresponding to the velocity of 77 m s^{-1} was underpredicted.

3.2.2 Sensitivity of the skin simulant response to the input failure strain

Figure 11 shows the sensitivity of V_{th} to the input failure strain. Note that the developed strain rates in the simulations at the investigated V_i values were in the range of $2,500$ – $4,500 \text{ s}^{-1}$. The limiting strain corresponding to input strain rates of $2,800 \text{ s}^{-1}$ and $4,200 \text{ s}^{-1}$ was $\sim 1 \text{ mm mm}^{-1}$. Hence, the failure strain of $\sim 1 \text{ mm mm}^{-1}$ at these strain rates varied for the parametric studies. When the input failure strain was based on the limiting strain estimated by the Gent model, the difference in V_{th} between the simulation and the experiment was not significant ($<10\%$). However, when the failure

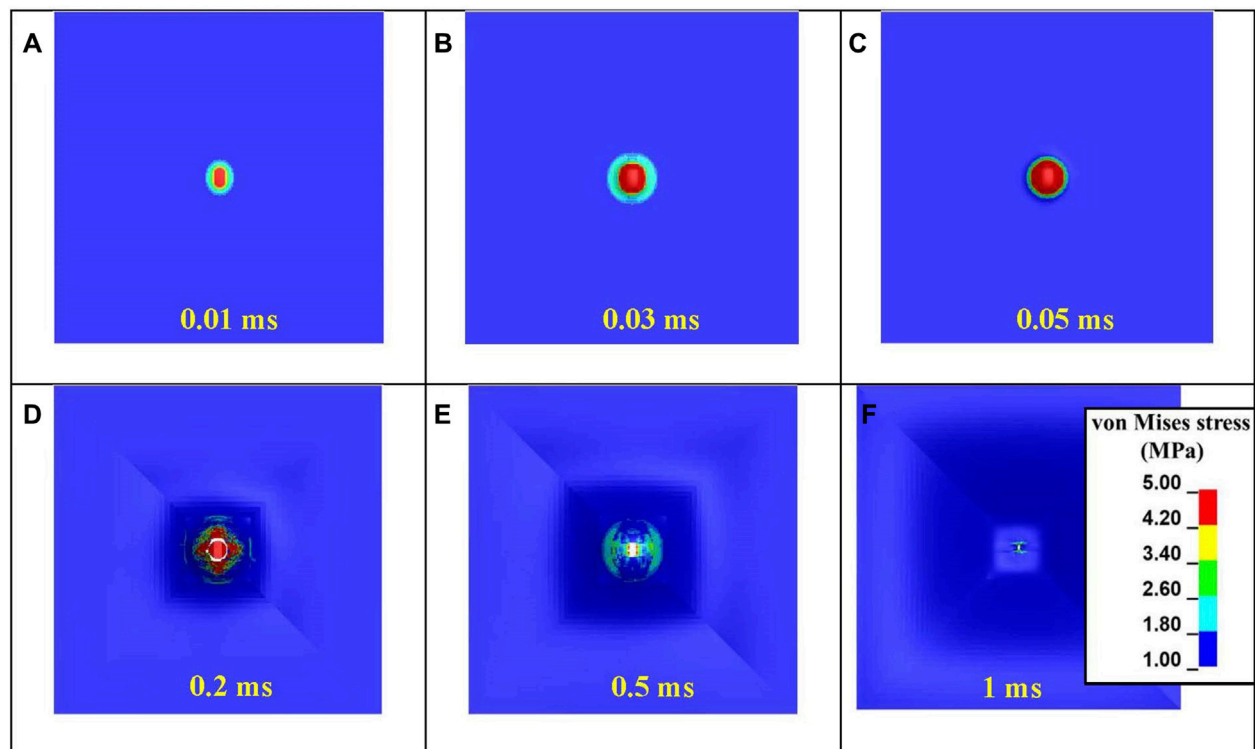


FIGURE 8
Evolution of the von Mises stress during various stages of the interaction of the FSP with the skin simulant: (A) initial contact; (B, C) stretching of the skin simulant; (D) cavity generation; (E) elastic recovery after complete perforation; (F) final cavity generated after complete unloading.

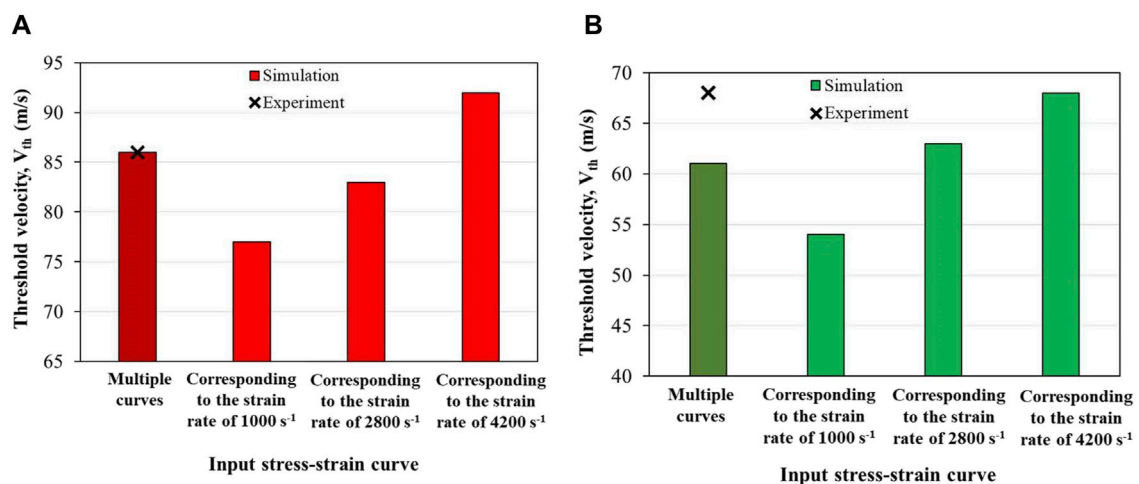


FIGURE 9
Sensitivity of the threshold velocity (V_{th}) to the input stress–strain curve with (A) 1.10 g and (B) 2.79 g FSPs.

strain was less than the limiting strain, the difference in V_{th} between the simulation and experiment was pronounced. For example, for input failure strains of 0.8, 0.6, and 0.4, the V_{th} from the simulations were underpredicted by ~20%, ~33%, and ~52%, respectively, as compared to the V_{th} obtained experimentally. A near-plateau trend in the V_{th} was observed when the input failure strain exceeded the limiting strain.

3.2.3 Effects of FSP velocity (constant mass) and FSP mass (constant impact energy)

Figure 12 shows the displacements of the skin simulant in the direction of impact (Figure 12A), maximum principal strain (Figure 12B), and maximum principal stress (Figure 12C) within a cross section (c/s) on the rear face. Representative results along the x-axis are shown for the 1.10 g FSP. Results for $V_i = 86 \text{ m s}^{-1}$ (low

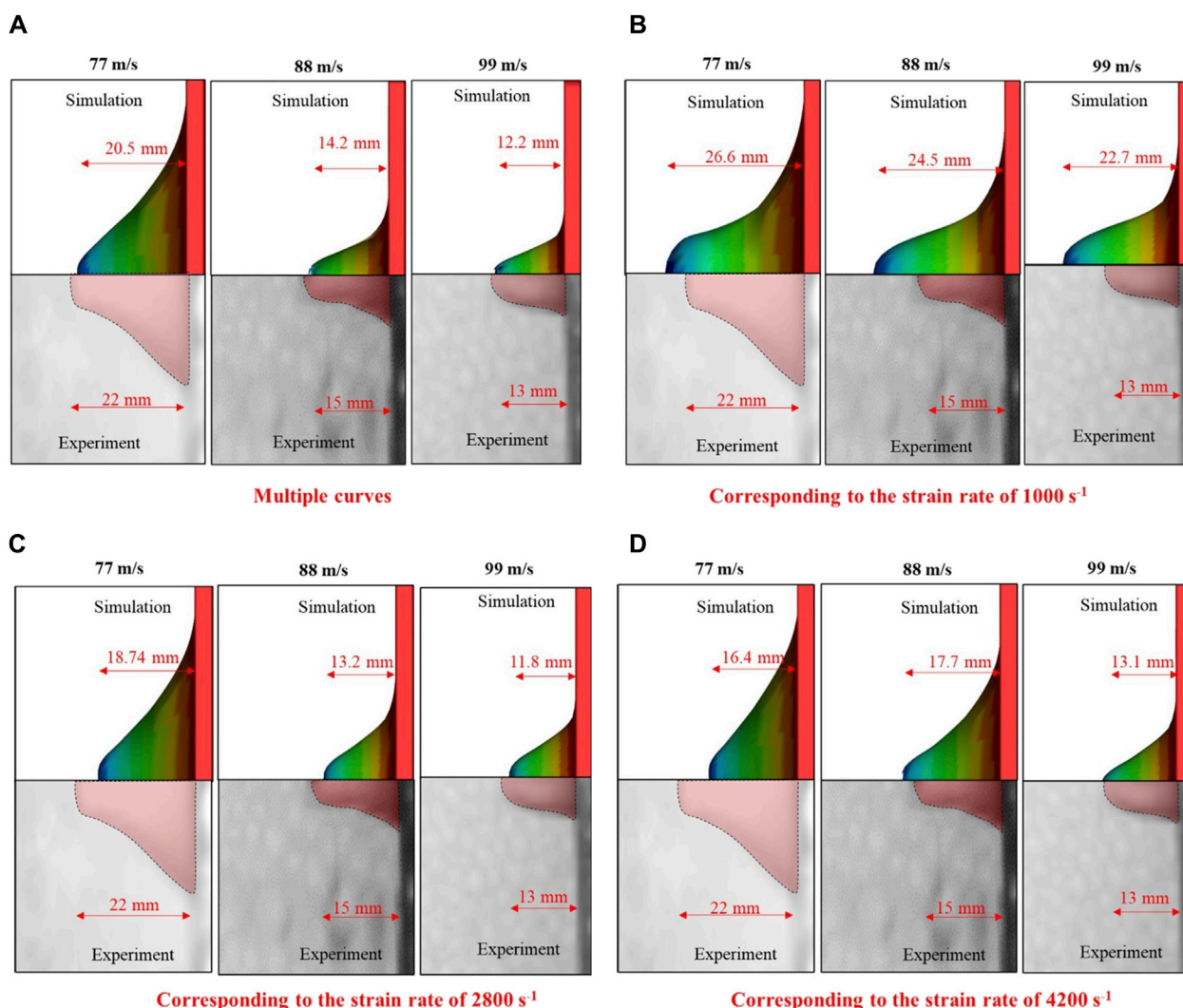


FIGURE 10 Peak displacement of the skin simulant with respect to input stress-strain curve (A) multiple curves (B) corresponding to the strain rate of 1000 s^{-1} (C) corresponding to the strain rate of 2800 s^{-1} (D) corresponding to the strain rate of 4200 s^{-1} . Representative results for 1.10-g FSP are depicted. Similar trends are observed for 2.79-g FSP.

value corresponding to the V_{th} of the 1.10 g FSP) and $V_i = 300 \text{ m s}^{-1}$ (relatively high value) are presented, showing notable distinctions between the low and high V_i cases. The FSP with high V_i induced relatively smaller amplitude deformations (solid lines in Figure 12A) and higher stresses (solid lines in Figure 12C) over a localized area, facilitating relatively easier penetration of the skin simulant over a shorter time ($\sim 0.03 \text{ ms}$). For the low V_i case, relatively larger amplitude deformations (dotted lines in Figure 12A) and lower stresses (dotted lines in Figure 12C) were developed. Interestingly, the penetration process for low velocity required approximately one order of magnitude more time ($\sim 0.3 \text{ ms}$) than the high-velocity impact. Hence, the deformation and stress encompassed a relatively larger c/s area. Similar trends were observed along the y -axis and for the 2.79 g FSP.

When the mass of the FSP was changed (Figure 13) while maintaining the same impact energy (i.e., 5 J), the FSP with a smaller mass induced relatively smaller amplitude deformations (dotted lines in Figure 13A) and higher stresses (dotted lines in

Figure 13C) over a localized area. Thus, for the same impact energy, the FSP with the smaller mass achieved relatively easier perforation due to the higher V_i .

3.2.4 Effect of the FSP material

Table 5 shows the V_{th} and E_{th}/A values when the FSP material was changed from mild steel to BB and PVC plastics. The mass of the FSP was maintained constant (i.e., 1.1 g). Owing to the differences in the densities of BB and PVC plastics with respect to mild steel, the sizes of the BB and PVC FSPs increased proportionally even as the same shape of the FSP was maintained. Compared to the V_{th} of the mild steel FSP, the V_{th} values of BB and PVC FSPs were higher by $\sim 22\%$ and $\sim 33\%$, respectively. These increases in V_{th} are attributed to the larger cross-sectional areas (Table 5), which result in load distributions over wider areas.

Compared to the E_{th}/A of the mild steel FSP, the E_{th}/A of BB and PVC FSPs were lower by $\sim 39\%$ and $\sim 44\%$, respectively. Despite the reductions in E_{th}/A with respect to mild steel, the E_{th}/A values of BB

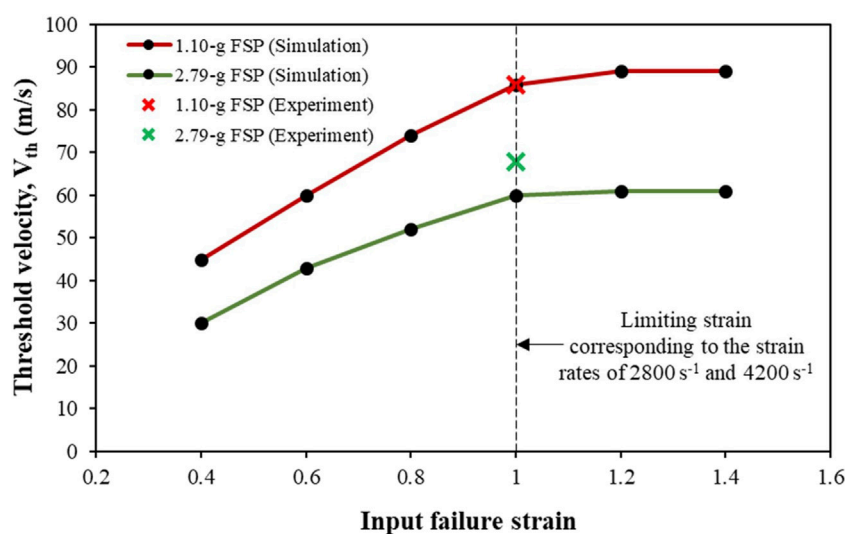


FIGURE 11
Sensitivity of the threshold velocity (V_{th}) to the input failure strain values.

(0.11 J mm⁻²) and PVC (0.10 J mm⁻²) exceeded the proposed contusion threshold of 0.0252 J mm⁻² (Park et al., 2011). Furthermore, considerable stresses were generated (e.g., above the laceration threshold of 1 MPa (Park et al., 2011)) over a larger area (Figure 14).

3.2.5 Effect of the skin simulant thickness

Figure 15 shows V_{th} as a function of the skin simulant thickness, which exhibits a linear relationship ($R^2 = 0.99$).

4 Discussion

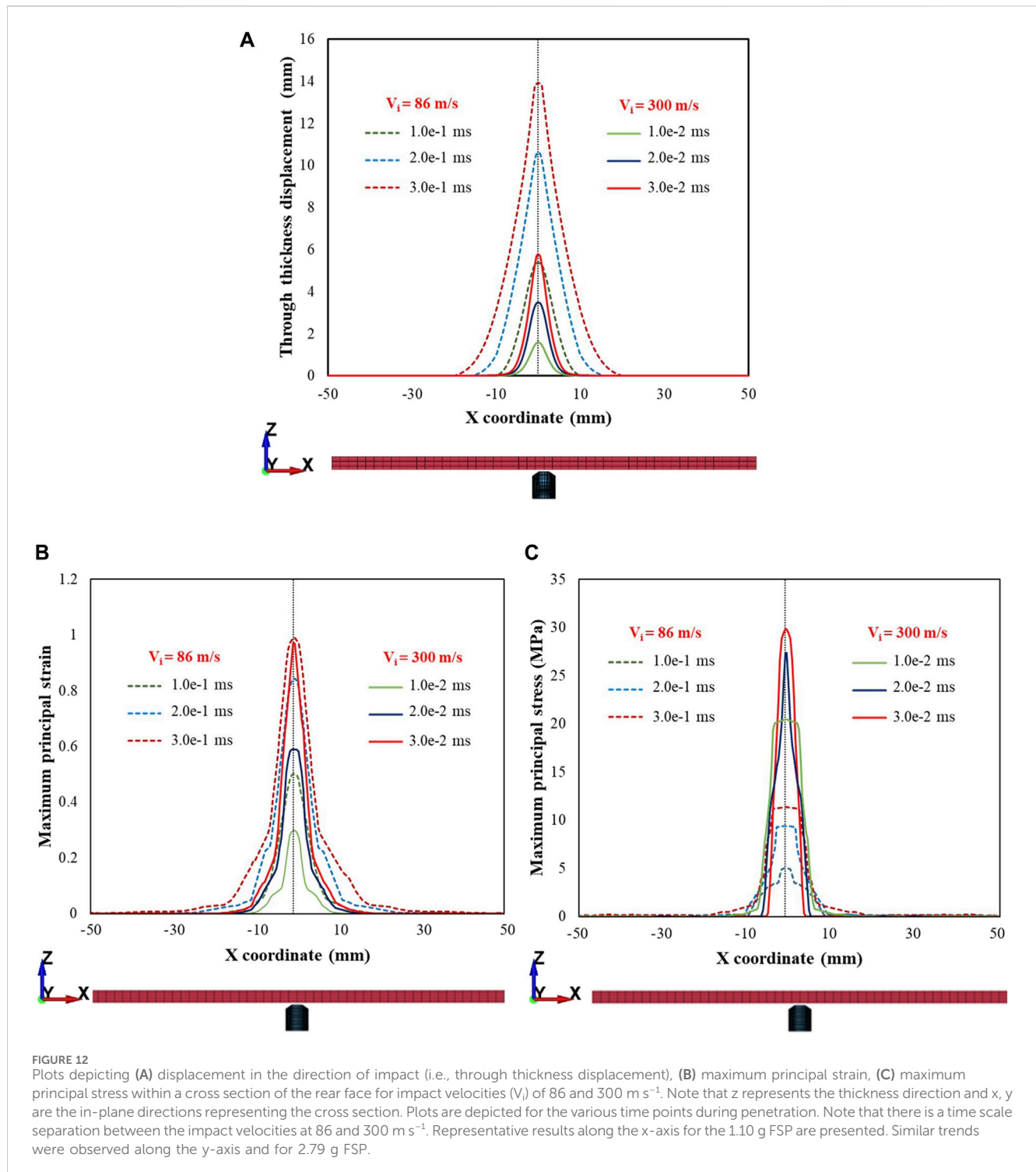
In this work, the responses of the skin simulant to ballistic impact were investigated using experiments and concurrent simulations. Simulations were further used to conduct parametric studies by incorporating the rate-dependent material responses at different strain rates (i.e., quasi-static, 1,000 s⁻¹, 2,800 s⁻¹, and 4,200 s⁻¹). Note that the developed strain rates in the simulations at the investigated impact velocities were in the range of 2,500–4,500 s⁻¹. Hence, the stress-strain curves at the chosen strain rates (i.e., 1,000–4,200 s⁻¹) were found to be suitable and related to the experimental velocity ranges. The full spectrum of stress-strain responses at the aforementioned strain rates were used as the inputs unless stated otherwise.

The V_{th} and E_{th}/A values decreased as the FSP size increased (Table 4). This trend is consistent with observations in literature. For instance, Breeze et al. (2013) estimated V_{50} values (i.e., velocity corresponding to 50% probability of perforation) of chisel-nosed FSPs weighing 0.16 g, 0.49 g, and 1.10 g for perforation of goat skin and noted that the 0.16 g and 1.10 g FSPs offered the highest and lowest V_{50} values, respectively. Breeze and Clasper (2013) also compiled data from various experiments involving fragment impact on either skin or skin simulant, and their comparative analysis revealed a consistent inverse relationship between the fragment size and V_{50} value. Furthermore, the range of E_{th}/A (i.e., 0.12–0.18 J mm⁻²) obtained in this work is commensurate

with that reported in literature for skin or skin simulant perforation (Kneubuehl, 2011; Bir et al., 2012; Jin et al., 2019).

We observed that the V_{th} , E_{th}/A , and peak displacement values of the skin simulant were sensitive to the strain rate (Figures 9, 10). These results demonstrate an interesting paradigm based on the input stress-strain curve. The aforementioned values from the simulations matched reasonably well with those from the experiments (Figures 5, 6; Table 4) when a full spectrum of stress-strain responses at different strain rates were used as the inputs. This is because the material model appropriately interpolates the data at the strain rates realized in the simulations based on the input stress-strain curves. When a single curve was applied, the results did not match with those from experiments. The V_{th} was underpredicted and overpredicted when stress-strain curves corresponding to strain rates of 1,000 s⁻¹ and 4,200 s⁻¹ were used as inputs, respectively (Figure 9). When a single stress-strain curve corresponding to a strain rate of 1,000 s⁻¹ was used, the peak displacements at higher impact velocities (i.e., 88 and 99 m s⁻¹) were overpredicted. On the contrary, when a single stress-strain curve corresponding to a strain rate of either 2,800 s⁻¹ or 4,200 s⁻¹ was used, the peak displacement at a lower V_i (i.e., 77 m s⁻¹) was underpredicted (Figure 10). These responses are attributed to stiffening of the material with increase in the strain rate. Upadhyay et al. (2020, 2021) also reported a similar rate-dependent stiffening response in a similar silicone-based soft material. Similar rate-dependent behaviors were also observed in polymers (Li and Lambros, 2001; Chen et al., 2024). Our results underscore that the strain-rate-dependent material response should be incorporated when modeling skin and skin surrogates under ballistic impact. Currently, very few models incorporate strain-rate-dependent behaviors (see Joodaki and Panzer (2018) and the references therein; Liu et al., 2014).

The failure mechanism of the skin simulant involved shearing followed by elastic hole enlargement (Figures 7, 8). The skin simulant stretched in the direction of impact of the FSP until it reached the failure strain (Figure 7i–iii). The subsequent unloading



phase involved lateral stretching by the FSP as the skin simulant attempted to undergo elastic recovery but was constrained by the presence of the FSP (Figure 7iv), a phenomenon known as elastic hole enlargement. After complete perforation (Figure 7v), the final size of the generated cavity induced by shearing remained smaller than the diameter of the FSP (Figure 7vi). This occurrence of a smaller cavity in the skin simulant compared to the FSP size due to elastic retraction is consistent with findings documented in existing literature (Inchingolo et al., 2011;

Kneubuehl et al., 2011; Baptista et al., 2014; Carr et al., 2014; Serraino et al., 2020).

Interestingly, we observed that the peak displacements of the skin simulant at impact velocities corresponding to perforation were lower than those corresponding to non-perforation (Figures 6, 10). As the velocity of the FSP increases, the rate of loading increases and failure strain decreases (Li and Lambros, 2001; Shergold et al., 2006; Lim et al., 2011; Khatam et al., 2014; Ottenio et al., 2015; Joodaki and Panzer, 2018; Chen et al., 2024). Hence, the deformation becomes

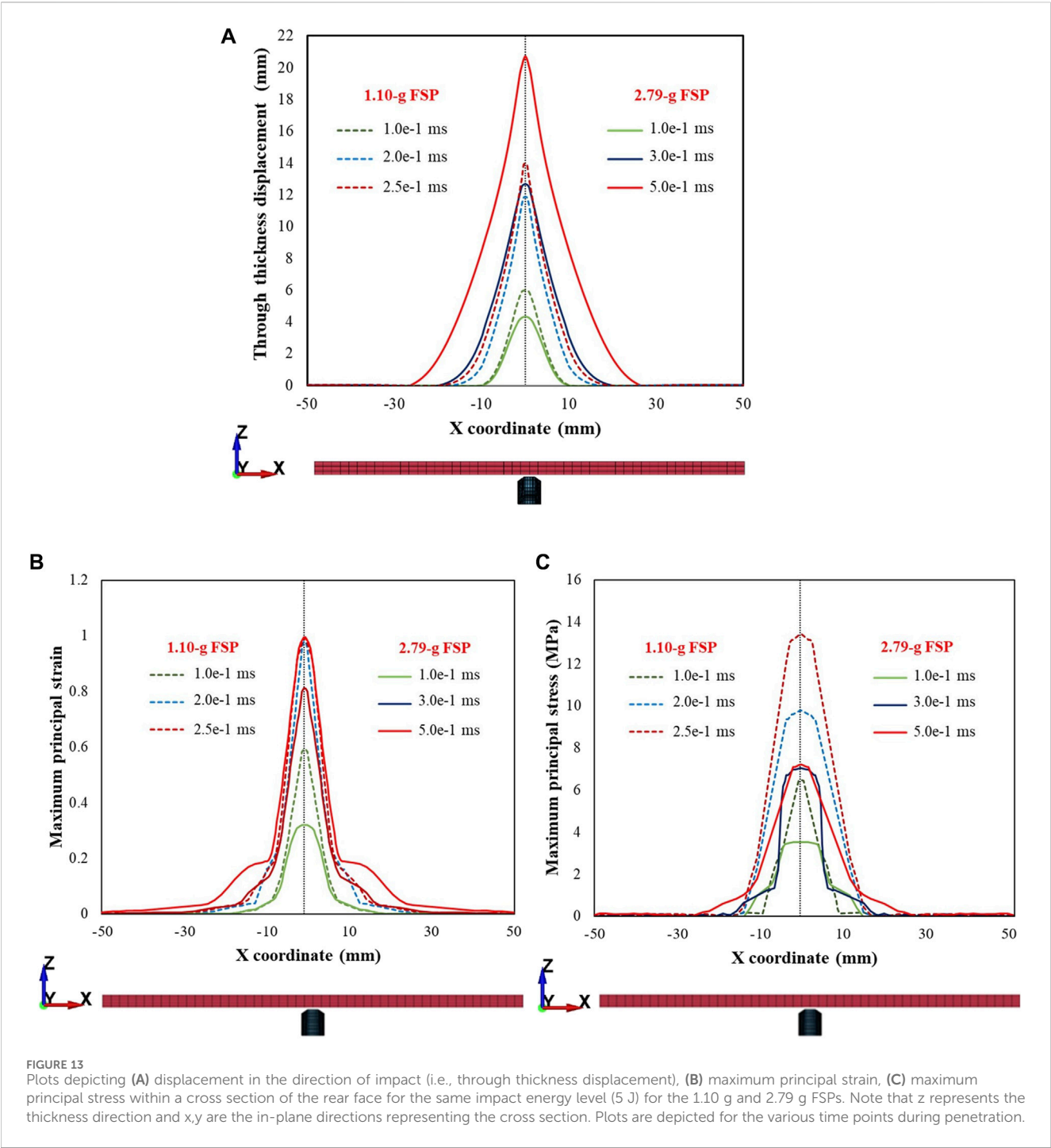


TABLE 5 Effects of the FSP materials on the threshold velocities (V_{th}). Results are presented for the 1.10 g FSPs.

FSP material	Cross-sectional area, A (mm ²)	V_{th} (m/s)	E_{th}/A (J mm ²)
Mild steel	22.72	86	0.18
BB plastic	56.00	105	0.11
PVC plastic	73.60	115	0.10

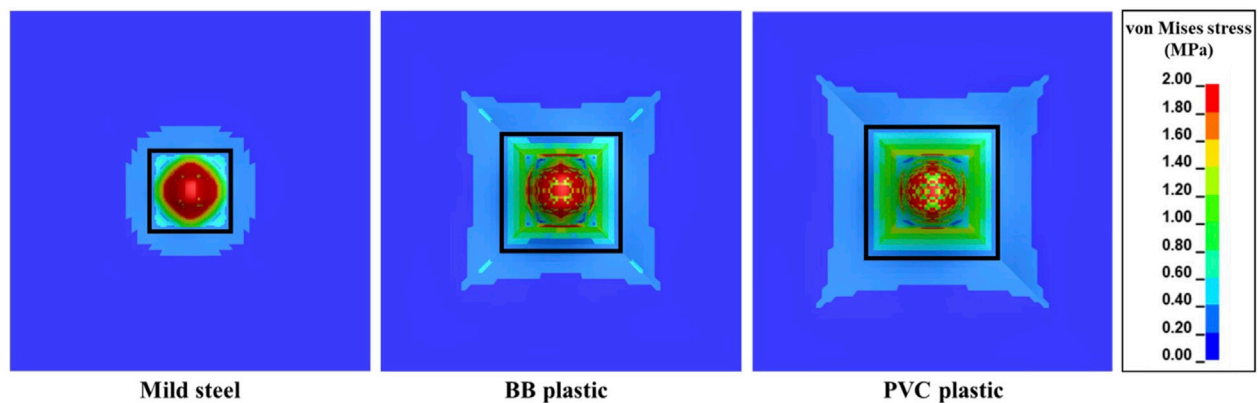


FIGURE 14
von Mises stress contours of the skin simulant during interaction with FSPs made of different materials for an impact velocity (V_i) of 86 m s^{-1} . The von Mises stress in the region bounded by the black rectangle is above the laceration threshold of 1 MPa , indicating increases in the affected area for FSPs made of BB and PVC plastics.

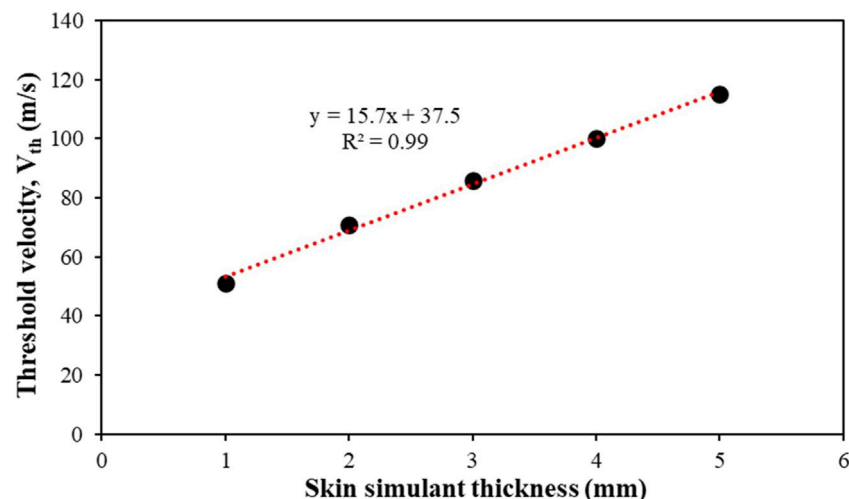


FIGURE 15
Effect of skin simulant thickness on the threshold velocity (V_{th}). Results are presented for the 1.10 g FSP.

more localized with a relatively smaller amplitude (Figures 12A, 13A) and generates high stresses (Figures 12C, 13C) over a small area in a short time. This suggests that failure is stress driven (for additional details, see [Supplementary Material](#)), facilitating relatively easier perforation of the skin simulant at velocities corresponding to perforation (Figures 12, 13). The shorter times required for perforation at higher velocities result in relatively smaller peak displacements of the skin simulant compared to those at lower velocities (Figures 6, 10).

The V_{th} values were sensitive to the input failure strain (Figure 11). Owing to the absence of experimental data on failure strain, we estimated the failure strains using the Gent model, which gives the limiting or maximum extensibility. The V_{th} from the simulation matched the experimental V_{th} (Figure 11) when the input failure strain was based on the estimate from the Gent model (or within 10% of the estimates from the Gent model). For input failure strain values lower than those estimated by the Gent model,

the V_{th} values were underpredicted. The V_{th} exhibited a near-plateau trend when the input failure strain was above the limiting strain estimated by the Gent model. This underscores the importance of the input failure strain value. Our results suggest that the limiting strain obtained from the Gent model is a reasonable estimate of the failure strain. This is especially noteworthy considering the typical lack of high-strain-rate experimental data up to failure strain in literature (Joodaki and Panzer, 2018).

We investigated the influence of the FSP material on the ballistic responses of the skin simulant (Table 5). FSPs made of three different materials (mild steel, BB plastic, and PVC plastic) and having the same mass (1.10 g) were studied. Even though V_{th} increased by 22%–33% with the plastic FSPs, these increases may not be sufficient to qualify plastic FSPs as non-lethal. A few investigations suggest that projectiles made of BB plastic can penetrate the skin (Grocock et al., 2006; Tsui et al., 2010; Jin et al., 2019) when expelled with considerable velocity (90 – 160 m

s^{-1}). Furthermore, the energy densities (Table 5) of the plastic FSPs exceeded the contusion threshold of 0.0252 J mm^{-2} (Park et al., 2011) and generated stresses in the skin simulant by exceeding the laceration threshold of 1 MPa (Park et al., 2011) (Figure 14). Considerable stresses were also generated over larger areas. These observations are critical as plastic projectiles are generally used as non-lethal projectiles to control or disperse crowds during law enforcement (Bir et al., 2005; Rezende-Neto et al., 2009; Bir et al., 2012).

We also found a linear relation between V_{th} and skin simulant thickness (Figure 15). In this work, we used narrow ranges of velocities ($60\text{--}100 \text{ m s}^{-1}$) and masses (1.10 g; 2.79 g) of chisel-nosed FSPs. Hence, in this work, the linear relationship between V_{th} and skin simulant thickness is independent of the FSP velocity and mass. In the future, it would be interesting to investigate whether the linear relation between V_{th} and skin simulant thickness is applicable for wider ranges of velocities, masses, and shapes of the FSPs.

5 Limitations

The present work has a few limitations. In this work, similar stress-strain responses were assumed under compression and tension; this is mainly due to the lack of compression data on the skin simulant used in this work. It should be noted that soft polymeric materials of this class often behave asymmetrically under tension and compression (Donato and Bianchi, 2012; Pellegrino et al., 2015; Siviour and Jordan, 2016; Chen et al., 2024). Efforts will therefore be made in the future to obtain and utilize compression stress-strain data for the skin simulant.

6 Conclusion

In this study, we investigated the rate-dependent ballistic responses of the skin simulant under fragment impact. A finite-element model was developed alongside experimental testing, and reasonable agreement was observed between the numerical simulation and experimental results. The following key conclusions are drawn from this study.

- The threshold velocity (V_{th}) and energy density (E_{th}/A) decrease with increasing size of the FSP.
- The energy density (E_{th}/A) was in a narrow range ($0.12\text{--}0.18 \text{ J mm}^{-2}$) for investigated FSPs.
- The V_{th} and peak displacement of the skin simulant exhibited sensitivity to the strain rate. V_{th} was underpredicted when using a single stress-strain curve corresponding to a strain rate of $1,000 \text{ s}^{-1}$ and overpredicted when using a single stress-strain curve at a strain rate of $4,200 \text{ s}^{-1}$. The closest match between the simulated and experimental V_{th} was achieved when the stress-strain curves were considered across the full spectrum of strain rates (quasi-static, $1,000 \text{ s}^{-1}$, $2,800 \text{ s}^{-1}$, and $4,200 \text{ s}^{-1}$). Similar trends were observed for the peak displacement of the skin simulant.
- The peak displacement of the skin simulant was a function of the impact velocity. The peak displacements of the skin simulant at lower impact velocities (during non-

perforation) were higher compared to those at higher velocities (during perforation). This was attributable to the stress-driven failure.

- The failure mechanism of the skin simulant primarily entailed cavity shearing followed by elastic hole enlargement. The final size of the resulting cavity remained smaller than the size of the corresponding FSP.
- The V_{th} from simulation best matched the experimental V_{th} when the input failure strain was close to the limiting strain estimated from the Gent model.
- Although 1.10 g FSPs made of BB and PVC plastics demonstrated higher V_{th} than mild steel FSPs of the same size, they exhibited significant threats of contusion and laceration.
- A linear relationship was noted between V_{th} and skin simulant thickness.

Data availability statement

The original contributions presented in the study are included in the article/Supplementary Material, and any further inquiries may be directed to the corresponding author.

Author contributions

PP: conceptualization, data curation, formal analysis, investigation, methodology, software, validation, and writing—original draft. SG: conceptualization, funding acquisition, supervision, and writing—review and editing.

Funding

The authors declare that financial support was received for the research, authorship, and/or publication of this article. This work was supported by the Armaments Research Board (grant number ARMREB-ASE-2018-198).

Acknowledgments

SG acknowledges financial support from the Armaments Research Board under grant number ARMREB-ASE-2018-198.

Conflict of interest

The authors declare that the research was conducted in the absence of any commercial or financial relationships that could be construed as a potential conflict of interest.

Publisher's note

All claims expressed in this article are solely those of the authors and do not necessarily represent those of

their affiliated organizations or those of the publisher, editors, and reviewers. Any product that may be evaluated in this article or claim that may be made by its manufacturer is not guaranteed or endorsed by the publisher.

References

- Allen, F., and Sperrazza, J. (1956). *New casualty criteria for wounding by fragments ballistic research laboratories, aberdeen proving ground*. Maryland Report.
- Baptista, M. V., d'Ávila, S. C., and d'Ávila, A. M. M. (2014). Histopathological detection of entry and exit holes in human skin wounds caused by firearms. *J. forensic Leg. Med.* 25, 49–52. doi:10.1016/j.jflm.2014.04.017
- Bir, C. A., Ressler, M., and Stewart, S. (2012). Skin penetration surrogate for the evaluation of less lethal kinetic energy munitions. *Forensic Sci. Int.* 220, 126–129. doi:10.1016/j.forsciint.2012.02.008
- Bir, C. A., Stewart, S. J., and Wilhelm, M. (2005). Skin penetration assessment of less lethal kinetic energy munitions. *J. Forensic Sci.* 50, JFS2004551–4. doi:10.1520/jfs2004551
- Bolduc, V., and Jager, H. (2016). “Summary of newly ratified NATO standard AEP 2920, ed. A, V1,” in *Personal armour systems symposium PASS 2016 proceeding book*, 25–40.
- Bowyer, G., Cooper, G., and Rice, P. (1995). Management of small fragment wounds in war: current research. *Ann. R. Coll. Surg. Engl.* 77, 131–134. doi:10.1097/00005373-199603001-00037
- Breeze, J., and Clasper, J. C. (2013). Determining the velocity required for skin perforation by fragment simulating projectiles: a systematic review. *a Syst. Rev. BMJ Mil. Health* 159, 265–270. doi:10.1136/jramc-2013-000070
- Breeze, J., James, G., and Hepper, A. (2013). Perforation of fragment simulating projectiles into goat skin and muscle. *BMJ Mil. Health* 159, 84–89. doi:10.1136/jramc-2013-000065
- Breeze, J., Sedman, A., James, G., Newbery, T., and Hepper, A. (2014). Determining the wounding effects of ballistic projectiles to inform future injury models: a systematic review. *a Syst. Rev. BMJ Mil. Health* 160, 273–278. doi:10.1136/jramc-2013-000099
- Carr, D., Kieser, J., Mabbott, A., Mott, C., Champion, S., and Girvan, E. (2014). Damage to apparel layers and underlying tissue due to hand-gun bullets. *Int. J. Leg. Med.* 128, 83–93. doi:10.1007/s00414-013-0856-1
- Carr, D. J., Lewis, E., and Horsfall, I. (2017). A systematic review of military head injuries. *BMJ Mil. Health* 163, 13–19. doi:10.1136/jramc-2015-000600
- Champion, H. R., Bellamy, R. F., Roberts, C. P., and Leppaniemi, A. (2003). A profile of combat injury. *J. Trauma Acute Care Surg.* 54, S13–S19. doi:10.1097/01.ta.0000057151.02906.27
- Chanda, A. (2018). Biomechanical modeling of human skin tissue surrogates. *Biomimetics* 3, 18. doi:10.3390/biomimetics3030018
- Chanda, A., Unnikrishnan, V., Flynn, Z., and Lackey, K. (2017). Experimental study on tissue phantoms to understand the effect of injury and suturing on human skin mechanical properties. *Proc. Institution Mech. Eng. Part H J. Eng. Med.* 231, 80–91. doi:10.1177/0954411916679438
- Chanda, A., and Upchurch, W. (2018). Biomechanical modeling of wounded skin. *J. Compos. Sci.* 2, 69. doi:10.3390/jcs2040069
- Chen, C., Cheng, Y., Zhu, X., Cai, Y., Xue, Y., Kong, N., et al. (2020). Ultrasound assessment of skin thickness and stiffness: the correlation with histology and clinical score in systemic sclerosis. *Arthritis Res. & Ther.* 22, 197–198. doi:10.1186/s13075-020-02285-x
- Chen, W. W. (2016). Experimental methods for characterizing dynamic response of soft materials. *J. Dyn. Behav. Mater.* 2, 2–14. doi:10.1007/s40870-016-0047-5
- Chen, Y., Quino, G., and Pellegrino, A. (2024). A comprehensive investigation on the temperature and strain rate dependent mechanical response of three polymeric syntactic foams for thermoforming and energy absorption applications. *Polym. Test.* 130, 108287. doi:10.1016/j.polymertesting.2023.108287
- Deka, L., Bartus, S., and Vaidya, U. (2008). Damage evolution and energy absorption of E-glass/polypropylene laminates subjected to ballistic impact. *J. Mater. Sci.* 43, 4399–4410. doi:10.1007/s10853-008-2595-0
- Donato, G. H. B., and Bianchi, M. (2012). Pressure dependent yield criteria applied for improving design practices and integrity assessments against yielding of engineering polymers. *Eng. Polym. J. Mater. Res. Technol.* 1, 2–7. doi:10.1016/s2238-7854(12)70002-9
- Fenton, L., Horsfall, I., and Carr, D. (2020). Skin and skin simulants. *J. Forensic Sci.* 52, 96–106. doi:10.1080/00450618.2018.1450896
- Gent, A. N. (1996). A new constitutive relation for rubber. *Rubber Chem. Technol.* 69, 59–61. doi:10.5254/1.3538357
- Grocock, C., McCarthy, R., and Williams, D. J. (2006). Ball Bearing (BB) guns, ease of purchase and potential for significant injury. *Ann. R. Coll. Surg. Engl.* 88, 402–404. doi:10.1308/003588406x98630
- Guo, L., and Wang, Y. (2020). High-rate tensile behavior of silicone rubber at various temperatures. *Rubber. Chem. Technol.* 93, 183–194. doi:10.5254/rct.19.81562
- Hazell, P. J. (2022). *Armour: materials, theory, and design*. CRC press.
- Henderson, J. (2010). *ALethality criteria for debris generated from accidental explosions*. Ministry Def. Lond.
- Horgan, C., and Saccomandi, G. (2022). A description of arterial wall mechanics using limiting chain extensibility constitutive models. *Biomechanics Model. Mechanobiol.* 1, 251–266. doi:10.1007/s10237-002-0022-z
- Inchingolo, F., Tatullo, M., Marrelli, M., Inchingolo, A. D., Pinto, G., Inchingolo, A. M., et al. (2011). Short report of an unusual ballistic trauma. *Int. J. Surg. case Rep.* 2, 272–274. doi:10.1016/j.ijscr.2011.08.009
- Jin, Y., Haitao, L., Cheng, W., Wang, X., Han, R., Li, R., et al. (2019). The experimental and numerical investigation on the ballistic limit of BB—gun pellet versus skin simulant. *Forensic Sci. Int.* 298, 393–397. doi:10.1016/j.forsciint.2019.02.033
- Joodaki, H., and Panzer, M. B. (2018). Skin mechanical properties and modeling: a review. *A Rev. Proc. Institution Mech. Eng. Part H J. Eng. Med.* 232, 323–343. doi:10.1177/0954411918759801
- Jor, J. W., Parker, M. D., Taberner, A. J., Nash, M. P., and Nielsen, P. M. (2013). Computational and experimental characterization of skin mechanics: identifying current challenges and future directions. *Syst. Biol. Med.* 5, 539–556. doi:10.1002/wsbm.1228
- Kalra, A., Lowe, A., and Al-Jumaily, A. (2016). Mechanical behaviour of skin: a review. *J. Mater. Sci. Eng.* 5, 1000254. doi:10.4172/2169-0022.1000254
- Khatam, H., Liu, Q., and Ravi-Chandar, K. (2014). Dynamic tensile characterization of pig skin. *Acta Mech. Sin.* 30, 125–132. doi:10.1007/s10409-014-0042-9
- Khodadadi, A., Liaghat, G., Ahmadi, H., Bahramian, A. R., Anani, Y., Razmkhah, O., et al. (2019a). Numerical and experimental study of impact on hyperelastic rubber panels. *Iran. Polym. J.* 28, 113–122. doi:10.1007/s13726-018-0682-x
- Khodadadi, A., Liaghat, G., Ahmadi, H., Bahramian, A. R., and Razmkhah, O. (2019b). Impact response of Kevlar/rubber composite. *Compos. Sci. Technol.* 184, 107880. doi:10.1016/j.compscitech.2019.107880
- Kneubuehl, B. P. (2011). *Wound ballistics: basics and applications*. Springer science & business media.
- Kneubuehl, B. P., Coupland, R. M., Rothschild, M. A., and Thali, M. J. (2011). “Wound ballistics and forensic medicine,” in *Wound ballistics* (Springer), 253–303.
- Kolling, S., Du Bois, P., Benson, D., and Feng, W. (2007). A tabulated formulation of hyperelasticity with rate effects and damage. *Comput. Mech.* 40, 885–899. doi:10.1007/s00466-006-0150-x
- Laurent, A., Mistretta, F., Bottiglioli, D., Dahel, K., Goujon, C., Nicolas, J. F., et al. (2007). Echographic measurement of skin thickness in adults by high frequency ultrasound to assess the appropriate microneedle length for intradermal delivery of vaccines. *Natl. Libr. Med.* 25, 6423–6430. doi:10.1016/j.vaccine.2007.05.046
- Li, Z., and Lambros, J. (2001). Strain rate effects on the thermomechanical behavior of polymers. *Int. J. Solids Struct.* 38, 3549–3562. doi:10.1016/s0020-7683(00)00223-7
- Lim, J., Hong, J., Chen, W. W., and Weerasooriya, T. (2011). Mechanical response of pig skin under dynamic tensile loading. *Int. J. Impact Eng.* 38, 130–135. doi:10.1016/j.ijimpeng.2010.09.003
- Limbirt, G. (2017). Mathematical and computational modelling of skin biophysics: a review. *a Rev. Proc. R. Soc. A Math. Phys. Eng. Sci.* 473, 20170257. doi:10.1098/rspa.2017.0257
- Liu, H., Chen, J., Kang, J.-y., Li, X.-x., and Azhari, I. (2014). Finite element analysis of the dynamic response of the cardiovascular system to the blunt ballistic impact. *Computer Modelling and new. Technologies* 18, 44–49.
- LSTC (2021). “LS-DYNA keyword user's manual,” California, United States: Livermore Software Technology Corporation.

Supplementary material

The Supplementary Material for this article can be found online at: <https://www.frontiersin.org/articles/10.3389/fbioe.2024.1422685/full#supplementary-material>

- Marechal, L., Bolland, P., Lindenroth, L., Petrou, F., Kontovounisios, C., and Bello, F. (2021). Toward a common framework and database of materials for soft robotics. *Soft Robot.* 8, 284–297. doi:10.1089/soro.2019.0115
- Muhr, A. (2005). Modeling the stress-strain behavior of rubber. *Rubber Chem. Technol.* 78, 391–425. doi:10.5254/1.3547890
- NATO (2003). “NATO standardization agreement (STANAG 2920): ballistic test method for personal armour materials and combat clothing,” in *NATO standardization agency*. 2nd ed.
- Ogden, R. W. (1972). Large deformation isotropic elasticity—on the correlation of theory and experiment for incompressible rubberlike solids Proceedings of the Royal Society of London. *A Math. Phys. Sci.*, 565–584. doi:10.1098/rspa.1972.0026
- Ottenio, M., Tran, D., Annaidh, A. N., Gilchrist, M. D., and Bruyère, K. (2015). Strain rate and anisotropy effects on the tensile failure characteristics of human skin. *J. Mech. Behav. Biomed. Mater.* 41, 241–250. doi:10.1016/j.jmbbm.2014.10.006
- Park, J.-J., Haddadin, S., and Song, J.-B. (2011). “Albu-Schäffer A Designing optimally safe robot surface properties for minimizing the stress characteristics of human-robot collisions,” in *2011 IEEE international conference on robotics and automation (IEEE)*, 5413–5420.
- Pavie, J., Langlet, A., Eches, N., and Jacquet, J.-F. (2015). On ballistic parameters of less lethal projectiles influencing the severity of thoracic blunt impacts. *Engineering* 18, 192–200. doi:10.1080/10255842.2013.789101
- Pellegrino, A., Tagarielli, V., Gerlach, R., and Petrinic, N. (2015). The mechanical response of a syntactic polyurethane foam at low and high rates of strain. *Int. J. Impact Eng.* 75, 214–221. doi:10.1016/j.ijimpeng.2014.08.005
- Rashid, B., Destrade, M., and Gilchrist, M. D. (2014). Mechanical characterization of brain tissue in tension at dynamic strain rates. *J. Mech. Behav. Biomed. Mater.* 33, 43–54. doi:10.1016/j.jmbbm.2012.07.015
- Regasa, L. E., Kaplan, D. A., Martin, E. M. M., Langbein, J., Johnson, F., and Chase, L. C. (2018). Mortality following hospital admission for US active duty service members diagnosed with penetrating traumatic brain injury. *J. Head Trauma Rehabilitation* 33, 123–132. doi:10.1097/htr.0000000000000380
- Rezende-Neto, J., Silva, F. D., Porto, L. B., Teixeira, L. C., Tien, H., and Rizoli, S. B. (2009). Penetrating injury to the chest by an attenuated energy projectile: a case report and literature review of thoracic injuries caused by “less-lethal. *munitions World J. Emerg. Surg.* 4, 1–5. doi:10.1186/1749-7922-4-26
- Rosenberg, Z., and Dekel, E. (2012) *Terminal ballistics*. Springer.
- Sachs, D., Wahlsten, A., Kozerke, S., Restivo, G., and Mazza, E. (2021). A biphasic multilayer computational model of human skin. *Biomechanics Model. Mechanobiol.* 20, 969–982. doi:10.1007/s10237-021-01424-w
- Serraino, S., Milone, L., Picone, D., Argo, A., Salerno, S., and Midiri, M. (2020). “Imaging for ballistic trauma: other applications of forensic imaging in the living,” in *Radiology in forensic medicine* (Springer), 169–180.
- Shergold, O. A., Fleck, N. A., and Radford, D. (2006). The uniaxial stress versus strain response of pig skin and silicone rubber at low and high strain rates. *Int. J. Impact Eng.* 32, 1384–1402. doi:10.1016/j.ijimpeng.2004.11.010
- Siviour, C. R., and Jordan, J. L. (2016). High strain rate mechanics of polymers: a review. *J. Dyn. Behav. Mater.* 2, 15–32. doi:10.1007/s40870-016-0052-8
- Smooth-on. Smooth-on Dragon Skin™ Series Addition Cure Silicone Rubber Compounds. Technical Bulletin. Available at: https://www.smooth-on.com/tb/files/DRAGON_SKIN_SERIES_TB.pdf
- Sperrazza, J., and Kokinakis, W. (1968). Ballistic limits of tissue and clothing. *Ann. N. Y. Acad. Sci.* 152, 163–167. doi:10.1111/j.1749-6632.1968.tb11973.x
- Tsui, C., Tsui, K., and Tang, Y. (2010). Ball bearing (BB) gun injuries. *J. Emerg. Med.* 17, 488–491. doi:10.1177/102490791001700510
- Upadhyay, K., Spearot, D., and Subhash, G. (2021). Validated tensile characterization of the strain rate dependence in soft materials. *Soft Mater. Int. J. Impact Eng.* 156, 103949. doi:10.1016/j.ijimpeng.2021.103949
- Upadhyay, K., Subhash, G., and Spearot, D. (2020). Visco-hyperelastic constitutive modeling of strain rate sensitive soft materials. *J. Mech. Phys. Solids* 135, 103777. doi:10.1016/j.jmps.2019.103777
- Wahlsten, A., Pensalfini, M., Stracuzzi, A., Restivo, G., Hopf, R., and Mazza, E. (2019). On the compressibility and poroelasticity of human and murine skin. *skin Biomechanics Model. Mechanobiol.* 18, 1079–1093. doi:10.1007/s10237-019-01129-1
- Yoganandan, N., and Pintar, F. A. (1997). Biomechanics of penetrating trauma. *Engineering* 25, 485–501. doi:10.1615/critrevbiomedeng.v25.i6.10
- Zecevic, B., Terzic, J., Razic, F., and Kadic, S. (2015). Lethal influence factors of natural and performed fragmentation projectiles DAAAM. *Int. Sci. Book*, 219–234. doi:10.2507/daaam.scibook.2015.20



OPEN ACCESS

EDITED BY

Xuanzhen Cen,
Óbuda University, Hungary

REVIEWED BY

Michael Voor,
University of Louisville, United States
Zixiang Gao,
University of Calgary, Canada

*CORRESPONDENCE

Alireza Rastegarpanah,
✉ a.rastegarpanah@bham.ac.uk

RECEIVED 26 September 2023

ACCEPTED 25 September 2024

PUBLISHED 27 November 2024

CITATION

Rastegarpanah A and Taylor SJG (2024) A wireless buckle transducer for measurement of human forearm tendon tension: operational principles and finite element study. *Front. Bioeng. Biotechnol.* 12:1278740. doi: 10.3389/fbioe.2024.1278740

COPYRIGHT

© 2024 Rastegarpanah and Taylor. This is an open-access article distributed under the terms of the [Creative Commons Attribution License \(CC BY\)](https://creativecommons.org/licenses/by/4.0/). The use, distribution or reproduction in other forums is permitted, provided the original author(s) and the copyright owner(s) are credited and that the original publication in this journal is cited, in accordance with accepted academic practice. No use, distribution or reproduction is permitted which does not comply with these terms.

A wireless buckle transducer for measurement of human forearm tendon tension: operational principles and finite element study

Alireza Rastegarpanah^{1*} and Stephen J. G. Taylor²

¹School of Metallurgy and Materials, University of Birmingham, Birmingham, United Kingdom, ²Division of Surgery and Interventional Science, Royal National Orthopaedic Hospital, Institute of Orthopaedics and Musculoskeletal Science, University College London, Stanmore, United Kingdom

Introduction: Conventional methods for evaluating the management of spasticity, a complex neuromuscular disorder, typically fail to directly measure the muscle forces and loads applied through tendons, which is crucial for accurate diagnostics and treatment. To bridge this gap, we developed a novel modular buckle transducer (BT) designed to measure tendon forces *in vivo*. This device adjusts to accommodate tendon sizes ranging from 3 mm to 5 mm, maintaining accuracy within this range and avoiding the need for identical tendon calibration.

Methods: This study first presents the mechanical principles for determining tendon tension T using several strain gauges appropriately positioned to allow for varying angles of passage of the tendon through the device. Next, we present a finite element (FE) model that uses multiple linear regression to determine T while varying tendon diameter and lateral placement within the device for several candidate strain gauge locations on the device base plate. Finally, we posit several alternative ways of combining gauge strains.

Results: Initial simulation results demonstrated that this placement facilitates effective pre-implementation calibration, with the device accommodating tendon variations from 3 mm to 5 mm in diameter for a range of gauge placements.

Discussion: Future validation of this technology will involve direct testing on explanted human/equine tendons to verify the practical utility of the BT, aiming to establish a new standard for assessing and managing neuromuscular disorders such as spasticity.

KEYWORDS

buckle transducer, tendon, calibration, regression, finite element analysis

1 Introduction

Spasticity is a motor disorder arising from anomalies in the brain or spinal cord, manifesting through increased muscle tone and exaggerated tendon jerks due to neurophysiological changes [Mukherjee and Chakravarty \(2010\)](#). Tendons serve as essential conduits, transmitting muscle forces to bones; the tensile force transmitted via

tendons may be determined using both invasive and non-invasive techniques. Invasive methods, such as the direct implantation of force transducers, pose risks such as infection, signal loss, and moisture ingress, making them less favourable for long-term applications. On the other hand, non-invasive techniques, while safer, often lack the precision required for dynamic, *in vivo* measurements of tendon forces. The buckle transducer (BT) bridges this gap by offering a minimally invasive solution that enables accurate and direct tendon force measurements.

In recent years, non-invasive methods for tendon force measurement have been proposed, utilizing technologies such as ultrasound and shear wave propagation. Pourcelot et al. demonstrated that tendon forces can be non-invasively estimated by analyzing the propagation of ultrasonic waves along the tendon [Pourcelot et al. \(2005\)](#). Additionally, a shear wave tensiometer introduced by Martin et al. uses skin-mounted sensors to measure tendon vibrations, providing a non-invasive method for estimating tendon loads during dynamic activities such as walking and running [Martin et al. \(2018\)](#). While these methods offer valuable alternatives, they are typically limited to superficial tendons and rely on optimal acoustic coupling with the skin for accuracy. Furthermore, they may not provide the precision required for more complex, *in vivo* measurements, especially in deeper tendons. In contrast, buckle transducers (BT) provide a direct and highly accurate measurement of tendon forces, particularly in scenarios where non-invasive methods may fall short due to tendon depth or the need for precise, dynamic measurements.

While natural asymmetry between the left and right limbs, such as differences in muscle mass, tendon length, and joint structure, may impact tendon force transmission, this study focuses on measuring the force within the specific tendon into which the transducer is inserted. Our goal is to provide accurate measurements for the targeted tendon, irrespective of potential asymmetry between limbs. Among these techniques, buckle transducers (BTs) are notable for their ability to measure forces directly by placing the BT around the tendon such that it senses the force applied to it by the tendon without injury. These BTs, classified under extensometry transducers, measure the *in vivo* force exerted by tendons, with strain gauges embedded in the device to reflect these forces [Ravary et al. \(2004\)](#).

Buckle transducers function by utilizing the natural tendency of a tendon, when intertwined between the deformable arms of the device, to straighten upon tensile loading. As the tendon straightens, it exerts a force that deforms the transducer's arms. This deformation is captured by strain gauges mounted on the device, which convert the physical strain into electrical signals for analysis. This method allows for the measurement of forces within the tendon without causing tissue damage, making BTs suitable for *in vivo* applications.

Various BT designs have been developed over the years, including the E-form, oval, and rectangular form configurations ([Figure 1](#)), each suited to different biomechanical applications. The E-form design, for example, offers ease of insertion and removal, making it ideal for *in vivo* applications. The oval and rectangular form configurations provide greater contact area with the tendon, which can enhance measurement sensitivity but may require more complex calibration. These designs represent alternative approaches

to tendon tension measurement, rather than an evolutionary progression.

This study introduces a modular buckle transducer (BT) designed to accommodate various Flexor Carpi Radialis tendon sizes. We hypothesize that the BT can be effectively calibrated across different tendon thicknesses and tension loads, particularly in vitro environments. Our approach involved mathematical modelling followed by Solidworks simulations to record the impact of varying forces on the BT using multiple bearing sizes. These simulations were instrumental in determining the optimal locations for installing gauge sensors on the buckle's baseplate, aiming to maximise accuracy.

1.1 Buckle transducers reported in human studies

Buckle Transducers (BTs) have garnered extensive attention due to their instrumental significance in diagnosing tendon issues, facilitating treatment, and investigating the biomechanics of tendons and ligaments. In human studies, BTs find wide applicability in assessing Achilles tendon force, a pivotal element in normal walking. The anatomical location of the Achilles tendon allows for safe implementation of the BT around the tendon, minimizing risks to surrounding tissues [Gregor et al. \(1987\)](#), [Fukashiro et al. \(1993\)](#), [Komi \(1990\)](#). In one study, a small S-shaped BT was implanted in subjects with spasticity to measure the force of the knee's distal spastic semitendinosus tendon [Ateş et al. \(2016\)](#). Another research endeavor employed a BT to measure loads on knee ligaments during knee flexion, contributing to the validation of a reconstruction technique [Coobs et al. \(2010\)](#). Furthermore, a custom-designed rectangular BT was utilized for *in vitro* testing, enabling the study of intact ankle ligament properties at varying loads using a hydraulic material testing machine [Best et al. \(2016\)](#). These diverse applications underscore the versatility and significance of BTs in biomechanical research and clinical investigations.

Indeed, BTs have also found application in upper-limb studies. For instance, a study reported *in vivo* measurement of hand tendon forces using an S-shaped force transducer [Schuind et al. \(1992\)](#). In another study, a BT was implanted in the tendons of the index finger to measure flexor tendon forces [Edsfeldt et al. \(2015\)](#). Furthermore, a strain gauge-based BT was employed to measure tension in wrist flexor tendons [Fridén et al. \(2010\)](#). These investigations underscore the adaptability and utility of BTs across various upper-limb scenarios, contributing valuable insights into the biomechanics and function of tendons in these regions.

1.2 Buckle transducers reported in animal studies

In animal studies, BTs have been applied to diverse contexts. For instance, an E-shaped stainless steel BT equipped with a metal foil strain gauge was employed to measure Achilles tendon force in a goat [Lee et al. \(2011\)](#). In another investigation involving horses, an E-type BT was implanted in eight subjects to gauge the force required for optimal intraoperative left arytenoid cartilage

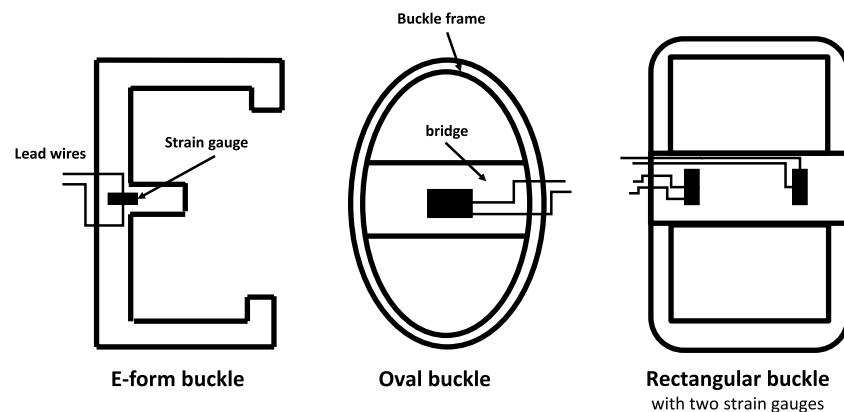


FIGURE 1

Some alternative designs of buckle transducer in the literature, with sectional view Keegan et al. (1991); Roberts (1994); Stone et al. (1983); the E-form (and its variant, the S-form) allow buckle insertion and removal *in vivo*; others require a removable crossbar Ravary et al. (2004).

abduction, aiding in laryngoplasty surgery Witte et al. (2010b). Transducer calibration, conducted before and after implantation, served to validate transducer sensitivity, with linear regression establishing the correlation between force and voltage output. Another E-type transducer was developed to measure forces exerted on surgical sutures Witte et al. (2010a). Regression measurement yielded predictions of actual force with a mean error of 4%, deemed an acceptable prediction margin for *in-vitro* calibration.

In a separate study, the performance characteristics of an internal BT were evaluated analytically *in vivo* Herzog et al. (1996). The findings revealed that even minor angular displacements and corresponding bone rotations could significantly influence transducer output. While internal force transducers do produce reliable signals *in vivo*, precise determination of tissue forces can prove challenging, especially during animal locomotion. These varied applications highlight the value of BTs in animal biomechanical research, offering insights into physiological processes and aiding surgical interventions.

1.3 Sizes of BT and associated risks of implantation

The sizes of implanted BTs have been tailored to match the dimensions of the respective tendons. For instance, in animal studies, an implantable E-form BT was reported to have dimensions of approximately $9 \times 5 \text{ mm}^2$ Wehrle et al. (2001), while in human studies, dimensions were around $34 \times 20 \text{ mm}$ Ravary et al. (2004). In another example, an S-shape BT measuring $20 \times 12 \times 9 \text{ mm}$ with a maximal force range of 400 N was employed to measure the force exerted on human spastic muscles during knee flexion Yucesoy et al. (2017). These diverse sizes reflect the adaptability of BTs to varying anatomical requirements and research objectives, making them a versatile tool in biomechanical investigations.

Long-term implantation of BTs in the body can lead to notable discomfort, particularly when the transducers are bulky. A study

found that pain levels were significantly alleviated upon reducing the size of the BT Komi et al. (1987). The duration required for wound healing and the return to normal walking after BT implantation varied, ranging from 2 to 3 weeks in humans Ravary et al. (2004), to 1 week in cats Walmsley et al. (1978). Two potential risks associated with BT implantation include tissue shortening and bone impingement, both of which can be mitigated by employing smaller BTs. Each application often demands a specific BT geometry tailored to the unique requirements of the study.

A primary advantage of BTs lies in their capacity to offer a mechanical average of force, reducing errors stemming from unmeasured sections of the tendon Fleming and Beynnon (2004). However, even slight misalignment of the transducer's axis relative to the axis of tendon fibers can induce significant fluctuations in the output signal for a given externally applied load Ravary et al. (2004). This underscores the importance of meticulous positioning and alignment of BTs to ensure accurate and reliable measurements.

1.4 Calibration issues

Similar to any measurement device used in inaccessible environments, the accuracy of *in vivo* readings obtained from BTs relies on dependable and reproducible calibration, either before or after the experiment. In the case of permanently implanted devices, particularly in humans, calibration must be conducted beforehand using materials that closely resemble the tendon's properties. However, this task is challenging due to the non-homogeneous nature of tendons and the complexities of replicating their characteristics outside the body within a calibration setting. Instances in the literature highlight situations where inadequate calibration, failing to account for local movement or shape changes of the tendon *in vivo*, resulted in unreliable measurements. Typically, calibration involves clamping the ends of a substitute material mimicking the tendon on either side of the transducer within a tensile testing machine. Ideally, the substitute material should have similar properties and geometry to the actual tendon. However, in cases where the transducer's sensitivity to changes in tendon geometry comes into play, this calibration

approach proves inadequate due to unknown morphological changes occurring with load. Hence, calibration is a critical step that requires careful consideration and adaptation to account for the intricacies of the biomechanical context. Addressing the challenges associated with proper calibration ensures that the measurements obtained from BTs accurately reflect the forces within tendons and support meaningful interpretations of biomechanical phenomena.

Interpreting the data obtained post-calibration presents challenges due to the potential influence of local variations in tendon geometry on the relationship established between the transducer signal and tendon load during calibration. It becomes evident that *in vitro* calibration necessitates independent validation methods to accurately align with the *in vivo* conditions Ravary et al. (2004). For example, a study by An et al. An et al. (1990) developed a low-profile transducer equipped with two uniaxial strain gauges to measure loads ranging from 0 to 50 N. The findings indicated that repeated loading and the consequent alterations in tendon thickness have an impact on the calibration factor. Additionally, tendon thickness emerged as a parameter that could be leveraged to affect the calibration factor. These complexities emphasize the significance of comprehensive calibration procedures that consider the intricate interplay between transducer signals, tendon geometry, and load. Addressing these challenges ensures that the collected data accurately reflects the biomechanical dynamics within tendons and supports robust and meaningful interpretations of the results.

It is evident that prior research, whether conducted in humans or animals, has predominantly relied on either post-calibration of tendons (in the case of animals) or attempting to estimate *in vivo* tendon thickness while tolerating uncertainties about the forces by calibrating with materials of similar geometry. In this context, the primary contribution of this paper lies in presenting a proof-of-concept for a modular BT design that overcomes the limitations of conventional approaches. This novel design enables the measurement of tendon tension in a manner that is independent of the tendon's cross-sectional area and its position within the BT, using multiple strain gauges to avoid the need for pre- or post-calibration using the target tendon.

2 Methodology

This study introduces a novel design for a BT featuring a detachable central bearing, as depicted in Figure 2. The integration of both measurement and data telemetry capabilities within a single hermetically sealed unit presented several challenges. These included maintaining strain sensitivity (which required the use of temperature-sensitive silicon strain gauges), allocating sufficient space for the amplifiers, analog-to-digital converters, and telemetry circuitry, and ensuring the hermetic seal remained intact to protect the electronics from environmental factors. Additionally, the design had to allow for effective near-field coil coupling, using the same pair of coils for both power supply and data telemetry. While these challenges were addressed in the design, further optimization, especially concerning strain sensitivity, remains a potential area for improvement.

This study currently restricts itself to a finite element, and while the design is optimized to accommodate these components, no *in*

vivo testing has yet been conducted. The integration of power supply and telemetry circuitry remains theoretical at this stage. An implanted coil within the device would enable inductive coupling with an external coil, serving the dual purpose of power supply and data telemetry. This innovative approach aligns with the pursuit of streamlined and integrated solutions for tendon force measurement and data transmission.

2.1 Design of modular buckle transducer

The study at hand focuses on the modelling of a BT with dimensions of 20 × 11 × 13 mm (Length-Width-Height). This design incorporates a cavity on the underside of the transducer to accommodate strain gauges, electronics, and an induction coil. The selected dimensions are in practical alignment with the feasibility of manufacturing such a transducer. Notably, the BT's design has been tailored for surgical convenience, enabling the central bearing to be removed and subsequently repositioned over the tendon. This feature facilitates the passage of the tendon through the transducer, with bearing surfaces present at both ends and at the central bearing. This design approach prioritizes usability during surgical procedures while maintaining the essential functionalities of the transducer.

As the tendon tension increases, the natural response of the tendon is to attempt to straighten. This action places direct mechanical load on the three positioned bearings within the BT. Depending upon the tendon's diameter, it will be deflected through the BT with a varying small angle. This will impose a combination of axial and shear forces on the end bearings, which will vary the proportion of strain in gauges located at different distances from the centre. The challenge is to interpret these strains to measure the tensile force in the tendon, independent of the tendon position and shape.

A study by Weber et al. Weber et al. (2015) measured the cross-section of the FCR tendon across multiple specimens, revealing diameter variations ranging from 3 mm to 5 mm. Correspondingly, our BT was designed to feature six distinct removable rod sizes, specifically 3 mm, 3.4 mm, 3.8 mm, 4.2 mm, 4.6 mm, and 5 mm, which correspond to the typical tendon sizes encountered in the tendons of interest (Figure 4). The current design has not been tested on tendons outside this range. If applied to tendons significantly larger or smaller than these sizes, the measurement accuracy could be affected. Expanding the central rod size range would require further calibration and testing to ensure accuracy across a broader range of tendon sizes. This array of sizes empowers surgeons to select the optimal bearing size during surgery, effectively ensuring a suitable deflection angle (angle of passage) that enables the achievement of a desirable strain magnitude at the strain gauges. Importantly, this approach prevents overstretching of the tendon while maintaining the capacity to generate adequate strain magnitudes.

2.2 Mathematical modelling of buckle transducer

A 2D mechanical analysis was carried out to establish relationships between strains at candidate strain gauge sites on the BT's baseplate, the tension within the tendon (T), and the

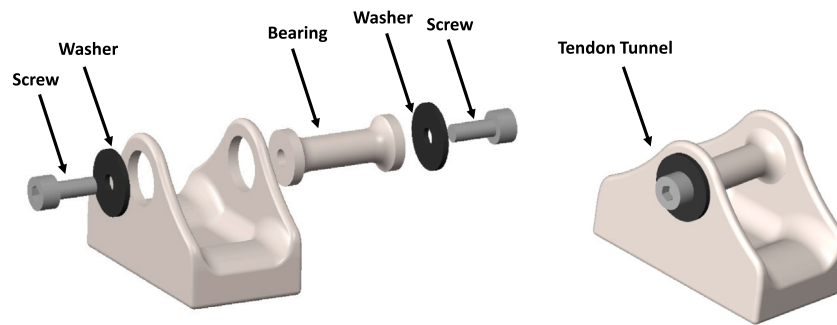


FIGURE 2
Designed CAD model of the modular buckle transducer in disassembled view (left) and assembled view (right).

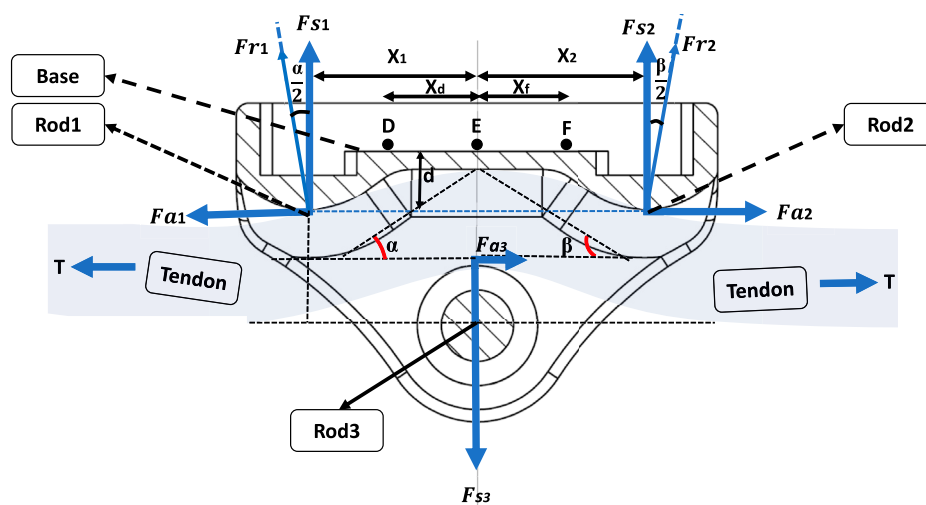


FIGURE 3
Free body diagram of the designed buckle transducer in cross-section view.

angles of passage (α , β) on either side of the transducer (Figure 3). This analytical investigation treated the BT as an unconstrained frictionless free body. It was reasonably assumed that the BT is effectively rigid compared to the tendon and the loads generated. The analysis considered force vectors acting on the rods, which arise from the magnitude of T and the two angles of passage (α , β). The alteration in the tendon's direction around each bearing surface gives rise to two orthogonal forces at each bearing, the vertical (shear - F_s) and horizontal (axial - F_a) components of the resultant force (F_r) acting on bearing one are given by Equations 1a-c:

$$F_{a1} = F_{r1} \sin\left(\frac{\alpha}{2}\right) \quad (1a)$$

$$F_{s1} = F_{r1} \cos\left(\frac{\alpha}{2}\right) \quad (1b)$$

$$F_{r1} = 2T \sin\left(\frac{\alpha}{2}\right) \quad (1c)$$

At bearing 2, given by Equations 2a-c:

$$F_{a2} = F_{r2} \sin\left(\frac{\beta}{2}\right) \quad (2a)$$

$$F_{s2} = F_{r2} \cos\left(\frac{\beta}{2}\right) \quad (2b)$$

$$F_{r2} = 2T \sin\left(\frac{\beta}{2}\right) \quad (2c)$$

Therefore, the relations between T and its orthogonal components are as follows:

At bearing 1, given by Equations 3a-b:

$$F_{a1} = 2T \sin^2\left(\frac{\alpha}{2}\right) = T(1 - \cos \alpha) \quad (3a)$$

$$F_{s1} = 2T \cos\left(\frac{\alpha}{2}\right) \sin\left(\frac{\alpha}{2}\right) = T \sin(\alpha) \quad (3b)$$

At bearing 2, given by Equations 4a-b:

$$F_{a2} = 2T \sin^2\left(\frac{\beta}{2}\right) = T(1 - \cos \beta) \quad (4a)$$

$$F_{s2} = 2T \cos\left(\frac{\beta}{2}\right) \sin\left(\frac{\beta}{2}\right) = T \sin(\beta) \quad (4b)$$

At bearing 3, given by Equations 5a-b:

$$F_{s3} = T \sin \alpha + T \sin \beta \quad (5a)$$

$$F_{a3} = T \cos \beta - T \cos \alpha \quad (5b)$$

These forces lead to the generation of bending moments within the baseplate, along with slight axial forces. In order to differentiate the sensitivities to T , α , and β , a total of six separate strain gauges were simulated. One pair was located at each of the designated points (D, E, F) on the BT, one gauge per side of the buckle (Figure 3).

In the subsequent analysis, we consider the transducer to be in a state of static equilibrium around the tendon, characterized by the following conditions, given by Equations 6a-b:

$$F_{s1} + F_{s2} = F_{s3} \quad (6a)$$

$$F_{a2} + F_{a3} = F_{a1} \quad (6b)$$

Where the tendon is of uniform cross section throughout the BT, the buckle exhibits symmetry, and coupled with the absence of friction between the tendon and the bearings, the following relationships, Equations 7a-b, hold:

$$F_{s1} = F_{s2} = \frac{F_{s3}}{2} \quad (7a)$$

$$F_{a1} = F_{a2}; F_{a3} = 0; \alpha = \beta \quad (7b)$$

However, in more general scenarios, the tendon thickness does not remain constant, leading to $\alpha \neq \beta$. In such cases, there are three unknown variables (T , α , β) that need to be determined. To establish the relationships between these variables and the three strains (or pairs of strains) at points D, E, and F, we derive three equations. The axial and shear forces applied to the buckle's bearing surfaces due to the tendon induce components of strain. Treating the structure as a beam with simple supports at the end bearings and subject to a concentrated shear force F_{s3} , we observe that no moments are sustained at the end bearings. Consequently, the bending moments at points D, E, and F can be expressed by Equations 8a-c:

$$M_D = F_{s1}(X_1 - X_d) + (d \times F_{a1}) \quad (8a)$$

$$M_E = F_{s1}X_1 + (d \times F_{a1}) \quad (8b)$$

$$M_F = F_{s2}(X_2 - X_f) + (d \times F_{a2}) \quad (8c)$$

Where d is the perpendicular distance from the line of action of F_{a1} , F_{a2} to the strain gauged surface. Substituting T , α , β for the forces using Equations 3, 4 we find (Equations 9a-c):

$$M_D = T \sin \alpha (X_1 - X_d) + dT(1 - \cos \alpha) \quad (9a)$$

$$M_E = T \sin \alpha \times X_1 + dT(1 - \cos \alpha) = T \sin \beta \times X_2 + dT(1 - \cos \beta) \quad (9b)$$

$$M_F = T \sin \beta (X_2 - X_f) + dT(1 - \cos \beta) \quad (9c)$$

And using the relationships between bending and strain at each site, including tensile strains due to axial forces F_{a1} , F_{a2} , given by Equations 10a-d:

$$\epsilon_D = \frac{(T \sin \alpha (X_1 - X_d) + dT(1 - \cos \alpha))y_D}{I_D E} - \frac{T(1 - \cos \alpha)}{A_D E} \quad (10a)$$

$$\epsilon_E = \frac{(T \sin \alpha \times X_1 + dT(1 - \cos \alpha))y_D}{I_E E} - \frac{T(1 - \cos \alpha)}{A_E E} \quad (10b)$$

$$\epsilon_E = \frac{(T \sin \beta \times X_2 + dT(1 - \cos \beta))y_E}{I_E E} - \frac{T(1 - \cos \beta)}{A_E E} \quad (10c)$$

$$\epsilon_F = \frac{(T \sin \beta (X_2 - X_f) + dT(1 - \cos \beta))y_F}{I_F E} - \frac{T(1 - \cos \beta)}{A_F E} \quad (10d)$$

Where y_n is the distance from the neutral axis to the gauge site, I_n is the second moment of the area at each cross-section, and A_n is the local cross-sectional area ($n=D,E,F$) where Y_n , I_n and A_n are all known. These equations may be solved to determine T , α and β , independent of locally varying angles of passage. In practice, the sensitivity coefficients are found using multiple linear regression in pre-implantation calibration using a range of tendons or substitute materials over the diameter range 4–5 mm (with appropriate sized central rod).

2.3 Finite Element Analysis in simulation

To determine the optimal locations for the strain gauges within the practical transducer, the Finite Element Analysis (FEA) toolbox in Solidworks was employed. This analysis aimed to ascertain the strains generated along the baseplate of the modelled BT in response to the tendon tension, T , and the angles of passage, α and β . The purpose was to characterize the strain behaviour in terms of its sensitivity to T , as well as its response to changes in tendon diameter and its position within the buckle. For each tendon size, ranging from 4mm to 5 mm in diameter with 0.2 mm increments, a corresponding sized central rod was employed to accommodate the tendon with appropriate angles of passage. This ensured a consistent angle of passage (13°) across all tendon diameters, which represented a suitable angle for achieving adequate strain sensitivity. A range of five tensile loads, from 100N to 500N, was applied to assess linearity, while 500 N was used for all other variables tested. The vertical and horizontal components of the force, both in magnitude and direction, acting on the rods were calculated using Equations 3–5. These forces were then applied to the bearing surfaces as distributed loads. To simplify the analysis, the tendon itself was not explicitly modeled in the simulation. Rather, the force distribution applied to the contact surfaces between the buckle and the tendon were modelled as depicted in Figure 4.

2.4 Determining the best location for mounting the gauges on the baseplate

Five alternative gauge placements were tested, each with six point strains measured from the FE model. In each case the six gauges were placed symmetrically about X and Y-axes and at $X = 0$, on the flat transducer baseplate; Table 1. The following load case sets were applied:

- 100–500 N in 100 N increments for 4.4 mm tendon diameter, tendon centred;
- 500 N for six increments of tendon diameter from 4 to 5 mm, tendon centred;

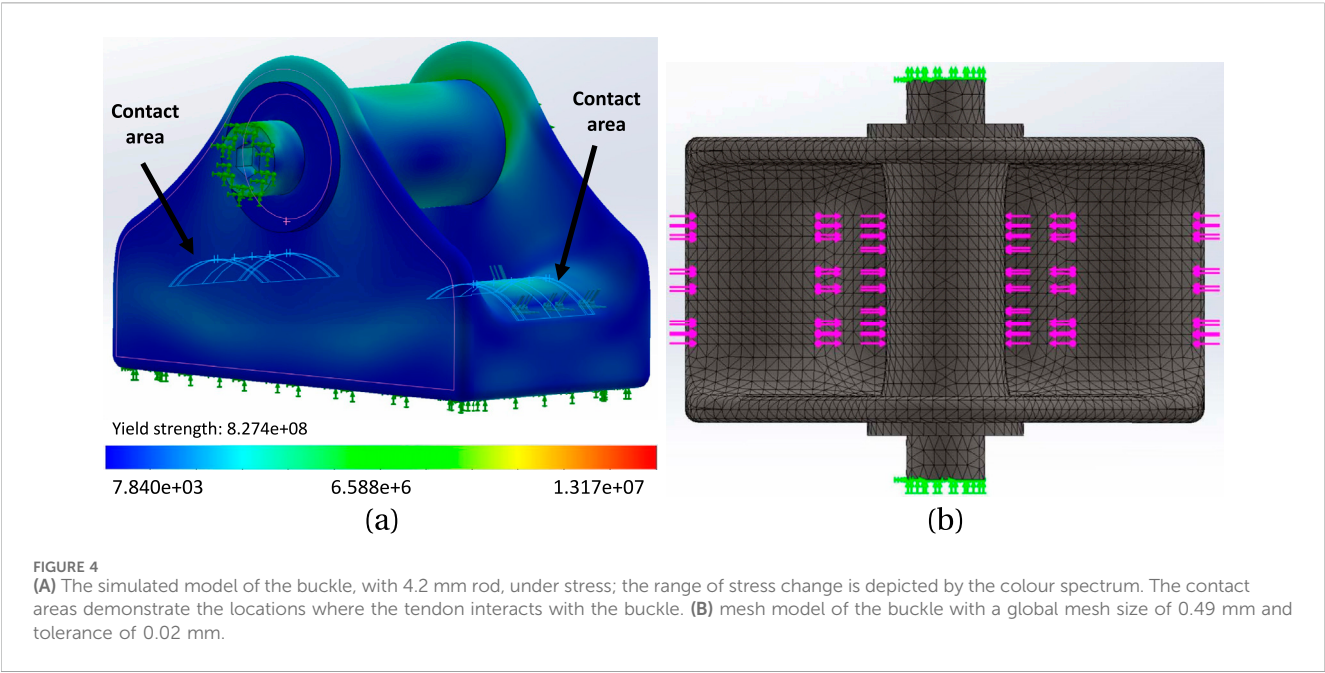
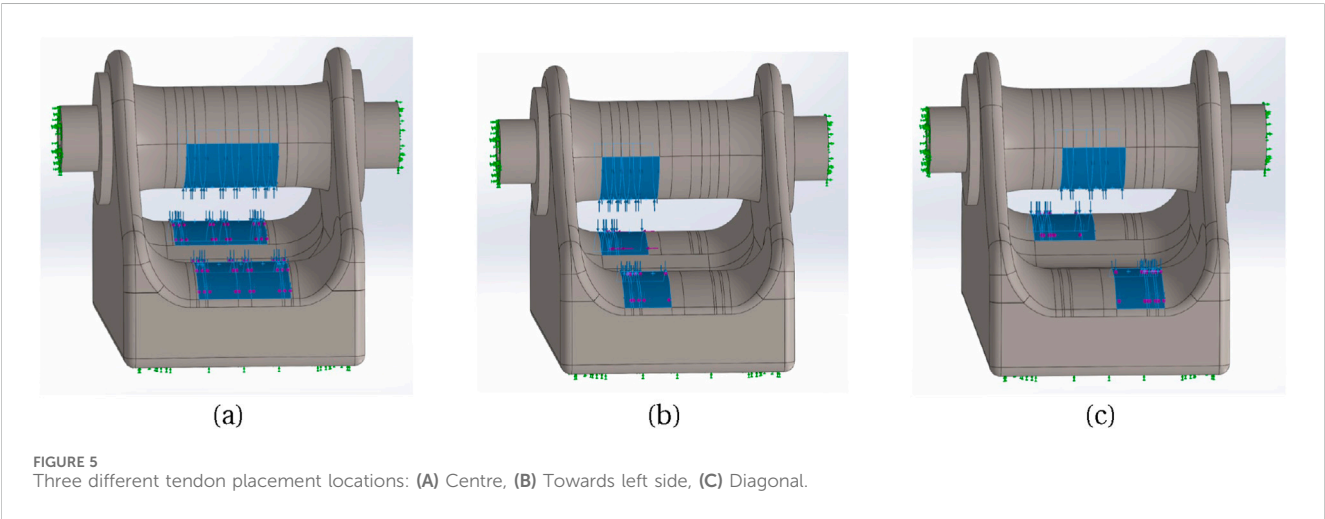


TABLE 1 Location of sensors X, Y (mm).

Cases	Sensor 1	Sensor 2	Sensor 3	Sensor 4	Sensor 5	Sensor 6
1	(-1.9, 2.5)	(-1.9, -2.5)	(0, 2.5)	(0, -2.5)	(1.9, 2.5)	(1.9, -2.5)
2	(-1.9, 3)	(-1.9, -3)	(0, 3)	(0, -3)	(1.9, 3)	(1.9, -3)
3	(-2.9, 3)	(-2.9, -3)	(0, 3)	(0, -3)	(2.9, 3)	(2.9, -3)
4	(-4.1, 2.5)	(-4.1, -2.5)	(0, 2.5)	(0, -2.5)	(4.1, 2.5)	(4.1, -2.5)
5	(-4.1, 3)	(-4.1, -3)	(0, 3)	(0, -3)	(4.1, 3)	(4.1, -3)



3. 500 N for 4.2 mm tendon diameter; three different positions of the tendon in the buckle: centred (Figure 5A), towards one side (Figure 5B), diagonal (Figure 5C). Extreme side and diagonal cases were also analysed (not shown).

Figure 6 illustrates the distribution of X, Y direct strains and XY shear strain across the baseplate, for one load case of set 2, showing strain gradients along X and Y-axes. Table 2 lists three alternative ways of combining the six measured strains; these combinations

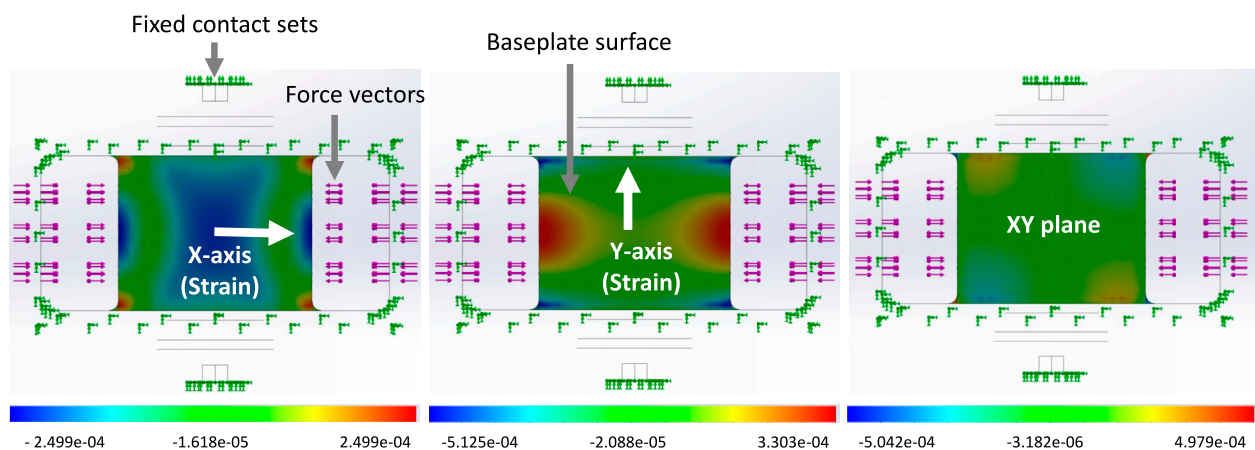


FIGURE 6

An example of Strain distribution on the baseplate when a 500N tension load was applied to the buckle with a 5 mm installed rod. The strain distribution is depicted from left to right: direct X, direct Y, XY shear. The figures display a bottom view of the buckle.

TABLE 2 Three alternative combinations of the 6 strains, referred to in table 3.

Strain combination	Strain values
1	$S = [S_1, S_2, S_3, S_4, S_5, S_6]$
2	$S = [\frac{(S_1 + S_2)}{2}, \frac{(S_3 + S_4)}{2}, \frac{(S_5 + S_6)}{2}]$
3	$S = [\frac{(S_1 + S_2 + S_5 + S_6)}{4}, \frac{(S_3 + S_4)}{2}]$

were explored in the analysis, as potentially combining gauges electrically within a later experimental transducer would reduce the bandwidth requirements for data transmission. In practice the gauge locations would be determined by practical considerations as well as modelled results; strain gauges are a finite size and would have some tolerance on positioning, so by varying the locations in the model it is possible to ascertain how critical the experimental placements might have to be.

2.5 Linear regression with least squares method

Following the determination of sensor positions on the baseplate, linear regression using the least squares method was employed to compute the residual vector for both tendon load and diameter. The gathered dataset comprises n paired observations encompassing the independent variables \mathbf{X} and the dependent variable \mathbf{Y} . Consequently, the fitting model is given by Equation 11:

$$\mathbf{Y} = \zeta_0 + \zeta_1 \mathbf{X} + \epsilon \quad (11)$$

where ϵ represents the error vector, uncorrelated across measurements, while ζ signifies the parameter vector. In the present study, the applied tension load and tendon diameter serve as independent variables, with strain values as dependent variables. As indicated in Table 2, the strain matrix $S_{i,j}$ can adopt varying dimensions based on the predictor presentation format. We explore three distinct strain combinations relative to the strain gauge positions: (i) $S_{11,6}$, where

$i \in 1, 2, \dots, 11$ signifies the number of observations, and $j \in 1, 2, \dots, 6$ represents individual strain values calculated across six sensors; (ii) $S_{11,3}$, where $i \in 1, 2, \dots, 11$ signifies observations, and $j \in 1, 2, 3$ represents three pairs of averaged strain values; (iii) $S_{11,2}$, where $i \in 1, 2, \dots, 11$ indicates observations, and $j \in 1, 2$ signifies averaged strain values for outer and inner sensors. The sensor locations, labeled one through 6, are illustrated in Figure 7.

In the analysis, we utilized Excel to conduct linear regression, facilitating the computation of coefficients ζ_0 and ζ_1 . The residual vector, denoted as \mathbf{e} , is determined by Equation 12a. To ascertain the matrix error \mathbf{e}_{ij} —where i signifies the number of observations and j signifies the number of dependent variables—for the prediction of both tendon load and diameter, a structured approach was adopted. Initially, a matrix $\mathbf{A}_{m \times n}$ was created, encompassing coefficients of dependent variables. In this context, m represents the count of dependent variables, while n denotes the number of independent variables. For instance, the residual error in predicting tendon tension and diameter, where strains are presented in the format of $S_{11,2}$ (corresponding to Strain combination two from Table 2), is given by Equations 12a, 12b:

$$\mathbf{e}_{(i,1)}^{\text{load}} = \left(\mathbf{A}^T \times (\mathbf{A} \times \mathbf{A}^T)^{-1} \right)^T \times \mathbf{S}_{(ix3)}^T - L_i, \quad i \in \{1, 2, \dots, 11\} \quad (12a)$$

$$\mathbf{e}_{(i,2)}^{\text{Thickness}} = \left(\mathbf{A}^T \times (\mathbf{A} \times \mathbf{A}^T)^{-1} \right)^T \times \mathbf{S}_{(ix3)}^T - Q_i, \quad i \in \{1, 2, \dots, 11\} \quad (12b)$$

Where L and Q represent the initial tension and diameter values respectively, and they were used as input in the regression model. As in some cases the matrices were non-square, the appropriate version of the Moore-Penrose pseudo inverse technique was used to make them invertible.

2.6 Effect of non-central location of the tendon

The initial study was devised around three key independent variables: the tendon's diameter, the load it carried, and its position

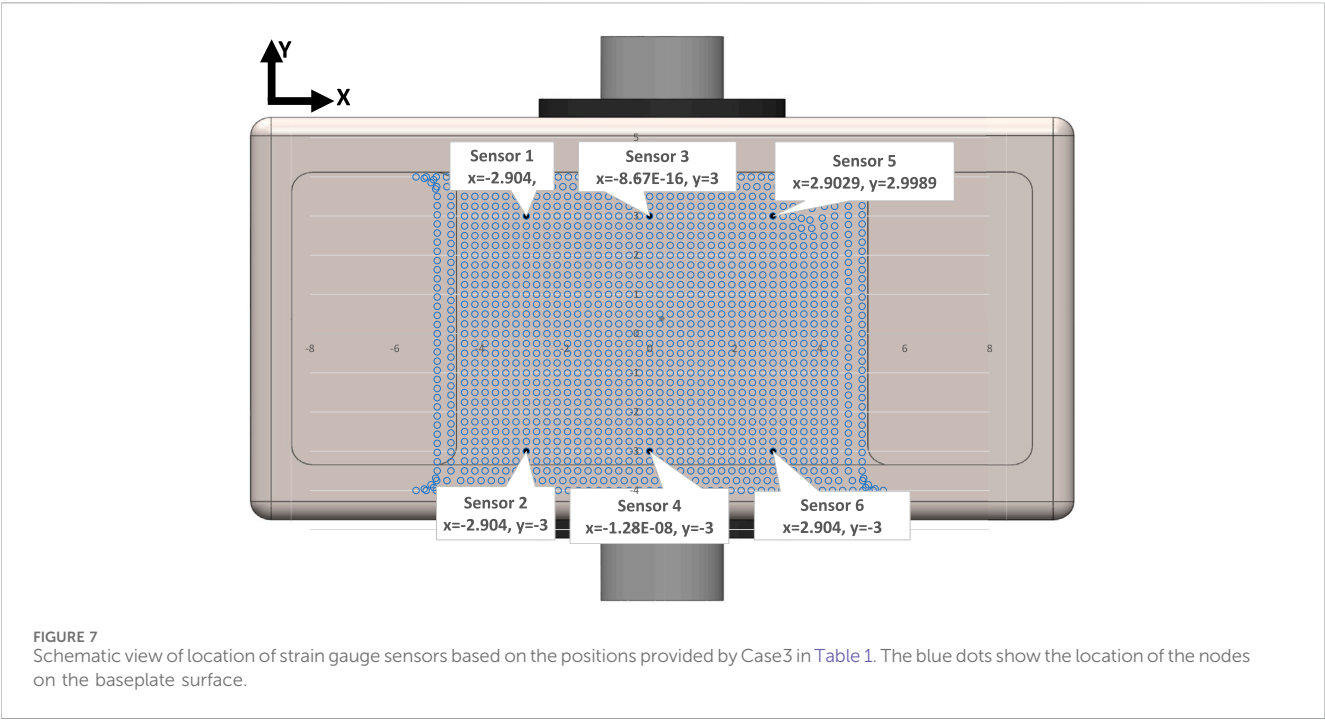


TABLE 3 Strain gauge coordinates, considered cases and resulting errors (load, N and tendon diameter, mm) for each gauge coordinate position.

Series	Location of sensors - cases (Table 1)	Strain combination (Table 2)	Position of the tendon	Average load error (N)	SD of load error	Average position error (mm)	SD of position error
1	1	2	central positions only	7	3	0.0	0.1
2	2	2	central positions only	−19	11	−0.5	0.2
3	3	2	central positions only	2	1	−0.1	0.0
4	3	2	central, left and cross positions	2	1	−0.1	0.1
5	4	2	central positions only	9	4	0.1	0.1
6	5	2	central positions only	36	16	0.4	0.2
7	3	1	central positions only	2	1	−0.1	0.0
8	3	3	central positions only	2	1	−0.1	0.0

SD: Standard Deviation

within the buckle. To examine scenarios where the tendon was not centrally seated within the buckle, three primary situations for tendon contact with the end bearings were simulated: i) *Central*: This situation entails the tendon aligning precisely along the buckle’s midline on the Y-axis. ii) *Diagonal*: Here, the tendon is positioned diagonally across the buckle. iii) *One-side*: This involves situating the tendon on one side (either right or left) of the bearing, in close proximity to a side wall. These represent possible extreme displacements, for which we still look for adequate measurement accuracy.

3 Results

A series of model analyses was undertaken to assess the accuracy of the BT in measuring tendon force for variations in load, tendon size and position (Table 3 reports a subset of these). Several gauge locations were tested as per Table 1; for each location the tendon size and position were also varied, but only listed for one gauge location (Table 1, case 3) for brevity, as this was the only set of gauge placements of those tested which gave results which were

TABLE 4 X strains for 500N and 4.4 mm diameter tendon, for the 5 cases of Table 1.

Table 1 cases	D	E	X strain	X strain
	X,Y (mm)	X,Y (mm)		
1	1.9; 2.5	0; 2.5	-3.55E-05	-3.67E-05
2	1.9; 3.0	0; 3.0	-3.34E-05	-3.13E-05
3	2.9; 3.0	0; 3.0	-2.19E-05	-3.13E-05
4	4.1; 2.5	0; 2.5	2.96E-06	-3.67E-05
5	4.1; 3.0	0; 3.0	1.13E-05	-3.13E-05

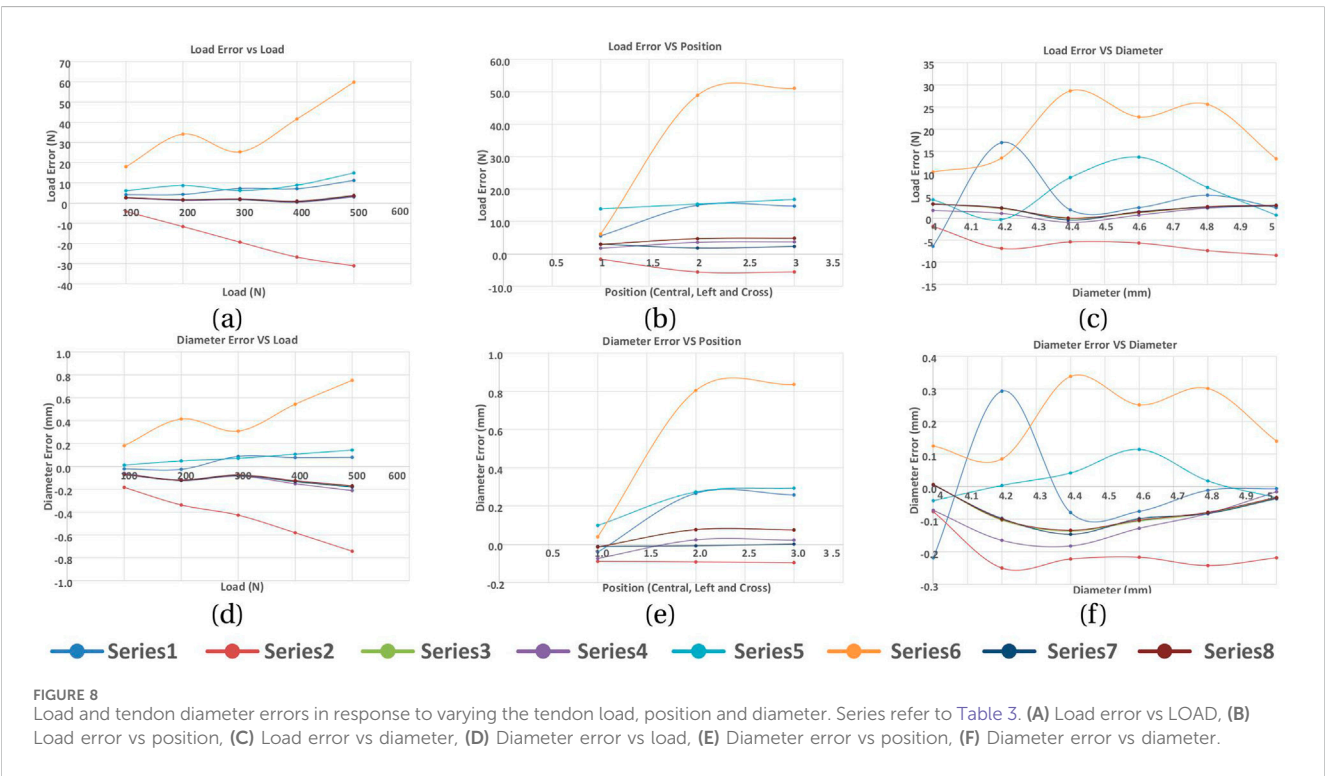
satisfactory for the tendon located centrally and in line with the buckle. All other locations (Table 1, cases 1,2,4,5) gave errors in load (Table 3). Four of the six gauges are placed symmetrically about X and Y-axes (with the remaining two placed along the Y-axis in line with the central rod), and the modelled strains were in broad agreement with those expected from cantilever loading produced by the tendon. Strains in the X direction for each of the five gauge positions of Table 1 are shown in Table 4, for 500N tendon force and 4.4 mm tendon diameter. The strains at the outer gauge locations (sensors 1,2,5,6, Table 1) were in general lowest at the outer bearings and increased towards the centre, as shown by the strain gradient plot of Figure 6. For the one gauge location which gave satisfactory results for gauge locations (Table 1, case 3), the results for variation in tendon size and position were also satisfactory (within 2N error); Table 3, series 4. There was no change in these results when the other two strain combinations (Table 2 rows 1,3) were used; Table 3, series 7,8. For each of the eight series combinations of Table 3, the errors in predicted load and tendon diameter are shown in Figure 8, for

variations in load, tendon diameter and position. Series 3,4,7,8 show best overall performance, all having X = 3 mm.

4 Discussion

In this study, a prototype buckle transducer instrumented with several strain gauges has been FE modelled with loads applied directly to the end bearing surfaces and central rod, upon which the tendon would bear. Combinations of axial and shear forces were applied according to the angle of passage with which the tendon would pass through the transducer. Instead of modelling the morphology of a real tendon, we recognised that this would be true of only one tendon, and so we instead applied a distributed load to each bearing, and varied the centre and distribution of these loads to observe changes in the predicted tendon tension resulting from a regression model. Within a limited range of tendon diameters (3–5 mm), and corresponding central rod sizes to maintain an angle of passage which gave suitably large strains whilst reducing the tendon path length, strains were computed at several sites on the baseplate and used in linear regressions to determine the sensitivities to change in load and tendon thickness. The resulting load errors when varying load, tendon thickness and position were found to be acceptably small for a limited range of gauge positions around 3 mm from the baseplate centre in X and Y directions.

From the simple mathematical analysis presented earlier (Equations 10a-d,), a significantly different magnitude of strain is required between central and outer gauges for the unknowns (T , α , β) to be determined. Our results show that this is only realised for gauge locations around X = 3 mm (Table 4). For X = 2 mm the strains are higher but more similar to X = 0; for X = 4 mm the strains are opposite in sign and becoming too low to enable sufficient load



resolution in a practical transducer. This highlights the importance of choosing appropriate gauge locations for the method to be able to yield satisfactory load errors irrespective of changes in tendon position and size (within the constraints of the BT). In a practical transducer the strain gauges occupy a finite area of the baseplate, thus averaging strains across the gauge grid; there is also less room for siting gauges appropriately, although the findings of this study would allow for suitable gauge sites practically. Moreover, these gauge locations are within regions of slowly changing strain fields, allowing for some immunity to positional errors.

The design of our BT attempted to allow for the inclusion of a cavity for electronics for *in vivo* measurement and telemetry. This necessarily stiffened the structure, such that the developed strains were low, Table 4, which would require the use of semiconductor strain gauges to achieve adequate load sensitivity. Future designs could aim to reduce this stiffness, minimising especially sidewall height which stiffens the cantilever action. Further refinement could include improved tendon contact simulation or even the inclusion of the tendon itself rather than its contacts with the transducer.

One aspect of the design which we did not explicitly test here is the ability of the transducer to determine loads over a range of angles of passage through the device, although the theory supports this. The next design iteration will include this.

We have shown here that an approach using multiple strain gauges is able to determine the tendon load independent of a certain range of tendon thickness and position in the buckle. This is shown theoretically by the mathematical analysis presented, although in a practical device, as in this FE study, the sensitivities would be found by regression.

5 Conclusion

This study introduces a miniaturized modular BT that offers adjustability to accommodate various Flexor Carpi Radialis tendon sizes. The initial hypothesis posits that the BT can be effectively calibrated regardless of tendon thickness and tension load. To explore this, the buckle was subjected to mathematical modeling and subsequent Solidworks simulations. By applying different forces to the buckle with varying bearing sizes, strain values were recorded across different cases. A sequence of regression analyses was devised to achieve two main objectives: I) determine the optimal location for installing gauge sensors on the buckle's baseplate, and II) assess the model's accuracy in calibrating the buckle while considering tendon position and tension load independence. The most favorable outcomes were achieved when the gauges were positioned with a maximum separation distance, avoiding proximity to the baseplate edges. The refined modular design of the BT indicates its potential readiness for the pilot study phase, involving its manufacturing and testing with Series 4 configuration for the installation of strain gauges. This particular configuration has demonstrated promising outcomes, notably in its capacity to facilitate the accurate determination of tendon tension while remaining unaffected by variations in local thickness. Our initial hypothesis was that the BT could be calibrated regardless of tendon thickness, placement and tension load. While the design shows promise in achieving this independence, variations in the angle of passage (AoP) within the

BT were not adequately explored. As a result, further research is required to test for variation in AoP across different rod sizes and assess the accuracy of the transducer under these conditions. Subsequent phases of this research involve constructing a prototype BT for testing with human FCR tendons, aiming to compare real-world results against those attained through simulation. Furthermore, future possibilities entail *in vivo* device implantation to characterize forearm spasticity.

Data availability statement

The raw data supporting the conclusions of this article will be made available by the authors, without undue reservation.

Author contributions

AR: Conceptualization, Methodology, Software, Investigation, Validation, Data curation, Formal analysis, Visualization, Project administration, Writing-original draft, Writing-review and editing. ST: Conceptualization, Methodology, Investigation, Validation, Formal analysis, Resources, Supervision, Funding acquisition, Project administration, Writing-original draft, Writing-review and editing.

Funding

The author(s) declare that financial support was received for the research, authorship, and/or publication of this article.

Acknowledgments

We would like to thank Professor Rui Loureiro and Dr. Tom Quick for their support of this study (under the RESPONSS project: Rehabilitation Technologies Supporting Clinical and Self-management of Spasticity - Grant number: 538267, funded by the Leslie Foundation).

Conflict of interest

The authors declare that the research was conducted in the absence of any commercial or financial relationships that could be construed as a potential conflict of interest.

Publisher's note

All claims expressed in this article are solely those of the authors and do not necessarily represent those of their affiliated organizations, or those of the publisher, the editors and the reviewers. Any product that may be evaluated in this article, or claim that may be made by its manufacturer, is not guaranteed or endorsed by the publisher.

References

- An, K.-N., Berglund, L., Cooney, W. P., Chao, E. Y., and Kovacevic, N. (1990). Direct *in vivo* tendon force measurement system. *J. biomechanics* 23, 1269–1271. doi:10.1016/0021-9290(90)90384-f
- Ateş, F., Temelli, Y., and Yucesoy, C. A. (2016). The mechanics of activated semitendinosus are not representative of the pathological knee joint condition of children with cerebral palsy. *J. Electromyogr. Kinesiol.* 28, 130–136. doi:10.1016/j.jelekin.2016.04.002
- Best, R., Böhle, C., Mauch, F., and Brüggemann, P. G. (2016). Preventive lateral ligament tester (pllt): a novel method to evaluate mechanical properties of lateral ankle joint ligaments in the intact ankle. *Knee Surg. Sports Traumatol. Arthrosc.* 24, 963–970. doi:10.1007/s00167-014-3190-3
- Coobs, B. R., Wijdicks, C. A., Armitage, B. M., Spiridonov, S. I., Westerhaus, B. D., Johansen, S., et al. (2010). An *in vitro* analysis of an anatomical medial knee reconstruction. *Am. J. sports Med.* 38, 339–347. doi:10.1177/0363546509347996
- Edsfieldt, S., Rempel, D., Kurska, K., Diao, E., and Lattanza, L. (2015). *In vivo* flexor tendon forces generated during different rehabilitation exercises. *J. Hand Surg. Eur. Volume* 40, 705–710. doi:10.1177/1753193415591491
- Fleming, B. C., and Beynnon, B. D. (2004). *In vivo* measurement of ligament/tendon strains and forces: a review. *Ann. Biomed. Eng.* 32, 318–328. doi:10.1023/b:abme.0000017542.75080.86
- Fridén, J., Shillito, M. C., Chehab, E. F., Finneran, J. J., Ward, S. R., and Lieber, R. L. (2010). Mechanical feasibility of immediate mobilization of the brachioradialis muscle after tendon transfer. *J. hand Surg.* 35, 1473–1478. doi:10.1016/j.jhsa.2010.06.003
- Fukashiro, S., Komi, P., Järvinen, M., and Miyashita, M. (1993). Comparison between the directly measured achilles tendon force and the tendon force calculated from the ankle joint moment during vertical jumps. *Clin. Biomech.* 8, 25–30. doi:10.1016/s0268-0033(05)80006-3
- Gregor, R., Komi, P., and Järvinen, M. (1987). Achilles tendon forces during cycling. *Int. J. sports Med.* 8, S9–S14. doi:10.1055/s-2008-1025698
- Herzog, W., Archambault, J., Leonard, T., and Nguyen, H. (1996). Evaluation of the implantable force transducer for chronic tendon-force recordings. *J. biomechanics* 29, 103–109. doi:10.1016/0021-9290(95)00019-4
- Keegan, K., Baker, G., Boero, M., and Pijanowski, G. (1991). “Measurement of suspensory ligament strain using a liquid mercury strain gauge: evaluation of strain reduction by support bandaging and alteration of hoof wall angle,” in *Proceedings of the 37th annual convention of the American association of equine practitioners, San Francisco, California (1991–1992)*, 243–244.
- Komi, P., Salonen, M., Järvinen, M., and Kokko, O. (1987). *In vivo* registration of achilles tendon forces in man. *Int. J. Sports Med.* 8, S3–S8. doi:10.1055/s-2008-1025697
- Komi, P. V. (1990). Relevance of *in vivo* force measurements to human biomechanics. *J. biomechanics* 23, 23–34. doi:10.1016/0021-9290(90)90038-5
- Lee, S. S., de Boef Miara, M., Arnold, A. S., Biewener, A. A., and Wakeling, J. M. (2011). Emg analysis tuned for determining the timing and level of activation in different motor units. *J. Electromyogr. Kinesiol.* 21, 557–565. doi:10.1016/j.jelekin.2011.04.003
- Martin, J. A., Brandon, S. C., Keuler, E. M., Hermus, J. R., Ehlers, A. C., Segalman, D. J., et al. (2018). Gauging force by tapping tendons. *Nat. Commun.* 9, 1592. doi:10.1038/s41467-018-03797-6
- Mukherjee, A., and Chakravarty, A. (2010). Spasticity mechanisms—for the clinician. *Front. neurology* 1, 149. doi:10.3389/fneur.2010.00149
- Pourcelot, P., Defontaine, M., Ravary, B., Lemâtre, M., and Crevier-Denoix, N. (2005). A non-invasive method of tendon force measurement. *J. Biomechanics* 38, 2124–2129. doi:10.1016/j.jbiomech.2004.09.012
- Ravary, B., Pourcelot, P., Bortolussi, C., Konieczka, S., and Crevier-Denoix, N. (2004). Strain and force transducers used in human and veterinary tendon and ligament biomechanical studies. *Clin. Biomech.* 19, 433–447. doi:10.1016/j.clinbiomech.2004.01.008
- Roberts, C. (1994). *In vivo* measurement of human anterior cruciate ligament forces during knee extension exercises. *Trans. ORS* 15, 84.
- Schuijnd, F., Garcia-Elias, M., Cooney III, W. P., and An, K.-N. (1992). Flexor tendon forces: *in vivo* measurements. *J. hand Surg.* 17, 291–298. doi:10.1016/0363-5023(92)90408-h
- Stone, J., Madsen, N., Milton, J., Swinson, W., and Turner, J. (1983). Developments in the design and use of liquid-metal strain gages. *Exp. Mech.* 23, 129–139. doi:10.1007/bf02320400
- Walmsley, B., Hodgson, J., and Burke, R. (1978). Forces produced by medial gastrocnemius and soleus muscles during locomotion in freely moving cats. *J. neurophysiology* 41, 1203–1216. doi:10.1152/jn.1978.41.5.1203
- Weber, J., Agur, A., Fattah, A., Gordon, K., and Oliver, M. (2015). Tensile mechanical properties of human forearm tendons. *J. Hand Surg. Eur. Volume* 40, 711–719. doi:10.1177/1753193415584715
- Wehrle, G., Nohama, P., Kalinowski, H. J., Torres, P. I., and Valente, L. C. G. (2001). A fibre optic bragg grating strain sensor for monitoring ventilatory movements. *Meas. Sci. Technol.* 12, 805–809. doi:10.1088/0957-0233/12/7/309
- Witte, T. H., Cheetham, J., Rawlinson, J. J., Soderholm, L. V., and Ducharme, N. G. (2010a). A transducer for measuring force on surgical sutures. *Can. J. veterinary Res.* 74, 299–304.
- Witte, T. H., Cheetham, J., Soderholm, L. V., Mitchell, L. M., and Ducharme, N. G. (2010b). Equine laryngoplasty sutures undergo increased loading during coughing and swallowing. *Veterinary Surg.* 39, 949–956. doi:10.1111/j.1532-950x.2010.00742.x
- Yucesoy, C. A., Temelli, Y., and Ateş, F. (2017). Intra-operatively measured spastic semimembranosus forces of children with cerebral palsy. *J. Electromyogr. Kinesiol.* 36, 49–55. doi:10.1016/j.jelekin.2017.07.003



OPEN ACCESS

EDITED BY

Zhen (Jeff) Luo, University of Technology
Sydney, Australia

REVIEWED BY

Dhananjay T. Tambe,
University of South Alabama, United States
Yen-Liang Liu,
China Medical University, Taiwan

*CORRESPONDENCE

Alessandra Carriero,
✉ acarriero@ccny.cuny.edu

RECEIVED 17 September 2024

ACCEPTED 11 December 2024

PUBLISHED 06 January 2025

CITATION

Muñoz A, Docaj A, Fernandez J and Carriero A
(2025) *FiberO* for an automated quantitative
analysis of fibers orientation and organization in
biological fibrous tissues.
Front. Bioeng. Biotechnol. 12:1497837.
doi: 10.3389/fbioe.2024.1497837

COPYRIGHT

© 2025 Muñoz, Docaj, Fernandez and Carriero.
This is an open-access article distributed under
the terms of the [Creative Commons Attribution
License \(CC BY\)](#). The use, distribution or
reproduction in other forums is permitted,
provided the original author(s) and the
copyright owner(s) are credited and that the
original publication in this journal is cited, in
accordance with accepted academic practice.
No use, distribution or reproduction is
permitted which does not comply with these
terms.

FiberO for an automated quantitative analysis of fibers orientation and organization in biological fibrous tissues

Asier Muñoz, Anxhela Docaj, Julen Fernandez and
Alessandra Carriero*

Department of Biomedical Engineering, The City College of New York, New York, NY, United States

Many biological fibrous tissues exhibit distinctive mechanical properties arising from their highly organized fibrous structure. In disease conditions, alterations in the primary components of these fibers, such as type I collagen molecules in bone, tendons, and ligaments, assembly into a disorganized fibers architecture generating a weak and/or brittle material. Being able to quantitatively assess the fibers orientation and organization in biological tissue may help improve our understanding of their contribution to the tissue and organ mechanical integrity, and assess disease progress and therapy effect. In this work, we present *FiberO*, a new open-source available software that automatically quantifies fibers orientation, by performing morphological image openings, and fibers organization within the tissue, by determining and plotting their continuity in groups. *FiberO* performance is here evaluated using second harmonic generation microscopy images of mouse bones and tendons as examples of biological fibrous tissues. *FiberO* outperformed *Directionality* and *OrientationJ*, two open-source plugins available in ImageJ, and *FiberFit* and *CT-FIRE*, in the calculation and plotting of fibers orientation in reference images with known fibers orientation. Additionally, *FiberO* is currently the sole software to date able to accurately track the continuity of aligned fibers, and it quantifies and displays the organized surface(s) in the tissue of interest. *FiberO* can be used in the wider engineering and science field to investigate the fibers orientation and organization of different natural and synthetic fibrous tissues.

KEYWORDS

fiber, orientation, organization, continuity, fibrous tissue

Introduction

Biological fibrous tissues are an incredible source of inspiration for new man-made materials. Their composite nature and complex hierarchical structure confer them ultimate material properties that are difficult to find in new materials. In particular, bone, the tissue constituting our skeleton, is a biological composite material made of a mineral phase, based on hydroxyapatite mineral crystals, embedded in a collagen protein mesh. The hierarchical arrangement of its primary components makes bone a strong and tough material (Muñoz et al., 2021). Tendons and ligaments are soft connective tissues able to sustain high tensile loads thanks to their collagenous hierarchical organization. Similarly to skin and blood vessels, which are also composed by elastin, they are energy store tissues able to regain their original shape after being loaded in elastic conditions. These biological fibrous tissues are a

great source of inspiration for newly generated materials; yet we still do not know how exactly the hierarchical structure confers them their material properties. Therefore, knowing how their primary components are organized within the material, particularly their fibers arrangement, will help reveal how these biological materials develop their material properties, i.e., stiffness, strength and toughness. Indeed, despite a good amount of research conducted in the field, it is still unclear the link between the structural and compositional properties of fibers (in particular collagen and other fibrous proteins organization) in biological materials and their mechanical properties.

Imaging fibers structure and organization within the biological tissues can be very informative to (i) understand the biomechanical properties of the tissue, (ii) detect and study progression of disease, and (iii) assess efficacy of treatments. Particularly, second harmonic generation (SHG) microscopy, a derivative of multiphoton microscopy, has a unique ability to directly image collagen fibers structure in different tissues, including tendon, ligament, bone (Millard et al., 2003), and lung (Kottmann et al., 2015) tissue without the need for labeling with either fluorophores or fluorescent proteins (Williams et al., 2001; Zipfel et al., 2003). Type I collagen generally produces a very strong signal in both backward and forward SHG microscopy, whereas collagen type II, III, V, XI, XXIV and XXVII generate weaker and sometimes not sufficient signal (Yoshioka et al., 2022; Ranjit et al., 2015; Chen et al., 2012; Lilledahl et al., 2011). Apart from collagen, acto-myosin, microtubules and elastin have been previously imaged using SHG microscopy in their endogenous tissues, yet collagen type I signal remains the most efficient SHG source proteins with subsequently brightest signal compared to any other fibrous protein (Campagnola et al., 2002; Chu et al., 2004; Dombek et al., 2003; Le et al., 2007; Mansfield et al., 2009). One of the principal advantages of SHG microscopy over many other imaging techniques is that it achieves a high level of penetration in both thick and dense tissue samples, allowing for visualization of the collagen assembly with no need for fixation. Additionally, live cell and tissue imaging is also possible since there is no excitation of molecules nor photobleaching of the tissue (Williams et al., 2001; Kim et al., 2000). SHG microscopy imaging allows for visualization of collagen protein assembly and organization at the sub-micrometer and micrometer scales (Campagnola et al., 2002; Chu et al., 2004). This particular imaging technique has its origin in the induction of intense laser radiation in tissue samples resulting in frequency doubling, i.e., the optical effect in which two incident photons combine and emit a single photon with visible light (Millard et al., 2003; Campagnola et al., 1999; Mohler et al., 2003; Roth and Freund, 1981).

In diseases or pathological conditions that are associated with fibers disorganization such as fibrosis (Kottmann et al., 2015; Parra et al., 2006; Rittié, 2017), cancers (Rittié, 2017; Cloos et al., 2003; Zunder et al., 2020), atherosclerosis (Le et al., 2007), cleft lip (Noor et al., 2022), or cases pertaining to connective tissues and disorders such as tendinopathy (Knapik and Pope, 2020), osteoarthritis (Yoshioka et al., 2022), fracture healing (Nair et al., 2022), skin damage (Mostaço-Guidolin et al., 2017), Paget's disease (Cloos et al., 2003) or osteogenesis imperfecta (OI) (Shapiro et al., 2021), alterations of fibrous proteins orientations have been previously observed using polarized light and SHG microscopy. However, the inability to quantify their orientation and organization has left us

with very interesting questions that researchers are trying to solve regarding the assessment of their direct contribution to their endogenous tissue's mechanical properties. Similarly, tissue engineering research also sees a rising need for a better understanding of the link between fibers structure organization and tissue mechanics to create new materials with formidable mechanical performances (Kim et al., 2021).

The orientation of biological tissue fibers visualized with SHG microscopy has been previously quantified using a variety of computational methods. These include the 2D Fourier transform (Bueno et al., 2013; Sivaguru et al., 2010), Fourier transform followed by power spectral density determination (Bayan et al., 2009), Fourier transform combined with a Radon transform (McLean, 2015), edge detection technique (Hill et al., 2012), watershed (Koch et al., 2014), and wavelet transforms (Tilbury et al., 2014). Some of these methods require significant image pre-processing steps that can delete useful information or amplify the noise in images with poor signal-to-noise ratio (Bredfeldt et al., 2014). For instance, Fourier transform often requires extensive noise reduction, contrast enhancement and image scaling to improve the accuracy of frequency domain analysis (Singh and Mittal, 2014). Similarly, edge detection methods involve pre-processing steps like smoothing or thresholding to isolate relevant edges while the watershed algorithm requires careful image smoothing and segmentation, especially in cases where boundaries are unclear (Zhao and Xie, 2013). Others are based on computationally expensive image transformation techniques (Barbhuiya and Hemachandran, 2013; Deans, 2007). However, it is still challenging to automatically and quantitatively determine how these fibers are arranged within the tissue, and discern the regions of organized and disorganized fibers. These regions are usually visually inspected and manually separated in the images of interest (Hedjazi et al., 2022). Human perception can be appropriate for visually detecting well-organized fiber structures from images, such as those from SHG microscopy, but this would only be as far as a qualitative analysis, and it would fail at a quantitative assessment of such information, especially when the comparison between samples of different groups is necessary. Therefore, for an accurate evaluation of fibers organization in SHG microscopy images, a methodology that is based on a quantitative and automated analysis of fibers continuity is essential, and this has been the focus of this work.

The development of a reliable, open-source, quantitative approach that enhances our understanding of the fibers alignment and organization in biological tissues, such as bone, can help identify diseases, assess their progress and efficacy of treatments in the clinical community. Importantly, having an open-source tool that provides accurate results offers the opportunity to compare results in consistent manner using a standardized platform at no cost for the researchers worldwide. Here we present *FiberO*, a new quantitative and objective software that automatically identifies fibers, and quantifies their orientation and organization within the tissues, according to the fibers contiguous structure. The morphological opening applied to the SHG microscopy images used in this study allows the creation of maps depicting the collagen fibers orientation. Furthermore, the application of 8-neighbor connectivity of the angular data from the output images of the previous step enables to trace tissue organization in terms of fibers continuity. This standardized and

unbiased method for interpreting greyscale images of fibers, as those obtained from SHG microscopy images, can be used to support material characterization, clinical studies of biopsies, tissue engineering as well as any other analysis of fibrous tissues.

Methods

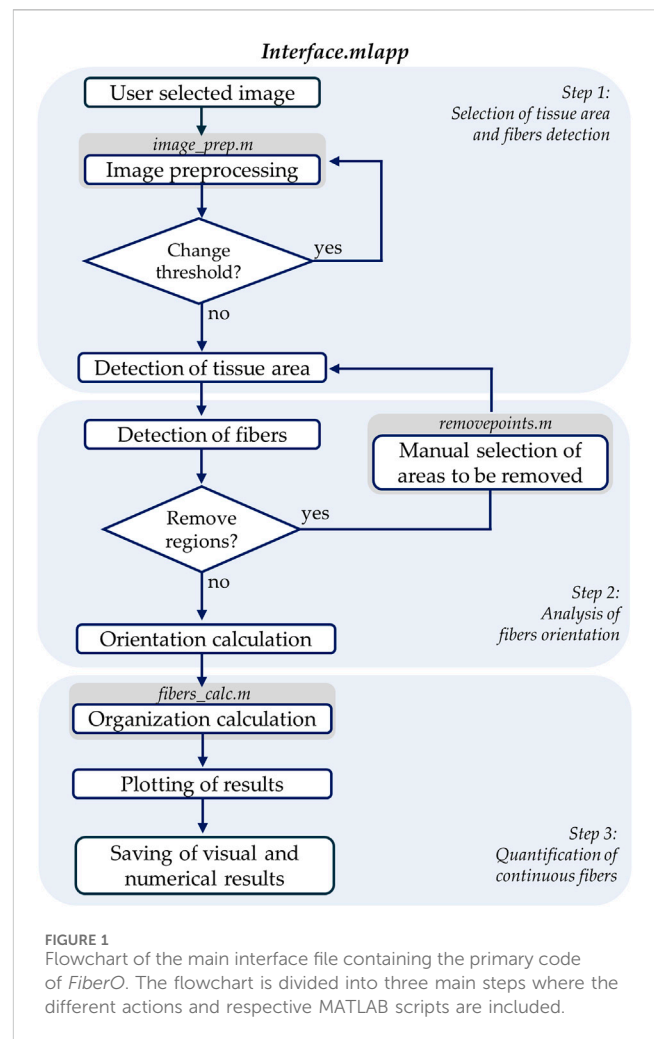
Images of fibers within tissues: SHG microscopy images of bone and tendon

To demonstrate the value and performance of *FiberO*, our new methodology, we considered SHG microscopy images of tibial bone and tail tendons of 14 week old *oim/oim* (B6C3fe-a/acolla2^{*oim/oim*}) mouse model of OI, known to have disoriented and disorganized fibers (Hedjazi et al., 2022; Blouin et al., 2019; Nadiarnykh et al., 2007; Fratzl et al., 1996), bone fragility (Carriero et al., 2014a; Carriero et al., 2014b; Carriero et al., 2014c), and joint and tendon hyper-elasticity (Chipman et al., 1993; Enderli et al., 2016). Tissues from their wild type (WT) counterparts were used as healthy control references of well aligned, continuous fibers within tissues. The *oim* mouse model of OI presents with a naturally occurring collagen type I mutation and similar phenotypic expressions to humans with moderate to severe OI (Chipman et al., 1993; Enderli et al., 2016). Here, we are using *oim* bone and tendon tissue as a model of disorganized collagen fibers as previously observed using polarized light microscopy, SHG microscopy (Hedjazi et al., 2022; Blouin et al., 2019; Nadiarnykh et al., 2007) and small angle X-ray scattering (Fratzl et al., 1996). Yet these observations remained qualitative in nature (Blouin et al., 2019).

To prepare the bone samples, mouse tibiae transverse or longitudinal cross-sections (3 mm thick) at approximately 37% mid-diaphyseal tibial length were cut using a slow speed saw machine with a diamond blade, glued on microscope slides, and polished starting with 400 grit silicon carbide paper to a progressively higher finish until a final polishing with 0.5 μm diamond suspension solution. To prepare the tendon samples, mouse tails were excised from the body and the skin removed to expose the tail tendon. Bone and tendon samples were imaged using a Prairie Tech. Ultima IV Multiphoton Microscope (Bruker; Madison, WI) while maintained hydrated in saline solution (PBS). The microscope was equipped with a commercial titanium sapphire femtosecond two-photon laser tuned at 920 nm excitation wavelength to achieve high energies sufficient for a SHG signal and allow for optimal birefringence. The 460/50 nm bandpass filter used to detect emitted signals granted a spectral window between 410 nm and 510 nm. Backward SHG microscopy images were obtained from the transversely cut sections using a 40 \times 0.8 N.A. water immersion objective lens. Images acquired were of three possible resolutions, (512 \times 512, or 1024 \times 1024 or 2048 \times 2048 pixels) with a pixel size of 0.11 μm . Frame averaging was set at four and dwell time per pixel was defined as 0.8 s.

FiberO algorithm

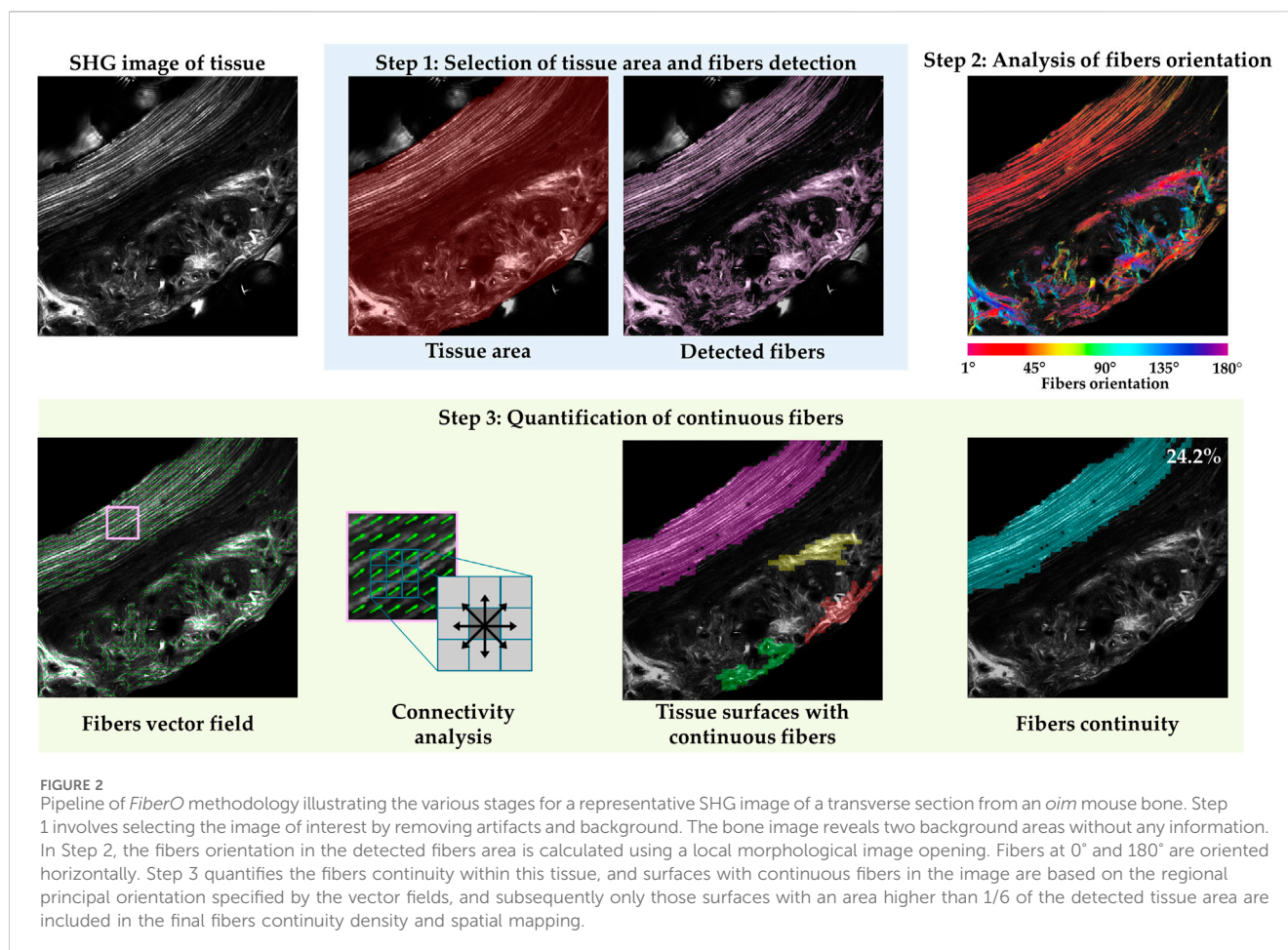
We created a custom MATLAB algorithm with a user interface, called *FiberO*, to automatically identify and measure the orientation of fibers as well as the quantity of organized fibers in images of fibrous tissues (Figure 1). The software is available on GitHub for



public access and use in the following link: <https://github.com/CarrieroLab/FiberO>.

Step 1: selection of tissue area and fibers detection

SHG microscopy can effectively capture collagen-specific images of bone sections or tendon segments, but these images can also be characterized by low signal-to-noise ratio in areas with little collagen, or in the background, and the appearance of artifacts, such as those arising from laser power fluctuations, imaging artifacts and possible air bubbles forming while imaging in wet conditions. Therefore, the first step of the methodology is to remove the unwanted pixels of background and artifacts (e.g., air bubbles in SHG images) from the images with an automatic threshold that determines the minimum intensity value of a pixel to proceed further with the analysis (Figure 2 Step 1). Additionally, a visual inspection can be performed, allowing the user to manually select and remove remaining background and artifacts pixels in the raw images by clicking on various points to define the vertices of a polygonal area for elimination. Next, the images are divided in a total of 100 by 100 facets (which size in pixels depends on the size of our images, e.g., 50 \times 50 pixels for 512 \times 512 pixel images, 100 \times 100 pixels for 1024 \times 1024 pixel images, and 200 \times 200 pixels for 2048 \times 2048 pixel images). At this point, facets with noisy data were assigned as NaN values and were not considered for the next



processing steps. This denoising step allows for a boost in the performance of the custom written code and a reduction in the overall computational time. If artifact areas are within the tissue, they count as part of total tissue area of interest; however, if they are connected with the edge of the image, they do not count towards the total tissue area of interest. Besides this, artifact areas do not interfere with subsequent analysis steps.

Step 2: analysis of fibers orientation

Firstly, the detection of fibers is necessary to identify which pixels should be considered for the orientation calculation. To achieve this, image sharpening is applied to enhance fine details and edges within the image. This process utilizes gradients in pixel intensities along the horizontal and vertical directions to identify areas where fibers are likely to be present, making them more distinguishable for subsequent analysis (Joshi and Koju, 2012). After computing the gradients, adaptive thresholding is applied, which takes into account the intensity variations within smaller regions, or neighborhoods, of the image. This adaptive approach helps overcome challenges existing in some type of imaging, such as SHG microscopy, including issues like non-uniform illumination or varying fiber intensities. After these processes, fibers located in the foreground of the image are differentiated from the dark background of the image. However, it is important to note that some of the detected patterns might not be bright enough to be considered as collagen fibers. To ensure precise detection of fibers a final intensity threshold is applied.

At this point the code calculates *the fibers density* (quantity of the fibers in the tissue) and *the fibers average intensity* (quality of the fibers in the tissue), and assesses *the fibers orientation* in the tissue.

To assess the orientation of fibers, a mathematical morphology technique with an opening of an image is implemented to erode away the boundaries of regions of foreground pixels, followed by a dilation to add pixels to the boundaries of objects in images (Figure 2 Step 2). By applying them sequentially, foreground regions that match the shape of the structuring element used in the operation can be preserved, while all other pixel regions are removed. At this point, a structural element with the shape of a line, which assimilates to the shape of fibers, is rotated starting from an angle of 1° up to 180°, and for every pixel position, the orientation in which the output image has the most intense value is saved. Obtaining the orientation for every pixel, the fibers orientation colormaps are generated (Figure 2 Step 2). These images show the direction of the fibers in the entire tissue section.

Step 3: quantification of continuous fibers

To determine how the fibers are organized in the tissue, *the fibers continuity* is assessed. As a first step, the vector field indicating the regional preferential orientation of the fibers is generated. For this step, the images are again divided in a grid of 50 x 50 facets. Because the images are divided in a grid of facets, the mode or the most frequent orientation value for all the pixels inside every facet is calculated, representing the main orientation of the fibers within each facet (Figure 2 Step 3 Fibers vector field). Pixels with very low

intensity values and a preferential orientation of 180° are not accurately characterized by the morphological opening, significantly affecting the direction of the vectors in the vector field. As a result, they are excluded from further consideration. Next, we performed the analysis of tissue surfaces with continuous fibers by considering the eight neighbors' connectivity for every facet (Figure 2 Step 3 Connectivity analysis). In this process, each facet is considered to be connected to the adjoining facets if the difference of their principal orientation is smaller or equal to 20° . Doing this, the whole set of surfaces that compose the bone sections are obtained. Only groups of continuous fibers whose surfaces covered more than 30 facets (over the total 50×50 facets) are displayed. Next, the surfaces are sorted in descending order based on of their overall surface area (Figure 2 Step 3 Tissue surfaces with continuous fibers), and only those surfaces with an area bigger than a sixth of the firstly detected fibers surface area in the analyzed image are maintained and considered as surfaces with continuous well-oriented fibers (Figure 2 Step 3 Fibers continuity). Finally, the percentage of tissue with continuous fibers is obtained as the ratio between the sum of the surfaces with continuous fibers and the detected tissue area.

Validation

The precision of *FiberO* in determining fibers orientation was verified by comparing it with various well-established techniques typically employed for analyzing fiber networks. A dataset of 75 images featuring artificial fiber networks was created for this validation (Supplementary Figures 1, 2), as previously done in the literature (Morrill et al., 2016). These images contained 120 lines each representing a different fibers configuration and were divided into two distinct groups to understand the accuracy of our technique when working with images containing different fiber sizes and degree of isotropy. The first subset of images consisted of 25 images featuring three different fiber widths (0.5, 1, and 1.5). The fibers were randomly arranged, with 70% (or $\alpha = 0.7$) aligned in the preferred direction. The second subset of images contained 50 images with fibers that were arranged in random orientations with varying values of isotropy ($\alpha = 0.2, 0.4, 0.6, 0.8$, and 1) and had a fiber width of 1.

The performance of *FiberO* was evaluated against *Directionality* (Liu, 1991) and *OrientationJ* (Püspöki et al., 2016), two plugins available in ImageJ, as well as *FiberFit* (Morrill et al., 2016) and *CT-FIRE* (Bredfeldt et al., 2014), standalone tools developed by researchers for analyzing fibrous images. *Directionality* offers two different solutions: the first one is based on Fourier spectrum analysis and the second one is based on the derivation of the local gradient orientation (Liu, 1991). *OrientationJ* computes the orientations based on the gradient structure tensor in a local neighborhood (Püspöki et al., 2016). *FiberFit* utilizes the Fourier transform to generate fiber angle distributions (Morrill et al., 2016), while *CT-FIRE* employs the fast discrete curvelet transform for image denoising and fiber edge enhancement, followed by the *FIRE* fiber extraction algorithm, enabling the precise identification and analysis of individual fibers in complex fibrous tissues (Bredfeldt et al., 2014). The errors between the measured and real principal angle, and between the measured and real amount of fibers oriented within the preferred orientation α were analyzed. To compute α , the sum of counts from the center of the histogram (\pm the standard deviation of the distribution) was divided by the total

counts in the histogram. Statistical analysis was conducted using SPSS (IBM v.28.0) to assess significant differences in the effectiveness of the different image analysis tools. The assumptions for parametric tests were first assessed using the Kolmogorov-Smirnov (K-S) test to evaluate normal distribution and Levene's test to determine homogeneity of variance across the techniques. As the assumptions were not satisfied, statistical differences were evaluated using the Kruskal-Wallis test, a non-parametric alternative to ANOVA. P-values were adjusted for multiple comparisons using the modified Bonferroni correction, as the focus was on evaluating *FiberO*'s performance in relation to each individual tool, rather than comparing the rest of the tools to one another. A visual inspection of the orientation colormaps produced by four different techniques (*FiberO*, *Directionality* in both modes, and *OrientationJ*) was performed using a representative SHG microscopy image of bone to assess the effectiveness of these spatial image processing methods. *FiberFit* and *CT-FIRE* were not included as they do not provide fibers orientation map.

Results

Here we present an automated and quantitative evaluation of fibers orientation and organization in bone and tendon SHG microscopy images as assessed by our novel *FiberO* software. Figure 3 shows the outcome of *FiberO* image processing steps for different bone and tendon SHG microscopy images. These images show the original SHG microscopy images on the first column, the preprocessed image (with fibers density and average fibers intensity) on the second column, the fibers orientation on the third column, followed by the tissue surfaces with continuous fibers, and finally by the mapping (and density) of the fibers continuity.

Case A: mouse cortical bone cross-section with organized fibers

The sequence of images in Figure 3A exhibit a bone section mostly composed of concentric lamellae oriented principally around the endosteum and periosteum of an *oim* mouse bone, following its natural curvature. In the output image, most of the collagen is highlighted, with some collagen fibers oriented perpendicular to the main direction of the remaining collagen fibers in the regions of blood vessels. Angiogenesis precedes osteogenesis and therefore it is interesting to visualize how the bone fibers well align around the intracortical blood vessels. Nevertheless, these continuous fibers groups are too small to be counted in the fibers continuity.

Case B: mouse cortical bone cross-section with disorganized fibers

Figure 3B reveals a bone section with a defined preferential orientation of the collagen fibers in the left half of the image, and a more disorganized matrix in the right side of the image. *FiberO* is able to pick up these two areas automatically, and quantifies the area of collagen fibers continuity to be only 14% of the detected bone tissue area in an *oim* mouse bone.

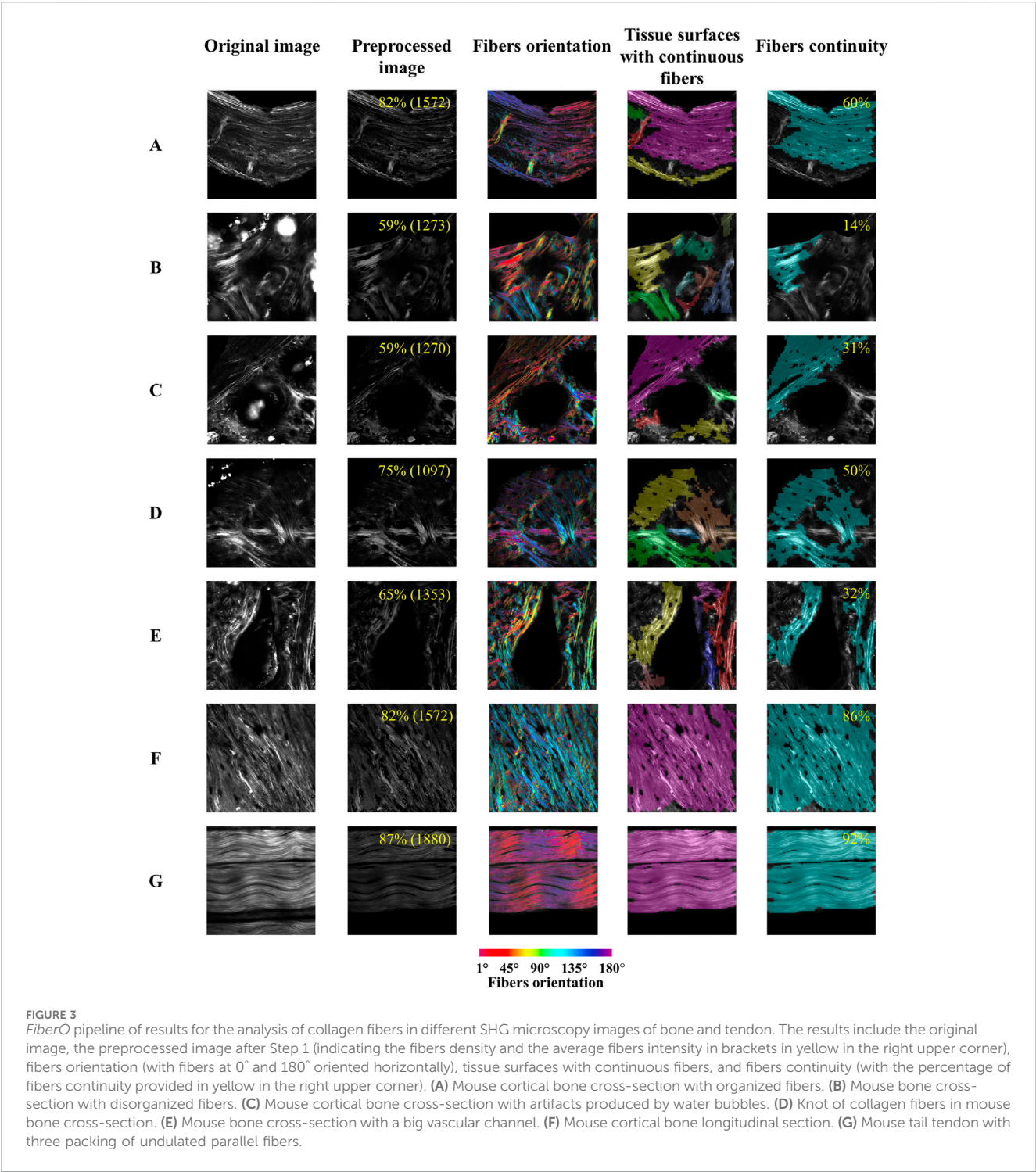


FIGURE 3
FiberO pipeline of results for the analysis of collagen fibers in different SHG microscopy images of bone and tendon. The results include the original image, the preprocessed image after Step 1 (indicating the fibers density and the average fibers intensity in brackets in yellow in the right upper corner), fibers orientation (with fibers at 0° and 180° oriented horizontally), tissue surfaces with continuous fibers, and fibers continuity (with the percentage of fibers continuity provided in yellow in the right upper corner). (A) Mouse cortical bone cross-section with organized fibers. (B) Mouse bone cross-section with disorganized fibers. (C) Mouse cortical bone cross-section with artifacts produced by water bubbles. (D) Knot of collagen fibers in mouse bone cross-section. (E) Mouse bone cross-section with a big vascular channel. (F) Mouse cortical bone longitudinal section. (G) Mouse tail tendon with three packing of undulated parallel fibers.

Case C: mouse cortical bone cross-section with artifacts produced by water bubbles

Figure 3C is characterized by a region with continuous collagen lamellae with a preferred orientation on the top, next to an area of disorganized collagen fiber tissues in an *oim* mouse bone. Two bubbles are depicted in this image and they cover large portion of the disorganized tissue area. *FiberO* here detects the artifacts and does not analyze these three parts of the image. Furthermore, *FiberO* automatically and correctly

selects the area of collagen fiber continuity and estimates it to be 31% of the total bone surface in the image.

Case D: knot of collagen fibers in mouse bone cross-section

The collagen fibers arrangement in Figure 3D shows a knot pattern in a WT mouse bone. The orientation of the fibers at the

knot region seems to overlap, and are mostly well-aligned, and continuous for 50% of the entire bone surface imaged as calculated by *FiberO* software.

Case E: mouse bone cross-section with a big vascular channel

Figure 3E presents the fiber tissue surrounding a big vascular canal of irregular shape in a WT mouse bone. In this bone 32% of the tissue fibers are continuous and mainly located around the edges of the canal, following its shape.

Case F: mouse cortical bone longitudinal section

Figure 3F is a SHG microscopy image of a longitudinal bone section in a WT mouse cortical bone. In this image most of the collagen fibers are oriented at an angle of 120° . In the output image of *FiberO*, 86% of the fibrous surface is highlighted with continuous fibers as the low-signal facets are not considered as continuous parts.

Case G: mouse tail tendon with three packing of undulated parallel fibers

Figure 3G shows the continuous collagen fibers of an *oim* mouse tail tendon. Fibers follow a wavy shape in a given direction. 92% of the entire tissue surface is composed by continuous fibers and is described by our software *FiberO*.

Validation

The performance of the here developed code was analyzed comparing the results provided by *FiberO* for the analysis of new images generated with known fibers thickness and orientation (Supplementary Figures 1, 2) with the ones obtained using reliable fibers orientation determination tools: 1) *Directionality*, which computes the fiber orientations based on the Fourier spectra or the local gradient orientation (Liu, 1991), 2) *OrientationJ*, which is based on the gradient structure tensor in a local neighborhood similarly to our *FiberO* software (Püspöki et al., 2016), 3) *FiberFit*, which also employs the Fourier transform to generate fiber angle distributions (Morrill et al., 2016), and 4) *CT-FIRE*, which combines the fast discrete curvelet transform for image denoising and fiber enhancement with the FIRE algorithm for fiber extraction (Bredfeldt et al., 2014). The graphs in Figures 4A, B present the validation results for all the techniques with varying fibers width in terms of the error for the detected preferential orientation angle and the amount of fibers oriented at this specific direction α . When changing fibers width, *FiberO*'s angle error for different fiber thicknesses was only outperformed by very little ($<0.2^\circ$) by the Fourier spectra-based *Directionality* method for fibers measuring 0.5 and 1.5 in width. In contrast, both *OrientationJ* and *CT-FIRE* performed worse than *FiberO*, exhibiting significantly higher angle errors at different fiber widths. Additionally, when

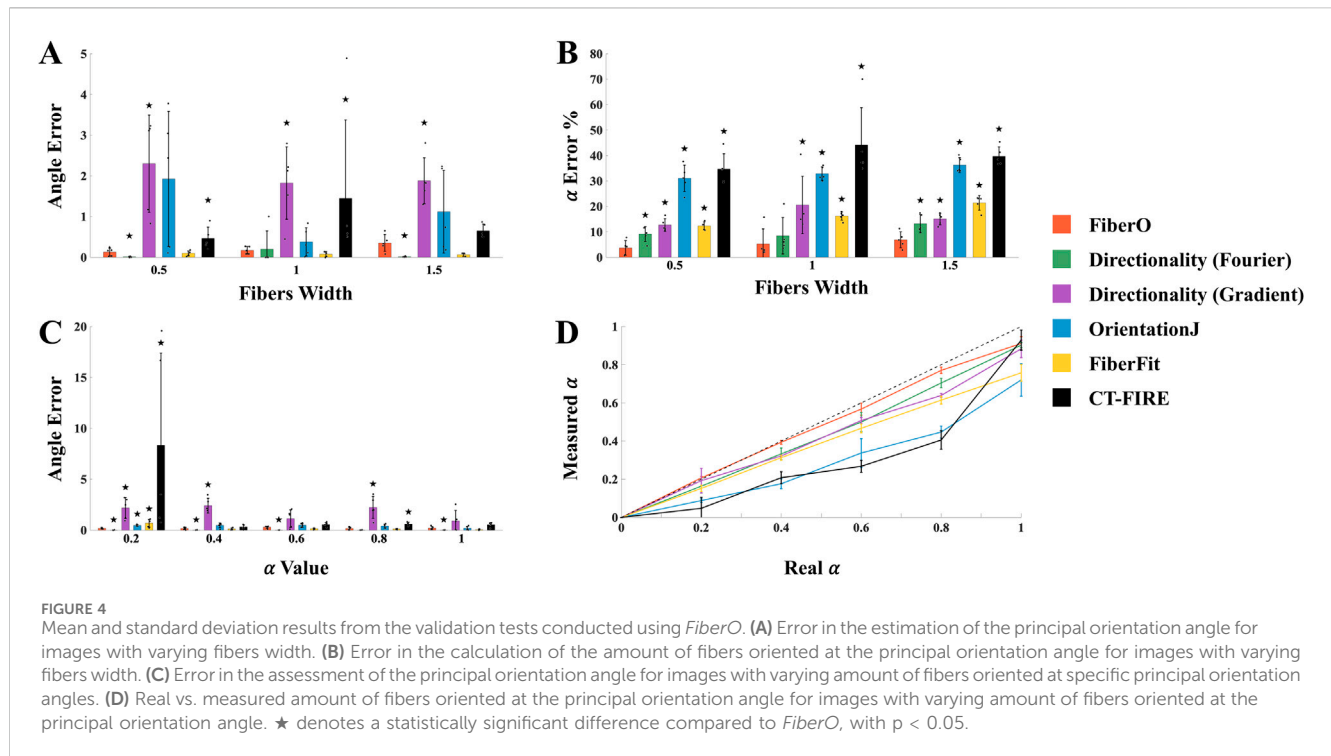
evaluating the percentage error between the actual and measured number of fibers aligned at the preferential orientation α , *FiberO* outperformed all other methods, with an error rate of $5.3\% \pm 4.1\%$. It was followed by the Fourier spectra-based *Directionality* method, then the local gradient-based *Directionality* method, *FiberFit*, *OrientationJ*, and finally *CT-FIRE*, with an average error of $10.3\% \pm 5.0\%$, $16.1\% \pm 7.1\%$, $16.7\% \pm 4.3\%$, $33.4\% \pm 4.1\%$, and $39.6\% \pm 9.6\%$, respectively (Figure 4B). These results show that *Directionality*, *FiberFit*, *CT-FIRE*, and *OrientationJ* methods underestimate the amount of fibers that follow the preferential orientation of the network.

Figure 4C presents the angle error data obtained from the set of images with different values of α . Once again, the smallest error between the real and the measured preferential orientation was obtained using the Fourier spectra *Directionality* method, closely followed by *FiberO*, which achieved a significantly lower error compared to the other techniques across various levels of anisotropy, with the poorest performance observed in the local gradient-based *Directionality* method. When a high level of disorganization was present, with numerous fibers exhibiting random orientations and lacking a clear preferential direction, *CT-FIRE* was unable to produce results that accurately reflected the actual fibers arrangement. Finally, Figure 4D displays the difference between the measured and real α for the different evaluated techniques (with a mean error value of $3.4\% \pm 3.7\%$, $7.9\% \pm 3.9\%$, $9.9\% \pm 4.6\%$, $13.3\% \pm 7.3\%$, $22.9\% \pm 12.8\%$, and $24.6\% \pm 9.5\%$ for *FiberO*, *Directionality* with Fourier spectra, *Directionality* with local gradient orientation, *FiberFit*, *CT-FIRE*, and *OrientationJ*, respectively) and indicates that *FiberO* best estimates the number of fibers oriented at the principal orientation angle.

The orientation maps generated using the four different available techniques (*FiberO*, *Directionality* in both modes, and *OrientationJ*) for a representative SHG microscopy image of an *oim* mouse bone cross-section are shown in Figure 5. This figure shows that although the *Directionality* method based on Fourier spectra is powerful for calculating global fiber orientations (as seen in Figure 4A), it does not perform well when representing their local orientation values in the form of orientation color maps, generating images that do not show the different orientations of the fibers (Figure 5). A similar behavior is found when analyzing the results for the *Directionality* method based on the local gradient orientation, where only the orientation of the most intense fibers is highlighted by a pink-like color (Figure 5). *FiberO* and *OrientationJ* provide the visually most comprehensive fibers orientation colormaps, with detailed regional orientation of the primary orientations of the collagen fibers (Figure 5). Figure 5 also shows that in the areas with less collagen content, such as the center of the bone cortex, the intensity of the colors indicating the direction of the collagen fibers computed by *OrientationJ* is reduced compared to the colors displayed by *FiberO*, which instead clearly exhibit the regional principal orientation of the collagen fibers with the color mapping.

Discussion

A new open-source available accurate software for the automatic and quantitative analysis of fibers orientation and organization



within a tissue is presented in this work. This method, named *FiberO*, conducts the analysis of the fibers orientation and continuity in the tissue starting from gray scale images of fibers, such as those but not limited to the ones obtained using SHG microscopy imaging, which, for example, allows the visualization of collagen type I fibers within connective tissues. In biological materials, the hierarchical organization of the primary components of the extracellular matrix of connective tissues plays a crucial role in their mechanical properties. Understanding the orientation and assembly of collagen fibers in connective tissues, such as bone and tendons, is important in determining how these structures relate to the tissue mechanical properties, or are affected by disease and if therapies can improve them. This extends to other fibrous non-collagenous proteins as long as they can be visualized and distinguished from surrounding matrix via any imaging modality, not just SHG microscopy. For example, picrosirius red staining of biological tissue is another well-known histochemical technique used to study tissue fibers (Rittié, 2017). However, so far, the use of these imaging and histological techniques, and the understanding of the contribution of the fibers structure and assembly to the biological tissue mechanics has been limited by the inability to quantify fibers orientation and organization in these tissues.

The presented work provides the first open-source software that allows users to automatically and quantitatively evaluate the orientation and organization of fibers in tissues, such as in those from connective tissues, including bone and tendons. *FiberO* program is written in the high-level engineering language MATLAB and it is customizable for the users as needed. In addition, a user-friendly interface has been implemented to facilitate program control for user less experienced in coding. This allows users to specify properties and visualize the tissue sections at different steps of the analysis.

FiberO software was originally designed to measure bone and tendons collagen type I fibers orientation and organization, but because many living tissues are composed of extracellular fibrous proteins, it can be generalized to study other fibrous tissues, such as lung sections that are composed of elastin fibers, also visible with SHG microscopy, as well as fibers in other natural or artificial materials such as in food, rocks, engineering materials, etc.

The technique presented here has been validated against other open-source methods, which have been used for the study of fibers network orientation (Sensini et al., 2018; Reznikov et al., 2013; Fee et al., 2016; Taufalele et al., 2019), including *Directionality* (Liu, 1991), *OrientationJ* (Püspöki et al., 2016), *FiberFit* (Morrill et al., 2016), and *CT-FIRE* (Bredfeldt et al., 2014). *FiberO* is the method that most accurately determines the amount of fibers oriented at the preferential orientation angle of known fibers networks. Furthermore, *FiberO* is only outperformed by very little ($<0.2^\circ$) by *Directionality* method based on the Fourier spectra in calculating the value of the preferential orientation of the fibers networks. However, although the Fourier Transform *Directionality* method proved more efficient in capturing the global information of the fiber network, it loses to localize the fibers orientation as the spatial understanding of the Fourier Transform *Directionality* method is compromised during the transition from frequency space to the spatial domain, as evidenced by the dimmed orientation maps. Therefore, when analyzing the spatial distribution of the collagen fibers network, *Directionality* method based on the Fourier spectra is not accurate and does not provide important information on the orientation, as instead is done by *FiberO*.

Besides *Directionality* and *OrientationJ*, other open-source software have been developed for the automatic calculation of fibers orientation on grayscale images. Examples of these include the software *FiberFit*, which was used to evaluate the analysis of fibers

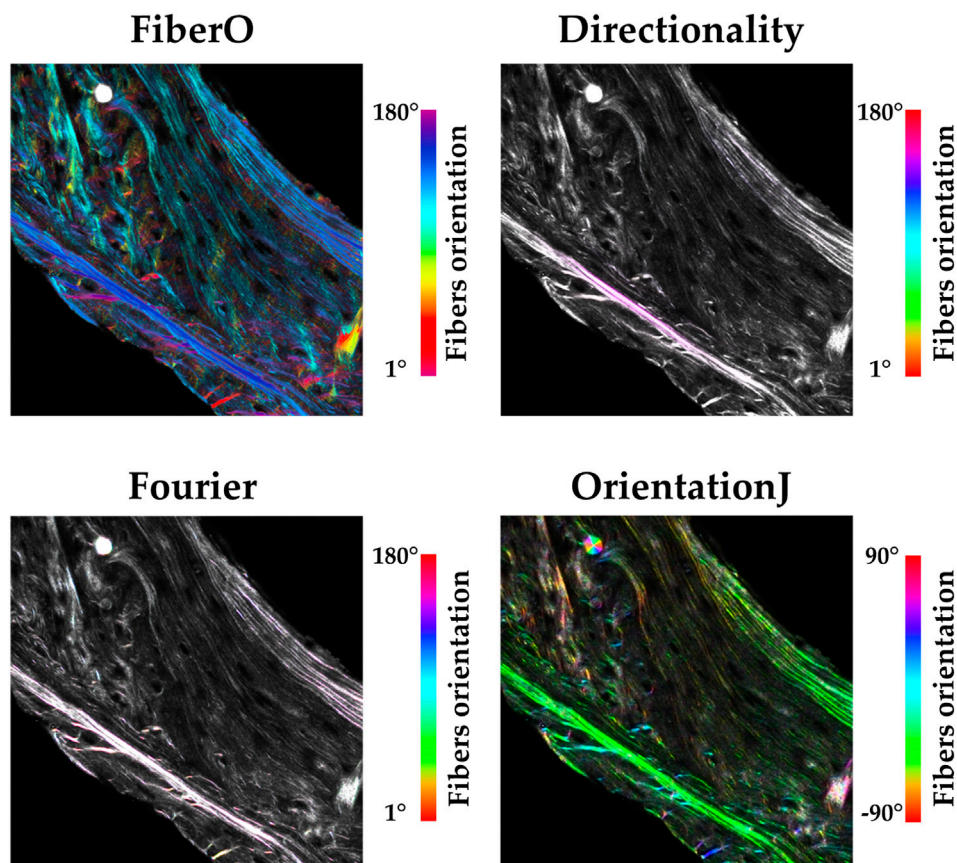


FIGURE 5

Fibers orientation colormaps obtained using *FiberO*, *Directionality* using local gradient and Fourier spectra, and *OrientationJ* for a representative bone cross-section imaged with SHG microscopy. A different color code for the fibers orientation is used for each method, accordingly to their approach. Only *FiberO* and *OrientationJ* show an intelligible distribution of the fiber orientations. Fibers are however more visible when using *FiberO*.

from confocal images of ligaments and only computes a single value of the global orientation distribution for the entire image, and hence does not generate the colormaps showing the local orientation of the fibers (Morrill et al., 2016). Similarly, the software *CT-FIRE* also offers the ability to measure specific characteristics of individual fibers, encompassing aspects such as orientation, size, linearity, and thickness (Bredfeldt et al., 2014), as well as notable is the work conducted in this direction by many other researchers in this field (Sivaguru et al., 2010; Bayan et al., 2009; Koch et al., 2014; Zyablitskaya et al., 2017). However, *FiberFit* and *CT-FIRE* did not demonstrate better performance than *FiberO* in the analysis of images with fibers with known width and orientation. Furthermore, because they do not provide the capability to visualize orientation maps, they are limited tools for analyzing the spatial orientation of fibers in biological tissues. Therefore, *FiberO* is to date the open-source software that best quantifies fibers orientation in the tissue with contour mapping. *FiberO* has been developed to work with 2D images. However, its implementation on stacks of images can be used to obtain the analysis of 3D images with respect of a plane of reference, as we have done previously to analyze fibers organization in tendons (Manrique et al., 2023).

To our knowledge, *FiberO* is the first and only software that based on the fibers regional organization information

automatically detects the surface(s) with continuous fibers that contribute to the overall tissue imaged. This task was till now done manually by researchers to distinguish the areas of tissue with organized and disordered collagen fibers in SHG microscopy images of bone (Hedjazi et al., 2022). Manual selection increases the time required to process the data and possibly introduces subjectivity into the results. Instead, *FiberO* accurately differentiated region(s) in the analyzed images in an automatic and rapid manner based on the quantitative analysis of their fibers orientation and continuity.

In conclusion, we developed an open-source software, called *FiberO*, that based on morphological image openings can automatically and accurately quantify the main regional orientations of fibers and determine their organization in biological tissues from grey scale images, such as from those of bone and tendon collagen fibers taken with SHG microscopy. *FiberO*'s fibers orientation quantification and plotting outperformed five different open-source techniques currently used to track fibers orientations. *FiberO* is also currently the only open-source available software providing organization information of the fibers within the tissue. This study provides a novel tool for researchers to investigate the fibers orientation and organization in different natural and artificially made fibrous tissues.

Data availability statement

The original contributions presented in the study are included in the article/Supplementary Material and in the Git-Hub folder of *FiberO* (<https://github.com/CarrieroLab/FiberO>), further inquiries can be directed to the corresponding author.

Author contributions

AM: Conceptualization, Data curation, Formal Analysis, Investigation, Methodology, Software, Validation, Visualization, Writing—original draft, Writing—review and editing. AD: Conceptualization, Data curation, Formal Analysis, Investigation, Methodology, Software, Validation, Writing—original draft, Writing—review and editing. JF: Conceptualization, Formal Analysis, Investigation, Methodology, Software, Validation, Visualization, Writing—original draft, Writing—review and editing. AC: Conceptualization, Data curation, Formal Analysis, Funding acquisition, Investigation, Methodology, Project administration, Resources, Software, Supervision, Validation, Visualization, Writing—original draft, Writing—review and editing.

Funding

The author(s) declare that financial support was received for the research, authorship, and/or publication of this article. This work

was supported by the National Science Foundation (CBET-1829310).

Conflict of interest

The authors declare that the research was conducted in the absence of any commercial or financial relationships that could be construed as a potential conflict of interest.

The author(s) declared that they were an editorial board member of *Frontiers*, at the time of submission. This had no impact on the peer review process and the final decision.

Publisher's note

All claims expressed in this article are solely those of the authors and do not necessarily represent those of their affiliated organizations, or those of the publisher, the editors and the reviewers. Any product that may be evaluated in this article, or claim that may be made by its manufacturer, is not guaranteed or endorsed by the publisher.

Supplementary material

The Supplementary Material for this article can be found online at: <https://www.frontiersin.org/articles/10.3389/fbioe.2024.1497837/full#supplementary-material>

References

- Barbhuiya, A., and Hemachandran, K. (2013). Wavelet transformations and its major applications in digital image processing. *Int. J. Eng. Res. and Technol. (IJERT)*, ISSN 2 (3), 1–5. doi:10.17577/IJERTV2IS3538
- Bayan, C., Levitt, J. M., Miller, E., Kaplan, D., and Georgakoudi, I. (2009). Fully automated, quantitative, noninvasive assessment of collagen fiber content and organization in thick collagen gels. *J. Appl. Phys.* 105 (10), 102042. doi:10.1063/1.3116626
- Blouin, S., Fratzl-Zelman, N., Roschger, A., Cabral, W. A., Klaushofer, K., Marini, J. C., et al. (2019). Cortical bone properties in the Brtl/+ mouse model of Osteogenesis imperfecta as evidenced by acoustic transmission microscopy. *J. Mech. Behav. Biomed. Mater.* 90, 125–132. doi:10.1016/j.jmbm.2018.10.010
- Bredfeldt, J. S., Liu, Y., Pehlke, C. A., Conklin, M. W., Szulcowski, J. M., Inman, D. R., et al. (2014). Computational segmentation of collagen fibers from second-harmonic generation images of breast cancer. *J. Biomed. Opt.* 19 (1), 016007. doi:10.1117/1.jbo.19.1.016007
- Bueno, J. M., Palacios, R., Chessey, M. K., and Ginis, H. (2013). Analysis of spatial lamellar distribution from adaptive-optics second harmonic generation corneal images. *Biomed. Opt. express* 4 (7), 1006–1013. doi:10.1364/boe.4.001006
- Campagnola, P. J., Millard, A. C., Terasaki, M., Hoppe, P. E., Malone, C. J., and Mohler, W. A. (2002). Three-dimensional high-resolution second-harmonic generation imaging of endogenous structural proteins in biological tissues. *Biophys. J.* 82 (1 Pt 1), 493–508. doi:10.1016/s0006-3495(02)75414-3
- Campagnola, P. J., Wei, M. D., Lewis, A., and Loew, L. M. (1999). High-resolution nonlinear optical imaging of live cells by second harmonic generation. *Biophys. J.* 77 (6), 3341–3349. doi:10.1016/s0006-3495(99)77165-1
- Carriero, A., Bruse, J. L., Oldknow, K. J., Millán, J. L., Farquharson, C., and Shefelbine, S. J. (2014a). Reference point indentation is not indicative of whole mouse bone measures of stress intensity fracture toughness. *Bone* 69, 174–179. doi:10.1016/j.bone.2014.09.020
- Carriero, A., Zimmermann, E. A., Paluszny, A., Tang, S. Y., Bale, H., Busse, B., et al. (2014b). How tough is brittle bone? Investigating osteogenesis imperfecta in mouse bone. *J. Bone Min. Res.* 29 (6), 1392–1401. doi:10.1002/jbmr.2172
- Carriero, A., Zimmermann, E. A., Shefelbine, S. J., and Ritchie, R. O. (2014c). A methodology for the investigation of toughness and crack propagation in mouse bone. *J. Mech. Behav. Biomed. Mater.* 39, 38–47. doi:10.1016/j.jmbm.2014.06.017
- Chen, X., Nadiarynk, O., Plotnikov, S., and Campagnola, P. J. (2012). Second harmonic generation microscopy for quantitative analysis of collagen fibrillar structure. *Nat. Protoc.* 7 (4), 654–669. doi:10.1038/nprot.2012.009
- Chipman, S. D., Sweet, H. O., McBride, D. J., Davison, M. T., Marks, S. C., Shuldiner, A. R., et al. (1993). Defective pro alpha 2(I) collagen synthesis in a recessive mutation in mice: a model of human osteogenesis imperfecta. *Proc. Natl. Acad. Sci. U. S. A.* 90 (5), 1701–1705. doi:10.1073/pnas.90.5.1701
- Chu, S. W., Chen, S. Y., Chern, G. W., Tsai, T. H., Chen, Y. C., Lin, B. L., et al. (2004). Studies of $\chi(2)/\chi(3)$ tensors in submicron-scaled bio-tissues by polarization harmonics optical microscopy. *Biophys. J.* 86 (6), 3914–3922. doi:10.1529/biophysj.103.034595
- Cloos, P. A., Fledelius, C., Christgau, S., Christiansen, C., Engsig, M., Delmas, P., et al. (2003). Investigation of bone disease using isomerized and racemized fragments of type I collagen. *Calcif. Tissue Int.* 72 (1), 8–17. doi:10.1007/s00223-002-2034-1
- Deans, S. R. (2007). The Radon transform and some of its applications. *Cour. Corp.* doi:10.1080/713821644
- Dombeck, D. A., Kasischke, K. A., Vishwasrao, H. D., Ingelsson, M., Hyman, B. T., and Webb, W. W. (2003). Uniform polarity microtubule assemblies imaged in native brain tissue by second-harmonic generation microscopy. *Proc. Natl. Acad. Sci. U. S. A.* 100 (12), 7081–7086. doi:10.1073/pnas.0731953100
- Enderli, T. A., Burtch, S. R., Templet, J. N., and Carriero, A. (2016). Animal models of osteogenesis imperfecta: applications in clinical research. *Orthop. Res. Rev.* 8, 41–55. doi:10.2147/orr.s85198
- Fee, T., Downs, C., Eberhardt, A., Zhou, Y., and Berry, J. (2016). Image-based quantification of fiber alignment within electrospun tissue engineering scaffolds is related to mechanical anisotropy. *J. Biomed. Mater. Res. A* 104 (7), 1680–1686. doi:10.1002/jbm.a.35697
- Fratzl, P., Paris, O., Klaushofer, K., and Landis, W. J. (1996). Bone mineralization in an osteogenesis imperfecta mouse model studied by small-angle x-ray scattering. *J. Clin. Invest.* 97 (2), 396–402. doi:10.1172/jci118428
- Hedjazi, G., Guterman-Ram, G., Blouin, S., Schemenz, V., Wagermaier, W., Fratzl, P., et al. (2022). Alterations of bone material properties in growing Ifitm5/BRIL p.S42 knock-in mice, a new model for atypical type VI osteogenesis imperfecta. *Bone* 162, 116451. doi:10.1016/j.bone.2022.116451

- Hill, M. R., Duan, X., Gibson, G. A., Watkins, S., and Robertson, A. M. (2012). A theoretical and non-destructive experimental approach for direct inclusion of measured collagen orientation and recruitment into mechanical models of the artery wall. *J. biomechanics* 45 (5), 762–771. doi:10.1016/j.jbiomech.2011.11.016
- Joshi, S. R., and Koju, R. (2012). *Study and comparison of edge detection algorithms*. 2012 Third Asian Himalayas international conference on internet (IEEE).
- Kim, B. M., Eichler, J., Reiser, K. M., Rubenchik, A. M., and Da Silva, L. B. (2000). Collagen structure and nonlinear susceptibility: effects of heat, glycation, and enzymatic cleavage on second harmonic signal intensity. *Lasers Surg. Med.* 27 (4), 329–335. doi:10.1002/1096-9101(2000)27:4<329::aid-lsm5>3.0.co;2-c
- Kim, J., Boys, A. J., Estroff, L. A., and Bonassar, L. J. (2021). Combining TGF- β 1 and mechanical anchoring to enhance collagen fiber formation and alignment in tissue-engineered menisci. *ACS Biomater. Sci. Eng.* 7 (4), 1608–1620. doi:10.1021/acsbomaterials.0c01791
- Knapik, J. J., and Pope, R. (2020). Achilles tendinopathy: pathophysiology, epidemiology, diagnosis, treatment, prevention, and screening. *J. Spec. Oper. Med.* 20 (1), 125–140. doi:10.55460/qxtx-a72p
- Koch, R. G., Tsamis, A., D'Amore, A., Wagner, W. R., Watkins, S. C., Gleason, T. G., et al. (2014). A custom image-based analysis tool for quantifying elastin and collagen micro-architecture in the wall of the human aorta from multi-photon microscopy. *J. Biomech.* 47 (5), 935–943. doi:10.1016/j.jbiomech.2014.01.027
- Kottmann, R. M., Sharp, J., Owens, K., Salzman, P., Xiao, G. Q., Phipps, R. P., et al. (2015). Second harmonic generation microscopy reveals altered collagen microstructure in usual interstitial pneumonia versus healthy lung. *Respir. Res.* 16 (1), 61. doi:10.1186/s12931-015-0220-8
- Le, T. T., Langohr, I. M., Locker, M. J., Sturek, M., and Cheng, J. X. (2007). Label-free molecular imaging of atherosclerotic lesions using multimodal nonlinear optical microscopy. *J. Biomed. Opt.* 12 (5), 054007. doi:10.1117/1.2795437
- Lilledahl, M. B., Pierce, D. M., Ricken, T., Holzapfel, G. A., and Davies, C. L. (2011). Structural analysis of articular cartilage using multiphoton microscopy: input for biomechanical modeling. *IEEE Trans. Med. Imaging* 30 (9), 1635–1648. doi:10.1109/tmi.2011.2139222
- Liu, Z.-Q. (1991). Scale space approach to directional analysis of images. *Appl. Opt.* 30 (11), 1369–1373. doi:10.1364/ao.30.001369
- Manrique, L., Docaj, A., Munoz, A., and Carriero, A. (2023). *Effect of collagen mutations on 3D fiber organization in Achilles and tail tendons* (Dallas, Texas: Orthopaedic Research Society ORS).
- Mansfield, J., Yu, J., Attenburrow, D., Moger, J., Tirlapur, U., Urban, J., et al. (2009). The elastin network: its relationship with collagen and cells in articular cartilage as visualized by multiphoton microscopy. *J. Anat.* 215 (6), 682–691. doi:10.1111/j.1469-7580.2009.01149.x
- McLean, J. (2015). *A linear method for quantification of collagen fiber orientation in Cornea*. 2015 41st Annual Northeast Biomedical Engineering Conference (NEBEC) (IEEE).
- Millard, A. C., Campagnola, P. J., Mohler, W., Lewis, A., and Loew, L. M. (2003). Second harmonic imaging microscopy. *Methods Enzymol.* 361, 47–69. doi:10.1016/s0076-6879(03)61005-0
- Mohler, W., Millard, A. C., and Campagnola, P. J. (2003). Second harmonic generation imaging of endogenous structural proteins. *Methods* 29 (1), 97–109. doi:10.1016/s1046-2023(02)00292-x
- Morrill, E. E., Tulepbergenov, A. N., Stender, C. J., Lamichhane, R., Brown, R. J., and Lujan, T. J. (2016). A validated software application to measure fiber organization in soft tissue. *Biomech. Model. Mechanobiol.* 15 (6), 1467–1478. doi:10.1007/s10237-016-0776-3
- Mostaço-Guidolin, L., Rosin, N. L., and Hackett, T.-L. (2017). Imaging collagen in scar tissue: developments in second harmonic generation microscopy for biomedical applications. *Int. J. Mol. Sci.* 18 (8), 1772. doi:10.3390/ijms18081772
- Muñoz, A., Docaj, A., Ugarteburu, M., and Carriero, A. (2021). Poor bone matrix quality: what can be done about it? *Curr. Osteoporos. Rep.* 19 (5), 510–531. doi:10.1007/s11914-021-00696-6
- Nadiarykh, O., Plotnikov, S., Mohler, W. A., Kalajzic, I., Redford-Badwal, D., and Campagnola, P. J. (2007). Second harmonic generation imaging microscopy studies of osteogenesis imperfecta. *J. Biomed. Opt.* 12 (5), 051805. doi:10.1117/1.2799538
- Nair, A., Chuang, S.-C., Lin, Y.-S., Chen, C.-H., Fang, T.-C., Chiu, H.-C., et al. (2022). Characterization of collagen response to bone fracture healing using polarization-SHG. *Sci. Rep.* 12 (1), 18453. doi:10.1038/s41598-022-21876-z
- Noor, R. A. M., Shah, N. S. M., Zin, A. A. M., Sulaiman, W. A. W., and Halim, A. S. (2022). Disoriented collagen fibers and disorganized, fibrotic orbicularis oris muscle fiber with mitochondrial myopathy in non-syndromic cleft lip. *Arch. Oral Biol.* 140, 105448. doi:10.1016/j.archoralbio.2022.105448
- Parra, E. R., Teodoro, W. R., Velosa, A. P., de Oliveira, C. C., Yoshinari, N. H., and Capelozzi, V. L. (2006). Interstitial and vascular type V collagen morphologic disorganization in usual interstitial pneumonia. *J. Histochem. Cytochem.* 54 (12), 1315–1325. doi:10.1369/jhc.6a6969.2006
- Püspöki, Z., Storath, M., Sage, D., and Unser, M. (2016). Transforms and operators for directional bioimage analysis: a survey. *Adv. Anat. Embryol. Cell Biol.* 219, 69–93. doi:10.1007/978-3-319-28549-8_3
- Ranjit, S., Dvornikov, A., Stakic, M., Hong, S. H., Levi, M., Evans, R. M., et al. (2015). Imaging fibrosis and separating collagens using second harmonic generation and phasor approach to fluorescence lifetime imaging. *Sci. Rep.* 5, 13378. doi:10.1038/srep13378
- Reznikov, N., Almany-Magal, R., Shahar, R., and Weiner, S. (2013). Three-dimensional imaging of collagen fibril organization in rat circumferential lamellar bone using a dual beam electron microscope reveals ordered and disordered sub-lamellar structures. *Bone* 52 (2), 676–683. doi:10.1016/j.bone.2012.10.034
- Rittié, L. (2017). Method for picosirius red-polarization detection of collagen fibers in tissue sections. *Methods Mol. Biol.* 1627, 395–407. doi:10.1007/978-1-4939-7113-8_26
- Roth, S., and Freund, I. (1981). Optical second-harmonic scattering in rat-tail tendon. *Biopolymers* 20 (6), 1271–1290. doi:10.1002/bip.1981.360200613
- Sensini, A., Gualandri, C., Zucchelli, A., Boyle, L. A., Kao, A. P., Reilly, G. C., et al. (2018). Tendon fascicle-inspired nanofibrous scaffold of polylactic acid/collagen with enhanced 3D-structure and biomechanical properties. *Sci. Rep.* 8 (1), 17167. doi:10.1038/s41598-018-35536-8
- Shapiro, J., Maguire, K., Swami, S., Zhu, H., Flynn, E., Wang, J., et al. (2021). Histopathology of osteogenesis imperfecta bone. Supramolecular assessment of cells and matrices in the context of woven and lamellar bone formation using light, polarization and ultrastructural microscopy. *Bone Rep.* 14, 100734. doi:10.1016/j.bonr.2020.100734
- Singh, G., and Mittal, A. (2014). Various image enhancement techniques-a critical review. *Int. J. Innovation Sci. Res.* 10 (2), 267–274.
- Sivaguru, M., Durgam, S., Ambekar, R., Luedtke, D., Fried, G., Stewart, A., et al. (2010). Quantitative analysis of collagen fiber organization in injured tendons using Fourier transform-second harmonic generation imaging. *Opt. Express* 18 (24), 24983–24993. doi:10.1364/oe.18.024983
- Taufalele, P. V., Vanderburgh, J. A., Muñoz, A., Zanolli, M. R., and Reinhart-King, C. A. (2019). Fiber alignment drives changes in architectural and mechanical features in collagen matrices. *PLoS One* 14 (5), e0216537. doi:10.1371/journal.pone.0216537
- Tilbury, K., Hocker, J., Wen, B. L., Sandbo, N., Singh, V., and Campagnola, P. J. (2014). Second harmonic generation microscopy analysis of extracellular matrix changes in human idiopathic pulmonary fibrosis. *J. Biomed. Opt.* 19 (8), 086014. doi:10.1117/1.jbo.19.8.086014
- Williams, R. M., Zipfel, W. R., and Webb, W. W. (2001). Multiphoton microscopy in biological research. *Curr. Opin. Chem. Biol.* 5 (5), 603–608. doi:10.1016/s1367-5931(00)00241-6
- Yoshioka, N. K., Young, G. M., Khajuria, D. K., Karuppagounder, V., Pinamont, W. J., Fanburg-Smith, J. C., et al. (2022). Structural changes in the collagen network of joint tissues in late stages of murine OA. *Sci. Rep.* 12 (1), 9159. doi:10.1038/s41598-022-13062-y
- Zhao, F., and Xie, X. (2013). An overview of interactive medical image segmentation. *Ann. BMVA* 2013 (7), 1–22.
- Zipfel, W. R., Williams, R. M., Christie, R., Nikitin, A. Y., Hyman, B. T., and Webb, W. W. (2003). Live tissue intrinsic emission microscopy using multiphoton-excited native fluorescence and second harmonic generation. *Proc. Natl. Acad. Sci. U. S. A.* 100 (12), 7075–7080. doi:10.1073/pnas.0832308100
- Zunder, S. M., Gelderblom, H., Tollenaar, R. A., and Mesker, W. E. (2020). The significance of stromal collagen organization in cancer tissue: an in-depth discussion of literature. *Crit. Rev. Oncol. Hematol.* 151, 102907. doi:10.1016/j.critrevonc.2020.102907
- Zyablitskaya, M., Takaoka, A., Munteanu, E. L., Nagasaki, T., Trokel, S. L., and Paik, D. C. (2017). Evaluation of therapeutic tissue crosslinking (TXL) for myopia using second harmonic generation signal microscopy in rabbit sclera. *Invest. Ophthalmol. Vis. Sci.* 58 (1), 21–29. doi:10.1167/iops.16-20241



OPEN ACCESS

EDITED BY

Peter Quesada,
University of Louisville, United States

REVIEWED BY

Svitlana Kopyl,
University of Aveiro, Portugal
Sheng Zhou,
Nanjing Drum Tower Hospital, China

*CORRESPONDENCE

Yanru Xue,
✉ xueyanru@tyut.edu.cn
Xiaogang Wu,
✉ wuxiaogangtyut@163.com
Weiyi Chen,
✉ chenweiyi@tyut.edu.cn

RECEIVED 24 August 2024

ACCEPTED 13 January 2025

PUBLISHED 03 February 2025

CITATION

Liu C, Zhao L, Dong H, Hua Z, Wang Y, Wang Y, Li P, Wei X, Zhang K, Xue Y, Wu X and Chen W (2025) Experimental investigation on the reverse mechano-electrical effect of porcine articular cartilage.
Front. Bioeng. Biotechnol. 13:1485593.
doi: 10.3389/fbioe.2025.1485593

COPYRIGHT

© 2025 Liu, Zhao, Dong, Hua, Wang, Wang, Li, Wei, Zhang, Xue, Wu and Chen. This is an open-access article distributed under the terms of the [Creative Commons Attribution License \(CC BY\)](https://creativecommons.org/licenses/by/4.0/). The use, distribution or reproduction in other forums is permitted, provided the original author(s) and the copyright owner(s) are credited and that the original publication in this journal is cited, in accordance with accepted academic practice. No use, distribution or reproduction is permitted which does not comply with these terms.

Experimental investigation on the reverse mechano-electrical effect of porcine articular cartilage

Chunsheng Liu¹, Le Zhao¹, Hao Dong¹, Zekun Hua¹, Yanqin Wang¹, Yongxing Wang², Pengcui Li³, Xiaochun Wei³, Kai Zhang⁴, Yanru Xue^{1*}, Xiaogang Wu^{1*} and Weiyi Chen^{1*}

¹College of Biomedical Engineering, Taiyuan University of Technology, Taiyuan, China, ²Taiyuan Great Health Technology Health Management Co., Ltd., Taiyuan, China, ³Shanxi Provincial Key Laboratory for Repair of Bone and Soft Tissue Injury, Taiyuan, China, ⁴Huajin Orthopaedic Hospital, Taiyuan, China

Introduction: The electric signals within the cartilage tissue are essential to biological systems and play a significant role in cartilage regeneration. Therefore, this study analyzed and investigated the reverse mechano-electrical effect in porcine articular cartilage and its related influencing factors.

Methods: The deflection of cartilage samples in an electric field was measured to analyze the mechanisms of different factors affecting the reverse mechano-electrical effect in articular cartilage.

Results: The results showed that the cartilage thickness, water content, and externally applied voltage all impacted the deflection of the cartilage. The reduction in cartilage water content resulted in a decrease in cartilage thickness, following the same influencing mechanism as thickness. On the other hand, an increase in the externally applied voltage led to an increase in the electric field force within the cartilage space, consequently increasing the deflection of the cartilage in the electric field. Additionally, the externally applied voltage also caused a slight temperature rise in the vicinity of the cartilage specimens, and the magnitude of the temperature increase was proportional to the externally applied voltage.

Discussion: The fitting results of the experimental data indicated that cartilage thickness influenced the dielectric constant and moment of inertia of the cartilage in the electric field, thereby affecting the magnitude of the electric field force and deflection of the cartilage. This may provide valuable insights for further investigation into the microscopic mechanisms of cell proliferation, differentiation, and cartilage regeneration induced by electrical stimulation.

KEYWORDS

articular cartilage, reverse mechano-electrical effect, cartilage's thickness, deflection, external electric field

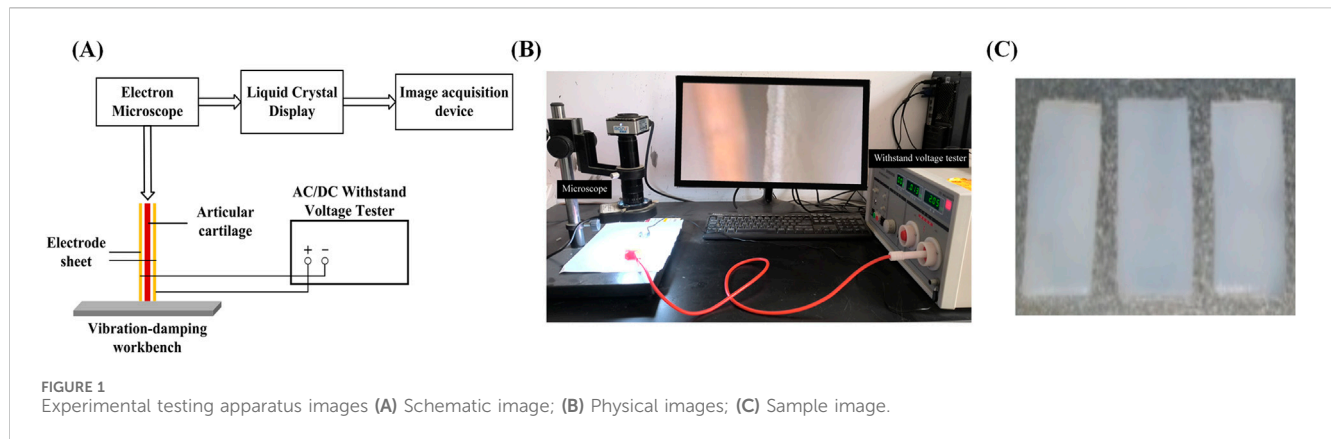
1 Introduction

Osteoarthritis is one of the most common diseases among the global adult population, affecting hundreds of millions of people worldwide. Furthermore, its prevalence is expected to continue increasing in the coming years (Glyn-Jones et al., 2015; Disease et al., 2018). Due to the avascular nature of articular cartilage, it cannot naturally regenerate after injury. Therefore, clinical treatment is typically required when damage or disease occurs

(Hunziker, 1999). The therapeutic effects of currently used clinical treatment modalities are not entirely satisfactory (Zhou et al., 2022). Therefore, it is necessary to seek a new approach that can effectively stimulate and accelerate cartilage regeneration. In recent years, electrical stimulation (ES) has been widely recognized as a promising method to promote cartilage regeneration. It can facilitate cartilage regeneration by directly applying electrical stimulation or harnessing the endogenous bioelectricity within the cartilage (Hu et al., 2014; Clark et al., 2014). These pathways alter gene expression in the cells and promote the production of growth factors (Leppik et al., 2020). Additionally, electrical fields can stimulate the expression of aggrecan and type II collagen mRNA, as well as increase the production of proteoglycans and collagen in human osteoarthritic cartilage explants (Brighton et al., 2008). Bioelectricity within cartilage tissue stands as an essential component of the biological system. Endogenous electric fields, characterized by weak electrical signals emanating from cartilage during daily physiological activities, play a pivotal role in early embryonic development and tissue regeneration (Kapat et al., 2020). These electrical signals have the potential to impact crucial processes such as cell migration, proliferation, and differentiation within cartilage tissue. Recognizing the significance of bioelectricity, a range of electric stimulation techniques have been devised for clinical applications, encompassing the acceleration of wound healing, deep brain stimulation, and tissue regeneration. Given the pervasive nature of bioelectric signals throughout the body, electrical stimulation emerges as a key strategy in promoting the regeneration of cartilage tissue (Kwon et al., 2016; Curry et al., 2020). In the past few decades, electrical stimulation has gained increasing attention due to its applications in regenerative medicine (Zimmermann et al., 2023). As early as 1972, Becker and Spadaro (1972) discovered that altering wound polarity by applying exogenous electrical stimulation in mammals could improve wound healing and potentially induce tissue regeneration response. Zuzzi et al. (2013) conducted a 35-day electrical stimulation on rat articular cartilage defects. The results revealed that continuous electrical stimulation led to the increased thickness of collagen fibers in the cartilage and a higher number of chondrocytes, indicating a promoting effect of electrical stimulation on articular cartilage repair. Furthermore, Vaca-Gonzalez et al. (2019) demonstrated that electrical stimulation can promote cell proliferation and stimulate the synthesis of matrix molecules associated with articular cartilage cells, such as type II collagen, proteoglycans, and glycosaminoglycans. Despite significant research endeavors, the translation of these findings into clinical applications in the relevant field remains elusive. This challenge can be attributed to the limited scope of conclusions drawn from preclinical *in vitro* and *in vivo* experiments, which may not yield directly applicable insights for clinical implementation. Therefore, it is necessary to consider the effects of exogenous electrical stimulation on the organism itself. Leppik et al. (2015) demonstrated the good tolerance of the organism to long-term direct current electrical stimulation by applying it to a rat amputation model. Moreover, no additional side effects were noted, including weight changes, decreased vitality, signs of infection, or tumor development. This confirmation underscores the effectiveness of electrical stimulation as a therapeutic approach for osteoarthritis.

The cartilage reverse mechano-electrical effect involves the mechanical deformation of the cartilage surface induced by external electrical field stimulation. This phenomenon leads to ion flow and changes in electric potential within the cartilage, thereby influencing its normal physiological functions. Specifically, the mechanical deformation resulting from the reverse mechano-electrical effect triggered by electrical stimulation can alter the local microenvironment at the site of cartilage defects, activate signaling pathways on cell membranes, and regulate the expression of relevant genes to enhance chondrocyte activity and promote cartilage regeneration (Zhang et al., 2014; Wieland et al., 2015; Papachroni et al., 2009). Currently, research on the reverse mechano-electrical effect is mainly focused on cartilage regeneration, including chondrocyte proliferation, differentiation, and migration (Housmans et al., 2023). It utilizes low-intensity direct current electric fields to promote cartilage regeneration, reduce symptoms of arthritis, and thereby improve articular function and restore the articular structure. In recent years, significant progress has been made in the research on the reverse mechano-electrical effect in cartilage. For example, Hiemer et al. (2018) have demonstrated that the direct application of exogenous electrical stimulation to cartilage can effectively mimic the endogenous electric potentials generated within the cartilage tissue during articular motion and mechanical loading processes. This stimulation facilitates the healing process, guides the development of cartilage cells, and supports cartilage tissue regeneration. Consequently, the researchers explored the effects of electric fields on human chondrocytes, mesenchymal stem cells, and co-cultures of both. The outcomes demonstrated that applying electrical stimulation to cartilage did not impact the metabolic activity of chondrocytes or bone marrow mesenchymal stem cells. Moreover, osteoarthritis presents significant challenges for the individual, such as pain and limited mobility. Pelletier et al. (2015) discovered that the pain caused by arthritis is not only a result of pathological changes in the peripheral tissues surrounding the cartilage but also involves sensitization of the central and peripheral nervous systems and a decrease in descending pain inhibition. Additionally, the application of electrical stimulation to cartilage has a Neuromodulation effect. Therefore, electrical stimulation can effectively alleviate the pain caused by Antal et al. (2010). Therefore, delving into the cartilage reverse mechano-electrical effect can offer crucial references for clinical practice to enhance osteoarthritis conditions and advance cartilage tissue regeneration through the application of electrical stimulation to the cartilage.

In 1996, Aschero et al. (1996) experimentally validated the existence of the reverse mechano-electrical effect in fresh bovine bone. The researchers placed cylindrical specimens of bovine bone, measuring approximately 10 mm in thickness, into a specialized dual-chamber extensometer. They applied an electric field with an intensity of 10 kV/m and recorded measurements of bone thickness changes along and across the electric field lines. The results revealed that the bovine bone specimens exhibited a displacement deflection of approximately 3 μ m under the influence of the applied high electric field, thus confirming the presence of the reverse mechano-electrical effect in bovine bone tissue. Given the similarities in properties between bone and cartilage, this study suggests employing a similar methodology to conduct experiments targeting articular cartilage. The goal is to explore the potential



physical mechanisms underlying the deflection and flexural behavior of cartilage when exposed to electrical stimulation. This will provide valuable insights for further investigation into the microscopic mechanisms of cell proliferation, differentiation, and cartilage regeneration induced by electrical stimulation. Compared to previous studies, we introduced non-contact electric fields for the first time in our experiments, evaluating the characteristics of cartilage by utilizing displacement signals generated through the reverse mechano-electrical effect.

2 Materials and methods

2.1 Preparation of cartilage specimens

Shortly after slaughter, the cartilaginous tissue of the pig's hind leg articular is detached for sampling. The pig meat and cartilage utilized for post-slaughter experimentation do not necessitate approval procedures. Carefully remove the muscles around the cartilage on the clean table, open the joint capsule to expose the cartilage, and then remove the fascia. Observe the cartilage surface, cut the cartilage specimen with a smooth position without slit, and then cut with a scalpel to obtain a 20 mm 10 mm rectangular specimen. The specimen is milky white and smooth in texture, as shown in Figure 1C. After sampling, the specimen thickness was controlled at 1–2 mm by polishing the cartilage on 1,000 target sandpaper. Additionally, to minimize structural discrepancies among specimens, ensure that sandpaper grinding is consistently directed from bottom to top, thereby minimizing variations across different regions of the specimen.

2.2 Reverse mechano-electrical effect testing device

The experimental setup, as shown in Figure 1, includes a high-pressure endurance testing device, a high-magnification industrial microscope, a computer monitor, a cartilage fixation device, and two copper electrode plates. First, fix the prepared cartilage specimen onto the fixation device. Then, utilize the external high-pressure endurance testing device to apply different direct-current fields. The electron microscope (AO-HD228S) captures the deflection and

flexure of the non-fixed end of the cartilage specimen and transmits these changes in real-time to the computer monitor. By selecting appropriate observation points in the monitor and pre-calibrating them, the deflection and flexure of the cartilage can be determined. To study the reverse mechano-electrical effect, we measured the deflection and flexure of pig articular cartilage under the influence of an electric field. The experimental samples were obtained from the articular cartilage of pig joints, specifically from the articular surface. The experiments were conducted using samples of varying thickness: 1, 1.2, 1.4, 1.6, 1.8, and 2.0 mm (all with a length and width of 10 mm). The articular cartilage specimens were placed within an external electric field generated by two electrode plates connected to a high-voltage steady-state direct current power supply (LK2674 Pressure Tester). The deflection and flexure of the free end of the cartilage specimens were observed and calculated using a high-magnification electron microscope and digital image processing techniques. This allowed us to explore various properties of the reverse mechano-electrical effect in cartilage. Before the experiment, the cartilage samples were soaked in 0.9% physiological saline solution, and the surface of the cartilage was wiped to remove any excess moisture before the experiment commenced.

3 Results

3.1 The effect of different thicknesses on cartilage deflection deformation

Figure 2A presents a schematic diagram illustrating the deflection of the cartilage specimen within an electric field, showing how the cartilage bends and flexes in response to the applied electric field force. In Figure 2B, the magnitude of deflection and flexure induced by the reverse mechano-electrical effect in cartilage is depicted under varying thicknesses (1, 1.2, 1.4, 1.6, 1.8, and 2.0 mm) when an external electric field is applied. The applied voltage is maintained at 600 V, and the water content is maintained between 75% and 80%. For example, with an applied voltage of 600 V, as the cartilage thickness decreases from 2.0 mm to 1.0 mm, the deflection and flexure within the electric field increase from 11.7 μm to 16.2 μm . This trend holds across different voltage groups, indicating that a reduction in cartilage thickness leads to a

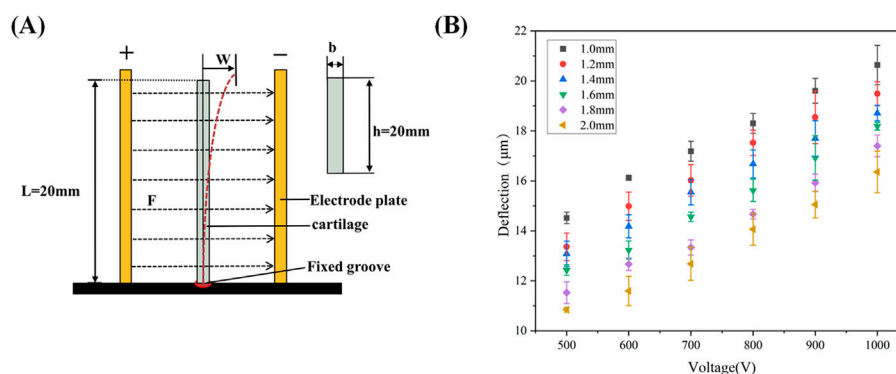


FIGURE 2
(A): Schematic diagram of cartilage displacement in an electric field; (B) Deflection of cartilage of different thicknesses under different voltages.

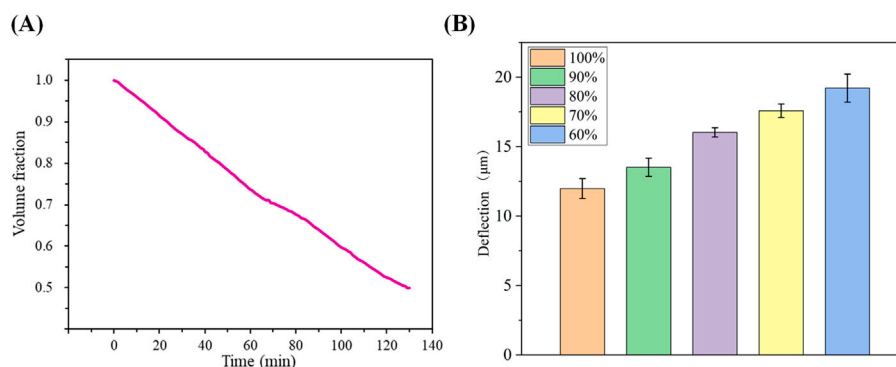


FIGURE 3
(A): Average dehydration of cartilage over time at room temperature; (B) Magnitude of cartilage deflection due to different water contents.

gradual increase in deflection and flexure within the electric field, demonstrating an inverse relationship between these variables.

3.2 The effect of different moisture content on cartilage deflection deformation

The fitted curve in Figure 3A illustrates the average dehydration rate of the cartilage specimens at room temperature. It indicates that it takes approximately 129.5 min for the cartilage to lose water from a saturated state (after soaking in physiological saline for 24 h) to reach 50% water content. This fitting result also suggests that the dehydration rate of the cartilage specimens under room temperature conditions follows a linear change. The dehydration rate of the sample volume fraction is approximately 24% per hour. In Figure 3B, the deflection displacement generated by cartilage at a thickness of 1.0 mm under an applied voltage of 600 V is shown for different water contents. The results reveal that as the water content gradually decreases, the deflection displacement of the cartilage in the electric field increases from 13.9 μm at water saturation to 17.4 μm at 60% water content. This indicates an inverse relationship

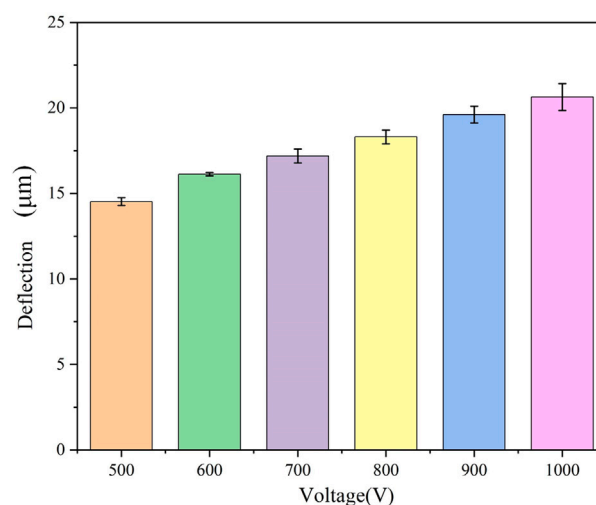


FIGURE 4
Magnitude of cartilage deflection produced under different voltages.

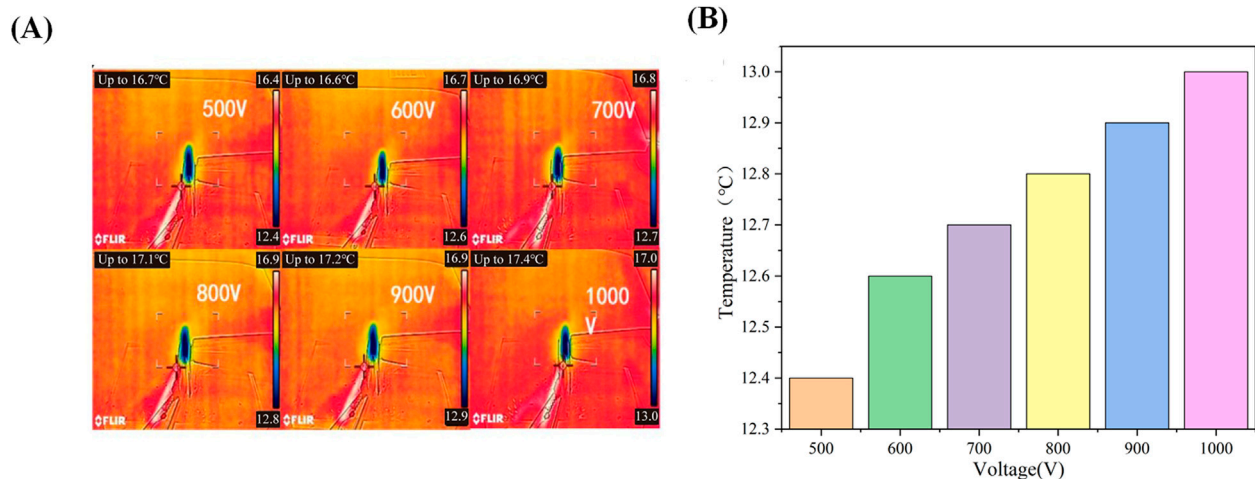


FIGURE 5
(A): Infrared thermal imaging of cartilage under different voltages; (B) Surface temperature of cartilage under different voltages.

between the deflection displacement in the electric field and the water content of the articular cartilage under the same external conditions.

3.3 The effect of different voltages on cartilage deflection deformation

We conducted tests to examine the effect of various applied external electric fields (500, 600, 700, 800, 900, and 1000 V) on the deflection displacement generated by cartilage due to the reverse mechano-electrical effect replaced, while maintaining a constant cartilage thickness (1.0 mm) and water content range (75%–80%). The experimental findings, illustrated in Figure 4, demonstrate that the magnitude of the applied external electric field notably influences the deflection displacement resulting from the inverse piezoelectric effect in cartilage. When using an applied external electric field of 500 V, the measured deflection displacement of the cartilage was 14.3 μm . As the applied external electric field gradually increased, the deflection displacement of the cartilage specimen also showed an increase. At an external electric field reached 1000 V, the corresponding deflection displacement of the cartilage rose to 20.2 μm . Hence, it can be concluded that increasing the applied external voltage results in a proportional increase in the deflection displacement generated by the reverse mechano-electrical effect in cartilage, indicating a significant positive correlation between the two factors.

3.4 The effect of external voltages on cartilage temperature variation

Due to the influence of the water content of the cartilage on the specimen's thickness during the experiment, changes in water content are significantly affected by the external temperature. Therefore, we conducted tests to measure the temperature variations of the cartilage specimen itself and its surrounding

environment at various applied voltages (500, 600, 700, 800, 900, and 1000 V). Figure 5A presents the infrared thermal images of the cartilage and electrodes at different applied voltages. As the cartilage specimens had been soaked in physiological saline for 24 h, it is evident that the temperature of the cartilage is significantly lower than the ambient temperature. Upon applying the external voltage, there is a slight increase in the temperature around the cartilage. As the applied voltage increases, the temperature around the cartilage also rises. The corresponding results are depicted in Figure 5B. The relationship between the two can be approximated as an increase of 0.1°C increase in the temperature around the cartilage for every 100 V increase in the applied external voltage.

4 Discussion

The magnitude of deflection displacement exhibited by articular cartilage in an electric field is a result of both the inherent structural characteristics of the cartilage itself and the external loading conditions. Macroscopic studies focusing on the reverse mechano-electrical effect in cartilage offer valuable insights into various physiological processes, such as cell proliferation and differentiation within cartilage, which are triggered by microscopic-level electrical stimulation signals. In our study, we conducted a comprehensive examination of the deflection displacement induced by the inverse piezoelectric effect in pig articular cartilage when subjected to an electric field. We thoroughly analyzed how cartilage dimensions and external conditions influence the extent of deflection displacement, while also taking into account the impact of external voltage on the surface temperature of the cartilage. Through meticulous analysis and fitting of experimental data, we discovered that the thickness of the cartilage plays a crucial role in determining the dielectric constant and moment of inertia of the cartilage within the electric field. These factors, in turn, influence the magnitude of electric field forces and resulting deflection displacement in the cartilage.

With the advancement of biomedical technology and tissue engineering, electrical stimulation for cartilage regeneration has gained increasing attention. Numerous studies have robustly demonstrated that electrical stimulation can effectively enhance the self-healing capacity of cartilage and promote cartilage tissue regeneration (Zhou et al., 2023; Krueger et al., 2021; Vaiciuleviciute et al., 2023). However, the direct application of high-voltage external electrical stimulation to cartilage tissue can pose a risk of damage to the organism itself (Victoria et al., 2009). Therefore, it is crucial to find a suitable approach that is sensitive to electrical stimulation signals to promote cartilage repair while minimizing potential damage to the organism itself. In recent years, with the rise of tissue engineering research, the use of implantation of alternative materials to promote cartilage repair has become a reliable clinical treatment approach (Liu et al., 2022). This technique heavily relies on the selection of implant materials. Given the beneficial effects of electrical stimulation on cartilage repair, piezoelectric materials that are sensitive to electrical stimulation signals appear to be a promising choice. These materials can mimic the microenvironment within cartilage and generate stimulating biological responses. Additionally, they can generate electrical signals themselves to promote tissue repair. Therefore, combining the reverse mechano-electrical effect with biomaterials for articular research seems to be an effective approach to enhance and promote cartilage regeneration. Consequently, we conducted research on the mechanisms and related influencing factors of the reverse mechano-electrical effect in cartilage.

The study indicates that there is a significant correlation between the deflection displacement of cartilage in an electric field and the moment of inertia of the cartilage itself, as well as the magnitude of the electric field force applied externally. The specific relationship between these factors can be described as in Equation 1 (Philpot, 2008):

$$w = -\frac{FL^4}{8E_p I_y} \quad (1)$$

w represents the deflection displacement of cartilage in the electric field, F represents the magnitude of the electric field force applied to the cartilage specimen, L represents the length of the cartilage specimen, E_p represents the elastic modulus of the cartilage specimen, and I_y represents the moment of inertia of the cartilage.

In the experiment, we measured the average elastic modulus of the cartilage specimen with a thickness of 1.0 mm as 6.13 MPa. Therefore, we only need to investigate the relationship between the cartilage thickness and the electric field force F and moment of inertia I_y . Since the cartilage specimen is placed between two electrode plates, we can approximate the experimental setup as a parallel plate capacitor. Thus, the electric field force can be described as follows Equation 2:

$$F = Q \cdot E \quad (2)$$

Q represents the charge between the two electrode plates, and E represents the electric field intensity. The relationship between Q and E can be described as in Equations 3, 4:

$$Q = C \cdot U \quad (3)$$

$$E = \frac{U}{d} \quad (4)$$

C represents the capacitance, U represents the magnitude of the applied voltage, and d represents the distance between the two electrode plates. The capacitance C is defined as in Equation 5:

$$C = \frac{\epsilon S}{4\pi k d} \quad (5)$$

where: ϵ represents the dielectric constant of the cartilage, S represents the relative area between the two electrode plates, and k represents the electrostatic force constant. Based on the above equations, we can conclude Equation 6:

$$F = \frac{\epsilon S U^2}{4\pi k d^2} \quad (6)$$

According to the definition of the moment of inertia, it can be described as follows:

$$I_y = \frac{bh^3}{12} \quad (7)$$

where: b represents the thickness of the cartilage, and h represents the width of the cartilage specimen. Therefore, we obtain the relationship between the deflection value of cartilage in the electric field and the thickness of the cartilage as follows:

$$w = -\frac{3\epsilon S U^2 L^3}{8\pi k d^2 b E_p h^3} \quad (8)$$

From Equations 7, 8, it is evident that when the thickness b of the cartilage specimen is altered while keeping other conditions constant, the moment of inertia I_y of the cartilage decreases with decreasing thickness b , thereby affecting the deflection displacement w of the cartilage. Additionally, since changes in cartilage thickness result in variations in the cartilage's dielectric constant ϵ , the electric field strength between the two electrodes remains constant under the same voltage. However, due to the different thicknesses leading to different dielectric constants ϵ , the electric field force F experienced by the cartilage becomes inconsistent. The combined effect of these factors significantly influences the deflection of the cartilage induced by the reverse mechano-electrical effect.

As we can observe the magnitude of cartilage deflection in the electric field through a high-magnification industrial microscope during the experiment, the magnitude of the electric field force F cannot be directly determined due to the unknown dielectric constant ϵ . Thus, we can deduce the magnitude of the electric field force from the deflection values, allowing us to explore the relationship between cartilage thickness and the electric field force F as well as the dielectric constant ϵ . The specific relationship is depicted in Figure 6, with the following external conditions set: the relative area (S) of the two electrodes is 20 mm × 12 mm, the applied voltage (U) is 600 V, the cartilage specimen width (h) is 10 mm, the length (L) is 20 mm, and the distance (d) between the two electrodes is 8 mm. The fitting results indicate a linear relationship between cartilage thickness and the electric field force F , the deflection w as well as the dielectric constant ϵ . In other words, as the cartilage thickness increases, the electric field

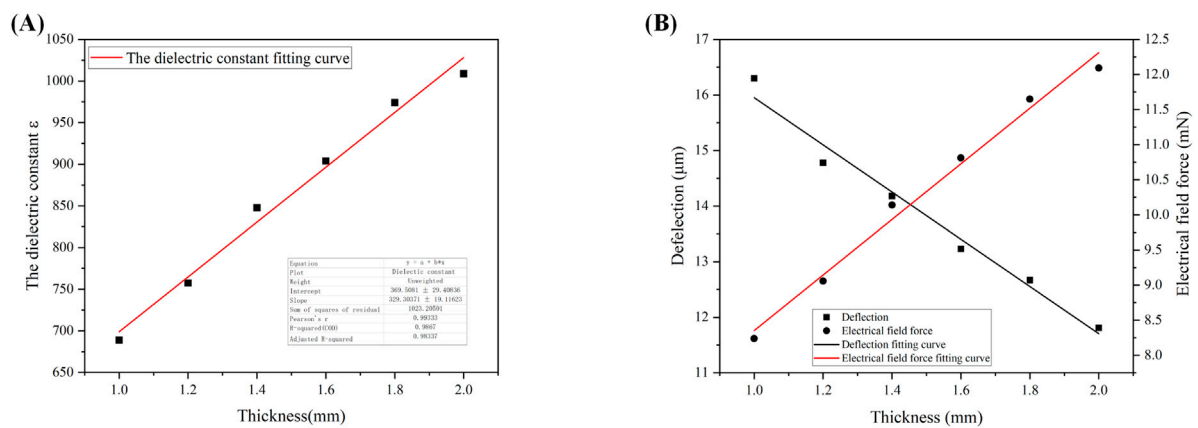


FIGURE 6 (A): Fitted curve of dielectric constant as a function of cartilage thickness; (B) Fitted curves of deflection and electric field force as a function of cartilage thickness.

force F , the deflection w and the dielectric constant ϵ also increase. This relationship can be described by the Equations 9–11:

$$\epsilon = 329303.71b + 369.51 \quad (9)$$

$$F = \frac{82325.93bSU^2 + 92.38SU^2}{\pi kd^2} \quad (10)$$

$$w = -\frac{123488.89bSU^2L^3 + 138.57SU^2L^3}{\pi kd^2bE_p h^3} \quad (11)$$

The specific interpretation is as follows: When the thickness of the cartilage specimen increases, it becomes more difficult for the specimen to be penetrated, resulting in a larger dielectric constant.

Furthermore, Equation 8 indicates an inverse relationship between the deflection displacement w and the cartilage thickness b . This is consistent with our fitting results for the relationship between cartilage thickness and deflection displacement shown in Equation 11 and Figure 6B, thus validating the reliability of the data obtained in our experiment.

The thickness of the cartilage sample emerges as a critical determinant in our exploration of the reverse mechano-electrical effect, underscoring its pivotal role in our research. To maintain methodological rigor and ensure precision in our comparisons, we systematically tested identical samples with varying thicknesses, progressing from thicker to thinner specimens. Throughout these experiments, we upheld consistency in other influential variables such as cartilage area and the applied external voltage. The experimental findings, elegantly depicted in Figure 2B, unveil a pronounced and noteworthy relationship between cartilage thickness and deflection displacement within the electric field under unwavering external conditions. This observed correlation elegantly mirrors an anticipated negative trajectory, closely aligning with our initial hypotheses. This association can be traced back to the experimental setup where one end of the cartilage is anchored, while changes in specific markers at the opposing end are meticulously tracked post-voltage application. This setup profoundly influences the electric field force acting on the cartilage and the cartilage's moment of inertia. The thickness of the cartilage profoundly impacts both its dielectric constant and

moment of inertia, culminating in a discernible negative correlation between cartilage thickness and deflection displacement in the electric field.

Cartilage is characterized by its high water content, a defining feature (Ansari et al., 2019). However, due to the relatively thin thickness of the cartilage specimens, they tend to lose water rapidly at room temperature. The application of voltage can potentially elevate the surrounding temperature of the cartilage, further expediting the dehydration process. Hence, water content is a crucial factor that cannot be overlooked in the study of the reverse mechano-electrical effect in cartilage. To mitigate this concern, we procured cartilage samples and stored them in physiological saline to ensure adequate hydration during the experiments. Before initiating the experiments, we initially plotted the average dehydration curve of the cartilage samples. The fitted results, as depicted in Figure 3A, indicate that the cartilage dehydration follows a linear trend over time at room temperature. In our study, we examined three sets of cartilage specimens, with individual variations having minimal impact on cartilage dehydration. Therefore, we identified specific points on the dehydration curve and recorded the corresponding time required to reach those points. The impact of water content on the deflection displacement induced by the reverse mechano-electrical effect in cartilage is shown in Figure 3B. As the water content decreases, under consistent conditions of cartilage thickness (1.0 mm) and applied external voltage (600 V), the deflection displacement of the cartilage in the electric field increases. This observation may be attributed to the decreased water content within the cartilage, leading to a thinner cartilage thickness and subsequently influencing the deflection displacement in the electric field. In experiments, it is important to acknowledge the inherent error that may arise from the equipment setup. Firstly, there is a degree of uncertainty in the measurements captured by the high-power microscope, although this error is deemed insignificant relative to the screen resolution. The electric field error introduced by the pressure tester was carefully controlled to be within 1 V, but still had a slight adverse effect on the precision of the experiment. Additionally, the selection of a semi-flexible fixation

method for the fixation device was chosen for the convenience of conducting multiple measurements, yet its potential impact on the experiment remains unpredictable.

In the experiment, we observed a significant impact of different applied voltages on the deflection of the cartilage in an electric field. Therefore, we examined the pattern of variation in the reverse mechano-electrical effect in cartilage by adjusting the applied voltage. [Figure 4](#) illustrates the deflection of the cartilage samples at various voltages (500, 600, 700, 800, 900, 1000 V). The results reveal a notable positive correlation between the applied voltage and the deflection of the cartilage, suggesting that higher applied voltages result in increased deflection. This phenomenon can be elucidated as follows: during the experiment, the cartilage specimens are placed between two electrode plates, and upon applying voltage, an electric field is generated between these plates. The electric field exerts a force on the cartilage, causing a corresponding deflection. According to [Equation 4](#), the electric field intensity escalates with increasing applied voltage. With other conditions constant, the electric field force acting on the cartilage also increases, leading to a larger deflection in the electric field. Thus, based on the experimental results, it can be inferred that the applied voltage significantly influences the deflection of cartilage in an electric field, exhibiting a positive correlation between the two.

In light of the high voltage levels utilized in our experimental setup, it is imperative to address the inevitable temperature fluctuations that arise. Consequently, we diligently monitored the temperature variations surrounding the cartilage specimens both before and after the application of varying external voltages. To maintain the reliability of our experimental data, we ensured a period of stabilization, allowing the temperature to return to normal room levels before proceeding with subsequent measurements. The results, elegantly depicted in [Figure 5](#), shed light on the thermal effects induced by the application of voltage on the cartilage specimens. As expected, our findings indicate a noticeable increase in temperature following the voltage application. Noteworthy is the direct correlation observed; as the applied voltage intensifies, so too does the magnitude of temperature elevation in the vicinity of the cartilage samples. Nevertheless, during the voltage increase from 500 V to 1000 V, the temperature rise around the cartilage specimens remains below 1°C, indicating a relatively small temperature increase. Furthermore, we conducted a thorough investigation into the repercussions of these temperature variations on the water content and thickness variability of the cartilage specimens. Strikingly, our findings revealed minimal differences in both water content and thickness when exposed to these temperature fluctuations. Particularly noteworthy is the negligible impact on the thickness of the cartilage specimens ([Walker and Madihally, 2015](#)). Based on these compelling results, we can confidently conclude that while the application of voltage does lead to a slight increase in temperature within the cartilage specimens, this temperature rise has negligible implications for the thickness variations of the cartilage under standard room temperature conditions.

Additionally, this study has several limitations. Firstly, the precision of the high-voltage tester during the application of external voltage is limited, leading to a potential error of up to 10 V in the applied voltage. This introduces a slight deviation in the measured deflection values. Secondly, in the sampling process, the

cartilage specimens were manually cut and polished, which unavoidably introduces some errors. Consequently, the size of each sample is not precisely identical, with an error of less than 0.02 mm. To mitigate this, we computed the average values to minimize this error. In addition, it is worth noting that high external voltages can cause a slight temperature increase, which has the potential to influence the cartilage's dielectric constant within the electric field. However, since the temperature difference observed before and after applying the voltage was found to be insignificant, we chose to overlook this particular impact in our study. Furthermore, due to various factors related to both the cartilage itself and the specifics of our testing setup, a period of approximately 30 s is necessary to properly adjust the applied voltage value after securing the cartilage in the testing apparatus. During this period, the cartilage's water content evaporates to some extent, resulting in a decrease in water content of approximately 2%. These limitations should be taken into consideration when interpreting the results and further research can be conducted to address these limitations and enhance the accuracy of the findings. In previous research, inevitable discrepancies were observed between experimental outcomes and real physiological indicators, influenced by factors such as temperature variations and the intensity of the electric field ([Fukada and Yasuda, 2007](#)). Moving forward, we plan to refine our experimental approach by conducting studies in environments that closely replicate physiological conditions. This adjustment aims to mitigate any discrepancies and better align our experimental results with real-world physiological responses.

Electric stimulation plays a crucial role in cartilage repair, with its impact primarily seen in several key areas. Firstly, it promotes the proliferation of chondrocytes, accelerating the regeneration and repair of cartilage tissue. Through targeted electric stimulation, chondrocyte growth and differentiation are activated, facilitating the formation of new cartilage tissue. Additionally, it enhances the synthesis of cartilage matrix by stimulating chondrocytes, leading to increased production of essential components like collagen and chondroitin sulfate, thus supporting the repair and regeneration of cartilage tissue ([Fukada and Yasuda, 2007](#); [Halperin et al., 2004](#)).

Furthermore, electric stimulation improves chondrocyte function by boosting metabolic activity, enhancing cell function and biological activity, ultimately contributing to the health and stability of cartilage tissue. By reducing the inflammatory response in damaged areas and alleviating pain and swelling, appropriate electric stimulation facilitates a smoother cartilage repair process. In summary, electric stimulation comprehensively impacts various stages of cartilage repair, including cell proliferation, matrix synthesis, cell function, and inflammation response, ultimately promoting the healing and repair of cartilage damage.

5 Conclusion

In summary, this study investigated the reverse mechano-electrical effect in articular cartilage and its related influencing factors. The findings reveal that applying an external electric field leads to corresponding deflection and flexure of the cartilage. This phenomenon was consistently observed throughout the entire experimental process.

- (1) The thickness of cartilage serves as a critical factor influencing the deflection and flexure induced by the reverse mechano-electrical effect within the cartilage. As the cartilage thickness decreases, the deflection and flexure resulting from this effect intensify. Our thorough analysis of the data fitting highlights that changes in cartilage thickness directly impact the cartilage's dielectric constant within the electric field, consequently affecting the magnitude of the electric field force exerted. Moreover, the cartilage's moment of inertia is intricately linked to its thickness. The synergistic effect of these elements leads to varying degrees of deflection and flexure within the electric field in response to fluctuations in thickness.
- (2) The water content within cartilage is a crucial factor that impacts the deflection and flexure induced by the reverse mechano-electrical effect. This is due to the highly hydrated nature of cartilage, where a decrease in water content leads to a gradual reduction in cartilage thickness. Consequently, this reduction in thickness results in an increased deflection and flexure within the electric field.
- (3) In our experimental investigations, we conducted separate tests to quantify the degree of cartilage deflection and flexure across different voltage settings. Our analysis underscores the significant impact of the external electric field strength on the deflection and flexure induced by the reverse mechano-electrical effect in cartilage. These variables demonstrate a positive correlation, illustrating that an escalation in the external electric field intensity directly corresponds to an increase in the deflection and flexure experienced by the cartilage.
- (4) Due to the application of a high external electric field, it is inevitable that there will be changes in temperature around the cartilage specimen. Our findings reveal that when an external voltage of 500 V is applied, it causes an approximate temperature increase of 0.1°C around the cartilage. With the applied voltage increases to 1000 V, the temperature rises to 0.7°C. Notably, the temperature increase is approximately 0.1°C for every 100 V increase in voltage.

Data availability statement

The original contributions presented in the study are included in the article/supplementary material, further inquiries can be directed to the corresponding authors.

Ethics statement

Ethical approval was not required for the studies on animals in accordance with the local legislation and institutional requirements because only commercially available established cell lines were used.

References

Ansari, S., Khorshidi, S., and Karkhaneh, A. (2019). Engineering of gradient osteochondral tissue: from nature to lab. *Acta Biomater.* 87, 41–54. doi:10.1016/j.actbio.2019.01.071

Author contributions

CL: Writing–original draft. LZ: Writing–original draft. HD: Writing–original draft. ZH: Writing–original draft. YaW: Methodology, Supervision, Writing–original draft, Writing–review and editing. YoW: Conceptualization, Investigation, Writing–review and editing. PL: Writing–review and editing. XCW: Writing–review and editing. KZ: Writing–review and editing. YX: Conceptualization, Data curation, Formal Analysis, Funding acquisition, Methodology, Project administration, Supervision, Writing–original draft, Writing–review and editing. XGW: Data curation, Formal Analysis, Funding acquisition, Investigation, Resources, Supervision, Writing–original draft, Writing–review and editing. WC: Writing–review and editing.

Funding

The author(s) declare that financial support was received for the research, authorship, and/or publication of this article. This work was supported by the Regional Innovation Joint Fund of the National Natural Science Foundation of China (Key Project) (U21A20353), Regional Innovation Joint Fund of the National Natural Science Foundation of China (Integrated Project: U23A6009), the National Natural Science Foundation of China (Grant Nos. 12272250, 12372310, and 82172503), China Postdoctoral Science Foundation (Grant No. 2020M680913), Shanxi Province Returned Overseas Foundation (Grant No. 2022–081), the Shanxi Province Basic Research Program (Grant No. 202203021212254), and the Graduate Innovation Program of Shanxi Province (Grant No. 2023–125).

Conflict of interest

Author YoW was employed by Taiyuan Great Health Technology Health Management Co., Ltd.

The remaining authors declare that the research was conducted in the absence of any commercial or financial relationships that could be construed as a potential conflict of interest.

Publisher's note

All claims expressed in this article are solely those of the authors and do not necessarily represent those of their affiliated organizations, or those of the publisher, the editors and the reviewers. Any product that may be evaluated in this article, or claim that may be made by its manufacturer, is not guaranteed or endorsed by the publisher.

Antal, A., Terney, D., Kuhn, S., and Paulus, W. (2010). Anodal transcranial direct current stimulation of the motor cortex ameliorates chronic pain and reduces short intracortical inhibition. *J. Pain Symptom Manage* 39 (5), 890–903. doi:10.1016/j.jpainsymman.2009.09.023

- Aschero, G., Gizdulich, P., Mango, F., and Romano, S. M. (1996). Converse piezoelectric effect detected in fresh cow femur bone. *J. Biomechanics* 29 (9), 1169–1174. doi:10.1016/0021-9290(96)00011-5
- Becker, R. O., and Spadaro, J. A. (1972). Electrical stimulation of partial limb regeneration in mammals. *Bull. N. Y. Acad. Med.* 48 (4), 627–641. doi:10.1111/j.1749-6632.1974.tb26815.x
- Brighton, C. T., Wang, W., and Clark, C. C. (2008). The effect of electrical fields on gene and protein expression in human osteoarthritic cartilage explants. *JBJS* 90 (4), 833–848. doi:10.2106/jbjs.f.01437
- Clark, C. C., Wang, W., and Brighton, C. T. (2014). Up-regulation of expression of selected genes in human bone cells with specific capacitively coupled electric fields. *J. Orthop. Res.* 32 (7), 894–903. doi:10.1002/jor.22595
- Curry, E. J., Le, T. T., Das, R., Ke, K., Santorella, E. M., Paul, D., et al. (2020). Biodegradable nanofiber-based piezoelectric transducer. *Proc. Natl. Acad. Sci. U. S. A.* 117 (1), 214–220. doi:10.1073/pnas.1910343117
- Disease, G. B. D., Injury, I., Prevalence, C., Abay, S. M., Abbafati, C., Abbasi, N., et al. (2018). Global, regional, and national incidence, prevalence, and years lived with disability for 354 diseases and injuries for 195 countries and territories, 1990–2017: a systematic analysis for the Global Burden of Disease Study 2017. *Lancet* 392 (10159), 1789–1858. doi:10.1016/s0140-6736(18)32279-7
- Fukada, E., and Yasuda, I. (2007). On the piezoelectric effect of bone. *J. Phys. Soc. Jpn.* 12 (10), 1158–1162. doi:10.1143/JPSJ.12.1158
- Glyn-Jones, S., Palmer, A. J., Agricola, R., Price, A. J., Vincent, T. L., Weinans, H., et al. (2015). Osteoarthritis. *Lancet* 386 (9991), 376–387. doi:10.1016/s0140-6736(14)60802-3
- Halperin, C., Mutchnik, S., Agronin, A., Molotskii, M., Urenski, P., Salai, M., et al. (2004). Piezoelectric effect in human bones studied in nanometer scale. *Nano Lett.* 4 (7), 1253–1256. doi:10.1021/nl049453i
- Hiemer, B., Krogull, M., Bender, T., Ziebart, J., Krueger, S., Bader, R., et al. (2018). Effect of electric stimulation on human chondrocytes and mesenchymal stem cells under normoxia and hypoxia. *Mol. Med. Rep.* 18 (2), 2133–2141.
- Housmans, B. A. C., van den Akker, G. G. H., Neeffes, M., Timur, U. T., Cremers, A., Peffers, M. J., et al. (2023). Direct comparison of non-osteoarthritic and osteoarthritic synovial fluid-induced intracellular chondrocyte signaling and phenotype changes. *Osteoarthr. Cartil.* 31 (1), 60–71. doi:10.1016/j.joca.2022.09.004
- Hu, W. W., Hsu, Y. T., Cheng, Y. C., Li, C., Ruaan, R. C., Chien, C. C., et al. (2014). Electrical stimulation to promote osteogenesis using conductive polypyrrole films. *Mater. Sci. Eng. C Mater. Biol. Appl.* 37, 28–36. doi:10.1016/j.msec.2013.12.019
- Hunziker, E. B. (1999). Articular cartilage repair: are the intrinsic biological constraints undermining this process insuperable. *Osteoarthr. Cartil.* 7 (1), 15–28. doi:10.1053/joca.1998.0159
- Kapat, K., Shubhra, Q. T. H., Zhou, M., and Leeuwenburgh, S. (2020). Piezoelectric nano-biomaterials for biomedicine and tissue regeneration. *Adv. Funct. Mater.* 30 (44). doi:10.1002/adfm.201909045
- Krueger, S., Riess, A., Jonitz-Heincke, A., Weizel, A., Seyfarth, A., Seitz, H., et al. (2021). Establishment of a new device for electrical stimulation of non-degenerative cartilage cells *in vitro*. *Int. J. Mol. Sci.* 22 (1), 394. doi:10.3390/ijms22010394
- Kwon, H. J., Lee, G. S., and Chun, H. (2016). Electrical stimulation drives chondrogenesis of mesenchymal stem cells in the absence of exogenous growth factors. *Sci. Rep.* 6, 39302. doi:10.1038/srep39302
- Leppik, L., Oliveira, K. M. C., Bhavsar, M. B., and Barker, J. H. (2020). Electrical stimulation in bone tissue engineering treatments. *Eur. J. Trauma Emerg. Surg.* 46 (2), 231–244. doi:10.1007/s00068-020-01324-1
- Leppik, L. P., Froemel, D., Slavici, A., Ovadia, Z. N., Hudak, L., Henrich, D., et al. (2015). Effects of electrical stimulation on rat limb regeneration, a new look at an old model. *Sci. Rep.* 5, 18353. doi:10.1038/srep18353
- Liu, Y., Dzidotor, G., Le, T. T., Vinikoor, T., Morgan, K., Curry, E. J., et al. (2022). Exercise-induced piezoelectric stimulation for cartilage regeneration in rabbits. *Sci. Transl. Med.* 14 (627), eabi7282. doi:10.1126/scitranslmed.abi7282
- Papachroni, K. K., Karatzas, D. N., Papavassiliou, K. A., Basdra, E. K., and Papavassiliou, A. G. (2009). Mechanotransduction in osteoblast regulation and bone disease. *Trends Mol. Med.* 15 (5), 208–216. doi:10.1016/j.molmed.2009.03.001
- Pelletier, R., Higgins, J., and Bourbonnais, D. (2015). Addressing neuroplastic changes in distributed areas of the nervous system associated with chronic musculoskeletal disorders. *Phys. Ther.* 95 (11), 1582–1591. doi:10.2522/ptj.20140575
- Philpot, T. A. (2008). *Mechanics of materials: an integrated learning system*. John Wiley and Sons.
- Vaca-Gonzalez, J. J., Guevara, J. M., Moncayo, M. A., Castro-Abril, H., Hata, Y., and Garzon-Alvarado, D. A. (2019). Biophysical stimuli: a review of electrical and mechanical stimulation in hyaline cartilage. *Cartilage* 10 (2), 157–172. doi:10.1177/1947603517730637
- Vaiciuleviciute, R., Uzieliene, I., Bernotas, P., Novickij, V., Alaburda, A., and Bernotiene, E. (2023). Electrical stimulation in cartilage tissue engineering. *Bioengineering* 10, 454. doi:10.3390/bioengineering10040454
- Victoria, G., Petrisor, B., Drew, B., and Dick, D. (2009). Bone stimulation for fracture healing: what's all the fuss? *Indian J. Orthop.* 43 (2), 117–120. doi:10.4103/0019-5413.50844
- Walker, K. J., and Madhally, S. V. (2015). Anisotropic temperature sensitive chitosan-based injectable hydrogels mimicking cartilage matrix. *J. Biomed. Mater. Res. Part B, Appl. Biomaterials* 103 (6), 1149–1160. doi:10.1002/jbm.b.33293
- Wieland, D. C., Krywka, C., Mick, E., Willumeit-Romer, R., Bader, R., and Kluess, D. (2015). Investigation of the inverse piezoelectric effect of trabecular bone on a micrometer length scale using synchrotron radiation. *Acta Biomater.* 25, 339–346. doi:10.1016/j.actbio.2015.07.021
- Zhang, J., Ding, C., Ren, L., Zhou, Y., and Shang, P. (2014). The effects of static magnetic fields on bone. *Prog. Biophys. Mol. Biol.* 114 (3), 146–152. doi:10.1016/j.biombio.2014.02.001
- Zhou, Z., Cui, J., Wu, S., Geng, Z., and Su, J. (2022). Silk fibroin-based biomaterials for cartilage/osteocondral repair. *Theranostics* 12 (11), 5103–5124. doi:10.7150/thno.74548
- Zhou, Z., Zheng, J., Meng, X., and Wang, F. (2023). Effects of electrical stimulation on articular cartilage regeneration with a focus on piezoelectric biomaterials for articular cartilage tissue repair and engineering. *Int. J. Mol. Sci.* 24 (3), 1836. doi:10.3390/ijms24031836
- Zimmermann, J., Sahm, F., Arbeiter, N., Bathel, H., Song, Z., Bader, R., et al. (2023). Experimental and numerical methods to ensure comprehensible and replicable alternating current electrical stimulation experiments. *Bioelectrochemistry* 151, 108395. doi:10.1016/j.bioelechem.2023.108395
- Zuzzi, D. C., Ciccone Cde, C., Neves, L. M., Mendonca, J. S., Joazeiro, P. P., and Esquisatto, M. A. (2013). Evaluation of the effects of electrical stimulation on cartilage repair in adult male rats. *Tissue Cell* 45 (4), 275–281. doi:10.1016/j.tice.2013.02.003



OPEN ACCESS

EDITED BY

Zhen Luo,
University of Technology Sydney, Australia

REVIEWED BY

Wenxin Niu,
Tongji University, China
Valerio Giustino,
University of Palermo, Italy
Claire Hiller,
The University of Sydney, Australia

*CORRESPONDENCE

Jie Lyu,
✉ lvj@sumhs.edu.cn
Jia Han,
✉ jia.han@canberra.edu.au

RECEIVED 30 June 2024

ACCEPTED 20 January 2025

PUBLISHED 07 February 2025

CITATION

Wang X, Wang Z, Adams R, Gao Y, Lyu J and Han J (2025) Effects of stair riser height on ankle proprioception in individuals with and without chronic ankle stability.
Front. Bioeng. Biotechnol. 13:1457233.
doi: 10.3389/fbioe.2025.1457233

COPYRIGHT

© 2025 Wang, Wang, Adams, Gao, Lyu and Han. This is an open-access article distributed under the terms of the [Creative Commons Attribution License \(CC BY\)](https://creativecommons.org/licenses/by/4.0/). The use, distribution or reproduction in other forums is permitted, provided the original author(s) and the copyright owner(s) are credited and that the original publication in this journal is cited, in accordance with accepted academic practice. No use, distribution or reproduction is permitted which does not comply with these terms.

Effects of stair riser height on ankle proprioception in individuals with and without chronic ankle stability

Xueying Wang^{1,2}, Zheng Wang³, Roger Adams^{4,5}, Yang Gao¹, Jie Lyu^{5*} and Jia Han^{5,6*}

¹Department of Sport and Physical Education, Faculty of Arts and Social Sciences, Hong Kong Baptist University, Kowloon Tong, Hong Kong SAR, China, ²School of Exercise and Health, Shanghai University of Sport, Shanghai, China, ³Shanghai Sixth People's Hospital Affiliated to Shanghai Jiao Tong University School of Medicine, Shanghai, China, ⁴Research Institute for Sport and Exercise, Faculty of Health, University of Canberra, Canberra, ACT, Australia, ⁵College of Rehabilitation Sciences, Shanghai University of Medicine and Health Sciences, Shanghai, China, ⁶Science, Technology, Engineering and Mathematics (STEM) College, RMIT University, Melbourne, VIC, Australia

Background: Ankle sprains during stair descent are prevalent, especially in those with chronic ankle instability (CAI), which may be attributed to diminished ankle proprioception associated with CAI.

Objective: This study aimed to determine whether individuals with CAI have lower ankle proprioceptive performance during stair descent and to determine to what extent stair riser height may affect ankle proprioception.

Methods: 40 university students, including 21 CAI (9 males and 12 females, mean age 22.38 years, mean height 169.97 cm and mean weight 64.88 kg) and 19 healthy controls (11 males and 8 females, mean age 23.05 years, mean height 169.42 cm and mean weight 65.18 kg) volunteered. The Ankle Inversion Discrimination Apparatus for Stair Descent (AIDASD) was used to measure ankle inversion proprioception across 3 different riser heights: 15 cm, 17.5 cm, and 20 cm during stair descent.

Results: ANOVA showed that individuals with CAI performed significantly worse than health group across all tested riser heights ($F = 44.066$, $p < 0.001$), with a significant main effect of riser height ($F = 13.288$, $p < 0.001$). Significant differences in proprioceptive acuity were found between 15 cm and higher risers ($p < 0.001$), but not between 17.5 cm and 20 cm ($p = 0.675$), alongside a significant linear downward trend with increasing riser height ($F = 15.476$, $p < 0.001$). No significant interaction was observed between the group and riser height ($F = 0.745$, $p = 0.478$).

Conclusion: The presence of ankle instability and increased riser height significantly negatively affected ankle inversion proprioceptive performance during stair descent, which may increase the risk of ankle sprain.

Application: Potential applications of this research include the assessment of ankle proprioception during stair descent attributable to effective ankle instability rehabilitation and riser height selection for safe stair design.

KEYWORDS

chronic ankle instability, motor control, ankle proprioception, stair descent, biomechanics

Introduction

Acute lateral ankle sprains are the most common musculoskeletal injuries (Herzog et al., 2019; Wang et al., 2024; Witt and Witt, 2013). In addition, acute ankle sprains have a high rate of recurrence and residual symptoms, which may lead to the development of chronic ankle instability (CAI) (Roos et al., 2017). CAI has been defined as a condition characterized by persistent perceived or episodic giving away and ongoing symptoms such as pain, weakness and reduced self-reported function (Gribble et al., 2016; Hertel and Corbett, 2019).

Over 25% of ankle sprains requiring hospital care over a 4-year period result from a fall downstairs (Waterman et al., 2010). Stair descent is a challenging locomotor task that necessitates complex balance control and involves greater forward acceleration of the upper body compared to level walking (Novak et al., 2016). Furthermore, stair descent places increased demands on the muscle, force, and movement at the ankle joint (Jacobs, 2016). During this process, the ankle joint bears weight and is plantar-flexed, one posture seen in ankle sprains (Wright et al., 2000). In participants with a history of unilateral ankle sprain, participants experiencing increased perceived instability were likely to show greater ankle inversion and plantarflexion during stair descent (Cao et al., 2020). Furthermore, when compared to healthy controls without a history of an ankle sprain, patients with CAI demonstrated excessive tibiotalar inversion during stair descent (Cao et al., 2019).

However, much of the current knowledge about motor control deficits in ankle instability during stair descent is based on biomechanical methods such as kinematics (Cao et al., 2022; Cao et al., 2020; Cao et al., 2019), kinetics, and electromyography (Ghaderi et al., 2021), with fewer studies focusing on the role of proprioception in stair descent, although this plays an essential role in movement control (Henry and Baudry, 2019; Witchalls et al., 2012a).

Proprioception is the capacity to receive sensory input from mechanoreceptors and integrate it with all pertinent sensory information to determine body position and movement, ultimately producing an appropriate motor response (Han et al., 2016). The crucial role of ankle complex proprioception in movement and balance control has been widely acknowledged (Fournier Belley et al., 2016; Han et al., 2015b; Horak and Nashner, 1986). During stair descent, the ankle complex—which includes the ankle joint, the talocrural joint, the subtalar joint, and the inferior tibiofibular joint—is the essential part of the human body in contact with the support surface. Through its distinct mechanoreceptors, ankle joint provides critical sensory information for locomotion regulation in the central nervous system (CNS) (Nurse et al., 2005). Previous research has suggested that individuals with CAI have difficulties in accurately

detecting the position of their ankle joint before initial impact for landing, which may increase the likelihood of recurrent ankle sprain (Konradsen and Voigt, 2002). More research on ankle proprioception during stair descent would enable researchers and clinicians to better understand the high risk of ankle sprains, and the pathological alteration after ankle sprains.

To assess the extent of ankle proprioception impairment in CAI during stair descent, we developed a novel apparatus, i.e., the Ankle Inversion Discrimination Apparatus for Stair Descent (AIDASD). This novel apparatus replicates the stair descent task and has demonstrated reliability in evaluating ankle proprioceptive acuity in individuals with and without CAI (Wang et al., 2024). Significant differences were found between the Non-CAI and CAI groups in terms of ankle movement discrimination sensitivity during stair descent.

Improved stair design, including factors such as riser height (the vertical distance from one step to the next), has been stressed as a way to significantly minimize the incidence of stair injuries (Roys, 2001; Tse, 2005). However, much of the knowledge about stair descending deficits in CAI is primarily based on riser height. Increasing riser height has been found to further increase the demands of stair descent by increasing ankle displacements, moments, and powers, along with increased muscle activations, in healthy young adults (Jacobs, 2016; Spanjaard et al., 2008).

Although previous results from studies have shown stair descent deficits in individuals with CAI, no studies have yet examined the impact of different riser heights on ankle proprioception, which may be an essential factor in reducing the incidence of ankle sprain during stair descent.

Our previous studies have shown that in a relaxed, standing, weight-bearing position, the ability to differentiate between different ankle inversion movements worsened as inversion depth increased (Black et al., 2014; Symes et al., 2010). Symes et al. pointed out that this finding is associated with the angles at which the ankle is usually positioned during daily tasks. To be more specific, when the extent of ankle inversion exceeds the range typically encountered during daily activities, there is a notable decline in proprioceptive discrimination of movement at the ankle (Symes et al., 2010). Because individuals may frequently face varying elevations of steps in their everyday experiences and have adapted to diverse step heights, the height of steps may not affect proprioceptive ability. In contrast, there has been an indication of a relationship between the magnitude of displacement towards a goal and error in joint position matching, whereby an increase in the range of movement in the criterion movement is related to a higher degree of error in accurately matching its position in the reproduction movement (Goble, 2010). Goble proposed that individuals employ distance information when replicating joint positions, implying that the error in the results may be influenced by the distance of movement (Goble, 2010). Similarly, our recent studies, using the accuracy of

TABLE 1 Participant demographic information (Mean \pm SD).

Characteristic	Group		Difference between groups
	CAI	Non-CAI	
N	21	19	
Gender	M9 F12	M11 F8	
Age (y)	22.38 \pm 2.78	23.05 \pm 1.43	$t = 0.973, p = 0.338$
Height (cm)	169.97 \pm 9.79	169.42 \pm 8.69	$t = -0.189, p = 0.851$
Weight (Kg)	64.88 \pm 14.23	65.18 \pm 13.14	$t = 0.070, p = 0.945$
CAIT score	17.00 \pm 3.19	29.10 \pm 1.48	$t = 15.094, p < 0.001$

SD = standard deviation, CAI = chronic ankle instability, N = number, M/F = male/female, CAIT = cumberland ankle instability tool.

discrimination between movements of different distances made as proprioceptively determined targets, showed worsening discrimination towards the more distant targets when individuals raise the upper limb to overhead targets (Han et al., 2021a), which implies that the acuity of proprioception may decrease with increase in riser height due to the greater movement distance.

Therefore, this study was conducted to investigate the effect of varying riser height on ankle inversion proprioceptive performance in individuals with and without CAI. We hypothesized that, with the riser height of the stairs increasing, the proprioceptive function of individuals both with and without CAI may decrease, with ankle proprioceptive scores being significantly lower in people with CAI.

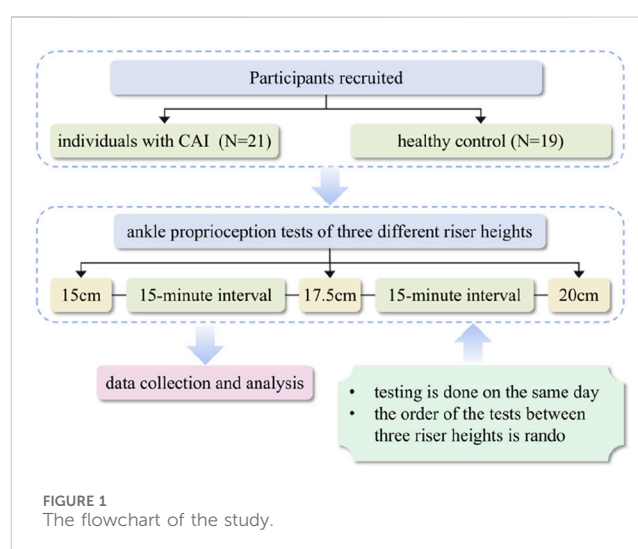
Materials and methods

This cross-sectional study was approved by the Committee for Ethics in Human Research at Shanghai University of Sport (approval number: 102772021RT123) and all participants provided written informed consent before data collection commenced.

Participants

The G*Power software package was used to determine the sample size for 90% power and an expected effect size of 0.25 SD units. It showed that to meet these specifications, there should be at least 18 participants in each group.

In this cross-sectional design study, 40 participants, including 21 with CAI and 19 healthy controls, were recruited via advertisements at Shanghai University of Sport from September 2021 to November 2021. Individuals were classified as having CAI if they had a history of at least 1 significant lateral ankle sprain, a history of at least 2 episodes of ankle joint “giving away” in the 6 months before study enrolment, and a score of ≤ 24 on the Cumberland Ankle Instability Tool (CAIT). For the healthy control group, the inclusion was no history of ankle injury. Participants were excluded from the study if they had a history of previous surgeries to the lower limb, a history of a fracture in the lower limb, and any lower limb musculoskeletal injury in the last 3 months that interrupted desired physical activity for at least 1 day. Demographic information is reported in Table 1.



Instrumentation

The Ankle Inversion Discrimination Apparatus for Stair Descent (AIDASD) tests proprioceptive ability to discriminate between different angles of ankle inversion when participants step onto the wedged platform in a task of stair descent, and its reliability and validity have been verified previously (Wang et al., 2024). The AIDASD apparatus consists of three steps to ensure a full stair gait cycle, the last of which having a wedged landing platform for the testing foot. For each trial, participants were instructed to stand upright on the top of the staircase and to descend stairs at a self-selected speed. The 4 different wedged platforms could provide 4 possible ankle inversion test angles (10°, 12°, 14° and 16°).

In this study, we aimed to identify the influence of riser height on ankle proprioception performance in individuals with and without CAI during stair descent. Standard riser heights in the Australian and Chinese documented public residential stair dimensions were taken into account when selecting the risers employed in this study (15 cm, 17.5 cm, and 20 cm) (Cao et al., 2019; Dundas et al., 2014; Chinese Standard, 2019). The Australian Building Standards AS1657 for stair riser height specify a minimum of 130 mm and a maximum of 255 mm. Therefore, based on the original apparatus of stair geometry, we built three separate custom 3-step wooden

staircases without handrails for the testing protocol with different riser heights (X cm × 29 cm × 60 cm, height × depth × width, with X = 15 cm, 17.5 cm, and 20 cm).

Testing protocols

Testing took place in a university clinical laboratory and was conducted by a professional therapist. To standardize the sensory experience from the footplate, all participants were barefoot for AIDASD testing.

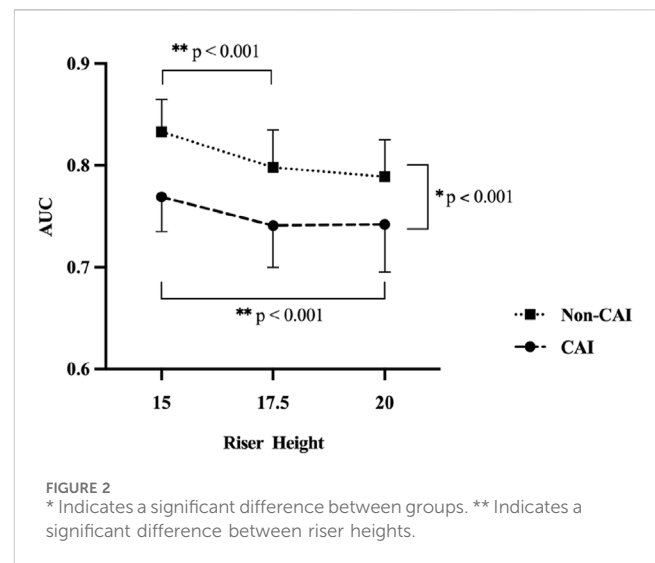
The data from 3 tests in total on the AIDASD at different riser heights was collected, with a participant completing the test on the same day. To avoid any learning effect, the test sequence was randomised by drawing cards, with tests separated by 15 min of rest (Figure 1).

During the proprioceptive testing process at each riser height, participants were first given a familiarization session in which they experienced the four ankle inversion positions in order three times, going from the smallest (Position 1 = 10°) through to the largest (Position 4 = 16°), for 12 inversion movements in total. After that, the data test was conducted with individuals with CAI who started descending the stairs with their non-symptomatic ankles and control participants starting with the non-dominant lower extremity, with the dominant leg defined as the one they prefer to use when kicking a ball (Xiao et al., 2024). During the process at each riser height, participants were instructed to keep their heads up and eyes directed forwards and not to look down at the apparatus, to eliminate the availability of visual information about the wedged platform. At each riser height participants undertook 40 trials without feedback in total, with 10 randomly presented trials for each different inversion position. On each trial, participants identified the ankle inversion position experienced based on proprioceptive information and responded with a number (1, 2, 3, or 4) reflecting the ankle inversion position they felt that they had just experienced.

Data analysis

Data were analyzed using SPSS version 24 (IBM Corporation Route 100, Somers, NY 10589). Each participant's proprioceptive acuity at the ankle complex was assessed by calculating a movement discrimination score. To obtain this acuity score, raw data were initially put into a 4 × 4 matrix indicating the frequency with which each response was made for each stimulus. Three pair-wise receiver operating characteristic (ROC) curves were generated by non-parametric signal detection analysis. Following this, the mean area under the curve (AUC) was obtained using SPSS for each participant, giving an ankle proprioceptive discrimination score that could range from 0.5, equal to chance performance, to 1.0, a perfect score.

A 2-way repeated measures analysis of variance (ANOVA) was conducted using the factors of Group (CAI and non-CAI group) and Riser Height (15 cm, 17.5 cm, 20 cm). After a significant main effect, *post hoc* pairwise comparisons were carried out, with Bonferroni adjustment used to account for multiple comparisons. Effect sizes as partial eta squared (η_p^2) were determined. Effect sizes greater than or



equal to 0.25, 0.09, and 0.01 were considered large, moderate, and small, respectively (Cronk, 2019). Polynomial trend analysis was employed to examine the shape of the ankle proprioceptive discrimination sensitivity function across different stair riser heights. A significance level of $p < 0.05$ was adopted for all analyses.

Results

There was no significant interaction between the Group and Riser Height factors for ankle proprioceptive discrimination sensitivity ($F = 0.745$, $p = 0.478$, $\eta_p^2 = 0.019$). There was a significant group main effect, indicating that the overall AUC proprioceptive discrimination scores in individuals with CAI were significantly lower than in participants without CAI ($F = 44.066$, $p < 0.001$, $\eta_p^2 = 0.537$). Riser height had a significant main effect on ankle proprioceptive acuity ($F = 13.288$, $p < 0.001$, $\eta_p^2 = 0.259$). *Post hoc* pair-wise comparisons revealed a significant difference at 15 cm compared to 17.5 cm ($p < 0.001$, 95% CI = 0.018, 0.045) and 20 cm ($p < 0.001$, 95% CI = 0.021, 0.049), with no significant difference between 17.5 cm and 20 cm ($p = 0.675$, 95% CI = -0.014, 0.021).

The polynomial trend analysis result showed that the linear trend component was significant ($F = 15.476$, $p < 0.001$) without a significant quadratic trend ($F = 1.770$, $p = 0.188$), indicating that both groups reduced their ankle proprioceptive performance in a similar linear fashion as riser height increased (Figure 2).

Discussion

This study aimed to examine the impact of changes in riser height on ankle inversion proprioception in individuals with and without CAI. The main effect of riser height observed here showed that riser height can affect ankle proprioceptive ability for both groups, with increased riser height being likely to reduce ankle inversion proprioceptive performance during stair descent. In addition, the group main effect observed here demonstrated that

the CAI group had worse ankle proprioceptive performance during stair descent than the non-CAI group. Given the importance of stair descent in daily life and the increased risk of ankle sprain during descending stairs, slight modifications in step geometry can help to reduce the risk. The findings here can be used to inform changes in stair safety codes and standards.

Riser height is identified as a critical element in stairway safety that can help reduce stair injuries (Novak et al., 2016). In this study, results indicate that proprioceptive ability deteriorated as riser height increased, with both groups showing reduced ankle proprioceptive performance in a similar linear pattern as riser height went up. This is consistent with the results observed in the upper limb proprioceptive tasks in a previous study, which reflected worsening discrimination toward the more distant targets (Han et al., 2021a). Previous studies have evaluated the effects of stair riser height on stair descent by using biomechanical methods, with results that show that as riser height increases, the stability of movement reduces, with further demands for the movement system including increasing lower extremity muscle activity (Gerstle et al., 2018) and ground reaction forces (Novak et al., 2016). It has been shown that movement planning is concerned with the specification of feedback gains, and movement control is the use of these feedback gains to driver movement (Gallivan et al., 2018). Among these feedback gains, proprioceptive information may be the more trustworthy source because when vision is employed to track activity in the external environment, the central nervous system may place greater emphasis on proprioceptive information from particular parts of the body for movement control according to the sensory reweighting hypothesis (Han et al., 2015a; Pasma et al., 2012). Therefore, we may speculate that with riser height increasing, the motor system needs to produce a series of changes such as increasing muscle activity to compensate for reduced proprioceptive feedback (Luo et al., 2024).

However, *post hoc* pair-wise comparisons here indicated a significant difference at 15 cm when compared to 17.5 cm and 20 cm, but no significant pairwise difference between 17.5 cm and 20 cm was found. This infers that participants were able to integrate multi-joint proprioceptive inputs more effectively from the hip and knee to help determine the ankle position and movement in space when the riser height was more than 17.5 cm. Dynamic stabilization of joints is accomplished through the integrated functioning of individual joints in the lower limb, collectively creating the lower kinetic chain (Chan et al., 2022). It has previously been shown that CAI patients transitioned the ankle landing strategy from the rearfoot to the forefoot (Gerstle et al., 2017) and increased lower extremity muscle activation (Gerstle et al., 2018) between riser heights of 15 cm and 25 cm, which may prepare for a less stable ankle joint position at landing and a distal foot load. These results suggest that control of the ankle joint deteriorates with riser height increasing and greater hip and knee motions may be required to compensate for maintaining stability. Indeed, kinematic methods have shown that individuals with increased perceived ankle instability are likely to increase hip adduction, hip flexion, knee adduction and knee flexion (Cao et al., 2020). The riser height they used was 18 cm, ranging from 17.5 cm to 20 cm. Therefore, as the riser height increases, irrespective of ankle stability conditions, individuals may change their movement patterns by increasing hip and knee movements to compensate for ankle instability,

which leads to more reliance on hip and knee proprioceptive information input. The stair descent task involves a sequence of overlapping joint movements, requiring a complex interplay and coordination among joints (Tripp et al., 2006). It has been shown that proximal joint stability is important for optimal distal function (Tripp et al., 2006). We speculate that this adaptive strategy in CAI with increasing riser height during stair descent may contribute to increasing distal ankle stability and therefore decreasing the risk of re-injury. Thus, further studies could focus on sensory-motor mechanisms of control during stair descent by combining kinesiological methods and dynamic proprioception tests.

Although the two groups reduced their ankle proprioceptive performance in a similar linear pattern as riser height increased, results also showed a significant group main effect, meaning that, overall, individuals with CAI performed worse than those without CAI in ankle inversion proprioceptive tests during stair descent, regardless of riser height. This is consistent with our previous research, where the AIDASD assessment was found to be reliable and capable of discriminating between individuals with and without CAI (Wang et al., 2024). Additionally, previous studies have shown ankle proprioceptive deficits during dynamic and functional tasks such as stepping, and landing (Han et al., 2021b; Witchalls et al., 2012b). However, a systematic review found no significant difference between individuals with and without CAI when using proprioception assessments, including JPS and TTPDM (Hiller et al., 2011). These conflicting results indicate that JPS and TTPDM may not be sufficiently sensitive to detect the proprioceptive deficits of CAI. Research has demonstrated that ankle proprioception in individuals with CAI is specific to certain tasks and should be assessed while imitating the conditions of an ankle injury (Han et al., 2022; Thompson et al., 2018). Being the same as the Ankle Inversion Discrimination Apparatus for Landing (AIDAL) (Han et al., 2021b), the AIDASD test involves complete weight-bearing, voluntary active movement, and testing by replicating the ankle sprain “action at injury” with a dynamic and functional movement. In addition, different tasks are used to measure ankle proprioception (Han et al., 2016), but their outcomes often are not associated (Yang et al., 2020), suggesting that different tests may target different neurophysiological characteristics of proprioception (Han et al., 2020). Han and his colleague pointed out the distinction between “imposed” and “obtained” proprioception, which might explain why AIDASD is sensitive enough to detect proprioceptive deficits associated with CAI (Han et al., 2020). Unlike “imposed” proprioception assessed by JPS and TTPDM that focuses on threshold activity in mechanoreceptors, the AIDASD task requires “obtain” proprioception, exposing the central processing impairments in individuals with CAI. The AIDASD test appears to be more specific in recognizing central processing issues and sensitive in detecting proprioceptive impairments seen in normal activities, such as stair descent. Its ability to detect deficits during dynamic tasks indicates a central processing deficit rather than peripheral injury rather than peripheral injury, suggesting that additional studies are needed. Further studies could use brain imaging techniques such as functional near-infrared spectroscopy (fNIRS) to explore changes in neural processing between the CNS and CAI-affected ankles, as observed differences in bilateral prefrontal cortex (PFC) and supplementary motor area (SMA) activations might indicate a

compensatory mechanism from proprioceptive disruptions after an initial ankle sprain (Luo et al., 2024).

The current study contains several limitations. First, although the participants in the CAI group met the CAI selection criteria recommended by the International Ankle Consortium, some factors including the level of physical activity were not collected and should be considered in future studies. Second, the results of this study may be generalized only to the young population due to the fact that our participants consisted of university student volunteers. Stairs have been identified as a common source of injurious falls among older adults (Jacobs, 2016; Startzell et al., 2000). Further, ankle proprioceptive acuity falls markedly after 75 years of age (Yang et al., 2019). Therefore, future studies should investigate the ankle proprioception performance during stair descent in older adults. Thirdly, the current study only focuses on riser height. Besides riser height, other stair architecture such as tread width (the horizontal distance between edges of adjacent steps), and handrail availability (Jacobs, 2016; Novak et al., 2016). Further study may explore the effect of other stair design factors on ankle proprioception performance.

From the perspective of practical implications, given the importance of stair descent in participation in the community, this study highlights that consideration should be given to having the smallest riser height possible when designing community and domestic spaces for safety. In addition, for clinicians, targeting assessments and interventions at deficits in ankle proprioception during stair descent may also be important for effective CAI rehabilitation.

Conclusion

The current study demonstrated a significant impact of ankle instability and stair riser height on ankle proprioceptive performance during stair descent. The findings highlight the underlying proprioceptive mechanisms associated with more frequent ankle injuries during stair descent, as well as the association between riser height and ankle injuries. Given the importance of stair descent in participation in the community, this study highlights that consideration should be given to having the smallest riser height possible when designing community and domestic spaces for safety.

References

- Black, G., Waddington, G., and Adams, R. (2014). Relative sensitivity of depth discrimination for ankle inversion and plantar flexion movements. *Percept. Mot. Ski.* 118 (1), 115–125. doi:10.2466/26.24.PMS.118k10w7
- Cao, S., Wang, C., Jiang, S., Yu, Y., Zhang, C., Huang, J., et al. (2022). Concomitant osteochondral lesions of the talus affect the stair descent biomechanics of patients with chronic ankle instability: a pilot study. *Gait Posture* 96, 306–313. doi:10.1016/j.gaitpost.2022.06.009
- Cao, S., Wang, C., Ma, X., Jiang, S., Yu, Y., Wang, X., et al. (2020). Stair descent biomechanics reflect perceived instability in people with unilateral ankle sprain history. *Clin. Biomech.* 72, 52–57. doi:10.1016/j.clinbiomech.2019.11.022
- Cao, S., Wang, C., Ma, X., Wang, X., Huang, J., Zhang, C., et al. (2019). *In vivo* kinematics of functional ankle instability patients and lateral ankle sprain copers during stair descent. *J. Orthop. Res.* 37 (8), 1860–1867. doi:10.1002/jor.24303
- Chan, L. Y. T., Sim, Y. T. N., Gan, F. K., and Bin Abd Razak, H. R. (2022). Effect of chronic ankle instability on lower extremity kinematics, dynamic postural stability, and muscle activity during unilateral jump-landing tasks: a systematic review and meta-analysis. *Phys. Ther. Sport* 55, 176–188. doi:10.1016/j.ptsp.2022.04.005
- Chinese Standard (2019). *Unified standard for design of civil buildings* (GB 50352-2019).
- Cronk, B. C. (2019). *How to use SPSS®: a step-by-step guide to analysis and interpretation*. Routledge.
- Dundas, M. A., Gutierrez, G. M., and Pozzi, F. (2014). Neuromuscular control during stepping down in continuous gait in individuals with and without ankle instability. *J. Sports Sci.* 32 (10), 926–933. doi:10.1080/02640414.2013.868917
- Fournier Belley, A., Bouffard, J., Brochu, K., Mercier, C., Roy, J. S., and Bouyer, L. (2016). Development and reliability of a measure evaluating dynamic proprioception during walking with a robotized ankle-foot orthosis, and its relation to dynamic postural control. *Gait Posture* 49, 213–218. doi:10.1016/j.gaitpost.2016.07.013

Data availability statement

The raw data supporting the conclusions of this article will be made available by the authors, without undue reservation.

Ethics statement

The studies involving humans were approved by the Committee for Ethics in Human Research at Shanghai University of Sport. The studies were conducted in accordance with the local legislation and institutional requirements. The participants provided their written informed consent to participate in this study.

Author contributions

XW: Writing—original draft. ZW: Writing—review and editing. RA: Writing—review and editing. YG: Writing—review and editing. JL: Writing—review and editing. JH: Writing—review and editing.

Funding

The author(s) declare that no financial support was received for the research, authorship, and/or publication of this article.

Conflict of interest

The authors declare that the research was conducted in the absence of any commercial or financial relationships that could be construed as a potential conflict of interest.

Publisher's note

All claims expressed in this article are solely those of the authors and do not necessarily represent those of their affiliated organizations, or those of the publisher, the editors and the reviewers. Any product that may be evaluated in this article, or claim that may be made by its manufacturer, is not guaranteed or endorsed by the publisher.

- Gallivan, J. P., Chapman, C. S., Wolpert, D. M., and Flanagan, J. R. (2018). Decision-making in sensorimotor control. *Nat. Rev. Neurosci.* 19 (9), 519–534. doi:10.1038/s41583-018-0045-9
- Gerstle, E. E., Keenan, K. G., O'Connor, K., and Cobb, S. C. (2018). Lower extremity muscle activity during descent from varying step heights. *J. Electromyogr. Kinesiol.* 42, 57–65. doi:10.1016/j.jelekin.2018.06.006
- Gerstle, E. E., O'Connor, K., Keenan, K. G., and Cobb, S. C. (2017). Foot and ankle kinematics during descent from varying step heights. *J. Appl. Biomechanics* 33 (6), 453–459. doi:10.1123/jab.2016-0301
- Ghaderi, F., Shahmoradi, E., Moghadam Salimi, M., Asghari Jafarabadi, M., and Goljarian, S. (2021). The effect of heel height of shoe on ankle muscle activation pattern in women with functional ankle instability during stair descending. *Muscles, Ligaments Tendons J. (MLTJ)* 11 (4), 666. doi:10.32098/mltj.04.2021.08
- Goble, D. J. (2010). Proprioceptive acuity assessment via joint position matching: from basic science to general practice. *Phys. Ther.* 90 (8), 1176–1184. doi:10.2522/ptj.20090399
- Gribble, P. A., Bleakley, C. M., Caulfield, B. M., Docherty, C. L., Fourchet, F., Fong, D. T.-P., et al. (2016). Evidence review for the 2016 International Ankle Consortium consensus statement on the prevalence, impact and long-term consequences of lateral ankle sprains. *Br. J. Sports Med.* 50 (24), 1496–1505. doi:10.1136/bjsports-2016-096189
- Han, J., Adams, R., and Waddington, G. (2020). “Imposed” and “obtained” ankle proprioception across the life span—Commentary on Djajadikarta et al. *J. Appl. Physiology* 129 (3), 533–534. doi:10.1152/jappphysiol.00541.2020
- Han, J., Adams, R., Waddington, G., and Han, C. (2021a). Proprioceptive accuracy after uni-joint and multi-joint patterns of arm-raising movements directed to overhead targets. *Somatosens. Mot. Res.* 38 (2), 127–132. doi:10.1080/08990220.2021.1876017
- Han, J., Anson, J., Waddington, G., Adams, R., and Liu, Y. (2015a). The role of ankle proprioception for balance control in relation to sports performance and injury. *BioMed Res. Int.* 2015, 1–8. doi:10.1155/2015/842804
- Han, J., Waddington, G., Adams, R., Anson, J., and Liu, Y. (2016). Assessing proprioception: a critical review of methods. *J. Sport Health Sci.* 5 (1), 80–90. doi:10.1016/j.jshs.2014.10.004
- Han, J., Waddington, G., Anson, J., and Adams, R. (2015b). Level of competitive success achieved by elite athletes and multi-joint proprioceptive ability. *J. Sci. Med. Sport* 18 (1), 77–81. doi:10.1016/j.jsams.2013.11.013
- Han, J., Yang, Z., Adams, R., Ganderton, C., Witchalls, J., and Waddington, G. (2021b). Ankle inversion proprioception measured during landing in individuals with and without chronic ankle instability. *J. Sci. Med. Sport* 24 (7), 665–669. doi:10.1016/j.jsams.2021.02.004
- Han, J., Yang, Z., Witchalls, J., Ganderton, C., Adams, R., and Waddington, G. (2022). Ankle inversion proprioception impairment in persons with chronic ankle instability is task-specific. *Percept. Mot. Ski.* 129 (6), 1736–1748. doi:10.1177/00315125221125608
- Henry, M., and Baudry, S. (2019). Age-related changes in leg proprioception: implications for postural control. *J. Neurophysiology* 122 (2), 525–538. doi:10.1152/jn.00067.2019
- Hertel, J., and Corbett, R. O. (2019). An updated model of chronic ankle instability. *J. Athl. Train.* 54 (6), 572–588. doi:10.4085/1062-6050-344-18
- Herzog, M. M., Kerr, Z. Y., Marshall, S. W., and Wikstrom, E. A. (2019). Epidemiology of ankle sprains and chronic ankle instability. *J. Athl. Train.* 54 (6), 603–610. doi:10.4085/1062-6050-447-17
- Hiller, C. E., Nightingale, E. J., Lin, C. W., Coughlan, G. F., Caulfield, B., and Delahunty, E. (2011). Characteristics of people with recurrent ankle sprains: a systematic review with meta-analysis. *Br. J. Sports Med.* 45 (8), 660–672. doi:10.1136/bjsm.2010.077404
- Horak, F. B., and Nashner, L. M. (1986). Central programming of postural movements: adaptation to altered support-surface configurations. *J. Neurophysiology* 55 (6), 1369–1381. doi:10.1152/jn.1986.55.6.1369
- Jacobs, J. V. (2016). A review of stairway falls and stair negotiation: lessons learned and future needs to reduce injury. *Gait Posture* 49, 159–167. doi:10.1016/j.gaitpost.2016.06.030
- Konradsen, L., and Voigt, M. (2002). Inversion injury biomechanics in functional ankle instability: a cadaver study of simulated gait. *Scand. J. Med. Sci. Sports* 12 (6), 329–336. doi:10.1034/j.1600-0838.2002.00108.x
- Luo, X., Huang, B., Huang, Y., Li, M., Niu, W., and Wang, T. (2024). Central imaging based on near-infrared functional imaging technology can be useful to plan management in patients with chronic lateral ankle instability. *J. Orthop. Surg. Res.* 19 (1), 361. doi:10.1186/s13018-024-04790-0
- Novak, A. C., Komisar, V., Maki, B. E., and Fernie, G. R. (2016). Age-related differences in dynamic balance control during stair descent and effect of varying step geometry. *Appl. Ergon.* 52, 275–284. doi:10.1016/j.apergo.2015.07.027
- Nurse, M. A., Hulliger, M., Wakeling, J. M., Nigg, B. M., and Stefanyshyn, D. J. (2005). Changing the texture of footwear can alter gait patterns. *J. Electromyogr. Kinesiol.* 15 (5), 496–506. doi:10.1016/j.jelekin.2004.12.003
- Pasma, J. H., Boonstra, T. A., Campfens, S. F., Schouten, A. C., and Van der Kooij, H. (2012). Sensory reweighting of proprioceptive information of the left and right leg during human balance control. *J. Neurophysiology* 108 (4), 1138–1148. doi:10.1152/jn.01008.2011
- Roos, K. G., Kerr, Z. Y., Mauntel, T. C., Djoko, A., Dompier, T. P., and Wikstrom, E. A. (2017). The epidemiology of lateral ligament complex ankle sprains in national collegiate athletic association sports. *Am. J. Sports Med.* 45 (1), 201–209. doi:10.1177/0363546516660980
- Roys, M. S. (2001). Serious stair injuries can be prevented by improved stair design. *Appl. Ergon.* 32 (2), 135–139. doi:10.1016/s0003-6870(00)00049-1
- Spanjaard, M., Reeves, N. D., van Dieën, J. H., Baltzopoulos, V., and Maganaris, C. N. (2008). Lower-limb biomechanics during stair descent: influence of step-height and body mass. *J. Exp. Biol.* 211 (Pt 9), 1368–1375. doi:10.1242/jeb.014589
- Startzell, J. K., Owens, D. A., Mulfinger, L. M., and Cavanagh, P. R. (2000). Stair negotiation in older people: a review. *J. Am. Geriatrics Soc.* 48 (5), 567–580. doi:10.1111/j.1532-5415.2000.tb05006.x
- Symes, M., Waddington, G., and Adams, R. (2010). Depth of ankle inversion and discrimination of foot positions. *Percept. Mot. Ski.* 111 (2), 475–484. doi:10.2466/06.25.26.Pms.111.5.475-484
- Thompson, C., Schabrun, S., Romero, R., Bialocerkowski, A., van Dieën, J., and Marshall, P. (2018). Factors contributing to chronic ankle instability: a systematic review and meta-analysis of systematic reviews. *Sports Med.* 48 (1), 189–205. doi:10.1007/s40279-017-0781-4
- Tripp, B. L., Uhl, T. L., Mattacola, C. G., Srinivasan, C., and Shapiro, R. (2006). A comparison of individual joint contributions to multijoint position reproduction acuity in overhead-throwing athletes. *Clin. Biomech.* 21 (5), 466–473. doi:10.1016/j.clinbiomech.2005.12.015
- Tse, T. (2005). The environment and falls prevention: do environmental modifications make a difference? *Aust. Occup. Ther. J.* 52 (4), 271–281. doi:10.1111/j.1440-1630.2005.00525.x
- Wang, X., Wang, Z., Adams, R., Ganderton, C., Lyu, J., and Han, J. (2024). Ankle inversion proprioception measured during stair descent can identify chronic ankle instability. *Musculoskelet. Sci. Pract.* 72, 102958. doi:10.1016/j.msksp.2024.102958
- Waterman, B. R., Owens, B. D., Davey, S., Zaccilli, M. A., and Belmont, P. J., Jr. (2010). The epidemiology of ankle sprains in the United States. *J. Bone Jt. Surg.* 92 (13), 2279–2284. doi:10.2106/jbjs.L01537
- Witchalls, J., Blanch, P., Waddington, G., and Adams, R. (2012a). Intrinsic functional deficits associated with increased risk of ankle injuries: a systematic review with meta-analysis. *Br. J. Sports Med.* 46 (7), 515–523. doi:10.1136/bjsports-2011-090137
- Witchalls, J., Waddington, G., Blanch, P., and Adams, R. (2012b). Ankle instability effects on joint position sense when stepping across the active movement extent discrimination apparatus. *J. Athl. Train.* 47 (6), 627–634. doi:10.4085/1062-6050-47.6.12
- Witt, B. L., and Witt, S. L. (2013). Acute ankle sprains: a review of literature. *Osteopath. Fam. Physician* 5 (5), 178–184. doi:10.1016/j.osfp.2013.04.001
- Wright, I. C., Neptune, R. R., van den Bogert, A. J., and Nigg, B. M. (2000). The influence of foot positioning on ankle sprains. *J. Biomechanics* 33 (5), 513–519. doi:10.1016/s0021-9290(99)00218-3
- Xiao, S., Shen, B., Xu, Z., Zhan, J., Zhang, C., Han, J., et al. (2024). Balance control deficits are associated with diminished ankle force sense, not position sense, in athletes with chronic ankle instability. *Archives Phys. Med. Rehabilitation* 105 (11), 2127–2134. doi:10.1016/j.apmr.2024.06.019
- Yang, N., Waddington, G., Adams, R., and Han, J. (2019). Age-related changes in proprioception of the ankle complex across the lifespan. *J. Sport Health Sci.* 8 (6), 548–554. doi:10.1016/j.jshs.2019.06.003
- Yang, N., Waddington, G., Adams, R., and Han, J. (2020). Joint position reproduction and joint position discrimination at the ankle are not related. *Somatosens. Mot. Res.* 37 (2), 97–105. doi:10.1080/08990220.2020.1746638



OPEN ACCESS

EDITED BY

Zhen Luo,
University of Technology Sydney, Australia

REVIEWED BY

Qiang Chen,
Southeast University, China
Yifei Jin,
University of Nevada, United States

*CORRESPONDENCE

Yongtao Lyu,
✉ yongtaolu@dlut.edu.cn
Lei Li,
✉ spinecmull@163.com

[†]These authors share first authorship

RECEIVED 29 September 2024

ACCEPTED 13 January 2025

PUBLISHED 12 February 2025

CITATION

Lai R, Jiang J, Huo Y, Wang H, Bosiakov S, Lyu Y and Li L (2025) Design of novel graded bone scaffolds based on triply periodic minimal surfaces with multi-functional pores. *Front. Bioeng. Biotechnol.* 13:1503582. doi: 10.3389/fbioe.2025.1503582

COPYRIGHT

© 2025 Lai, Jiang, Huo, Wang, Bosiakov, Lyu and Li. This is an open-access article distributed under the terms of the [Creative Commons Attribution License \(CC BY\)](#). The use, distribution or reproduction in other forums is permitted, provided the original author(s) and the copyright owner(s) are credited and that the original publication in this journal is cited, in accordance with accepted academic practice. No use, distribution or reproduction is permitted which does not comply with these terms.

Design of novel graded bone scaffolds based on triply periodic minimal surfaces with multi-functional pores

Rongwu Lai^{1,2†}, Jian Jiang^{1,3†}, Yi Huo², Hao Wang², Sergei Bosiakov⁴, Yongtao Lyu^{2,5*} and Lei Li^{3*}

¹Department of Spinal Surgery, Central Hospital of Dalian University of Technology, Dalian, China,

²School of Mechanics and Aerospace Engineering, Dalian University of Technology, Dalian, China,

³Department of Orthopaedic Surgery, Shengjing Hospital of China Medical University, Shenyang, Liaoning, China, ⁴Faculty of Mechanics and Mathematics, Belarusian State University, Minsk, Belarus,

⁵DUT-BSU Joint Institute, Dalian University of Technology, Dalian, China

Background: Various mechanical and biological requirements on bone scaffolds were proposed due to the clinical demands of human bone implants, which remains a challenge when designing appropriate bone scaffolds.

Methods: In this study, novel bone scaffolds were developed by introducing graded multi-functional pores onto Triply Periodic Minimal Surface (TPMS) structures through topology optimization of unit cell. The performance of these scaffolds was evaluated using finite element (FE) analysis and computational fluid dynamics (CFD) method.

Results: The results from FE analysis indicated that the novel scaffold exhibited a lower elastic modulus, potentially mitigating the issue of stress shielding. Additionally, the results from CFD demonstrated that the mass transport capacity of the novel scaffold was significantly improved compared to conventional TPMS scaffolds.

Conclusion: In summary, the novel TPMS scaffolds with graded multi-functional pores presented in this paper exhibited enhanced mechanical properties and mass transport capacity, making them ideal candidates for bone repair. A new design framework was provided for the development of high-performance bone scaffolds.

KEYWORDS

bone scaffold, triply periodic minimal surface, multi-functional pore, mechanical behavior, mass transport capacity

1 Introduction

The high prevalence of orthopedic diseases worldwide underscores the urgent clinical need for bone scaffolds that demonstrate excellent performance (Campana et al., 2014; Wallace et al., 2017; Li Y et al., 2018). Currently, there is a demand for functionally graded bone scaffolds to facilitate the transition from cancellous bone to cortical bone in the gradient region of human bone defects (Fernandez de Grado et al., 2018). Nowadays, triply periodic minimal surface (TPMS) bone scaffolds are widely developed in bone implants (Davoodi et al., 2020). However, scaffolds designed based on TPMS structures cannot fully address two critical issues, i.e., the stress-shielding effect caused by a high elastic modulus

and the insufficient mass transport capacity due to low permeability (Jiang et al., 2024; Vijayavenkataraman et al., 2020).

Since the performance of TPMS bone scaffolds mainly depends on their geometrical structure, how to improve the performance of bone scaffolds through rational structural design has become the focus and difficulty in current research studies. The high elastic modulus of bone scaffolds can cause the implanted artificial bone scaffolds to bear most of the mechanical loads, which resulted in a stress-shielding effect and further led to interface loosening (Barba et al., 2019). For functionally graded bone scaffolds, selecting an appropriate gradient transition is critical for achieving optimal performance, which remains a key challenge in current research studies. Peng et al. (2023) highlighted that the elastic modulus and permeability of bone scaffolds represent conflicting performance requirements, making it difficult to simultaneously optimize both properties. Moreover, seldom has research been conducted to completely address this problem. Therefore, it is a primary focus to resolve this trade-off issue in current studies. Although the elastic modulus of TPMS bone scaffolds is lower than that of traditional cubic porous structures, it is still higher than that of cancellous bone. Sevilla et al. (2007) reported that the elastic modulus of cancellous bone was 1.08 GPa. Wu et al. (2018) investigated the elastic modulus of cancellous bone under different loading directions. The results indicated that the modulus of cancellous bone was 3.47 GPa in the longitudinal direction and 2.57 ± 0.28 GPa in the transverse direction. Although there were discrepancies in the elastic moduli of cancellous bone between the studies, it was generally agreed that the elastic modulus of a bone scaffold should not exceed 3.00 GPa to align with that of the cancellous bone. Khaleghi et al. (2021) reported that the elastic modulus of a Schwarz P (i.e., one type of TPMS) scaffold with a porosity of 70% was 5.60 GPa, which was greater than that of cancellous bone. Rabiati et al. (2021) stated that the permeability of cancellous bone is in the range of $3.66 \times 10^{-8} \text{ m}^2$ to $1.90 \times 10^{-7} \text{ m}^2$. However, Santos et al. (2020) found that the permeability of a TPMS structure is in the range of $4.31 \times 10^{-10} \text{ m}^2$ to $8.44 \times 10^{-9} \text{ m}^2$. Accordingly, it is necessary to optimize the topologies of TPMS bone scaffolds.

Recent studies on functionally graded TPMS bone scaffolds have made significant progress in improving gradient transitions to enhance both mechanical and biological performances. Wang et al. (2022) demonstrated that scaffolds with graded porosities improved load-bearing capacity while maintaining a high permeability, but it cannot be fully ensured that the challenges in optimizing the gradient transition are mitigated to prevent stress shielding. Zhang et al. (2020) found that mechanical strength and fluid transport were balanced by continuous gradient designs but struggled with achieving excellent performance by different porosities. Kim et al. (2020) reported that cell proliferation was enhanced using graded TPMS scaffolds. However, the mass transport capacity was limited by the low permeability. Li et al. (2021) improved mechanical anisotropy and acknowledged that achieving an ideal balance between elastic modulus and permeability for bone scaffolds remains a key challenge. Xu et al. (2020) highlighted that although graded designs show potential in addressing the mismatch of elastic modulus, further improvement was also needed to ensure mechanical stability and clinical applicability. The limitations of achieving an optimal balance between mechanical properties and permeability still exist, and therefore improved design strategies are needed.

In this study, a novel graded bone scaffold with multi-functional pores was developed based on the Schwarz P structure. The finite element (FE) analysis and computational fluid dynamics (CFD) method were applied to evaluate the performance of the novel functionally graded bone scaffolds with different porosities, and it was found that its mechanical properties and mass transport capacities were more excellent than those of conventional scaffolds, which indicated that novel bone scaffold may be a better candidate for bone repair (Hollister and Kikuchi, 1994).

2 Methodology

In this section, the Schwarz P structure is introduced, followed by a detailed description of the methodology for designing novel TPMS bone scaffolds with multi-functional pores. Methods for evaluating the mechanical properties of TPMS bone scaffolds were then described, including the evaluations of the elastic modulus and the anisotropy of the novel scaffolds using numerical homogenization methods. Finally, a numerical simulation method to evaluate the permeability is presented.

2.1 Design of novel TPMS bone scaffolds with graded multi-functional pores

A minimal surface has the smallest area subject to certain constraints and is mathematically defined as a surface with a mean curvature of 0 at any point (Yoo, 2011). TPMS is a minimal surface that possesses periodical array in three orthogonal base directions, and its topology is determined by functional expressions. Common TPMS structures include Schwarz P, Gyroid, Diamond, and I-WP (Blanquer et al., 2017). Schwarz P was proposed by the scientist Schwarz who first introduced the concept of minimal surfaces in 1883 (Strömberg, 2021). The continuous surface structure of TPMS reduces the stress concentration, and thus the stress bearing is more uniform. Meanwhile, the continuous surface structure of TPMS has better connectivity and larger specific surface area, and it was shown by cell culture that bone marrow stromal cells (BMSCs) exhibited better adhesion, proliferation, and osteogenic differentiation behaviors on the TPMS structural scaffold (Guo et al., 2023). Among the various TPMS structures (Diamond, Gyroid, Fischer-Koch S, etc.), the Schwarz P possesses cubic symmetry (Lu et al., 2019; Lu et al., 2020) and is more suitable for opening multi-functional pores in its surfaces, which is one major novelty in the present study. Therefore, the Schwarz P structure was selected as the example for structural design in this study. The Schwarz P structure was created by incorporating the thickness of the minimal surface. The Schwarz P structure can be characterized by the following mathematical function (Blanquer et al., 2017).

$$f(x, y, z) = \cos\left(\frac{2\pi}{n}x\right) + \cos\left(\frac{2\pi}{n}y\right) + \cos\left(\frac{2\pi}{n}z\right) - c, \quad (1)$$

where f determines the TPMS topology type; x, y, z are the coordinates of a point in the design space; n denotes the length of a unit cell; and constant c is used to control the two-phase domain, which determines the porosity of the structure (Peng et al., 2023).

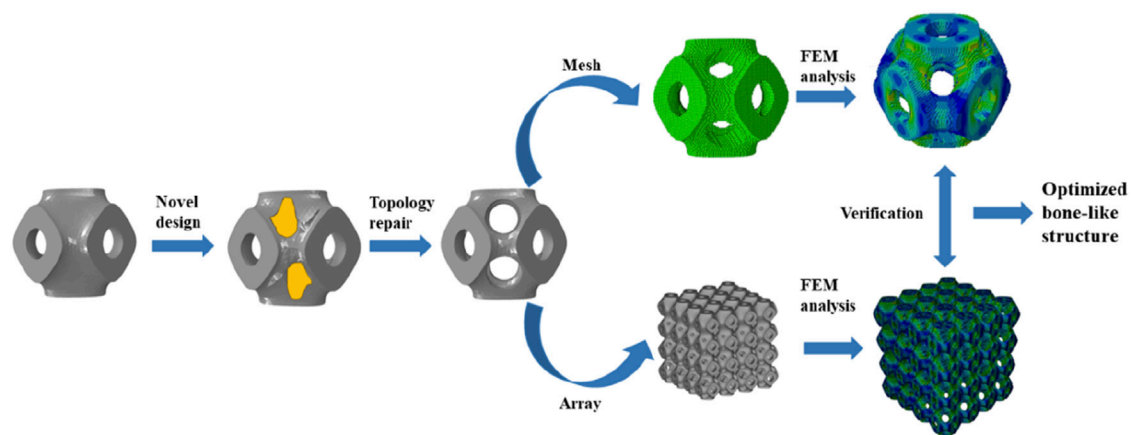


FIGURE 1
Schematic diagram of the design process of the novel structure.

The mass transport capacity of bone scaffolds depends on the pore size and the obstructed area (Kurtz et al., 2007; Ali et al., 2020). The structures with different porosities can be formed using various parameters, as illustrated in Equation 1. However, parameter c in Equation 1 is a unique variable to control the surface of the unit cell, which is related to porosity. Consequently, it was noted that multi-functional pores have been integrated into the scaffolds to enhance the mass transport capability and reduce the elastic modulus. Next, the process of generating multi-functional pores by the structural optimization method was briefly analyzed, and the differences between the gradient transition methods commonly used in previous studies for bone scaffolds and the newly proposed multi-functional pore gradient transition methods were described in detail.

The constitutive relation of stress σ and strain ϵ of the Schwarz P structure can be expressed as Equation 2. Since Schwarz P has cubic symmetry with three independent elastic constants, the stiffness matrix can be simplified as follows (Gere and Goodno, 2009).

$$\begin{pmatrix} \sigma_{11} \\ \sigma_{22} \\ \sigma_{33} \\ \sigma_{12} \\ \sigma_{13} \\ \sigma_{23} \end{pmatrix} = \begin{bmatrix} C_{11} & C_{12} & C_{12} & 0 & 0 & 0 \\ C_{12} & C_{11} & C_{12} & 0 & 0 & 0 \\ C_{12} & C_{12} & C_{11} & 0 & 0 & 0 \\ 0 & 0 & 0 & C_{44} & 0 & 0 \\ 0 & 0 & 0 & 0 & C_{44} & 0 \\ 0 & 0 & 0 & 0 & 0 & C_{44} \end{bmatrix} \begin{pmatrix} \epsilon_{11} \\ \epsilon_{22} \\ \epsilon_{33} \\ \epsilon_{12} \\ \epsilon_{13} \\ \epsilon_{23} \end{pmatrix}, \quad (2)$$

where C_{11} , C_{12} , and C_{44} are the three independent elastic constants of the Schwarz P structure.

The derived expression for the elastic modulus of the Schwarz P structure is given by a computational simplification with the introduction of boundary conditions as Equation 3 (Ma et al., 2021; Feng et al., 2021; Lee et al., 2017).

$$E = \frac{18w^{(1)}w^{(2)} - 2[w^{(2)}]^2}{3V[3w^{(1)} + w^{(2)}]} = \frac{18v_\epsilon^{(1)}v_\epsilon^{(2)} - 2[v_\epsilon^{(2)}]^2}{3[3v_\epsilon^{(1)} + v_\epsilon^{(2)}]}, \quad (3)$$

where V represents the volume of the Schwarz P structure and $v_\epsilon = \frac{w}{V}$ represents the strain energy density.

We intend to reduce the elastic modulus of the Schwarz P bone scaffold, and the optimization framework is expressed in Equation 4 (Jiang et al., 2024).

$$\begin{cases} \text{find } v_\epsilon = (v_\epsilon^{(1)}, v_\epsilon^{(2)}) \\ \min f(v_\epsilon) = \frac{18v_\epsilon^{(1)}v_\epsilon^{(2)} - 2[v_\epsilon^{(2)}]^2}{3[3v_\epsilon^{(1)} + v_\epsilon^{(2)}]}, \\ \text{subject to } \begin{cases} 0.5 \leq V_{\text{frac}} \leq 0.8 \\ t \geq 0.2\text{mm} \end{cases} \end{cases} \quad (4)$$

where V_{frac} represents the volume fraction of the Schwarz P scaffold and t represents the thickness of the scaffold.

Calculations were carried out using Abaqus (v2023, Dassault Systems SIMULIA Ltd. Providence, RI, United States) according to the optimization framework, and the Solid Isotropic Material Penalty (SIMP, one type of topology optimization) was used. As shown in Figure 1, the new structure was obtained by iterative computation, and then topological repair was performed to generate a unit cell with multi-functional pores, and a novel bone scaffold was designed based on the unit cell. According to the unit cell design method for multi-functional pores with different porosities, a unit cell graded Schwarz P bone scaffold with a porosity of 65% was obtained, as shown in Figure 2B. A linear transition was taken (Karuna et al., 2022), and the gradient transition method in this study are expressed as Equation 5.

$$\frac{V_1}{V_2} = 2.0, \quad (5)$$

where V_1 and V_2 denote the volume sizes of the top unit cell and the bottom unit cell, respectively.

The strategy of the proposed optimized design was to add graded multi-functional pores, which can form a new topology of TPMS. The graded multi-functional pore bone scaffolds with a porosity of 65% were designed, as shown in Figure 2C. Two bone scaffolds with different gradient transitions were obtained with an overall porosity of 65%. It is worth noting that the structures with the same porosity imply the same volume of the solid material according to the definition of porosity, which can ensure comparability among different structures.

As shown in Figure 2A, a uniform Schwarz P bone scaffold with a porosity of 65% was also established as a control group. Therefore,

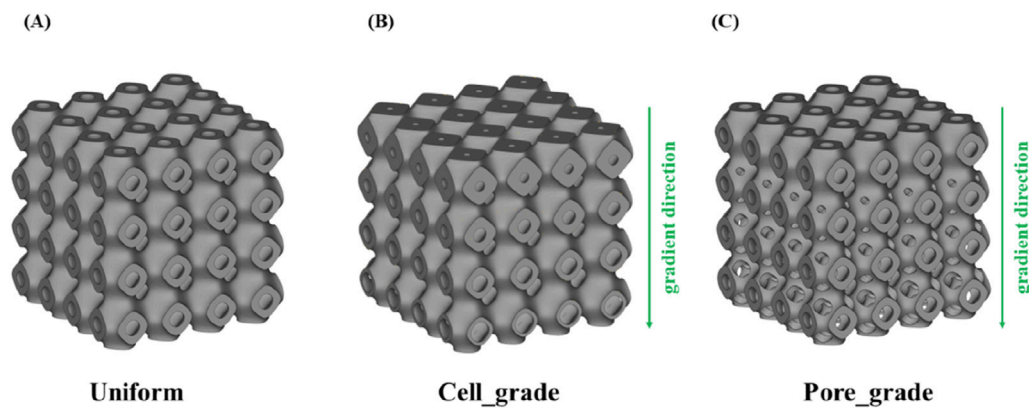


FIGURE 2

Three types of bone scaffolds. (A) Uniform Schwarz P bone scaffold with a porosity of 65%. (B) Cell gradient Schwarz P bone scaffold with a porosity of 65%. (C) Multi-functional pore-graded Schwarz P bone scaffold with a porosity of 65%.

three bone scaffolds with an overall porosity of 65% were compared to evaluate their performances. Similarly, two sets of bone scaffolds with porosities of 70% and 75% were designed, and the performance of these bone scaffolds was also compared using the same methods. All bone scaffold structures were generated using the software Flatt Pack (v3.31, University of Nottingham, United Kingdom), and the models were reprocessed using Materialise Magics (v24.0, Lovaine, Belgium). Additionally, the direction of gradient transition was set to the Y-direction for all graded bone scaffolds, while the X and Z directions remained unchanged.

2.2 Mechanical simulations and analysis

To evaluate the mechanical behavior of the novel scaffolds, the FE simulation was performed. Based on the parameters of the stiffness matrix, the Zener anisotropy indexes were calculated. The elastic moduli and Zener anisotropy indexes were used to evaluate the performance of novel scaffolds. For the FE simulations, the boundary conditions were set as Equations 6, 7:

$$\begin{cases} \Delta I_x|_{x=l_x} = 0.001I_x \\ \Delta I_x|_{x=0} = \Delta I_y|_{y=0} = \Delta I_y|_{y=l_y} = \Delta I_z|_{z=0} = \Delta I_z|_{z=l_z} = 0 \end{cases} \quad (6)$$

$$\begin{cases} \Delta I_x|_{x=l_x} = 0.0005I_x, \Delta I_z|_{x=l_x} = 0.0005I_x \\ \Delta I_z|_{x=0} = \Delta I_y|_{y=0} = \Delta I_y|_{y=l_y} = \Delta I_z|_{z=l_z} = \Delta I_x|_{z=0} = 0 \end{cases} \quad (7)$$

The material of the bone scaffold was set as TC4 (i.e., a titanium alloy material) with a Young's modulus of 110.0 GPa and a Poisson's ratio of 0.34, which is widely used in bone implants (Montazerian et al., 2017). The parameters in Equation 2 were obtained by calculating the effective elastic modulus of the bone scaffold (Jiang et al., 2024). The elastic constants can be calculated as follows (Peng et al., 2023).

$$C_{ij} = \bar{\sigma} = \frac{1}{V} \int_V \sigma_{ij} dV. \quad (8)$$

Regarding the convergence analysis of the mesh, an FE model with an element size of 0.06 mm was used in this study, and results were independent of the mesh size (Jiang et al., 2024). To evaluate

the mechanical anisotropy of the bone scaffold, the Zener anisotropy index, which is most commonly used to evaluate the anisotropic properties of materials, was used, and its expression is given as below (Chen et al., 2019).

$$A = \frac{2C_{44}}{C_{11} - C_{12}}. \quad (9)$$

When the Zener anisotropy index is equal to 1, the structure is isotropic, and when larger than 1, the anisotropy is more pronounced. After obtaining all the elastic constants C_{ij} through Equation 8, the Zener anisotropy index for each structure can therefore be calculated by substituting the elastic constants into Equation 9. Additionally, the stiffness matrix of bone scaffolds was homogenized using MATLAB (R2023a, MathWorks, Inc., Natick, Massachusetts, United States), and each Young's modulus surface was colored according to the magnitude of the effective stiffness.

2.3 Mass transport simulations and analysis

The mass transport capacity of bone scaffolds was mainly evaluated by the permeability, and high permeability can facilitate nutrient transport and accelerate bone growth. Therefore, CFD was performed in COMSOL (v6.0, COMSOL Multiphysics, Stockholm, Sweden) to simulate the fluid flow process in the bone scaffolds. The permeability of the bone scaffolds was calculated before and after the optimal design of the structure. The unit cells were arrayed into a $4 \times 4 \times 4$ bone scaffold structure with an overall size of $10.0 \text{ mm} \times 10.0 \text{ mm} \times 10.0 \text{ mm}$. Since the analysis of permeability needs to be carried out on the fluid domain, Boolean operations were performed on the bone scaffold to obtain the fluid region. To avoid the boundary conditions caused by the inlet and outlet regions, a fluid domain of $10.0 \text{ mm} \times 10.0 \text{ mm} \times 5.0 \text{ mm}$ was established at both the fluid inlet and outlet, which can ensure that a more stable state was achieved in the fluid through the region of the bone scaffold. In this way, a $10.0 \text{ mm} \times 10.0 \text{ mm} \times 20.0 \text{ mm}$ parallel hexagonal fluid domain was established, as shown in Figure 3. The specific boundary conditions

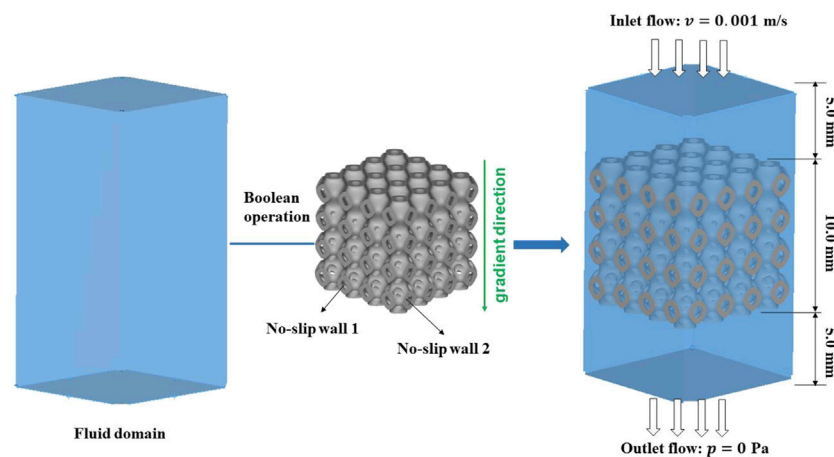


FIGURE 3
Modeling process of the fluid domain and the boundary conditions in CFD analysis.

for permeability calculations were set in TPMS bone scaffolds (Zhang et al., 2020). The rate of inlet flow was 0.001 m/s, and the outlet pressure was 0.0 Pa. The inner and outer surfaces of the bone scaffolds were set to no-slip walls. The permeability was based on Darcy's law expressed as Equation 10 (Peng et al., 2023).

$$Re = \frac{\nu \rho D}{\mu}, \quad (10)$$

where Re denotes the Reynolds number; ν denotes the fluid flow rate (m/s); ρ denotes the fluid density (kg/m^3); and D denotes the radius of the pore. The pressure drop between the inlet and outlet can be obtained by CFD calculation, and the permeability K of the bone scaffold can be calculated as Equations 11, 12.

$$K = \frac{\nu \mu L}{\Delta P}, \quad (11)$$

$$\nu = \frac{Q}{A}, \quad (12)$$

where K denotes the permeability of the bone scaffold; μ denotes the coefficient of kinetic viscosity of the fluid ($\text{Pa} \cdot \text{s}$); L denotes the straight length in the fluid direction (m); ΔP denotes the pressure difference between the inlet and outlet (Pa); Q denotes the volume of fluid flowing through the structure per unit of time (m^3/s); and A denotes the cross-sectional area of the fluid domain (m^2). The fluid flowing through the bone scaffold was set to be water with the following specific parameters: $\rho = 1000 \text{ kg/m}^3$; $\mu = 0.001 \text{ Pa} \cdot \text{s}$; $\nu = 0.001 \text{ m/s}$. The fluid volume of the bone scaffold was set to be water.

3 Results

3.1 Mechanical properties of the novel structures

3.1.1 Comparison of the effective elastic modulus among three types of bone scaffolds

The von Mises stress distribution of the three bone scaffolds was calculated. The von Mises stress distribution under uniaxial

compression for the scaffolds at 65% porosity is presented in Figure 4. The uniform Schwarz P scaffold exhibited a homogeneous and periodic stress distribution, which aligns with the typical properties of TPMS structures. In contrast, for the multi-functional pore-graded Schwarz P scaffolds, a more pronounced variation in stress distribution was observed in the Y-direction due to the gradient transition from the top to the bottom. A smoother stress variation was found in the multi-functional pore-graded scaffold compared to the single-cell gradient scaffold, indicating improved homogeneity in stress distribution and reduced directional variability in mechanical properties. Similar patterns were observed in the unidirectional shear von Mises stress distribution (Figure 5), where a gentler transition was noted in the multi-functional pore-graded scaffold compared to the single-cell gradient scaffold, while the non-gradient transition direction exhibited uniformity.

Comparison in the effective elastic moduli in the three groups of bone scaffolds at the porosities of 65%, 70%, and 75% is illustrated in Figure 6. The uniform bone scaffold was served as a control in the comparison. For the unit cell graded bone scaffolds with the porosities of 65%, 70%, and 75%, the difference in the effective compressive moduli between the X and Y directions was found to be 11.4%, 27.3%, and 18.4%, respectively, while the corresponding values for the bone scaffolds with functionally graded pores were 6.3%, 6.9%, and 5.9%, respectively. Therefore, it can be concluded that the difference in the effective compressive modulus between X and Y directions in the bone scaffolds with functionally graded pores was significantly reduced at different porosities.

By analyzing the elastic modulus of bone scaffolds on the three types, several results were obtained. At a porosity of 65%, the effective compressive modulus of the uniform bone scaffold was 6.58 GPa in both X and Y directions. For the unit cell graded bone scaffold, the elastic modulus was 6.64 GPa in the X direction and 5.96 GPa in the Y direction. The bone scaffold with multi-functionally graded pores exhibited a compressive modulus of 5.59 GPa in the X direction and a compressive modulus of 5.26 GPa in the Y direction. At a porosity of 70%, the uniform bone scaffold had an effective compressive modulus of 5.95 GPa

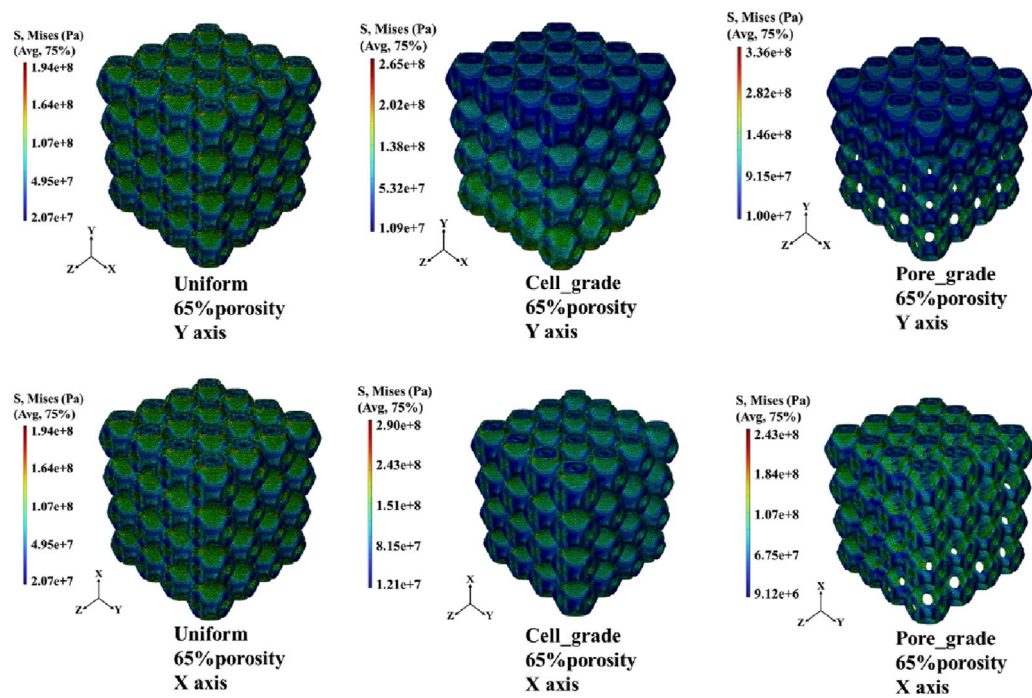


FIGURE 4
Von Mises stress distribution of three types of Schwarz P bone scaffolds with porosity 65% under uniaxial compression.

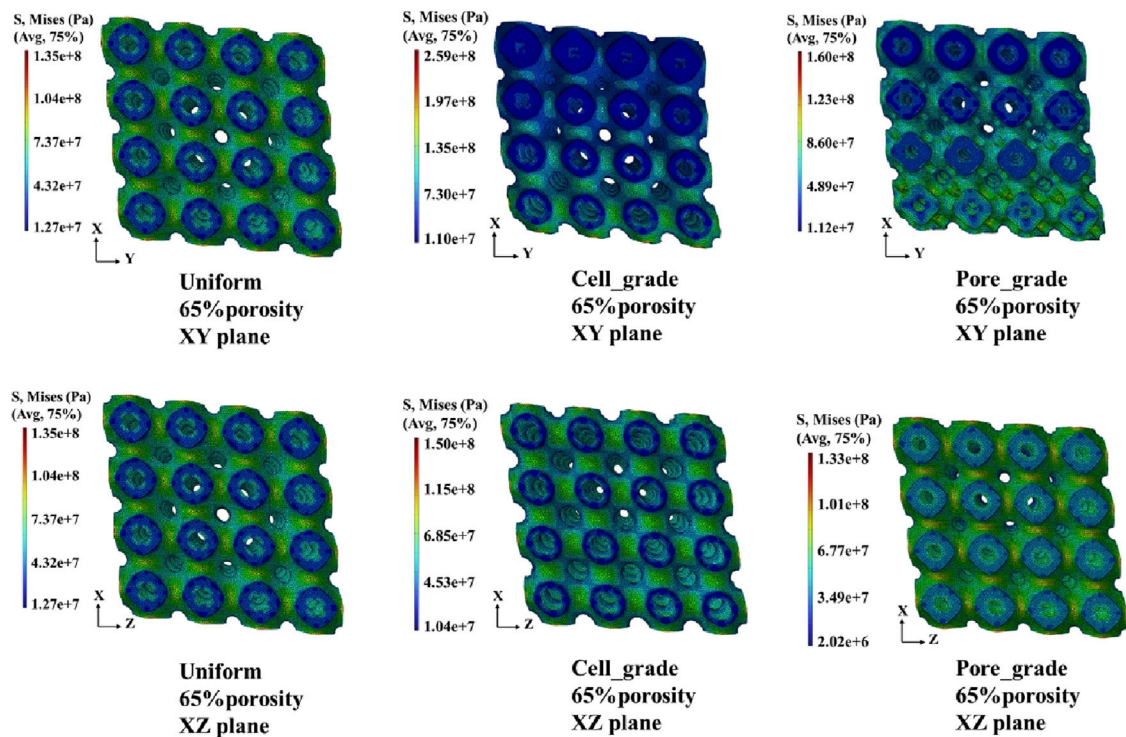


FIGURE 5
Von Mises stress distribution of three types of Schwarz P bone scaffolds with porosity 65% under unidirectional shear loading.

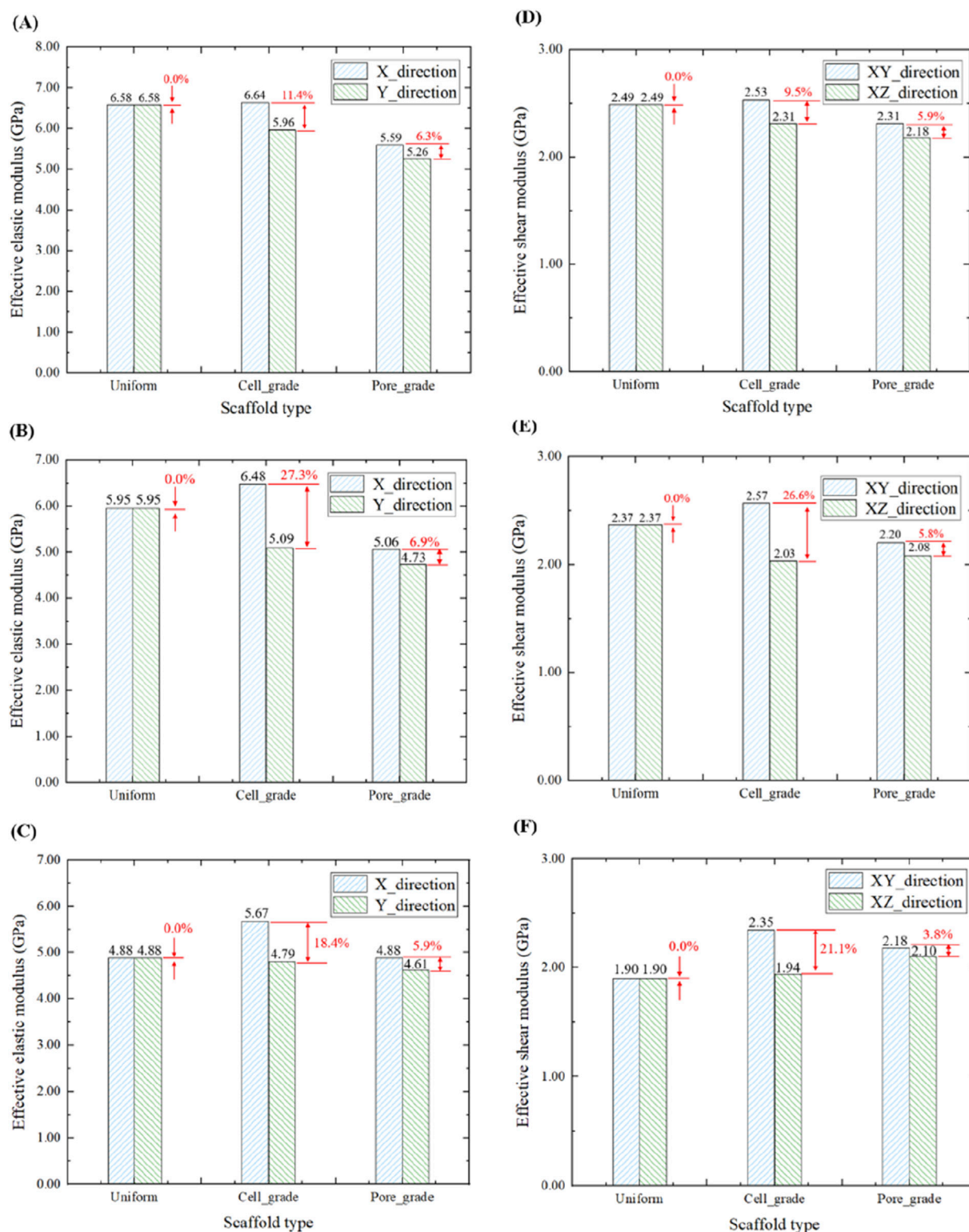


FIGURE 6

Comparison of the elastic moduli in three groups of bone scaffolds. (A) Effective elastic modulus of bone scaffolds with a porosity of 65%. (B) Effective elastic modulus of bone scaffolds with a porosity of 70%. (C) Effective elastic modulus of bone scaffolds with a porosity of 75%. (D) Effective shear modulus of bone scaffolds with a porosity of 65%. (E) Effective shear modulus of bone scaffolds with a porosity of 70%. (F) Effective shear modulus of bone scaffolds with a porosity of 75%.

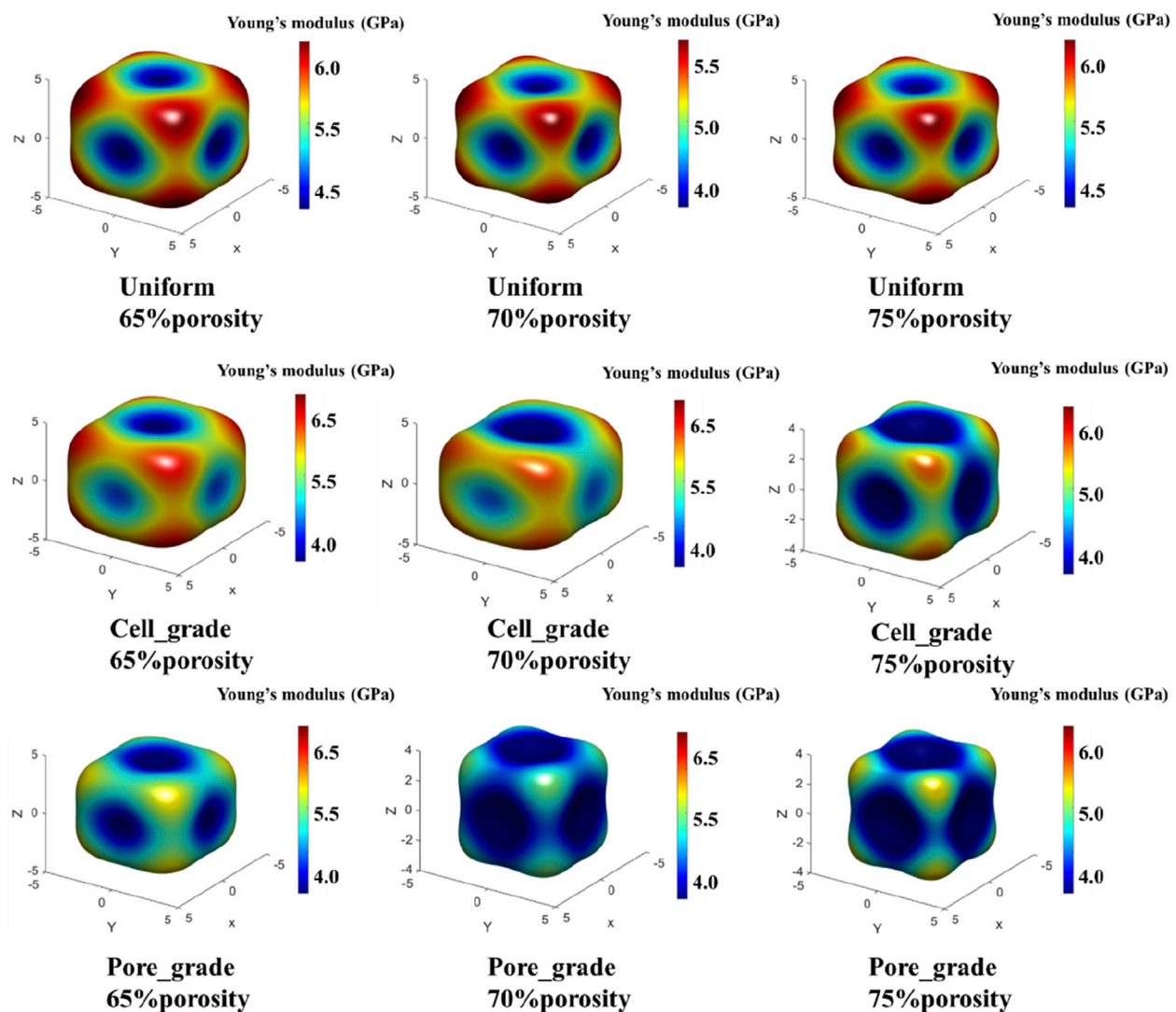


FIGURE 7
Comparison of the three-dimensional spatial distribution of the effective elastic modulus for three types of Schwarz P bone scaffolds.

in both X and Y directions. The unit cell gradient bone scaffold exhibited an elastic modulus of 6.48 GPa in the X-direction and an elastic modulus of 5.09 GPa in the Y-direction. The bone scaffold with multi-functionally graded pores displayed an elastic modulus of 5.06 GPa in the X-direction and an elastic modulus of 4.73 GPa in the Y-direction. At a porosity of 75%, the uniform bone scaffold had an elastic modulus of 4.88 GPa in both X and Y directions. The unit cell gradient bone scaffold showed an elastic modulus of 5.67 GPa in the X-direction and an elastic modulus of 4.79 GPa in the Y-direction, while the bone scaffold with multi-functionally graded pores exhibited elastic moduli of 4.88 GPa and 4.61 GPa in the X and Y directions, respectively. It was shown that the unit cell graded bone scaffolds had a larger effective compressive modulus in the non-gradient transition direction when the porosity was the same, which may exacerbate the occurrence of stress shielding and was not conducive to the long-term stability of the bone scaffolds. In contrast, bone scaffolds with multi-functionally graded pores exhibited

smaller effective compressive moduli in both gradient transition and non-gradient transition directions, which is beneficial for mitigating stress shielding. For the effective shear modulus, at three different porosities of 65%, 70%, and 75%, the difference in the effective shear modulus of the unit cell graded bone scaffolds in different directions was 9.5%, 26.6%, and 21.1%, respectively, while those in the bone scaffolds with multi-functionally graded pores were 5.9%, 5.8%, and 3.8%, respectively. Similar to the analysis of effective compressive modulus, the difference in the effective shear modulus of the bone scaffolds with multi-functionally graded pores in different directions reduced greatly at different porosities.

3.1.2 Comparison of the spatial distribution of effective elastic modulus among three types of bone scaffolds

The anisotropy of bone scaffolds was analyzed using the spatial distribution of the elastic modulus in three dimensions, as shown in

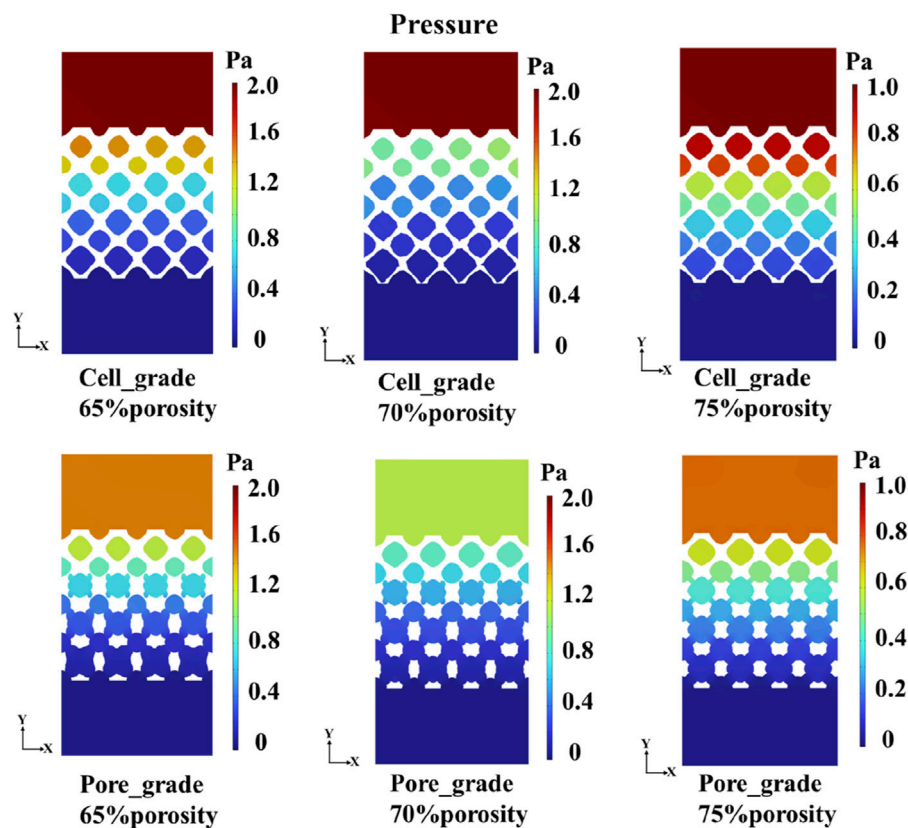


FIGURE 8
Pressure distribution of functionally graded Schwarz P bone scaffolds.

Figure 7. Since the Schwarz P structure is cubic symmetric, there are only three independent elastic constants C_{11} , C_{12} , and C_{44} in the stiffness matrix. However, a porosity gradient is introduced to the functionally graded Schwarz P bone scaffold in one direction, so it is no longer a cubically symmetric structure, and the independent elastic constants are increased by 2. The Zener anisotropy index in Equation 9 was calculated using the three independent elastic constants C_{11} , C_{12} , and C_{44} , which was not suitable for the functionally graded bone scaffolds. Thus, the anisotropy of the bone scaffolds was examined through the three-dimensional spatial distribution of the elastic modulus.

The distribution of elastic modulus for both the unit cell graded bone scaffolds and the bone scaffolds with multi-functionally graded pores was similar. The elastic modulus was lower in the central region of the eight faces of the cube and higher in the direction of the eight corner points of the cube. At all three porosities with 65%, 70%, and 75%, the difference between the highest and the lowest elastic modulus of the bone scaffolds with multi-functionally graded pores was relatively smaller, whereas that of the unit cell gradient bone scaffold was relatively larger. For instance, at a porosity of 65%, although both scaffolds showed the highest elastic modulus in the direction of the cube corner point, the difference among the moduli in the direction of the cube corner point and the other directions was larger in the unit cell graded bone scaffold, implying greater anisotropy. In contrast, the anisotropy of bone scaffolds with multi-functionally graded pores was not as significant as that of the unit cell gradient bone scaffold.

3.2 Comparison in mass transport capacity between functionally graded Schwarz P bone scaffolds

Comparisons in the mass transport capacity between two functionally graded bone scaffolds were conducted. Jiang et al. (2024) investigated the significantly higher mass transport capacity of unit cell gradient bone scaffolds compared to uniform bone scaffolds. Accordingly, the mass transport capacity of two functionally graded bone scaffolds was only compared in the study. A cross-section through the center of the multi-functional pore was chosen to represent the pressure drop in the bone scaffold structure, as shown in Figure 8. For each porosity, the pressure drop of the graded multi-functional pore bone scaffold was smaller than that of the unit cell gradient bone scaffold, and the reduction in pressure drop is favorable to the enhancement in permeability. Therefore, better mass transport capacity was achieved by adding the graded multi-functional pores. Additionally, from the fluid flow domain analysis, it can be seen that the fluid flow domain of both gradient bone scaffolds gradually increased along the gradient direction. This was because the porosity was gradually increasing from the top to the bottom of the gradient bone scaffold, and the corresponding fluid flow domain was getting bigger, which may be favorable for mass transport.

The flow region of the unit cell graded bone scaffolds was still independent on each other, despite the increase in the size of the region. In contrast, the flow region in the bone scaffolds with multi-

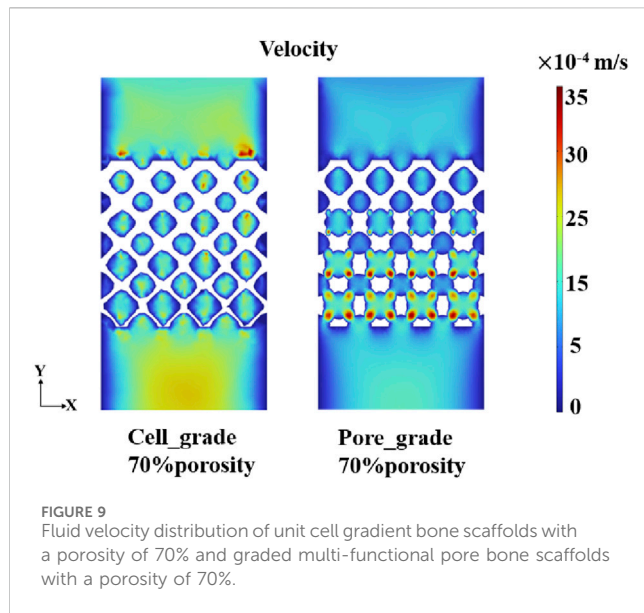


FIGURE 9
Fluid velocity distribution of unit cell gradient bone scaffolds with a porosity of 70% and graded multi-functional pore bone scaffolds with a porosity of 70%.

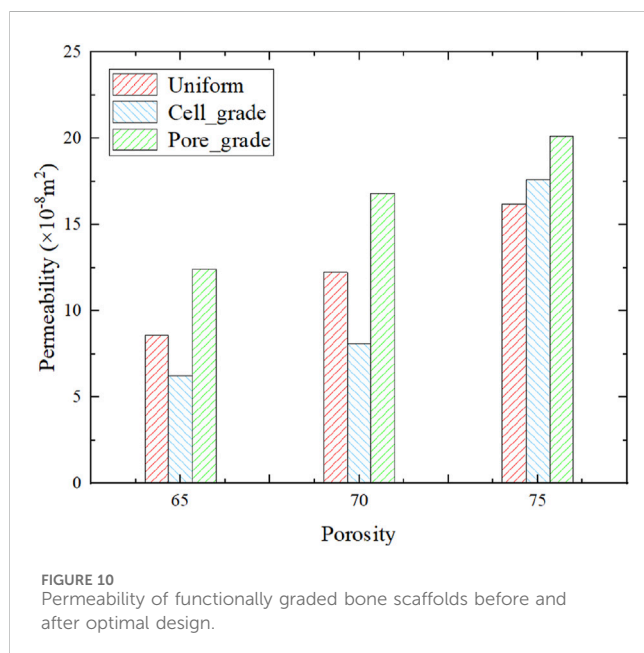


FIGURE 10
Permeability of functionally graded bone scaffolds before and after optimal design.

functionally graded pores not only increased gradually but also achieved full connectivity near the bottom. The mass transport capacity can be greatly improved, due to the superiority of multi-functional pores. At a porosity of 70%, unit cell gradient bone scaffolds and bone scaffolds with multi-functionally graded pores were selected and analyzed for the velocity of fluid flow, as shown in Figure 9. It can be seen that the flow velocity in the bone scaffolds with multi-functionally graded pores increased with an increase in the fluid flow region, and the effect of flow velocity increase became more obvious as the flow region gradually connected.

After obtaining the pressure drop of the bone scaffolds, the permeability can be calculated from Equation 11, as shown in Figure 10. The bone scaffolds with multi-functionally graded pores had the highest permeability at each porosity. The

permeability of each bone scaffolds increased with the increase in porosity.

4 Discussion

Currently, bone scaffolds based on TPMS structures are widely used because their properties are closest to those of human bones. However, the performance of the TPMS bone scaffolds, such as elastic modulus, anisotropy, and permeability still cannot fully meet the needs of human bones. To address the problems, a novel bone scaffold with multi-functionally graded pores was proposed based on the TPMS structure. The performance of the designed bone scaffold was characterized and analyzed by numerical calculation methods. Some interesting findings were revealed in this study.

First, the elastic modulus of the novel bone scaffold was significantly lower, which can mitigate the effect of stress shielding. The optimized bone scaffolds with multi-functionally graded pores have a smaller difference on the effective compressive modulus and the effective shear modulus in different directions at three different porosities, namely, 65%, 70%, and 75%, which can meet the needs of some specific bone implants. The elastic modulus of the novel scaffold designed in the present study is closer to that of human bones, compared to the traditional scaffolds. It is reported in the literature that the elastic modulus of human cortex bones is approximately from 1.08 to 3.47 GPa (Sevilla et al., 2007; Wu et al., 2018), the elastic modulus of traditional scaffolds is approximately from 5.01 to 6.58 GPa (Khaleghi et al., 2021; Jiang et al., 2024; Li et al., 2024), and the elastic modulus of the scaffold in this study can reach approximately 4.61 GPa. Therefore, it is believed the optimized scaffold could better reduce the stress shielding, compared to traditional scaffolds, but this requires further direct investigation in the future. Moreover, the gradient transition structure of the novel bone scaffold was similar to the gradient transition structure of human natural bone, i.e., geometrically similar to human bone.

Second, the differences between the highest and lowest moduli of elasticity for bone scaffolds with multi-functionally graded pores at porosities of 65%, 70%, and 75% were relatively small, whereas the differences were relatively large for bone scaffolds with unit cell gradients. This also confirms that the elastic modulus of the bone scaffolds with multi-functionally graded pores matches better with that of human bone.

Third, the mass transport capacity of designed bone scaffolds with multi-functionally graded pores was higher than that of unit cell gradient bone scaffold and uniform bone scaffold, which can be beneficial for nutrient transport and cell growth. It should be noted that the permeability of the bone scaffold may also be anisotropic due to the gradient variation in the Y direction. However, the anisotropic analysis of permeability is not the focus of the study. The permeability of bone scaffolds was analyzed along the gradient transition direction to obtain the fluid flow velocity and structural permeability. The permeability of designed bone scaffolds with multi-functionally graded pores was higher than that of the unit cell gradient bone scaffolds, which may be greater mass transport capability.

Some limitations in the present work should be noted. First, the experimental test of the novel bone scaffold was not performed. The experimental part has been demonstrated by the uniform bone

scaffolds and the unit cell gradient bone scaffolds (Peng et al., 2023). Therefore, it can be assumed that the results in this study were reliable. Additionally, it should be noted that the calculations were performed using linear-elastic material settings, without considering the plastic phase. This aspect will be addressed in future research by defining a complete material constitutive model for more accurate calculations, and the compressive and tensile strength could be evaluated afterward. Second, the mass transfer capability was investigated only in one direction as the direction of the gradient transition is a very important point to focus on. Third, the fluid used in the mass transport simulations was simplified to Newtonian water. It is acknowledged that the assumption of using Newtonian water in these simulations oversimplifies the rheological behavior of bone tissue fluids (e.g., blood and bone marrow). We thus incorporate a non-Newtonian fluid model in future work for a more accurate assessment (Wang et al., 2022). Nevertheless, the use of water as the fluid is considered reliable for studies focusing on the overall feasibility of mass transport. Last but not the least, cell and animal experiments have not been conducted either. This will be studied in depth in the future in order to further realize clinical applications.

5 Conclusion

In this study, a novel functionally graded TPMS bone scaffold was designed by introducing multi-functional pores as a novel geometric variable into traditional bone scaffolds. The performance of the novel new bone scaffolds was evaluated and compared to those of uniform and unit cell graded scaffolds. The main findings are as follows:

- 1) Compared to the commonly used unit cell graded bone scaffolds, the effective compression modulus and effective shear modulus of the bone scaffolds with multi-functionally graded pores are significantly lower, which contributes to the reduction in the stress-shielding effect.
- 2) Compared to the traditionally cell graded bone scaffolds, the elastic modulus of the bone scaffolds with multi-functionally graded pores was more spatially and uniformly distributed, with smaller differences in the values of the elastic modulus in different directions, which aligns more closely with the goal of mimicking the mechanical behavior of natural bone.
- 3) The designed bone scaffolds with multi-functionally graded pores have a higher permeability compared to the unit cell graded bone scaffolds and uniform bone scaffolds, suggesting greater mass transport capabilities.

This study focuses on designing a novel Schwarz P structure with multi-functional pores by using a unit cell optimization method. These pores were used to create graded bone scaffolds with functional gradients and mechanical anisotropy, suitable for implantation in areas like the femur and vertebrae. The results demonstrate that, compared to the widely used bone scaffolds, the bone scaffolds with multi-functionally graded pores exhibit lower directional variation in effective modulus and possess higher mass transport capabilities. The smaller directional difference in effective modulus results in lower stress shielding, whereas the enhanced mass transport capacity promotes

nutrient transport and supports cell growth. The novel graded multi-functional pore scaffolds successfully met the mechanical anisotropy and mass transport requirements needed for bone scaffolds with excellent performance. The novel TPMS bone scaffold offers two key advantages: 1) its gradient porosity transition structure closely resembles the natural gradient structure found in human bone, providing a geometric similarity that is beneficial for bone integration, and 2) the equivalent compressive modulus and shear modulus exhibit minimal directional variation, which results in a more isotropic mechanical performance. This feature is particularly important for implantation in load-bearing regions such as the vertebrae, where mechanical homogeneity is essential to ensure proper function and support. In the end, this design approach expands the design space of functional gradient TPMS bone scaffolds and provides a theoretical basis for the development of high-performance bone scaffolds.

Data availability statement

The raw data supporting the conclusions of this article will be made available by the authors, without undue reservation.

Author contributions

RL: methodology, software, and writing—original draft. JJ: funding acquisition, investigation, and writing—review and editing. YH: methodology and writing—original draft. HW: supervision and writing—review and editing. SB: writing—review and editing and supervision. YL: writing—review and editing, conceptualization, formal analysis, and methodology. LL: writing—review and editing and investigation.

Funding

The author(s) declare that financial support was received for the research, authorship, and/or publication of this article. This study is funded by the National Key R&D Program of China(2024YFE0213500), the National Natural Science Foundation of China (12072066; 12211530062), the Dalian University of Technology and Affiliated Central Hospital joint research fund (2022ZZXYG45, DUT23YG217), and the DUT-BSU Joint Institute Fund (ICR2303).

Conflict of interest

The authors declare that the research was conducted in the absence of any commercial or financial relationships that could be construed as a potential conflict of interest.

Generative AI statement

The author(s) declare that no Generative AI was used in the creation of this manuscript.

Publisher's note

All claims expressed in this article are solely those of the authors and do not necessarily represent those of their affiliated

References

- Ali, D., Ozalp, M., Blanquer, S. B. G., and Onel, S. (2020). Permeability and fluid flow-induced wall shear stress in bone scaffolds with TPMS and lattice architectures: a CFD analysis. *Eur. J. Mechanics-B/Fluids* 79, 376–385. doi:10.1016/j.euromechflu.2019.09.015
- Barba, D., Alabort, E., and Reed, R. (2019). Synthetic bone: design by additive manufacturing. *Acta Biomater.* 97, 637–656. doi:10.1016/j.actbio.2019.07.049
- Blanquer, S. B. G., Werner, M., Hannula, M., Sharifi, S., Lajoinie, G. P. R., Eglon, D., et al. (2017). Surface curvature in triply-periodic minimal surface architectures as a distinct design parameter in preparing advanced tissue engineering scaffolds. *Biofabrication* 9 (2), 025001. doi:10.1088/1758-5090/aa6553
- Campana, V., Milano, G., Pagano, E., Barba, M., Cicione, C., Salonna, G., et al. (2014). Bone substitutes in orthopaedic surgery: from basic science to clinical practice. *J. Mater. Sci. Mater. Med.* 25, 2445–2461. doi:10.1007/s10856-014-5240-2
- Chen, Z., Xie, Y. M., Wu, X., Wang, Z., Li, Q., and Zhou, S. (2019). On hybrid cellular materials based on triply periodic minimal surfaces with extreme mechanical properties. *Mater. and Des.* 183, 108109. doi:10.1016/j.matdes.2019.108109
- Davoodi, E., Montazerian, H., Khademhosseini, A., and Toyserkani, E. (2020). Sacrificial 3D printing of shrinkable silicone elastomers for enhanced feature resolution in flexible tissue scaffolds. *Acta Biomater.* 117, 261–272. doi:10.1016/j.actbio.2020.10.001
- Feng, J., Liu, B., Lin, Z., and Fu, J. (2021). Isotropic porous structure design methods based on triply periodic minimal surfaces. *Mater. and Des.* 210, 110050. doi:10.1016/j.matdes.2021.110050
- Fernandez de Grado, G., Keller, L., Idoux-Gillet, Y., Wagner, Q., Musset, A. M., Benkirane-Jessel, N., et al. (2018). Bone substitutes: a review of their characteristics, clinical use, and perspectives for large bone defects management. *J. tissue Eng.* 9, 2041731418776819. doi:10.1177/2041731418776819
- Gere, J. M., and Goodno, B. J. (2009). *Mechanics of materials*. Independence, KY, USA: Cengage learning, Inc.
- Guo, W., Yang, Y., Liu, C., Bu, W., Guo, F., Li, J., et al. (2023). 3D printed TPMS structural PLA/GO scaffold: process parameter optimization, porous structure, mechanical and biological properties. *J. Mech. Behav. Biomed. Mater.* 142, 105848. doi:10.1016/j.jmbbm.2023.105848
- Hollister, S. J., and Kikuchi, N. (1994). Homogenization theory and digital imaging: a basis for studying the mechanics and design principles of bone tissue. *Biotechnol. Bioeng.* 43 (7), 586–596. doi:10.1002/bit.260430708
- Jiang, J., Huo, Y., Peng, X., Wu, C., Zhu, H., and Lyu, Y. (2024). Design of novel triply periodic minimal surface (TPMS) bone scaffold with multi-functional pores: lower stress shielding and higher mass transport capacity. *Front. Bioeng. Biotechnol.* 12, 1401899. doi:10.3389/fbioe.2024.1401899
- Karuna, C., Poltue, T., Khruaduangkham, S., and Promoppatum, P. (2022). Mechanical and fluid characteristics of triply periodic minimal surface bone scaffolds under various functionally graded strategies. *J. Comput. Des. Eng.* 9 (4), 1258–1278. doi:10.1093/jcde/qwac052
- Khaleghi, S., Dehnavi, F., Baghani, M., Safdari, M., Wang, K., and Baniassadi, M. (2021). On the directional elastic modulus of the TPMS structures and a novel hybridization method to control anisotropy. *Mater. Des.* 210, 110074. doi:10.1016/j.matdes.2021.110074
- Kurtz, S., Ong, K., Lau, E., Mowat, F., and Halpern, M. (2007). Projections of primary and revision hip and knee arthroplasty in the United States from 2005 to 2030. *Jbjs* 89 (4), 780–785. doi:10.2106/JBJS.F.00222
- Lee, D. W., Khan, K. A., and Al-Rub, R. K. A. (2017). Stiffness and yield strength of architected foams based on the Schwarz Primitive triply periodic minimal surface. *Int. J. Plasticity* 95, 1–20. doi:10.1016/j.iplas.2017.03.005
- Li, K., Liao, R., Zheng, Q., Zuo, C., Yin, B., Ji, C., et al. (2024). Design exploration of staggered hybrid minimal surface magnesium alloy bone scaffolds. *Int. J. Mech. Sci.* 281, 109566. doi:10.1016/j.ijmecsci.2024.109566
- Li, Y., Xia, Q., Yoon, S., Lee, C., Lu, B., and Kim, J. (2021). Simple and efficient volume merging method for triply periodic minimal structures. *Comput. Phys. Commun.* 264, 107956. doi:10.1016/j.cpc.2021.107956
- Li, Y., Zhou, J., Pavanram, P., Leeflang, M., Fockaert, L., Pouran, B., et al. (2018). Additively manufactured biodegradable porous magnesium. *Acta biomater.* 67, 378–392. doi:10.1016/j.actbio.2017.12.008
- Lu, Y., Cheng, L. L., Yang, Z., Li, J., and Zhu, H. (2020). Relationship between the morphological, mechanical and permeability properties of porous bone scaffolds and the underlying microstructure. *PloS one* 15 (9), e0238471. doi:10.1371/journal.pone.0238471
- Lu, Y., Zhao, W., Cui, Z., Zhu, H., and Wu, C. (2019). The anisotropic elastic behavior of the widely-used triply-periodic minimal surface based scaffolds. *J. Mech. Behav. Biomed. Mater.* 99, 56–65. doi:10.1016/j.jmbbm.2019.07.012
- Ma, Q., Zhang, L., Ding, J., Qu, S., Fu, J., Zhou, M., et al. (2021). Elastically-isotropic open-cell minimal surface shell lattices with superior stiffness via variable thickness design. *Addit. Manuf.* 47, 102293. doi:10.1016/j.addma.2021.102293
- Montazerian, H., Davoodi, E., Asadi-Eydivand, M., Kadkhodapour, J., and Solati-Hashjin, M. (2017). Porous scaffold internal architecture design based on minimal surfaces: a compromise between permeability and elastic properties. *Mater. and Des.* 126, 98–114. doi:10.1016/j.matdes.2017.04.009
- Peng, X., Huo, Y., Zhang, G., Cheng, L., Lu, Y., Li, J., et al. (2023). Controlled mechanical and mass-transport properties of porous scaffolds through hollow strut. *Int. J. Mech. Sci.* 248, 108202. doi:10.1016/j.ijmecsci.2023.108202
- Rabiatul, A., Fatihhi, S., Md, S., Zakaria, A., and Harun, M. N. (2021). Fluid-structure interaction (FSI) modeling of bone marrow through cancellous bone structure under compression. *Biomechanics Model. Mechanobiol.* 20, 957–968. doi:10.1007/s10237-021-01423-x
- Santos, J., Pires, T., Gouveia, B., Castro, A. P., and Fernandes, P. R. (2020). On the permeability of TPMS scaffolds. *J. Mech. Behav. Biomed. Mater.* 110, 103932. doi:10.1016/j.jmbbm.2020.103932
- Sevilla, P., Aparicio, C., Planell, J. A., and Gil, F. (2007). Comparison of the mechanical properties between tantalum and nickel-titanium foams implant materials for bone ingrowth applications. *J. Alloys Compd.* 439 (1–2), 67–73. doi:10.1016/j.jallcom.2006.08.069
- Strömberg, N. (2021). Optimal grading of TPMS-based lattice structures with transversely isotropic elastic bulk properties. *Eng. Optim.* 53 (11), 1871–1883. doi:10.1080/0305215X.2020.1837790
- Vijayavenkataraman, S., Kuan, L., and Lu, W. (2020). 3D-printed ceramic triply periodic minimal surface structures for design of functionally graded bone implants. *Mater. Des.* 191, 108602. doi:10.1016/j.matdes.2020.108602
- Wallace, I., Worthington, S., Felson, D., Jurmain, R. D., Wren, K. T., Maijanen, H., et al. (2017). Knee osteoarthritis has doubled in prevalence since the mid-20th century. *Proc. Natl. Acad. Sci.* 114 (35), 9332–9336. doi:10.1073/pnas.1703856114
- Wang, L., Wang, J., Chen, Q., Li, Q., Mendieta, J. B., and Li, Z. (2022). How getting twisted in scaffold design can promote bone regeneration: a fluid-structure interaction evaluation. *J. Biomechanics* 145, 111359. doi:10.1016/j.jbiomech.2022.111359
- Wu, D., Isaksson, P., Ferguson, S. J., and Persson, C. (2018). Young's modulus of trabecular bone at the tissue level: a review. *Acta Biomater.* 78, 1–12. doi:10.1016/j.actbio.2018.08.001
- Yoo, D. J. (2011). Computer-aided porous scaffold design for tissue engineering using triply periodic minimal surfaces. *Int. J. Precis. Eng. Manuf.* 12, 61–71. doi:10.1007/s12541-011-0008-9
- Zhang, L., Song, B., Yang, L., and Shi, Y. (2020). Tailored mechanical response and mass transport characteristic of selective laser melted porous metallic biomaterials for bone scaffolds. *Acta Biomater.* 112, 298–315. doi:10.1016/j.actbio.2020.05.038



OPEN ACCESS

EDITED BY

Zhen Luo,
University of Technology Sydney, Australia

REVIEWED BY

Rui B. Ruben,
Polytechnic Institute of Leiria, Portugal
Cristian Indino,
Humanitas San Pio X Hospital, Italy

*CORRESPONDENCE

Xin Ma,
✉ maxin@sjtu.edu.cn
Dahang Zhao,
✉ dahang@vip.126.com

†These authors have contributed equally to this work

RECEIVED 01 October 2024

ACCEPTED 20 January 2025

PUBLISHED 27 February 2025

CITATION

Yu J, Li C, Lyu J, Cao S, Zhang C, Ma X and Zhao D (2025) Statistical shape modeling of shape variability of the human distal tibia: implication for implant design of the tibial component for total ankle replacement. *Front. Bioeng. Biotechnol.* 13:1504897. doi: 10.3389/fbioe.2025.1504897

COPYRIGHT

© 2025 Yu, Li, Lyu, Cao, Zhang, Ma and Zhao. This is an open-access article distributed under the terms of the [Creative Commons Attribution License \(CC BY\)](https://creativecommons.org/licenses/by/4.0/). The use, distribution or reproduction in other forums is permitted, provided the original author(s) and the copyright owner(s) are credited and that the original publication in this journal is cited, in accordance with accepted academic practice. No use, distribution or reproduction is permitted which does not comply with these terms.

Statistical shape modeling of shape variability of the human distal tibia: implication for implant design of the tibial component for total ankle replacement

Jian Yu^{1†}, Chengke Li^{2†}, Jinyang Lyu^{3†}, Shengxuan Cao³,
Chao Zhang³, Xin Ma^{1,3*} and Dahang Zhao^{4*}

¹Department of Orthopedics, Shanghai Sixth People's Hospital Affiliated to Shanghai Jiao Tong University School of Medicine, Shanghai, China, ²Department of Hand and Foot Microsurgery, Shunde Hospital Affiliated to Jinan University, Foshan, Guangdong, China, ³Department of Orthopedics, Huashan Hospital, Fudan University, Shanghai, China, ⁴Department of Orthopedics, Ruijin Hospital Affiliated to Shanghai Jiao Tong University School of Medicine, Shanghai, China

Introduction: Understanding the morphological variability of the distal tibia can help design tibial components of total ankle implants. This study aimed to assess the shape variability of the distal tibial bone, utilizing the statistical shape modeling (SSM) technique.

Methods: A total of 229 tibial bones were analyzed through CT scans to develop SSM models. Principal component analysis (PCA) was employed to characterize shape variation across the male, female, and overall groups. The geometric parameters of the resected surfaces at the 10-mm level above the distal tibial articular surface were compared.

Results: The first seven principal component analysis (PCA) modes accounted for approximately 24.9%–40% of the shape variation, totaling 71.5%–75.6%. Considerable variabilities were observed among these three groups and all principal modes of variation. Notably, the male tibia had a bigger medial malleolus, anterior part of the fibular notch, and posterior malleolus. In the 10-mm resection surface of the distal tibia, anterior–posterior and medial–lateral distances were the main sources of variation. In addition, variations were frequently detected at both the anterior and posterior corners of the fibular notch in the resection surface of the distal tibia.

Conclusion: The SSM technique has been shown to be an effective method in finding mean shape and principal variability. Size plays a crucial role in both inter- and intra-groups, and morphological differences vary across different sizes. Therefore, these considerations should be taken into account while designing tibial components for total ankle implants.

KEYWORDS

distal tibial morphology, human anatomy, statistical shape modeling, total ankle replacement, implant design

Introduction

Total ankle arthroplasty (TAA) is an effective procedure to treat end-stage ankle arthritis (Raikin et al., 2014). The implant survival rate for TAA is improving (Gougoulas et al., 2010; Daniels et al., 2014), yet it is not comparable to that of total knee or hip arthroplasty (Lee et al., 2018; Clough et al., 2019; Mäkelä et al., 2014; Victor et al., 2014). During TAA, the damaged distal tibia was replaced by a metallic artificial implant. Novel tibial components of total ankle implants, considering maximum distal tibial coverage (Gross et al., 2018), require detailed measurements of the anatomy of distal tibia and its resection surface. In addition, understanding the three-dimensional (3D) shape variability of the distal tibia can help identify the shape morphological similarities and differences in patients with pathological changes in the tibia, such as the tibial fracture, anterior impingement, and osteochondral lesions of the distal tibia (Mitchell et al., 2019; Blom et al., 2019).

However, the shape of the distal tibia is complex and not fully understood, with size and gender differences (Claassen et al., 2019; Ataoğlu et al., 2020). Current clinical evaluation methods of the measurement of the bone rely on plain radiographic images or images from computed tomography (CT) or magnetic resonance imaging (MRI). After the selection of feature points on the anatomic landmark of the images, distances, angles, or areas can be measured to describe the bone anatomy (Yu et al., 2022; Nguyen et al., 2020; Kuo et al., 2016). However, only a limited amount of image information is utilized, and selection bias might exist when choosing feature points. Statistical shape modeling (SSM) serves as a robust analytical tool for analyzing anatomical data by constructing a mean shape and several variations from a collection of medical images (Heimann and Meinzer, 2009; Lenz et al., 2021). Although several studies (Bredbenner et al., 2010; Audenaert et al., 2019; Peiffer et al., 2022; Nelson et al., 2017; Gabrielli et al., 2020) focused on the tibia or ankle joint, which included morphological studies of the distal tibia, to the best of our knowledge, we found no articles specifically studying the SSM of distal tibia and reporting the shape change at the distal tibial resection surface.

In this study, we aimed to qualitatively evaluate the shape variability of the distal tibial bone using the SSM method. Male and female tibiae were registered separately and used to generate two separate SSMs, thereby producing two sex-specific mean tibia shapes that were then analyzed for gender differences between SSM models. The resection surfaces in the distal tibia for total ankle replacement were compared among different shape modes.

Materials and methods

With the Institutional Review Board approval, the computed tomography (CT) scan data on 123 healthy Chinese participants (59 females and 64 males, 106 participants contributed both ankles; 23.78 ± 3.19 years of age, 168.52 ± 7.70 cm of height, and 63.08 ± 13.42 kg of body weight; body mass index: 22.06 ± 3.50) from previous studies were used (Yu et al., 2023; Wang et al., 2023). Two orthopedic surgeons independently evaluated all CT images (scanned by Brilliance iCT, Philips, Cleveland, U.S. with 120 kV of voltage, 250 mA of current, 0.67 mm of slice thickness,

and 512×512 pixels of matrix) (Yu et al., 2022) to exclude previous trauma, severe deformity, or degenerative changes in the ankle, such as ankle arthritis and osteochondral lesions of the distal tibia.

3D reconstruction

A total of 229 3D models of tibia were reconstructed in Mimics (Materialise NV, Belgium) from the Digital Imaging and Communications in Medicine (DICOM) file of CT images. All right tibiae were mirrored and grouped together with the left tibia in 3-matic Medical (Materialise NV, Belgium). A parallel cut was made at 25 mm above the distal tibial articular surface of each tibial bone to create the distal tibia (Hvid et al., 1985). A sensitivity analysis of the selection on the articular surface of the distal tibia for plane fitting on one of the subjects was performed (See Supplementary Figure S1; Supplementary Table S1 of the supplementary document).

Statistical shape modeling

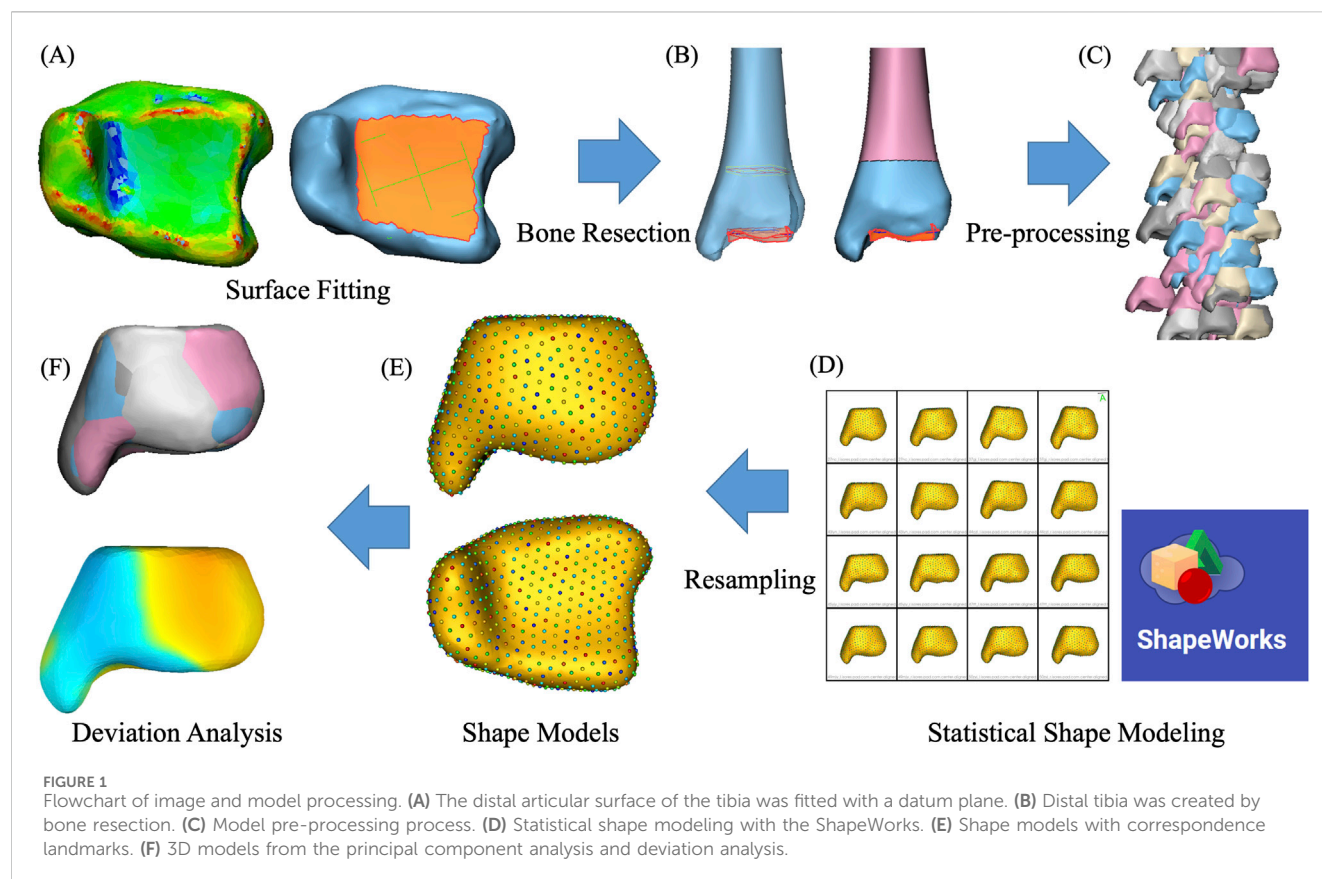
An open-source SSM (ShapeWorks, University of Utah, Salt Lake City, UT, United States) was used for the statistical shape modeling of the distal tibia (Cates et al., 2017). Each tibia was first aligned to a randomly chosen “master” tibia using the iterative closest point method. Then, surface meshes were converted to volumetric datasets in the form of distance transforms. ShapeWorks software used 1,024 anatomical landmarks to represent each distal tibia, and the correspondence landmark locations of all tibiae can be analyzed for mean shapes and shape variations.

Analysis

Principal component analysis (PCA) can reduce high-dimensional SSM correspondence data and yield non-zero eigenvalues that characterize the amount of variance. Each uncorrelated dimension of variation was defined as “modes” based on the order of the eigenvalues. For each significant mode of tibia, the mean and ± 3 standard deviations (SD) of the surface model were exported in Geomagic Studio 2013 (Geomagic, Morrisville, North Carolina, United States). Deviation analysis was performed to visualize anatomical differences within a mode of variation, in which the mean tibial bone was used as the reference model, while the ± 3 SD tibia was used as a target model. The SSM process is presented in Figure 1.

Post-processing

The recommended tibial bone resection level for total ankle replacement ranges from 5 mm to 11 mm among different implant systems (Yu et al., 2020). To maintain consistency and create a resection surface for total ankle replacement, the tibial bone was resected at 10-mm level superior to tibial plafond with the protection



of medial malleolus under the guidance of senior foot and ankle surgeons (Yu et al., 2022).

At the 10-mm resection surface, the medial anterior–posterior (M-AP) dimension was taken as the medial largest anteroposterior length. The lateral anterior–posterior (L-AP) dimension was taken as the length of the line drawn parallel to the M-AP and passing through the medial-most point in the fibula notch of the distal tibia. The C-AP is the anterior–posterior distance of the surface along the middle line of M-AP and L-AP. Perpendicular to M-AP, anterior medial–lateral (A-ML) and posterior medial–lateral (P-ML) dimensions were taken as the anterior and posterior longest mediolateral lengths of the resected distal tibial surface, respectively, while C-ML represented the shortest mediolateral length of the resected distal tibial surface (Figure 2C). These geometric parameters of the 10-mm resection surface of the distal tibia were compared for each mode of variation.

Results

Tibial shape variation for the overall, male, and female groups

Seven PCA components for the overall tibiae represented 40.0%, 11.2%, 7.1%, 5.9%, 4.6%, 3.8%, and 3.1% of the overall variation, respectively, which contributed to a cumulative total of 75.6% of the overall shape variation. For the female group, the first seven modes accounted for 26.5%, 14.5%, 10.9%, 6.8%, 5.4%, 4.8%, and 4.1% of the overall tibial variation, respectively, collectively representing

73.0% of the female shape variation. For male groups, the first seven modes represented 25.9%, 13.7%, 8.8%, 7.4%, 7.0%, 5.2%, and 3.6% of the overall tibial variation, respectively, representing 71.5% of the male shape variation in total (see Figures 3).

Deviation analyses of the shape variations (± 3 SD) with respect to their mean shapes are presented in Figures 4–6 and Supplementary Table S2 of the supplementary document.

In the overall group, the first mode of variation showed a remarkable variation in the tibia from inner–outer and top–bottom directions changing from a short and thick shape to a long and thin shape. Differences in the second mode of variation included a variation in the tibia at the anterior–posterior and medial–lateral dimensions. The third mode of variation showed a variation in the tibia from anterior–lateral to posterior–medial directions. The fourth mode of variation exhibited a variation in the tibia from anterior–bottom to posterior–top directions. The fifth mode of variation described a variation in anterior–posterior lengths between a wider medial side and narrow lateral side to the opposite with the associated thickening of the medial malleolus. The sixth mode of variation was a combination of a variation in the anterior–posterior and up–down directions. The seventh mode of variation includes small changes at the tip of the medial malleolus, the anterior lateral, and posterior edge of the tibia.

The seven modes of variation in both the female and male groups shared the same trend with the overall group. Small differences were presented in the fourth, fifth, and sixth modes of variation between the female and overall groups. The fourth mode of variation in the female group exhibited a variation in

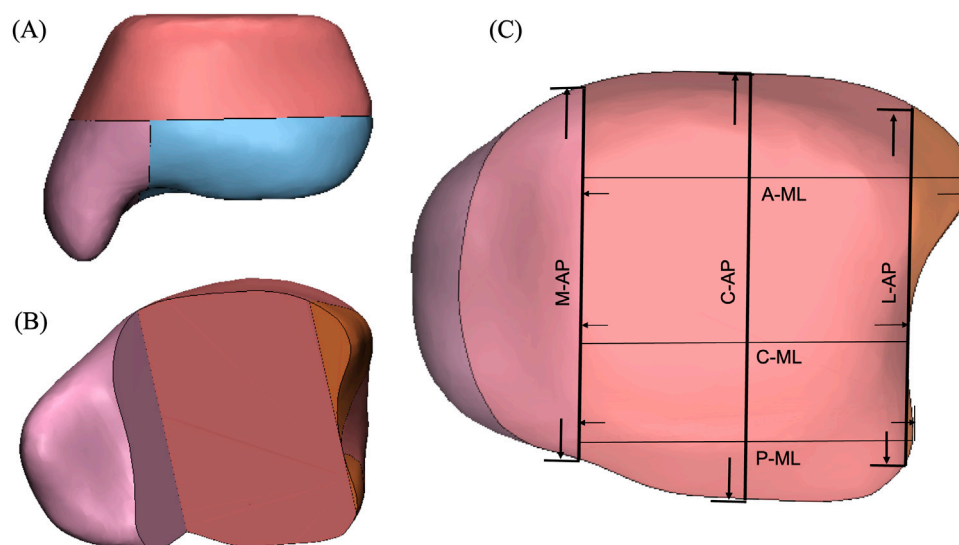


FIGURE 2

Schematic representation of the distal tibial resected surface showing the measurement methods used in the CT analysis. (A) Distal tibial cut was made at 10-mm level superior to tibial plafond with the protection of the medial malleolus. (B) Perspective view of the distal tibia after the removal of the 10-mm bone fragment of the distal tibia. (C) Two-dimensional illustration of the geometric parameters of the 10-mm resection surface of the distal tibia. M-AP, C-AP, and L-AP represented the anterior–posterior distances, while A-ML, C-ML, and P-ML represented the medial–lateral distances.

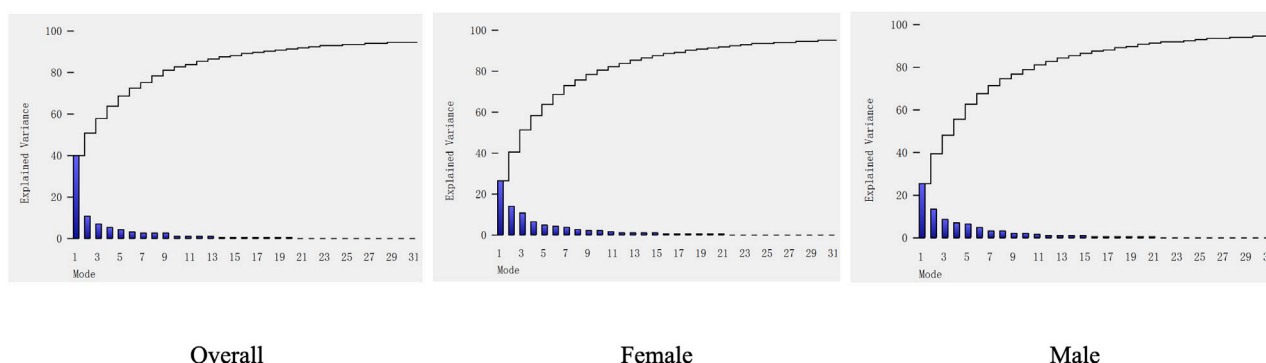


FIGURE 3

Cumulative shape variation in significant PCA modes of the overall, male, and female groups. PCA modes are ordered based on the associated variance (bar), which determined the cumulative shape variation (curve).

the tibia from posterior–medial to anterior–lateral directions. The fifth mode of variation described a variation at the anterior lateral and posterior edges of the tibia. The sixth mode of variation showed small changes at the anterior and posterior edges of the medial malleolus. Differences between the male and overall groups were noticed in the fourth modes of variation, where the male group displayed a combination of a variation in up–down directions and around the upper and bottom edges.

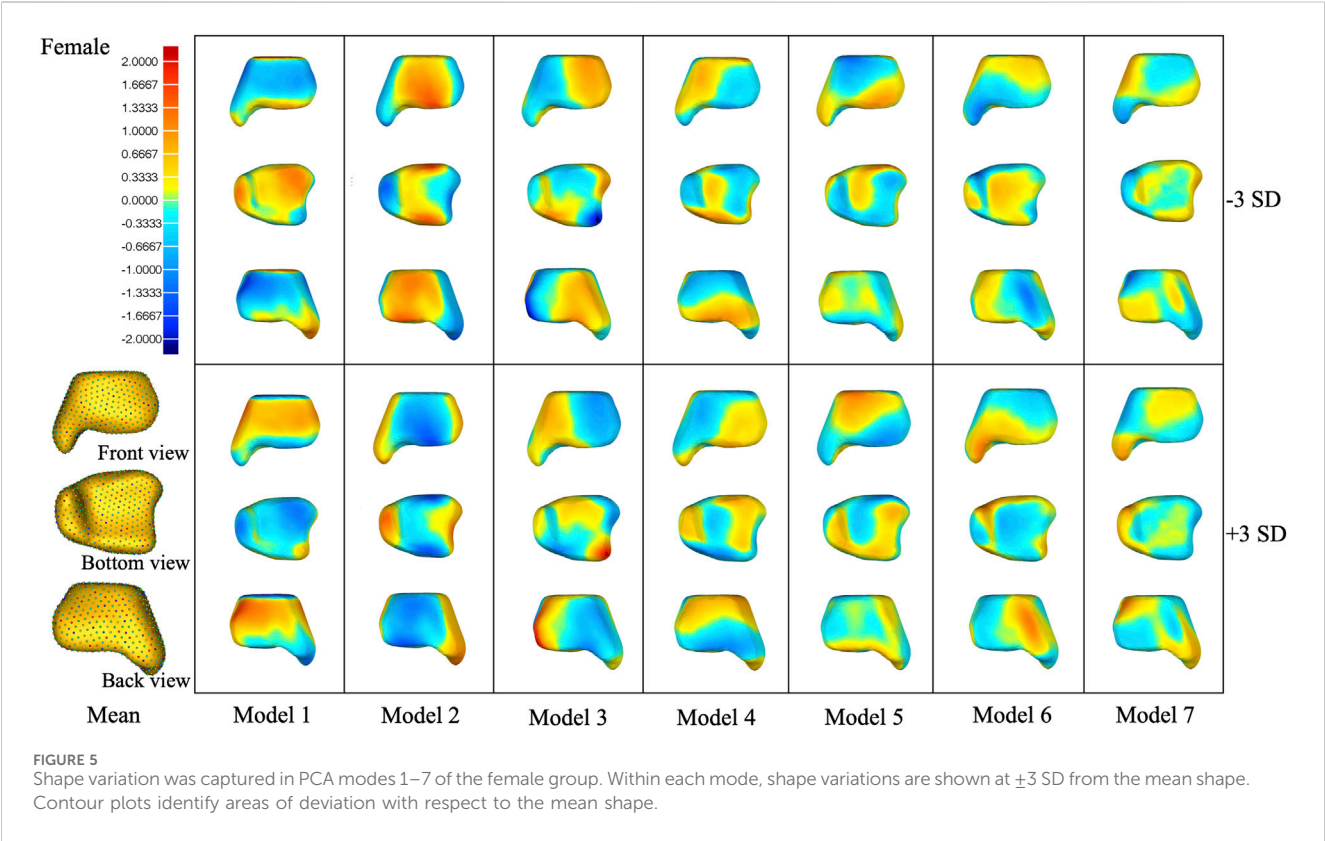
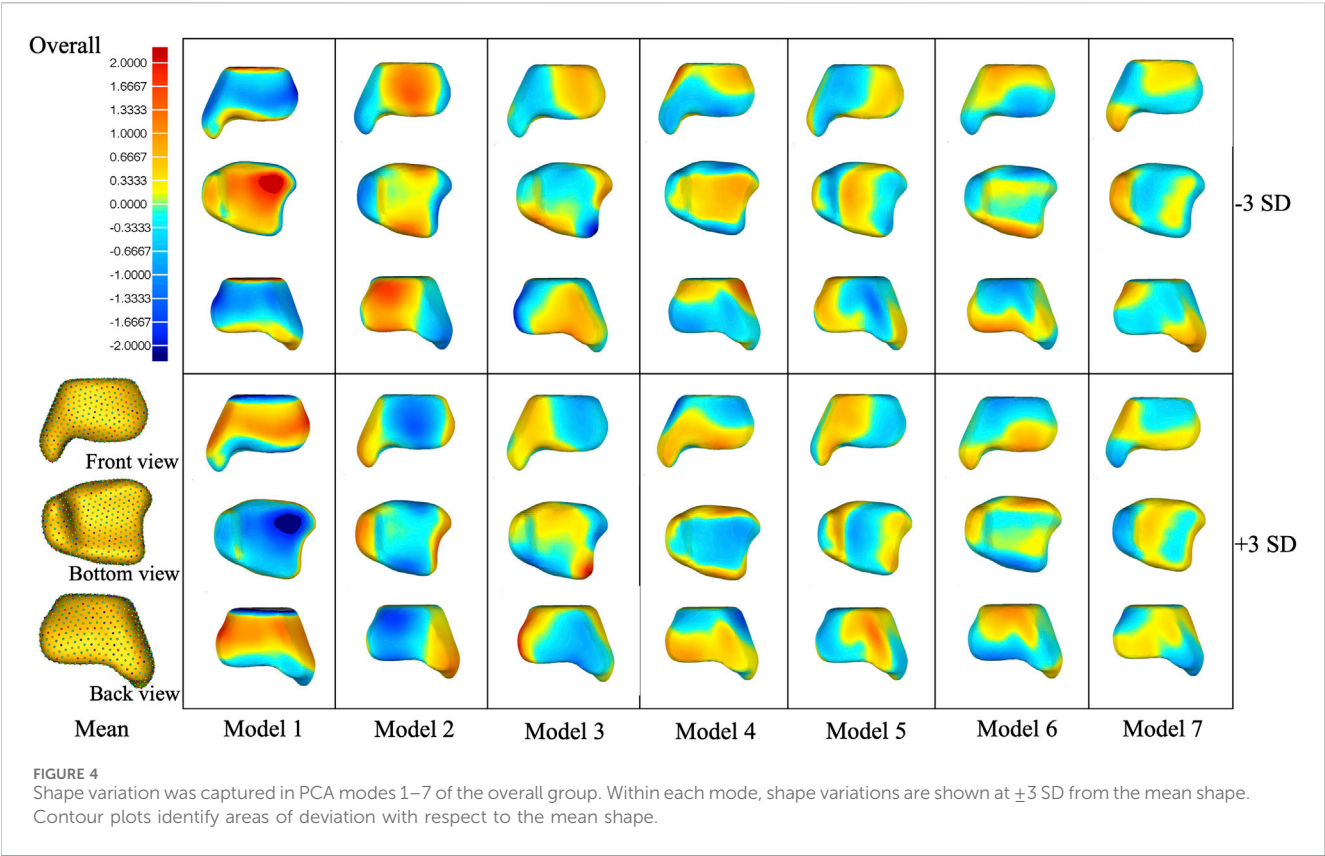
Gender differences between mean models

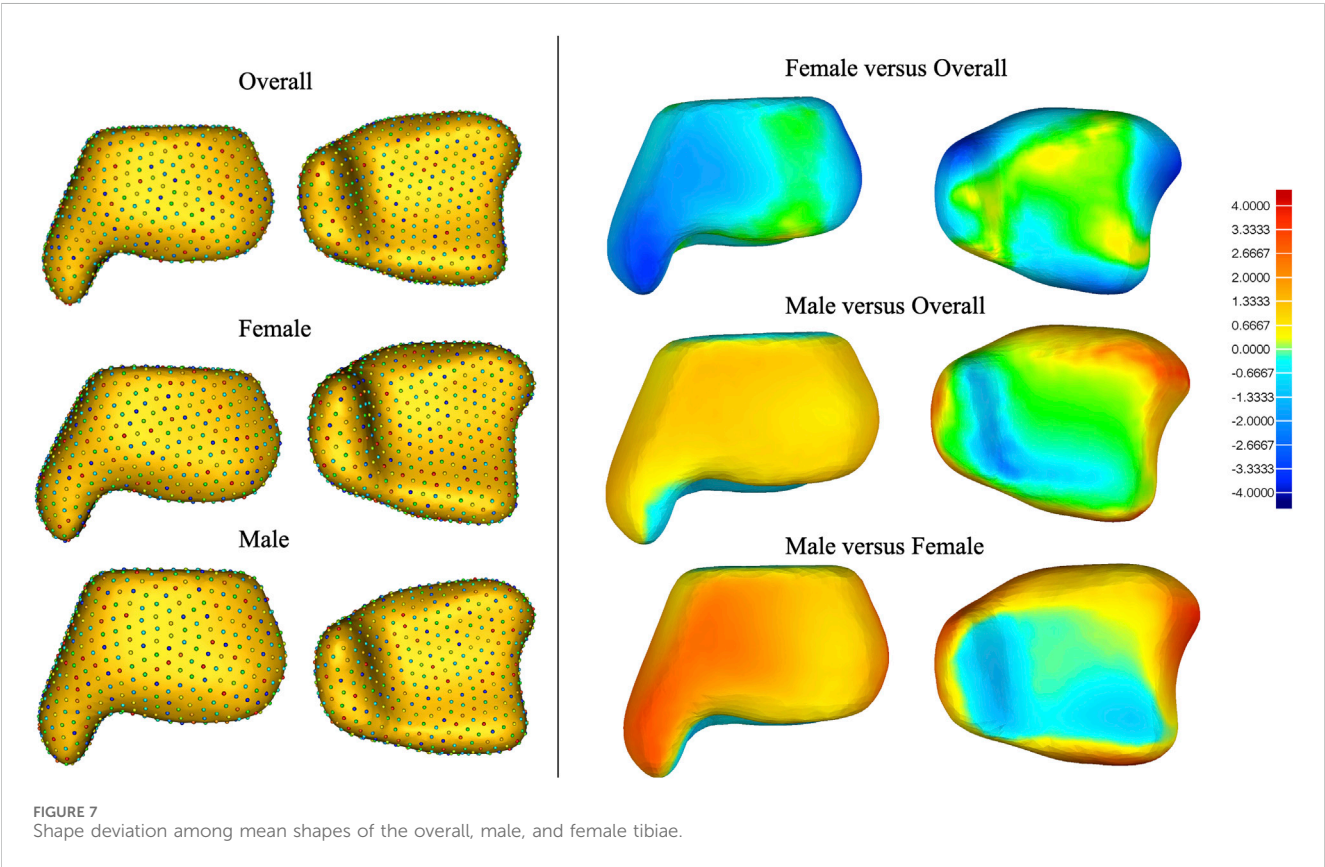
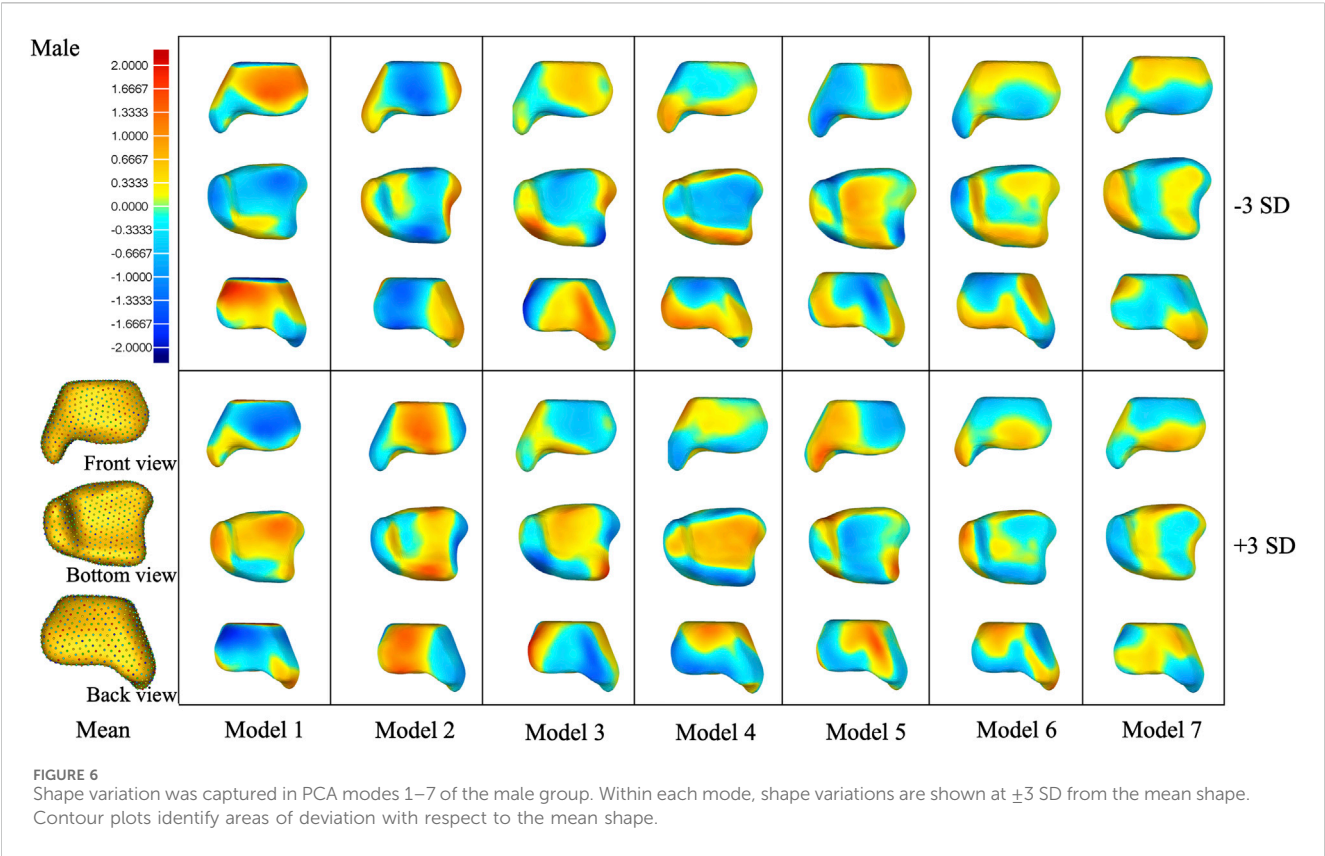
Shape deviations of mean shapes among the three groups are presented in Figure 7 and in Supplementary Table S3 of the

supplementary document. It was noted that the mean shape of the male tibia generally has a large size than the female tibia, especially around the medial malleolus, anterior part of the fibular notch, and posterior malleolus.

Curve variation in the resection surface of PCA modes 1–7 of the overall group

The first mode of variation showed a remarkable variation in size along the anterior–medial to posterior–lateral directions. The +3 SD model of the first mode generally has a bigger anterior–posterior and medial–lateral distance than the –3 SD model and is rotated clockwise (Figure 8; Table 1). However, the L-APs of +3 or –3 SD models of the first mode were smaller than





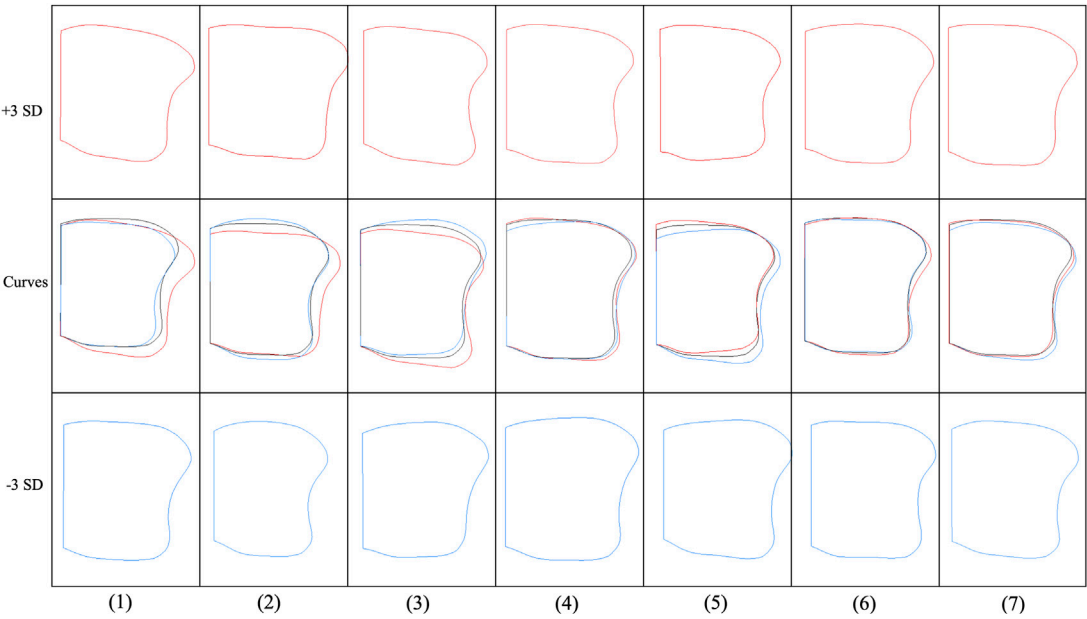


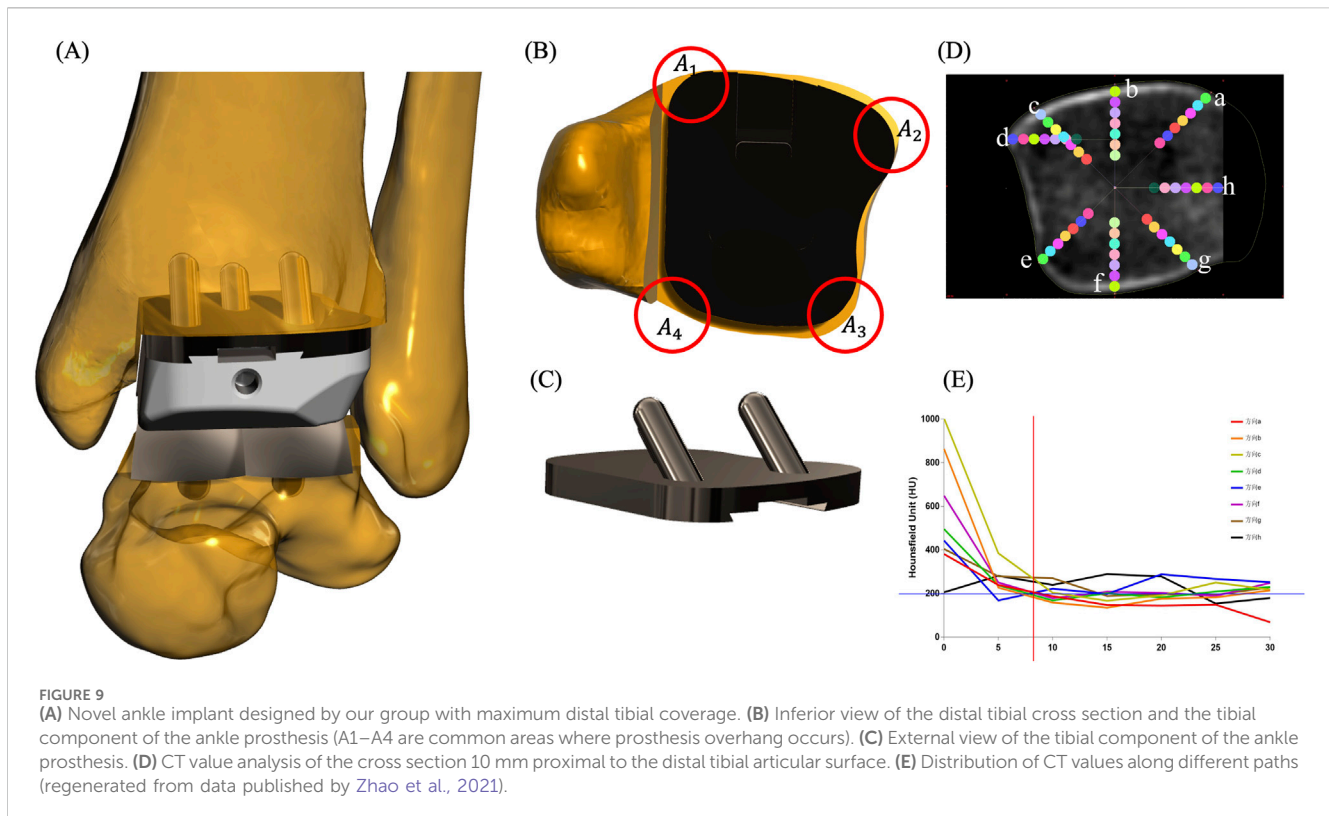
FIGURE 8
Curve variation in the resection surface of PCA modes 1–7 of the overall group. Within each mode, curve variations are shown at ± 3 SD from the mean shape (the red curves represent +3 SD models, the black curves represent mean models, and the blue curves represent –3 SD models).

TABLE 1 Geometric parameters of the 10-mm resection surface of the distal tibia.

Overall group	M-AP (mm)	C-AP (mm)	L-AP (mm)	A-ML (mm)	C-ML (mm)	P-ML (mm)
Mean	31.81	36.26	30.33	32.86	27.72	28.38
Mode 1+3SD	31.83	38.08	29.77	37.24	29.67	29.72
Mode 1–3SD	30.79	34.46	28.76	31.77	26.17	26.54
Mode 2+3SD	30.11	33.34	25.66	35.95	28.24	29.25
Mode 2–3SD	31.51	38.73	33.27	33.01	27.29	28.37
Mode 3+3SD	30.68	35.81	32.93	33.66	28.70	30.46
Mode 3–3SD	31.45	36.84	29.33	34.39	27.88	27.88
Mode 4+3SD	32.15	36.56	31.10	33.99	28.78	29.68
Mode 4–3SD	30.1	35.88	29.77	33.83	28.84	29.16
Mode 5+3SD	33.22	35.98	28.64	32.67	27.89	28.41
Mode 5–3SD	29.14	35.97	32.26	34.29	28.8	29.46
Mode 6+3SD	31.15	36.77	30.06	34.23	28.02	28.09
Mode 6–3SD	31.76	35.44	30.74	32.64	27.99	28.94
Mode 7+3SD	32.17	36.31	28.28	33.46	27.63	27.68
Mode 7–3SD	30.92	36.34	20.66	34.14	28.43	28.99

those of the mean model, indicating that the variation models were reducing in anterior–posterior distance on the lateral side. Differences in the second mode of variation included a variation from the medial–lateral direction. The +3 SD model of the second mode was wider but thinner than the –3 SD model (the +3 SD model of the second mode has smaller M-AP, C-AP, and L-AP but larger A-ML, C-ML, and P-ML).

The third mode of variation showed an obvious variation at both the anterior and posterior corners of the fibular notch. The fourth mode of variation exhibited a small variation at the anterior–medial edge and the lateral side of the resection surface. The fifth mode of variation described a small variation in the tibia at the anterior–medial, anterior–lateral, and posterior–lateral edge. Small variations in sixth and seventh modes are located around the lateral edge of the resection surfaces.



Discussion

In this study, we developed SSMs of the distal tibia from CT images of 229 tibiae. Considerable variabilities were observed among these three groups and all principal modes of variation, highlighting the complexity of the 3D shape of the distal tibia, which cannot be clearly represented by two-dimensional (2D) radiographs or described using 2D measurements. The first seven principal component analysis modes accounted for approximately 24.9%–40% of the shape variation, totaling 71.5%–75.6%. Although 75.6% from first seven principal components may not fully explain the morphology of the distal tibia, seven modes of morphological variation are enough for implant design of the tibial component of the total ankle implant. Although ignorance of other principal components may result in the loss of some information, it may also prevent noise and the interpretation of random variation in the data. Future studies should further include the quantitative method, such as parallel analysis, to determine the significance of each mode.

Notably, the overall groups have a higher explained variance in the first PCA mode or the cumulative explained variance for the first seven PCA modes. It can be explained that the variances caused by the difference in the mean shape between males and females are much larger than the within-group variation, resulting in a significantly higher explained variance by the first PCA mode in the overall group. Gender differences revealed substantial size variation between the mean shape of male and female tibiae, especially in the medial malleolus and the anterior part of the fibular notch. Sex-specific implants with different shapes might play an important role in future implant designs. Chinese female

patients, in particular, frequently experience issues with undersized implant and mismatch, which requires further investigation on these anatomical data. Of course, future studies should further investigate the shape variance, following size normalization in all distal tibiae.

The tibial components of several new-generation total ankle implants have been anatomically designed to support three cortices (see Figures 9A–C for illustration) and reduce fibular impingement (Gross et al., 2018; Integra, 2017). Such a design is highly related to the morphological variability of the distal tibial resection surface. Our previous studies have shown that bone density in the distal tibia decreases rapidly within 5 mm of the bony edge (Zhao et al., 2021) (Figures 9D, E), and the weight-bearing area of the distal tibia is primarily located in the peripheral cortical bone (Yu et al., 2022). Therefore, the implant should ideally reach the distal tibial bony edge to obtain the maximum support. However, oversizing in localized regions would result in overhang, which could cause bone or soft tissue impingement, especially at the four corners (A1–A4 regions) of the tibial component (Figure 9B). At the anteromedial aspect of the prosthesis (A1 region), impingement of the tibialis anterior tendon and the extensor hallucis longus tendon may occur; at the anterolateral aspect (A2 region), impingement with the extensor digitorum longus tendon or the anterior border of the fibula may occur; at the posterolateral aspect (A3 region), impingement of the peroneus longus tendon, the peroneus brevis tendon, or the anterior border of the fibula may occur; at the posteromedial aspect (A4 region), impingement of the tibialis posterior tendon may occur. These issues can cause peri-ankle pain, limited range of motion, and even surgical failure requiring implant removal.

The resection surface analysis showed substantial variation among the modes of variation in the overall group at the 10-mm resection surface. Anterior–posterior and medial–lateral distances were main sources of variation. In addition, variation frequently existed at both the anterior and posterior corners of the fibular notch in the resection surface of the distal tibia. For the tibial components of off-the-shelf total ankle implants considering maximizing cortical coverage, excessive prominence in the A2–A3 region should be avoided to prevent the prosthesis edge from overhanging the bone due to anatomical variations.

The current study has several limitations. First, the current SSM only involves CT images of healthy young participants. Future work should expand the recruitment to include the elderly population with more image modalities, such as MRI to account for the joint cartilage of the tibia (Forney et al., 2011; Nott et al., 2021). In addition, a 10-mm resection level did not fit all total ankle implant systems. Future studies should include more resection levels. Finally, the interpretation of deviation results of principal modes of variation has inherent subjectivity. Thus, more quantitative measurements should be developed in future studies to better identify the shape variability of the tibia. We should measure all actual models to obtain the maximum and minimum values of non-size-related parameters including the aspect ratio, curvature of the articular surface, medial malleolus morphology, anterior malleolus morphology, posterior malleolus morphology, fibular notch morphology, and the orientation of the distal tibial articular surface. Such data can be used to verify the authenticity of different SD models and determine each mode of variation, capturing a specific percentage of the variation. More statistical tools such as linear discriminant analysis should be included for precise and direct shape comparison.

In conclusion, SSM is an effective method of finding mean shape and principal variability. Considerable variabilities were noticed among these three groups and all principal modes of variation. Size plays a crucial role in both inter- and intra-groups, and morphological differences vary across different sizes. The male tibia has a bigger medial malleolus, anterior part of the fibular notch, and posterior malleolus. In addition, in the 10-mm resection surface of the distal tibia, variation existed along the anterior–posterior and medial–lateral directions and at both the anterior and posterior corners of the fibular notch. Such information is crucial for the implant design of the tibial components for total ankle replacement.

Data availability statement

The original contributions presented in the study are included in the article/Supplementary Material; further inquiries can be directed to the corresponding authors.

Ethics statement

The studies involving humans were approved by the Ethics Committee of Huashan Hospital, Fudan University. The studies were conducted in accordance with the local legislation and institutional requirements. The participants provided their written informed consent to participate in this study.

Author contributions

JY: Conceptualization, Data curation, Methodology, Software, Validation, Writing–original draft, Writing–review and editing. CL: Investigation, Software, Visualization, Writing–review and editing. JL: Data curation, Software, Writing–original draft. SC: Data curation, Writing–review and editing. CZ: Software, Validation, Writing–review and editing. XM: Funding acquisition, Writing–review and editing. DZ: Conceptualization, Funding acquisition, Supervision, Writing–review and editing.

Funding

The authors declare that financial support was received for the research, authorship, and/or publication of this article. This study was funded by the National Natural Science Foundation of China (Grant Nos 82072388 and 82372363).

Acknowledgments

The authors would like to gratefully acknowledge the support from the National Natural Science Foundation of China (Grant Nos 82072388 and 82372363). They would also like to thank Yunchao Zhu (Ph.D. candidate of Fudan University) for helping us respond to the reviewers' comments.

Conflict of interest

The authors declare that the research was conducted in the absence of any commercial or financial relationships that could be construed as a potential conflict of interest.

Generative AI statement

The authors declare that no Generative AI was used in the creation of this manuscript.

Publisher's note

All claims expressed in this article are solely those of the authors and do not necessarily represent those of their affiliated organizations, or those of the publisher, the editors and the reviewers. Any product that may be evaluated in this article, or claim that may be made by its manufacturer, is not guaranteed or endorsed by the publisher.

Supplementary material

The Supplementary Material for this article can be found online at: <https://www.frontiersin.org/articles/10.3389/fbioe.2025.1504897/full#supplementary-material>

References

- Ataoglu, M. B., Tokgöz, M. A., Köktürk, A., Ergişi, Y., Hatipoğlu, M. Y., and Kanath, U. (2020). Radiologic evaluation of the effect of distal tibiofibular joint anatomy on arthroscopically proven ankle instability. *Foot Ankle Int.* 41 (2), 223–228. doi:10.1177/1071100719884555
- Audenaert, E. A., Pattyn, C., Steenackers, G., De Roeck, J., Vandermeulen, D., and Claes, P. (2019). Statistical shape modeling of skeletal anatomy for sex discrimination: their training size, sexual dimorphism, and asymmetry. *Front. Bioeng. Biotechnol.* 7, 302. doi:10.3389/fbioe.2019.00302
- Blom, R. P., Meijer, D. T., de Muinck Keizer, R. O., Stufkens, S. A. S., Sierevelt, I. N., Schepers, T., et al. (2019). Posterior malleolar fracture morphology determines outcome in rotational type ankle fractures. *Injury* 50 (7), 1392–1397. doi:10.1016/j.injury.2019.06.003
- Bredbenner, T. L., Eliason, T. D., Potter, R. S., Mason, R. L., Havill, L. M., and Nicoletta, D. P. (2010). Statistical shape modeling describes variation in tibia and femur surface geometry between Control and Incidence groups from the osteoarthritis initiative database. *J. Biomech.* 43 (9), 1780–1786. doi:10.1016/j.jbiomech.2010.02.015
- Cates, J., Elhajian, S., and Whitaker, R. (2017). “ShapeWorks: particle-based shape correspondence and visualization software,” in *Statistical shape and deformation analysis*. Editors G. Zheng, S. Li, and G. Székely (Academic Press), 257–298.
- Claassen, L., Luedtke, P., Yao, D., Ettinger, S., Daniilidis, K., Nowakowski, A. M., et al. (2019). Ankle morphometry based on computerized tomography. *Foot Ankle Surg.* 25 (5), 674–678. doi:10.1016/j.fas.2018.08.002
- Clough, T., Bodo, K., Majeed, H., Davenport, J., and Karski, M. (2019). Survivorship and long-term outcome of a consecutive series of 200 Scandinavian Total Ankle Replacement (STAR) implants. *Bone Jt. J.* 101-B (1), 47–54. doi:10.1302/0301-620X.101b1.bjj-2018-0801.r1
- Daniels, T. R., Younger, A. S. E., Penner, M., Wing, K., Dryden, P. J., Wong, H., et al. (2014). Intermediate-term results of total ankle replacement and ankle arthrodesis: a COFAS multicenter study. *J. Bone Jt. Surg. Am.* 96 (2), 135–142. doi:10.2106/jbjs.101597
- Forney, M., Subhas, N., Donley, B., and Winalski, C. S. (2011). MR imaging of the articular cartilage of the knee and ankle. *Magn. Reson. Imaging Clin. N. Am.* 19 (2), 379–405. doi:10.1016/j.mric.2011.02.005
- Gabrielli, A. S., Gale, T., Hogan, M., and Anderst, W. (2020). Bilateral symmetry, sex differences, and primary shape factors in ankle and hindfoot bone morphology. *Foot Ankle Orthop.* 5 (1), 2473011420908796. doi:10.1177/2473011420908796
- Gougoulas, N., Khanna, A., and Maffulli, N. (2010). How successful are current ankle replacements? a systematic review of the literature. *Clin. Orthop. Relat. Res.* 468 (1), 199–208. doi:10.1007/s11999-009-0987-3
- Gross, C. E., Palanca, A. A., and DeOrio, J. K. (2018). Design rationale for total ankle arthroplasty systems: an update. *J. Am. Acad. Orthop. Surg.* 26 (10), 353–359. doi:10.5435/jaaos-d-16-00715
- Heimann, T., and Meinzer, H. P. (2009). Statistical shape models for 3D medical image segmentation: a review. *Med. Image Anal.* 13 (4), 543–563. doi:10.1016/j.media.2009.05.004
- Hvid, I., Rasmussen, O., Jensen, N. C., and Nielsen, S. (1985). Trabecular bone strength profiles at the ankle joint. *Clin. Orthop. Relat. Res.* 199, 306–12.
- Integra. (2017). *Cadence total ankle system surgical technique*.
- Kuo, C. C., Lu, H. L., Lu, T. W., Leardini, A., Kuo, M. Y., and Hsu, H. C. (2016). Validity and reliability of ankle morphological measurements on computerized tomography-synthesized planar radiographs. *Biomed. Eng. Online.* 15 92. doi:10.1186/s12938-016-0215-9
- Lee, G.-W., Wang, S.-H., and Lee, K.-B. (2018). Comparison of intermediate to long-term outcomes of total ankle arthroplasty in ankles with preoperative varus, valgus, and neutral alignment. *J. bone Jt. Surg. Am.* 100 (10), 835–842. doi:10.2106/jbjs.17.00703
- Lenz, A. L., Krahenbuhl, N., Peterson, A. C., Lisonbee, R. J., Hintermann, B., Saltzman, C. L., et al. (2021). Statistical shape modeling of the talocrural joint using a hybrid multi-articulation joint approach. *Sci. Rep.* 11 (1), 7314. doi:10.1038/s41598-021-86567-7
- Mäkelä, K. T., Matilainen, M., Pulkkinen, P., Fenstad, A. M., Havelin, L., Engesaeter, L., et al. (2014). Failure rate of cemented and uncemented total hip replacements: register study of combined Nordic database of four nations. *BMJ Br. Med. J.* 348, f7592. doi:10.1136/bmj.f7592
- Mitchell, P. M., Harms, K. A., Lee, A. K., and Collinge, C. A. (2019). Morphology of the posterior malleolar fracture associated with a spiral distal tibia fracture. *J. Orthop. Trauma* 33 (4), 185–188. doi:10.1097/bot.0000000000001398
- Nelson, A. E., Golightly, Y. M., Lateef, S., Renner, J. B., Jordan, J. M., Aspden, R. M., et al. (2017). Cross-sectional associations between variations in ankle shape by statistical shape modeling, injury history, and race: the Johnston County Osteoarthritis Project. *J. Foot Ankle Res.* 10, 34. doi:10.1186/s13047-017-0216-3
- Nguyen, C. V., Greene, J. D., Cooperman, D. R., and Liu, R. W. (2020). An anatomic and radiographic study of the distal tibial epiphysis. *J. Pediatr. Orthop.* 40 (1), 23–28. doi:10.1097/bpo.0000000000001088
- Nott, E., Matheny, L. M., Clanton, T. O., Lockard, C., Douglass, B. W., Tanghe, K. K., et al. (2021). Accessibility and thickness of medial and lateral talar body cartilage for treatment of ankle and foot osteochondral lesions. *Foot Ankle Int.* 42 (10), 1330–1339. doi:10.1177/10711007211015189
- Peiffer, M., Burssens, A., Duquesne, K., Last, M., De Mits, S., Victor, J., et al. (2022). Personalised statistical modelling of soft tissue structures in the ankle. *Comput. Methods Programs Biomed.* 218, 106701. doi:10.1016/j.cmpb.2022.106701
- Raikin, S. M., Rasouli, M. R., Espandar, R., and Maltenfort, M. G. (2014). Trends in treatment of advanced ankle arthropathy by total ankle replacement or ankle fusion. *Foot Ankle Int.* 35 (3), 216–224. doi:10.1177/1071100713517101
- Victor, J., Ghijssels, S., Tajdar, F., Van Damme, G., Deprez, P., Arnout, N., et al. (2014). Total knee arthroplasty at 15–17 years: does implant design affect outcome? *Int. Orthop.* 38 (2), 235–241. doi:10.1007/s00264-013-2231-8
- Wang, S., Yu, J., Lyu, J., Zhao, D., Zhang, C., Huang, J., et al. (2023). Statistical shape modeling of mean shape and principal variability of the human talar bone in the Chinese population. *J. Orthop. Surg. Hong Kong* 31 (3), 10225536231206534. doi:10.1177/10225536231206534
- Yu, J., Cao, S., Wang, C., Zhao, D., Wang, S., Zhang, C., et al. (2023). *In vivo* evaluation of the position and orientation of the geometric Axis of the tibiotalar joint. *Appl. Bionics Biomech.* 2023, 1–7. doi:10.1155/2023/2763099
- Yu, J., Zhang, C., Chen, W. M., Zhao, D., Chu, P., Wang, S., et al. (2020). Finite-element analysis of the influence of tibial implant fixation design of total ankle replacement on bone-implant interfacial biomechanical performance. *J. Orthop. Surg. Hong Kong* 28 (3), 2309499020966125. doi:10.1177/2309499020966125
- Yu, J., Zhao, D., Wang, S., Chu, P., Zhang, C., Huang, J., et al. (2022). Finite element analysis of the biomechanical effect of bone resection depth in the distal tibia after total ankle replacement. *J. Med. Biol. Eng.* 42 (4), 422–428. doi:10.1007/s40846-022-00722-7
- Zhao, D., Zhang, G., Huang, D., Yu, J., Wang, K., Wang, X., et al. (2021). Investigation on the contour and bone mineral density of the distal tibial cutting surface used for total ankle arthroplasty. *J. Orthop. Surg. Hong Kong* 29 (2), 23094990211028048. doi:10.1177/23094990211028048

Frontiers in Bioengineering and Biotechnology

Accelerates the development of therapies,
devices, and technologies to improve our lives

A multidisciplinary journal that accelerates the
development of biological therapies, devices,
processes and technologies to improve our lives
by bridging the gap between discoveries and their
application.

Discover the latest Research Topics

[See more →](#)

Frontiers

Avenue du Tribunal-Fédéral 34
1005 Lausanne, Switzerland
frontiersin.org

Contact us

+41 (0)21 510 17 00
frontiersin.org/about/contact



Frontiers in
Bioengineering
and Biotechnology

